UNIVERSITAT DE BARCELONA

A hotspot for posttranslational modifications on the androgen receptor dimer interface drives pathology and anti-androgen resistance

Andrea Alegre Martí

ADVERTIMENT. La consulta d'aquesta tesi queda condicionada a l'acceptació de les següents condicions d'ús: La difusió d'aquesta tesi per mitjà del servei TDX (**www.tdx.cat**) i a través del Dipòsit Digital de la UB (**diposit.ub.edu**) ha estat autoritzada pels titulars dels drets de propietat intel·lectual únicament per a usos privats emmarcats en activitats d'investigació i docència. No s'autoritza la seva reproducció amb finalitats de lucre ni la seva difusió i posada a disposició des d'un lloc aliè al servei TDX ni al Dipòsit Digital de la UB. No s'autoritza la presentació del seu contingut en una finestra o marc aliè a TDX o al Dipòsit Digital de la UB (framing). Aquesta reserva de drets afecta tant al resum de presentació de la tesi com als seus continguts. En la utilització o cita de parts de la tesi és obligat indicar el nom de la persona autora.

ADVERTENCIA. La consulta de esta tesis queda condicionada a la aceptación de las siguientes condiciones de uso: La difusión de esta tesis por medio del servicio TDR (**www.tdx.cat**) y a través del Repositorio Digital de la UB (**diposit.ub.edu**) ha sido autorizada por los titulares de los derechos de propiedad intelectual únicamente para usos privados enmarcados en actividades de investigación y docencia. No se autoriza su reproducción con finalidades de lucro ni su difusión y puesta a disposición desde un sitio ajeno al servicio TDR o al Repositorio Digital de la UB. No se autoriza la presentación de su contenido en una ventana o marco ajeno a TDR o al Repositorio Digital de la UB (framing). Esta reserva de derechos afecta tanto al resumen de presentación de la tesis como a sus contenidos. En la utilización o cita de partes de la tesis es obligado indicar el nombre de la persona autora.

WARNING. On having consulted this thesis you're accepting the following use conditions: Spreading this thesis by the TDX (**www.tdx.cat**) service and by the UB Digital Repository (**diposit.ub.edu**) has been authorized by the titular of the intellectual property rights only for private uses placed in investigation and teaching activities. Reproduction with lucrative aims is not authorized nor its spreading and availability from a site foreign to the TDX service or to the UB Digital Repository. Introducing its content in a window or frame foreign to the TDX service or to the UB Digital Repository is not authorized (framing). Those rights affect to the presentation summary of the thesis as well as to its contents. In the using or citation of parts of the thesis it's obliged to indicate the name of the author.

UNIVERSITAT DE BARCELONA

Facultat de Farmàcia i Ciències de l'Alimentació

A hotspot for posttranslational modifications on the androgen receptor dimer interface drives pathology and anti-androgen resistance

Andrea Alegre Martí

2023

UNIVERSITAT DE BARCELONA

FACULTAT DE FARMÀCIA I CIÈNCIES DE L'ALIMENTACIÓ

Ph.D. PROGRAMME IN BIOTECHNOLOGY 2020 – 2023

A hotspot for posttranslational modifications on the androgen receptor dimer interface drives pathology and anti-androgen resistance

Memòria presentada per Andrea Alegre Martí
per optar al títol de doctora per la Universitat de Barcelona

Prof. Eva Estébanez Perpiñá	Prof. Pablo Fuentes Prior	Andrea Alegre Martí
Tutora i directora de la tesi	Co-director de la tesi	Doctoranda de la tesi

Barcelona, 2023

X-ray crystallography is a wonderful adventure in which you must be perseverant and patient to find the treasure hidden in protein crystals.

It is a journey to the universe of molecules where beauty is found in every detail and the secret of life is hidden in every atom.

Ada Yonath

Acknowledgements

The experience of pursuing this doctoral thesis has allowed me to fulfil my largest professional goal so far: investigating intro the molecular mechanisms behind the emergence of extremely complex diseases, such as cancer, and doing so by delving into some of the atomic roots of the problems. My thesis advisors, Prof. Eva Estébanez-Perpiñá and Prof. Pablo Fuentes-Prior, share this same Science philosophy with me. Before the functional consequences that we can observe by altering the conditions of cells and animals commonly used in biomedical research, from which we can draw valuable conclusions, we firmly believe that the root cause of a certain disease may lie in something much more concrete but incredible difficult sometimes to envision: the structure of proteins, which are one of the major key players in all cellular functions. Eva and Pablo have helped me to explore the complex world of elucidating the structure of macromolecules, especially proteins. With the foundation they have provided me, I hope to continue fulfilling the objective that motivated me to enter the field of Structural Biology.

Thank you very much, Eva, for always seeking the best opportunities to make the early years of my professional career as thorough as possible. I am proud of the curriculum I have achieved after my time in your laboratory. Although you always would say that the merit is mine, it is you who have provided me with the required resources and opportunities to achieve it. Thank you for being there day and night, literally, to guide me during the development and completion of my project and to nurture my mind by discussing countless issues, of note those related to the world outside and inside of Science, which may seem to have little to do with it but that in fact are related to the constant struggle we face as women in Science. Your perspective has always been encouragingly optimistic and motivating. These characteristics define you, and I expect they will also define me from now on!

Thank you so much, Pablo, for instilling in me the rigor that we should analyse our structural data, as well as those from others and any other type of experiment. I am constantly amazed by your exceptional ability to work in the field of Biomedical Sciences, coming from a background in Physics and Mathematics. I aspire to be a Renaissance scientist just like you, to possess the mental capacity to master so many and so different areas of Science as you have demonstrated, while also retaining the cultural knowledge you have tried to impart to Alba and me. Breaking the seriousness and certainty of our result analyses by challenging us to see if we knew about Mayarí, Blondie, or "The Good, the Bad and the Ugly" has been the most enjoyable way to make our research more engaging without ceasing to stimulate our minds.

Although they have not been officially my thesis advisors, Dr. Álvaro Aytés and Prof. Annabel F. Valledor have welcomed me into their laboratories during a significant time of my Ph.D. journey. They have taught me the importance of collaborating and of combining expertise to unleash the full potential of a project to be excellent. With them, I have learned that the "win-win" philosophy is the best formula for achieving significant goals. In fact, I have had the privilege of collaborating with many different groups and being part of a great multidisciplinary team that has made my thesis, in my humble opinion, very complete. Therefore, I would like to express special gratitude to all the researchers with whom we have collaborated to complete the projects presented in this thesis: Dr. Rana El Bizri and Dr. Lidia Franco (from Dr. Aytés group, IDIBELL), and Dr. Josep Maria Piulats (ICO-IDIBELL); Dr. Joan Font-Diaz (from Prof. Valledor group), Prof. Carme Caelles, M. Nuria Peralta-Moreno and Prof. Jaime Rubio-Martínez (UB); Dr. Rosa Antón (IIB-Sant Pau); Dr. Juan Fernández-Recio (ICVV); Dr. Ana M. Rojas (CABD-CSIC), Dr. Ulrich Eckhard and Dr. Marta Nadal (IBMB-CSIC), Dr. Lisa Sevilla and Dr. Paloma Pérez (IBV-CSIC); Dr. Coralie Poulard and Dr. Muriel Le Romancer (CRCL, France); Prof. Gordon Hager and his group (NCI-NIH, USA); Dr. Ana Paredes and Dr. Mercedes Ricote (CNIC); Dr. Marta Taulès (CCiTUB); Dr. Marta Vilaseca and Dr. Marina Gay (IRB core services); Dr. Eugenia Ruiz and Dr. Jaume Mercadé (GAT Therapeutics S.L.); and the team of the Xaloc Beamline at the ALBA-CELLS synchrotron. Thank you very much also to Prof. Josefa Badia (UB), coordinator of the doctoral program, who has helped me tremendously in all the bureaucratic processes during these last years.

However, without my incredible lab colleagues, it would not have been possible to achieve my dream of working in Biomedical research either. They have taught me all the experimental techniques, and together we have deciphered a jigsaw piece of the molecular mechanisms that lead to the development of diseases. I am grateful to Montserrat Abella, our lab technician, who has become much more than a lab mate, for teaching me protein expression, purification, and crystallization techniques. Thank you, Montse, for inspiring me with the precision, accuracy, rigor, and organization that characterise your work. We have had countless conversations about life that provided me with invaluable advice and to help me grow as a person. You are a great role model to follow.

My colleagues and now fellow doctors, Alba Jiménez-Panizo and Adrián Martínez-Tébar, have been the most understanding and constant support I could have wished for. Alba and Adri, we have not only gone through the same learning process together and shared countless hours of

work, but also have you proven to be invaluable friends that I hope to maintain for life, even though we may be working in different places from now on. I have enjoyed working with both of you tremendously; I believe we make a fantastic team. You are already admirable scientists, and you still have a fruitful path ahead of you. In an ideal world, I would choose to work with you in the same group for a lifetime, without a doubt.

Indiscutiblemente, junto con Alba y Adri, mi familia ha sido un gran pilar durante este proceso y, por supuesto, durante mi vida. Todos ellos han celebrado tanto o incluso más que yo todos los logros conseguidos hasta ahora, y han disfrutado viéndome avanzar y apoyándome en cada decisión que he tomado. Mis padres, Marga y Ciriaco, mi hermana Carla, mi abuela Andrea, mi pareja Rafa, el resto de mi familia, y mi gatita Nami, que llegó a la familia para darme el empujón final que necesitaba durante el último año de mi tesis. Rafa, siempre has estado a mi lado durante este trayecto, desde que empecé la carrera hasta el depósito de mi tesis, y has sabido darme el espacio que necesitaba para abordar todo el trabajo que me ha supuesto este logro sin alejarte de mí, ayudándome de todas las formas que has sabido, haciéndome reír, solucionado todos y cada uno de los problemas informáticos que este mundo de la Biología Estructural me deparaba, y creciendo junto a mí como persona. Carla, durante nuestra infancia y juventud, he aprendido contigo a ser una persona responsable, organizada y cuidadosa, y como mi hermana pequeña me lo has puesto super fácil gracias a tu increíble personalidad. Estas virtudes que he adquirido contigo me han servido enormemente durante esta travesía. Abuela, cada día des de que entré en la universidad te has asegurado de que llegara sana y salva a casa, dado que te preocupa enormemente el mundo que nos rodea hoy en día a todos, pero en especial a las mujeres. El informe diario vía telefónica sobre mi posición precisa en todo momento una vez he salido del laboratorio y hasta que he llegado a casa, me ha mantenido con los pies sobre la tierra, recordándome que ante todo lo más importante es mi salud, cosa que he olvidado en varias ocasiones por estar demasiado enfrascada en mi trabajo. Por último, muchas gracias mama y papa por brindarme absolutamente todo lo que habéis podido para hacer posible que cumpliera este gran sueño, porque gracias a vosotros todo esto empezó con las vacaciones tan divertidas que habéis organizado cada año para Carla y para mí, llenas de naturaleza y actividades que sin vosotros quizás no habría probado nunca. En especial, todo este proyecto empezó con nuestras vacaciones en Almería, donde hicimos submarinismo por primera vez, donde por fin descubrí lo maravillosa que es la naturaleza y donde decidí qué quería ser de mayor: “científica de los seres vivos”.

Abstract

Nuclear receptors (NRs) are a superfamily of ligand-activated transcription factors that function as biological sensors to regulate gene expression in a time- and tissue-specific and manner. The coordinated actions of NRs affect the proliferation, differentiation, and apoptosis of different cell types. This thesis unravels new structural and functional information regarding the implications for human pathophysiology of two evolutionary highly related members of this superfamily that are regulated by steroid hormones, the androgen (AR) and glucocorticoid (GR) receptors.

The AR directs male development, phenotype maintenance and adult physiology and reproduction. AR mutations associated with prostate cancer and androgen insensitivity syndromes may profoundly influence its structure, protein interaction network, and binding to chromatin, resulting in altered transcription signatures and drug responses. Current structural information fails to explain the effect of pathological mutations on AR structure–function relationship. In this thesis dissertation, we have thoroughly studied the effects of five selected mutations that span the complete dimer interface of AR ligand–binding domain (AR-LBD) using X-ray crystallography in combination with *in vitro*, *in silico*, and cell-based assays. These variants alter AR-dependent transcription and responses to anti-androgens by inducing a previously undescribed allosteric switch in the AR-LBD that increases exposure of a major methylation target, Arg^{761}. We also corroborate the relevance of residues Arg^{761} and Tyr^{764} for AR dimerization and function. Together, our results reveal allosteric coupling of AR dimerization and posttranslational modifications as a disease mechanism with relevant implications for precision medicine.

The GR is a ubiquitously expressed protein that controls metabolic and homeostatic processes essential for life. Although numerous crystal structures of the GR ligand-binding domain (GR-LBD) have been previously reported, the functional, (patho)-physiologically relevant oligomeric state of the full-length receptor (FL-GR) remains disputed. We have recently presented a catalogue of 20 different dimeric arrangements of the GR-LBD, including both transcriptionally active and self-repressed, antagonistic bound GR-LBD homodimers, with important implications for FL-GR multimerization in living cells. In this thesis, we go further and present evidence of the heterodimerization of AR and GR, a complex that has been hypothesized to have important implications in the pathophysiology of castration-resistant prostate cancer.

Abstract (català)

Els receptors nuclears (NR) són una superfamília de factors de transcripció activats per lligands que funcionen com a sensors biològics per regular l'expressió gènica de manera específica en temps i teixit. Les accions coordinades dels NR afecten la proliferació, diferenciació i apoptosi de diferents tipus cel·lulars. Aquesta tesi aporta nova informació estructural i funcional sobre les implicacions en la fisiopatologia humana de dos receptors d'aquesta superfamília, estretament relacionats evolutivament, que estan regulats per hormones esteroides, els d'andrògens (AR) i els de glucocorticoides (GR).

L'AR dirigeix el desenvolupament i manteniment del fenotip masculí, així com la fisiologia i la reproducció en l'adultesa. Les mutacions a l'AR associades al càncer de pròstata i a la síndrome d'insensibilitat als andrògens poden afectar la seva estructura, xarxa d'interacció de proteïnes i unió a la cromatina, resultant en l'alteració del patró de transcripció de l'AR i de la resposta cel·lular a fàrmacs. La informació estructural actual no explica l'efecte de les mutacions patològiques en l'estructura-funció de l'AR. En aquesta tesi, hem estudiat a fons els efectes de cinc mutacions de la interfície de dimerització del domini d'unió a lligand de l'AR (AR-LBD) utilitzant cristal·lografia de raigs X en combinació amb assajos *in vitro*, *in silico* i en cèl·lules. Aquestes variants alteren la transcripció dependent d'AR i la resposta als anti-andrògens mitjançant un canvi al·lostèric prèviament desconegut en l'AR-LBD que augmenta l'exposició d'un important lloc de metilació, la Arg^{761}. També corroborem la rellevància dels residus Arg^{761} i Tyr^{764} per a la dimerització i funció de l'AR. En conjunt, els nostres resultats mostren la comunicació al·lostèrica entre dimerització i modificació post-traduccional de l'AR com a mecanisme patogènic amb implicacions rellevants pels fàrmacs de precisió.

El GR és una proteïna expressada de manera ubiqua que controla processos metabòlics i homeostàtics essencials per la vida. Tot i que s'han reportat nombroses estructures cristal·logràfiques del GR-LBD, l'estat oligomèric funcional i fisiològicament rellevant del receptor complert (FL-GR) segueix sent objecte de disputa. Recentment hem presentat un catàleg de 20 disposicions dimèriques diferents del GR-LBD, incloent tant aquelles transcripcionalment actives com auto-reprimides, amb implicacions importants per la oligomerització de FL-GR en cèl·lules vives. En aquesta tesi, anem més enllà i presentem evidència de la heterodimerització de l'AR i el GR, un complex que es proposa que té importants efectes en la fisiopatologia del càncer de pròstata resistent a la castració.

Table of contents

ACKNOWLEDGEMENTS I
ABSTRACT IV
ABSTRACT (CATALÀ) V
TABLE OF CONTENTS VI
INDEX OF FIGURES AND TABLES X
LIST OF ABBREVIATIONS XII
INTRODUCTION 1
1. General insights into the nuclear receptor superfamily 1
Fig. 1. Phylogenetic distribution of nuclear receptors subfamilies and their cognate ligands. *2*
Fig. 2. Schematic representation of nuclear receptor oligomerization modes. *3*
Fig. 3. Classification of nuclear receptors. *5*
2. Steroid receptors oligomerization regulates their functions 5
2.1. Building blocks: domain organization and structure 5
Fig. 4. Domain organization of oxosteroid receptors compared to the related estrogen receptor. *6*
Fig. 5. Cartoons depicting the structure of steroid receptors DNA- and ligand-binding domains. *8*
2.2. Quaternary assemblies of nuclear receptors regulate transcription 9
Fig. 6. Oligomerization modes of DNA-binding domains of nuclear receptors. *10*
Fig. 7. Canonical versus non-canonical dimerization modes of steroid receptors. *12*
Fig. 8. Three-dimensional structures of multidomain steroid receptors. *13*
3. Human physiology of the androgen and glucocorticoid receptors 14
3.1. Androgens and glucocorticoids synthesis and signalling pathways 14
Fig. 9. Steroids release through the hypothalamic-pituitary-adrenal and -gonadal axes. *15*
Fig. 10. Life cycle of the glucocorticoid receptor and DNA binding models. *17*
3.2. Allosteric regulation of androgen and glucocorticoid receptors 18
Fig. 11. Allosteric remodelling of the ligand binding domain upon ligand binding. *19*
Fig. 12. Sequence alignment of androgen and glucocorticoid receptors highlighting post-translational modifications sites. *20*
4. The androgen and glucocorticoid receptors in human disease 23
4.1. Glucocorticoid receptor-associated pathologies 23
4.2. Androgen receptor-related diseases 24
Fig. 13. Pathogenic mutations on the ligand binding domain of androgen and glucocorticoid receptors. *25*
4.3. Glucocorticoid receptor in castration resistant prostate cancer 26
OBJECTIVES 28
Fig. 14. Chronogram of completed objectives during the current Ph.D. thesis. *29*

MATERIALS AND METHODS 31
1. *In vivo* cell-based assays 31
1.1. Cell lines and plasmids 31
1.2. Luciferase reporter assay 31
1.3. Cell proliferation 32
1.4. Cell viability 33
1.5. Immunoprecipitation 33
1.6. Transcriptomic analysis 34
1.7. Enrichment analysis 35
1.8. Real time qPCR 36
1.9. Proximity ligation assay 37
2. Biochemical and biophysical experiments 38
2.1. Cloning and mutagenesis 38
2.2. Recombinant proteins expression and purification 38
2.3. Differential scanning fluorimetry 40
2.4. Limited proteolysis 41
2.5. Crystallization and structure determination 41
2.6. Mass spectrometry analysis of protein dimerization in solution 41
2.7. Surface plasmon resonance (Biacore) 43
Fig. 15. Schematic representation of surface plasmon resonance experiments 44
3. *In silico* computational analyses 44
3.1. Docking experiments and dimeric interface analysis 44
3.2. Estimated energetic impact of AR point mutations 45
3.3. Statistical coupling analysis 46
3.4. Molecular dynamic simulations 46
RESULTS 48
1. Mutants of the androgen receptor dimer interface impact its functionality 48
1.1. Mutations affect cell proliferation and response to anti-androgens 48
Fig. 16. Mutations impact androgen receptor transactivation activity and cellular phenotypes. 49
Fig. 17. Mutations confer different cellular response to antiandrogens. 50
1.2. Deregulation of androgen-targeted transcription programs upon mutation 51
Fig. 18. The transcriptional profiles of AR mutants differ from that of the wild-type receptor (I). 52
Fig. 19. The transcriptional profiles of AR mutants differ from that of the wild-type receptor (II). 53

2. Mutational impact on the androgen receptor ligand binding domain (AR-LBD) 54
2.1. Mutations do not compromise AR-LBD folding but lead to a reduced stability 54
Fig. 20. In solution and in silico characterization of AR-LBD dimer interface mutants. *55*
Fig. 21. AR-LBD dimer interface mutations alter sensitivity to proteolysis of the domain. *56*
2.2. Mutants show structural rearrangements in key areas of the AR-LBD 57
Table 1. X-ray crystallography data collection, refinement statistics and model quality. *59*
Fig. 22. AR-LBD dimer interface mutants induce local and distant structural changes. *60*
Fig. 23. AR-LBD dimer interface mutants display local flexibility differences. *62*
Fig. 24. Molecular dynamics of wild type and mutant structures demonstrate local changes in flexibility. *64*
Fig. 25. Mutations induce conformational changes in specific regions of the AR-LBD. *65*
3. Towards the identification of a mechanism underlying mutations pathogenicity 66
3.1. Non-canonical dimerization of the AR-LBD is conserved upon mutations 66
Fig. 26. Dimer interface mutants do not impair homodimer formation. *66*
3.2. The recurrent Tyr764Cys point mutation highlights the ability of AR-LBD dimer interface to adopt different relative orientations 68
Fig. 27. Mutant Y764C enhances homodimerization with a symmetric Cys-Cys' covalent bound. *69*
Table 2. Summary of Cys-Cys' covalently linked peptides in the Y764C LBD dimer identified by MS/MS. *70*
Table 3. Summary of BMB-crosslinked peptides in the Y764C LBD dimer identified by MS/MS. *70*
3.3. The Arg761 zone undergoes large conformational rearrangements 71
Fig. 28. The Arg761-zone conformation is differentially rearranged by AR-LBD mutants. *72*
3.4. AR-LBD dimer interface mutations affect *in vivo* methylation of Arg761 73
Fig. 29. Arg761 and Ser792 are more solvent exposed in AR-LBD dimer interface mutants. *74*
Fig. 30. Androgen receptor is preferentially monomethylated in living cells by the PRMT5. ..... *76*
Fig. 31. Model of the interaction between androgen receptor and PRMT5·MEP50 methylosome complex. *78*
4. Characterization of androgen and glucocorticoid receptors heterodimerization 78
Fig. 32. Purification of recombinant androgen and glucocorticoid receptor core modules. *80*
Fig. 33. Immobilised androgen and glucocorticoid receptor cores interact with their cognate hormone response elements in solution. *81*
Fig. 34. Androgen and glucocorticoid receptors form both homo- and heterodimers in solution. *82*
Fig. 35. The homodimerization interface of the AR-LBD could also play a role for its heterodimerization with the glucocorticoid receptor. *84*
DISCUSSION 85
Fig. 36. Cascade of post-translational modifications affecting the AR-LBD. *89*
CONCLUSIONS 92
REFERENCES 94

SUPPLEMENTARY MATERIALS 114
1. Supplementary figures 114
Fig. S1. The cellular phenotypes and the transcriptional profiles of AR mutants differ from that of the wild-type receptor. *115*
Fig. S2. Supraphysiological dihydrotestosterone concentrations suppress cell growth of AR-responsive cell lines. *116*
Fig. S3. In silico characterization of AR-LBD dimer interface mutants. *118*
Fig. S4. AR-LBD interface mutants are predicted to dimerize essentially as non-canonical wild type AR-LBD. *120*
Fig. S5. Dynamics of R761-zone large conformational reorientations. *122*
2. Supplementary tables 124
Table S1. Reported mutations in the major functional areas of the AR-LBD. *125*
Table S2. Summary of clinical and biological information on AR-LBD dimer interface mutants. *127*
3. Publications 129
3.1. A hotspot for posttranslational modifications on the androgen receptor dimer interface drives pathology and anti-androgen resistance 129
3.2. The multivalency of the glucocorticoid receptor ligand-binding domain explains its manifold physiological activities 191
3.3. γ-Linolenic acid in maternal milk drives cardiac metabolic maturation 243
3.4. The mineralocorticoid receptor modulates timing and location of genomic binding by glucocorticoid receptor in response to synthetic glucocorticoids in keratinocytes 273
3.5. Glucocorticoid resistance: Interference between the glucocorticoid receptor and the MAPK signalling pathways 294
APPENDIX 317
1. Manuscripts in preparation 317
2. Conferences 317
2.1. Oral presentations 317
2.2. Poster presentation 318
2.3. Congress attendance 319
3. Courses / Workshops 320
4. Short stays at collaborator laboratories 320
5. Participation in funded research projects 321
6. Other merits 321

Index of figures and tables

Fig. 1. Phylogenetic distribution of nuclear receptors subfamilies and their ligands. 2

Fig. 2. Schematic representation of nuclear receptor oligomerization modes. 3

Fig. 3. Functional classification of nuclear receptors. 5

Fig. 4. Domain organization of oxosteroid receptors compared to the related estrogen receptor. 6

Fig. 5. Structure of steroid receptors DNA- and ligand-binding domains. 8

Fig. 6. Oligomerization modes of DNA-binding domains of nuclear receptors. 10

Fig. 7. Canonical versus non-canonical dimerization modes of steroid receptors. 12

Fig. 8. Three-dimensional structures of multidomain steroid receptors. 13

Fig. 9. Steroids release through the hypothalamic-pituitary-adrenal and -gonadal axes. 15

Fig. 10. Life cycle of the glucocorticoid receptor and DNA binding models. 17

Fig. 11. Allosteric remodelling of the ligand binding domain upon ligand binding. 19

Fig. 12. Sequence alignment of androgen and glucocorticoid receptors highlighting post-translational modifications sites. 20

Fig. 13. Pathogenic mutations on the ligand binding domain of androgen and glucocorticoid receptors. 25

Fig. 14. Chronogram of completed objectives during the current Ph.D. thesis. 29

Fig. 15. Schematic representation of surface plasmon resonance experiments. 44

Fig. 16. Mutations impact androgen receptor transactivation activity and cellular phenotypes. 49

Fig. 17. Mutations confer different cellular response to antiandrogens. 50

Fig. 18. The transcriptional profiles of AR mutants differ from that of the wild-type receptor (I). 52

Fig. 19. The transcriptional profiles of AR mutants differ from that of the wild-type receptor (II). 53

Fig. 20. In solution and *in silico* characterization of AR-LBD dimer interface mutants. 55

Fig. 21. AR-LBD dimer interface mutations alter sensitivity to proteolysis of the domain. 55

Table 1. X-ray crystallography data collection, refinement statistics and model quality. 58

Fig. 22. AR-LBD dimer interface mutants induce local and distant structural changes. 59

Fig. 23. AR-LBD dimer interface mutants display local flexibility differences. 60

Fig. 24. Molecular dynamics of wild type and mutant structures demonstrate local changes in flexibility. 63

Fig. 25. Mutations induce conformational changes in specific regions of the AR-LBD. 65

Fig. 26. Dimer interface mutants do not impair homodimer formation. 66

Fig. 27. Mutant Y764C enhances homodimerization with a symmetric Cys-Cys' covalent bound. 68

Table 2. Summary of Cys-Cys' covalently linked peptides in the Y764C LBD dimer identified by MS/MS. 69

Table 3. Summary of BMB-crosslinked peptides in the Y764C LBD dimer identified by MS/MS. 69

Fig. 28. The Arg761-zone conformation is differentially rearranged by AR-LBD mutants. 71

Fig. 29. Arg761 and Ser792 are more solvent exposed in AR-LBD dimer interface mutants. 73

Fig. 30. Androgen receptor is preferentially monomethylated in living cells by the PRMT5.....75

Fig. 31. Model of the interaction between androgen receptor and PRMT5·MEP50 methylosome complex...77

Fig. 32. Purification of recombinant androgen and glucocorticoid receptor core modules. 79

Fig. 33. Immobilised androgen and glucocorticoid receptor cores interact with their cognate hormone response elements in solution. 80

Fig. 34. Androgen and glucocorticoid receptors form both homo- and heterodimers in solution. 81

Fig. 35. The homodimerization interface of the AR-LBD could also play a role for its heterodimerization with the glucocorticoid receptor. 83

Fig. 36. Cascade of post-translational modifications affecting the AR-LBD. 88

Fig. S1. The cellular phenotypes and the transcriptional profiles of AR mutants differ from that of the WT receptor. 114

Fig. S2. Supraphysiological DHT concentrations suppress cell growth of AR-responsive cell lines. 115

Fig. S3. *In silico* characterization of AR-LBD dimer interface mutants. 117

Fig. S4. AR-LBD interface mutants are predicted to dimerize essentially as non-canonical WT AR-LBD. .119

Fig. S5. Dynamics of R761-zone large conformational reorientations. 121

Table S1. Reported mutations in the major functional areas of the AR-LBD. 124

Table S2. Summary of clinical and biological information on AR-LBD dimerization interface mutants. 126

Note: all figures are original content created specifically for this thesis or for the publications derived from it, unless otherwise specified.

List of abbreviations

AF	Activation function
AIS	Androgen insensitivity syndrome
AR	Androgen receptor
AREs	Androgen response elements
AT	After TEV protease treatment
BF-3	Binding function-3
BMB	1,4-bis(maleimido)butane
BMOE	Bis(maleimido)ethane
CAIS	Complete androgen insensitivity syndrome
CHIP	C-terminus of Hsp70 interacting protein
CNT	AR-null PC3 control cell line
CRPC	Castration-resistant prostate cancer
DBD	DNA binding domain
DEG	Differentially expressed genes
DEX	Dexamethasone
DHT	Dihydrotestosterone
DMSO	Dimethyl sulfoxide
DTT	Dithiothreitol
DU145	Human Caucasian prostate adenocarcinoma cell line (brain metastasis)
Cryo-EM	Cryogenic electron microscopy
E	Elution
ER	Estrogen receptor
ERG	Estrogen-responsive gene
FDR	False discovery rate
FL	Full-length

FT	Flow through
GCs	Glucocorticoids
GR	Glucocorticoid receptor
GRE	Glucocorticoid response element
GSEA	Gene set enrichment analysis
KEGG	Kyoto encyclopaedia of genes and genomes
K_D	Dissociation constant
HRE	Hormone response elements
IMAC	Immobilized metal affinity chromatography
LBD	Ligand binding domain
LBP	Ligand binding pocket
MAIS	Mild androgen insensitivity syndrome
MD	Molecular dynamics simulations
MMA	Monomethylated arginine
MR	Mineralocorticoid receptor
MSigDB	Molecular signature database
NIP	Normalized interface propensity
NTD	N-terminal domain
NRs	Nuclear receptors
PAIS	Partial androgen insensitivity syndrome
PC3	Human Caucasian prostate adenocarcinoma cell line (bone metastasis)
PCa	Prostate cancer
PCA	Principal component analysis
PDB	Protein data bank
PLA	Proximity ligation assay
PR	Progesterone receptor

PROGENy	Pathway responsive genes
RMSD	Root-mean-square deviation
RMSF	Root-mean-square fluctuation
RNA-seq	Ribonucleic acid sequencing
RNF6	Ring finger protein 6
RU	Resonance units
RXR	Retinoid x receptor
22Rv1	Human Caucasian prostate adenocarcinoma cell line
RWPE1	Human Caucasian normal epithelial cell line
SCS	Second coordination shell
SDMA	Symmetrically dimethylated arginine
SDS-PAGE	Sodium dodecyl-sulfate polyacrylamide gel electrophoresis
SPR	Surface plasmon resonance
SRs	Steroid receptors
SRC	Steroid receptor coactivator
TEV	*Tobacco etch* virus
Tm	Melting temperature
TMPRSS2	Transmembrane protease serine 2
vdW	Van der Waals
VST	Variance stabilizing transformation
W	Wash
WB	Western blotting
WT	Wild type

Introduction

1. General insights into the nuclear receptor superfamily

Nuclear Receptors (NRs) comprise a large superfamily of evolutionary related transcription factors that control pivotal biological processes by binding to specific DNA hormone response elements (HRE), which in turn triggers either activation or repression of cognate target genes. Most NRs are ligand-regulated, while some are regarded as orphan receptors because their endogenous ligands are still to be identified or agreed upon. Ligand binding induces conformational changes that eventually result in the recruitment of coregulators, the transcriptional and chromatin-remodelling complexes to key NR interacting surfaces (Schütz et al., 1995; Aranda and Pascual, 2001; Lonard and O'Malley, 2007; Bridgham et al., 2010; Huang et al., 2010; Weikum et al., 2018). Main NR ligands are cholesterol-derived hormones, retinoids, thyroid hormones, and vitamins, among others. NRs play important roles in virtually every aspect of human physiology, including development, reproduction, immune response, vascular and cardiac function, tissue growth, toxin clearance, and carbohydrate and lipid metabolism (Schütz et al., 1995; Sonoda et al., 2008). Since NRs are involved in such core physiological processes, their dysregulated actions and altered signalling pathways are linked to major human diseases such as cancer, metabolic syndrome, and chronic inflammation, to name a few. Therefore, NRs are major pharmaceutical targets driving billion dollar markets (Huang et al., 2010; Xu, 2015): one in six FDA-approved drugs target a NR (Santos et al., 2017; Nemetchek et al., 2022).

Phylogenetic analyses of NR sequences from about 40 broadly sampled animal phyla revealed shared conserved domains between all NRs (Bridgham et al., 2010). These analyses showed that both ligand-independent and ligand-dependent receptors are scattered across the evolutionary tree and that there is no relationship between the evolutionary origin of a receptor and the chemical nature of its ligand (Gronemeyer et al., 2004). Hence, it has been proposed that NRs have evolved from a ligand-independent ancestral orphan receptor, acquiring ligand binding capability and specificity afterwards (Escriva et al., 1997). This hypothesis is supported by (1) the absence of orthologs of classically liganded endocrine receptors outside the vertebrate subphylum, suggesting a late appearance of liganded receptors during evolution (Markov and Laudet, 2011); (2) NRs regulation through conformational changes in a ligand-independent manner, for example by post-translational modifications (PTMs) (Rochette-Egly, 2003; Markov

and Laudet, 2011); and (3) the unrelated synthesis pathways of the different NR ligands. However, current evidence shows that NRs are promiscuous, being able to bind some ligands with high affinity (in the nanomolar range) while other chemically unrelated compounds are bound with lower (micromolar) affinity, which may be important for NR cross-talk (Fig. 1) (Markov and Laudet, 2011). Furthermore, although it is true that PTMs may trigger conformational changes, the orphan ancestral hypothesis implies that complex functions such as the allosteric regulation of NRs upon ligand binding, evolved de novo several independent times among the different subfamilies, which seems unlikely. Instead, sensitivity to different ligands may have evolved thanks to subtle modifications of the ancestral ligand-binding pocket (LBP), while ligand-independent activation may have appeared repeatedly as a consequence of mutations that stabilized the active conformation in the absence of ligand, as it occurs in some pathological conditions (Bridgham et al., 2010; Markov and Laudet, 2011). For all these reasons, it cannot be discarded that the ancestral NR was a ligand-activated receptor.

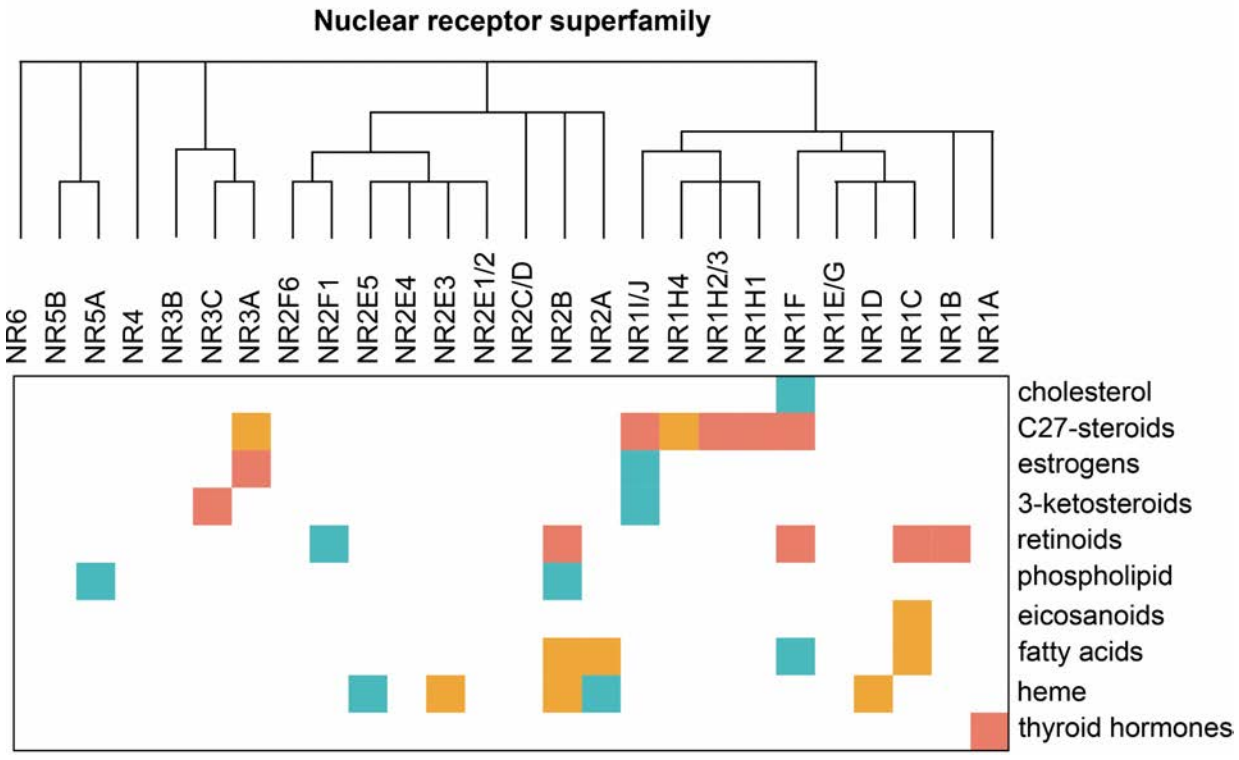

Fig. 1. Phylogenetic distribution of nuclear receptors subfamilies and their cognate ligands.
Ligands that bind to given group of receptors with nanomolar affinity are highlighted with red squares, and those binding with micromolar affinity are in yellow. Blue squares indicate ligands whose binding affinities have not been fully characterized to date (Bertrand et al., 2004; Markov and Laudet, 2011).

In addition to ligand binding, several regulatory mechanisms can modify the conformation of NRs and thus their transcriptional activities. Similar to other transcription factors involved in complex regulatory networks and processes, NRs monomers are able to interact with themselves (homo-interactions) or other members of the superfamily (hetero-interactions) to form ordered supramolecular assemblies known as oligomers (Kumari and Yadav, 2019). This process allows fine-tuned modulation of protein activity and confers the capacity of NRs to extend their functions and to integrate complex metabolic cues (De Bosscher et al., 2020). Diverse multimeric arrangements have been found in the NR superfamily, including homo- and heterodimers as well as higher order oligomers (Fig. 2) (Mangelsdorf and Evans, 1995; Germain and Bourguet, 2013; Presman and Hager, 2017). NR oligomerization modes will be addressed in detail in section 2.2 below. In addition, NRs can also form complexes with many different coregulatory proteins that can either promote or repress transcription. Together with ligands, coregulators determine tissue and time specificities of NRs function (Nader et al., 2009; Duez and Staels, 2010). Among the most important protein families that belong to the NRs interactome are the steroid/nuclear receptors coactivators family (SRC or NCoA), E3 ubiquitin-protein ligases, cyclin-dependent kinases (CDK), MAP kinases (MAPK), protein methyl transferases (PRMT), and nuclear receptor corepressors (NCoR) (Rochette-Egly, 2003; Lonard and O'Malley, 2007, 2012; Hokayem et al., 2017; Sevilla and Pérez, 2018).

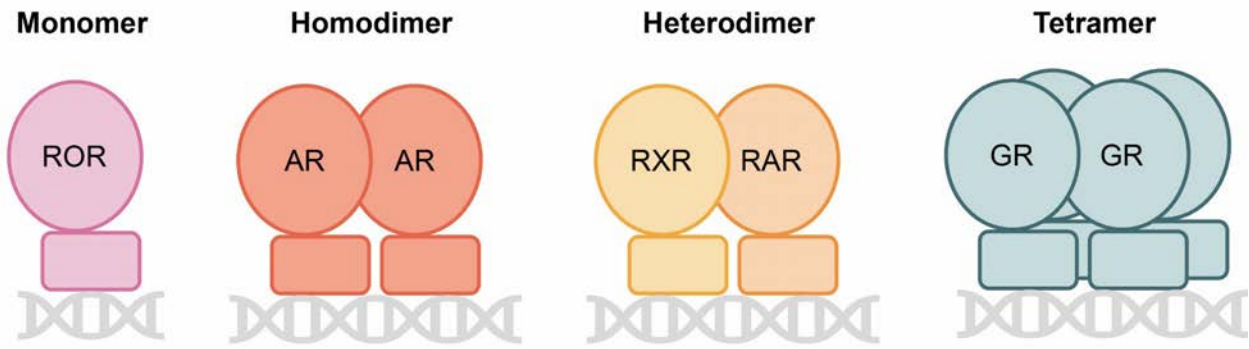

Fig. 2. Schematic representation of nuclear receptor oligomerization modes.

While some NRs are known to function as monomers, most of them work as either homo- or heterodimers. Higher order oligomers such as tetramers are less well characterized and are currently the subject of intense investigation (see section 2.2). The NRs chosen as examples of each dimerization mode are RAR-related orphan receptor (ROR) in purple, androgen receptor (AR) in red, retinoic X receptor (RXR) in yellow, retinoic acid receptor (RAR) in orange, and glucocorticoid receptor (GR) in blue.

There are 48 NRs in humans, which can be classified in seven families based on their phylogenetic relationships (Fig. 1) (Weikum et al., 2018) although alternative classification systems according to the chemical nature of their cognate ligands, their oligomerization mode or their biological functions have also been proposed (Fig. 3) (Schütz et al., 1995; Laudet, 1997; Sonoda et al., 2008). Endocrine receptors comprise steroid (SR) and non-steroid receptors, which bind to hormones and vitamins, respectively. SRs are known to bind to DNA as homodimers, while biologically active forms of non-steroid receptors can be both homodimers and heterodimers with RXR (Evans and Mangelsdorf, 2014). The second group are the orphan receptors, whose endogenous ligands have not been identified yet (Mangelsdorf and Evans, 1995; Gallastegui et al., 2015). Some receptors in this group may be ligand-independent, but their regulation may be controlled by covalent modifications (PTMs) and/or coactivator availability instead (Sonoda et al., 2008). Receptors in this group have been shown to function as either monomers or homodimers. Finally, adopted NRs constitute the third group of NRs, which were initially considered as orphan receptors but for which *bona fide* endogenous ligands have been identified later on. A wide range of small-molecule compounds such as bile acids and phospholipids as well as dietary lipids have been reported as ligands of this group. Most of the adopted NRs bind DNA as heterodimers with the funding member of this group, RXR (Ingraham and Redinbo, 2005; Schupp and Lazar, 2010; Evans and Mangelsdorf, 2014; Gallastegui et al., 2015). Prior to its ‘deorphanization’, the crystal structure of ligand-free (apo) RXR revealed a collapsed LBP, suggesting a ligand-independent mechanism of activation (Bourguet et al., 1995). The identification of LBP-bound 9-cis retinoic acid in a later crystal structure of liganded (holo) RXR was the first experimental evidence of ligand-induced conformational changes and activation of a NR. These structures revealed the enormous malleability of the LBP (Mangelsdorf et al., 1990; Bourguet et al., 1995; Gallastegui et al., 2015).

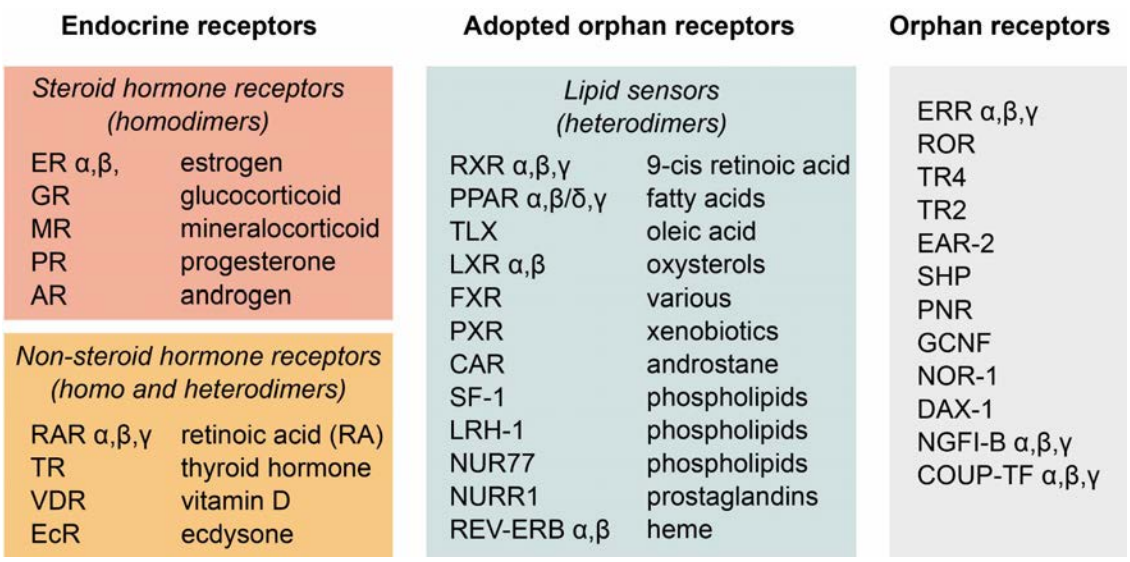

Fig. 3. Classification of nuclear receptors.

NRs are commonly classified based on the chemical nature of their ligands (steroid hormone, non-steroid hormone, lipid, or non-liganded) and their oligomerization modes (homo- and/or heterodimers). Alternative classifications are also used, based for instance on phylogenetics relationships or their biological activities.

2. Steroid receptors oligomerization regulates their functions

SRs belong to the endocrine family 3 of NRs, which is further subdivided into subfamilies A, comprising estrogen receptors α (ERα/NR3A1) and β (ERβ/NR3A2) (Walter et al., 1985; Greene et al., 1986; Moore et al., 1998); B, including estrogen-like receptors α (ERRα/NR3B1), β (ERRβ/NR3B2), and γ (ERRγ/NR3B3) (Giguère et al., 1988; Hong et al., 1999); and C (also known as oxosteroid receptors, see below), formed by the glucocorticoid (GR/NR3C1; Hollenberg et al., 1985; Miesfeld et al., 1986), mineralocorticoid (MR/NR3C2; Arriza et al., 1987), progesterone (PR/NR3C3; Jeltsch et al., 1986; Misrahi et al., 1987; Conneely et al., 1989) and androgen receptors (AR/NR3C4; Lubahn et al., 1988; Tilley et al., 1989).

2.1. Building blocks: domain organization and structure

Similar to other NRs, SRs have a modular structure (Fig. 4): a variable in size and intrinsically disordered N-terminal domain (NTD), which is followed by a highly conserved DNA-binding domain (DBD), a poorly conserved interdomain linker or hinge, and a C-terminal ligand-binding domain (LBD) (Bourguet et al., 1995; Jenster et al., 1995; Moras and Gronemeyer, 1998; Weikum et al., 2018). In the following, the multidomain DBD-hinge-LBD stretch will be termed ‘core’ NR.

The NTD is the least conserved region within the NR superfamily and is the main PTM target (Faus and Haendler, 2006). It features the so-called activation function 1 (AF-1), which is required for autonomous transcriptional activation in a ligand-independent manner (Xu, 2015). Early investigations revealed that AF-1 engages in transient contacts with the C-terminal LBD, termed N-C interactions, which contribute to stabilize the overall protein structure and thus regulate DNA and coregulator binding (Langley et al., 1998; He and Wilson, 2002; Bai et al., 2005). Experimental structural information on the NTD is missing, as it lacks stable secondary and tertiary structures under physiological conditions (Tora et al., 1989; Bevan et al., 1999; Wärnmark et al., 2001). However, the result of biochemical and biophysical studies suggest that it undergoes at least partial folding ('helicity induction') to modulate the formation of transcription activation complexes organized around the receptor (Kumar et al., 2004; McEwan et al., 2007; De Mol et al., 2016, 2018).

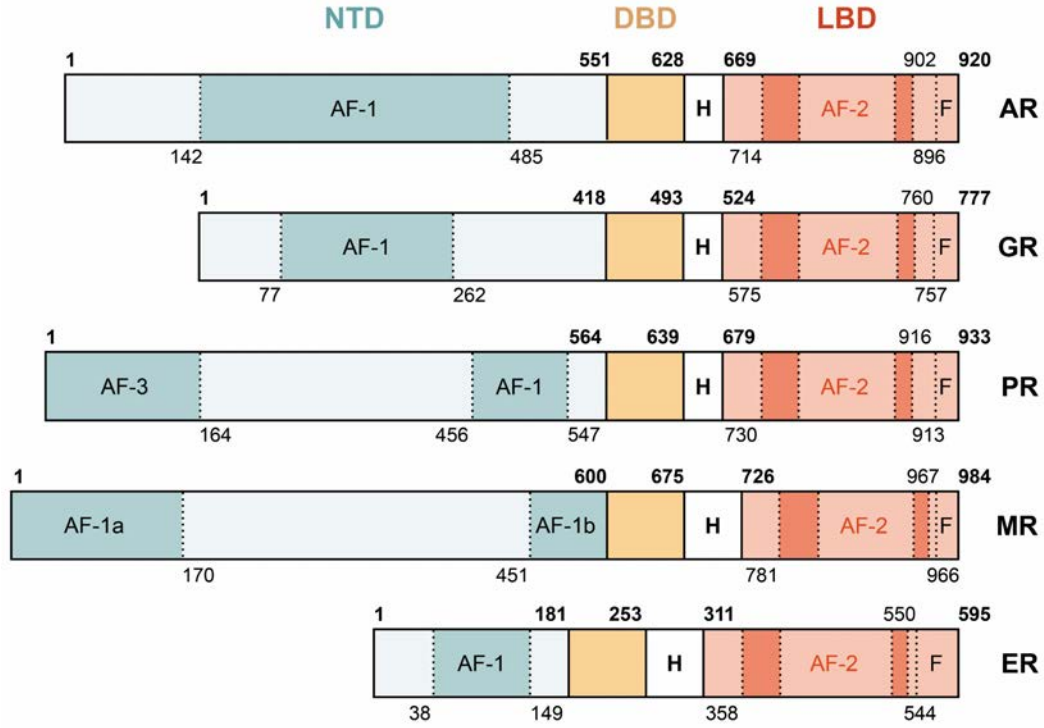

Fig. 4. Domain organization of oxosteroid receptors compared to the related estrogen receptor.
The modular structure of canonical human SR isoforms is depicted (ARα, GRα, MRα, PRβ, and ERα). The first and last residue numbers of each functional area are given. Major domains are NTD in blue, DBD in yellow, hinge (H) in white, and LBD in red. The F domain is also marked, and AF pockets are shaded in darker colour. Note that PR presents an extra region in the NTD, termed AF-3, which comprises two LXXLL motifs that engage in intramolecular interactions with the LBD in a progesterone-dependent manner (Sartorius et al., 1994; Dong et al., 2004).

The DBDs of NRs are arranged into two α-helices, comprising two zinc fingers (Fig. 5, A and B). Some NRs present an additional a-helix in the more N-terminal part of the hinge, which some researchers have described as a C-terminal extension (CTE) of the actual DBD. Each of the zinc fingers is considered a subdomain and contains four cysteine residues that coordinate a zinc ion. The first subdomain features the DNA-reading helix, which makes base-specific interactions with the major groove of the bound DNA. The second subdomain makes non-specific contacts with the DNA backbone and contains residues essential for receptor dimerization. The extra helix within the CTE makes additional base-specific contacts with the DNA minor groove (Evans and Umesono, 1989; Gronemeyer and Moras, 1995; Centenera et al., 2008; Weikum et al., 2018). The hexameric DNA sequence of HREs, 5'-(A/G)GGTCA-3', is recognized by all NRs (Yamamoto, 1985), but mutations and extensions of this core motif together with the arrangement of two motifs in different orientations, confer selectivity to the different receptors (Gronemeyer et al., 2004). In particular, SRs bind symmetric indirect or palindromic (→ n ←) repeats with the consensus half-site 5′–AGAACA–3' (5′–AGGTCA–3' for ER), while other NRs bind to direct (→ n →) or everted (← n →) repeats (Forman and Evans, 1995; Khorasanizadeh and Rastinejad, 2001; Martin and Tremblay, 2010). The hinge region plays a major role in the communication between the globular DBD and LBD modules, and also harbours a bipartite nuclear localization signal as well as key PTMs sites (Tanner et al., 2010; Burns et al., 2011).

The LBD of NRs is a globular three-layer antiparallel α-helical sandwich usually comprising twelve α-helices, although SRs lack helix 2 (H2). This is in addition to four small β-strands (Bourguet et al., 1995). The LBD contains the cocooned LBP, an internal hydrophobic cavity that encapsulates ligands (Fig. 5, C and D). Another functionally important element of the LBD is the activation function 2 (AF-2), an exposed hydrophobic surface responsible for the interaction with coregulatory proteins as well as with the NTD. This cleft is formed by residues from H3, H4, H5 and H12, and recruits transcriptional coregulators that harbour a LXXLL motif (where L stands for leucine, and X can be any residue). Unlike AF-1, AF-2 function and recruitment of coactivators are ligand-dependent (Aranda and Pascual, 2001; Xu, 2015; Weikum et al., 2018). Another hydrophobic surface adjacent to AF-2 was first described in AR, binding function 3 (BF-3), and is composed of residues from H1, the loop between H3-5 and H9 (Estébanez-Perpiñá et al., 2007). This surface is an important binding site for coregulators such as co-chaperones, triggering allosteric signal transmission to other functional regions of the AR-LBD (Fig. 5D). Increasing evidence for physiologically equivalent sites in other NRs suggests

that this interaction surface is a conserved feature across the superfamily (Buzón et al., 2011; Kirschke et al., 2014; Badders et al., 2018; Jiménez-Panizo et al., 2022; Kamaraj et al., 2022; Dube et al., 2023). In addition, the LBD of SRs presents a unique CTE, termed F domain for historical reasons. This stretch is a major differentiation element in SRs. In the phylogenetically closer subgroup of oxosteroid receptors (GR, MR, PR, and AR), the well-conserved F domain folds back and covers part of the globular LBD. In striking contrast, the equivalent sequence in ERα/β is completely unrelated and is not involved in any interactions with the LBD, while other NRs lack an F domain altogether. The sequence and structural differences of F domains in oxosteroid receptors have important consequences for their dimerization mechanism (Fuentes-Prior et al., 2019; Jiménez-Panizo et al., 2019).

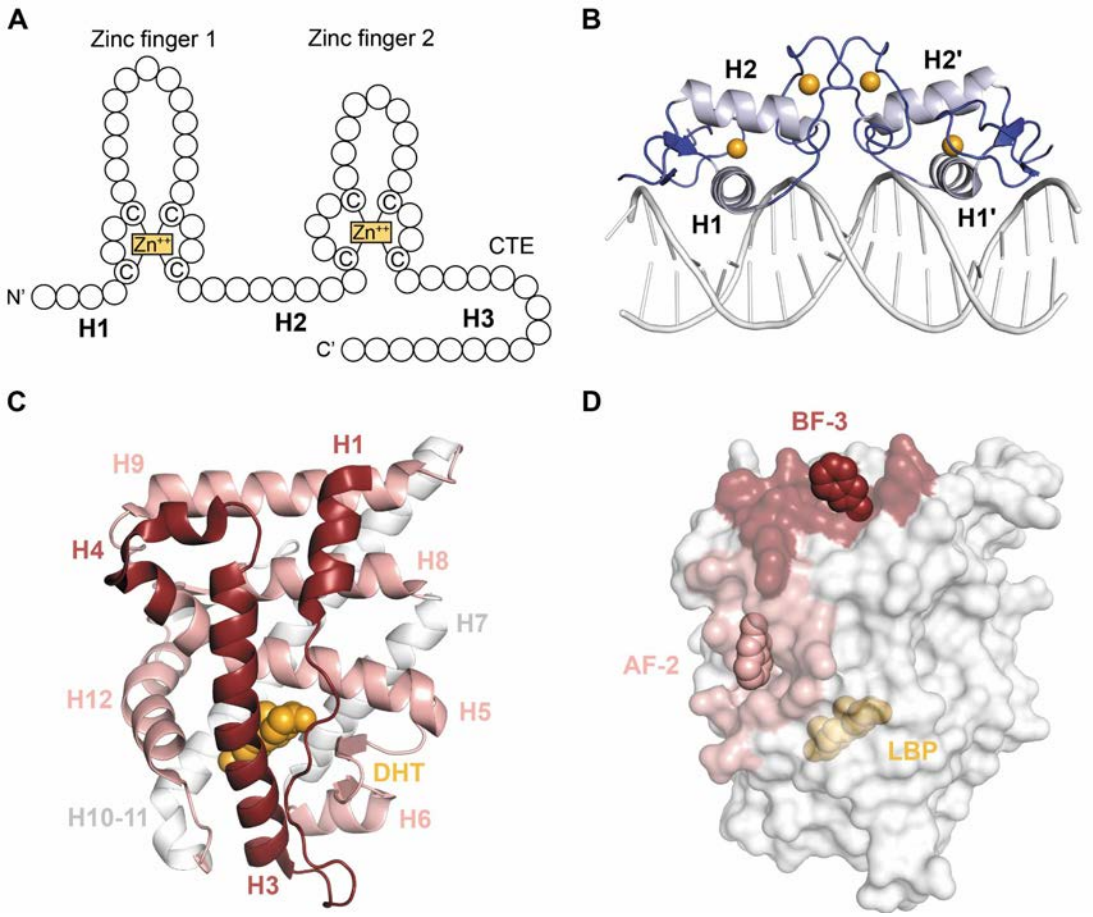

Fig. 5. Cartoons depicting the structure of steroid receptors DNA- and ligand-binding domains.
(A) Generic and schematic representation of NRs DBD subdomains. *(B)* Crystal structure of dimeric GR-DBD bound to DNA (protein data bank code (PDB): 5CBX) with α-helices in light blue and zinc ions in yellow. *(C-D)* Crystal structure of monomeric AR-LBD (PDB: 2PIU) bound to its natural ligand dihydrotestosterone (DHT, yellow) showing *(C)* the three layers of the α-helical sandwich coloured in raspberry, pink and grey, and *(D)* the functional pockets AF-2, BF-3, and LBP.

2.2. Quaternary assemblies of nuclear receptors regulate transcription

Binding of steroid hormones to SRs that are complexed to chaperones in the cytoplasm trigger an intricate sequence of events in which hormones, chaperones, coregulator proteins and chromatin cooperate to modulate SR mediated gene expression (see below). The precise regulation of this network is still a matter of intense investigation. It is now well stablished that a major regulatory element of SRs function is their oligomerization state in each specific cellular context. The equilibrium between monomeric, dimeric, and even higher order oligomeric assemblies of SRs (as well as other NRs) is critical for the transcriptional regulation in both normal and pathogenic conditions, as well as for the therapeutic outcome of clinically approved drugs against pathologies associated with SRs (Presman and Hager, 2017; Fuentes-Prior et al., 2019; Jiménez-Panizo et al., 2019; De Bosscher et al., 2020).

Likely, oligomerization may involve all the NR domains. While there is a wealth of functional and structural data on the dimerization modes of DBD and LBD modules, the molecular determinants of NTD oligomerization are still poorly characterized. DBD oligomerization is mostly dictated by the geometry of the two hexameric half-sites comprising the HREs, which can be arranged as direct, inverted or everted repeats, as explained above (Rastinejad et al., 2013; De Bosscher et al., 2020). Accordingly, structural data has revealed several oligomerization modes for NR-DBDs, including monomers, homodimers and heterodimers with RXR, which in turn can be differentiated into head-to-head and head-to-tail arrangements (Fig. 6) (Helsen et al., 2012; Evans and Mangelsdorf, 2014; Gallastegui et al., 2015; Weikum et al., 2018). SR-DBDs bind as homodimers to palindromic or inverted repeats (Härd et al., 1990; Schwabe et al., 1993; Shaffer et al., 2004; Roemer et al., 2006; Hudson et al., 2014), although AR-DBD has also been found to bind to direct repeats (Zhou et al., 1997; Weikum et al., 2018).

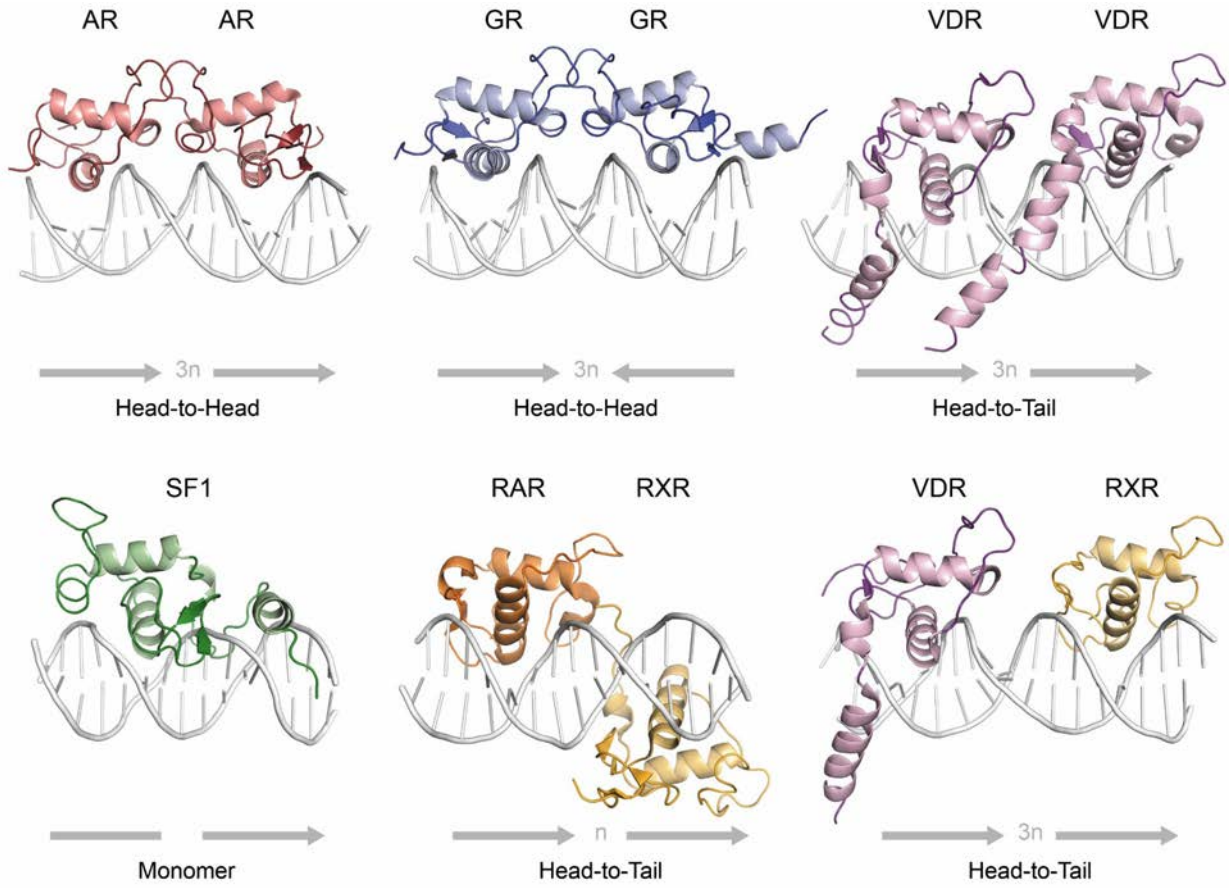

Fig. 6. Oligomerization modes of DNA-binding domains of nuclear receptors.
Three-dimensional X-ray structures of DNA-bound NR-DBDs in different oligomeric conformations. The corresponding PDB codes are 1R4I (AR), 3G6P (GR), 1KB4 (vitamin D receptor, VDR), 2FF0 (Steroidogenic factor 1, SF1), 1DSZ (RAR·RXR), and 1YNW (VDR·RXR). The number of bases between the two hexameric repeats (grey arrows) is noted as "n".

In the case of LBD modules, two major dimerization modes have been structurally characterized. An arrangement typical of heterodimers with RXR (Mangelsdorf and Evans, 1995; Chandra et al., 2008, 2017; Lou et al., 2014) is shared by homodimers of the ER and the hepatocyte nuclear factor-4α (HNF4) (Brzozowski et al., 1997; Chandra et al., 2013). This dimerization mode is called 'canonical' and is centred on aliphatic residues from helices H10-11 of both monomers (Fig. 7A). In striking contrast, oxosteroid receptors lack the signature of hydrophobic residues at the N-terminal end of H10-11 and feature an F domain that partially covers the canonical dimerization interface. These features preclude dimerization of oxosteroid receptors according to the canonical model, but leave open other possibilities (Fig. 7, B and C) (Tanenbaum et al., 1998; Williams and Sigler, 1998; Fuentes-Prior et al., 2019; Jiménez-Panizo et al., 2019, 2022).

In particular, the crystal structure of the AR-LBD homodimer revealed a symmetrical, head-to-head arrangement centred on helices H5, with additional contacts provided by residues from adjacent helices and loops (Fig. 7B) (Nadal et al., 2017). This H5-centred dimeric arrangement has been confirmed in solution and in cells (Nadal et al., 2017), as well as in low resolution cryogenic electron microscopy (cryo-EM) structures of core AR (Wasmuth et al., 2022) and of full-length AR (FL-AR) bound to DNA (Yu et al., 2020). Further, topologically equivalent, LBD dimerization interfaces have been identified in GR (Bledsoe et al., 2002) and in constitutive androstane receptor (CAR), an orphan receptor of the NR1 family (Shan et al., 2004). Of note, CAR forms canonical heterodimers with RXR as well as AR-like non-canonical homodimers (Xu et al., 2004), demonstrating that alternative dimeric conformations can be adopted by the same NR depending on a number of cellular parameters (Fuentes-Prior et al., 2019). Therefore, current evidence points towards a complex structural landscape, as illustrated not only by the AR-like dimerization mode (Fig. 7B) but also by the multiple non-canonical LBD homodimers that have been described for PR (Tanenbaum et al., 1998; Williams and Sigler, 1998) and GR (Fig. 7C) (Jiménez-Panizo et al., 2022), as well as for non-steroid NRs such as the thyroid receptor-β (e.g., PDB 2PIN) and for orphan receptors of the NR4 family, Nur77 (e.g., PDB 3V3E) and Nurr1 (e.g., PDB 1OVL).

To distinguish physiologically relevant dimerization modes, structural and functional data of multidomain core and FL receptors is required (Jiménez-Panizo et al., 2022). In contrast to the large number of reported structures of isolated DBD and LBD modules from almost all NR families, only a few core or FL receptors have been structurally characterized, and no common quaternary architecture among these multidomain NRs complexes has been identified (Evans and Mangelsdorf, 2014; Fuentes-Prior et al., 2019). Furthermore, this structural data has challenged the oversimplified dogma of one-domain-one-function. Most notably, the bidirectional interdomain communication between DBD, hinge and LBD modules, as well as protein-DNA interactions mediated not only by the DBD, profoundly impact the stability of core NR structures, and critically modulate DNA binding. This has been strikingly demonstrated in a series of crystallographic and cryo-EM structures of NRs bound to different sets of coregulators and HREs and is supported by additional biochemical experiments.

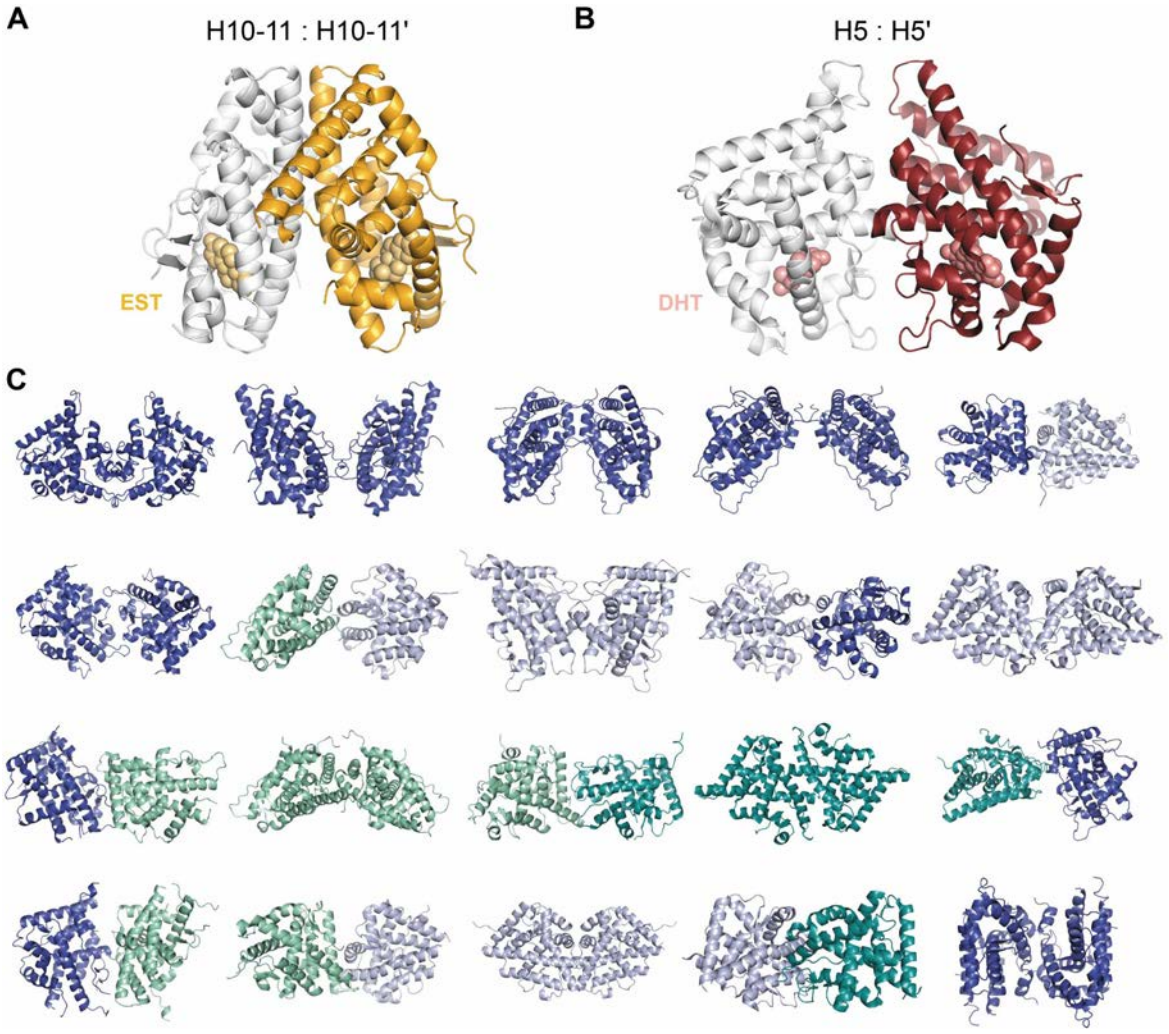

Fig. 7. Canonical versus non-canonical dimerization modes of steroid receptors.
(A) The ER-LBD homodimer adopts the canonical H10-11 centred dimerization mode (PDB: 1ERE). The estrogen molecule (EST) bound in the LBP is shown as yellow spheres. *(B)* AR-LBD homodimer in the non-canonical H5 centred conformation (PDB: 5JJM). DHT is shown as pink spheres. *(C)* Catalogue of non-canonical homodimerization modes for isolated GR-LBD crystals (Jiménez-Panizo et al., 2022).

RXR heterodimerization partners use a common surface patch on their LBDs to engage in domain-domain interactions with their DBDs, which is called the 'confluence zone' and acts as an allosteric transmission centre that propagates signals across the whole core NRs (Chandra et al., 2008, 2013, 2017; Lou et al., 2014; Fuentes-Prior et al., 2019). In the case of homodimeric SRs, low-resolution cryo-EM structures of FL human ERα and AR (Yi et al., 2015; Yu et al., 2020), and core AR (Fig. 8, A to C) (Wasmuth et al., 2022), as well as a recent crystal structure of core GR (Fig. 8D) (Postel et al., 2023) suggest important cross-talk between NTD, DBD and LBD moieties. Further, studies of SR oligomerization in living cells have provided strong evidence for GR, AR and PR tetramerization in the presence of cognate DNA, while ERα

remains mostly dimeric (Presman et al., 2016; Paakinaho et al., 2017; Presman and Hager, 2017; Jiménez-Panizo et al., 2022). Finally, an increasing number of experimental observations point to multiple combinations of SRs as 'atypical' heterodimers, which do not rely on canonical interactions with RXR for activity. These heterodimers are particularly relevant for SR-linked pathologies, but their characterization is still incomplete and in some cases is limited to *in vitro* observations that still require *in vivo* confirmation (Amoutzias et al., 2007; De Bosscher et al., 2020).

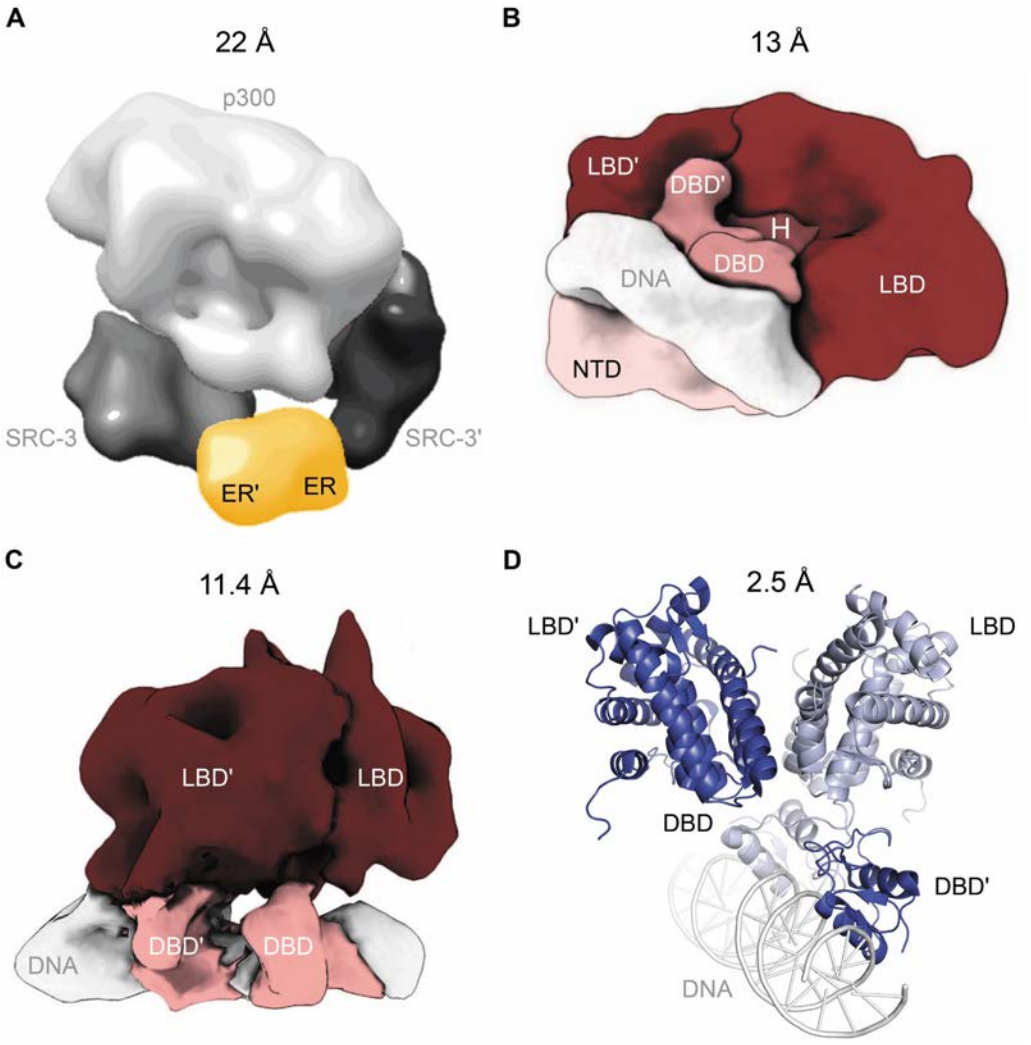

Fig. 8. Three-dimensional structures of multidomain steroid receptors.

(A) Full length ERα structure (yellow) in complex with its major coactivators: steroid receptor coactivator 3 (SRC-3) and p300, a histone acetyltransferase (grey). The EMDB code of the complex is EMD-8832. Note that low resolution prevents the visualization of individual ER domains. *(B-C)* Full length (B) and core (C) AR structures (red shaded) bound to DNA (grey) (EMD-22079 and EMD-25132, respectively). *(D)* Crystal structure of a dimeric GR core (blue cartoons) bound to DNA (grey) (PDB code 7PRW). The reported resolutions are indicated in each case.

In summary, current evidence reveals quite diverse arrangements of NR quaternary assemblies and bidirectional cross-talk between individual NR domains with each other and with cognate DNA. Since NRs engage in pivotal physiological processes, dysregulated actions are linked to major human diseases, explaining their role as important prognostic markers and pharmacological targets. Thus, further structural investigations together with studies in living cells and animal models are required to advance towards a complete taxonomy of possible quaternary architectures for the NR superfamily, and to fully apprehend their relevance in normal physiology and pathology.

3. Human physiology of the androgen and glucocorticoid receptors

3.1. Androgens and glucocorticoids synthesis and signalling pathways

The endogenous steroid hormones are derived from cholesterol in the adrenal and gonadal glands, upon regulation of the hypothalamic-pituitary-adrenal (HPA) and -gonadal (HPG) axes, respectively. Acting on nearly every tissue in the body, glucocorticoids (GCs) maintain homeostasis by regulating a plethora of physiological processes, including metabolism, immune response, skeletal growth, cardiovascular function, reproduction and cognition (Sapolsky et al., 2000; Timmermans et al., 2019). On the other hand, androgens drive not only human sexual development and reproduction, but they also modulate the functions of other tissues functions including brain, bone, muscle, adipose tissue, skin, hair and the cardiovascular system, affecting growth, body shape and human behaviour (Elzenaty et al., 2022). In addition to their manifold functions, both GCs and androgens keep balanced feed-forward and feedback loops to maintain normal functioning of the HPA and HPG axes (Fig. 9) (Oakley and Cidlowski, 2013; Handa and Weiser, 2014; Elzenaty et al., 2022).

In response to physiological cues and stressors, the hypothalamus releases corticotropin-releasing hormone (CRH) to the anterior pituitary to stimulate the secretion of adrenocorticotropic hormone (ACTH) in a circadian-dependent manner, which in turn triggers the synthesis and secretion of GCs in the cortex of the adrenal gland (Fig. 9A) (Oakley and Cidlowski, 2013; Timmermans et al., 2019). Similarly, production of androgens in the gonads is controlled by the HPG axis in a developmental specific fashion, through the hypothalamic secretion of gonadotropin-releasing hormone (GnRH) that stimulates the pituitary release of luteinizing hormone (LH) and follicular-stimulating hormone (FSH) (Fig. 9B) (Elzenaty et al., 2022). This system is sex specific, mediated by the testes or the ovaries as target organs of HPG

axis hormones. Leydig cells in the testis produce and secrete testosterone abundantly, which is then converted to the most potent endogenous androgen in terms of affinity for the AR the DHT (Wilson, 2001). By contrast in the ovary, theca cells produce androstenedione, a 'weak' androgen according to its low affinity towards AR, which is mostly used as estrogen precursor, while only small amounts are secreted into the bloodstream (Skiba et al., 2019). The adult adrenal cortex can also produce weak androgens, which can be metabolised to more potent androgens (testosterone or DHT) in peripheral tissues (Rege et al., 2013; Turcu et al., 2014, 2020). However, unlike androgen production in the HPG axis, the exact regulation of adrenal androgen production is still not fully elucidated (Miller et al., 2020).

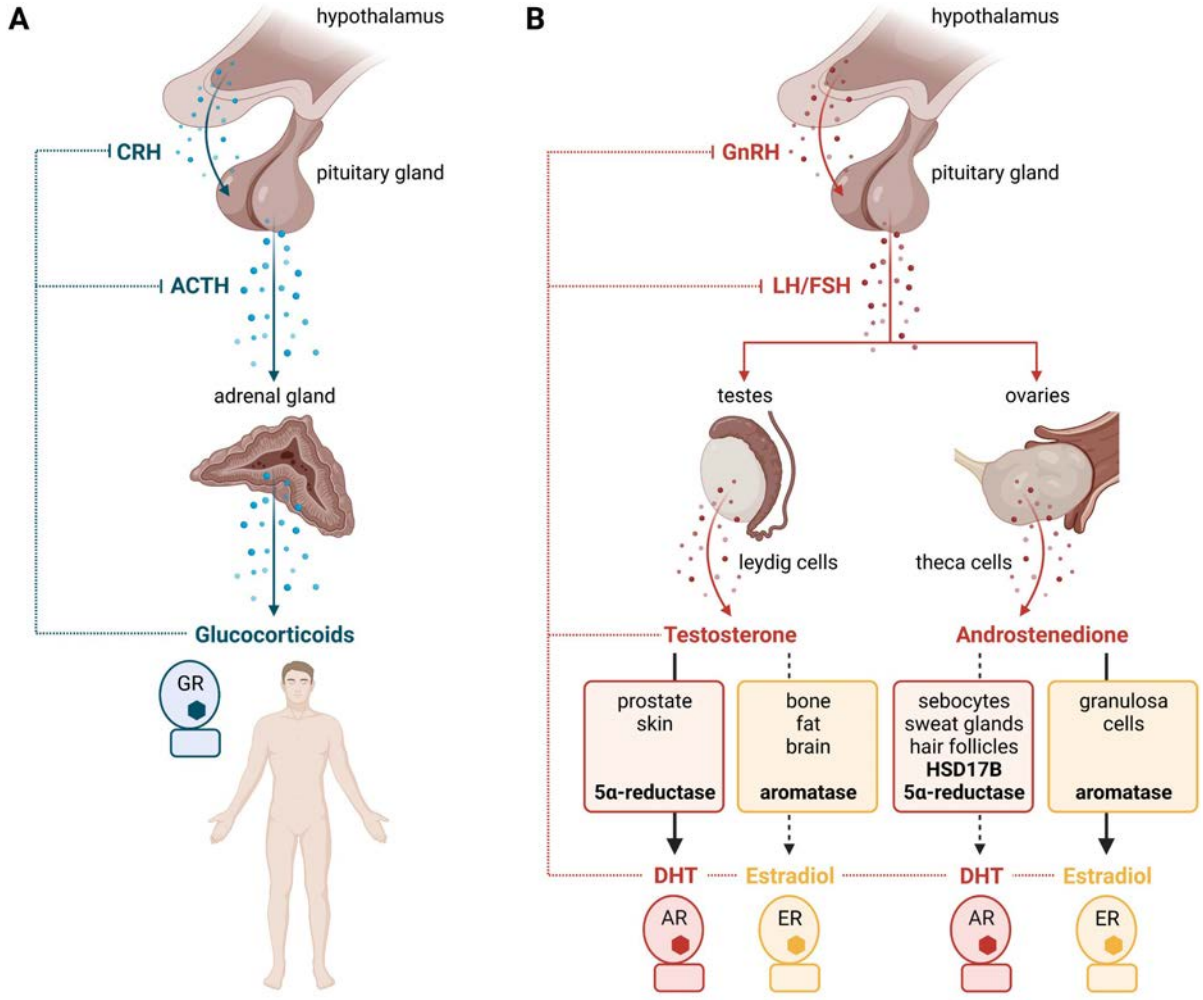

Fig. 9. Steroids release through the hypothalamic-pituitary-adrenal and -gonadal axes.

(A) Representation of GCs release regulation through the HPA axis. *(B)* Sex-specific control of androgen and estrogen release through the HPG axis. Enzymes that transform testosterone or androstenedione into DHT or estradiol are in bold. In women, androstenedione is transformed into testosterone by the 17β-hydroxysteroid dehydrogenase (HSD17B) prior to its reduction to DHT by the 5α-reductase.

Created with BioRender.com

Newly synthesized AR and GR may adopt a folded conformation in which the LBP remains inaccessible to hormones, preventing untimely activation. The structural conformation of the LBD required for AR and GR activation follows multiple cycles of association and release from multichaperone complexes, which partially unfold these receptors into a stable, hormone-competent conformation (Fig. 10) (Prescott and Coetzee, 2006). The first chaperone complex interacts co-translationally with the receptors in the ribosome, and is comprised of heat shock protein 70 (Hsp70) and a co-chaperone of the Hsp40 family (Fliss et al., 1999; Prescott and Coetzee, 2006; Timmermans et al., 2019). This AR/GR-chaperone complex is stabilized and prolonged by the co-chaperone, Hip, until the Hop co-chaperone binds to recruit Hsp90 (Höfeld et al., 1995; Dittmar et al., 1997; Freeman et al., 2000; Ricketson et al., 2007). To stabilize AR or GR in a hormone-competent, transcriptionally inactive intermediate conformation, p23 chaperone and FKBP51 immunophilin bind to Hsp90 within the complex, releasing Hip, Hop and Hsp70 (Freeman et al., 2000; Hernández et al., 2002; Prescott and Coetzee, 2006; Oakley and Cidlowski, 2013; Timmermans et al., 2019). Upon hormone binding, the AR/GR-chaperone complex is further reorganized: FKBP51 replaces FKBP52, and AR/GR undergoes a conformational change that exposes their nuclear localization signals followed by their trafficking to the nucleus (Riggs et al., 2003; Prescott and Coetzee, 2006; Vandevyver et al., 2012; Timmermans et al., 2019). The chaperone complex mediates the continuous nuclear-cytoplasmic shuttling of AR and GR, which determines the levels of AR/GR proteins in the nucleus and thus the strength of receptors' transcriptional activities through their binding to androgen (ARE) and glucocorticoid (GRE) response elements (Owens-Grillo et al., 1996; Hager et al., 2000; Prescott and Coetzee, 2006; Vandevyver et al., 2012).

Within the nucleus, SRs are known to interact with chromatin as oligomers, as previously explained (Presman et al., 2016; Paakinaho et al., 2017; Presman and Hager, 2017; Jiménez-Panizo et al., 2022). However, the exact sequence of chaperone complex dissociation and AR/GR monomer-to-oligomer transition within the nucleus has not been precisely elucidated yet (Schaufele et al., 2005; Centenera et al., 2008; Vandevyver et al., 2012; Nadal et al., 2017). Pioneer studies suggested that oligomerization precedes chromatin binding and demonstrated that DNA binding is redox-dependent (Kokontis and Liao, 1999). Traditionally, GR binding to GREs has been described following the so called 'dissociated model', where depending on chromatin context and specific DNA sequence, GREs can either stimulate transcription upon binding of GR dimers (positive GREs) (Oakley and Cidlowski, 2013; Hudson et al., 2014), or

transrepress gene expression by recruiting two GR monomers that do not dimerize (negative GREs) (Hudson et al., 2013; Timmermans et al., 2019). Besides, AR dimerization was shown to enhance chromatin remodelling to modulate gene expression (Jin et al., 2013).

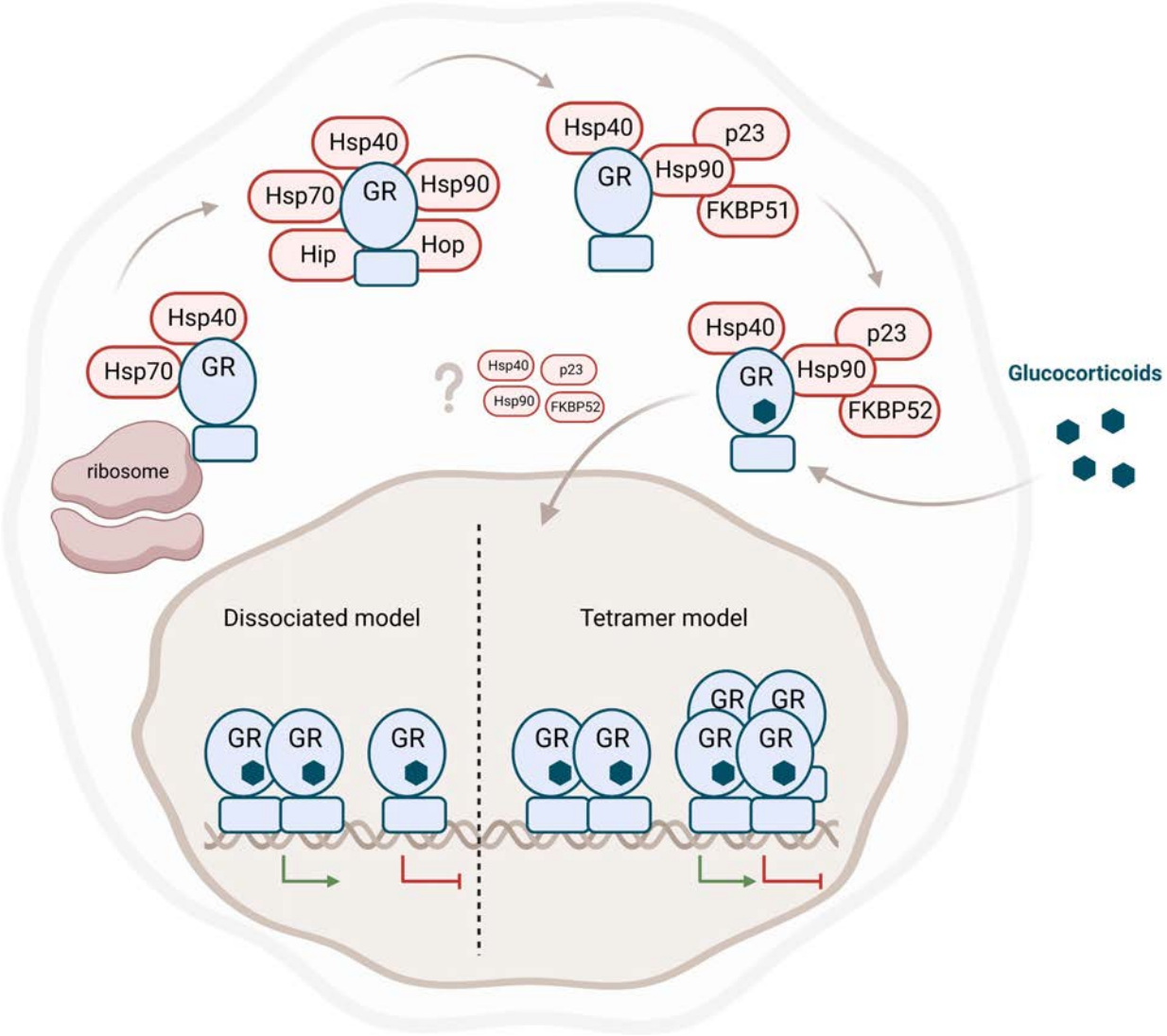

Fig. 10. Life cycle of the glucocorticoid receptor and DNA binding models.

Schematic representation of the multiple cycles of association and release from multichaperone complexes underlying the GR cell cycle from its synthesis to hormone binding, activation, and nuclear translocation. The details of the chaperone-dissociation process are still to be worked out. The dissociated model of GR regulation of GRE-dependent transcription postulates that GR transactivation (green arrows) and transrepression (red arrows) are performed by dimeric and monomeric forms of the receptor, respectively (lower left side). However, the results of recent experiments in living cells do not support this model and indicate that higher GR (homo)multimers underlie both actions instead (lower right side). Created with BioRender.com

However, recent studies of SRs trafficking in living cells have dramatically advanced our understanding of this process, forcing a paradigm shift in the field (Presman et al., 2014, 2016; Paakinaho et al., 2017, 2019; Jiménez-Panizo et al., 2019). These studies have demonstrated that the GR variant previously reported to interact as a monomer with GREs to repress gene-expression is actually capable of dimerizing in living cells, explaining its retained DNA-binding capacity (Paakinaho et al., 2019). Thus, the inability of a dimerization-defective mutant to efficiently bind chromatin and therefore to trigger any gene response, suggests that monomeric GR has a minimal function *in vivo* and is unlikely to contribute significantly to the physiologically relevant activities of the receptor (Johnson et al. 2021). Furthermore, quantitation of GR and AR single-molecules at chromatin level has revealed that the dimeric forms of these receptors are intermediate states toward their biologically active, tetrameric arrangements ('dimers of dimers') (Fig. 10) (Presman et al., 2016; Paakinaho et al., 2017, 2019). The intricate links between NR oligomeric state, affinity for ligands (hormones), binding cooperativity and recruitment to specific chromatin sites needs further investigation (Fuentes-Prior et al., 2019).

3.2. Allosteric regulation of androgen and glucocorticoid receptors

NRs are allosteric proteins (Kuriyan, 2004; Del Sol et al., 2006; McEwan, 2012; Mackinnon et al., 2014), in which information signals are transmitted from a functional site to another, and the AR and GR are no exception in this regard (Estébanez-Perpiñá et al., 2007; Grosdidier et al., 2012; Jiménez-Panizo et al., 2019). Regulation of receptor signalling is not only exerted by the differential expression of various protein isoforms, but through allosteric switches alternating between different conformations induced by binding of chaperones, ligands, DNA, and other interactors. Ligand binding and the exchange of chaperones by coactivators are allosterically coupled, as it was previously mentioned (Hur et al., 2004; Estébanez-Perpiñá et al., 2005). In particular, hormone binding to the LBP triggers allosteric remodelling of the AF-2 and BF-3 surfaces (Fig. 11). In this manner, occupancy of the LBP regulates the dynamics and stability of surfaces that recognize coregulators and is thus allosterically coupled to the recruitment of these proteins to the AR or GR (Estébanez-Perpiñá et al., 2005, 2007). Although a proteomics study has identified essentially overlapping, agonist-specific interactomes of both AR and GR (Lempiäinen et al., 2017), the detailed molecular determinants of NR binding to a large number of coregulators are far from being well characterized.

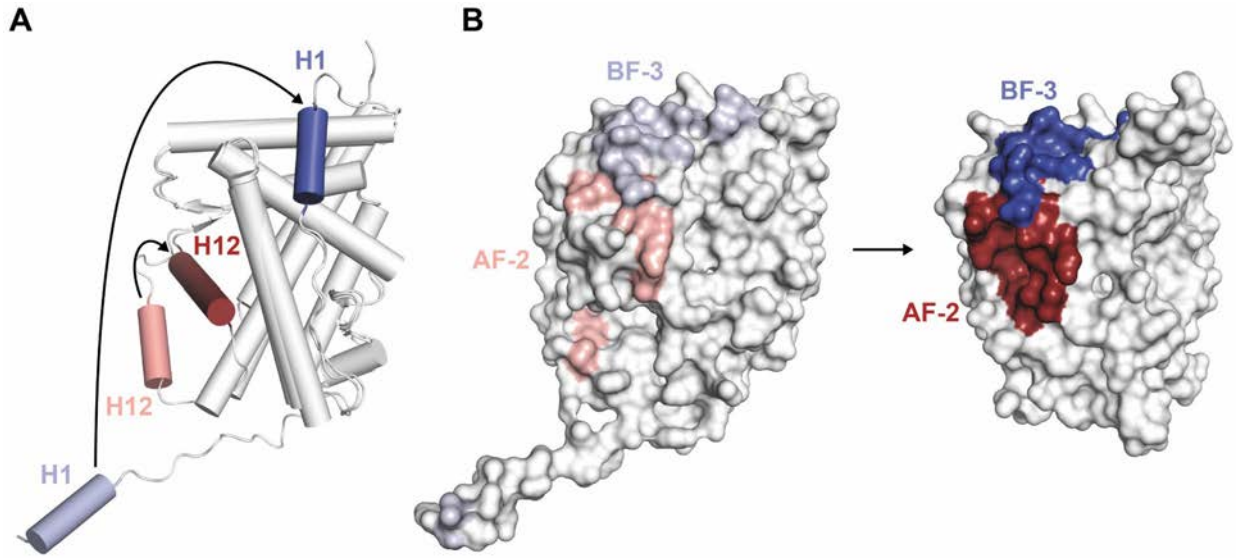

Fig. 11. Allosteric remodelling of the ligand binding domain upon ligand binding.

(A) Cartoon representation of GR-LBD showing the rearrangement of helices H1 and H12 induced by ligand binding. The crystal structure of GR-LBD bound to an antagonist (light blue and red, PDB: 4MDD) shows a partial displacement of H12, preventing co-activator binding to the AF-2 pocket, as well as a complete unfolding of H1. By contrast, both helices are integral parts of the globular GR-LBD when bound to an agonist (dark blue and red, PDB: 1M2Z). *(B)* Surface representation of GR-LBD bound to antagonist (left) and agonist (right) highlighting AF-2 residues and AR-topologically equivalent BF-3 pocket residues.

Among the ~ 200 reported coregulator proteins of the AR and GR interactomes, enzymes that add or remove covalent PTMs are especially relevant as messengers of physiological context information distinct from that provided by hormone ligands. PTMs can trigger allosteric transitions, modify protein interaction surfaces, and affect protein ligand response, localization, stability, regulatory activity, and DNA binding in a context-specific manner (Faus and Haendler, 2006). Main PTMs affecting both AR and GR include the addition of phosphate, acetyl, methyl, ubiquitin, and SUMO groups (Fig. 12) (Gioeli and Paschal, 2012; Weikum et al., 2017; Wen et al., 2020). Further, GR has also been reported to undergo nitrosylation of cysteine residues within the zinc-finger domains (Galigniana et al., 1999; Paul-Clark et al., 2003; Scheschowitsch et al., 2017; Weikum et al., 2017).

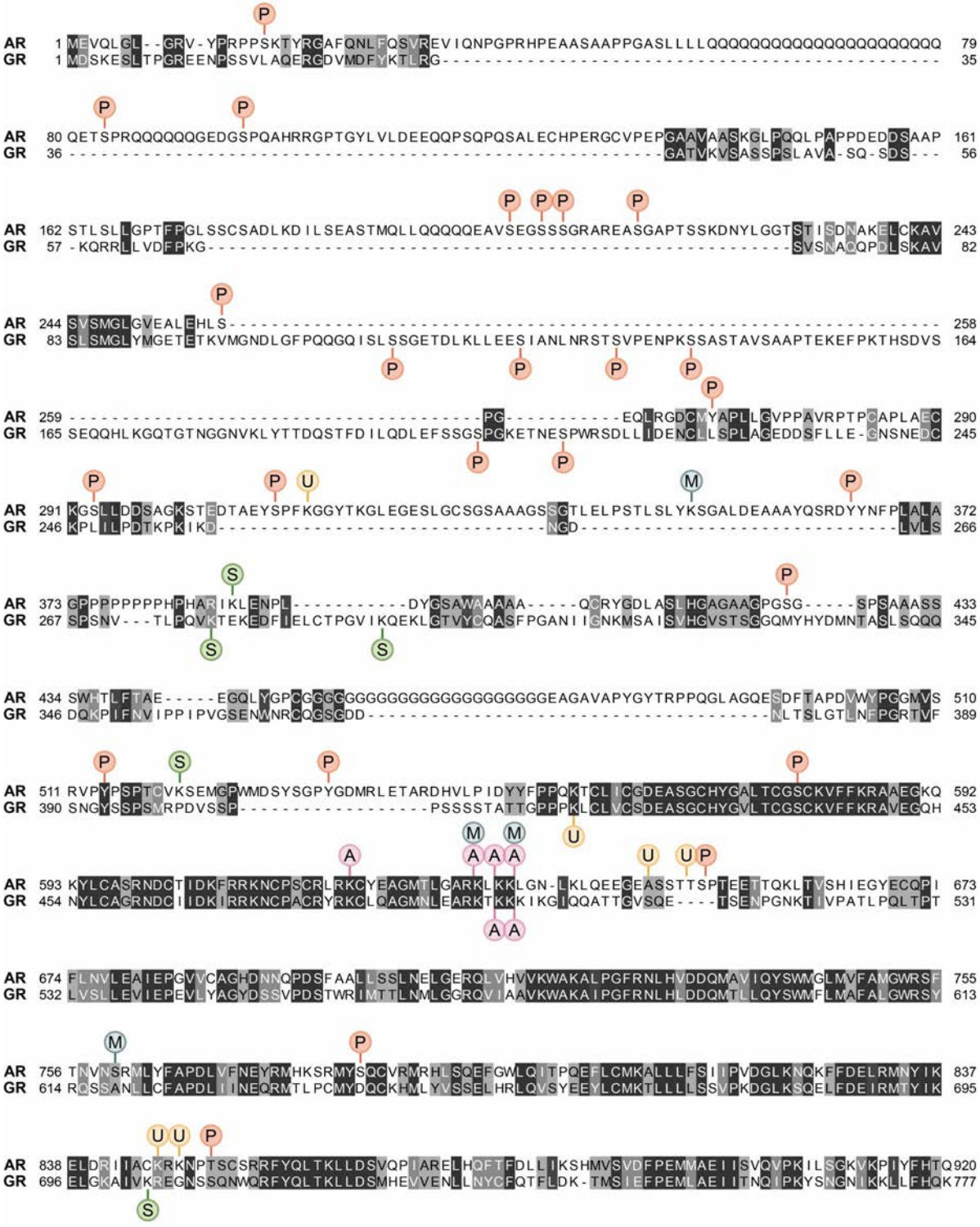

Fig. 12. Sequence alignment of androgen and glucocorticoid receptors highlighting post-translational modifications sites.

Reported PTMs of these NRs include phosphorylation (P, red), methylation (M, blue), acetylation (A, purple), sumoylation (S, green), and ubiquitination (U, yellow). The degree of conservation between AR and GR, is indicated with grey shading (from dark grey for identical residues to white for non-conserved residues). Note that most PTMs are receptor-specific.

Phosphorylation is the most common PTM of AR and GR, mostly affecting the NTD. AR phosphorylation occurs mainly in response to androgens, although a few sites are also phosphorylated in an androgen-independent manner (Koryakina et al., 2014; Wen et al., 2020). GR maintains a basal level of phosphorylation, and some additional sites are phosphorylated upon ligand binding. Kinases reported to phosphorylate both AR and GR are cyclin-dependent kinases (CDKs), mitogen protein kinases (MAPKs) and JUN N-terminal kinases (JNKs). AR is further phosphorylated by protein kinase B (AKT), serine/threonine kinase PIM-1 and Aurora kinases (AURKA, AURKB); GR can be also phosphorylated by glycogen synthase kinase-3 (GSK-3). Phosphorylation is most commonly reversed by protein phosphatases 1 (PP1α), 2A (PP2A), and 5 (PP5) (Ward and Weigel, 2009; Koryakina et al., 2014; Weikum et al., 2017; Wen et al., 2020).

Lysine acetylation sites in AR and GR are located in the KXKK motifs within the hinge region. This PTM has been described as a key modification modulating the recruitment of coregulators, which appears to be important for nuclear translocation. Cross-talks between AR kinases and acetyltransferases (HATs) that target the AR have been identified (Fu et al., 2004). Furthermore, AR and GR are direct substrates of histone deacetylases (HDACs). AR is acetylated by p300, P/CAF and Tip60, and deacetylated by HDAC1. GR acetylation by the HAT protein termed circadian locomotor output cycles protein kaput (CLOCK) has been shown to reduce its ability to regulate transcriptional activity and to be critical for circadian rhythm maintenance (Kino and Chrousos, 2011). Further, GR deacetylation by HDAC2 is important for repression of NF-κB-regulated genes (Ito et al., 2006).

Two of the lysines residues in the AR hinge region can also be methylated, pointing to an additional cross-talk between these two PTMs. Lysines methylation is performed by histone-lysine N-methyltransferase SET9 (Ko et al., 2011; Malbeteau et al., 2022). In addition to a third lysine in the NTD, Arg761 in the LBD can also be methylated by protein methyltransferase 5 (PRMT5), which has important implications for prostate cancer (see section 3.3) (Mounir et al., 2016; Malbeteau et al., 2022). GR is also methylated by PRMT5 in the cell nucleus (Poulard et al., 2020). However, the targeted arginine residue(s) and the role of this modification in GR activity are still under investigation.

Lysine ubiquitination promotes protein turnover by targeting them to the proteasome for degradation. For both AR and GR, this PTM is necessary for sustained transcription at a given promoter allowing precise control of key transcriptional events (Faus and Haendler, 2006). However, ubiquitination of specific lysine residues enhances AR function rather than targeting the SR for degradation (Wen et al., 2020). Main enzymes responsible for AR and GR ubiquitination are the E3 ubiquitin-protein ligases MDM2, ring finger protein 6 (RNF6) and C-terminus of Hsp70 interacting protein (CHIP), while reversion of the ubiquitination is exerted by Usp10 and Usp26 deubiquitinating enzymes (Wallace and Cidlowski, 2001; Xu et al., 2009; Li et al., 2014).

Finally, SUMOylation of a few lysine residues in AR and GR has commonly been linked to transcription repression, but its functions are context-dependent. It also affects protein stability and nuclear-cytoplasm trafficking. AR can be modified by E3 SUMOylation ligases PIAS1 and PIAS-α in a ligand-dependent manner, while GR is modified by the SUMO conjugase Ubc9 (Faus and Haendler, 2006; Gioeli and Paschal, 2012; Weikum et al., 2017; Wen et al., 2020).

In addition to allosteric rearrangements elicited by hormone binding and coregulators along the AR and GR signalling pathways, the target DNA sequences to which receptors bind also induce important rearrangements of the receptor structure (Fuentes-Prior et al., 2019; Jiménez-Panizo et al., 2019; Timmermans et al., 2019). Cognate DNA-binding sequences of the GR have been shown to function as *bona fide* allosteric modulators, which are capable of affecting receptor conformation and thus regulate its activity (Meijsing et al., 2009; Watson et al., 2013; Love et al., 2017; Weikum et al., 2017; Frank et al., 2018). Nucleotides directly flanking a GR-binding site not only modulate its 3D structure, but also that of the GR–DBD and even the multimeric conformation of the receptor (Schöne et al., 2016). Most notably, a change in a single base pair resulted in up to 10-fold higher affinity in the activation of a GRE reporter gene in response to ligand. This implies that GR activity can be modulated by both sequence composition and DNA shape to achieve fine-tuning of the GR structure and activity downstream of binding. These features are likely to be shared by other oxosteroid receptors, given the almost identical sequences of their DBDs and some conserved sequence features of interdomain hinges. Further, specific flanking nucleotide sequences could enforce unique DNA conformations required for an optimal transcriptional response thus explaining how receptors predicted to recognize similar binding motifs show distinct DNA-binding preferences. In summary, binding of AR and GR DBDs binding to their cognate DNA sequences triggers intra- and interdomain conformational changes that affect the overall quaternary structure of the receptor, including its LBD (Jiménez-Panizo et al., 2019).

4. The androgen and glucocorticoid receptors in human disease

Tight spatial and temporal regulation of AR and GR activity is critical for the proper functioning of tissue-specific signalling cascades. Therefore, dysfunctions of the AR or GR regulated pathways have profound pathophysiological consequences (Knudsen and Penning, 2010; Vitellius et al., 2018; Estébanez-Perpiñá et al., 2021; Regazzo et al., 2022).

4.1. Glucocorticoid receptor-associated pathologies

The dysregulation of endogenous GC secretion or the overuse of exogenous hormones manifest wide-ranging and devastating effects on most organ systems (Raff et al., 2014). Excess of GCs leading to Cushing's syndrome or adrenal insufficient secretion of GCs underlying Addison's disease are the two major human conditions related to unbalanced levels of hormones (Munir et al., 2022; Gutiérrez et al., 2023). On the other hand, alterations in GR function, either due to mutations of the encoding gene or to other molecular changes along the GR signalling pathway, are manifested as either GC resistance or hypersensitivity (Nicolaides and Charmandari, 2015, Nicolaides et al., 2015b; Wilkinson et al., 2018).

Primary generalized GC resistance (PGGR or Chrousos syndrome), results from impaired GR function and thus a decreased sensitivity to GCs in all organs, due to heterozygous variants in the GR encoding gene including point mutations, insertions, or deletions. Alterations in the GR function include dysregulation of the GC-mediated negative feedback mechanisms, which results in compensatory activation of the HPA axis that leads to hypersecretion of ACTH and cortisol (highly variable, ranging from severe symptoms to subclinical hypercortisolism). Thus, this condition may result in increased production of other adrenal steroids such as androgens and mineralocorticoids, explaining the clinical signs related to such hormone excess in patients affected by this syndrome (Kino and Chrousos, 2001; Kino et al., 2002; Nicolaides et al., 2010, 2015b, 2015a; Charmandari et al., 2013; Nicolaides and Charmandari, 2015; Wilkinson et al., 2018). Computer simulations suggest that the primary cause of GC resistance in Chrousos syndrome is an overall destabilization of the LBD due to single amino acid replacements that affect the LBP and/or AF-2 (Hurt et al., 2016). Functional studies indicate that most of the 26 mutations that have been described in the human *GR* gene, impair several steps of GC signalling including hormone recognition, GR nuclear translocation, DNA binding and interactions with the coactivator, GRIP1, which ultimately leads to reduced or absent GR-dependent transactivation (Fig. 13A) (Vitellius et al., 2016, 2018; Nicolaides and Charmandari, 2017; Vitellius and Lombes, 2020).

By contrast, primary generalized GC hypersensitivity (PGGH) is a rare syndrome with clinical signs of metabolic disorder without hypercortisolism, due to compensatory hypoactivation of the HPA axis (Nicolaides and Charmandari, 2017). This disease mostly correlates with *GR* polymorphisms (N363S, ER22/23EK and BclI restriction fragment length polymorphisms) while to date, a single patient harbouring a point mutation in the NTD (p.D401H) exhibited clinical symptoms of GC hypersensitivity including obesity, type 2 diabetes and hypertension (Charmandari et al., 2008).

4.2. Androgen receptor-related diseases

Upregulated AR activity is the dominant driver of one of the leading cancers in adult men, prostate cancer (PCa), making AR a central therapeutic target for PCa treatment (Tilley et al., 1990; Knudsen and Penning, 2010; Robinson et al., 2015; Quigley et al., 2018; Estébanez-Perpiñá et al., 2021). On the other hand, impaired response to androgens leads to an X-chromosome linked disorder of sex development in genetic males termed androgen insensitivity syndrome (AIS) (Lubahn et al., 1989; Hiort et al., 1996; Hughes et al., 2012). Many point mutations in the AR gene associated with either resistance to PCa therapeutic drugs (antiandrogens) (Sack et al., 2001,Bohl et al., 2005a, 2007) and/or with AIS have been reported (Fig. 13, B and C, table S1) (Gottlieb et al., 2012). Knowledge of the structure of the wild type (WT) protein does not allow to predict the structural and functional impact of point mutations and therefore their pathogenicity and clinical implications in patients (Nadal et al., 2017; Jiménez-Panizo et al., 2019; Wasmuth et al., 2022). Whereas mutations causing AIS occur in the germline, PCa-linked mutations are mostly somatic and occur prior to endocrine treatment or are induced by the selective pressure of antiandrogen therapies (Jiménez-Panizo et al., 2019; Estébanez-Perpiñá et al., 2021). While few mutations in PCa have been described as oncogenic or drivers (causative of the disease), most are considered passenger or silent mutations, although a contribution to PCa development and/or progression cannot be excluded (McPhaul et al., 1991; Hyytinen et al., 2002; Culig et al., 2003; Gottlieb et al., 2012).

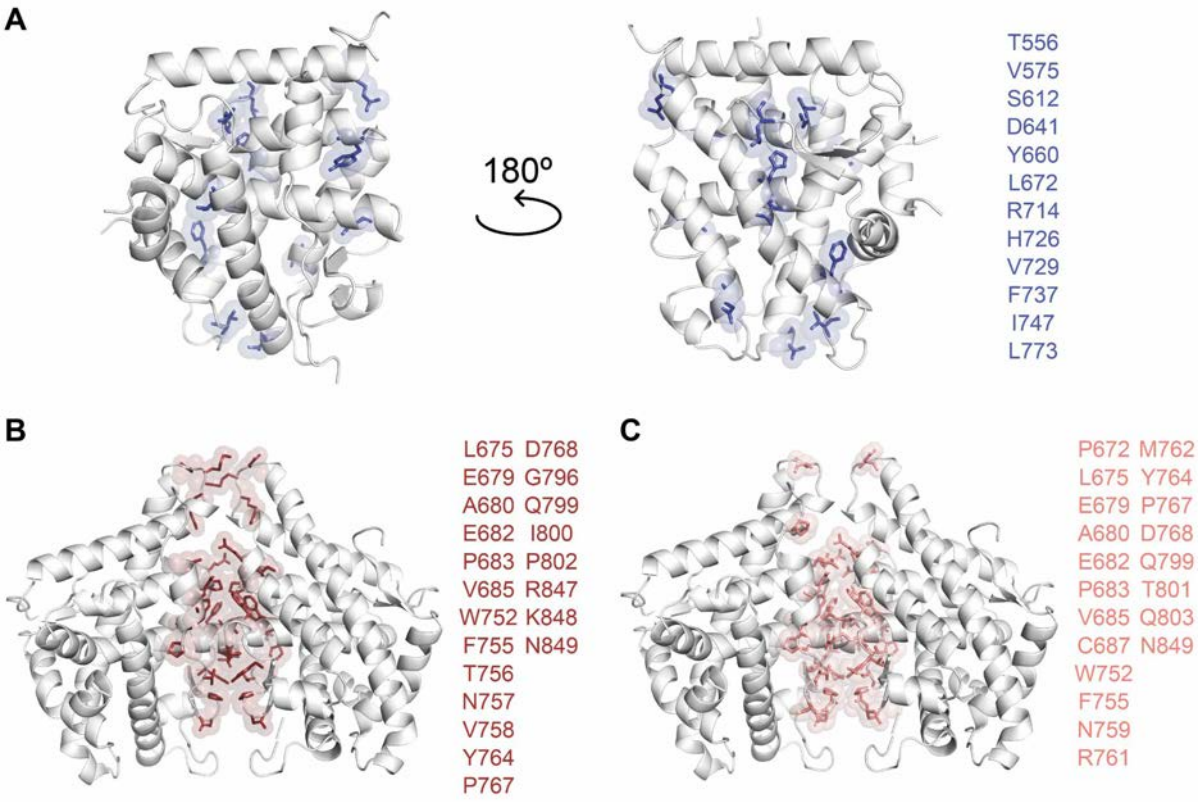

Fig. 13. Pathogenic mutations on the ligand binding domain of androgen and glucocorticoid receptors. *(A)* Mutated residues of the GR-LBD linked to GC resistance are shown as blue sticks and listed to the right. (B-C) AR-LBD homodimer with mutations link to PCa (red, B) and AIS (pink, C) highlighted as sticks and listed to the right.

To date, only three AR-LBD point-mutants have been structurally characterized out of the over 350 reported variants. These oncogenic mutations (W742L, H875Y, and T878A) map to the internal LBP and are responsible for rendering the antiandrogens cyproterone acetate, flutamide and bicalutamide ineffective, respectively. Comparison of the WT AR-LBD and these mutant structures did not reveal any overall conformational changes. However, these mutations change the volume and shape of the LBP allowing the receptor to remain active even in the presence of antagonists, thus explaining tumour escape from therapeutic control (Sack et al., 2001,Bohl et al., 2005a, 2007; Estébanez-Perpiñá et al., 2021). On the other hand, phenotypes associated with AR gene mutations in AIS patients, range from mild symptoms (mild AIS, MAIS) to partial (partial AIS, PAIS) or completely feminized phenotypes (complete AIS, CAIS) (Lubahn et al., 1989; Brown et al., 1990; Hiort et al., 1996; Radmayr et al., 1998; Hughes et al., 2012). Not surprisingly, about half of the CAIS-linked mutations map to the AR-LBD but only a few of them can be easily rationalized as directly affecting hormone binding (Gottlieb et al., 2012; Jiménez-Panizo et al., 2019).

AR-LBD pathogenic mutations outside the LBP may affect AR-dependent gene signatures through modulation of the monomer-oligomer equilibrium, accessibility of PTM sites, and/or by altering dynamic interactions with coregulators and chromatin. These processes are likely to be intricately intertwined and coupled via allosteric signalling transmission both within the AR monomer and across its dimerization interface (Shaffer et al., 2004; Nadal et al., 2017; Jiménez-Panizo et al., 2019; Yu et al., 2020; Wasmuth et al., 2022).

4.3. Glucocorticoid receptor in castration resistant prostate cancer

The best characterized mechanisms of acquired antiandrogen-resistance leading to PCa ultimate stage, castration resistant prostate cancer (CRPC), are point-mutations in the AR protein allowing non-androgens to activate AR, together with the expression of AR splice variants, *AR* gene amplification, intratumoral androgen synthesis, AR activation by ligands other than DHT, AR-mediated chromosomal rearrangements leading to the fusion of transmembrane protease serine 2 with transcriptional regulator estrogen-responsive genes (TMPRSS2-ERG) and altered epigenetic mechanisms (Chen et al., 2004; Scher and Sawyers, 2005; Knudsen and Penning, 2010; Dehm and Tindall, 2011; Centenera et al., 2013; Park et al., 2014; Robinson et al., 2015; Reig et al., 2016; Narayanan et al., 2016; Ruggero et al., 2018; Li et al., 2018; Quigley et al., 2018; Berglund et al., 2019; Karthaus and Sawyers, 2019). In addition, emerging evidence suggests that GCs may also contribute to the failure of chemotherapy and tumour progression towards CRPC (Chen et al., 1997; Moehren et al., 2008; Hartig et al., 2012; Arora et al., 2013; Claessens et al., 2014, 2017; Narayanan et al., 2016; Puhr et al., 2018; De Bosscher et al., 2020; Kumar, 2020).

In parallel to androgen deprivation therapies (ADT) and antiandrogens targeting AR, CRPC patients usually receive supplementary GCs or their precursors to prevent side effects, relieve pain during chemotherapy and further suppress adrenal androgen synthesis (Knudsen and Penning, 2010; Arora et al., 2013; Narayanan et al., 2016). In combination with mutations in *AR* arising during the progression of the disease, which lead to changes in AR ligand specificity, GCs can act as agonists for the AR. Thus, cortisol and its metabolite, cortisone, equally stimulate the growth of PCa tumoral cells and increase the secretion of prostate-specific antigen, a major biomarker for PCa diagnosis, in the absence of androgens (Zhao et al., 2000; Claessens et al., 2017). Moreover, GR can be upregulated upon ADT and atypically co-expressed with AR in prostate epithelial cells. In particular, enhanced GR expression has been observed in

enzalutamide-resistant tumour biopsies from PCa patients (Isikbay et al., 2014). Therefore, based on the high similarity between the DBDs of AR and GR (Shaffer et al., 2004), and the significant overlap in their transcriptomes (De Vos et al., 1993; Moehren et al., 2008; Claessens et al., 2017) and protein interactomes (Lempiäinen et al., 2017), it has been postulated that GR might take over the role of inhibited AR promoting a loss of antiandrogen control of proliferation and CRPC progression (Jääskeläinen et al., 2011; Arora et al., 2013; Isikbay et al., 2014; Puhr et al., 2018). Last but not least, GR–AR heterodimerization has been postulated as a potential mechanism explaining mutual inhibition of the transcriptional activity of the two receptors, leading to differential target gene expression (Chen et al., 1997; Zwart et al., 2017; Ide et al., 2018; Kanai et al., 2020; Ruiz et al., 2020; Quattrocelli et al., 2021; Timmermans et al., 2022). These differentially expressed genes might open novel therapeutic avenues in the ongoing battle against antiandrogen therapy resistance in PCa patients. However, the extent of the AR–GR physical association on a genome-wide scale in healthy prostate and in prostate cancer conditions remains to be determined (De Bosscher et al., 2020).

Objectives

The host laboratory previously presented the crystal structure of the transcriptionally active, dimeric AR-LBD (Nadal et al., 2017), later on corroborated with the low resolution, cryo-EM structures of the multidomain protein (Yu et al., 2020; Wasmuth et al., 2022). The structural analysis revealed that the dimerization interface is a hotspot for mutations identified in PCa and/or AIS patients (table S1) (Jiménez-Panizo et al., 2019). Interestingly, there was no clear-cut separation between PCa- and AIS-linked mutations, and some of these variants were linked to both conditions, albeit occurring in different developmental stages. These observations were the starting point for the major aim of this dissertation: to identify the mechanism(s) underlying the pathogenicity of disease-linked point mutants of the AR-LBD dimerization interface, based on a thorough functional and structural characterization of these AR variants. The specific goals of this project were the following:

1) To study the functionality of selected disease-linked AR mutants in living cells.
   a) To establish an appropriate cellular model for studying the cellular impact of AR variants in a background of metastatic PCa using the human cell line PC3.
   b) To assess the impact of AR mutants on cell viability, proliferation and response to standard-of-care anti-androgens compared to WT AR and parental, AR-null cell lines.
   c) To conduct transcriptomic analyses aimed at elucidating the differences between WT and mutant AR-dependent transcriptional programs.

2) To characterize the structure of AR-LBD mutants using biochemical and biophysical assays.
   a) To experimentally assess the impact of AR point mutations on folding, stability, and flexibility of isolated AR-LBD and to compare with the results of *in silico* predictions.
   b) To crystallize and resolve the crystal structures of agonist-bound AR-LBD mutants and analyse the structural rearrangements induced by point mutations both locally at the dimer interface and on the overall domain structure.
   c) To explore the coupling between the AR-LBD functional areas using molecular dynamics simulations.

3) To elucidate the impact of point mutants on the AR-LBD structure-function relationship and to identify possible pathogenic mechanism(s). We explored two major, not mutually exclusive, hypotheses:
   a) Mutations might affect the conformation of the transcriptionally active AR-LBD homodimer. To test this hypothesis, we performed thorough crosslinking – mass spectrometry analyses of WT and mutant AR-LBD homodimers formed in solution taking advantage of cysteine residues present at the dimer interface. Further, we predicted the binding energies of WT and mutant homodimers.
   b) Mutations might alter the functionality of the PTM hotspot in the AR-LBD, which overlaps with the dimerization interface. We aimed at studying the status of WT and mutant AR in living cells using phosphorylation and methylation-specific antibodies. Furthermore, we wished to study the interactions between AR and modifier enzymes both experimentally and computationally.

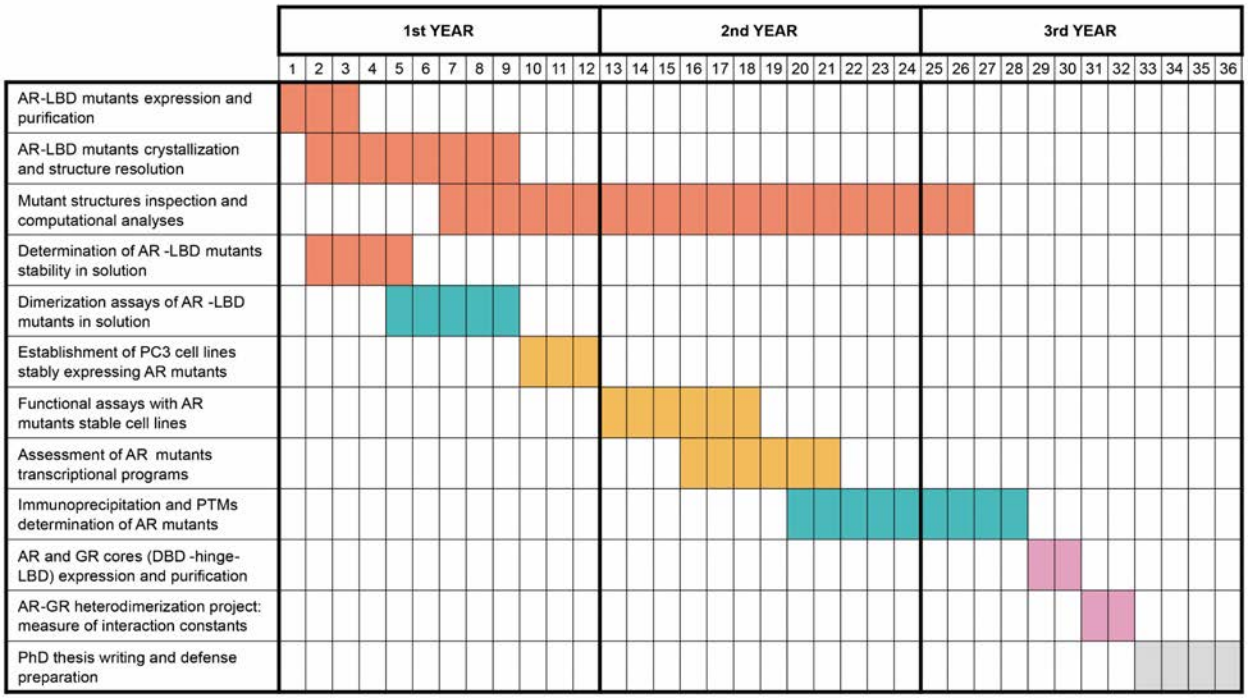

Fig. 14. Chronogram of completed objectives during the current Ph.D. thesis.

The chronogram shows the months allocated for each task, spanning from September to August each year (from 2020 to 2023). The tasks are color-coded based on whether they belong to objective 1 (yellow), 2 (red), or 3 (blue) of my main project on disease-linked AR mutants, and in purple for the current project on AR-GR heterodimerization. The time dedicated to Ph.D. thesis preparation is marked in grey.

In addition to point-mutations, other major pathogenic factors linked to the onset and progression of PCa need to be addressed to fully overcome the currently unmet clinical demands. As previously mentioned, the role of GR in the development of resistance to antiandrogens in PCa patients is not as well characterized as other molecular determinants that ultimately lead to CRPC. Important questions regarding the cross-talk between GC and androgen signalling pathways in both normal physiology and PCa remain to be resolved. Could GCs promiscuously activate AR? Can GR replace the related AR and regulate ARE-dependent transcription? Do AR and GR heterodimerize in living cells, and which structural elements form their heterodimerization interface? Is the hetero-interaction mutually inhibiting or activating? Aiming as future directions in our research enclosing the projects conducted so far in our laboratory regarding AR (Nadal et al., 2017) and GR oligomerization (Jiménez-Panizo et al., 2022), as well as the Ph.D. project hereby presented on disease-linked mutations of AR (Alegre-Martí et al., 2023), we set up to explore the involvement of AR-GR heterodimers in the pathogenesis of CRPC. Linked to this objective, we present ongoing data and future research avenues:

1) To assess the relative contribution of DBD and LBD modules of AR and GR to heterodimer formation by studying interactions of their isolated LBDs and cores (DBD-hinge-LBD).
2) To explore the interaction of AR and GR cores with their cognate AREs/GREs.
3) To characterize the heterodimerization landscape of AR and GR in solution.
4) To study AR-GR heterodimerization in living cells by means of proximity ligation assays of WT and disease-linked mutants of both nuclear receptors.
5) To solve the 3D structure of the DNA-bound AR-GR heterodimer by cryo-EM and X-ray crystallography.

Materials and methods

1. *In vivo* cell-based assays

1.1. Cell lines and plasmids

PC3, DU145, LNCaP, 22rv1 and RWPE-1 cell lines were purchased from and authenticated by ATCC (American Type Culture Collection). For maintenance, cells were cultured in RPMI-1640 or DMEM, respectively, supplemented with 10% FBS. For functional assay, cells were depleted of androgens using 10% Charcoal Stripped Serum (CSS; ThermoFisher). Site-directed mutagenesis of a commercial lentiviral-AR plasmid (pLENTI6.3/AR-GC-E2325, plasmid #85128, Addgene) was conducted to generate variants AR-F755V, AR-V758A, AR-Y764C, and AR-Q799E. For lentivirus production, HEK293-FT cells were cultured in DMEM (ThermoFisher) and the lentiviral packaging vectors psPAX2 and pCMV-VSV-G were co-transfected in 1 mg/mL polyethyleneimine (PEI) containing Opti-MEM® (ThermoFisher). After viral transduction using supernatants supplemented with 8 μg/mL polybrene, PC3 cells were incubated for 48 hours and selected with blasticidin (5 μg/mL) to generate control, WT-AR, and mutants cell lines.

1.2. Luciferase reporter assay

To assess AR transcriptional activity, a luciferase-based assay was performed in PC3 cells, which were seeded (15,000 cells/well) in white with clear flat-bottom 96-well plates (RPMI-1640 media supplemented with 10% CSS). After 24 h, 50% confluent cells were transfected using Lipofectamine™ 2000 transfection reagent (ThermoFisher), following the manufacturer's instructions. Renilla luciferase expression is controlled by a constitutive promoter for normalization (pRL-TK Renilla luciferase, Promega). On the other hand, Firefly luciferase plasmid (pARE-4X-Luciferase) contains four androgen response elements (AREs) cloned in tandem into pGL3 (Promega) (Soifer et al., 2012). Transfection was performed using 100 ng of pARE-4X-Luciferase and 10 ng of pRL-TK Renilla luciferase. Both luciferases are monomeric and neither requires post-translational processing, so they can function as genetic co-reporters immediately upon translation.

Transfection mixes were prepared in Opti-MEM® I (ThermoFisher). Six hours after transfection, the media was aspirated and replaced with RPMI-1640 media supplemented with 10% CSS. For the assay testing the transactivation level of AR mutants, cells were stimulated 24

h post-transfection for 4 h with vehicle or 20 nM DHT. For luciferase assay testing AR mutants' resistance to PCa treatment drugs, cells were treated for 30 minutes with abiraterone (40 or 80 µM) or enzalutamide (50 or 200 µM) prior to 20-nM DHT stimulation for 4 h. Luciferase activity was measured after cell incubation with the corresponding compounds with Dual-Glo® Luciferase Assay System (Promega) using a EnSpire Alpha plate reader (PerkinElmer). After background subtraction, the ratio of firefly to Renilla luciferase activity was calculated. Assays were performed in three independent experiments with five internal replicates each. GraphPad Prism 8.0 software was used to perform the statistical analyses using t-test, once confirmed the normal distribution of the values.

1.3. Cell proliferation

Colony formation. Approximately 30,000 PC3 cells were seeded in 6-well plates and grown in RPMI-1640 media supplemented with 10% CSS, in two independent replicates for each experiment. The next day (Day 1), cells were stimulated with 20 nM DHT. The stimulation was repeated every 2 days. Colonies were grown until Day 9 and stained with crystal violet (0.5% w/v in 10% EtOH and 90 % formaldehyde). After 30 minutes of incubation and several washes with water, colonies were scanned and quantified using ImageJ software (https://imagej.nih.gov/ij/). Colony formation capacity was normalized to control cells. Statistical analysis was performed using t-test, showing the differences with respect to PC3 AR-WT. For colony formation assays in other cell lines, cells were seeded based on their proliferation rate (DU145 8,000 cells/well, RWPE-1: 20,000 cells/well, 22Rv1: 30,000 cells/well, LNCaP: 80,000 cells/well). While DU145 and RWPE cells were cultured in CSS for this assay, 22Rv1 and LNCaP were cultured in FBS to prevent them from stopping proliferation. In all cases, media were supplemented with increasing concentrations of DHT.

Proliferation assays. Cells were trypsinised and counted (with trypan blue stain to discriminate living cells) every 2 days, starting at Day 3 and finishing at Day 7, the to follow time-course growth. To compare proliferation at Day 7, number of cells of each PC3 variant was normalized to their corresponding non-stimulated control (without DHT). Statistical analysis was performed using t-test, showing the differences with respect to PC3 AR-WT.

1.4. Cell viability

Approximately 4,000 cells (n=6) were seeded in 96-well plates in RPMI-1640 media containing 10% CSS. Cells were supplemented the next day with DHT combined with abiraterone acetate (Memorial Sloan Kettering Cancer Center), enzalutamide (MDV3100; Sigma-Aldrich) or apalutamide (Janssen) at different concentrations. After 72 h, cells were treated for 3 h with 10 µL/well of 5 mg/mL MTT (3-(4,5-dimethylthiazol-2-yl)-2,5-diphenyltetrazolium bromide), a yellow tetrazole that is reduced to purple formazan crystals by living cells. Formazan crystals were dissolved with 100 µL of solubilization buffer (10% SDS, 10 mM HCl) for 3 h. Plates were read at OD = 560 nm in a spectrophotometer and then the percentage of viable cells compared to the untreated wells was determined. In the case of abiraterone, the inhibitory concentration (IC50) was calculated using nonlinear regression fit in GraphPad Prism 8.0 software, normalizing to untreated cells. Statistical analysis was performed using parametric paired t-test comparing each PC3 AR-mutant regression curve versus PC3 AR-WT. Due to drug-resistance of PC3 cells against enzalutamide and apalutamide, data did not fit nonlinear regression models. To compare enzalutamide and apalutamide resistance, normalized cell viability (at 50 µM enzalutamide or 100 µM apalutamide) was expressed as a fold change percentage with respect to WT-AR. Statistical analysis was performed using a t-test, showing the differences between the PC3 WT-AR and its mutants. For viability assays of other cell lines, cells were seeded to reach confluence (90%) at the end of the experiment (DU145: 2,500 cells/well, LNCaP, 22Rv1 and RWPE-1: 5,000 cells/well). While DU145 and RWPE were cultured in CSS for this assay, 22Rv1 and LNCaP were cultured in FBS to prevent them from stopping proliferation. Media were supplemented with increasing concentrations of DHT.

1.5. Immunoprecipitation

For immunoprecipitation (IP) of FL-AR, PC3 cells were scraped off the plate and transferred to a microcentrifuge tube using Lysis Buffer (LyB) containing 50 mM Tris, 150 mM NaCl, 0.2% NP-40 and 10% glycerol supplemented with protease inhibitor cocktail (Roche), 1% phosphatase inhibitor cocktail 3 (Sigma), and 0.5% PMSF (Sigma) (in following, inhibitor mix). Samples were sonicated on ice three times for 5 sec each, amplitude 30%, and centrifuged. IP of the collected supernatant was performed using magnetic beads (Protein G and Protein A Mag Sepharose™ beads, ThermoFisher). AR XP® (Cell Signalling 5153, 1:50) and IgG (Rabbit IgG polyclonal - Isotype Control, Abcam, 1:50) antibodies were pre-incubated for 1 h with 25 µL of

A+G beads (1:1) at 4 ºC and cell lysates (1.6 mg) were pre-cleared with 5 µL of A+G beads (1:1). Beads were removed from the pre-cleared lysates and then transferred into AR or IgG tubes for IP at 4 ºC overnight in a rotating wheel. Afterwards, beads from the negative control (IgG tubes) and the immunoprecipitated samples were washed twice with LyB and 5 times with LyB lacking NaCl. Finally, beads were eluted with 70 µL of Laemmli buffer containing 10% β-mercaptoethanol for 5 minutes at 98 ºC and samples were analysed by Western blotting (WB).

For WB analysis of total protein extracts, PC3 cells were lysed with 1× buffer of radio-immunoprecipitation assay (RIPA, 10 mM Tris-HCl, pH 7.5, 0.1% SDS, 1% Triton X-100, 1% deoxycholate sodium salt, 0.15 M NaCl, 1 mM EDTA) supplemented with inhibitor mix. Proteins (30 µg per lane) were resolved by Sodium dodecyl-sulfate polyacrylamide gel electrophoresis (SDS-PAGE) and transferred onto a PVDF membrane (GE Healthcare, Amersham), which was blocked with PBS-T (phosphate-buffered saline and 0.1× Tween-20) containing 5% Bovine Serum Albumin (BSA; Sigma-Aldrich). Primary antibodies for WB were incubated at 4 ºC overnight: anti-AR (Abcam, 1:500), anti-mono methyl Arginine (R*GG) (Cell Signalling, 1:500) and anti-rabbit IgG HRP-linked antibodies (Cell Signalling, 1:10.000). HRP-conjugated secondary antibody was incubated for 1 h at room temperature. ECL Plus WB Detection Kit (ThermoScientific) was used for detection in a ChemiDoc MP Imaging System (BioRad).

1.6. Transcriptomic analysis

Approximately 500,000 PC3 cells were seeded in 10-cm plates in RPMI-1640 media supplemented with 10% CSS (hormone-depletion conditions) (n=3). After 48 h, cells were stimulated with 20 nM DHT for 4 h and collected. RNA was purified using the Maxwell® RSC simply RNA Tissue Kit (Promega), following manufacturer's instructions. RNA quality control, library preparation and 2x100 bp, >25 M PE reads, stranded mRNA-sequencing (RNA-seq) was performed using an Illumina HiSeq2500 platform. RNA-seq lanes were joined and reads were mapped with STAR (Dobin et al., 2013) to the primary assembly of the human reference genome (GRCh38) in conjunction with the complete gene annotation file available in GENCODE (Frankish et al., 2019). The gene read count was performed with the STAR parameter-quantMode GeneCounts. Results indicate on average 90% of reads uniquely mapped in all samples; around 80% of the reads are overlapping genes.

We used the IDEAmex service (Jimenez-Jacinto et al., 2019) to perform differential expression analysis using DESeq2 (Love et al., 2014) and limma methods (Ritchie et al., 2015). The count matrix was filtered considering 5 counts per million at least. To define differentially expressed genes (DEGs) we considered an absolute log2 fold change ≥ 1 and an adjusted p-value or false discovery rate (FDR) ≤ 0.05. The following differential expression analyses were performed: PC3 control versus WT AR, and point mutants F755V, V758A, Y764C and Q799E, as well as WT AR versus PC3, F755V, V758A, Y764C and Q799E. To identify the intersection of genes differentially expressed between contrasts we used the function UpSet from the package Complex heatmaps (Gu et al., 2016). Volcano plots were generated using the Enhanced Volcano R package on DESeq2. AR targets were recovered from DoRothEA (Garcia-Alonso et al., 2019).

For principal component analysis (PCA), raw counts were filtered to have at least three samples with 5 counts per million at least. Counts were transformed using the VST function (Anders and Huber, 2010). The PCA was calculated with the plotPCA function in DESeq2 and visualized with the ggplot2 package. For the VST data, we calculated the Euclidean distances between samples using the R function dist. We plotted the sample distance matrix with the rows/columns arranged by the distances, manually providing sampleDists to the clustering distance argument of the pheatmap function.

1.7. Enrichment analysis

Gene set enrichment analysis (GSEA) (Subramanian et al., 2005) was performed to assess the enrichment of the different mutant AR signatures against a reference signature of differentially expressed genes between control versus WT AR ranked according to the log2 fold change value and the clusterProfiler R package (Wu et al., 2021) on DESeq2 results. GSEA was also used to ascertain the enrichment in selected gene sets that match against the search for “prostate cancer” in Molecular Signature Database (MSigDB) or the entire Biological Pathways collection in the Kyoto Encyclopaedia of Genes and Genomes (KEGG) database. We performed GSEA against prostate cancer malignant signatures FOXM1, CENPF, and FOXM1+CENPF for each DESeq2 result between PC3 control versus WT AR, F755V, V758A, Y764C, or Q799E. Signatures recovered are defined as top 200 up- and downregulated DEGs (Aytes et al., 2014).

Transcription factor activity was estimated with the DoRothEA R package (Garcia-Alonso et al., 2019) using results from the limma package (Ritchie et al., 2015) between PC3 versus WT, F755V, V758A, Y764C, or Q799E AR. We estimated activity for pathways involved in cancer with pathway responsive genes (PROGENy) (Schubert et al., 2018). DGE results of PC3 control versus WT, F755V, V758A, Y764C, or Q799E AR using as input the list of genes ranked by the log2 fold change.

1.8. Real time qPCR

For qPCR, approximately 300,000 PC3 cells were seeded in 6-well plates in duplicates in RPMI-1640 media supplemented with 10% FBS. After 48 h, 70% confluent cells were hormone-depleted by using RPMI-1640 media supplemented with 10% CSS. After 24 h, cells were stimulated with 20 nM DHT for 4 h and collected. RNA was extracted using TRIzol reagent according to the manufacturer's instructions. After DNA digestion (DNAse, Amplification Grade, Invitrogen), cDNA was obtained using High-Capacity cDNA Reverse Transcription Kit (Applied Biosystems). Total cDNA was diluted 1:10 and quantitative PCR was performed using PowerUp SYBR Green Master Mix (Applied Biosystems) and plates were read with a LightCycler 480 (Roche). Results were normalized to GADPH expression level, and each sample was quantified in triplicate. Relative quantification considers GAPDH internal standard and control conditions (PC3-CNT without DHT) to normalize and compare samples. GraphPad Prism 8.0 software was used to perform the statistical analyses using t-test, which confirmed the normal distribution of the values. The following RT-qPCR primers were used to amplify:

- GAPDH: 5'-CATCTTCCAGGAGCGAGATC; 5'-GCTGTTGTCATACTTCTCATGG.
- TMPRSS2: 5'-CCTGACGCAGGCTTCCAAC; 5'-GGTCAAGGTGATGCACAGTG.
- FKBP5: 5'-GCGAAGGAGAAGACCACGACAT; 5'-TAGGCTTCCCTGCCTCTCCAAA.
- FOXA1: 5'-GCAATACTCGCCTTACGGCT; 5'-TACACACCTTGGTAGTACGCC.

1.9. Proximity ligation assay

Proximity ligation assays (PLA) were performed using reagents from the Naveniflex MR Kit (Navinci) essentially as previously described (Poulard et al., 2020). Briefly, cells were seeded onto coverslips in 12-well plates, fixed in methanol for 2 min, and then washed twice in 1× PBS. Fixed cells were stored at 4 °C for subsequent staining or saturated with the blocking solution for 1 h at 37 °C. All further steps were performed at this temperature. Cells were then incubated with different pairs of primary antibodies: (1) anti-AR (Cell Signaling #5153) and anti-PRMT5 (Santa Cruz sc-376937), (2) anti-AR (Santa Cruz sc-7305) and anti-monomethylated arginines (Cell Signaling #8711), or (3) anti-AR (Santa Cruz sc-7305) and anti-symmetrically dimethylated arginines (Cell Signaling #13222) for 1 h. After three washes in TBS-T, mouse and rabbit secondary antibodies conjugated with complementary oligonucleotides (‘Navenibodies’) were added and incubated for 1 h. Again, cells were washed three times in TBS-T and subsequently incubated with reaction reagents A, B and C to activate the oligos, to allow the interaction of Navenibodies that are in close proximity and the DNA hybridization and amplification of the proximity fluorescent probes (ATTO647), respectively. Finally, cells were washed 2 min in 1x TBS and incubated for 15 min with 0.1x TBS at room temperature. The samples were mounted using Duolink in situ mounting medium containing DAPI (Sigma #DUO82040). The edges of the coverslips were sealed using nail polish. Slides were then stored in the dark at 4 °C for a short-term or visualized under a Zeiss Fluorescence Microscope, and interactions were counted for at least 300 cells using ImageJ software (Schindelin et al., 2012). In some experiments, PRMT5 was downregulated using ON-TARGETplus Human SMART-pool siRNAs (Dharmacon #L-015817-00-0005). The unrelated siRNA ON-TARGETplus Non-targeting Control Pool (Dharmacon D-001810-10-05) was used as control in these siRNA experiments. Alternatively, PRMT5 activity was blocked by a 48 h pre-incubation of cells with a specific inhibitor, GSK595 (0.5 µM; Sigma). Cells incubated with the same volume of dimethyl sulfoxide (DMSO) were used as reference in these experiments.

2. Biochemical and biophysical experiments

2.1. Cloning and mutagenesis

Recombinant ancient variant, ancGR2-LBD (amino acids 529-777 of the human receptor) was cloned into a pMALCH10T vector to allow expression of GR-LBD as a fusion protein with an N-terminal maltose-binding protein (MBP) and a 6x histidine tag. Recombinant AR- and ancGR2-cores (amino acids 551-920 and 418-777, respectively) were cloned into a Pet28a vector as a fusion protein with an N-terminal 6x histidine tag in the case of AR core, and an N-terminal MBP and a 6x histidine tag in the case of GR core. Recombinant human AR-LBD (amino acids 641-920) was cloned into a modified pGEX vector. The resulting fusion protein consists of a glutathione S-transferase (GST) followed by a 6x histidine tag. In all cases, a *Tobacco etch* virus (TEV) cleavage site is also included before the corresponding sequence of the proteins of interest. The pGEX vector template encoding WT hAR-LBD was mutated using the Q5® Site-Directed Mutagenesis Kit (New England Biolabs) to generate AR-LBD mutants with the following primers:

- Y764C: 5'-CAGGATGCTCTgGCTTCGC, 5'- GAGTTGACATTGGTGAAGGATCG.
- V758A: 5'- TTCACCAATGcCAACTCCAGGATGCTC, 5'- GGATCGCCAGCCCATGGC.
- F755V: 5'- CTGGCGATCCgTCACCAATGT, 5'- CCCATGGCAAACACCATGAGC.
- F755L: 5'- CTGGCGATCCTTaACCAATGT, 5'- CCCATGGCAAACACCATGAGC.
- Q799E: 5'- TGGATGGCTCgAAATCACCCC, 5'- AACTCTTGAGAGAGGTGC.

2.2. Recombinant proteins expression and purification

Protein expression. The different constructs were transformed into BL21 *E. coli* cells. 1 µL of plasmid and 50 µL competent BL21 cells were treated for 45 s at 42 ºC following a standard heat shock protocol. Then 1 mL LB media was added, and the cells were incubated shaking at 37 ºC at the thermo-mixer for more than 1 h. Cells were plated on LB-agar plates containing 1 mM ampicillin (colonies transformed with LBD constructs) or 1 mM kanamycin (colonies transformed with core constructs). The plates were incubated O/N at 37 ºC. Colonies were picked and cultured 4 h shaking at 37 ºC and 200 rpm in 30 mL LB media containing 1 mM ampicillin or kanamycin. 1 L LB media supplemented with 1 mM ampicillin or kanamycin was inoculated with the pre-culture and incubated at 37 ºC and 200 rpm until an optical density at 600 nm between 0.6 and 0.8 was reached. After 1 h of cooling down to 4 ºC, cultures were

supplemented with 50 µM DHT (AR constructs) or dexamethasone (DEX, GR constructs) and protein expression was induced with 1 mM Isopropyl β-D-1-thiogalactopyranoside. Cultures inoculated with AR-LBD or GR-LBD were incubated O/N at 16 ºC and 200 rpm, those expressing AR core were incubated O/N at 18 ºC and GR core cultures were incubated both during 4h at 32 ºC and O/N at 16 ºC to compare the results and start optimizing the protocol.

Cell lysis and protein purification. Cells were harvested by centrifugation at 4000 rpm and 4 ºC during 30 min. Cell pellets were resuspended into 20 mL of lysis buffer, which is composed of the equilibration buffer (50mM Tris, 10 mM imidazole, 300mM NaCl, 10% Glycerol, 1mM dithiothreitol (DTT), 50 µM DEX or DHT, pH 8.0) supplemented with DNAase I and the complete protease inhibitor cocktail (Roche). Cells were lysed by sonication on ice for 4 min with an amplitude of 30% in 1 s pulse on/1 s pulse off intervals. The lysed cells were finally centrifuged at 4 ºC for 30 min at 20,000×g. Recombinant fusion proteins were purified to homogeneity by immobilized metal ion affinity chromatography (IMAC) using standard chromatographic procedures. The eluate of this first chromatography step was concentrated, treated with TEV protease to cleave the MBP-LBD linker, dialyzed to remove excess imidazole, and subjected to a second IMAC step. Chromatography steps were monitored by SDS-PAGE. Finally, protein concentrations were determined with Bradford assays. Details of the purification protocol are given below.

First IMAC step. Proteins were purified using 5-mL HisTrap™ HP columns prepacked with Ni Sepharose High Performance resin (HisTrap HP), with a flux of 1 mL/min and at 4 ºC. Columns were equilibrated with 5 column volumes of equilibration buffer. Then the lysate of the culture was filtered and immediately pump-loaded into the HisTrap column. The column was washed with the equilibration buffer with an increased concentration of 50 mM Imidazole to elute all proteins non-specifically bounded to the column. Finally, specifically bound proteins of interest ware eluted in 5 column volumes of the same buffer containing 300mM imidazole.

Tag cleavage and dialysis. Fractions containing purified fusion proteins were pooled and one aliquot of TEV protease (Sigma) at 1 mg/ml was added. The reaction mixture was put in a dialysis bag and dialyzed O/N at 4 ºC against 2 L of dialysis buffer (20mM HEPES, 25mM imidazole, 150mM Li_2SO_4, 10% glycerol, 1mM DTT, 50 µM DEX or DHT, pH 7.2). In this manner, cleavage of the GST-histidine, MBP-histidine and histidine tags and removal of excess imidazole were simultaneously achieved.

Second IMAC step. HisTrap™ HP columns were washed and equilibrated with the dialysis buffer. The reaction mixture (after TEV, AT, fraction) was loaded onto the column, so that tags containing histidine residues attached to the column while proteins of interest eluted. Column was then thoroughly washed with dialysis buffer with an increased concentration of 75 mM Imidazole, to ensure all protein of interest is eluted. Hence, flow-through (FT) and wash (W) fractions containing the desired protein were pooled and concentrated using Amicon Ultra 4/15 Centrifugal filters (Merck) and kept at -20 ºC for further experiments. Finally, specifically bound histidine-tag proteins were eluted (E fraction) with the same buffer containing 150 mM Imidazole and discarded. Columns were stored filled up with 20% ethanol.

Gel electrophoresis under denaturing conditions (SDS-PAGE). Samples from protein expression and purification steps were routinely analysed using 12% SDS-polyacrylamide gels. Protein samples were mixed with 6× SDS-loading buffer, heated at 95 ºC for 5-10 min and loaded into the gels. Gels were run for 45 min at 200 V. After electrophoresis, gels were stained with Coomassie Brilliant Blue for 5 minutes and finally bleached with buffer containing 10% methanol and 10% acetic acid for 1 h.

2.3. Differential scanning fluorimetry

Thermofluor experiments were performed in an iQ5 Multicolor Real-Time PCR Detection System (BIO-RAD) using 96-well plates (Hard-Shell® High-Profile Semi-Skirted PCR Plate, BIO-RAD) and a 25 µL total volume for each reaction essentially as previously described (Gustafsson et al., 2020). Melting curves were acquired from eight replicates to determine the average Tm. AR samples (0.5 mg/mL) were prepared in 20 mM HEPES, pH 8.0, 150 mM Li_2SO_4, 10% glycerol, 50 mM imidazole, 1 mM DTT, 50 µM DHT and centrifuged 5 min at 14,000 rpm. SYPRO Orange dye (Sigma-Aldrich) was firstly prepared at 80× in the protein buffer, starting from a 5000× commercial dilution. The final concentration of SYPRO Orange dye in each 25 µL reaction was 5×. The plates were sealed with optical quality sealing film (Microseal® B Seals, BIO-RAD) and centrifuged at 2,000g for 30 s. Samples were equilibrated for 60 s and analysed using a linear gradient from 16 to 95 ºC in increments of 1 ºC/min, recording the SYPRO orange fluorescence throughout the gradient in the iQ5 Optical System Software 2.0. Values were fitted using in the online tool JTSA with the Boltzmann four-parameter logistic equation, and the calculated fluorescence shift midpoints were compared via unpaired t test for equal variances in GraphPad Prism 8.

2.4. Limited proteolysis

Samples of recombinant WT AR-LBD and all studied mutants were buffered-exchanged into 25 mM Tris, pH 7.6, 10 mM $CaCl_2$, 1 mM DTT using a PD-10 column and concentrated to 0.5 mg/mL using a centrifugal filter device. Sequencing-grade Arg-C protease (Clostripain, P5214 Abnova) was added (50/1 w/w, protein/protease) and mixtures were incubated at 37 ºC with shaking. Aliquots of the proteolytic reactions were taken at indicated times, immediately mixed with reducing Laemmli buffer and heated at 95 ºC for 5 min. Reaction products were separated on SDS-polyacrylamide gels and stained with Coomassie Brilliant Blue.

2.5. Crystallization and structure determination

Purified, concentrated DHT-bound AR-LBD mutants (F755L, F755V, V758A, Y764C, and Q799E) were combined with a 2-fold molar excess of UBA3 peptide and incubated for one hour at RT. Drops of the AR-LBD mixture were equilibrated against 0.1 M Tris-HCl, pH 8.0, containing either 0.2 M sodium chloride, 2.0 M ammonium sulphate or 0.1 M ammonium acetate, 2.5 M sodium formate using the sitting drop vapor-diffusion method. Diffraction data were collected at 100 K at the XALOC beamline of the ALBA-CELLS synchrotron (https://www.cells.es/en/beamlines/bl13-xaloc) and processed with MOSFLM (http://www.mrc-lmb.cam.ac.uk/harry/mosflm/) and CCP4 (http://www.ccp4.ac.uk/). The crystal structures were solved and refined using MOLREP (https://www.ccp4.ac.uk/html/molrep.html#references), REFMAC5 (https://www2.mrc-lmb.cam.ac.uk/groups/murshudov/content/refmac/refmac.html) and COOT (https://www2.mrc-lmb.cam.ac.uk/personal/pemsley/coot/) from the CCP4 package. Crystal packing was analysed using PISA (http://www.ebi.ac.uk/), model quality was assessed with MolProbity (http://molprobity.biochem.duke.edu/), and structure figures were prepared with PyMOL (http://www.pymol.org).

2.6. Mass spectrometry analysis of protein dimerization in solution

Crosslinking experiments. Purified recombinant WT and mutant AR-LBD proteins were incubated with 4-fold molar excess of bis(maleimido)ethane (BMOE) or 1,4-bis(maleimido)butane (BMB) crosslinkers for 2 hours at 37 ºC following the manufacturer's instructions. Samples of the reaction mixtures were boiled in the presence of reducing Laemmli buffer and resolved by SDS-PAGE.

Y764C covalent dimerization in solution. Purified recombinant Y764C (3 mg/mL) was incubated in 20 mM HEPES, pH 8.0, 150 mM Li_2SO_4, 10% glycerol, 50 mM imidazole, 1 mM DTT, 50 µM DHT or in the same buffer without DTT after desalting using a PD-10 column (GE Healthcare). Y764C samples incubated under reducing and non-reducing conditions were boiled in the presence of reducing Laemmli buffer and resolved in a 10% SDS-polyacrylamide gel.

Nano-LC-MS/MS experiments. Bands corresponding to dimeric, BMB-crosslinked, or covalent-bound Y764C were excised from the gels and subjected to in-gel digestion following standard protocols. Briefly, excised bands were reduced (10 mM DTT) in 50 mM bicarbonate buffer, pH 8.0, for 45 min at 56 ºC, alkylated (50 mM iodoacetamide in 50 mM ammonium bicarbonate buffer for 30 min at 25 ºC) and digested with trypsin overnight at 37 ºC in 100 mM ammonium acetate buffer, pH 8 (Sequencing-grade endoproteases were from Promega). Following procedures have been performed as previously published (Jiménez-Panizo et al., 2022). Tryptic peptides were diluted in 1% formic acid (FA) and loaded onto a 180 µm x 20 mm C18 Symmetry trap column (Waters) at a flow rate of 15 µl/min using a nanoAcquity Ultra Performance LCTM chromatographic system (Waters). Peptides were separated using a C18 analytical column (BEH130 C18, 75 mm x 25 cm, 1.7 µm; Waters) with a 120-min run, comprising three consecutive linear gradients: from 1 to 35% B in 100 min, from 35 to 50% B in 10 min and from 50 to 85% B in 10 min (A= 0.1% FA in water, B= 0.1% FA in CH_3CN). The column outlet was directly connected to an Advion TriVersa NanoMate fitted on an LTQ-FT Ultra mass spectrometer (Thermo), which was operated in positive mode using the data-dependent acquisition mode. Survey MS scans were acquired in the FT-ICR cell with the resolution (defined at 400 m/z) set to 100,000. Up to six of the most intense ions per scan were fragmented and detected in the linear ion trap. The ion count target value was 1,000,000 for the survey scan and 50,000 for the MS/MS scan. Target ions already selected for MS/MS were dynamically excluded for 30 s. Spray voltage in the NanoMate source was set to 1.70 kV. Capillary voltage and tube lens on the LTQ-FT were tuned to 40 and 120 V, respectively. The minimum signal required to trigger MS to MS/MS switch was set to 1,000 and activation Q value was set at 0.25. Singly charged precursors were rejected for fragmentation.

2.7. Surface plasmon resonance (Biacore)

Surface plasmon resonance (SPR) is a sensitive tool for studying protein interactions with various analytes in solution (analytes defined in this technique as other proteins, DNA, peptides, or chemical scaffolds of varied sizes). Briefly, one of the interaction partners, the "ligand", is immobilized to the surface of a sensor chip and then various concentrations of the interacting molecule (the "analyte") are passed over (Fig. 15). Increases in surface density upon ligand-analyte interaction result in changes of the refractive index. Analysis of the generated binding curves ("sensorgrams") allows monitoring the binding process in real time and measurement of association (ka) and dissociation rates (kd), from which the equilibrium dissociation constant or affinity constant (K_D) can be calculated (Fig. 15).

In the current investigations, SPR analyses were performed at 25 ºC in a BIAcore T200 instrument (GE Healthcare). Highly purified, DEX- and DHT-bound recombinant GR and AR LBD and core modules were diluted in 10 mM sodium acetate, pH 5.0, and directly immobilized on CM5 chips (GE Healthcare) by amine coupling at three different densities (measured as resonance units, RUs) to perform the following sets of experiments:

1) Protein – DNA: GR and AR core modules were immobilized at 300-600 RUs. Sequences of duplex DNAs used in these assays are GRE-1 (5'-AAAAACAGAATGTTCA), ARE-1 (5'-TAGCGTGGCCAGAACATCATGTTCTCCGGTGCGAT), and ARE-2 (5'-CCAGAACATCAAGAACAC). The running buffer was 10 mM HEPES, 150 mM NaCl, 0.05% Tween-20, 10 mM ZnCl, and 10 mM Na molybdate, pH 3.00 – to avoid repulsion of between negatively charged dextran matrix of the chip and the DNA oligos.
2) Protein – protein interaction: GR and AR LBD and core modules were used both as analytes and as ligands, immobilized at densities around 100 RUs. The running buffer was 50 mM HEPES, 50 mM Li_2SO_4, 5% glycerol, 1 mM DTT, 0.05% Tween-20, and 5 µM DEX or DHT, pH 7.3.
3) Protein – peptide interaction: synthetic peptides corresponding to the AR-LBD non-canonical dimer interface were designed and custom-synthesised. Peptides were named indicating the first and last residue and the peptide length: WR10 (WRSFTNVNSR), WY13 (WRSFTNVNSRMLY) and CC18 (CQPIFLNVLEAIEPGVVC). For these assays, GR and AR LBD and core modules were immobilized at densities between 3000-6000 RUs. The running buffer was 1x PBS, 5% DMSO, 0.05% Tween-20.

Sensorgrams were analysed with the BIAcore T200 Evaluation software 3.0 and fitted according to the Langmuir 1:1 and multisite affinity models. Kinetics analysis was also conducted to calculate the half-life of the complexes (t1/2) as follows: $t_{1/2} = \ln(2)/k_d$.

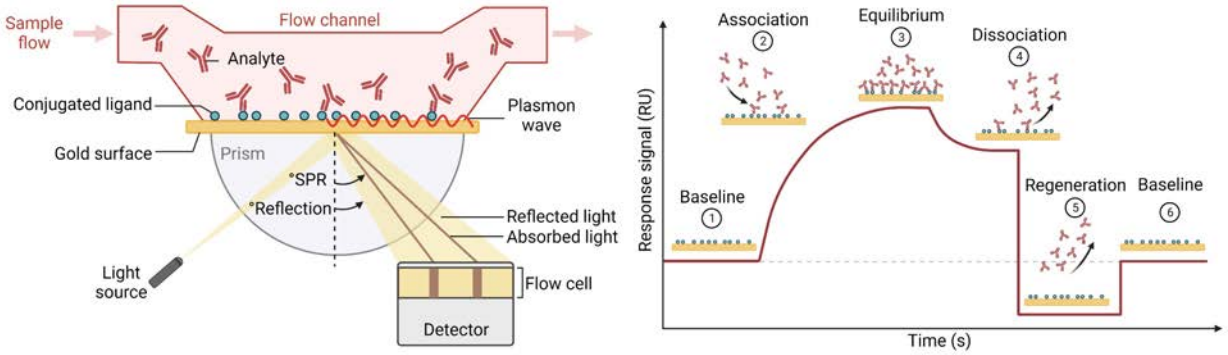

Fig. 15. Schematic representation of surface plasmon resonance experiments.

One binding partner, referred to as the ligand (blue sphere), is immobilized on a gold surface and the other binding partner, referred to as the analyte (red Y-shaped), flows across the sensor-chip surface. Changes in the refractive index with time are monitored. The generated sensorgrams (Response versus Time plot to the right) can be evaluated to derive kinetic and affinity constants.

Created with BioRender.com

3. *In silico* computational analyses

3.1. Docking experiments and dimeric interface analysis

The dimerization energy of the AR-LBD dimeric conformation found in the X-ray structure (PDB 5JJM, chains B:C) as well as that of the modelled mutant dimers (built by superimposition of the mutant monomeric structures onto the corresponding subunits of the crystallographic dimer) was computed with the pyDock bindEy module (Cheng et al., 2007) based on energy terms previously optimized for rigid-body docking. The pyDock binding energy is basically composed of Lennard-Jones van der Waals, Coulombic electrostatics, and implicit desolvation based on accessible surface area with atomic solvation parameters optimized for protein-protein interactions (Fernández-Recio et al., 2004). To avoid excessive penalization from possible clashes derived from the rigid-body approach, van der Waals total contribution was weighed by a factor of 0.1. For the same reason, van der Waals and electrostatic values per inter-molecular atom pair were restricted to a maximum of +1.0 kcal/mol, or to a range between -1.0 and +1.0 kcal/mol, respectively, BSA values of WT and mutants' dimers were computed as the difference in the accessible surface area between the dimer and the unbound molecules, using ICM-Browser (www.molsoft.com). In addition, homodimeric docking models of WT AR-LBD and

its mutants were built using pyDock docking and scoring method (Cheng et al., 2007). First, protein models were prepared by removing all cofactors and heteroatoms, and missing side chains were modelled with SCWRL 3.0 (Cheng et al., 2007). Then, the Fast Fourier Transform (FFT)-based docking programs FTDock (with electrostatics and 0.7 Å grid resolution) (http://www.sbg.bio.ic.ac.uk/docking/ftdock.html) and ZDOCK 2.1 (https://zdock.umassmed.edu/) were used to generate 10,000 and 2,000 rigid-body docking poses, respectively. These were merged in a single pool for subsequent pyDock scoring, as detailed above. From the resulting docking poses, normalized interface propensity (NIP) values were obtained for each residue with the built-in patch module of pyDock, implementing the pyDockNIP algorithm (Grosdidier and Fernández-Recio, 2008). A NIP value of 1 indicates that the corresponding residue is involved in all predicted interfaces of the 100 lowest energy docking solutions, while a value of 0 means that it appears as expected by random chance. Finally, a negative NIP value implies that the residue appears at the low-energy docking interfaces less often than random. Usually, residues with NIP $\geq$ 0.2 are considered as hotspot residues. Additionally, optimal docking areas (ODA) was obtained by computing surface patches with optimal desolvation energy generated from each surface residue (Fernandez-Recio et al., 2005). Residues with low ODA values, usually less than -10.0 kcal/mol, indicate regions with favourable desolvation energy upon interaction with a partner protein. Residues from Lys845 to Ser851 were removed from WT for all energy and docking calculations, for consistency in the comparative analysis, since these residues are missing in all mutant structures. Additional docking experiments were performed using the LZerD protein docking web server (https://lzerd.kiharalab.org/) with the structure of a hetero-tetrameric $(PRMT5)_2 \cdot (MEP50)_2$ complex as receptor (PDB 7L1G), and the current structure of AR-LBD(Q799E) as ligand. Solutions that satisfied the constraints (distance of Arg761-flanking residues to the PRMNT5 catalytic machinery < 6 Å) were visually inspected.

3.2. Estimated energetic impact of AR point mutations

We estimated the impact of the studied mutations on the overall protein stability with the FoldX empirical force (http://foldxsuite.crg.eu/) (Guerois et al., 2002). Ten iterations were conducted for each mutation, and later averaged. Computed free energy differences between mutant and WT proteins (estimated $\Delta\Delta G$) < 1 kcal/mol were considered not significant, those between 1 and 2, 2 and 4, and > 4 kcal/mol as slightly, mildly, and strongly destabilizing, respectively. (FoldX has an estimated error of ~0.7 kcal/mol).

3.3. Statistical coupling analysis

Following previously published protocol (Jiménez-Panizo et al., 2022), (DOI: 10.5281/zenodo.7274365), we identified two different sectors by using the SCA5 8/2011 version (Subramanian et al., 2005) and the updated version pySCA (Lockless and Ranganathan, 1999; Rivoire et al., 2016) with 880 alignments. The stability of the identified sectors was assessed with a statistical test based on hypergeometric calculations of the groups of residues belonging to given sectors between pairs of alignments. P-values were adjusted using FDR. Next, specific residues from the significant sectors were extracted and selected according to their rank.

3.4. Molecular dynamic simulations

System preparation. The crystal structure of monomeric AR-LDB·DHT (PDB 1T7T) was used to represent the WT receptor, while the X-ray mutant structures used were those determined in this work. In a first step, hydrogens were added to all protein residues in their corresponding protonation states at pH 7.0, and side chain orientations were adjusted using the Protein Preparation Wizard workflow included in Maestro v.10.0 software package (https://www.schrodinger.com/products/maestro). Missing residues in all the mutant structures (Lys845 to Ser851), were obtained from the WT structure by superposition. The parameters for DHT were obtained using the general amber force field (gaff2) (Wang et al., 2004) and charges were generated with the restrained electrostatic potential (Bayly et al., 1993) at the HF/6-31G(d,p) level using the Antechamber module of AMBER18 (https://ambermd.org/). Next, each system was placed in a cubic periodic box filled with Optimal Point Charge water molecules (Izadi et al., 2014), setting a minimum distance of 15 Å between the solute and the box walls. Water molecules closer than 1.0 Å to any complex atom were removed. Then, counter ions were added to neutralize the system following a grid-shaped procedure for mapping the electrostatic potential surface. All calculations were done using the ff19SB force field (Tian et al., 2020) with a cut-off of 10 Å for noncovalent interactions, applying the PME (Particle Mesh Ewald) method (Darden et al., 1993) for the treatment of the electrostatic interactions.

Molecular dynamics (MD). Before starting the molecular dynamics calculations, the structures were first relaxed to eliminate possible steric clashes with a 5000-steps minimization procedure using the steepest descent method. Then, the systems were stepwise heated to 300 K at a rate of 30 K every 20 ps, fixing the main atoms of the proteins with a harmonic positional

restriction of 5 kcal/mol·Å-2, using the Langevin thermostat algorithm with a collision frequency of 3 ps−1 under the NVT ensemble (heating). Subsequently, 100-ps simulations were performed at constant pressure (NPT ensemble) keeping fixed the main atoms with the same harmonic positional restrictions for density equilibration (density equilibration). Finally, conventional MD of 1 μs for all the mutants and 1.2 μs for the WT protein were carried out within the NVT ensemble in quadruplicate to increase the conformational sampling of the system (Perez et al., 2016). The ParmEd program was used to introduce hydrogen mass repartitioning to allow integration times of 4 fs (Hopkins et al., 2015) and the SHAKE algorithm (Ryckaert et al., 1977) was employed to constrain the bonds involving the hydrogen atoms (https://parmed.github.io/ParmEd/html/index.html).

Root-Mean Square Deviation (RMSD) and Root-Mean Square Fluctuation (RMSF). RMSD along the simulation time was computed using the CPPTRAJ module from AMBER18 (https://amber-md.github.io/cpptraj/CPPTRAJ.xhtml) for all the MD trajectories to assess the structural stability of the systems along time. RMSD was computed with respect to all the Cα atoms, using the not minimized X-ray structure of the WT as reference for all the systems. The resulting superimposed trajectories were employed to calculate the RMSF for each of the residues of the protein to obtain information about their conformational flexibility.

Residue pair distance (RPD). To quantify the effect of the different mutations on the distances between AR residue pairs, we implemented the algorithm described by Vatansever and co-workers (Vatansever et al., 2019). This algorithm is based on the concept of first coordination shell defined in the aussian network model but extended to a second coordination shell with a radius of ~9.1 Å to better account for the contribution of non-bonded pairs (Atilgan et al., 2004). Briefly, for each Cα,i atom the time-averaged distance to any other Cα,j atom that belongs to its second coordination shell was obtained for the WT ($\overline{\boldsymbol{R}}_{\boldsymbol{ij,WT}}$) and the studied mutants ($\overline{\boldsymbol{R}}_{\boldsymbol{ij,mut}}$). Then, the difference ($\Delta\overline{\boldsymbol{R}}_{\boldsymbol{ij}}$) between $\overline{\boldsymbol{R}}_{\boldsymbol{ij,WT}}$ and $\overline{\boldsymbol{R}}_{\boldsymbol{ij,mut}}$ was calculated, where $\Delta\overline{\boldsymbol{R}}_{\boldsymbol{ij}} = \overline{\boldsymbol{R}}_{\boldsymbol{ij,WT}} - \overline{\boldsymbol{R}}_{\boldsymbol{ij,mut}}$. To this end, we first calculated for all residues the changes in the time-averaged distance between residue i and all j residues that belong to its second coordination shell for the WT structure ($\overline{\boldsymbol{R}}_{\boldsymbol{ij,WT}}$) and for all mutants ($\overline{\boldsymbol{R}}_{\boldsymbol{ij,mut}}$). The obtained $\Delta\overline{\boldsymbol{R}}_{\boldsymbol{ij}}$ differences indicate the degree of distortion introduced by a specific mutation. Residue pairs (i, j) that have the largest positive ($\Delta\overline{\boldsymbol{R}}_{\boldsymbol{ij}} > 2.50$ Å) and negative distances ($\Delta\overline{\boldsymbol{R}}_{\boldsymbol{ij}} < -1.40$ Å) between WT and each mutant were highlighted.

Results

1. Mutants of the androgen receptor dimer interface impact its functionality

1.1. Mutations affect cell proliferation and response to anti-androgens

To assess the functional impact of point mutations that affect the AR-LBD dimer interface, we generated AR-null PC3 cell lines (CNT) stably expressing either WT AR or mutants Phe755Val (F755V) (Lobaccaro et al., 1993; Liu et al., 2009; Tadokoro et al., 2009), Val758Ala (V758A) (Marcelli et al., 2000; Shi et al., 2002; Zhou et al., 2010; Grosdidier et al., 2012; Hay and McEwan, 2012), Tyr764Cys (Y764C) (McPhaul et al., 1991; Murono et al., 1995; Quigley et al., 1995; Langley et al., 1998; Shi et al., 2002; Melo et al., 2003; Jääskeläinen et al., 2006; Liu et al., 2009; Hay and McEwan, 2012) or Gln799Glu (Q799E) (Batch et al., 1992; Murono et al., 1995; Quigley et al., 1995; Bevan et al., 1996; Wang et al., 1998; Hiort et al., 2000; Shi et al., 2002; Jääskeläinen et al., 2006; Hay and McEwan, 2012; Kalfa et al., 2013; Qi et al., 2013) (Fig. 16, A and B). As expected, WT expression resulted in a 24.5-fold increase in AR transactivation as measured by luciferase reporter expression under the control of a synthetic AR promoter. Interestingly, all four mutants displayed a significantly lower AR transactivation activity compared to WT (Fig. 16C). Further, expression of WT and V758A resulted in a nearly complete inhibition of colony formation (Fig. 16D and fig. S1A) and proliferation (Fig. 16, E and F) compared to CNT cells that was highly statistically significant. DHT treatment of AR-transduced DU145 (fig. S2, B to D) and of AR-sensitive LNCaP cells (fig. S2, E to G) resulted in comparable growth suppressive effects that were not observed in AR-negative parental DU145 cells (fig. S2, B to D), in a CRPC cell line, 22rv1 (fig. S2, H to J) or in AR-insensitive, normal epithelial cells (RWPE1; fig. S2, K to M). These observations confirm previous reports on the growth suppressive effect of AR stimulation in AR-responsive cells (Lam et al., 2020; Kumar et al., 2021). In striking contrast, F755V and Q799E had proliferation rates not significantly different from those of the CNT cells, while proliferation was only modestly impaired by Y764C (Fig. 16, E and F). Similarly, colony forming capacity was unchanged for F755V and partially, albeit significantly reduced in Glu799- and Cys764-expressing cells (Fig. 16D and fig. S1A).

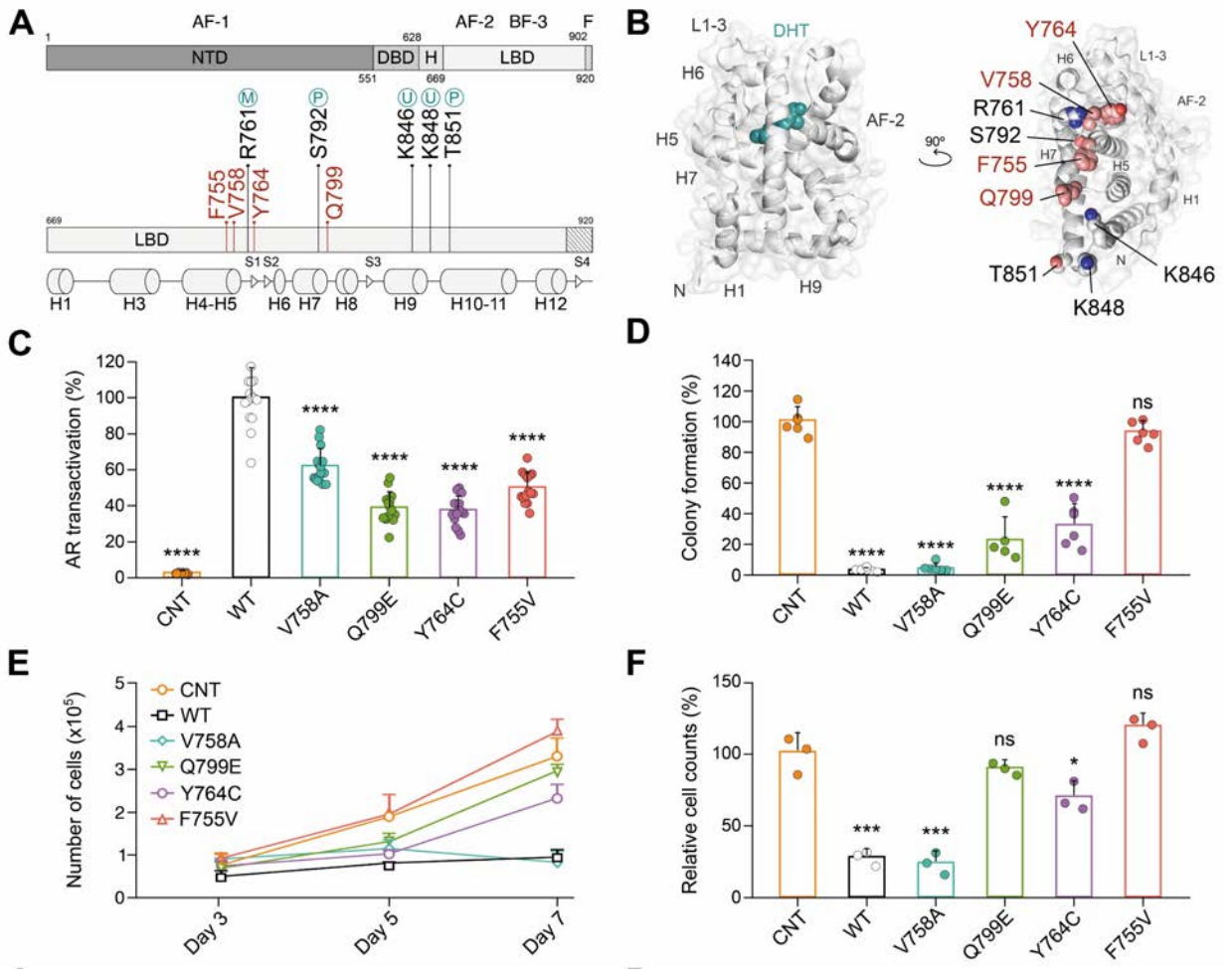

Fig. 16. Mutations impact androgen receptor transactivation activity and cellular phenotypes.

(A) Cartoon of AR domain organization. Physiologically relevant interaction sites (top; AF-1, AF-2, and BF-3), mutated AR-LBD residues (red; middle) and secondary structure elements (bottom; helices as H1-H12, cylinders, and β-strands as S1-S4, triangles) are indicated. Neighbouring residues of major PTM sites are shown (methylation (M), phosphorylation (P), and ubiquitination (U)). *(B)* 3D structure of AR-LBD (grey). Note that disease-linked residues (red spheres) and PTM sites (grey spheres) highlighted in (A) form an extended path on the AR-LBD dimer interface. *(C)* Relative AR transcriptional activity in CNT, WT and mutant AR-transduced PC3 cells (mean ± SD, n = 3). Differences against WT were calculated using a t-test and considered significant at p values < 0.1. (# $p < 0.1$ * $p < 0.05$, ** $p < 0.01$, *** $p < 0.001$ and **** $p < 0.0001$). The same p value guidelines and asterisk significance will be used through this thesis. *(D)* Clonogenicity assay quantification in transduced PC3 cells (mean ± SD, n = 3). Representative crystal violet-stained cultures are shown in fig. S1A. *(E)* Time course of transduced PC3 cells proliferation (mean ± SD, n = 3). Proliferation is completely suppressed with WT AR or V785A but no other mutants. *(F)* relative cell counts at day 7 after transduction. Differences against CNT in panels D and F were calculated using t-tests.

Next, we asked whether the differences in proliferation and clonogenicity displayed by the AR variants would translate into distinct responses to antiandrogenic treatments. WT or mutant AR expressing cells were treated with enzalutamide (Fig. 17, A and C), abiraterone (Fig. 17, B and D) or apalutamide (fig. S1B) and AR transactivation was measured. Remarkably, transactivation was significantly inhibited by enzalutamide and abiraterone in both WT and mutant AR cells (Fig. 17, A and B). Reduction in AR transactivation was not a consequence of impaired cell viability upon anti-androgen treatment (Fig. 17, C and D, fig. S1B). Specifically, V758A cells showed an 11.7, 20.6 and 16.1% increased viability compared to WT when treated with enzalutamide, apalutamide or abiraterone, respectively. On the contrary, F755V, Y764C, and Q799E mutant cells displayed a significantly increased sensitivity to all three antiandrogens (Fig. 17, C and D, fig. S1B).

Together, these results indicate that expression of ligand-bound WT AR in AR-null PCa cells induces a quiescent cell phenotype in AR-responsive cells without affecting the response to antiandrogen treatment. The data also demonstrates that, overall, point mutations at the AR dimerization surface negatively impact its ability to suppress proliferation and clonogenicity and mostly sensitize cells to antiandrogens (Fig. 16 and 17, fig. S1, A and B, and fig. S2).

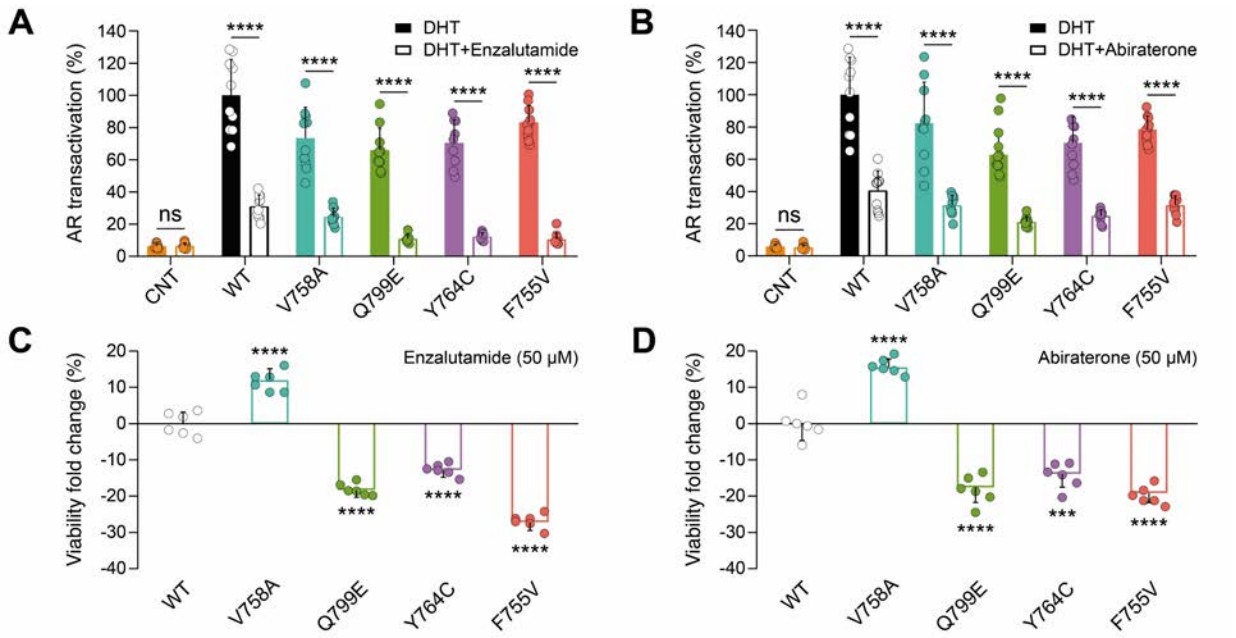

Fig. 17. Mutations confer different cellular response to antiandrogens.

(A-B) Effect of antiandrogens on the relative AR transcriptional activity (mean ± SD, n = 5). *(C-D)* PC3 cells viability fold change in response to antiandrogens relative to the CNT cells (mean ± SD, n = 3). Differences against CNT (panels G and H) or against WT (panels I and J) were calculated using t-tests.

1.2. Deregulation of androgen-targeted transcription programs upon mutation

Having demonstrated that dimerization surface mutations in the AR-LBD have an important impact on cellular functions, we next investigated whether these mutations alter gene expression patterns (Fig. 18 and fig. S1). Transcriptomic data was generated for WT and each mutant AR and compared to non-transduced cells as control. As expected, AR and canonical AR target genes such as *TMPRSS2*, *FKBP5*, and *TIPARP* were significantly upregulated in both WT and mutant AR expressing cells (Fig. 18A and fig. S1C), which was orthogonally validated in qPCR assays (fig. S1, G to I). In agreement with the functional evidence described above, the V758A mutant displayed AR target gene expression patterns most similar to WT AR (Fig. 18, C to E). Accordingly, GSEA showed that all four mutant AR signatures were similar to the WT signature (Fig. 18B). Although the AR regulon was conserved in all mutants, there were significant differences between the four variants. V758A showed a dynamic gene expression profile most similar to WT, while the differentially expressed gene sets of F755V, Y764C and Q799E were much smaller and shared fewer target genes compared to WT AR or V758A (Fig. 18C and fig. S1C). Variance assessment and clustering of expression profiles further confirmed the similarity of WT and V758A transcriptomes, on the one hand, and those of F755V, Y764C and Q799E, on the other. These two clusters were identified both by a principal component analysis (PCA) (Fig. 18D) and by clustering analysis computing sample-to-sample distances using Variance Stabilizing Transformation (VST) data (Fig. 18E). Further, gene expression in the AR regulon as defined by the DoRothEA collection of human regulons (Garcia-Alonso et al., 2019) showed that the set of activated AR target genes in WT and mutants remains largely conserved (Fig. 19A). However, only WT and V758A maintained a repressed gene set that included cancer drivers *FOXA1* and *MYC* as well as epithelial to mesenchymal transition drivers *SNAI2* (*SLUG*), *CDH2* (encoding N-cadherin), and *SOX4* (Fig. 19A and fig. S1I). This is consistent with the important reduction in proliferation and clonogenicity described above (Fig. 16, D to F and fig. S1A). In fact, GSEA analysis of the four AR mutants versus WT signatures evidenced again that V758A was not enriched in any of the PCa signatures in the MSigDB, as opposed to the significant enrichment demonstrated for F755V, Y764C and Q799E (Fig. 19B). Accordingly, only these three mutant signatures were found positively enriched in a previously defined upregulated gene signature strongly associated with poorer outcome in PCa patients (Aytes et al., 2014) (Fig. 19C).

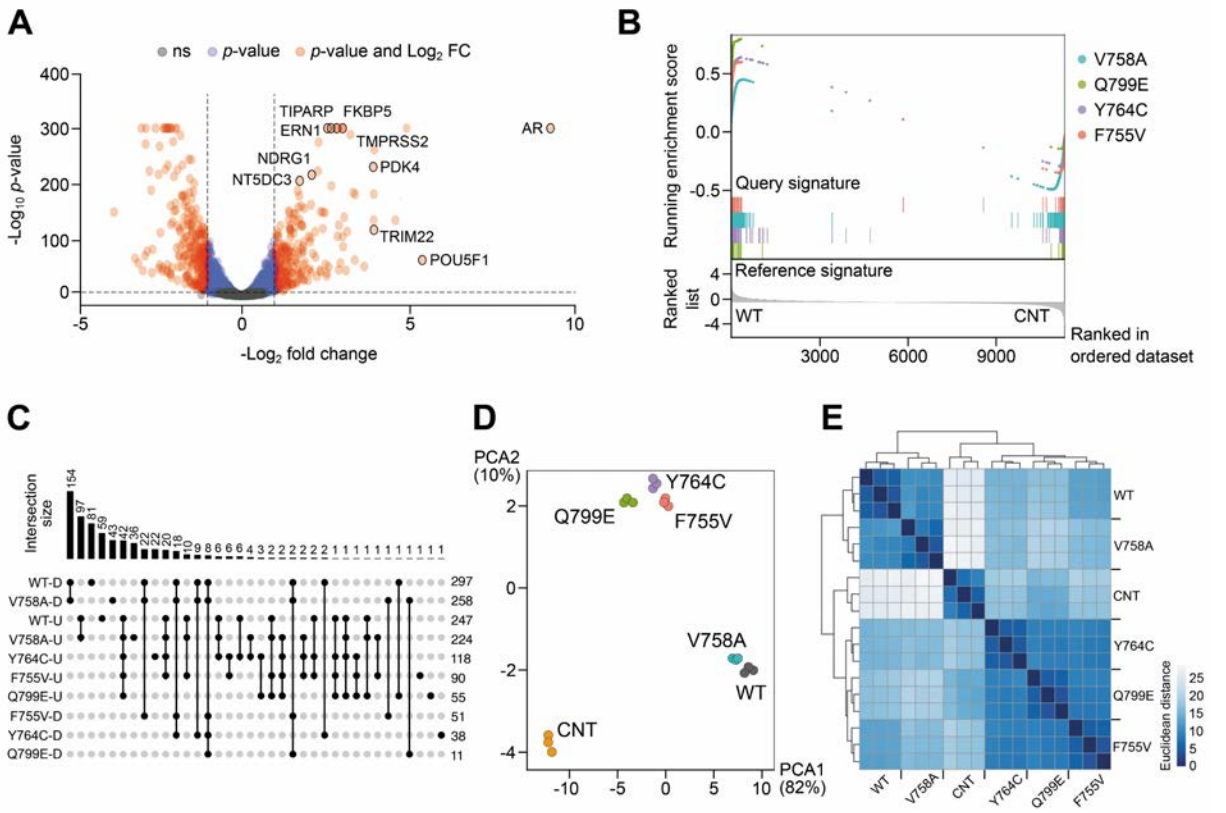

Fig. 18. The transcriptional profiles of AR mutants differ from that of the wild-type receptor (I).
The results of RNA-seq experiments conducted in triplicate for each cell line are summarized. *(A)* Differential expression analysis between CNT and AR-transduced cells. Genes with |log2(fold change)| ≥ 1 and $p \leq 0.05$ are shown in red. *(B)* GSEA demonstrates similar signatures of WT and mutant AR. *(C)* Differentially expressed genes overlap between WT-AR and its mutants. The bar plot (top) indicates the number of genes in the intersection between signatures, which are connected with vertical lines (bottom). For each WT and mutant AR, signatures are separately given for up- (U) and downregulated genes (D) and the size of the gene set is indicated (right). *(D-E)* PCA and heat map analysis of transcription profiles identifies three groups: (i) CNT, (ii) V785A and WT, and (iii) F755V, Y764C and Q799E.

Finally, querying the collection of KEGG database evidenced an unexpected enrichment for the Y764C mutant in biological pathways associated with pathogen infection and immune response including COVID-19 (fig. S1D), which was supported by the significant regulon enrichment in the mediator of type I interferon signalling, *STAT2* (fig. S1E) and the activation of the *JAK/STAT* pathway (fig. S1F) using the DoRothEA and the PROGENy algorithms. Together, these data suggest that the observed differences in cellular phenotype of the AR mutants are at least in part the result of a differentially reprogramed transcriptome in which WT and V758A show a less oncogenic and undifferentiated molecular phenotype compared to F755V, Y764C and Q799E.

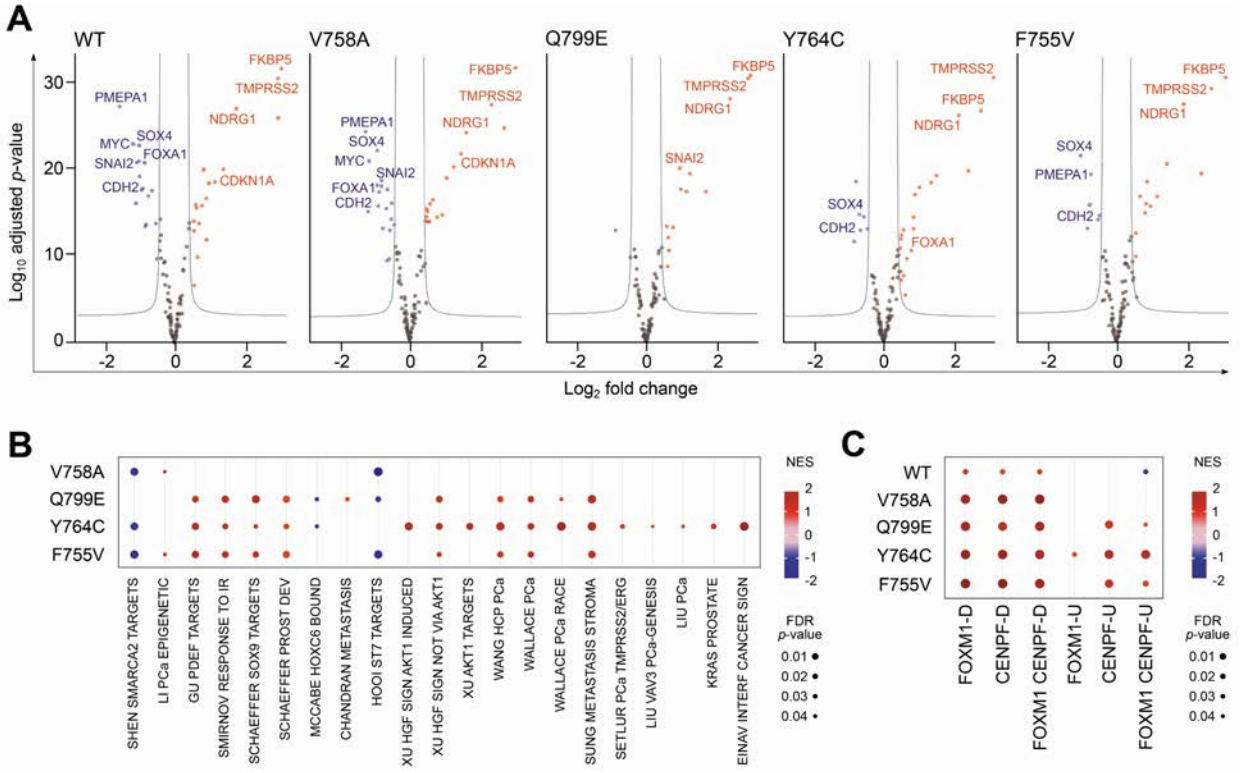

Fig. 19. The transcriptional profiles of AR mutants differ from that of the wild-type receptor (II).

(A) Volcano plots of AR target genes for WT and mutant AR. Canonical repressed (blue) and activated (red) AR targets are labelled. Note that repression of genes such as *MYC, SOX4, FOXA1* and *CDH2* is lost in Q799E, Y764C and F755V, but not in V785A. *(B)* GSEA of the mutant AR signatures against WT-AR on PCa gene sets. Of note, V758A signature shows very limited overall enrichment indicating its strong similarity with WT. *(C)* GSEA of WT and mutant AR against a previously defined PCa malignancy signature (Aytes et al., 2014). Enrichment for up- and downregulated targets of the malignancy signature drivers *FOXM1*, *CENPF* or both are shown separately. Interestingly, only the F755V, Y764C and Q799E signatures are enriched in the *FOXM1* and/or *CENPF* regulons. Normalized Enrichment Score (NES) scale and FDR *p* value thresholds are indicated.

2. Mutational impact on the androgen receptor ligand binding domain (AR-LBD)

2.1. Mutations do not compromise AR-LBD folding but lead to a reduced stability

To study the possible structural impact of point mutants located at the AR-LBD dimerization interface, we produced and purified to homogeneity WT AR-LBD and its point mutants F755L, F755V, V758A, Y764C and Q799E. Next, we characterized these recombinant proteins both biophysically using differential scanning fluorimetry and biochemically through limited proteolysis assays (Fig. 20 and 21). The results of these experiments demonstrated that all mutants are properly folded but have substantially lower thermal stability compared to the WT protein, as indicated by the reduced melting temperatures (Tm) (Fig. 20, A and B). In line with the RNA-seq results presented above, 'core' dimer interface mutants F755V, F755L and Y764C exhibited a remarkable drop in Tm compared to the WT protein (between 5 and 6 °C), the latter being the most thermolabile of all the studied variants. By contrast, the Tm of mutants V758A and Q799E was only 1 °C lower than the WT AR-LBD protein, demonstrating WT-like stability (Fig. 20, A and B). Energy estimations using FoldX based on previously reported structures of monomeric and dimeric AR-LBD also suggested that the studied missense mutations have an important impact on the domain stability (Fig. 20C), both in its monomeric and putative dimeric conformations. Mutations of the core interface, F755V/L and Y764C, are predicted to be particularly deleterious for homodimeric AR-LBD (Fig. 20C).

AR-LBD is a highly basic protein domain (isoelectric point (pI): 8.94) with 14 arginines (Fig. 21A) and 14 lysines outbalancing 11 negatively charged aspartate or glutamate residues. To assess whether the decrease in thermal stability of AR-LBD point mutants also manifests as an increased sensitivity to proteolysis, we incubated highly purified samples of WT AR-LBD and its point mutants with the endoproteinase, Arg-C, which cleaves peptide bonds at the C-terminus of Arg residues (Fig. 21, B to E). Again, the resulting cleavage pattern of V758A is most similar to that of WT AR-LBD (Fig. 21, B, C, E and F). Interestingly, and although the thermal stabilities of the two mutants are similar (Fig. 21, A and B), the proteolytic patterns of V758A and Q799E differ notably (Fig. 21, C to F and H). Mutants F755L (Fig. 21, B, E and G), F755V (Fig. 21, C, E and I) and Y764C (Fig. 21, D, E and H) have enhanced proteolytic susceptibility. In summary, point mutations of residues at the AR-LBD homodimerization interface appear to have an unanticipated global impact on the overall domain stability, as evidenced by notably lower Tm and enhanced sensitivity to proteolytic attack (Figs. 20 and 21).

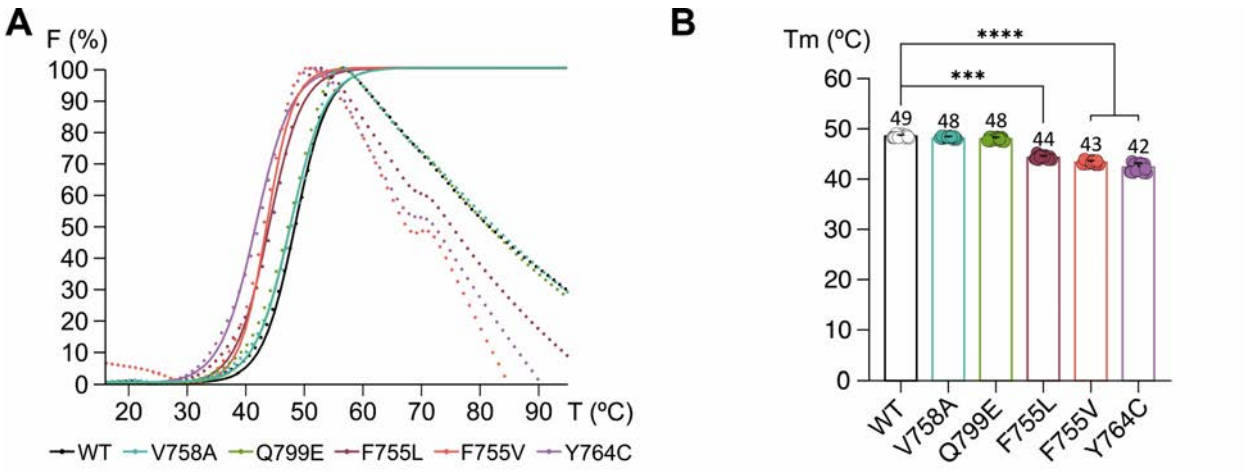

C

	Melting temperature (ºC)			Total Energy (kcal/mol)						Van der Waals Clashes (kcal/mol)					
	MUT	WT	Diff	MUT	Mon WT	Diff	MUT	Dim WT	Diff	MUT	Mon WT	Diff	MUT	Dim WT	Diff
V758A	48.12 ± 0.05	48.56 ± 0.29	**-0.44**	-75.73	-77.03	**1.30**	-269.70	-270.80	**1.50**	9.07	9.13	**-0.06**	33.55	33.57	**-0.03**
Q799E	47.71 ± 0.07	48.56 ± 0.29	**-0.85**	-76.43	-76.69	**0.26**	-270.12	-270.40	**0.28**	9.08	9.12	**-0.03**	33.65	33.65	**-0.00**
F755L	44.09 ± 0.08	48.56 ± 0.29	**-4.47**	-75.82	-76.81	**0.99**	-268.71	-270.39	**1.68**	9.13	8.98	**0.15**	34.28	33.65	**0.63**
F755V	43.65 ± 0.06	48.56 ± 0.29	**-4.91**	-74.05	-76.71	**2.66**	-268.01	-270.37	**2.36**	11.84	9.09	**2.75**	26.18	33.65	**2.53**
Y764C	41.68 ± 0.22	48.56 ± 0.29	**-6.89**	-73.36	-77.06	**3.70**	-267.70	-270.39	**2.69**	8.88	8.90	**-0.02**	33.64	33.67	**-0.03**

Fig. 20. In solution and in silico characterization of AR-LBD dimer interface mutants.

(A-B) Thermal shift assay of purified WT and mutant AR-LBDs. The melting curves of each sample (A) were analysed to calculate their melting temperatures (B) (mean ± SD, n = 4). Differences against WT AR-LBD were calculated using the t-test and considered significant at p values < 0.05. (*p < 0.05, ** p < 0.01, *** p < 0.001 and **** p < 0.0001). *(C)* Comparison between the experimentally determined melting temperatures (B) and the *in silico* calculated free energies of unfolding and Van der Waals clashes with FoldX.

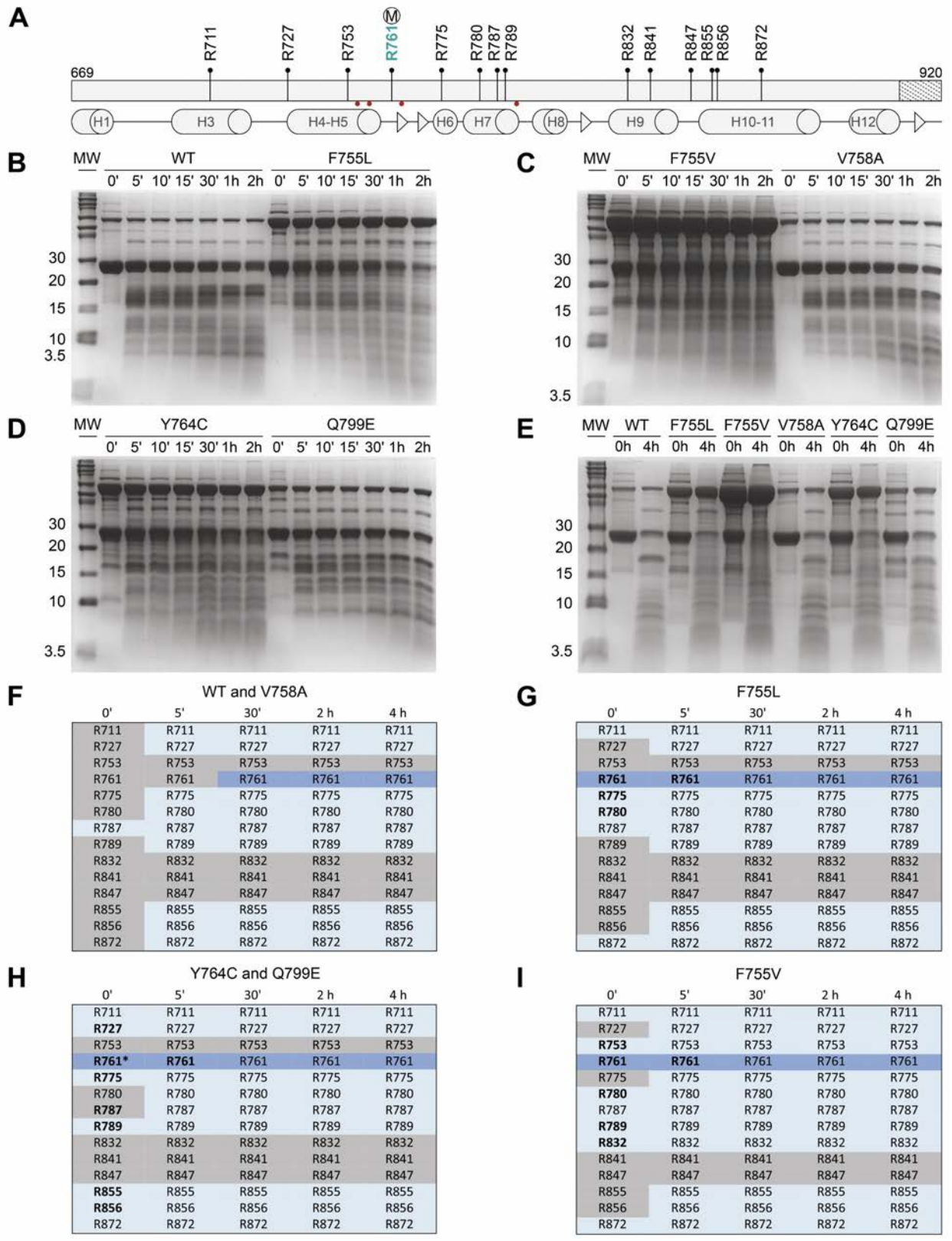

F — WT and V758A

0'	5'	30'	2 h	4 h
R711	R711	R711	R711	R711
R727	R727	R727	R727	R727
R753	R753	R753	R753	R753
R761	R761	R761	R761	R761
R775	R775	R775	R775	R775
R780	R780	R780	R780	R780
R787	R787	R787	R787	R787
R789	R789	R789	R789	R789
R832	R832	R832	R832	R832
R841	R841	R841	R841	R841
R847	R847	R847	R847	R847
R855	R855	R855	R855	R855
R856	R856	R856	R856	R856
R872	R872	R872	R872	R872

G — F755L

0'	5'	30'	2 h	4 h
R711	R711	R711	R711	R711
R727	R727	R727	R727	R727
R753	R753	R753	R753	R753
R761	**R761**	R761	R761	R761
R775	R775	R775	R775	R775
R780	R780	R780	R780	R780
R787	R787	R787	R787	R787
R789	R789	R789	R789	R789
R832	R832	R832	R832	R832
R841	R841	R841	R841	R841
R847	R847	R847	R847	R847
R855	R855	R855	R855	R855
R856	R856	R856	R856	R856
R872	R872	R872	R872	R872

H — Y764C and Q799E

0'	5'	30'	2 h	4 h
R711	R711	R711	R711	R711
R727	R727	R727	R727	R727
R753	R753	R753	R753	R753
R761*	**R761**	R761	R761	R761
R775	R775	R775	R775	R775
R780	R780	R780	R780	R780
R787	R787	R787	R787	R787
R789	R789	R789	R789	R789
R832	R832	R832	R832	R832
R841	R841	R841	R841	R841
R847	R847	R847	R847	R847
R855	R855	R855	R855	R855
R856	R856	R856	R856	R856
R872	R872	R872	R872	R872

I — F755V

0'	5'	30'	2 h	4 h
R711	R711	R711	R711	R711
R727	R727	R727	R727	R727
R753	R753	R753	R753	R753
R761	**R761**	R761	R761	R761
R775	R775	R775	R775	R775
R780	R780	R780	R780	R780
R787	R787	R787	R787	R787
R789	R789	R789	R789	R789
R832	R832	R832	R832	R832
R841	R841	R841	R841	R841
R847	R847	R847	R847	R847
R855	R855	R855	R855	R855
R856	R856	R856	R856	R856
R872	R872	R872	R872	R872

Fig. 21. AR-LBD dimer interface mutations alter sensitivity to proteolysis of the domain.

(A) Schematic representation of the AR-LBD secondary structure. The positions of the 14 arginine residues within the domain are indicated; the methylated Arg761 is labelled in blue (M). Red dots mark the position of the mutated residues in the current investigation. *(B-D)* Representative SDS-polyacrylamide gels showing the time course of proteolytic cleavage of WT and mutant AR-LBDs with Arg-C. *(E)* SDS-PAGE analysis of initial and end time points (limited proteolysis with Arg-C for 4 h). *(F-I)* Inferred proteolysis patterns for each mutant. Uncleaved arginines are shown in grey, cleaved Arg761 is coloured dark blue, and other cleaved arginines in sky blue. Bold-labelled arginines are cleaved with different kinetics compared to WT AR-LBD. Note that four different proteolysis patterns can be observed, corresponding to (F) WT and V758A, (G) F755L, (H) Y764C and Q799E, and (I) F755V.

2.2. Mutants show structural rearrangements in key areas of the AR-LBD

The results of the experiments described above demonstrate a significant impact of AR-LBD dimer interface mutants on AR transcriptional function, stability, and sensitivity to proteolytic attack. To assess whether these differences are reflected by noticeable structural rearrangements we expressed, crystallized, and refined at high resolution the X-ray crystal structures of the V758A, Y764C, F755V, F755L, and Q799E AR-LBD variants (Figs. 22 and 23). All mutant proteins crystallized as monomers in the orthorhombic space group ($P2_12_12_1$) (Figs. 22A and 23A, and fig. S3A; see fig. S3B and fig. 23B for comparison, Table 1). The "helical sandwich" fold typical of the nuclear receptor superfamily is conserved (Jiménez-Panizo et al., 2019) and the hormone (DHT) is bound inside the LBP essentially as in WT AR-LBD (Figs. 22A and 23A). The RMSD for the equivalent Cα atoms between the WT structure (PDB 1T7T) and the V758A, Y764C, F755V, Q799E and F755L mutants are 0.29, 0.33, 0.47, 0.52, and 0.54 Å, respectively.

Despite this overall conservation of the global protein fold, superimposition of the current mutant structures on previously solved structures of WT AR-LBD reveals important local structural changes on four specific distant sites of the domain (see Fig. 22A for an overall representation of the domain with these sites highlighted, and Fig. 22B to E for close-ups of these areas): the H5-S1-H7 area (from now on termed 'R761-zone', described in detail below) (Fig. 22B), the L1-3 loop, H6 and the C-t end of H11 (Fig. 22C), and two major functional sites, the BF-3 pocket comprising H9 and L9-10 (Fig. 22D), and the AF-2 pocket featuring the L3-4 loop and H12 (chaperone and coactivator binding sites, respectively) (Fig. 22E). In particular, several side chains of charged AF-2 residues exhibit conformational differences, most notably

the so-called charge-clamp residues, Lys721 and Glu894, which are known to stabilize bound coregulators at this protein-protein interaction site (Fig. 22E). Regarding the BF-3 pocket, and in addition to charged/polar residues such as Arg841 and Thr851, also the aromatic Phe827 exhibits a large flexibility (Fig. 22D). Noteworthy, Phe827 and Arg841 undergo major conformational changes upon small molecule binding to this surface-exposed pocket (Estébanez-Perpiñá et al., 2007). Loop L1-3 also exhibits side-chain conformational differences in several residues (Tyr774, His777 and Lys778), which we had previously identified as part of a secondary dimer interface in AR-LBD crystals to generate a tetrameric arrangement of the receptor (Fig. 22C) (Nadal et al., 2017).

These structural variations are also reflected by an overall enhanced flexibility of all mutants compared to WT AR-LBD (average B factor of 21.2 for the monomeric AR-LBD, PDB 1T7T), as demonstrated by the higher temperature factors (B-factors) of both main and side chain atoms in all variable regions (Fig. 23). Residues with particularly higher B-factors in the mutants are Asn693 and Gln694 (L1-3), Arg727 (L4-5), Asn759 and Arg761, a residue strictly conserved in AR from fish to humans, but not found in other steroidal receptors (H5 and loop H5-S1; fig. S3, C and D), Asp820 and Lys823 (L9-10), His886 (H6), and Glu894 (H12) (Fig. 23). Overall, mutants V758A and Y764C are most like the WT protein in this regard, while Q799E, F755L and F755V exhibit increased flexibility in H5, L1-3 and L9-10 (Fig. 23).

Our previous statistical coupling analysis (SCA) (Jiménez-Panizo et al., 2022) revealed that two groups of correlated residues or “sectors” define the internal circuits linking major interaction sites in the LBD of the related glucocorticoid receptor (GR). To analyse whether the AR-LBD dimerization surface is allosterically coupled to other functional regions we also performed SCA analysis, which identified 40 residues grouped in two sectors in the upper half of the domain (Fig. 22, F and G). Sector 1 residues cluster around the domain N-terminus (except the DHT ligand, Arg752), while sector 2 comprises LBP and AF-2 residues. Further, three residues common to both sectors are strategically located to cross-connect the LBP, AF-2 and BF-3, and dimerization interface (Fig. 22, F and G). Taken together, our results suggest that both sectors link functionally relevant regions thus coupling e.g., ligand binding to dimerization, coregulator binding or chaperone docking/release.

	V758A	Y764C	F755V	F755L	Q799E
PDB code	**7ZU1**	**7ZTZ**	**7ZTX**	**7ZTV**	**7ZU2**
Wavelength (Å)	0.979	0.979	0.979	0.979	0.979
Resolution range	66.17-1.68 (1.71-1.68)	65.84-1.40 (1.42-1.40)	65.82-1.89 (1.93-1.89)	56.2-1.94 (1.99-1.94)	44.55-1.74 (1.77-1.74)
Space group	$P2_12_12_1$	$P2_12_12_1$	$P2_12_12_1$	$P2_12_12_1$	$P2_12_12_1$
Cell constants a, b, c (Å) α, β, γ (°)	55.62, 66.17, 70.95 90, 90, 90	56.39, 65.84, 72.82 90, 90, 90	54.57, 65.82, 70.37 90, 90, 90	56.18, 65.80, 72.31 90, 90, 90	56.51, 66.04, 72.42 90, 90, 90
Molecules in the ASU	1	1	1	1	1
Total reflections	176567 (4168)	247697 (9727)	143549 (9454)	84880 (3942)	147708 (8184)
Unique reflections	29533 (1229)	53810 (2576)	20910 (1309)	18026 (1027)	28510 (1559)
Multiplicity	6.0 (3.4)	4.6 (3.8)	6.9 (7.2)	4.7 (3.8)	5.2 (5.2)
Completeness (%)	96.6 (80.4)	99.6 (98.2)	99.9 (100.0)	88.1 (79.8)	100.0 (100.0)
Mean I/sigma(I)	10.3 (0.7)	18.8 (0.5)	8.8 (0.7)	10.4 (2.8)	12.3 (1.5)
Wilson B-factor	27.1	27.0	38.2	22.8	26.1
R-meas	0.084 (2.026)	0.030 (1.692)	0.116 (3.399)	0.093 (0.720)	0.089 (2.398)
R-pim	0.033 (1.015)	0.014 (0.841)	0.045 (1.257)	0.042 (0.363)	0.039 (1.042)
CC1/2	0.998 (0.364)	1.000 (0.395)	0.998 (0.364)	0.989 (0.854)	0.999 (0.337)
Reflections used in refinement	28174	51127	19842	17086	27029
Reflections used for R-free	1235 (4.2)	2619 (4.9)	1020 (4.9)	888 (4.9)	1433 (5.0)
R-work	0.21	0.19	0.20	0.22	0.18
R-free	0.25	0.22	0.25	0.26	0.22
Number of atoms Protein, DHT, Water	2135 2008, 21, 81	2161 2010, 21, 120	2041 1973, 21, 32	2066 1997, 21, 44	2080 1985, 21, 64
RMS (bonds)	0.007	0.011	0.008	0.007	0.009
RMS (angles)	1.420	1.828	1.606	1.500	1.581
Ramachandran favoured (%)	98.76	98.74	98.32	98.33	99.16
Ramachandran allowed (%)	1.24	1.26	1.26	1.25	0.84
Clashscore	5.32	1.23	3.47	2.47	3.7
Average B-factor **Protein (main, side chain)** **DHT ligand** **Water**	40.4 40.0 (36.9, 42.8) 29.1 44.4	35.6 35.1 (32.0, 38.1) 25.4 42.8	48.2 48.1 (44.2, 51.9) 34.3 47.3	37.5 37.6 (34.3, 40.8) 25.3 36.3	37.3 37.2 (33.3, 40.9) 26.0 41.9

Table 1. X-ray crystallography data collection, refinement statistics and model quality.

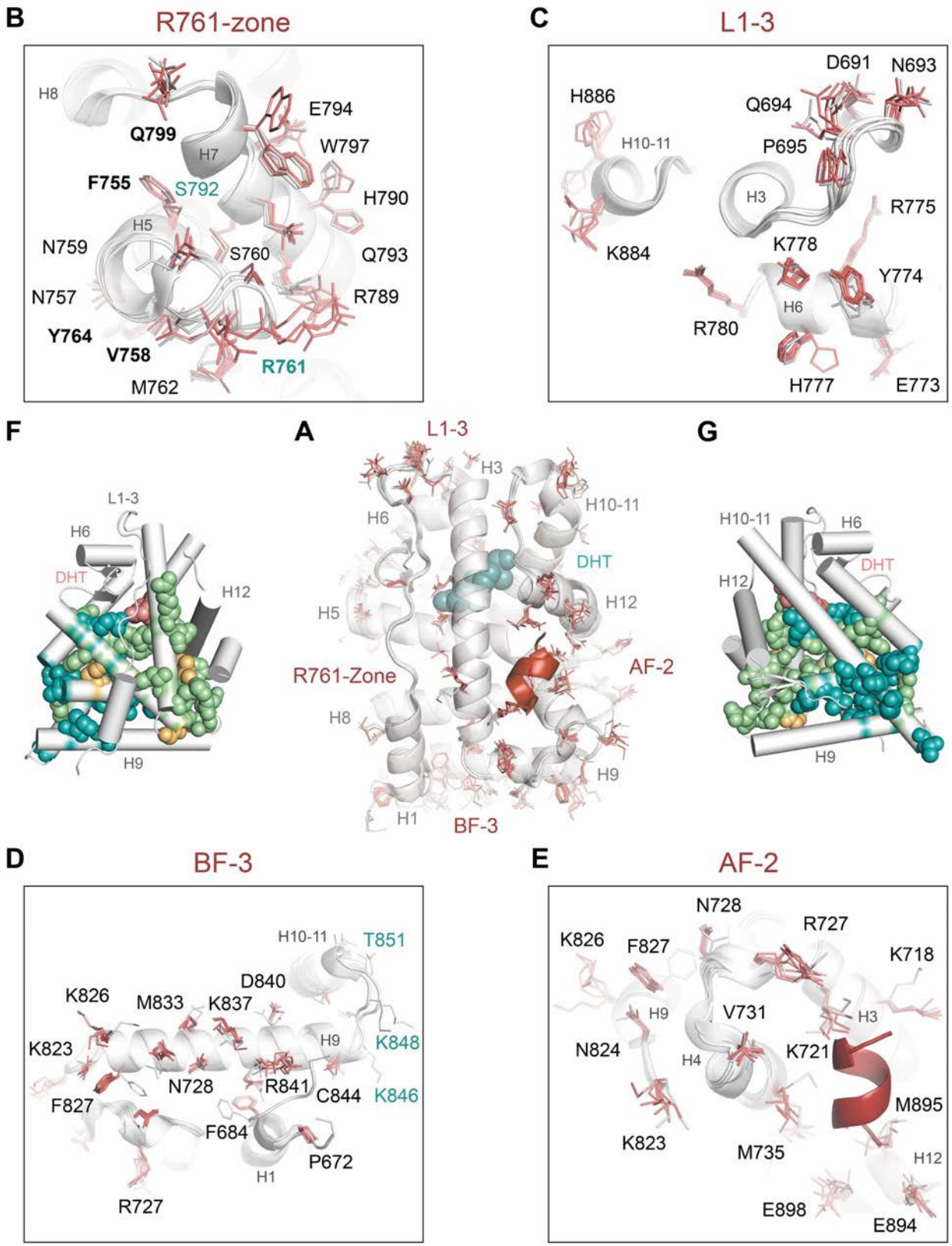

Fig. 22. AR-LBD dimer interface mutants induce local and distant structural changes.

(A) Superimposition of current high resolution crystal structures of mutant AR-LBDs on WT monomeric (PDB: 1T7T) and dimeric (PDB: 5JJM) forms of the domain. Secondary structure elements identical in all structures are depicted as a grey cartoon, with DHT as teal spheres and the AF-2-bound peptide (from 5JJM) in red. Large main- and/or side chain conformational changes cluster in four areas (panes B to E), highlighted by the major secondary structure elements (coral sticks). *(B)* Dimer interface core lined by H5 and H7, which in addition to the studied point-mutations (Phe755 and Val758 (H5), Tyr764 (S1), and Gln799 (H7) features mostly residues with non-polar / aromatic side chains, along with the positively charged Arg761. (C) The more distal part of the dimer interface formed by H3 and L1-3 (Tyr774 and His777 from (B) are shown for orientation). In this area several polar residues exhibit noticeable conformational changes. *(D)* BF-3 pocket, where multiple residues exhibit conformational changes, most notably those from H9. E, AF-2 pocket, where in addition to the charge-clamp residues, Lys721 and Glu894, known to stabilize bound coregulators at this interaction site, the side chains of both charged (Lys718, Arg727, Lys823, Glu898) and aliphatic residues (Met735, Met895) display conformational variability. *(F-G)* Sector 1 (teal) comprises 17 residues in and around H5, H7, H8, H9 and H10-11 (Met743, Phe748, Gly751, Arg753, Leu798, Ile800, Thr801, Met808, Leu811, Phe814, Glu838, Ile842, Thr851, Tyr858, Thre861, Lys862, Leu864), while sector 2 (green) features 20 residues mostly from H3, H5, H7, H8, S3 and H10-11 (Arg711, Leu713, Trp719, Ala720, Lys721, Phe726, Leu729, Gln734, Tyr739, Trp742, Gly744, Met746, Ala749, Trp752, Ser754, Leu791, Lys809, Leu813, Asp820, Arg856). Three residues (Gly725, Ile738 at the AF-2 groove and Phe805 at H7) belong to both sectors (yellow).

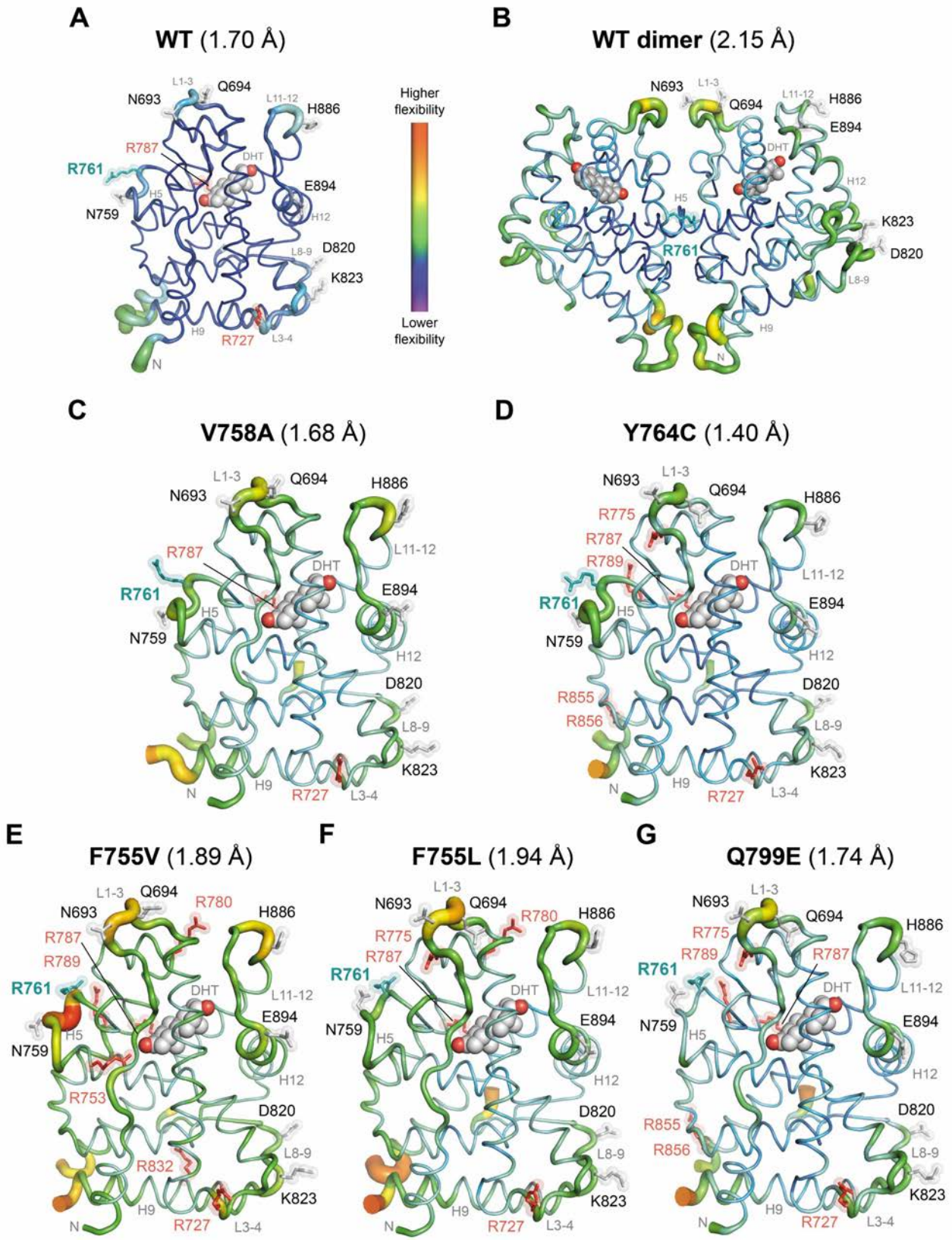

Fig. 23. AR-LBD dimer interface mutants display local flexibility differences.

(A-G) Visualization of protein mobility for WT and AR-LBD mutant proteins. Proteins are represented as ribbons sized by temperature factors (B-factors) and coloured according to the average B-factors of each residue (i.e., areas with larger atomic displacements appear thicker and are depicted with warmer colours (red, orange, yellow), whereas those with lower thermal motion are shown thinner and with cold colours (green, blue, violet)). DHT molecules bound inside the LBP pockets are shown as grey spheres with oxygen atoms in red. WT AR-LBD·DHT monomer (A, PDB 1T7T) and dimer (B, PDB 5JJM) are shown for comparison. Note that all mutants exhibit a larger mobility than WT AR-LBD.

To further explore the LBD dynamics and possible allosteric couplings between AR-LBD functional areas we performed four 1 μs-long (MD) simulations for both WT AR-LBD and all the mutants (Fig. 24 and fig. S3E). The analysis of the time evolution of the RMSD for all the Cα atoms using the experimental structure of WT AR-LBD as reference, confirms that the overall fold of the domain is stable against these point mutations and all structures show global structural stability. Moreover, global conformations do not vary remarkably for any of the mutants and their final RMSDs oscillate at around 2 Å (fig. S3E). To evaluate the flexibility of the mutants in more detail we analysed how a given residue fluctuates around a specific position with time. To this end, we quantified the fluctuations for all residues using the averaged RMSF value, averaged for the four MD replicas (Fig. 24 upper-right panel). As expected, more flexible regions correspond to those with higher B-factors in the current structures (compare Figs. 23 and 24). To analyse how specific mutations affect the dynamics of the different regions we calculate the RMSF differences between WT AR and the studied variants (Fig. 24). The stretch Lys884-Val888 (H10-H11) presents, for all the mutants, a markedly decreased flexibility compared to WT (Figs. 24 and Fig 22). On the other hand, the L1-3 loop (residues Cys687-Asn693) is notably more flexible in the V758A and F755L mutants. This behaviour is also observed in the Q799E mutant, although less pronounced, but neither in Y764C nor in F755V mutants. These two regions are located far from the mutated residues suggesting that mutations in the AR-LBD dimerization site induce conformational changes in the AF-2 pocket and thus that dimerization and coregulator binding are allosterically coupled.

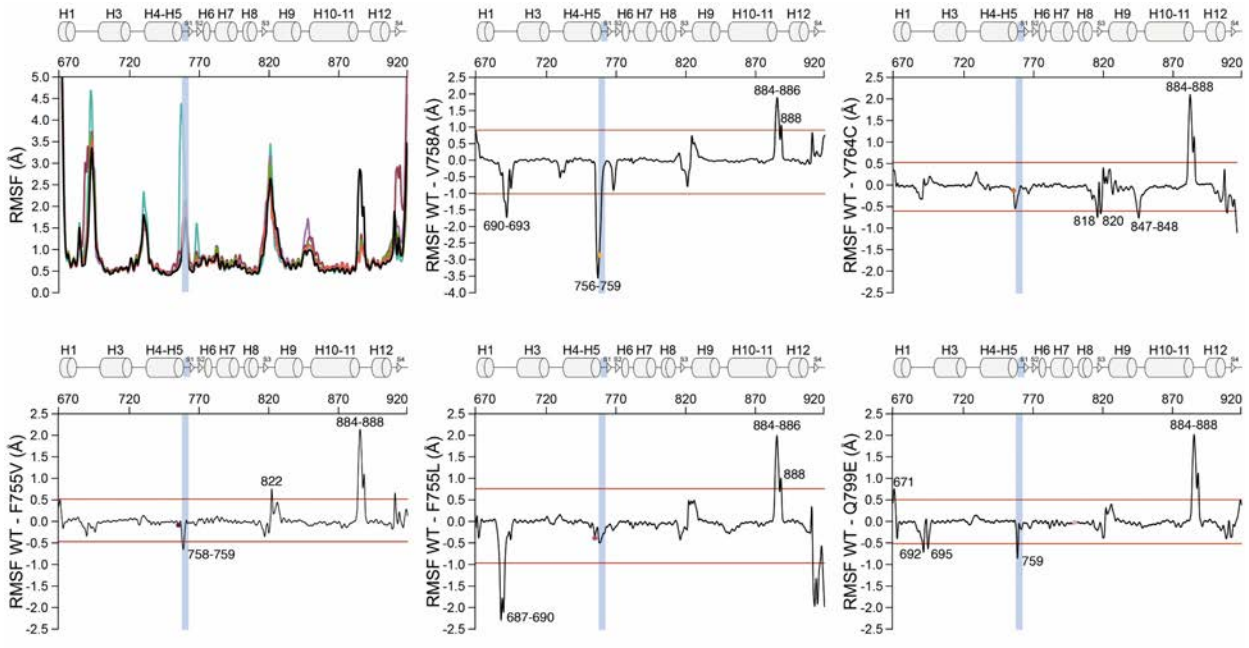

Fig. 24. Molecular dynamics of wild type and mutant structures demonstrate local changes in flexibility. Averaged RMSF of the four MD runs calculated for each structure: WT AR-LBD (black), V758A (blue), Y764C (purple), Q799E (green), F755L (violet), and F755V (red) (upper right plot). The remaining plots show the differences between the WT and mutant RMSF values. Residues with RMSF values higher than +2σ or lower than -2σ (indicating decreased or increased flexibility compared to WT, respectively) are labelled. Only changes with values greater than twice their standard deviations were considered significant (red lines). Major changes in flexibility around the mutation site were detected only for the V758A mutant. Mutant F755V only shows a minor change in this region while Q799E does not present any changes near the mutated residue but around Asn759 instead, in line with the experimental structure. Note that flexibility in the L5-S1 loop is remarkably higher in V758A, F755V and Q799E compared to WT (blue). On the contrary, the C-terminal end of H10-11 shows lower flexibility in all the mutants.

Next, and to complement the dynamic description of the impact of the different mutations we quantified local conformational changes by calculating the differences in the average Cα-Cα distances between spatially neighbouring residue pairs (extended up to the second coordination shell; ~9.1 Å). The results of these $\Delta\bar{R}_{ij}$ analyses are presented in Fig. 25. Overall, all mutant structures tend to have larger inter-residue distances compared to the WT protein, and some specific groups of residues show remarkable changes in their average pair distances. This is particularly true for residues Lys884-His886 and Val888-Phe892 at the C-terminal end of H10-H11 and the L11-12 loop (box A in Fig. 25). In line with the experimental findings, the R761-zone shows important changes in all the mutants (residues Asn759 to Tyr764, L5-S1 loop). This region presents two distinct groups of moving residues, consisting of the stretch from Arg789 to

Phe795 (helix H7) and Ser754-Val758 of H4-H5 (boxes B1 and B2 in Fig. 25, respectively). Furthermore, in all mutants, changes in average distances of residues Leu729-Asp733 (L3-4 loop and N-terminal end of H4-H5) and Gly821-Asn824 (S3-9 loop) are coupled (box C in Fig. 25). However, in this case, changes are negative for mutations Q779E and F755V, both negative and positive for Y764C and V758A mutants, or positive for F755L. Finally, residues Cys687 to Gln694 (L1-3) behave differently in each mutant. For F755L, this region shows negative changes in their average distances to residues Ala688-Arg711 (L1-3 and H3) and the Phe765-Leu769 stretch (boxes D1 and D2 in Fig. 25, respectively). Mutant V758A presents fewer changes in the average distances in the same regions, some of which are positive in the first one (box D1 in Fig. 25). For the Y764C mutant the first group of distances becomes completely positive while the second one practically disappears. No noticeable changes were detected for mutants F755V and Q799E. In summary, residue-pair distance analysis shows that the different interface mutations induce local conformational changes in AR-LBD. These changes are located far from the mutated residues in line with an allosteric mechanism. Moreover, although some changes are common to all the mutations, markedly different local responses were observed in specific AR regions.

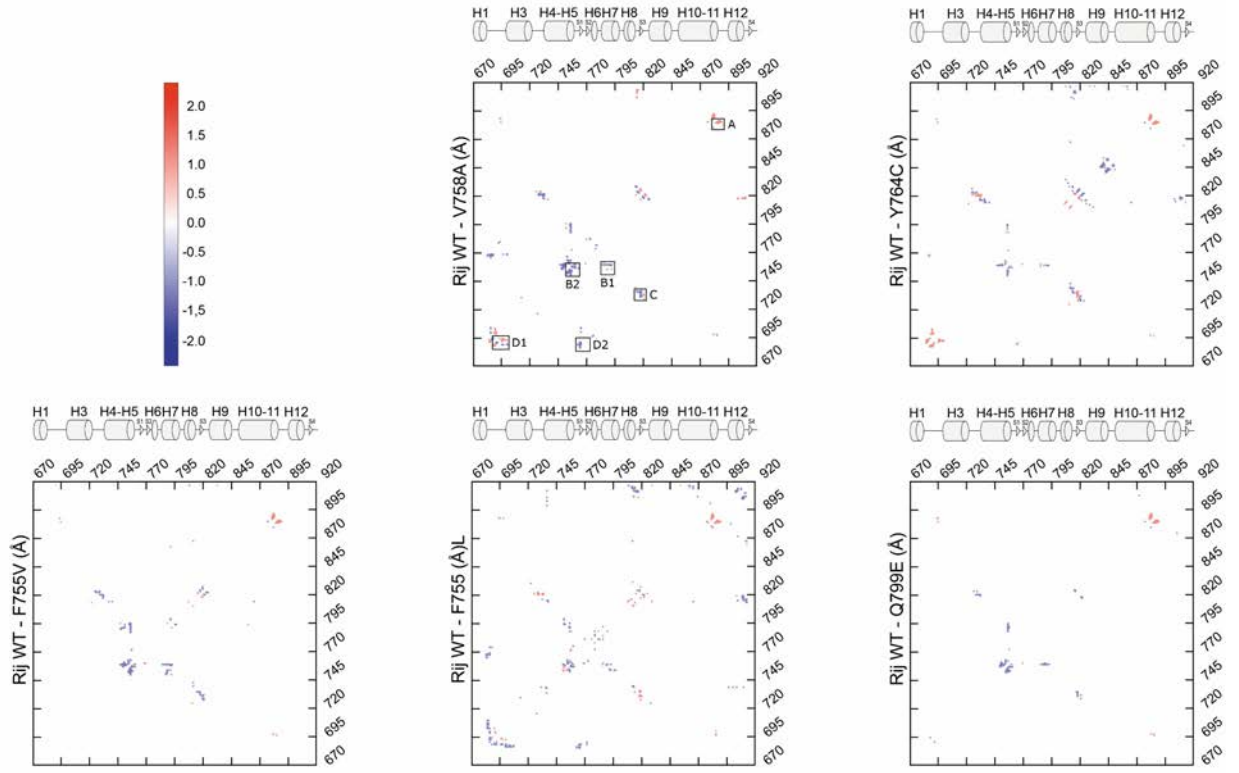

Fig. 25. Mutations induce conformational changes in specific regions of the AR-LBD.

Plots of the differences in average pairwise distances ($\Delta\bar{R}_{ij}$), with $\Delta\bar{R}_{ij} = \bar{R}_{ij,WT} - \bar{R}_{ij,mut}$, being $\bar{R}_{ij,WT}$ and $\bar{R}_{ij,mut}$ the average distances between Cα atoms of residues i (WT) and j (mutant) along the MD trajectories. Red and blue represent positive and negative $\Delta\bar{R}_{ij}$ values, corresponding to residue pairs whose average distances decrease or increase due to the mutation, respectively. Only residue pairs with $\Delta\bar{R}_{ij}$ > 2.50 or < - 1.40 which represent the most significant distance changes, are shown.

3. Towards the identification of a mechanism underlying mutations pathogenicity

3.1. Non-canonical dimerization of the AR-LBD is conserved upon mutations

The studied AR mutations are located at the non-canonical dimerization interface, so we next wondered whether they might impair homodimer formation (Fig. 26). We had previously shown that AR-LBD dimerization in solution could be demonstrated with the homo-bifunctional crosslinker, BMOE, which crosslinks residues Cys687 from two monomers (Nadal et al., 2017). To verify whether mutant proteins can dimerize as WT AR-LBD, we incubated purified samples of the recombinant proteins with either BMOE (spacer arm length: 8.0 Å) or a similar crosslinker with a larger spacer arm, BMB (10.9 Å), and analysed reaction products by SDS-PAGE. The results of these experiments revealed similar patterns of AR-LBD homodimer formation in all cases, indicating that receptor homodimerization is not compromised by point mutations of interface residues (Fig. 26A).

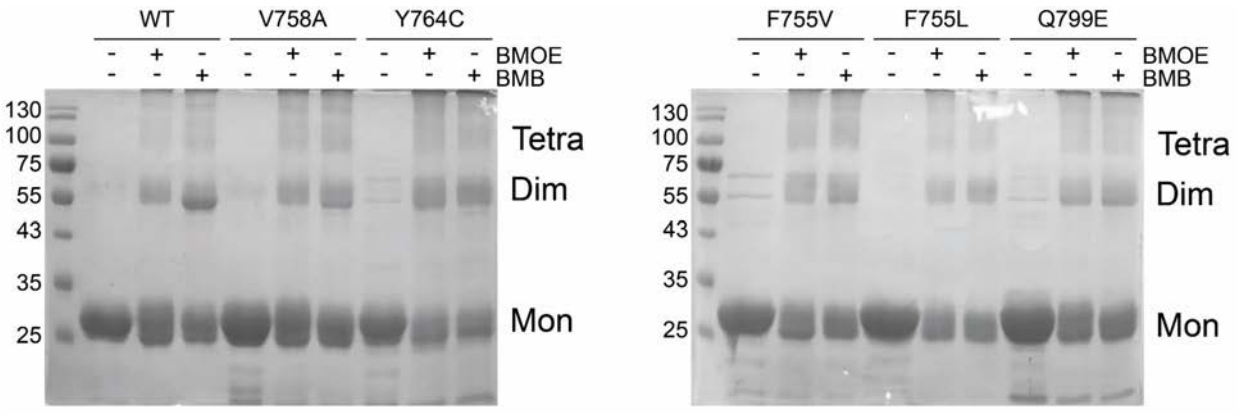

Fig. 26. Dimer interface mutants do not impair homodimer formation.

(A) SDS-PAGE analysis of WT and mutant AR-LBD samples treated with the bifunctional crosslinkers, BMOE or BMB. Note similar intensities of bands corresponding to dimeric AR-LBD in all cases, indicating that homodimer formation is not compromised by any of the studied point mutants.

Further, and to assess the possible impact of the studied mutants on the dimerization potential of AR-LBD mutants, we performed docking calculations using NIP (Grosdidier and Fernández-Recio, 2008) and optimal docking area (ODA) (Fernandez-Recio et al., 2005) (fig. S4). The computed binding energy of dimeric WT AR-LBD (PDB 5JJM (Fig. 23B), chains B and C, removing residues 845-851) was similar to that of V758A and Y764C mutants (assuming the same orientation as WT), and more favourable than that of the other mutants. Actually, the electrostatic energy contribution was much larger for WT than for any mutant, while the desolvation energy showed the opposite trend (fig. S4A). The size of the dimer interface as estimated from the buried surface area (BSA) was larger for WT than for the mutants, being V758A the one closest to WT (fig. S4A).

We also built alternative dimer arrangements by docking, based on WT (PDB 5JJM, chain B without residues 845-851) and current mutant monomeric structures (fig. S4B). Interestingly, the top ranked model in WT docking matched the X-ray dimer orientation (5.6 Å RMSD), with slightly better binding energy (fig. S4B). For all mutants, we also obtained similar orientations to the experimental dimer (RMSD < 10 Å), although not as the lowest-ranking models (fig. S4B). Binding energies for V758A and Y764C docking dimers were similar to those obtained by superimposition on the X-ray dimer, while in the rest of the mutants the binding energy of the docking dimer was more favourable (although showing slightly higher RMSD). NIP-based interface hot-spot residues predicted from docking (red residues in fig. S4C) were located at the X-ray dimer interface in WT and all mutants (except in F755V, which shows an additional NIP region around Asp829, Arg832, and Ile836), with residue at position 755 appearing among the highest NIP values in all cases but in F755V. Interestingly, desolvation areas predicted by ODA surface analysis were mostly located at the X-ray dimer interface in WT and all mutants (fig. S4D) indicating that a large part of the expected dimeric interface has favourable desolvation energy, especially the region around residue position 755. In general, predicted dimer interfaces from docking experiments and ODA are consistent with the X-ray dimer orientation (Nadal et al., 2017).

3.2. The recurrent Tyr764Cys point mutation highlights the ability of AR-LBD dimer interface to adopt different relative orientations

AR variant Tyr764Cys was first identified in a PAIS family and has since been repeatedly reported in AIS and PCa individuals worldwide (McPhaul et al., 1991; Murono et al., 1995; Quigley et al., 1995; Langley et al., 1998; Shi et al., 2002; Melo et al., 2003; Jääskeläinen et al., 2006; Liu et al., 2009; Hay and McEwan, 2012). Because this recurrent mutation introduces a solvent-exposed cysteine at the AR-LBD dimerization interface (Fig. 27A), we reasoned that the mutant protein would be more reactive, favouring formation of disulfide-bridged homodimers in solution. Indeed, Y764C but neither WT AR-LBD nor other mutants tested rapidly forms covalent dimers in solution at basic pH as assessed by non-reducing SDS-PAGE (Fig. 27B). To directly proof that residues Cys764/Cys764' from each monomer are responsible for disulfide bridge-mediated dimerization in solution, bands corresponding to the AR-LBD(Y764C) dimer were excised from the gel and subjected to enzymatic digestion with trypsin and GluC. MS/MS analysis of these digests allowed indeed the identification of *peaks* corresponding to Cys764-crosslinked peptides (Fig. 27C, Table 2). The dimeric AR-LBD conformation previously identified by X-ray crystallography (Fig. 23B) (Nadal et al., 2017) would not support reaction of neighbouring Cys764 residues (distance between Cβ atoms: 11 Å; Fig. 27A) but the recent structure of multidomain AR reveals the plasticity of this interface (Wasmuth et al., 2022). Therefore, and to provide additional evidence of the plasticity of the AR-LBD homodimer, we analysed by MS/MS the band corresponding to BMB-crosslinked, dimeric AR-LBD(Y764C) (Fig. 27D). The results corroborated the presence of a BMB-mediated linkage between Cys764 Sγ atoms from two monomers (Fig. 27D, Table 3).

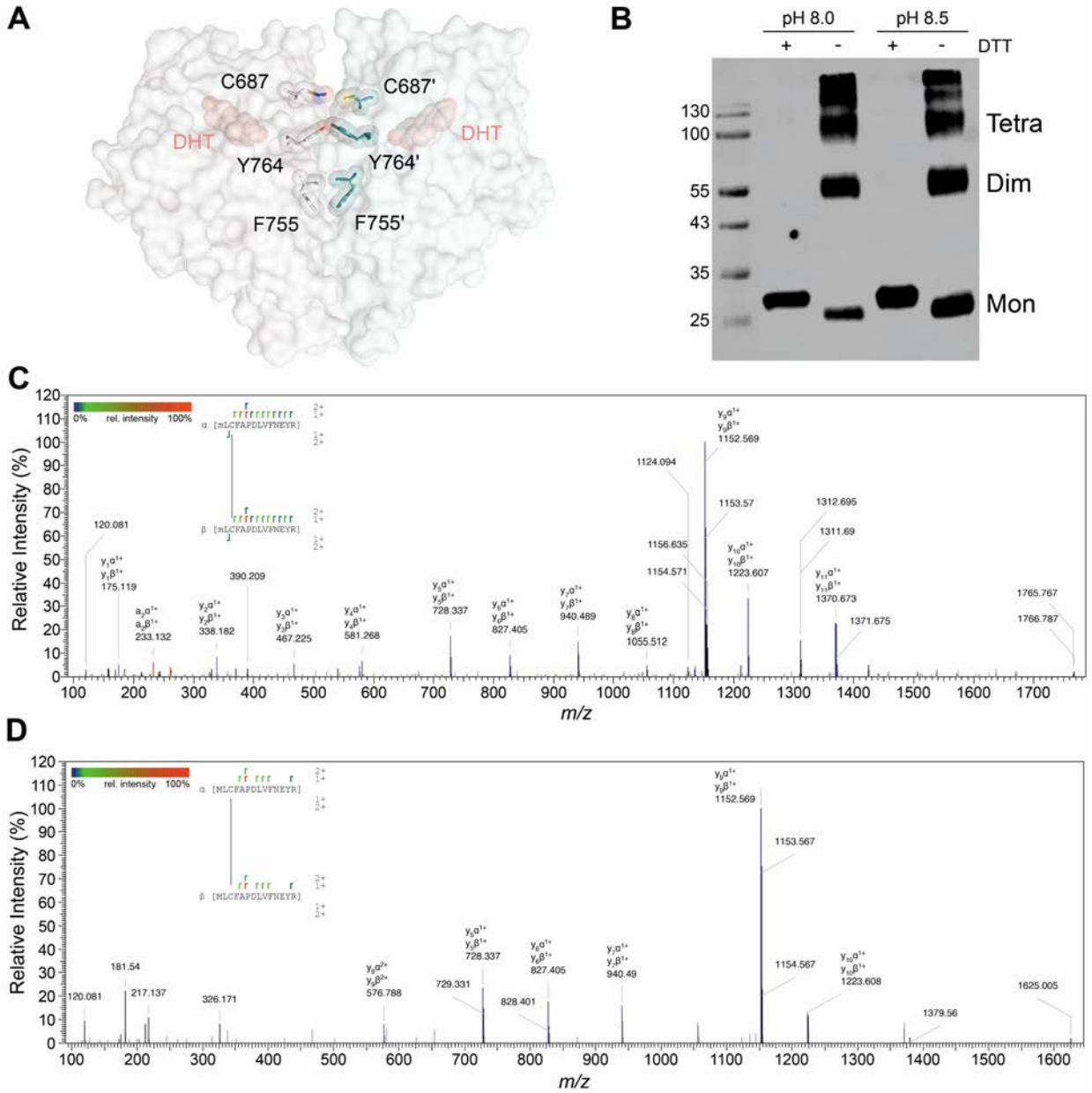

Fig. 27. Mutant Y764C enhances homodimerization with a symmetric Cys-Cys' covalent bound.

(A) 3D structure of the surface of AR-LBD dimer (PDB: 5JJM). Selected interface residues of both monomers (Cys687, Tyr764 and Phe755 (as reference)) are shown as sticks. The DHT molecule is depicted as salmon spheres. *(B)* SDS-PAGE analysis of AR-LBD(Y764C) behaviour under reducing (lanes 2 and 4, +DTT) and non-reducing conditions (lanes 3 and 5, -DTT). Note the spontaneous dimerization in solution when the protein is incubated under non-reducing conditions. *(C)* Representative MS/MS spectra demonstrating formation of a disulfide bridge between mutant Cys764 residues from two LBD monomers. m/z stands for mass-to-charge ratio. *(D)* Representative MS/MS spectra identifying BMB-crosslinked tryptic peptides between Cys764 residues from two LBD monomers.

AR-LBD(Y764C) Cys-Cys covalent bound peptides								
Site A	Site B	Sequence A	Sequence B	MeroX	XlinkX	Xi SEARCH	Max among Nodes	Stars
C-687	C-764	^{680}AIEPGVVCAGHDNNQPDSFAALLSSLNE^{707}	^{762}MLCFAPDLVFNE^{773}	5	3	2	5	***
			^{762}MLCFAPDLVFNEYR^{773}	1	9	4	9	***
	C-785	^{680}AIEPGVVCAGHDNNQPDSFAALLSSLNE^{707}	^{781}MYSQCVR^{787}			1	1	*
	C-807	^{680}AIEPGVVCAGHDNNQPDSFAALLSSLNE^{707}	^{795}FGWLQITPQEFLCMK^{809}	2	2	2	2	***
	C-853	^{680}AIEPGVVCAGHDNNQPD^{696}	^{849}NPTSCSR^{855}			1	1	*
		^{680}AIEPGVVCAGHDNNQPDSFAALLSSLNE^{707}	^{849}KNPTSCSR^{855}			1	1	*
			^{849}NPTSCSR^{855}			1	1	*
C-764	C-764	^{762}MLCFAPDLVFNE^{773}	^{762}MLCFAPDLVFNEYR^{775}			2	2	*
		^{762}MLCFAPDLVFNEYR^{775}	^{762}MLCFAPDLVFNE^{733}		1		1	*
			^{762}MLCFAPDLVFNEYR^{775}	7		4	7	**
	C-785	^{762}MLCFAPDLVFNE^{773}	^{781}MYSQCVR^{787}		2	3	3	**
		^{762}MLCFAPDLVFNEYR^{775}	^{781}MYSQCVR^{787}		14	6	14	**
	C-807	^{762}MLCFAPDLVFNE^{773}	^{795}FGWLQITPQEFLCMK^{809}			1	1	*
		^{762}MLCFAPDLVFNEYR^{775}	^{795}FGWLQITPQEFLCMK^{809}	3	7	4	7	***
	C-845	^{762}MLCFAPD^{768}	^{842}IIACK^{846}		1		1	*
		^{762}MLCFAPDLVFNE^{773}	^{842}IIACK^{846}	1	1		1	**
		^{762}MLCFAPDLVFNEYR^{775}	^{842}IIACK^{846}		8		8	*
	C-853	^{762}MLCFAPD^{768}	^{849}NPTSCSR^{855}		1	2	2	**
		^{762}MLCFAPDLVFNE^{773}	^{849}NPTSCSR^{855}			1	1	*
		^{762}MLCFAPDLVFNEYR^{775}	^{848}KNPTSCSR^{855}		1	1	1	**
			^{849}NPTSCSR^{855}		5	4	5	**

Table 2. Summary of Cys-Cys' covalently linked peptides in the Y764C LBD dimer identified by MS/MS.
The sequences of disulfide-bridged tryptic peptides identified in samples of dimeric Y764C are given along with the number of counts each peptide pair was detected with different software.

AR-LBD(Y764C) Cys-Cys crosslinked with BMB								
Site A	Site B	Sequence A	Sequence B	MeroX	XlinkX	Xi SEARCH	Unique CSM	Stars
C-764	C-764	^{762}MLCFAPDLVFNEYR^{775}	^{762}MLCFAPDLVFNEYR^{775}	5		5	8	**
	C-785	^{762}MLCFAPDLVFNEYR^{775}	^{781}MYSQCVR^{787}		6	5	9	**
	C-853	^{762}MLCFAPDLVFNEYR^{775}	^{849}NPTSCSR^{855}		1	2	3	**

Table 3. Summary of BMB-crosslinked peptides in the Y764C LBD dimer identified by MS/MS.
The number of counts each peptide pair was detected with different search tools is indicated. The only BMB-crosslinked tryptic peptides identified by MS involve the mutant Cys764, demonstrating its higher reactivity in solution.

3.3. The Arg761 zone undergoes large conformational rearrangements

In the AR-LBD homodimer, the major interface is formed by polar and hydrophobic residues from H5, β-strand S1 and their connecting loop, with additional contributions made by residues from H1 and H7-H9, and L1–3 (Fig. 28, A and B). The 'core' dimer interface features residues Val758-Arg761, along with the aromatic residues Trp752, Phe755, and Tyr764, which are involved in an intricate network of hydrogen bond and Van der Waals (VdW) interactions. Most notably, stacked residues Trp752 and Phe755 rigidify the H5-H5′ dimer interface, which is strengthened by strong VdW contacts of the latter with Pro802 as well as by hydrogen bonds between the guanidinium group of Arg761 and the main chain carbonyl oxygen atoms of Glu679, Ala680 and/or Glu682 from the neighbouring monomer (Fig. 28B). Unexpectedly, point mutations F755V/L (Fig. 28, F and G) and Q799E (Fig. 28H) resulted in a fully different conformation of H5-S1 loop residues compared to WT (Fig. 28C). Although residues Val755/Leu755 occupy essentially the same position as the WT Phe755, loss of stabilizing interactions mediated by the Phe755 phenol ring ultimately result in the exposure of the downstream Asn758-Arg761 sequence, which deviates by up to 4 Å from the more compact conformation commonly observed in structures of AR-LBD, and in which residue Ser760 is essentially buried (Fig. 28, C to H). Most notably, the side chain of Arg761 extends into bulk solvent and exhibits various degrees of freedom in the different mutants (Fig. 22B, Fig. 28, A to G). These residues are best defined by electron density in the F755L and Q799E crystals, in which the guanidinium group of Arg761 is sandwiched between the carboxylates of its "own" Glu773 and Asp829 from a crystal neighbour (Fig. 28, G and H). This extended conformation is stabilized by the side chain of Asn759, which accepts an H-bond from the main chain N atom of Arg761. The proline-like conformation adopted by the preceding residue, Ser760, is also noteworthy (Fig. 28G). Important contacts with a crystal neighbour constrain H5-S1 residues from larger displacements (Fig. 28, C to H). We reasoned that, in solution, these rearrangements could lead to even more extensive unfolding of the R761 switch zone. Indeed, important residue movements in this region were identified in our current MD simulations, some of which are larger than the deviations between mutant and WT in experimental structures (Fig. 24 and fig. S5).

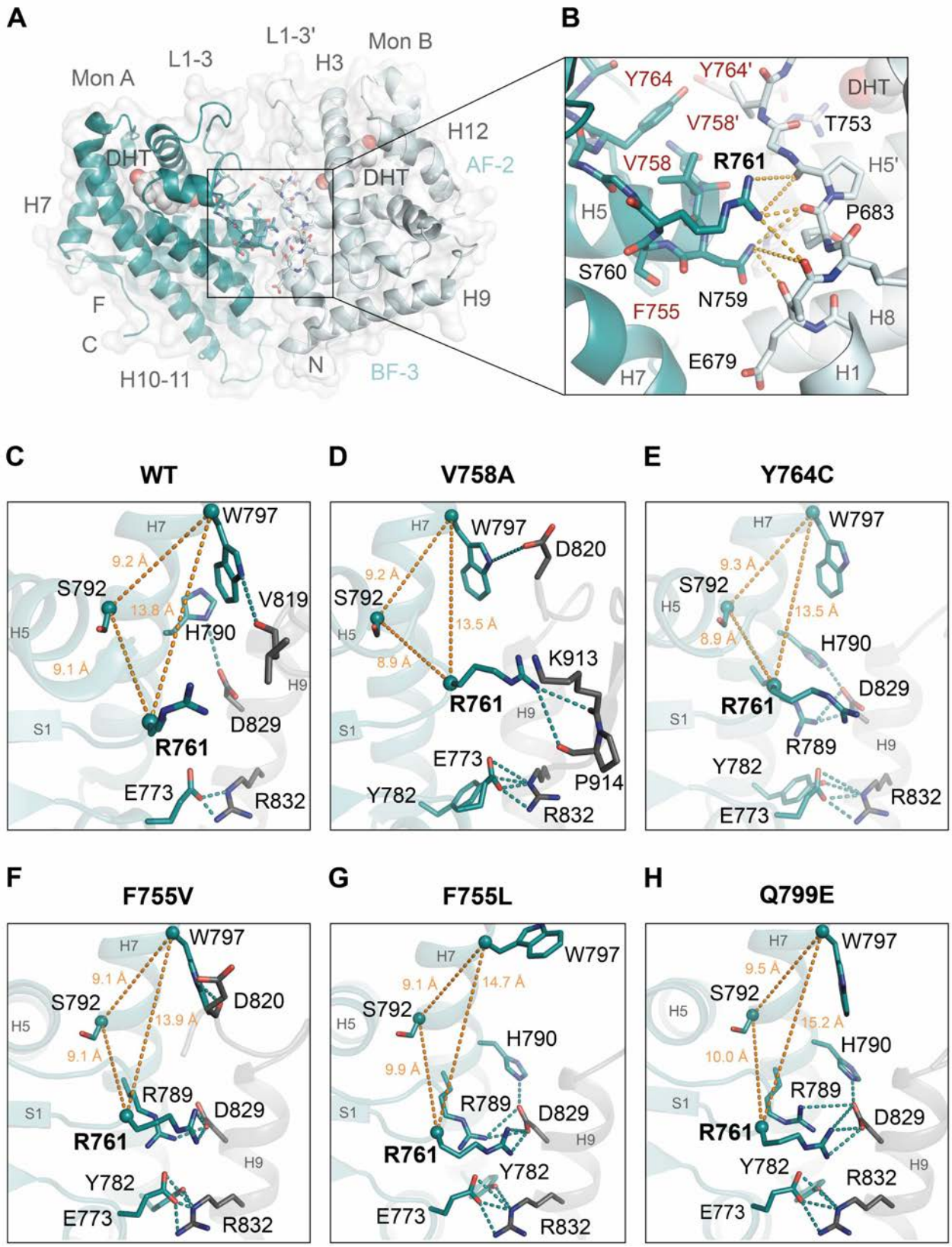

Fig. 28. The Arg761-zone conformation is differentially rearranged by AR-LBD mutants.

(A) Surface and cartoon representation of the AR-LBD·DHT dimer (PDB 5JJM). Residues comprising the core dimer interface are shown as color-coded sticks (oxygen, red; nitrogen, blue; carbon teal or sky-blue). *(B)* Close-up of the core dimer interface. Interface residues are shown as sticks and labelled. Major inter-domain hydrogen bonds are represented as orange dotted lines. *(C-H)* Close-ups of the R761-zone in the crystal structures of mutant AR-LBD (teal-coloured cartoons). The closest crystal neighbour is also shown in all cases (coloured dark grey), to highlight major interactions due to the crystal packing. Residues involved in the crystal contacts are represented as color-coded sticks. Note the tighter contacts involving the Arg761 side chain in mutants F755V (F), F755L (G) and Q799E (H) compared to WT (C), V758A (D) and Y764C (E), most notably salt bridges with the Asp829 carboxylate from the neighbouring monomer. Distances between the post-translationally modified residues, Arg761 and Ser792, and from both of them to the reference residue, Trp797, are also given.

3.4. AR-LBD dimer interface mutations affect *in vivo* methylation of Arg761

Our structural analysis of AR-LBD point mutants that affect the dimer interface revealed important structural rearrangements, which parallel the differences in the transcription profiles of these variants (see above). These observations prompted us to explore possible functional consequences of the studied mutations. Residue Arg761 adopts a markedly different, more exposed conformation in several mutants (Fig. 29, A to G), which together with minor changes in surrounding residues remodel this area, which ultimately results in an increased solvent accessibility of Ser792. Akt has been found to phosphorylate AR in residues Ser215 and Ser792 to modulate AR transactivation, cell survival and apoptosis (Wen et al., 2000; Lin et al., 2001, 2003). For this reason, we decided to verify whether Ser792 is differentially phosphorylated in AR mutants compared to WT AR, by using an antibody generated to detect this specific PTM. In a first replicate of this assay, only F755V, V758A and Q799E mutants were phosphorylated, although the corresponding bands are faint (Fig. 29H). Conversely, in a second replicate of this assay WT AR but none of the mutants were phosphorylated (data not shown). The results of these preliminary experiments suggest that phosphorylation of Ser792 may be cell cycle-dependent, and further experiments are needed (required) to assess the time course of this PTM.

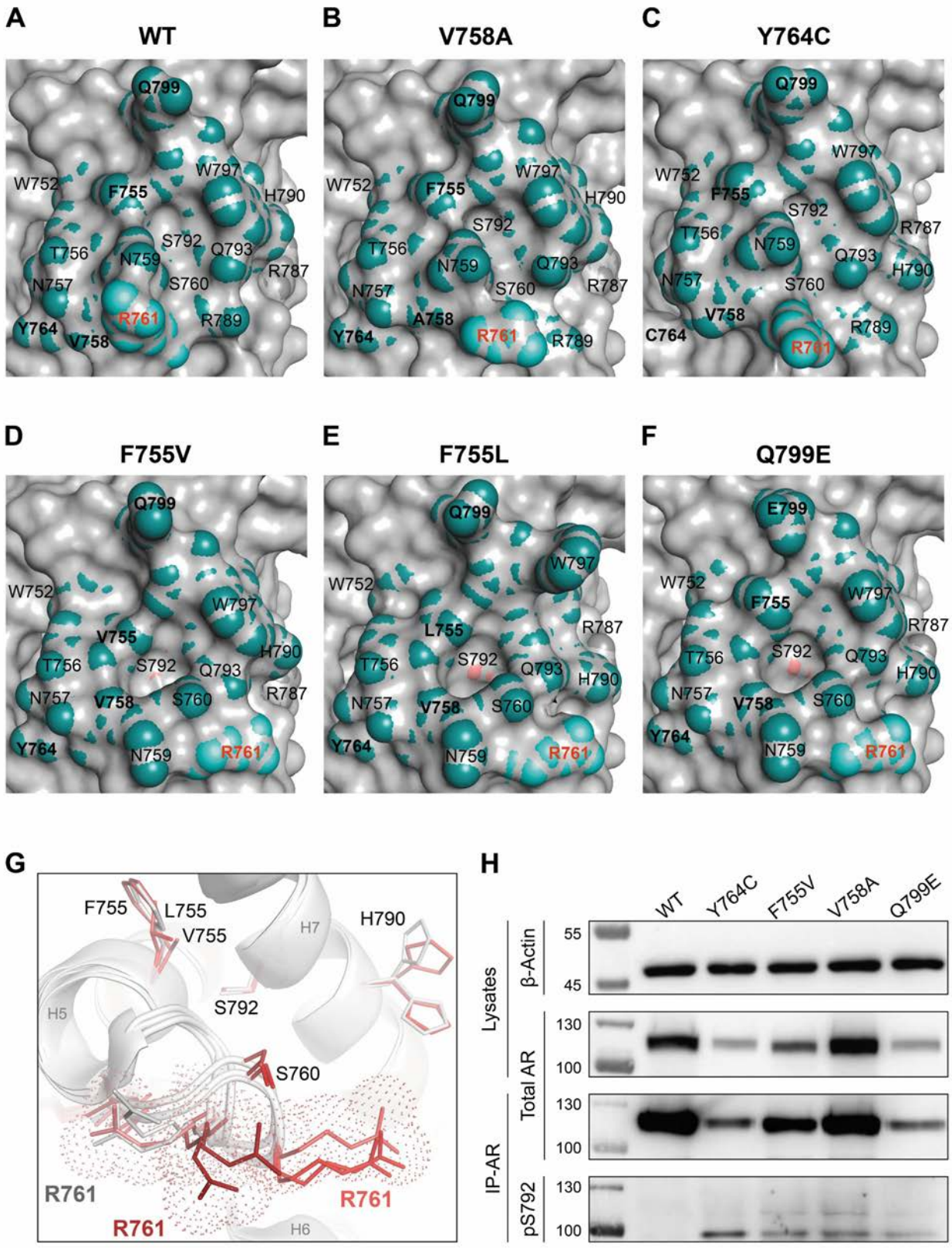

Fig. 29. Arg761 and Ser792 are more solvent exposed in AR-LBD dimer interface mutants.

(A-F) Surface representation of the AR-LBD pocket spanned by residues Trp752 and Phe755-Val758 (H5), Tyr764 (S1), Arg789-Gln793, Trp797, and Gln799 (H7) and Asn759-Arg761 (loop H5-S1). All residues are shown as teal spheres superimposed by a grey surface to highlight the pocket topography. Of note, Arg761 (red label) conformational changes and Ser792 (salmon) increasing solvent accessibility can be observed. *(G)* Cartoon representation of the Arg761-zone depicting the major dislodgement of loop H5-S1 triggered by pathological mutants, which can be appreciated by the different conformations adopted by the Arg761 side chain in the mutants structures (red shades) relative to WT (grey): from an intermediate state in V758A and Y764C (dark red, facing the viewer) to a right-oriented, more solvent-exposed position in F755V, F755L and Q799E (in salmon). *(H)* WB analysis of total and phosphorylated S792 (pS792) immunoprecipitated FL-AR (IP-AR) from PC3 cell lines expressing transduced WT or mutant AR. Note that lower bands in pS792 WB do not correspond to the molecular weight of FL-AR.

Arg761 has been reported as a substrate of a major type II arginine methyltransferase with both mono- and symmetrical dimethylation activity, protein arginine methyltransferase 5 (PRMT5), with important functional implications (Mounir et al., 2016). To assess direct physical interactions between FL-AR and endogenous PRMT5 in living cells, we performed PLA experiments. The results of these experiments demonstrated strong AR-PRMT5 interactions in PC3-WT and PC3-Q799E cells, which were significantly reduced in PRMT5-silenced cells (Fig. 30, A and B; note the 50% loss of AR-PRMT5 interactions for both WT and Q799E). Furthermore, PLA experiments demonstrated arginine monomethylation of FL-AR, as well as weaker symmetric dimethylation, which was reduced 50% upon incubation with the PRMT5-specific inhibitor, GSK595 (Fig. 30, D to F). In all PLA experiments, we observed heterogeneous patterns, with some nuclei showing strong AR-PRMT5 or methylation signals while others were practically devoid of these signals (Fig. 30, A and C). We also note that levels of Q799E mutant were remarkably lower in these experiments.

WB analysis of immunoprecipitated AR samples verified that Arg residues of both WT and mutant AR proteins were monomethylated in PC3 cells (Fig. 30G). Similar to the results of PLA experiments for the Q799E variant (Fig. 30C), the concentrations of mutant proteins were lower, and comparison of the relative intensities of bands corresponding to total and methylated AR fractions revealed that mutants were methylated to a lower extent. This feature is probably due to enhanced degradation of the mutant proteins, compared to WT AR (Fig. 20, A and B, and Fig. 21), rather than reduced expression. In this regard, recombinant WT AR-LBD and its mutants are produced at similar levels in a heterologous system (Fig. 30H). Considering the structural information presented above, these findings strongly suggest that residue Arg761 is preferentially monomethylated by PRMT5 in WT and AR-LBD mutants (Fig. 30).

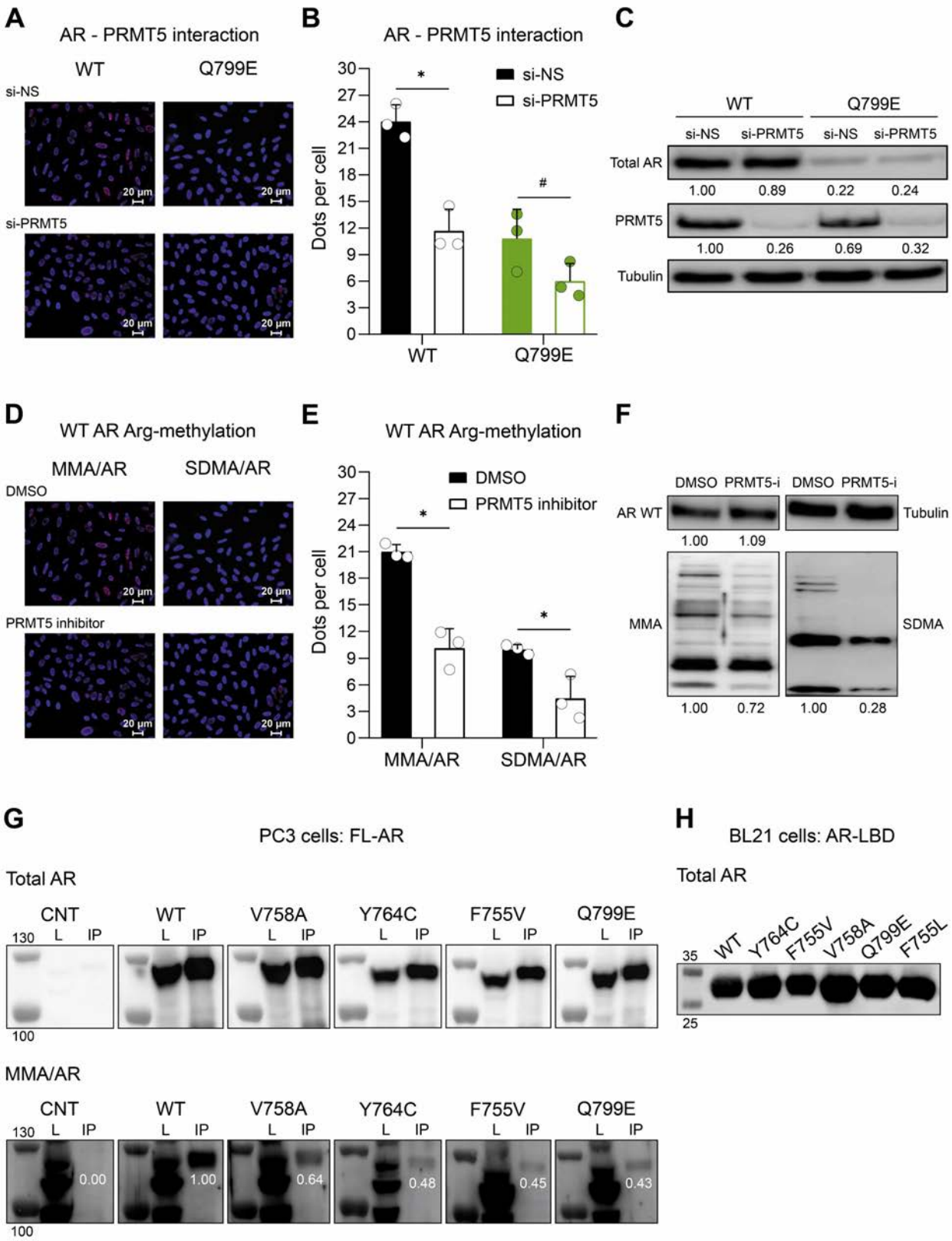

Fig. 30. Androgen receptor is preferentially monomethylated in living cells by the PRMT5.

(A and D) Representative PLA images demonstrating AR·PRMT5 physical interactions (A) and detected mono- (MMA) and symmetrically dimethylated arginine residues (SDMA) WT AR (D) in red dots. Nuclei were counterstained with DAPI (blue). To verify AR·PRMT5 interaction, PRMT5-silenced cells (si-PRMT5) were compared to non-silenced cells (si-NS) (A), and a PRMT5-specific inhibitor was used to verify that the methylation signal was PRMT5-dependent (D). *(B and E)* Quantified PRMT5-AR interactions are shown in B and the number of detected MMA/AR and SDMA/AR is shown in E (mean ± SEM, n = 3). Depicted differences were calculated using a t-test. *(C)* WB analysis and quantification of whole-cell extracts from (A). *(F)* WB analysis and quantification of whole-cell extracts from (D). Note that, while SDMA can be mediated only by PRMT5 and PRMT9, MMA can be catalysed by type I and II PRMTs. This explains the larger impact of the PRMT5-inhibitor on the SDMA. *(G)* WB analysis of total and MMA immunoprecipitated (IP) FL-AR from lysates (L) of PC3 cell lines expressing transduced WT or mutant AR. MMA/AR bands were double normalized against the total IP AR and against the MMA/AR-WT band (= 1.00), so that MMA levels of AR mutants are not biased by the amount of IP proteins. *(H)* Relative expression levels of WT and mutant AR-LBD in BL21 *Escherichia coli* cells.

In the absence of structural information on the mechanism of recognition and processing of globular, macromolecular substrates by the methylosome (the hetero-octameric PRMT5·MEP50 complex) and to explore possible binding modes of AR, we performed docking experiments using the current structure of AR-LBD Q799E mutant and previously reported structures of the PRMT5·MEP50 complex (Sun et al., 2011; Antonysamy et al., 2012; Ho et al., 2013; Mulvaney et al., 2021) (Fig. 31). Similar interactions could be expected for WT AR and other point mutants. The results of these docking experiments suggest how the extended H5-S1 loop in the AR-LBD would fit into the active site of the methyltransferase, supported by additional interactions of residues from the neighbouring PRMT5 monomer (Fig. 31). Further, inspection of the docking solutions suggests that the AR-PRMT5 complex might be stabilized by additional interactions of AR-DBD with the N-terminal subunit of the transferase, while the MEP50/WDR77 component could recognize methylated Arg residues within the AR-NTD (Fig. 31). Synergy between these different interactions would ultimately provide the necessary energy to enforce structural rearrangements required to insert the non-glycine side chains of Ser760 and Met762 in the corresponding subsites of the enzyme, thus allowing methylation of residue Arg761.

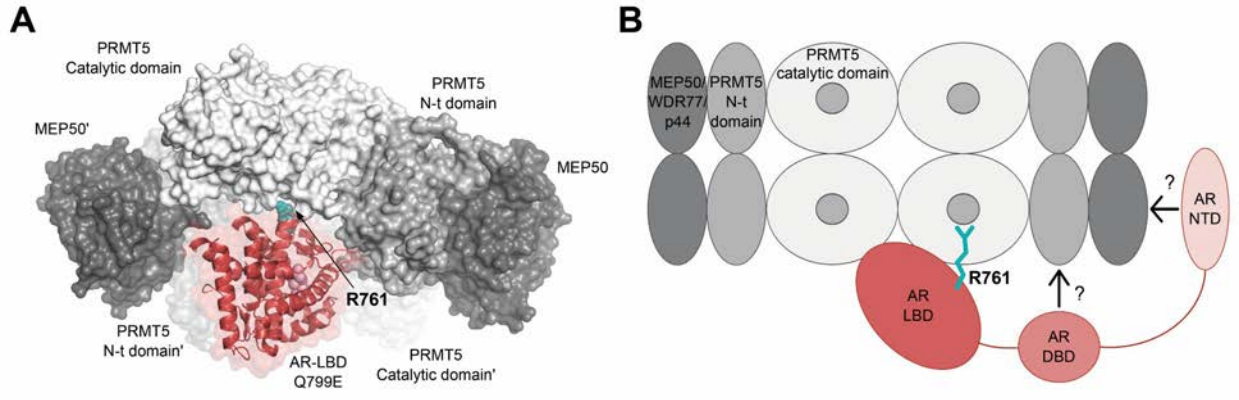

Fig. 31. Model of the interaction between androgen receptor and PRMT5·MEP50 methylosome complex. (A) Model of AR-LBD(Q799E) approaching the active site of the PRMT5·MEP50 methylosome. For simplicity, only a heterotetrameric (PRMT5)2·(MEP50)2 complex is shown (PDB 4GQB). Note that folded substrates such as AR-LBD would interact with two neighbouring catalytic subunits, in addition to NTD-MEP50 and DBD-PRMT5 contacts. fraction. *(B)* Diagram of putative interactions between AR domains and the methylosome.

4. Characterization of androgen and glucocorticoid receptors heterodimerization

We have thoroughly characterized the homodimerization landscape of AR and GR, in both the current work on pathogenic mutants affecting the AR dimer interface (Alegre-Martí et al., 2023), which is a follow-up of the prior study of AR homodimerization conducted by members of the host laboratory (Nadal et al., 2017), and the GR homodimerization to which I have contributed during my Ph.D. thesis (Jiménez-Panizo et al., 2022). Our multidisciplinary investigations have involved both *in vitro* biophysical assays with purified proteins and experiments in living cells. Building upon this foundational work, we now aim to broaden our study to the heterodimerization of these two receptors, which might hold significant implications for the pathophysiology of prostate cancer. In particular, this hetero-interaction appears to play a pivotal role in disease progression (Chen et al., 1997; Zwart et al., 2017; Ide et al., 2018; De Bosscher et al., 2020; Kanai et al., 2020; Ruiz et al., 2020; Quattrocelli et al., 2021; Timmermans et al., 2022). Also considering the potential pharmaceutical significance of the AR-GR interaction, our current project seeks to comprehensively characterize their heterodimerization mechanism. In this chapter, we present the preliminary data we have gathered so far in this project, which is currently being assembled into a draft.

To decipher the details of the interaction between these NRs in solution, we expressed and purified the LBD and core modules of AR and GR bound to the potent agonists DHT and DEX, respectively. As in our previous work on GR multimerization, we selected the ancient variant of the human GR, ancGR2, for these experiments. This construct recapitulates the characteristics of WT human GR-LBD and GR core and has repeatedly been employed in recent GR structure-function studies because of its higher solubility and stability *in vitro* (Weikum et al., 2017; Jiménez-Panizo et al., 2022). The expression and purification protocol for AR and GR cores is based on the already well established and optimized protocol for LBD modules, and consists of two consecutive affinity chromatography steps, as described in methods section 2.2, with minor adjustments to obtain large yields of highly purified multidomain proteins. For AR core (Figure 32A), this included an increase in the temperature during the O/N expression from 16 ºC to 18 ºC compared to the LBD protocol, and the addition of 1 mM of CHAPS, a zwitterionic surfactant that further solubilize AR core protein. Finally, and considering that AR-LBD copurifies with *E. coli* GroEL, the homologous protein of human Hsp60, we added 1 mM of ATP to the purification buffers to further activate GroEL and thus improve AR core folding.

On the other hand, the protocol for expressing and purifying the GR core is not fully optimized yet. We have made important advances regarding the purity of the elution fraction from the first IMAC step. However, the MBP-His-tag-GR fusion protein copurifies with two proteins of lower molecular weight, which appear to be C-terminally truncated forms of the protein (Figure 32B). So far, we have not been able to obtain a single band of this GR variant, neither by changing the expression conditions (e.g., from O/N at 16 ºC to 4 h at 32 ºC, to activate the cellular machinery), nor by introducing additional chromatography steps (Figure 32, B and C). Therefore, we decided to conduct preliminary experiments with this fraction while we continue optimizing the purification protocol in parallel.

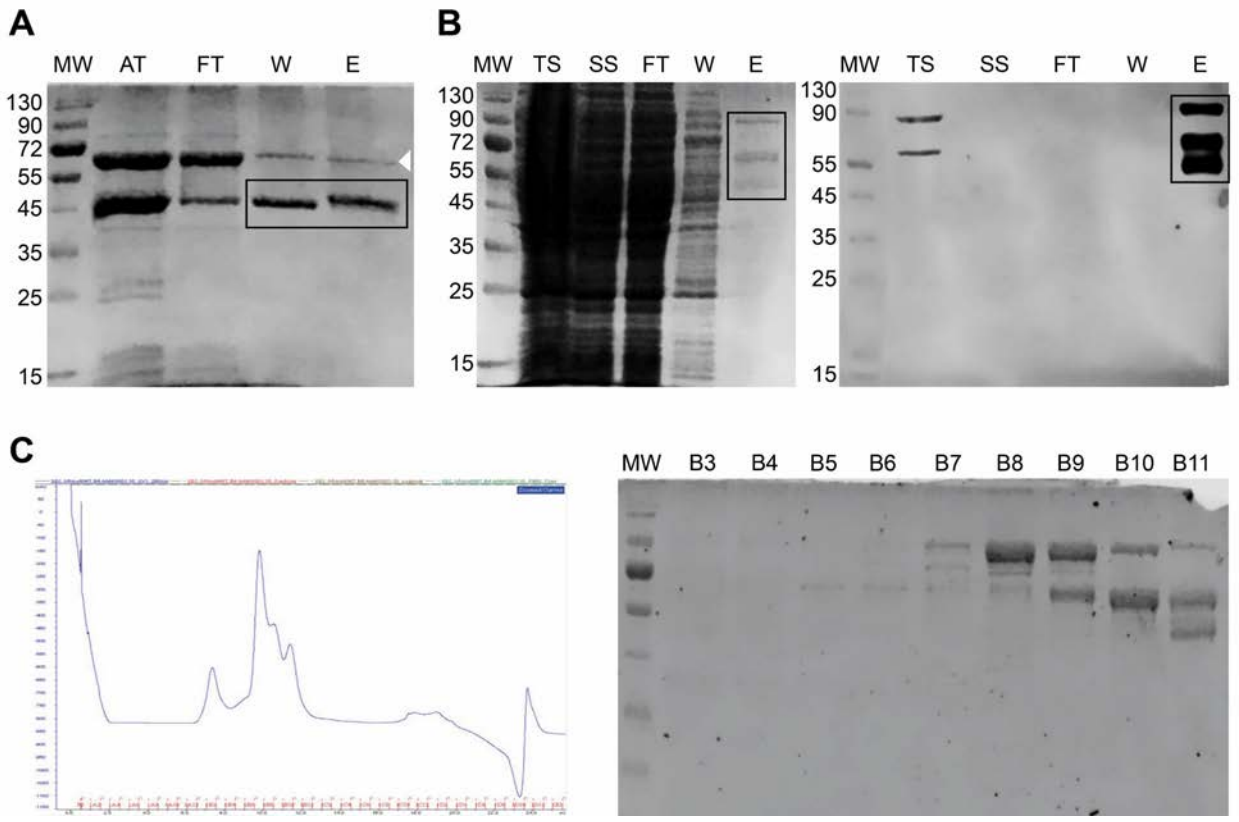

Fig. 32. Purification of recombinant androgen and glucocorticoid receptor core modules.
(A) SDS-PAGE analysis of second IMAC purification step of AR core. After TEV treatment (AT), the protein solution was applied again to the Ni-NTA column to remove the N-terminal tag and non-cleaved proteins. Samples of the flow-through (FT), wash (W) and elution (E) fractions were analysed. MW, molecular weight marker. The 60-kDa band marked with a white triangle corresponds to GroEL chaperonin, and the 52-kDa band to the AR core, W and E (fractions squared in black) were pooled, concentrated, and used in following experiments. *(B)* SDS-PAGE analysis of the first IMAC purification step of the GR core (left panel) and WB analysis of the same samples with a 6xHis tag antibody (right panel). Total sample (TS) corresponds to the cellular lysate after sonication, and soluble sample (SS) to the fraction after lysate centrifugation. *(C)* Chromatogram of the size exclusion purification of the bands squared in black in B (left), and SDS-PAGE analysis (right) of the fractions corresponding to the indicated fractions.

Purified, agonist-bound LBD and core modules of AR and GR were concentrated to 4 – 6 mg/mL immediately after the second IMAC purification and stored at – 20 ºC. To study the affinity and kinetics of the interactions between these receptors and their cognate HREs, we immobilized AR and GR cores on CM5 chips using standard amine coupling at a density of 300-600 RUs . Next, we ran over increasing concentrations (0.25 – 40 µM) of two selected AREs and one GRE duplex DNA sequences (see Methods section 2.7) and recorded the

corresponding sensorgrams. Analysis of the binding data according to the 1:1 Langmuir affinity model indicated that AR core binds to both ARE and GRE sequences with moderate affinity (K_D = 4 μM: Fig. 33, A to C). On the other hand, GR core binds with similar affinity to ARE1 (Fig. 33D), while binding to ARE2 and GRE does not fit the 1:1 model accurately (Fig. 33, E and F), as the statistical χ^2 values are of the same magnitude as the maximum responses (R_{max}). Ideally, the χ^2 values should be one order lower than the Rmax, indicating a better fit. These results demonstrate that AR and GR core recombinant proteins are functional and prompted us to perform additional experiments to assess their heterodimerization potential in solution.

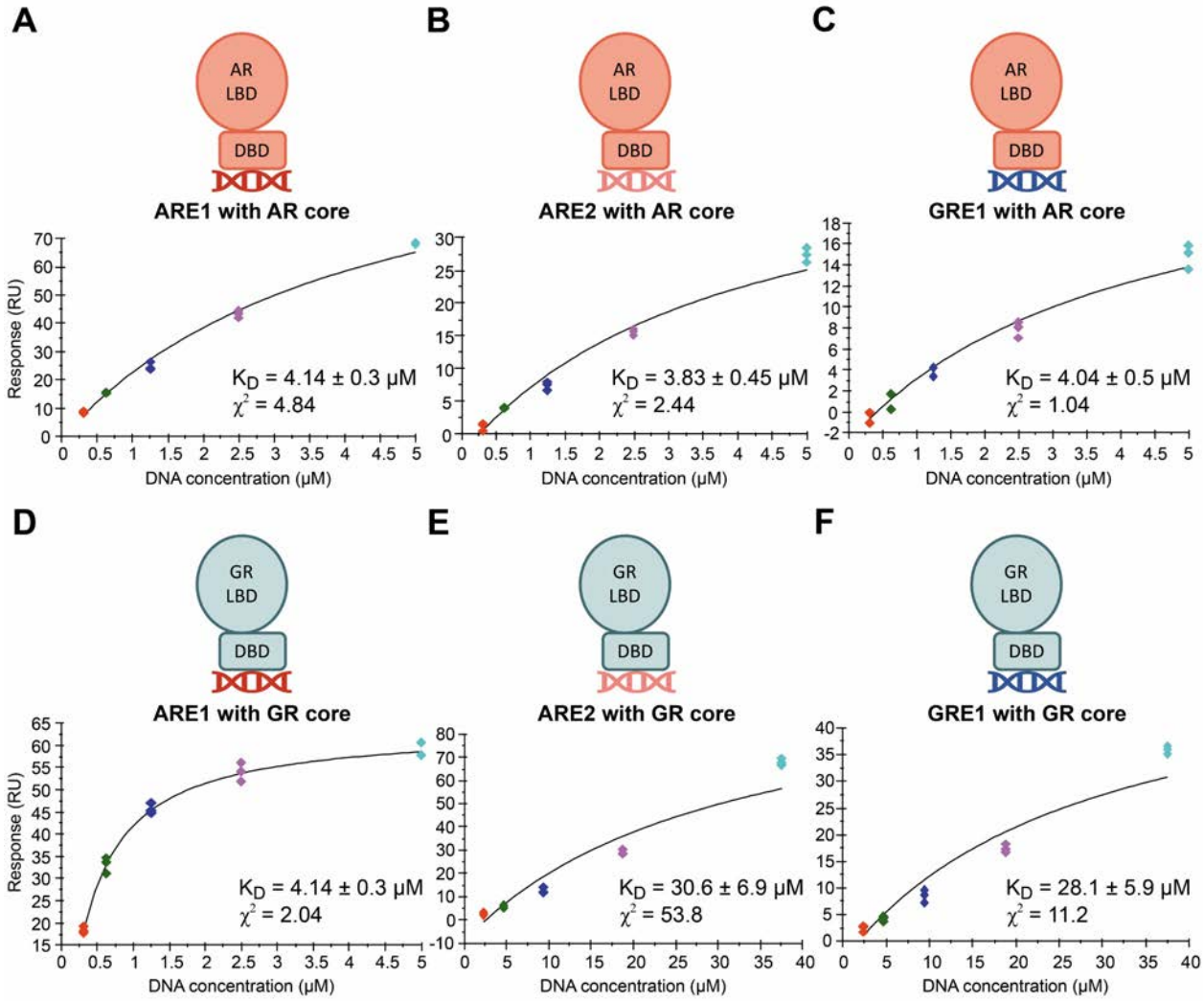

Fig. 33. Immobilised androgen and glucocorticoid receptor cores interact with their cognate hormone response elements in solution.

SPR analysis of the binding of AR *(A-C)* and GR *(D-F)* core modules to ARE1, ARE2 and GRE oligonucleotides. The accuracy of the data fitting to the 1:1 Langmuir model was assessed with the statistic χ^2.

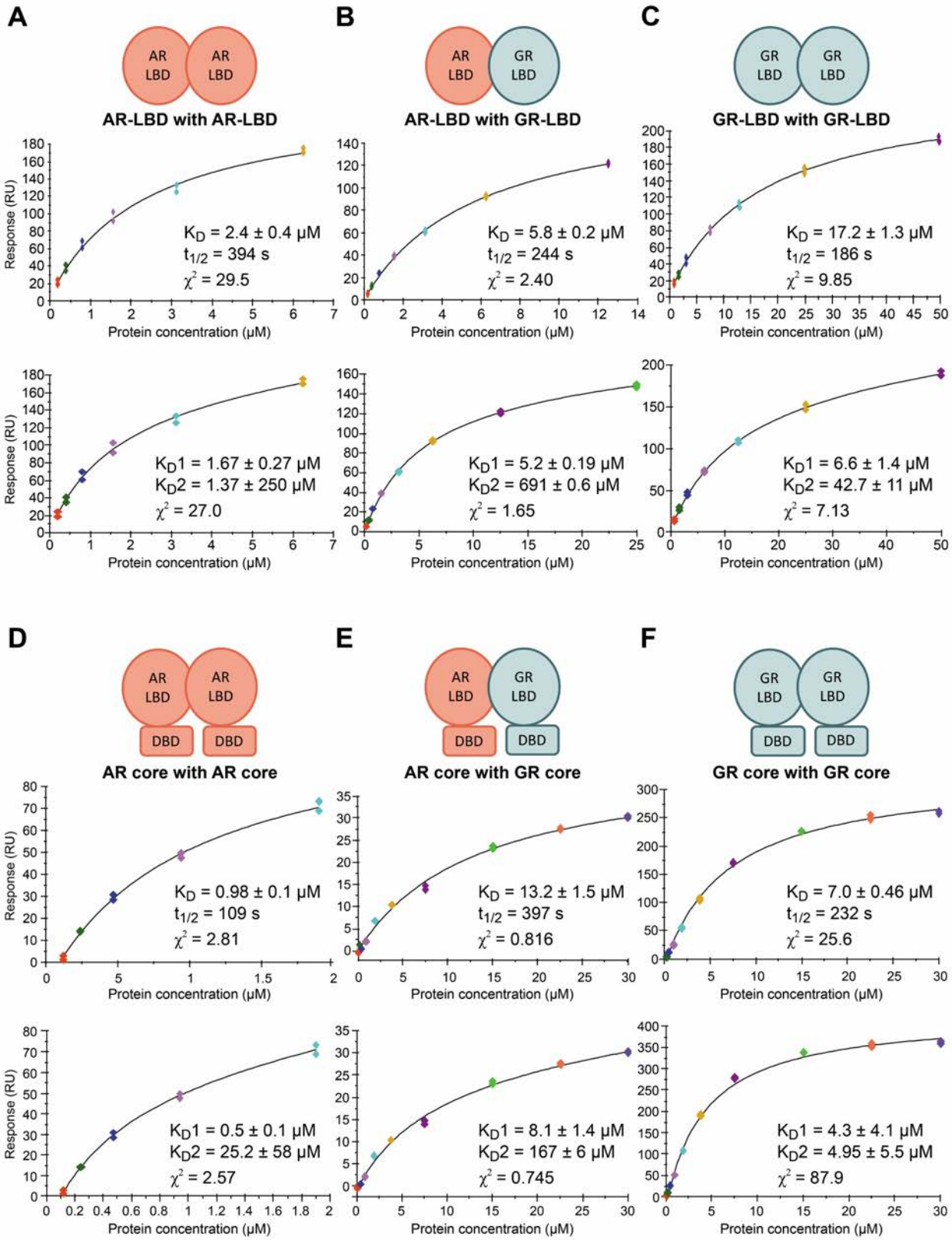

Fig. 34. Androgen and glucocorticoid receptors form both homo- and heterodimers in solution.

SPR analysis of the homo- and hetero-interactions between AR-LBD, GR-LBD *(A-C)*, AR core and GR core *(D-F)* according to 1:1 (upper plots in each panel) or multisite affinity models (lower plots in each panel). The results of experiments conducted in duplicate are shown along with the calculated affinity constants (K_D). Kinetics analysis was also conducted to calculate the half-life of the complexes ($t_{1/2}$). Statistical quality assessment of the data revealed that AR-LBD (A) and GR core (F) self-interaction data have χ^2 values too high for the obtained Rmax: AR-LBD presents 228.8 (1:1) and 180 RUs (multisite) and GR core has 341.8 (1:1) and 400 RUs (multisite). Further, the multisite fitting of the GR-LBD homo-interaction calculated a standard error of the same magnitude as the K_D2 (C, lower plot). For these reasons, AR-LBD, GR-LBD, and GR core datasets should be repeated to obtain conclusive data.

To this end, we immobilised purified LBD and core modules of AR and GR on CM5 chips at a density of about 100 RUs per channel and ran over increasing concentrations of the same protein samples (0.12 – 50 µM) as analytes. Several kinetics models were used to interpret the obtained SPR data using BiaEvalution software 3.0 (Fig. 34). All possible homo- and hetero-interactions could be fitted to both the 1:1 and multisite affinity models (Fig. 34). Although the multisite fittings show better statistics (χ^2 value, see legend to Fig. 34F), significance evaluation using the F-test demonstrate a significantly better fit to the multisite model only for GR core self-association. Therefore, data fitted to the 1:1 binding model were used to derive the half-life times of the complexes ($t_{1/2}$) from their dissociation constants (k_d). Among the LBD interactions, the AR-LBD homodimer is the most long-lived ($t_{1/2}$ = 394 s), followed by the AR-LBD·GR-LBD heterodimer (244 s) and finally the GR-LBD homodimer (186 s) (Fig. 34, A to C). Interestingly, the AR-GR core heterodimer is the most long-lived of all complexes (397 s), although it has a lower K_D (Fig. 34, D to F). In summary, SPR experiments suggest that AR and GR can interact as both homo- and heterodimers and as higher order oligomers, and the competition between homo- and hetero-interaction may depend on the cellular context. Further experiments are needed to fully characterize the nature of their interactions.

Finally, we assessed the possible relevance of the AR-LBD homodimerization interface for heterodimer formation with GR. We immobilised LBD and core modules of both SRs at densities of 3,000-6,000 RUs and studied their interactions with synthetic peptides derived from the AR non-canonical dimer interface (see Methods, section 2.7). Fig. 35 shows the affinity analysis of the protein–peptide interactions that could be fitted to the 1:1 Langmuir model. The three peptides showed high affinities for both the LBD (Fig. 35, A and B) and core modules of AR (Fig. 35D), as expected. GR core binds the WY13 peptide, although with lower affinity

compared to AR-peptide interactions (Fig. 35E). Finally, CC18 peptide binding to both LBD and core GR could not be accurately fitted to the 1:1 model (Fig. 35, C and F). Altogether, these results suggest that AR-LBD dimer interface may also be important for AR-GR heterodimerization.

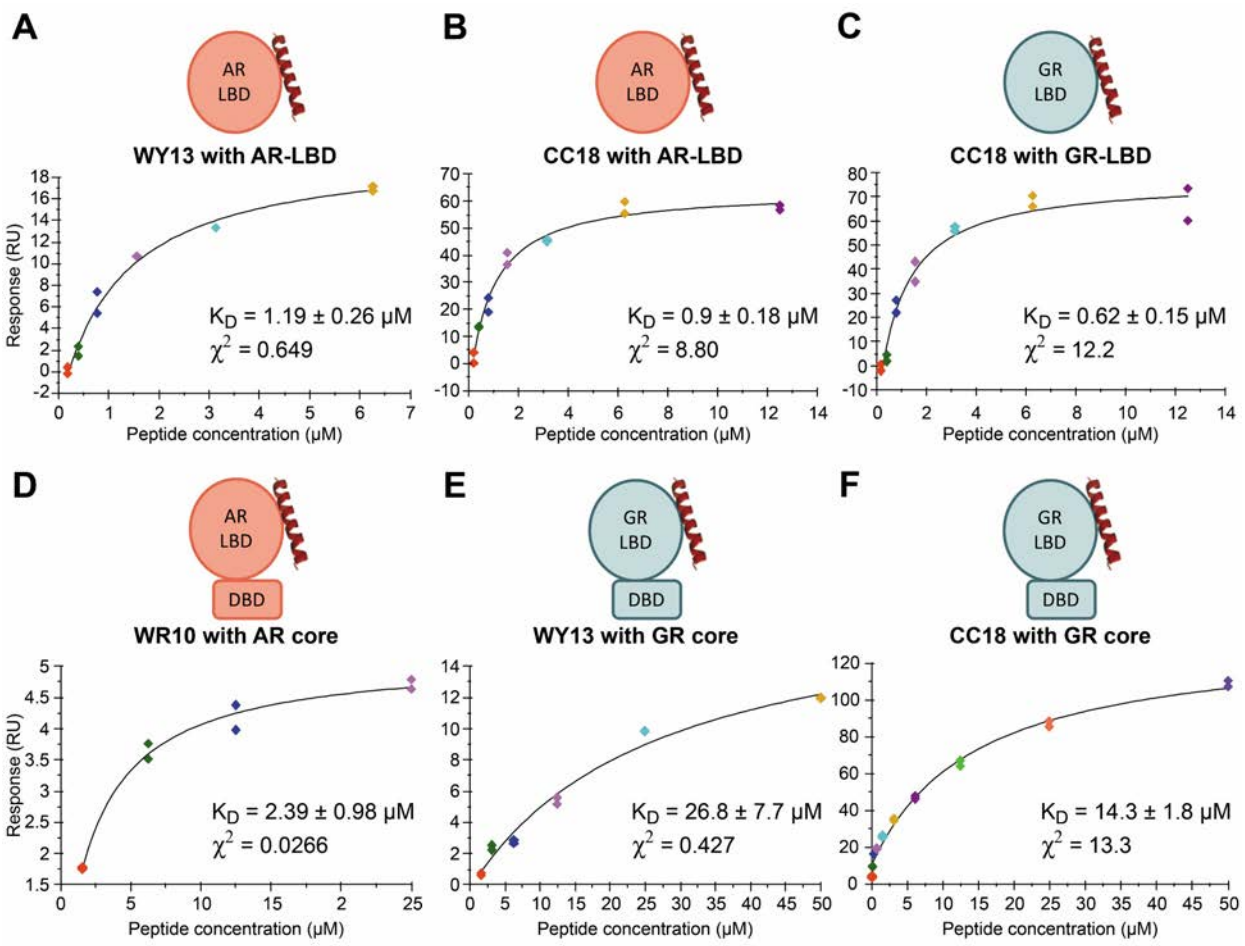

Fig. 35. The homodimerization interface of the AR-LBD could also play a role for its heterodimerization with the glucocorticoid receptor.

Affinity analysis of AR dimer interface peptides binding to LBD *(A-C)* and core *(D-F)* modules of AR and GR. Note that AR core was immobilized at 212 RUs -below the optimal density-, so we should expect an R_{max} of 5.6 RUs, as experimentally observed. This observation, in addition to the χ^2 value being two orders of magnitude lower than the Rmax (0.0266 and 5.65,respectively), validate the results of this dataset. Further assays will be performed to confirm these preliminary results.

Discussion

Although missense mutations of the *AR* gene have been repeatedly associated with conditions such as PCa and AIS (Gottlieb et al., 2012), the molecular mechanisms of disease causation and the affected pathways remain poorly understood to date. Previous structural analyses of AR point mutants have been limited to internal residues that line the LBP, which are particularly relevant because of their association with resistance to antiandrogen therapy in PCa patients (e.g., W742L, H875Y, and T878A) (Sack et al., 2001,Bohl et al., 2005b, 2007). Here we present a thorough multidisciplinary analysis of the structural and functional impact of several mutations that are buried at the AR-LBD dimer interface (Nadal et al., 2017), and which have been repeatedly linked to either AIS and/or PCa (F755L/V, V758A, Y764C, and Q799E). Although being essentially solvent-exposed residues in monomeric AR, and thus unlikely to compromise the overall folding of the protein, we show that these disease-linked variants have significant structural and functional implications. Most notably, transcriptomic analysis demonstrated that, despite overall conservation of AR programs, striking differences exist at the transcriptional level between WT AR and most mutants, including key drivers of PCa progression such as *FOXA1* and *MYC*. In general, mutations at the AR-LBD dimer interface impaired AR's ability to halt proliferation and colony formation while retaining sensitivity to AR targeting drugs, consistent with a role for the receptor as a master regulator of differentiation (Aytes et al., 2014). In fact, the growth suppressive role for ligand-bound AR had previously been shown (Lam et al., 2020; Kumar et al., 2021) and has been the basis for the proposed supraphysiologic testosterone treatment in PCa patients that is being evaluated in clinical settings as part of the bipolar androgen therapy (Schweizer et al., 2015). Mechanistically, AR signalling has been shown to be dichotomous, promoting or repressing growth at low or high activity levels, respectively (Nyquist et al., 2021), and distinct transcriptional outputs have been identified for patients responding to supraphysiologic testosterone (Qiu et al., 2022).

These significant differences in transcriptional programs were paralleled by a largely reduced stability of the mutant AR-LBD modules, as indicated by notably lower Tm of up to 6 °C and increased sensitivity to proteolysis in F755L/V and Y764C. Our current high-resolution crystal structures of the mutant domains reveal, in addition to changes in the targeted dimerization interface, an increased propensity to side chain movements of residues that cluster in previously described functional areas of the receptor: the exposed AF-2 and BF-3 pockets but also in the minor dimerization site identified in our previous crystal structure of multimeric AR-

LBD, and which evokes the tetrameric assemblies identified in living cells (Nadal et al., 2017). Similar movements were also identified in MD simulations of mutant proteins (Fig. 24 and 25, and fig. S3E and S5). Structural rearrangements are particularly noteworthy in variants F755L/V and Q799E, in which residues of the R761-zone (the H5-S1 loop) adopt a previously not observed, much more solvent-exposed conformation, which deviates by up to 4 Å from that observed in all previously reported structures of AR-LBD bound to both agonists and antagonists.

On the other hand, we showed that introduction of a cysteine in a solvent-exposed position at the dimer interface (Y764C) increases the propensity to non-productive dimer formation, which likely leads to further conformational changes in the FL protein. In this regard, the recently presented low-resolution cryo-EM structures of the "core" AR have revealed, in addition to an "entrenched" arrangement, which would correspond to our previously presented structure of dimeric AR-LBD (Nadal et al., 2017), a more open or "splayed" assembly of AR monomers (Wasmuth et al., 2022). The propensity to non-productive homodimerization by the Y764C variant might be particularly relevant in the crowded nuclear environment.

Our previous MD simulations of the V758A mutant indicated allosterically transmitted conformational changes in the AR-LBD (Grosdidier et al., 2012). The current crystal structures of AR-LBD point mutations that affect the dimerization interface confirm and extend these observations. Indeed, these replacements induce conformational changes at areas located in the diametrically opposed pole of the domain, most notably the AF-2 binding pocket (Fig. 16B and Fig. 22E). This is the first time that a mutation in the AR-LBD dimerization site has been linked to conformational changes in the AF-2 pocket, suggesting that dimerization and coregulator binding are allosterically coupled. Careful inspection of the crystal structures supported by MD and SCA analyses suggests allosteric pathways connecting the dimer interface with the LBP and the AF-2 and BF-3 sites in AR-LBD.

Previous investigations have revealed several functional defects in the studied mutants, including a lower affinity for agonists, which at least in the case of Y764C was shown to result from a more rapid dissociation of ligands without significant changes in the LBP, a significant to near complete loss of NTD-LBD (N/C) interactions, and a largely reduced transcriptional activity, in particular at physiological DHT concentrations (summarized in table S2). Altogether, these functional findings are in line with our current structural observations of increased mobility of AR-LBD mutants and have important consequences for the structure-function

relationship of the receptor. First, the overall decrease in domain stability together with subtle displacements of AF-2 residues might impair both intra- (N-/C-terminal) and intermolecular interactions with coregulators. Conversely, presence of the NTD would seem to stabilize the LBD upon N-/C- interactions, as suggested by the lower thermostability of a double mutant with a shortened polyQ stretch in the NTD in addition to the Y764C point mutation (McPhaul et al., 1991). This is also in line with the cryo-EM structures of FL-AR, which revealed a compact conformation with a central LBD surrounded by the NTD (Yu et al., 2020; Wasmuth et al., 2022), and with our recent identification of NTD-LBD interactions (Mosure et al., 2022; Sheikhhassani et al., 2022). Second, even mutations that do not affect the LBP directly can have a profound impact on DHT affinity, by facilitating its dissociation from the internal binding site. In this regard, hormone trafficking in and out the LBP is likely to involve displacements of residues in the H5-S1 loop similar to the ones observed in our current crystal structures, or perhaps of a larger magnitude. N/C interactions of the Q799E mutant were normal, however (Jääskeläinen et al., 2006), highlighting the unique molecular fingerprint of each mutation.

The PCa-associated transcription factor ERG was previously shown to recruit protein arginine methyltransferase PRMT5 to AR-target genes (Mounir et al., 2016). PRMT5 then methylates AR at position Arg761, ultimately downregulating AR transcriptional activity. Here we corroborate and extend these findings by showing a direct physical interaction of endogenous PRMT5 with both WT and the Q799E mutant of FL-AR in living cells. Further, we verified that AR is both mono- and, to a lesser extent, symmetrically dimethylated in cells in a PRMT5-dependent manner (Fig. 30, A to F). The presence of non-glycine residues both before and after Arg761 would seem to make its methylation less favourable than canonical Gly-Arg-Gly motifs, in light of current structural evidence for PRMT5 (Antonysamy et al., 2012; Ho et al., 2013) and other methylases (Zhang and Cheng, 2003). However, a recent systematic analysis of the human methylome has revealed a large number of substrates with bulky side chains preceding and/or following the modified arginine (Musiani et al., 2019). Our docking experiments suggest that Arg761 processing by the octameric $(PRMT5)_4 \cdot (MEP50)_4$ heterocomplex known as methylosome would depend on secondary interactions of residues in the immediate vicinity of the methylated arginine, on the one side, and exposed residues of the PRMT5 catalytic domain and the N-terminal subunit of a neighbouring molecule in the methylosome, on the other. Substrate recognition might be assisted by additional interactions with the highly acidic non-catalytic subunit of the methylosome, MEP50/WDR77, which have

been shown to orient substrate histones towards the buried active site of PRMT5 (Burgos et al., 2015). A summary of predicted AR interactions with the methylosome that might ultimately determine specific recognition and processing of Arg761 is schematically presented in Fig. 31.

Although the more exposed, protruding conformation of Arg761 in AR-LBD mutants would favour recognition and processing by the methylosome, we have actually observed a decrease in the total and methylated fractions of the studied AR mutants in cells. Point mutants of the AR-LBD are unlikely to affect protein expression, and indeed we have observed similar expression levels of recombinant WT AR-LBD and its mutants. Therefore, this apparent contradiction points to an enhanced degradation of mutant AR protein. AR is polyubiquitinated by several E3 ligases (Introduction; see Fig. 12 and 36), followed by its degradation in the proteasome. The tumour suppressor CHIP appears to be particularly relevant in this regard, as it couples the chaperone machinery to AR degradation, inducing mitotic arrest (Chymkowitch et al., 2011; Sarkar et al., 2014). Of particular clinical relevance, CHIP has been shown to modulate sensitivity to antiandrogen therapy in advanced PCa (Liu et al., 2018). These findings are also important with regard to the current development of proteolysis targeting chimeras (PROTACs) as pharmacological alternatives for PCa treatment (Mohler et al., 2021; Ha et al., 2022).

Multiple additional connections between the PRMT5·MEP50 methylosome, AR pathophysiological activity, and PCa aetiology have been reported. PRMT5 functions as an epigenetic activator of AR transcription in PCa (Deng et al., 2017), while the non-catalytic methylosome component, MEP50 (also termed androgen coactivator p44) has been previously identified as an AR interactor linked to PCa progression, which enhances AR-driven gene expression independently of PRMT5 catalytic activity. Accordingly, MEP50 expression levels are higher in PCa tissue than in adjacent, normal prostate tissue (Hosohata et al., 2003), and it has been associated with androgen independent PCa (Peng et al., 2008). Further, MEP50 is required for homeostasis of prostate epithelial cells by controlling the proper expression of AR-target genes, and its translocation from the nucleus into the cytoplasm in PCa cells results in exacerbated proliferation of prostate epithelial cells (Zhou et al., 2006). Altogether, the close relationship between methylosome and AR activity at the light of our current observations provokes a systematic analysis of AR methylation in PCa patients and suggests avenues for therapeutic intervention, in particular in *TMPRSS2:ERG* positive PCa (Mounir et al., 2016).

Another important PRMT5 substrate, AKT kinase, is also methylated at a non-canonical sequence that resembles the AR-LBD modification site (Gln-Arg-Leu) (Ha et al., 2022). The side chain of the methylated arginine residue, Arg391 is fully buried in the AKT protein core, indicating that large conformational changes are not uncommon in PRMT5 substrates. This finding is also relevant because AKT has been shown to phosphorylate AR at two canonical RXRXX(S/T) sites, Ser213 in the NTD and Ser792 in the LBD (Taneja et al., 2005; Xu et al., 2009; Gioeli and Paschal, 2012). Noteworthy, Ser792 is located close to Arg761, and it is more exposed in the mutants with an open H5-S1 loop. However, we have not detected significant differences in the degree of phosphorylation between WT and mutant AR (Fig. 29H).

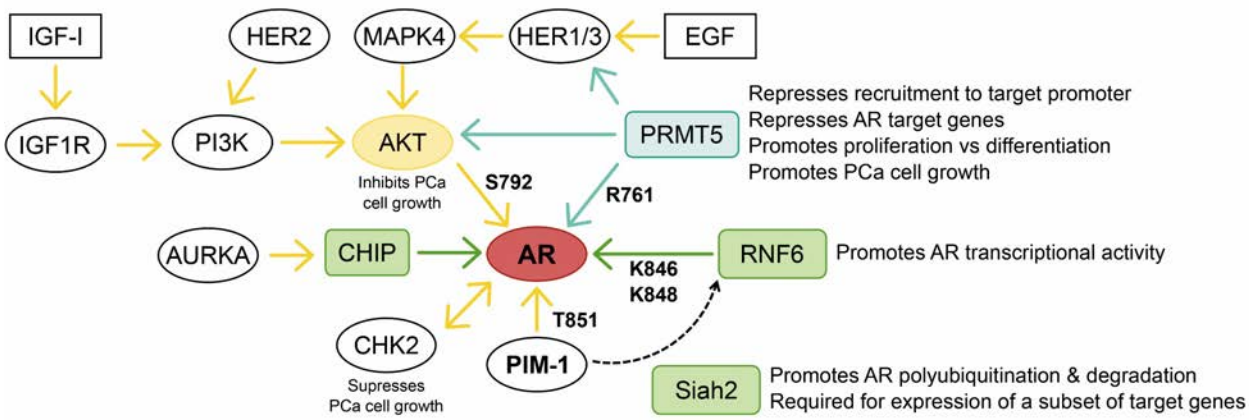

Fig. 36. Cascade of post-translational modifications affecting the AR-LBD.
Phosphorylation (yellow), methylation (blue), and ubiquitination (green) pathways are shown. Insulin-like growth factor 1 (IGF-1), IGF-1 receptor (IGF-1R), epidermal growth factor (EGF), epidermal growth factor receptor (HER1, 2 or 3), phosphoinositide 3-kinase (PI3K), checkpoint kinase 2 (CHK2), proto-oncogene serine/threonine-protein kinase (PIM-1) and E3 ubiquitin-protein ligase (Siah2). Of note, PRMT5 regulates the cascade at different levels, targeting EGFR/HER1, AKT and AR.

Inspection of the AR-LBD 3D structure reveals that the dimerization interface comprises, in addition to Arg761 and the nearby Ser792, several residues that have been previously reported as targets of post-translational modifications (Fig. 16A and 36). This extended patch includes in particular the pair of lysine residues at positions 846 and 848, which are ubiquitinated by RNF6 to modulate coactivator recruitment and AR transcriptional activity (van der Steen et al., 2013). Finally, residue Thr851 is phosphorylated by the PIM-1L isoform of this Ser/Thr kinase, which stabilizes AR by recruiting RNF6 (Linn et al., 2012; Koryakina et al., 2014). Interestingly, the phosphomimetic Thr851Asp mutation resulted in increased transcriptional activity due to enhanced recruitment of co-activators at AF-2 (Helsen et al., 2022), mirroring the impact of

several point mutations at the dimer interface characterized in the current work. Altogether, this AR surface emerges as a major hotspot for PTMs (a summary of AR-LBD PTMs and their functional consequences is given in Fig. 36). These findings underscore the realization that PTMs regulating DNA accessibility and transcription are not limited to histones but also affect other elements of the transcription machinery (extended histone code; Maksimovic and David, 2021). Future investigations should deepen on the cross-talk between PTMs and AR quaternary structure including interdomain motions and allosteric pathways connecting the different functional areas of the receptor and their impact on its proteasome-mediated degradation, as well as its interactions with specific coregulatory proteins.

One of the most intriguing interactors of AR in the complex landscape of PCa is the related GR, which is also regulated by PRMT5 (Poulard et al., 2020; Malbeteau et al., 2022) and has been postulated as an important contributor to the progression towards CRPC (Arora et al., 2013; Narayanan et al., 2016). Based on the GR enhanced expression in enzalutamide-resistant tumour biopsies from PCa patients and the high degree of similarity between its DBD and LBD modules with those of AR, it is plausible that the two SRs could form heterodimers under certain conditions. In fact, current evidence points to the AR-GR heterodimer as a potential mechanism explaining mutual inhibition of the transcriptional activity, leading to a differential target gene expression compatible with the CRPC scenario (Chen et al., 1997; Zwart et al., 2017; Ide et al., 2018; Ruiz et al., 2020; Quattrocelli et al., 2021; Timmermans et al., 2022).

Compared to the homodimerization mechanisms of AR and GR (Nadal et al., 2017; Yu et al., 2020; Jiménez-Panizo et al., 2022; Wasmuth et al., 2022), their heterodimerization is much less understood. Considering that both DBD and LBD globular domains might engage in intermolecular interactions, we decided to produce the AR and GR core proteins to assess AR-GR heterodimer formation in solution. The AR core was successfully overexpressed and purified to homogeneity with only traces of the GroEL chaperonin that is probably required for proper AR core folding and stabilization in the absence of its cognate DNA. In the case of GR, further optimization of the protocol is required to obtain a homogenous product without truncated versions of the MBP-His-tag-GR. Most probably, the molecular weight of the fusion protein may be at the limit of *E. coli* production capacity of recombinant proteins. Nonetheless, proper functionality of both AR and GR forms was demonstrated, since they bind to ARE with a moderate affinity of 4 μM, similar to the value previously reported from biolayer interferometry experiments (3 μM; ref Dalal et al., 2014).

Our protein-protein SPR assays demonstrate AR-GR heterodimerization in solution. In fact, both LBD and core modules of AR and GR can interact as homo- and heterodimers, the AR-GR core heterodimer turned out to be the most long-lived of all complexes despite having the lowest affinity. Interestingly, we previously obtained comparable results for the GR-MR heterodimer, suggesting that similar hetero-interaction mechanisms may be shared by several (and perhaps all) members of the oxosteroidal subfamily (Carceller-Zazo et al., 2023). Finally, our SPR results also suggest that the AR-LBD homodimer interface may also be relevant for AR-GR heterodimerization. We speculate that SRs might engage in various homo- and hetero-interactions depending on their relative concentrations and the cellular context, including post-translational modifications Further experiments are required to fully characterise AR-GR heterodimer formation *in vivo* and its biological relevance in PCa pathology. Most likely, disease-linked mutations in the AR-LBD dimer interface may also have important implications for heterodimerization.

In summary, the results of our multidisciplinary approach reveal a complex landscape of structure and function alterations induced by mostly conservative mutations that affect the dimerization interface of the AR-LBD, which opens various avenues for structure-guided modulation of AR function. The characterization of AR mutations presented here through a combination of complementary structural (X-ray crystallography coupled with docking experiments and MD simulations) and functional assays including transcriptome analysis could be straightforwardly extended to other pathological AR mutants including other oncogenic variants of the receptor. Early prognosis and precision pharmacology of AR-linked diseases would benefit from this integration of structural and cell biology studies under consideration of the interplay between AR mutations and PTM-driven pathology. Eventually, it might be possible to comprehensibly link all AR mutations to specific PCa subtypes, as has been achieved for the related ER in breast cancer (Robinson et al., 2015; Quigley et al., 2018), as an important step towards truly personalized treatment of PCa patients.

Conclusions

This Ph.D. dissertation presents five new, high resolution crystal structures of agonist-bound AR-LBD point-mutants found in patients with prostate cancer and/or androgen insensitivity syndrome and investigates the mechanism underlying the pathogenicity of these mutations, based on a thorough functional and structural characterization of these AR variants. To study the mutational impact on AR structure-function relationships, we used a battery of functional and transcriptomics analysis in living cells stably expressing WT or mutant AR, together with biophysical and biochemical experiments supported by bioinformatics analyses. The most relevant findings of the current research are:

1) Mutations at the AR-LBD dimer interface differently affect cell proliferation and response to anti-androgens. Expression of ligand-bound WT AR or V758A mutant in AR-null PCa cells induces a quiescent cell phenotype in AR-responsive cells without affecting the response to anti-androgen treatment. In contrast, F755V, Y764C and Q799E mutants negatively impact AR ability to suppress cellular proliferation and mostly sensitize cells to anti-androgens.

2) Androgen-dependent transcriptome is differentially reprogramed upon AR mutation. F755V, Y764C, and Q799E mutants show a more oncogenic and differentiated molecular phenotype compared to WT and V758A, which partially explains the observed differences in cellular phenotype between the distinct cell lines expressing each AR mutant.

3) AR-LBD homodimerization interface mutants do not compromise the folding of the domain but lead to an unexpected reduced thermal stability and increased sensitivity to proteolysis. Most notably, only the V758A mutant closely resembles the WT protein in terms of global domain stability, as evidenced by similar T_m values and cleavage patterns.

4) AR-LBD mutants exhibit an enhanced flexibility and distinct structural rearrangements in residues placed in the R761-zone that harbours the mutational sites, as well as in distant regions of the domain including L1-3, H6 and the two major functional sites, AF-2 and BF-3. Bioinformatics analyses further corroborate these findings and support that the changes induced in AR-LBD areas far from the mutated residues are in line with an allosteric mechanism connecting the major functional areas of the domain.

5) The non-canonical AR-LBD dimerization mode is conserved upon single point mutations of dimer interface residues. Moreover, the Y764C mutant illustrates the capacity of the AR-LBD dimer interface to engage distinct relative orientations within AR homodimers, as evidenced by the formation of covalently-bound homodimers.

6) FL-AR is preferentially monomethylated *in vivo* by the methyltransferase PRMT5, and disease-linked mutations significantly alter the conformation of the methylation site in the AR-LBD: Arg761. We propose that the most probable pathogenic mechanism of the studied mutations is their impact on the functionality of the PTM hotspot, which overlaps with the AR-LBD dimerization interface.

Following the same multidisciplinary approach of this thesis, which integrates structural and cell-based experiments, together with bioinformatics analyses, we will continue unravelling the molecular basis of AR related diseases. In this regard, we present preliminary results of our ongoing project seeking to decipher the implication of GR in CRPC. The results of these experiments in solution support the formation of AR-GR heterodimers and suggest that the AR-LBD dimerization interface is also involved in AR-GR heterodimerization. We are confident that our results open various avenues for structure-guided modulation of AR function and believe that future precision medicine attempts to tackle AR-linked diseases and in particular those aimed at prognosis and treatment of PCa patients, need to integrate structural biology with studies of the cellular effects of mutations, PTMs and AR-GR heterodimerization and the (intricate) mechanisms underlying pathology.

References

Alegre-Martí, A. *et al.* (2023) 'A hotspot for posttranslational modifications on the androgen receptor dimer interface drives pathology and anti-androgen resistance', *Science Advances*, 9(11). Available at: https://doi.org/10.1126/sciadv.ade2175.

Amoutzias, G.D. *et al.* (2007) 'A protein interaction atlas for the nuclear receptors: Properties and quality of a hub-based dimerisation network', *BMC Systems Biology*, 1, p. 34. Available at: https://doi.org/10.1186/1752-0509-1-34.

Anders, S. and Huber, W. (2010) 'Differential expression analysis for sequence count data', *Genome Biology*, 11(10), p. R106. Available at: https://doi.org/10.1186/gb-2010-11-10-r106.

Antonysamy, S. *et al.* (2012) 'Crystal structure of the human PRMT5:MEP50 complex', *Proceedings of the National Academy of Sciences of the United States of America*, 109(44), pp. 17960–17965. Available at: https://doi.org/10.1073/pnas.1209814109.

Aranda, A. and Pascual, A. (2001) 'Nuclear Hormone Receptors and Gene Expression', *Physiological Reviews*, 81(3), pp. 1269–1304. Available at: https://doi.org/10.1152/physrev.2001.81.3.1269.

Arora, V.K. *et al.* (2013) 'Glucocorticoid receptor confers resistance to antiandrogens by bypassing androgen receptor blockade', *Cell*, 155(6), pp. 1309–1322. Available at: https://doi.org/10.1016/j.cell.2013.11.012.

Arriza, J.L. *et al.* (1987) 'Cloning of human mineralocorticoid receptor complementary DNA: Structural and functional kinship with the glucocorticoid receptor', *Science*, 237(4812), pp. 268–275. Available at: https://doi.org/10.1126/science.3037703.

Atilgan, A.R., Akan, P. and Baysal, C. (2004) 'Small-World Communication of Residues and Significance for Protein Dynamics', *Biophysical Journal*, 86(1 I), pp. 85–91. Available at: https://doi.org/10.1016/S0006-3495(04)74086-2.

Aytes, A. *et al.* (2014) 'Cross-Species Regulatory Network Analysis Identifies a Synergistic Interaction between FOXM1 and CENPF that Drives Prostate Cancer Malignancy', *Cancer Cell*, 25(5), pp. 638–651. Available at: https://doi.org/10.1016/j.ccr.2014.03.017.

Badders, N.M. *et al.* (2018) 'Selective modulation of the androgen receptor AF2 domain rescues degeneration in spinal bulbar muscular atrophy', *Nature Medicine*, 24(4), pp. 427–437. Available at: https://doi.org/10.1038/nm.4500.

Bai, S., He, B. and Wilson, E.M. (2005) 'Melanoma antigen gene protein MAGE-11 regulates androgen receptor function by modulating the interdomain interaction', *Molecular and Cellular Biology*, 25(4), pp. 1238–1257. Available at: https://doi.org/10.1128/mcb.25.4.1238-1257.2005.

Batch, J. *et al.* (1992) 'Androgen receptor gene mutations identified by SSCP in fourteen subjects with androgen insensitivity syndrome', *Human Molecular Genetics*, 1(7), pp. 497–503. Available at: https://doi.org/10.1093/hmg/1.7.497.

Bayly, C.I. *et al.* (1993) 'A well-behaved electrostatic potential based method using charge restraints for deriving atomic charges: The RESP model', *Journal of Physical Chemistry*, 97(40), pp. 10269–10280. Available at: https://doi.org/10.1021/j100142a004.

Berglund, A.E. *et al.* (2019) 'Distinct transcriptional repertoire of the androgen receptor in ETS fusion-negative prostate cancer', *Prostate Cancer and Prostatic Diseases*, 22(2), pp. 292–302. Available at: https://doi.org/10.1038/s41391-018-0103-4.

Bertrand, S. *et al.* (2004) 'Evolutionary genomics of nuclear receptors: From twenty-five ancestral genes to derived endocrine systems', *Molecular Biology and Evolution*, 21(10), pp. 1923–1937. Available at: https://doi.org/10.1093/molbev/msh200.

Bevan, C.L. *et al.* (1996) ‘Functional analysis of six androgen receptor mutations identified in patients with partial androgen insensitivity syndrome’, *Human Molecular Genetics*, 5(2), pp. 265–273. Available at: https://doi.org/10.1093/hmg/5.2.265.

Bevan, C.L. *et al.* (1999) ‘The AF1 and AF2 domains of the androgen receptor interact with distinct regions of SRC1’, *Molecular and Cellular Biology*, 19(12), pp. 8383–8392. Available at: https://doi.org/10.1128/mcb.19.12.8383.

Bledsoe, R.K. *et al.* (2002) ‘Crystal structure of the glucocorticoid receptor ligand binding domain reveals a novel mode of receptor dimerization and coactivator recognition’, *Cell*, 110(1), pp. 93–105. Available at: https://doi.org/10.1016/S0092-8674(02)00817-6.

Bohl, C.E. *et al.* (2005a) ‘Structural basis for accommodation of nonsteroidal ligands in the androgen receptor’, *Journal of Biological Chemistry*, 280(45), pp. 37747–37754. Available at: https://doi.org/10.1074/jbc.M507464200.

Bohl, C.E. *et al.* (2005b) ‘Structural basis for antagonism and resistance of bicalutamide in prostate cancer’, *Proceedings of the National Academy of Sciences of the United States of America*, 102(17), pp. 6201–6206. Available at: https://doi.org/10.1073/pnas.0500381102.

Bohl, C.E. *et al.* (2007) ‘Crystal structure of the T877A human androgen receptor ligand-binding domain complexed to cyproterone acetate provides insight for ligand-induced conformational changes and structure-based drug design’, *Journal of Biological Chemistry*, 282(18), pp. 13648–13655. Available at: https://doi.org/10.1074/jbc.M611711200.

De Bosscher, K. *et al.* (2020) ‘Nuclear receptor crosstalk — defining the mechanisms for therapeutic innovation’, *Nature Reviews Endocrinology* [Preprint]. Available at: https://doi.org/10.1038/s41574-020-0349-5.

Bourguet, W. *et al.* (1995) ‘Crystal structure of the ligand-binding domain of the human nuclear receptor RXR-α’, *Nature*, 375(6530), pp. 377–382. Available at: https://doi.org/10.1038/375377a0.

Bridgham, J.T. *et al.* (2010) ‘Protein evolution by molecular tinkering: Diversification of the nuclear receptor superfamily from a ligand-dependent ancestor’, *PLoS Biology*. Edited by L.D. Hurst, 8(10), p. e1000497. Available at: https://doi.org/10.1371/journal.pbio.1000497.

Brown, T.R. *et al.* (1990) ‘Functional characterization of naturally occurring mutant androgenreceptors from subjects withcomplete androgen insensitivity’, *Molecular Endocrinology*, 4(12), pp. 1759–1772. Available at: https://doi.org/10.1210/mend-4-12-1759.

Brzozowski, A.M. *et al.* (1997) ‘Molecular basis of agonism and antagonism in the oestrogen receptor’, *Nature*, 389(6652), pp. 753–758. Available at: https://doi.org/10.1038/39645.

Burgos, E.S. *et al.* (2015) ‘Histone H2A and H4 N-terminal tails are positioned by the MEP50 WD repeat protein for efficient methylation by the PRMT5 arginine methyltransferase’, *Journal of Biological Chemistry*, 290(15), pp. 9674–9689. Available at: https://doi.org/10.1074/jbc.M115.636894.

Burns, K.A. *et al.* (2011) ‘Selective mutations in estrogen receptor α D-domain alters nuclear translocation and non-estrogen response element gene regulatory mechanisms’, *Journal of Biological Chemistry*, 286(14), pp. 12640–12649. Available at: https://doi.org/10.1074/jbc.M110.187773.

Buzón, V. *et al.* (2011) ‘A conserved surface on the ligand binding domain of nuclear receptors for allosteric control’. Available at: https://doi.org/10.1016/j.mce.2011.08.012.

Carceller-Zazo, E. *et al.* (2023) ‘The mineralocorticoid receptor modulates timing and location of genomic binding by glucocorticoid receptor in response to synthetic glucocorticoids in keratinocytes’, *FASEB Journal*, 37(1), p. e22709. Available at: https://doi.org/10.1096/fj.202201199RR.

Centenera, M.M. *et al.* (2008) 'Minireview: The Contribution of Different Androgen Receptor Domains to Receptor Dimerization and Signaling', *Molecular Endocrinology*, 22(11), pp. 2373–2382. Available at: https://doi.org/10.1210/me.2008-0017.

Centenera, M.M. *et al.* (2013) 'Ex vivo culture of human prostate tissue and drug development', *Nature Reviews Urology*, 10(8), pp. 483–487. Available at: https://doi.org/10.1038/nrurol.2013.126.

Chandra, V. *et al.* (2008) 'Structure of the intact PPAR-γ-RXR-α nuclear receptor complex on DNA', *Nature*, 456(7220), pp. 350–356. Available at: https://doi.org/10.1038/nature07413.

Chandra, V. *et al.* (2013) 'Multidomain integration in the structure of the HNF-4α nuclear receptor complex', *Nature*, 495(7441), pp. 394–398. Available at: https://doi.org/10.1038/nature11966.

Chandra, V. *et al.* (2017) 'The quaternary architecture of RARβ-RXRα heterodimer facilitates domain-domain signal transmission', *Nature Communications*, 8(1), pp. 1–9. Available at: https://doi.org/10.1038/s41467-017-00981-y.

Charmandari, E. *et al.* (2008) 'A novel point mutation in the amino terminal domain of the human glucocorticoid receptor (hGR) gene enhancing hGR-mediated gene expression', *Journal of Clinical Endocrinology and Metabolism*, 93(12), pp. 4963–4968. Available at: https://doi.org/10.1210/jc.2008-0892.

Charmandari, E., Kino, T. and Chrousos, G.P. (2013) 'Primary generalized familial and sporadic glucocorticoid resistance (chrousos syndrome) and hypersensitivity', *Endocrine Development*, pp. 67–85. Available at: https://doi.org/10.1159/000342505.

Chen, C.D. *et al.* (2004) 'Molecular determinants of resistance to antiandrogen therapy', *Nature Medicine*, 10(1), pp. 33–39. Available at: https://doi.org/10.1038/nm972.

Chen, S.Y. *et al.* (1997) 'Androgen and glucocorticoid receptor heterodimer formation: A possible mechanism for mutual inhibition of transcriptional activity', *Journal of Biological Chemistry*, 272(22), pp. 14087–14092. Available at: https://doi.org/10.1074/jbc.272.22.14087.

Cheng, T.M.K., Blundell, T.L. and Fernandez-Recio, J. (2007) 'PyDock: Electrostatics and desolvation for effective scoring of rigid-body protein-protein docking', *Proteins: Structure, Function and Genetics*, 68(2), pp. 503–515. Available at: https://doi.org/10.1002/prot.21419.

Chymkowitch, P. *et al.* (2011) 'The phosphorylation of the androgen receptor by TFIIH directs the ubiquitin/proteasome process', *EMBO Journal*, 30(3), pp. 468–479. Available at: https://doi.org/10.1038/emboj.2010.337.

Claessens, F. *et al.* (2014) 'Emerging mechanisms of enzalutamide resistance in prostate cancer', *Nature Reviews Urology*. Nature Publishing Group, pp. 712–716. Available at: https://doi.org/10.1038/nrurol.2014.243.

Claessens, F., Joniau, S. and Helsen, C. (2017) 'Comparing the rules of engagement of androgen and glucocorticoid receptors', *Cellular and Molecular Life Sciences*. Springer, pp. 2217–2228. Available at: https://doi.org/10.1007/s00018-017-2467-3.

Conneely, O.M. *et al.* (1989) 'The chicken progesterone receptor A and B isoforms are products of an alternate translation initiation event', *Journal of Biological Chemistry*, 264(24), pp. 14062–14064. Available at: https://doi.org/10.1016/s0021-9258(18)71642-6.

Culig, Z. *et al.* (2003) 'Studies on androgen receptor mutations and amplification in human prostate cancer.', *Methods in molecular medicine*, 81, pp. 267–275. Available at: https://doi.org/10.1385/1-59259-372-0:267.

Dalal, K. *et al.* (2014) 'Selectively targeting the DNA-binding domain of the androgen receptor as a prospective therapy for prostate cancer', *Journal of Biological Chemistry*, 289(38), pp. 26417–26429. Available at: https://doi.org/10.1074/jbc.M114.553818.

Darden, T., York, D. and Pedersen, L. (1993) ‘Particle mesh Ewald: An N·log(N) method for Ewald sums in large systems’, *The Journal of Chemical Physics*, 98(12), pp. 10089–10092. Available at: https://doi.org/10.1063/1.464397.

Dehm, S.M. and Tindall, D.J. (2011) ‘Alternatively spliced androgen receptor variants’, *Endocrine-Related Cancer*. Society for Endocrinology, pp. R183–R196. Available at: https://doi.org/10.1530/ERC-11-0141.

Deng, X. *et al.* (2017) ‘Protein arginine methyltransferase 5 functions as an epigenetic activator of the androgen receptor to promote prostate cancer cell growth’, *Oncogene*, 36(9), pp. 1223–1231. Available at: https://doi.org/10.1038/onc.2016.287.

Dittmar, K.D. *et al.* (1997) ‘Folding of the glucocorticoid receptor by the heat shock protein (hsp) 90-based chaperone machinery. The role of p23 is to stabilize receptor·hsp90 heterocomplexes formed by hsp90·p60·hsp70’, *Journal of Biological Chemistry*, 272(34), pp. 21213–21220. Available at: https://doi.org/10.1074/jbc.272.34.21213.

Dobin, A. *et al.* (2013) ‘STAR: Ultrafast universal RNA-seq aligner’, *Bioinformatics*, 29(1), pp. 15–21. Available at: https://doi.org/10.1093/bioinformatics/bts635.

Dong, X., Challis, J.R.G. and Lye, S.J. (2004) ‘Intramolecular interactions between the AF3 domain and the C-terminus of the human progesterone receptor are mediated through two LXXLL motifs’, *Journal of Molecular Endocrinology*, 32(3), pp. 843–857. Available at: https://doi.org/10.1677/jme.0.0320843.

Dube, N. *et al.* (2023) ‘Identification of an evolutionarily conserved allosteric network in steroid receptors’, *Journal of Chemical Information and Modeling*, 63(2), pp. 571–582. Available at: https://doi.org/10.1021/acs.jcim.2c01096.

Duez, H. and Staels, B. (2010) ‘Nuclear receptors linking circadian rhythms and cardiometabolic control’, *Arteriosclerosis, Thrombosis, and Vascular Biology*, pp. 1529–1534. Available at: https://doi.org/10.1161/ATVBAHA.110.209098.

Elzenaty, R.N., du Toit, T. and Flück, C.E. (2022) ‘Basics of androgen synthesis and action’, *Best Practice and Research: Clinical Endocrinology and Metabolism*. Bailliere Tindall Ltd. Available at: https://doi.org/10.1016/j.beem.2022.101665.

Escriva, H. *et al.* (1997) ‘Ligand binding was acquired during evolution of nuclear receptors’, *Proceedings of the National Academy of Sciences of the United States of America*, 94(13), pp. 6803–6808. Available at: https://doi.org/10.1073/pnas.94.13.6803.

Estébanez-Perpiñá, E. *et al.* (2005) ‘The molecular mechanisms of coactivator utilization in ligand-dependent transactivation by the androgen receptor’, *Journal of Biological Chemistry*, 280(9), pp. 8060–8068. Available at: https://doi.org/10.1074/jbc.M407046200.

Estébanez-Perpiñá, E. *et al.* (2007) ‘A surface on the androgen receptor that allosterically regulates coactivator binding’, *Proceedings of the National Academy of Sciences*, 104(41), pp. 16074–16079. Available at: https://doi.org/10.1073/pnas.0708036104.

Estébanez-Perpiñá, E., Bevan, C.L. and McEwan, I.J. (2021) ‘Eighty years of targeting androgen receptor activity in prostate cancer: The fight goes on’, *Cancers*. Multidisciplinary Digital Publishing Institute, pp. 1–19. Available at: https://doi.org/10.3390/cancers13030509.

Evans, R.M. and Mangelsdorf, D.J. (2014) ‘Nuclear receptors, RXR, and the big bang’, *Cell*, pp. 255–266. Available at: https://doi.org/10.1016/j.cell.2014.03.012.

Evans, R.M. and Umesono, K. (1989) ‘Determinants of target gene specificity for steroid /thyroid hormone receptors’, *Cell*, 57, pp. 1139–1146. Available at: https://doi.org/https://doi.org/10.1016/0092-8674(89)90051-2.

Faus, H. and Haendler, B. (2006) ‘Post-translational modifications of steroid receptors’, *Biomedicine and Pharmacotherapy*, 60(9), pp. 520–528. Available at: https://doi.org/10.1016/j.biopha.2006.07.082.

Fernandez-Recio, J. *et al.* (2005) ‘Optimal docking area: A new method for predicting protein-protein interaction sites’, *Proteins: Structure, Function and Genetics*, 58(1), pp. 134–143. Available at: https://doi.org/10.1002/prot.20285.

Fernández-Recio, J., Totrov, M. and Abagyan, R. (2004) ‘Identification of protein-protein interaction sites from docking energy landscapes’, *Journal of Molecular Biology*, 335(3), pp. 843–865. Available at: https://doi.org/10.1016/j.jmb.2003.10.069.

Fliss, A.E. *et al.* (1999) ‘Domain requirements of DnaJ-like (Hsp40) molecular chaperones in the activation of a steroid hormone receptor’, *Journal of Biological Chemistry*, 274(48), pp. 34045–34052. Available at: https://doi.org/10.1074/jbc.274.48.34045.

Forman, B.M. and Evans, R.M. (1995) ‘Nuclear hormone receptors activate direct, inverted, and everted repeats’, *Annals of the New York Academy of Sciences*, 761(1), pp. 29–37. Available at: https://doi.org/10.1111/j.1749-6632.1995.tb31366.x.

Frank, F., Okafor, C.D. and Ortlund, E.A. (2018) ‘The first crystal structure of a DNA-free nuclear receptor DNA binding domain sheds light on DNA-driven allostery in the glucocorticoid receptor’, *Scientific Reports*, 8(1), p. 13497. Available at: https://doi.org/10.1038/s41598-018-31812-9.

Frankish, A. *et al.* (2019) ‘GENCODE reference annotation for the human and mouse genomes’, *Nucleic Acids Research*, 47(D1), pp. D766–D773. Available at: https://doi.org/10.1093/nar/gky955.

Freeman, B.C. *et al.* (2000) ‘The p23 molecular chaperones act at a late step in intracellular receptor action to differentially affect ligand efficacies’, *Genes and Development*, 14(4), pp. 422–434. Available at: https://doi.org/10.1101/gad.14.4.422.

Fu, M. *et al.* (2004) ‘The androgen receptor acetylation site regulates cAMP and AKT but not ERK-induced activity’, *Journal of Biological Chemistry*, 279(28), pp. 29436–29449. Available at: https://doi.org/10.1074/jbc.M313466200.

Fuentes-Prior, P. *et al.* (2019) ‘Diversity of quaternary structures regulates nuclear receptor activities’, *Trends in Biochemical Sciences*, pp. 1–2. Available at: https://doi.org/10.1016/j.tibs.2018.11.004.

Galigniana, M.D., Piwien-Pilipuk, G. and Assreuy, J. (1999) ‘Inhibition of glucocorticoid receptor binding by nitric oxide’, *Molecular Pharmacology*, 55(2), pp. 317–323. Available at: https://doi.org/10.1124/mol.55.2.317.

Gallastegui, N. *et al.* (2015) ‘Advances in our structural understanding of orphan nuclear receptors’, *Trends in Biochemical Sciences*, pp. 25–35. Available at: https://doi.org/10.1016/j.tibs.2014.11.002.

Garcia-Alonso, L. *et al.* (2019) ‘Benchmark and integration of resources for the estimation of human transcription factor activities’, *Genome Research*, 29(8), pp. 1363–1375. Available at: https://doi.org/10.1101/gr.240663.118.

Germain, P. and Bourguet, W. (2013) ‘Dimerization of nuclear receptors’, in *Methods in Cell Biology*, pp. 21–41. Available at: https://doi.org/10.1016/B978-0-12-408143-7.00002-5.

Giguère, V. *et al.* (1988) ‘Identification of a new class of steroid hormone receptors’, *Nature*, 331(6151), pp. 91–94. Available at: https://doi.org/10.1038/331091a0.

Gioeli, D. and Paschal, B.M. (2012) ‘Post-translational modification of the androgen receptor’, *Molecular and Cellular Endocrinology*, pp. 70–78. Available at: https://doi.org/10.1016/j.mce.2011.07.004.

Gottlieb, B. *et al.* (2012) ‘The androgen receptor gene mutations database: 2012 update’, *Human Mutation*, 33(5), pp. 887–894. Available at: https://doi.org/10.1002/humu.22046.

Greene, G.L. *et al.* (1986) ‘Sequence and expression of human estrogen receptor complementary DNA’, *Science*, 231(4742), pp. 1150–1154. Available at: https://doi.org/10.1126/science.3753802.

Gronemeyer, H., Gustafsson, J.Å. and Laudet, V. (2004) ‘Principles for modulation of the nuclear receptor superfamily’, *Nature Reviews Drug Discovery*. Nature Publishing Group, pp. 950–964. Available at: https://doi.org/10.1038/nrd1551.

Gronemeyer, H. and Moras, D. (1995) ‘How to finger DNA’, *Nature*. Nature Publishing Group, pp. 190–191. Available at: https://doi.org/10.1038/375190a0.

Grosdidier, S. *et al.* (2012) ‘Allosteric conversation in the androgen receptor ligand-binding domain surfaces’, *Molecular Endocrinology*, 26(7), pp. 1078–1090. Available at: https://doi.org/10.1210/me.2011-1281.

Grosdidier, S. and Fernández-Recio, J. (2008) ‘Identification of hot-spot residues in protein-protein interactions by computational docking’, *BMC Bioinformatics*, 9(1), pp. 1–13. Available at: https://doi.org/10.1186/1471-2105-9-447.

Gu, Z., Eils, R. and Schlesner, M. (2016) ‘Complex heatmaps reveal patterns and correlations in multidimensional genomic data’, *Bioinformatics*, 32(18), pp. 2847–2849. Available at: https://doi.org/10.1093/bioinformatics/btw313.

Guerois, R., Nielsen, J.E. and Serrano, L. (2002) ‘Predicting changes in the stability of proteins and protein complexes: A study of more than 1000 mutations’, *Journal of Molecular Biology*, 320(2), pp. 369–387. Available at: https://doi.org/10.1016/S0022-2836(02)00442-4.

Gustafsson, R. *et al.* (2020) ‘Structure and characterization of phosphoglucomutase 5 from atlantic and baltic herring—an inactive enzyme with intact substrate binding’, *Biomolecules*, 10(12), pp. 1–23. Available at: https://doi.org/10.3390/biom10121631.

Gutiérrez, J., Latorre, G. and Campuzano, G. (2023) ‘Cushing syndrome’, *Medicina & Laboratorio*, 15, pp. 411–430. Available at: https://www.ncbi.nlm.nih.gov/books/NBK470218/.

Ha, S., Luo, G. and Xiang, H. (2022) ‘A comprehensive overview of small-molecule androgen receptor degraders: Recent progress and future perspectives’, *Journal of Medicinal Chemistry*, pp. 16128–16154. Available at: https://doi.org/10.1021/acs.jmedchem.2c01487.

Hager, G.L. *et al.* (2000) ‘Trafficking of nuclear receptors in living cells’, in *Journal of Steroid Biochemistry and Molecular Biology*, pp. 249–254. Available at: https://doi.org/10.1016/S0960-0760(00)00100-X.

Handa, R.J. and Weiser, M.J. (2014) ‘Gonadal steroid hormones and the hypothalamo-pituitary-adrenal axis’, *Frontiers in Neuroendocrinology*, pp. 197–220. Available at: https://doi.org/10.1016/j.yfrne.2013.11.001.

Härd, T. *et al.* (1990) ‘Solution structure of the glucocorticoid receptor DNA-binding domain’, *Science*, 249(4965), pp. 157–160. Available at: https://doi.org/10.1126/science.2115209.

Hartig, S.M. *et al.* (2012) ‘Feed-forward inhibition of androgen receptor activity by glucocorticoid action in human adipocytes’, *Chemistry and Biology*, 19(9), pp. 1126–1141. Available at: https://doi.org/10.1016/j.chembiol.2012.07.020.

Hay, C.W. and McEwan, I.J. (2012) ‘The impact of point mutations in the human androgen receptor: Classification of mutations on the basis of transcriptional activity’, *PLoS ONE*, p. 32514. Available at: https://doi.org/10.1371/journal.pone.0032514.

He, B. and Wilson, E.M. (2002) ‘The NH2-terminal and carboxyl-terminal interaction in the human androgen receptor’, *Molecular Genetics and Metabolism*, 75(4), pp. 293–298. Available at: https://doi.org/10.1016/S1096-7192(02)00009-4.

Helsen, C. *et al.* (2012) 'Structural basis for nuclear hormone receptor DNA binding', *Molecular and Cellular Endocrinology*, pp. 411–417. Available at: https://doi.org/10.1016/j.mce.2011.07.025.

Helsen, C. *et al.* (2022) 'The T850D phosphomimetic mutation in the sndrogen receptor ligand binding domain enhances recruitment at activation function 2', *International Journal of Molecular Sciences*, 23(3), pp. 1–21. Available at: https://doi.org/10.3390/ijms23031557.

Hernández, P.M., Chadli, A. and Toft, D.O. (2002) 'Hsp40 binding is the first step in the Hsp90 chaperoning pathway for the progesterone receptor', *Journal of Biological Chemistry*, 277(14), pp. 11873–11881. Available at: https://doi.org/10.1074/jbc.M111445200.

Hiort, O. *et al.* (1996) 'The clinical and molecular spectrum of androgen insensitivity syndromes', *American Journal of Medical Genetics*, 63(1), pp. 218–222. Available at: https://doi.org/10.1002/(SICI)1096-8628(19960503)63:1<218::AID-AJMG38>3.0.CO;2-P.

Hiort, O. *et al.* (2000) 'Significance of mutations in the androgen receptor gene in males with idiopathic infertility', *The Journal of Clinical Endocrinology & Metabolism*, 85(8), pp. 2810–2815. Available at: https://doi.org/10.1210/jcem.85.8.6713.

Ho, M.C. *et al.* (2013) 'Structure of the arginine methyltransferase PRMT5-MEP50 reveals a mechanism for substrate specificity', *PLoS ONE*, 8(2), p. e57008. Available at: https://doi.org/10.1371/journal.pone.0057008.

Höfeld, J., Minami, Y. and Hartl, F.U. (1995) 'Hip, a novel cochaperone involved in the eukaryotic hsc70/hsp40 reaction cycle', *Cell*, 83(4), pp. 589–598. Available at: https://doi.org/10.1016/0092-8674(95)90099-3.

Hokayem, J. El *et al.* (2017) 'Ubiquitination of nuclear receptors', *Clinical Science*, pp. 917–934. Available at: https://doi.org/10.1042/CS20160708.

Hollenberg, S.M. *et al.* (1985) 'Primary structure and expression of a functional human glucocorticoid receptor cDNA', *Nature*, 318(6047), pp. 635–641. Available at: https://doi.org/10.1038/318635a0.

Hong, H., Yang, L. and Stallcup, M.R. (1999) 'Hormone-independent transcriptional activation and coactivator binding by novel orphan nuclear receptor ERR3', *Journal of Biological Chemistry*, 274(32), pp. 22618–22626. Available at: https://doi.org/10.1074/jbc.274.32.22618.

Hopkins, C.W. *et al.* (2015) 'Long-time-step molecular dynamics through hydrogen mass repartitioning', *Journal of Chemical Theory and Computation*, 11(4), pp. 1864–1874. Available at: https://doi.org/10.1021/ct5010406.

Hosohata, K. *et al.* (2003) 'Purification and identification of a novel complex which is involved in androgen receptor-dependent transcription', *Molecular and Cellular Biology*, 23(19), pp. 7019–7029. Available at: https://doi.org/10.1128/mcb.23.19.7019-7029.2003.

Huang, P., Chandra, V. and Rastinejad, F. (2010) 'Structural overview of the nuclear receptor superfamily: Insights into physiology and therapeutics', *Annual Review of Physiology*, 72(1), pp. 247–272. Available at: https://doi.org/10.1146/annurev-physiol-021909-135917.

Hudson, W.H., Youn, C. and Ortlund, E.A. (2013) 'The structural basis of direct glucocorticoid-mediated transrepression', *Nature Structural and Molecular Biology*, 20(1), pp. 53–58. Available at: https://doi.org/10.1038/nsmb.2456.

Hudson, W.H., Youn, C. and Ortlund, E.A. (2014) 'Crystal structure of the mineralocorticoid receptor DNA binding domain in complex with DNA', *PLoS ONE*, 9(9), p. e107000. Available at: https://doi.org/10.1371/journal.pone.0107000.

Hughes, I.A. *et al.* (2012) 'Androgen insensitivity syndrome', in *The Lancet*. Elsevier, pp. 1419–1428. Available at: https://doi.org/10.1016/S0140-6736(12)60071-3.

Hur, E. *et al.* (2004) 'Recognition and accommodation at the androgen receptor coactivator binding interface', *PLoS Biology*, 2(9). Available at: https://doi.org/10.1371/journal.pbio.0020274.

Hurt, D.E. *et al.* (2016) 'Structural analysis on the pathologic mutant glucocorticoid receptor ligand-binding domains', *Molecular Endocrinology*, 30(2), pp. 173–188. Available at: https://doi.org/10.1210/me.2015-1177.

Hyytinen, E.R. *et al.* (2002) 'Pattern of somatic androgen receptor gene mutations in patients with hormone-refractory prostate cancer', *Laboratory Investigation*, 82(11), pp. 1591–1598. Available at: https://doi.org/10.1097/01.LAB.0000038924.67707.75.

Ide, H., Inoue, S. and Miyamoto, H. (2018) 'The role of glucocorticoid receptor signaling in bladder cancer progression', *Cancers*. Multidisciplinary Digital Publishing Institute, p. 484. Available at: https://doi.org/10.3390/cancers10120484.

Ingraham, H.A. and Redinbo, M.R. (2005) 'Orphan nuclear receptors adopted by crystallography', *Current Opinion in Structural Biology*, pp. 708–715. Available at: https://doi.org/10.1016/j.sbi.2005.10.009.

Isikbay, M. *et al.* (2014) 'Glucocorticoid receptor activity contributes to resistance to androgen-targeted therapy in prostate cancer', *Hormones and Cancer*, 5(2), pp. 72–89. Available at: https://doi.org/10.1007/s12672-014-0173-2.

Ito, K. *et al.* (2006) 'Histone deacetylase 2–mediated deacetylation of the glucocorticoid receptor enables NF-κB suppression', *The Journal of Experimental Medicine*, 203(1), pp. 7–13. Available at: https://doi.org/10.1084/jem.20050466.

Izadi, S., Anandakrishnan, R. and Onufriev, A. V. (2014) 'Building water models: A different approach', *Journal of Physical Chemistry Letters*, 5(21), pp. 3863–3871. Available at: https://doi.org/10.1021/jz501780a.

Jääskeläinen, J. *et al.* (2006) 'Human androgen receptor gene ligand-binding-domain mutations leading to disrupted interaction between the N- and C-terminal domains', *Journal of Molecular Endocrinology*, 36(2), pp. 361–368. Available at: https://doi.org/10.1677/jme.1.01885.

Jääskeläinen, T., Makkonen, H. and Palvimo, J.J. (2011) 'Steroid up-regulation of FKBP51 and its role in hormone signaling', *Current Opinion in Pharmacology*. Elsevier, pp. 326–331. Available at: https://doi.org/10.1016/j.coph.2011.04.006.

Jeltsch, J.M. *et al.* (1986) 'Cloning of the chicken progesterone receptor', *Proceedings of the National Academy of Sciences of the United States of America*, 83(15), pp. 5424–5428. Available at: https://doi.org/10.1073/pnas.83.15.5424.

Jenster, G. *et al.* (1995) 'Identification of two transcription activation units in the N-terminal domain of the human androgen receptor', *Journal of Biological Chemistry*, 270(13), pp. 7341–7346. Available at: https://doi.org/10.1074/jbc.270.13.7341.

Jimenez-Jacinto, V., Sanchez-Flores, A. and Vega-Alvarado, L. (2019) 'Integrative differential expression analysis for multiple experiments (IDEAMEX): A web server tool for integrated RNA-seq data analysis', *Frontiers in Genetics*, 10, p. 279. Available at: https://doi.org/10.3389/fgene.2019.00279.

Jiménez-Panizo, A. *et al.* (2019) 'Non-canonical dimerization of the androgen receptor and other nuclear receptors: Implications for human disease', *Endocrine-Related Cancer*, 26(8), pp. R479–R497. Available at: https://doi.org/10.1530/ERC-19-0132.

Jiménez-Panizo, A. *et al.* (2022) 'The multivalency of the glucocorticoid receptor ligand-binding domain explains its manifold physiological activities', *Nucleic acids research*, 50(22), pp. 13063–13082. Available at: https://doi.org/10.1093/nar/gkac1119.

Jin, H.J., Kim, J. and Yu, J. (2013) 'Androgen receptor genomic regulation', *Translational Andrology and Urology*. AME Publishing Company, pp. 158–177. Available at: https://doi.org/10.3978/j.issn.2223-4683.2013.09.01.

Kalfa, N. *et al.* (2013) 'Minor hypospadias: The "tip of the iceberg" of the partial androgen insensitivity syndrome', *PLoS ONE*, 8(4). Available at: https://doi.org/10.1371/journal.pone.0061824.

Kamaraj, R. *et al.* (2022) 'Allosteric antagonism of the pregnane x receptor (PXR): Current-state-of-the-art and prediction of novel allosteric sites', *Cells*. Multidisciplinary Digital Publishing Institute, p. 2974. Available at: https://doi.org/10.3390/cells11192974.

Kanai, A. *et al.* (2020) 'Significance of glucocorticoid signaling in triple-negative breast cancer patients: a newly revealed interaction with androgen signaling', *Breast Cancer Research and Treatment*, 180(1), pp. 97–110. Available at: https://doi.org/10.1007/s10549-020-05523-7.

Karthaus, W.R. and Sawyers, C.L. (2019) 'Strategies to identify and target cells of origin in prostate cancer', *Journal of the National Cancer Institute*. Oxford Academic, pp. 221–223. Available at: https://doi.org/10.1093/jnci/djy146.

Khorasanizadeh, S. and Rastinejad, F. (2001) 'Nuclear-receptor interactions on DNA-response elements', *Trends in Biochemical Sciences*, 26(6), pp. 384–390. Available at: https://doi.org/10.1016/S0968-0004(01)01800-X.

Kino, T. *et al.* (2002) 'Familial/sporadic glucocorticoid resistance syndrome and hypertension', in *Annals of the New York Academy of Sciences*. New York Academy of Sciences, pp. 101–111. Available at: https://doi.org/10.1111/j.1749-6632.2002.tb04416.x.

Kino, T. and Chrousos, G.P. (2001) 'Glucocorticoid and mineralocorticoid resistance/hypersensitivity syndromes', *Journal of Endocrinology*, 169(3), pp. 437–445. Available at: https://doi.org/10.1677/joe.0.1690437.

Kino, T. and Chrousos, G.P. (2011) 'Acetylation-mediated epigenetic regulation of glucocorticoid receptor activity: Circadian rhythm-associated alterations of glucocorticoid actions in target tissues', *Molecular and Cellular Endocrinology*, pp. 23–30. Available at: https://doi.org/10.1016/j.mce.2010.12.001.

Kirschke, E. *et al.* (2014) 'Glucocorticoid receptor function regulated by coordinated action of the Hsp90 and Hsp70 chaperone cycles', *Cell*, 157(7), pp. 1685–1697. Available at: https://doi.org/10.1016/j.cell.2014.04.038.

Knudsen, K.E. and Penning, T.M. (2010) 'Partners in crime: Deregulation of AR activity and androgen synthesis in prostate cancer', *Trends in Endocrinology and Metabolism*, pp. 315–324. Available at: https://doi.org/10.1016/j.tem.2010.01.002.

Ko, S. *et al.* (2011) 'Lysine methylation and functional modulation of androgen receptor by Set9 methyltransferase', *Molecular Endocrinology*, 25(3), pp. 433–444. Available at: https://doi.org/10.1210/me.2010-0482.

Kokontis, J.M. and Liao, S. (1999) 'Molecular action of androgen in the normal and neoplastic prostate', *Vitamins and Hormones*, 55(C), pp. 219–307. Available at: https://doi.org/10.1016/S0083-6729(08)60937-1.

Koryakina, Y., Ta, H.Q. and Gioeli, D. (2014) 'Androgen receptor phosphorylation: Biological context and functional consequences', *Endocrine-Related Cancer*. Bioscientifica Ltd, pp. T131–T145. Available at: https://doi.org/10.1530/ERC-13-0472.

Kumar, R. *et al.* (2004) 'Induced α-helix structure in AF1 of the androgen receptor upon binding transcription factor TFIIF', *Biochemistry*, 43(11), pp. 3008–3013. Available at: https://doi.org/10.1021/bi035934p.

Kumar, R. (2020) 'Emerging role of glucocorticoid receptor in castration resistant prostate cancer: A potential therapeutic target', *Journal of Cancer*, pp. 696–701. Available at: https://doi.org/10.7150/jca.32497.

Kumar, R. *et al.* (2021) 'Supraphysiologic testosterone induces ferroptosis and activates immune pathways through nucleophagy in prostate cancer', *Cancer Research*, 81(23), pp. 5948–5962. Available at: https://doi.org/10.1158/0008-5472.CAN-20-3607.

Kumari, N. and Yadav, S. (2019) 'Modulation of protein oligomerization: An overview', *Progress in Biophysics and Molecular Biology*, pp. 99–113. Available at: https://doi.org/10.1016/j.pbiomolbio.2019.03.003.

Kuriyan, J. (2004) 'Allostery and coupled sequence variation in nuclear hormone receptors', *Cell*. Elsevier B.V., pp. 354–356. Available at: https://doi.org/10.1016/S0092-8674(04)00125-4.

Lam, H.M. *et al.* (2020) 'Durable response of enzalutamide-resistant prostate cancer to supraphysiological testosterone is associated with a multifaceted growth suppression and impaired DNA damage response transcriptomic program in patient-derived xenografts', *European Urology*, 77(2), pp. 144–155. Available at: https://doi.org/10.1016/j.eururo.2019.05.042.

Langley, E., Kemppainen, J.A. and Wilson, E.M. (1998) 'Intermolecular NH2-/carboxyl-terminal interactions in androgen receptor dimerization revealed by mutations that cause androgen insensitivity', *Journal of Biological Chemistry*, 273(1), pp. 92–101. Available at: https://doi.org/10.1074/jbc.273.1.92.

Laudet, V. (1997) 'Evolution of the nuclear receptor superfamily: Early diversification from an ancestral orphan receptor', *Journal of Molecular Endocrinology*, pp. 207–226. Available at: https://doi.org/10.1677/jme.0.0190207.

Lempiäinen, J.K. *et al.* (2017) 'Agonist-specific protein interactomes of Glucocorticoid and androgen receptor as revealed by proximity mapping', *Molecular and Cellular Proteomics*, 16(8), pp. 1462–1474. Available at: https://doi.org/10.1074/mcp.M117.067488.

Li, B., Lu, W. and Chen, Z. (2014) 'Regulation of androgen receptor by E3 ubiquitin ligases: for more or less', *Receptors & Clinical Investigation*, 1(5). Available at: https://doi.org/10.14800/rci.122.

Li, Q. *et al.* (2018) 'Linking prostate cancer cell AR heterogeneity to distinct castration and enzalutamide responses', *Nature Communications*, 9(1), pp. 1–17. Available at: https://doi.org/10.1038/s41467-018-06067-7.

Lin, H.K. *et al.* (2001) 'Akt suppresses androgen-induced apoptosis by phosphorylating and inhibiting androgen receptor', *Proceedings of the National Academy of Sciences of the United States of America*, 98(13), pp. 7200–7205. Available at: https://doi.org/10.1073/pnas.121173298.

Lin, H.K. *et al.* (2003) 'Suppression versus induction of androgen receptor functions by the phosphatidylinositol 3-Kinase/Akt pathway in prostate cancer LNCaP cells with different passage numbers', *Journal of Biological Chemistry*, 278(51), pp. 50902–50907. Available at: https://doi.org/10.1074/jbc.M300676200.

Linn, D.E. *et al.* (2012) 'Differential regulation of androgen receptor by P1M-1 kinases via phosphorylation-dependent recruitment of distinct ubiquitin E3 ligases', *Journal of Biological Chemistry*, 287(27), pp. 22959–22968. Available at: https://doi.org/10.1074/jbc.M111.338350.

Liu, C. *et al.* (2018) 'Proteostasis by STUB1/HSP70 complex controls sensitivity to androgen receptor targeted therapy in advanced prostate cancer', *Nature Communications*, 9(1), pp. 1–16. Available at: https://doi.org/10.1038/s41467-018-07178-x.

Liu, Y.-H., Li, C. and Zhou, S.-F. (2009) 'Prediction of deleterious functional effects of non-synonymous single nucleotide polymorphisms in human nuclear receptor genes using a bioinformatics approach', *Drug Metabolism Letters*, 3(4), pp. 242–286. Available at: https://doi.org/10.2174/187231209790218145.

Lobaccaro, J.M. *et al.* (1993) 'An exonic point mutation creates a Maeill site in the androgen receptor gene of a family with complete androgen insensitivity syndrome', *Human Molecular Genetics*, pp. 1041–1043. Available at: https://doi.org/10.1093/hmg/2.7.1041.

Lockless, S.W. and Ranganathan, R. (1999) 'Evolutionarily conserved pathways of energetic connectivity in protein families', *Science*, 286(5438), pp. 295–299. Available at: https://doi.org/10.1126/science.286.5438.295.

Lonard, D.M. and O'Malley, B.W. (2007) 'Nuclear receptor coregulators: judges, juries, and executioners of cellular Regulation', *Cell*, 27, pp. 691–700. Available at: https://doi.org/10.1016/j.molcel.2007.08.012.

Lonard, D.M. and O'Malley, B.W. (2012) 'Nuclear receptor coregulators: Modulators of pathology and therapeutic targets', *Nature Reviews Endocrinology*, pp. 598–604. Available at: https://doi.org/10.1038/nrendo.2012.100.

Lou, X. *et al.* (2014) 'Structure of the retinoid X receptor α-liver X receptor β (RXRα-LXRβ) heterodimer on DNA', *Nature Structural and Molecular Biology*, 21(3), pp. 277–281. Available at: https://doi.org/10.1038/nsmb.2778.

Love, M.I. *et al.* (2017) 'Role of the chromatin landscape and sequence in determining cell type-specific genomic glucocorticoid receptor binding and gene regulation', *Nucleic Acids Research*, 45(4), pp. 1805–1819. Available at: https://doi.org/10.1093/nar/gkw1163.

Love, M.I., Huber, W. and Anders, S. (2014) 'Moderated estimation of fold change and dispersion for RNA-seq data with DESeq2', *Genome Biology*, 15(12), pp. 1–21. Available at: https://doi.org/10.1186/s13059-014-0550-8.

Lubahn, D.B. *et al.* (1988) 'Cloning of human androgen receptor complementary DNA and localization to the X chromosome', *Science*, 240(4850), pp. 327–330. Available at: https://doi.org/10.1126/science.3353727.

Lubahn, D.B. *et al.* (1989) 'Sequence of the intron/exon junctions of the coding region of the human androgen receptor gene and identification of a point mutation in a family with complete androgen insensitivity', *Proceedings of the National Academy of Sciences of the United States of America*, 86(23), pp. 9534–9538. Available at: https://doi.org/10.1073/pnas.86.23.9534.

Mackinnon, J.A.G. *et al.* (2014) 'Allosteric mechanisms of nuclear receptors: Insights from computational simulations', *Molecular and Cellular Endocrinology*, pp. 75–82. Available at: https://doi.org/10.1016/j.mce.2014.05.017.

Maksimovic, I. and David, Y. (2021) 'Non-enzymatic covalent modifications as a new chapter in the histone code', *Trends in Biochemical Sciences*, pp. 718–730. Available at: https://doi.org/10.1016/j.tibs.2021.04.004.

Malbeteau, L. *et al.* (2022) 'How protein methylation regulates steroid receptor function', *Endocrine Reviews*, 43(1), pp. 160–197. Available at: https://doi.org/10.1210/endrev/bnab014.

Mangelsdorf, D.J. *et al.* (1990) 'Nuclear receptor that identifies a novel retinoic acid response pathway', *Nature*, 345(6272), pp. 224–229. Available at: https://doi.org/10.1038/345224a0.

Mangelsdorf, D.J. and Evans, R.M. (1995) 'The RXR heterodimers and orphan receptors', *Cell*, pp. 841–850. Available at: https://doi.org/10.1016/0092-8674(95)90200-7.

Marcelli, M. *et al.* (2000) 'Androgen receptor mutations in prostate cancer', *Cancer Research*, 60, pp. 944–949. Available at: http://www.mcgill.ca/androgendb/data.htm.

Markov, G. V and Laudet, V. (2011) 'Origin and evolution of the ligand-binding ability of nuclear receptors', *Molecular and Cellular Endocrinology*, pp. 21–30. Available at: https://doi.org/10.1016/j.mce.2010.10.017.

Martin, L.J. and Tremblay, J.J. (2010) 'Nuclear receptors in Leydig cell gene expression and function', *Biology of Reproduction*. Oxford Academic, pp. 3–14. Available at: https://doi.org/10.1095/biolreprod.110.083824.

McEwan, I.J. *et al.* (2007) 'Natural disordered sequences in the amino terminal domain of nuclear receptors: lessons from the androgen and glucocorticoid receptors.', *Nuclear receptor signaling*. SAGE Publications, p. 1. Available at: https://doi.org/10.1621/nrs.05001.

McEwan, I.J. (2012) 'Nuclear hormone receptors: Allosteric switches', *Molecular and Cellular Endocrinology*. Elsevier, pp. 345–347. Available at: https://doi.org/10.1016/j.mce.2011.08.035.

McPhaul, M.J. *et al.* (1991) 'Molecular basis of androgen resistance in a family with a qualitative abnormality of the androgen receptor and responsive to high-dose androgen therapy.', *Journal of Clinical Investigation*, 87(4), pp. 1413–1421. Available at: https://doi.org/10.1172/JCI115147.

Meijsing, S.H. *et al.* (2009) 'DNA binding site sequence directs glucocorticoid receptor structure and activity', *Science*, 324(5925), pp. 407–410. Available at: https://doi.org/10.1126/science.1164265.

Melo, K.F. *et al.* (2003) 'Clinical, hormonal, behavioral, and genetic characteristics of androgen insensitivity syndrome in a Brazilian cohort: Five novel mutations in the androgen receptor gene', *Journal of Clinical Endocrinology and Metabolism*, 88(7), pp. 3241–3250. Available at: https://doi.org/10.1210/jc.2002-021658.

Miesfeld, R. *et al.* (1986) 'Genetic complementation of a glucocorticoid receptor deficiency by expression of cloned receptor cDNA', *Cell*, 46(3), pp. 389–399. Available at: https://doi.org/10.1016/0092-8674(86)90659-8.

Miller, W.L. *et al.* (2020) 'The adrenal cortex and its disorders', in *Sperling Pediatric Endocrinology: Expert Consult - Online and Print*. Elsevier, pp. 425–490. Available at: https://doi.org/10.1016/B978-0-323-62520-3.00014-2.

Misrahi, M. *et al.* (1987) 'Complete amino acid sequence of the human progesterone receptor deduced from cloned cDNA', *Biochemical and Biophysical Research Communications*, 143(2), pp. 740–748. Available at: https://doi.org/10.1016/0006-291X(87)91416-1.

Moehren, U. *et al.* (2008) 'Identification of androgen-selective androgen-response elements in the human aquaporin-5 and Rad9 genes', *Biochemical Journal*, 411(3), pp. 679–686. Available at: https://doi.org/10.1042/BJ20071352.

Mohler, M.L. *et al.* (2021) 'An overview of next-generation androgen receptor-targeted therapeutics in development for the treatment of prostate cancer', *International Journal of Molecular Sciences*. Multidisciplinary Digital Publishing Institute, pp. 1–20. Available at: https://doi.org/10.3390/ijms22042124.

De Mol, E. *et al.* (2016) 'EPI-001, a compound active against castration-resistant prostate cancer, targets transactivation unit 5 of the androgen receptor', *ACS Chemical Biology*, 11(9), pp. 2499–2505. Available at: https://doi.org/10.1021/acschembio.6b00182.

De Mol, E. *et al.* (2018) 'Regulation of androgen receptor activity by transient interactions of its transactivation domain with general transcription regulators', *Cell*, 26(1), pp. 145-152.e3. Available at: https://doi.org/10.1016/j.str.2017.11.007.

Moore, J.T. *et al.* (1998) 'Cloning and characterization of human estrogen receptor β isoforms', *Biochemical and Biophysical Research Communications*, 247(1), pp. 75–78. Available at: https://doi.org/10.1006/bbrc.1998.8738.

Moras, D. and Gronemeyer, H. (1998) 'The nuclear receptor ligand-binding domain: Structure and function', *Current Opinion in Cell Biology*, 10(3), pp. 384–391. Available at: https://doi.org/10.1016/S0955-0674(98)80015-X.

Mosure, S.A. *et al.* (2022) 'Structural basis of interdomain communication in PPARγ', *bioRxiv*, pp. 1–14. Available at: https://doi.org/10.1101/2022.07.13.499031.

Mounir, Z. *et al.* (2016) 'ERG signaling in prostate cancer is driven through PRMT5-dependent methylation of the androgen receptor', *eLife*, 5(MAY2016). Available at: https://doi.org/10.7554/eLife.13964.

Mulvaney, K.M. *et al.* (2021) 'Molecular basis for substrate recruitment to the PRMT5 methylosome', *Molecular Cell*, 81(17), pp. 3481-3495.e7. Available at: https://doi.org/10.1016/j.molcel.2021.07.019.

Munir, S., Rodriguez, B.S.Q. and Waseem, M. (2022) 'Addison disease', *StatPearls* [Preprint]. Available at: https://www.ncbi.nlm.nih.gov/books/NBK441994/.

Murono, K. *et al.* (1995) 'Human androgen insensitivity due to point mutations encoding amino acid substitutions in the androgen receptor steroid-binding domain', *Human Mutation*, 6(2), pp. 152–162. Available at: https://doi.org/10.1002/humu.1380060208.

Musiani, D. *et al.* (2019) 'Proteomics profiling of arginine methylation defines PRMT5 substrate specificity', *Science Signaling*, 12(575). Available at: https://doi.org/10.1126/scisignal.aat8388.

Nadal, M. *et al.* (2017) 'Structure of the homodimeric androgen receptor ligand-binding domain', *Nature Communications*, 8, p. 14388. Available at: https://doi.org/10.1038/ncomms14388.

Nader, N., Chrousos, G.P. and Kino, T. (2009) 'Circadian rhythm transcription factor CLOCK regulates the transcriptional activity of the glucocorticoid receptor by acetylating its hinge region lysine cluster: potential physiological implications', *The FASEB Journal*, 23(5), pp. 1572–1583. Available at: https://doi.org/10.1096/FJ.08-117697.

Narayanan, S., Srinivas, S. and Feldman, D. (2016) 'Androgen-glucocorticoid interactions in the era of novel prostate cancer therapy', *Nature Reviews Urology*, pp. 47–60. Available at: https://doi.org/10.1038/nrurol.2015.254.

Nemetchek, M.D. *et al.* (2022) 'A structural mechanism of nuclear receptor biased agonism', *Proceedings of the National Academy of Sciences of the United States of America*, 119(50), p. e2215333119. Available at: https://doi.org/10.1073/pnas.2215333119.

Nicolaides, N.C. *et al.* (2010) 'The human glucocorticoid receptor: Molecular basis of biologic function', *Steroids*, pp. 1–12. Available at: https://doi.org/10.1016/j.steroids.2009.09.002.

Nicolaides, N.C. *et al.* (2015a) 'A novel mutation of the hGR gene causing Chrousos syndrome', *European Journal of Clinical Investigation*, 45(8), pp. 782–791. Available at: https://doi.org/10.1111/eci.12470.

Nicolaides, N.C. *et al.* (2015b) 'Transient generalized glucocorticoid hypersensitivity', *European Journal of Clinical Investigation*, 45(12), pp. 1306–1315. Available at: https://doi.org/10.1111/eci.12554.

Nicolaides, N.C. and Charmandari, E. (2015) 'Chrousos syndrome: From molecular pathogenesis to therapeutic management', *European Journal of Clinical Investigation*, 45(5), pp. 504–514. Available at: https://doi.org/10.1111/eci.12426.

Nicolaides, N.C. and Charmandari, E. (2017) 'Novel insights into the molecular mechanisms underlying generalized glucocorticoid resistance and hypersensitivity syndromes', *Hormones*, 16(2), pp. 124–138. Available at: https://doi.org/10.14310/horm.2002.1728.

Nyquist, M.D. *et al.* (2021) 'Selective androgen receptor modulators activate the canonical prostate cancer androgen receptor program and repress cancer growth', *Journal of Clinical Investigation*, 131(10). Available at: https://doi.org/10.1172/JCI146777.

Oakley, R.H. and Cidlowski, J.A. (2013) 'The biology of the glucocorticoid receptor: New signaling mechanisms in health and disease', *Journal of Allergy and Clinical Immunology*, pp. 1033–1044. Available at: https://doi.org/10.1016/j.jaci.2013.09.007.

Owens-Grillo, J.K. *et al.* (1996) 'A model of protein targeting mediated by immunophilins and other proteins that bind to hsp90 via tetratricopeptide repeat domains', *Journal of Biological Chemistry*, 271(23), pp. 13468–13475. Available at: https://doi.org/10.1074/jbc.271.23.13468.

Paakinaho, V. *et al.* (2017) 'Single-molecule analysis of steroid receptor and cofactor action in living cells', *Nature Communications*, 8. Available at: https://doi.org/10.1038/ncomms15896.

Paakinaho, V. *et al.* (2019) 'Glucocorticoid receptor quaternary structure drives chromatin occupancy and transcriptional outcome', *Genome Research*, 29(8), pp. 1223–1234. Available at: https://doi.org/10.1101/gr.244814.118.

Park, K. *et al.* (2014) 'TMPRSS2: ERG gene fusion predicts subsequent detection of prostate cancer in patients with high-grade prostatic intraepithelial neoplasia', *Journal of Clinical Oncology*, 32(3), pp. 206–211. Available at: https://doi.org/10.1200/JCO.2013.49.8386.

Paul-Clark, M.J. *et al.* (2003) 'Glucocorticoid receptor nitration leads to enhanced anti-inflammatory effects of novel steroid ligands', *The Journal of Immunology*, 171(6), pp. 3245–3252. Available at: https://doi.org/10.4049/jimmunol.171.6.3245.

Peng, Y. *et al.* (2008) 'Distinct nuclear and cytoplasmic functions of androgen receptor cofactor p44 and association with androgen-independent prostate cancer', *Proceedings of the National Academy of Sciences of the United States of America*, 105(13), pp. 5236–5241. Available at: https://doi.org/10.1073/pnas.0712262105.

Perez, J.J., Tomas, M.S. and Rubio-Martinez, J. (2016) 'Assessment of the sampling performance of multiple-copy dynamics versus a unique trajectory', *Journal of Chemical Information and Modeling*, 56(10), pp. 1950–1962. Available at: https://doi.org/10.1021/acs.jcim.6b00347.

Postel, S. *et al.* (2023) 'Quaternary glucocorticoid receptor structure highlights allosteric interdomain communication', *Nature Structural and Molecular Biology*, 30(3), pp. 286–295. Available at: https://doi.org/10.1038/s41594-022-00914-4.

Poulard, C. *et al.* (2020) 'Using proximity ligation assay to detect protein arginine methylation', *Methods*, 175, pp. 66–71. Available at: https://doi.org/10.1016/j.ymeth.2019.09.007.

Prescott, J. and Coetzee, G.A. (2006) 'Molecular chaperones throughout the life cycle of the androgen receptor', *Cancer Letters*. Elsevier, pp. 12–19. Available at: https://doi.org/10.1016/j.canlet.2004.12.037.

Presman, D.M. *et al.* (2014) 'Live cell imaging unveils multiple domain requirements for in vivo dimerization of the glucocorticoid receptor', *PLoS Biology*, 12(3). Available at: https://doi.org/10.1371/journal.pbio.1001813.

Presman, D.M. *et al.* (2016) 'DNA binding triggers tetramerization of the glucocorticoid receptor in live cells', *Proceedings of the National Academy of Sciences of the United States of America*, 113(29), pp. 8236–8241. Available at: https://doi.org/10.1073/pnas.1606774113.

Presman, D.M. and Hager, G.L. (2017) 'More than meets the dimer: What is the quaternary structure of the glucocorticoid receptor?', *Transcription*, 8(1), pp. 32–39. Available at: https://doi.org/10.1080/21541264.2016.1249045.

Puhr, M. *et al.* (2018) 'The glucocorticoid receptor is a key player for prostate cancer cell survival and a target for improved antiandrogen therapy', *Clinical Cancer Research*, 24(4), pp. 927–938. Available at: https://doi.org/10.1158/1078-0432.CCR-17-0989.

Qi, J. *et al.* (2013) 'The E3 ubiquitin ligase siah2 contributes to castration-resistant prostate cancer by regulation of androgen receptor transcriptional activity', *Cancer Cell*, 23(3), pp. 332–346. Available at: https://doi.org/10.1016/j.ccr.2013.02.016.

Qiu, X. *et al.* (2022) 'Response to supraphysiological testosterone is predicted by a distinct androgen receptor cistrome', *JCI Insight*, 7(10). Available at: https://doi.org/10.1172/jci.insight.157164.

Quattrocelli, M. *et al.* (2021) 'Mechanisms and clinical applications of glucocorticoid steroids in muscular dystrophy', *Journal of Neuromuscular Diseases*. IOS Press, pp. 39–52. Available at: https://doi.org/10.3233/JND-200556.

Quigley, C.A. *et al.* (1995) 'Androgen receptor defects: Historical, clinical, and molecular perspectives', *Endocrine Reviews*, 16(3), pp. 271–321. Available at: https://doi.org/10.1210/edrv-16-3-271.

Quigley, D.A. *et al.* (2018) 'Genomic hallmarks and structural variation in metastatic prostate cancer', *Cell*, 174(3), pp. 758-769.e9. Available at: https://doi.org/10.1016/j.cell.2018.06.039.

Radmayr, C. *et al.* (1998) 'Analysis of a mutant androgen receptor offers a treatment modality in a patient with partial androgen insensitivity syndrome', *European Urology*, 33(2), pp. 222–226. Available at: https://doi.org/10.1159/000019540.

Raff, H., Sharma, S.T. and Nieman, L.K. (2014) 'Physiological basis for the etiology, diagnosis, and treatment of adrenal disorders: Cushing's syndrome, adrenal insufficiency, and congenital adrenal hyperplasia', *Comprehensive Physiology*, 4(2), pp. 739–769. Available at: https://doi.org/10.1002/cphy.c130035.

Rastinejad, F. *et al.* (2013) 'Understanding nuclear receptor form and function using structural biology', *Journal of Molecular Endocrinology*. Society for Endocrinology, pp. T1–T21. Available at: https://doi.org/10.1530/JME-13-0173.

Regazzo, D. *et al.* (2022) 'The Role of glucocorticoid receptor in the pathophysiology of pituitary corticotroph adenomas', *International Journal of Molecular Sciences*. Multidisciplinary Digital Publishing Institute, p. 6469. Available at: https://doi.org/10.3390/ijms23126469.

Rege, J. *et al.* (2013) 'Liquid chromatography-tandem mass spectrometry analysis of human adrenal vein 19-carbon steroids before and after ACTH stimulation', *Journal of Clinical Endocrinology and Metabolism*, 98(3), pp. 1182–1188. Available at: https://doi.org/10.1210/jc.2012-2912.

Reig, Ò. *et al.* (2016) 'TMPRSS2-ERG in blood and docetaxel resistance in metastatic castration-resistant prostate cancer', *European Urology*, 70(5), pp. 709–713. Available at: https://doi.org/10.1016/j.eururo.2016.02.034.

Ricketson, D. *et al.* (2007) 'A conformational switch in the ligand-binding domain regulates the dependence of the glucocorticoid receptor on Hsp90', *Journal of Molecular Biology*, 368(3), pp. 729–741. Available at: https://doi.org/10.1016/j.jmb.2007.02.057.

Riggs, D.L. *et al.* (2003) 'The Hsp90-binding peptidylprolyl isomerase FKBP52 potentiates glucocorticoid signaling in vivo', *EMBO Journal*, 22(5), pp. 1158–1167. Available at: https://doi.org/10.1093/emboj/cdg108.

Ritchie, M.E. *et al.* (2015) 'Limma powers differential expression analyses for RNA-sequencing and microarray studies', *Nucleic Acids Research*, 43(7), p. e47. Available at: https://doi.org/10.1093/nar/gkv007.

Rivoire, O., Reynolds, K.A. and Ranganathan, R. (2016) 'Evolution-based functional decomposition of proteins', *PLoS Computational Biology*, 12(6), p. e1004817. Available at: https://doi.org/10.1371/journal.pcbi.1004817.

Robinson, D. *et al.* (2015) 'Integrative clinical genomics of advanced prostate cancer', *Cell*, 161(5), pp. 1215–1228. Available at: https://doi.org/10.1016/j.cell.2015.05.001.

Rochette-Egly, C. (2003) 'Nuclear receptors: Integration of multiple signalling pathways through phosphorylation', *Cellular Signalling*, pp. 355–366. Available at: https://doi.org/10.1016/S0898-6568(02)00115-8.

Roemer, S.C. *et al.* (2006) 'Structure of the progesterone receptor-deoxyribonucleic acid complex: Novel interactions required for binding to half-site response elements', *Molecular Endocrinology*, 20(12), pp. 3042–3052. Available at: https://doi.org/10.1210/me.2005-0511.

Ruggero, K. *et al.* (2018) 'Epigenetic regulation in prostate cancer progression', *Current Molecular Biology Reports*, 4(2), pp. 101–115. Available at: https://doi.org/10.1007/s40610-018-0095-9.

Ruiz, D., Padmanabhan, V. and Sargis, R.M. (2020) 'Stress, sex, and sugar: Glucocorticoids and sex-steroid crosstalk in the sex-specific misprogramming of metabolism', *Journal of the Endocrine Society*. Oxford Academic. Available at: https://doi.org/10.1210/jendso/bvaa087.

Ryckaert, J.P., Ciccotti, G. and Berendsen, H.J.C. (1977) 'Numerical integration of the cartesian equations of motion of a system with constraints: molecular dynamics of n-alkanes', *Journal of Computational Physics*, 23(3), pp. 327–341. Available at: https://doi.org/10.1016/0021-9991(77)90098-5.

Sack, J.S. *et al.* (2001) 'Crystallographic structures of the ligand-binding domains of the androgen receptor and its T877A mutant complexed with the natural agonist dihydrotestosterone', *Proceedings of the National Academy of Sciences of the United States of America*, 98(9), pp. 4904–4909. Available at: https://doi.org/10.1073/pnas.081565498.

Santos, R. *et al.* (2017) ‘A comprehensive map of molecular drug targets’, *Nature Reviews Drug Discovery*, 16(1), pp. 19–34. Available at: https://doi.org/10.1038/nrd.2016.230.

Sapolsky, R.M., Romero, L.M. and Munck, A.U. (2000) ‘How do glucocorticoids influence stress responses? Integrating permissive, suppressive, stimulatory, and preparative actions’, *Endocrine Reviews*, 21(1), pp. 55–89. Available at: https://doi.org/10.1210/edrv.21.1.0389.

Sarkar, S. *et al.* (2014) ‘Androgen receptor degradation by the E3 ligase CHIP modulates mitotic arrest in prostate cancer cells’, *Oncogene*, 33(1), pp. 26–33. Available at: https://doi.org/10.1038/onc.2012.561.

Sartorius, C.A. *et al.* (1994) ‘A third transactivation function (AF3) of human progesterone receptors located in the unique N-terminal segment of the B-isoform’, *Molecular Endocrinology*, 8(10), pp. 1347–1360. Available at: https://doi.org/10.1210/mend.8.10.7854352.

Schaufele, F. *et al.* (2005) ‘The structural basis of androgen receptor activation: Intramolecular and intermolecular amino-carboxy interactions’, *Proceedings of the National Academy of Sciences of the United States of America*, 102(28), pp. 9802–9807. Available at: https://doi.org/10.1073/pnas.0408819102.

Scher, H.I. and Sawyers, C.L. (2005) ‘Biology of progressive, castration-resistant prostate cancer: Directed therapies targeting the androgen-receptor signaling axis’, *Journal of Clinical Oncology*. American Society of Clinical Oncology, pp. 8253–8261. Available at: https://doi.org/10.1200/JCO.2005.03.4777.

Scheschowitsch, K., Leite, J.A. and Assreuy, J. (2017) ‘New insights in glucocorticoid receptor signaling-more than just a ligand-binding receptor’, *Frontiers in Endocrinology*, p. 16. Available at: https://doi.org/10.3389/fendo.2017.00016.

Schindelin, J. *et al.* (2012) ‘Fiji: An open-source platform for biological-image analysis’, *Nature Methods*. Nature Publishing Group, pp. 676–682. Available at: https://doi.org/10.1038/nmeth.2019.

Schöne, S. *et al.* (2016) ‘Sequences flanking the core-binding site modulate glucocorticoid receptor structure and activity’, *Nature Communications*, 7(1), pp. 1–13. Available at: https://doi.org/10.1038/ncomms12621.

Schubert, M. *et al.* (2018) ‘Perturbation-response genes reveal signaling footprints in cancer gene expression’, *Nature Communications*, 9(1), pp. 1–11. Available at: https://doi.org/10.1038/s41467-017-02391-6.

Schupp, M. and Lazar, M.A. (2010) ‘Endogenous ligands for nuclear receptors: Digging deeper’, *Journal of Biological Chemistry*, pp. 40409–40415. Available at: https://doi.org/10.1074/jbc.R110.182451.

Schütz, G. *et al.* (1995) *The nuclear receptor superfamily: The second decade*, *Cell*. Available at: https://doi.org/10.1016/0092-8674(95)90199-x.

Schwabe, J.W.R. *et al.* (1993) ‘The crystal structure of the estrogen receptor DNA-binding domain bound to DNA: How receptors discriminate between their response elements’, *Cell*, 75(3), pp. 567–578. Available at: https://doi.org/10.1016/0092-8674(93)90390-C.

Schweizer, M.T. *et al.* (2015) ‘Effect of bipolar androgen therapy for asymptomatic men with castration-resistant prostate cancer: Results from a pilot clinical study’, *Science Translational Medicine*, 7(269). Available at: https://doi.org/10.1126/scitranslmed.3010563.

Sevilla, L.M. and Pérez, P. (2018) ‘Roles of the glucocorticoid and mineralocorticoid receptors in skin pathophysiology’, *International Journal of Molecular Sciences*, 19(1906), pp. 1–19. Available at: https://doi.org/10.3390/ijms19071906.

Shaffer, P.L. *et al.* (2004) ‘Structural basis of androgen receptor binding to selective androgen response elements’, *Proceedings of the National Academy of Sciences of the United States of America*, 101(14), pp. 4758–4763. Available at: https://doi.org/10.1073/pnas.0401123101.

Shan, L. *et al.* (2004) 'Structure of the murine constitutive androstane receptor complexed to androstenol: A molecular basis for inverse agonism', *Molecular Cell*, 16(6), pp. 907–917. Available at: https://doi.org/10.1016/j.molcel.2004.11.037.

Sheikhhassani, V. *et al.* (2022) 'Topological dynamics of an intrinsically disordered N-terminal domain of the human androgen receptor', *Protein Science*, 31(6), p. e4334. Available at: https://doi.org/10.1002/pro.4334.

Shi, X.B. *et al.* (2002) 'Functional analysis of 44 mutant androgen receptors from human prostate cancer', *Cancer Research*, 62(5), pp. 1496–1502. Available at: http://www.mcgill.ca/androgendb.

Skiba, M.A. *et al.* (2019) 'Androgens during the reproductive years: What is normal for women?', *Journal of Clinical Endocrinology and Metabolism*, 104(11), pp. 5382–5392. Available at: https://doi.org/10.1210/jc.2019-01357.

Soifer, H.S. *et al.* (2012) 'Direct regulation of androgen receptor activity by potent CYP17 inhibitors in prostate cancer cells', *Journal of Biological Chemistry*, 287(6), pp. 3777–3787. Available at: https://doi.org/10.1074/jbc.M111.261933.

Del Sol, A. *et al.* (2006) 'Residues crucial for maintaining short paths in network communication mediate signaling in proteins', *Molecular Systems Biology*, 2. Available at: https://doi.org/10.1038/msb4100063.

Sonoda, J., Pei, L. and Evans, R.M. (2008) 'Nuclear receptors: Decoding metabolic disease', *FEBS Letters*, pp. 2–9. Available at: https://doi.org/10.1016/j.febslet.2007.11.016.

van der Steen, T., Tindall, D.J. and Huang, H. (2013) 'Posttranslational modification of the androgen receptor in prostate cancer', *International Journal of Molecular Sciences*. Multidisciplinary Digital Publishing Institute, pp. 14833–14859. Available at: https://doi.org/10.3390/ijms140714833.

Subramanian, A. *et al.* (2005) 'Gene set enrichment analysis: A knowledge-based approach for interpreting genome-wide expression profiles', *Proceedings of the National Academy of Sciences of the United States of America*, 102(43), pp. 15545–15550. Available at: https://doi.org/10.1073/pnas.0506580102.

Sun, L. *et al.* (2011) 'Structural insights into protein arginine symmetric dimethylation by PRMT5', *Proceedings of the National Academy of Sciences of the United States of America*, 108(51), pp. 20538–20543. Available at: https://doi.org/10.1073/pnas.1106946108.

Tadokoro, R. *et al.* (2009) 'Comparison of the molecular consequences of different mutations at residue 754 and 690 of the androgen receptor (AR) and androgen insensitivity syndrome (AIS) phenotype', *Clinical Endocrinology*, 71(2), pp. 253–260. Available at: https://doi.org/10.1111/j.1365-2265.2008.03462.x.

Taneja, S.S. *et al.* (2005) 'Cell-specific regulation of androgen receptor phosphorylation in vivo', *Journal of Biological Chemistry*, 280(49), pp. 40916–40924. Available at: https://doi.org/10.1074/jbc.M508442200.

Tanenbaum, D.M. *et al.* (1998) 'Crystallographic comparison of the estrogen and progesterone receptor's ligand binding domains', *Proceedings of the National Academy of Sciences*, 95(11), pp. 5998–6003. Available at: https://doi.org/10.1073/pnas.95.11.5998.

Tanner, T.M. *et al.* (2010) 'A 629RKLKK633 motif in the hinge region controls the androgen receptor at multiple levels', *Cellular and Molecular Life Sciences*, 67(11), pp. 1919–1927. Available at: https://doi.org/10.1007/s00018-010-0302-1.

Tian, C. *et al.* (2020) 'Ff19SB: Amino acid-specific protein backbone parameters trained against quantum mechanics energy surfaces in solution', *Journal of Chemical Theory and Computation*, 16(1), pp. 528–552. Available at: https://doi.org/10.1021/acs.jctc.9b00591.

Tilley, W.D. *et al.* (1989) 'Characterization and expression of a cDNA encoding the human androgen receptor.', *Proceedings of the National Academy of Sciences of the United States of America*, 86(1), pp. 327–31. Available at: http://www.ncbi.nlm.nih.gov/pubmed/2911578%0A

Tilley, W.D. *et al.* (1990) 'Androgen receptor gene expression in human prostate carcinoma cell lines', *Cancer Research*, 50(17), pp. 5382–5386. Available at: http://aacrjournals.org/cancerres/article-pdf/50/17/5382/2440950/cr0500175382.pdf.

Timmermans, S., Souffriau, J. and Libert, C. (2019) 'A general introduction to glucocorticoid biology', *Frontiers in Immunology*, 10(1545), pp. 1–17. Available at: https://doi.org/10.3389/fimmu.2019.01545.

Timmermans, S., Vandewalle, J. and Libert, C. (2022) 'Dimerization of the glucocorticoid receptor and its importance in (patho)physiology: A primer', *Cells*. Multidisciplinary Digital Publishing Institute, p. 683. Available at: https://doi.org/10.3390/cells11040683.

Tora, L. *et al.* (1989) 'The human estrogen receptor has two independent nonacidic transcriptional activation functions', *Cell*, 59(3), pp. 477–487. Available at: https://doi.org/10.1016/0092-8674(89)90031-7.

Turcu, A. *et al.* (2014) 'Adrenal androgens and androgen precursors-Definition, synthesis, regulation and physiologic actions', *Comprehensive Physiology*, 4(4), pp. 1369–1381. Available at: https://doi.org/10.1002/cphy.c140006.

Turcu, A.F. *et al.* (2020) '11-Oxygenated androgens in health and disease', *Nature Reviews Endocrinology*. Nature Publishing Group, pp. 284–296. Available at: https://doi.org/10.1038/s41574-020-0336-x.

Vandevyver, S., Dejager, L. and Libert, C. (2012) 'On the trail of the glucocorticoid receptor: into the nucleus and back', *Traffic*. John Wiley & Sons, Ltd, pp. 364–374. Available at: https://doi.org/10.1111/j.1600-0854.2011.01288.x.

Vatansever, S., Erman, B. and Gümüş, Z.H. (2019) 'Oncogenic G12D mutation alters local conformations and dynamics of K-Ras', *Scientific Reports*, 9(1), pp. 1–13. Available at: https://doi.org/10.1038/s41598-019-48029-z.

Vitellius, G. *et al.* (2016) 'Three novel heterozygous point mutations of NR3C1 causing glucocorticoid resistance', *Human Mutation*, 37(8), pp. 794–803. Available at: https://doi.org/10.1002/humu.23008.

Vitellius, G. *et al.* (2018) 'Pathophysiology of glucocorticoid signaling', *Annales d'Endocrinologie*, 79(3), pp. 98–106. Available at: https://doi.org/10.1016/j.ando.2018.03.001.

Vitellius, G. and Lombes, M. (2020) 'Genetics in endocrinology: Glucocorticoid resistance syndrome', *European Journal of Endocrinology*, 182(2), pp. R15–R27. Available at: https://doi.org/10.1530/EJE-19-0811.

De Vos, P. *et al.* (1993) 'Interaction of androgen and glucocorticoid receptor DNA-binding domains with their response elements', *Molecular and Cellular Endocrinology*, 90(2), pp. R11–R16. Available at: https://doi.org/10.1016/0303-7207(93)90160-L.

Wallace, A.D. and Cidlowski, J.A. (2001) 'Proteasome-mediated glucocorticoid receptor degradation restricts transcriptional signaling by glucocorticoids', *Journal of Biological Chemistry*, 276(46), pp. 42714–42721. Available at: https://doi.org/10.1074/jbc.M106033200.

Walter, P. *et al.* (1985) 'Cloning of the human estrogen receptor cDNA', *Proceedings of the National Academy of Sciences of the United States of America*, 82(23), pp. 7889–7893. Available at: https://doi.org/10.1073/pnas.82.23.7889.

Wang, J. *et al.* (2004) 'Development and testing of a general Amber force field', *Journal of Computational Chemistry*, 25(9), pp. 1157–1174. Available at: https://doi.org/10.1002/jcc.20035.

Wang, Q. *et al.* (1998) 'Azoospermia associated with a mutation in the ligand-binding domain of an androgen receptor displaying normal ligand binding, but defective trans-activation', *The Journal of Clinical Endocrinology & Metabolism*, 83(12), pp. 4303–4309. Available at: https://doi.org/10.1210/jcem.83.12.5358.

Ward, R.D. and Weigel, N.L. (2009) 'Steroid receptor phosphorylation: Assigning function to site-specific phosphorylation', *BioFactors*, pp. 528–536. Available at: https://doi.org/10.1002/biof.66.

Wärnmark, A. *et al.* (2001) 'The N-terminal regions of estrogen receptor α and β are unstructured in vitro and show different TBP binding properties', *Journal of Biological Chemistry*, 276(49), pp. 45939–45944. Available at: https://doi.org/10.1074/jbc.M107875200.

Wasmuth, E. V. *et al.* (2022) 'Allosteric interactions prime androgen receptor dimerization and activation', *Molecular Cell*, 82(11), pp. 2021–2031. Available at: https://doi.org/10.1016/j.molcel.2022.03.035.

Watson, L.C. *et al.* (2013) 'The glucocorticoid receptor dimer interface allosterically transmits sequence-specific DNA signals', *Nature Structural and Molecular Biology*, 20(7), pp. 876–883. Available at: https://doi.org/10.1038/nsmb.2595.

Weikum, E.R. *et al.* (2017) 'Glucocorticoid receptor control of transcription: Precision and plasticity via allostery', *Nature Reviews Molecular Cell Biology*, 18(3), pp. 159–174. Available at: https://doi.org/10.1038/nrm.2016.152.

Weikum, E.R., Liu, X. and Ortlund, E.A. (2018) 'The nuclear receptor superfamily: A structural perspective', *Protein Science*, pp. 1876–1892. Available at: https://doi.org/10.1002/pro.3496.

Wen, S., Niu, Y. and Huang, H. (2020) 'Posttranslational regulation of androgen dependent and independent androgen receptor activities in prostate cancer', *Asian Journal of Urology*. Elsevier, pp. 203–218. Available at: https://doi.org/10.1016/j.ajur.2019.11.001.

Wen, Y. *et al.* (2000) 'HER-2/neu promotes androgen-independent survival and growth of prostate cancer cells through the Akt pathway', *Cancer Research*, 60(24), pp. 6841–6845. Available at: http://aacrjournals.org/cancerres/article-pdf/60/24/6841/2481520/ch240006841.pdf.

Wilkinson, L., Verhoog, N.J.D. and Louw, A. (2018) 'Disease-and treatment-associated acquired glucocorticoid resistance', *Endocrine Connections*, 7(12), pp. R328–R349. Available at: https://doi.org/10.1530/EC-18-0421.

Williams, S.P. and Sigler, P.B. (1998) 'Atomic structure of progesterone complexed with its receptor', *Nature*, 393(6683), pp. 392–396. Available at: https://doi.org/10.1038/30775.

Wilson, J.D. (2001) 'The role of 5α-reduction in steroid hormone physiology', *Reproduction, Fertility and Development*, 13(7–8), pp. 673–678. Available at: https://doi.org/10.1071/rd01074.

Wu, T. *et al.* (2021) 'clusterProfiler 4.0: A universal enrichment tool for interpreting omics data', *The Innovation*, 2(3), p. 100141. Available at: https://doi.org/10.1016/j.xinn.2021.100141.

Xu, H.E. (2015) 'Family reunion of nuclear hormone receptors: structures, diseases and drug discovery', *Nature*, 36(1), pp. 1–2. Available at: https://doi.org/10.1038/aps.2014.140.

Xu, K. *et al.* (2009) 'Regulation of androgen receptor transcriptional activity and specificity by RNF6-induced ubiquitination', *Cancer Cell*, 15(4), pp. 270–282. Available at: https://doi.org/10.1016/j.ccr.2009.02.021.

Xu, R.X. *et al.* (2004) 'A structural basis for constitutive activity in the human CAR/RXRα heterodimer', *Molecular Cell*, 16(6), pp. 919–928. Available at: https://doi.org/10.1016/j.molcel.2004.11.042.

Yamamoto, K.R. (1985) 'Steroid receptor regulated transcription of specific genes and gene networks', *Annual Review of Genetics*, 19(1), pp. 209–252. Available at: https://doi.org/10.1146/annurev.ge.19.120185.001233.

Yi, P. *et al.* (2015) 'Structure of a biologically active estrogen receptor-coactivator complex on DNA', *Molecular Cell*, 57(6), pp. 1047–1058. Available at: https://doi.org/10.1016/j.molcel.2015.01.025.

Yu, X. *et al.* (2020) 'Structural insights of transcriptionally active, full-length androgen receptor coactivator complexes', *Molecular Cell*, 79(5), pp. 812–823. Available at: https://doi.org/10.1016/j.molcel.2020.06.031.

Zhang, X. and Cheng, X. (2003) 'Structure of the predominant protein arginine methyltransferase PRMT1 and analysis of its binding to substrate peptides', *Structure*, 11(5), pp. 509–520. Available at: https://doi.org/10.1016/S0969-2126(03)00071-6.

Zhao, X.Y. *et al.* (2000) 'Glucocorticoids can promote androgen-independent growth of prostate cancer cells through a mutated androgen receptor', *Nature Medicine*, 6(6), pp. 703–706. Available at: https://doi.org/10.1038/76287.

Zhou, L. *et al.* (2006) 'Roles of the androgen receptor cofactor p44 in the growth of prostate epithelial cells', *Journal of Molecular Endocrinology*, 37(2), pp. 283–300. Available at: https://doi.org/10.1677/jme.1.02062.

Zhou, X.E. *et al.* (2010) 'Identification of SRC3/AIB1 as a preferred coactivator for hormone-activated androgen receptor', *Journal of Biological Chemistry*, 285(12), pp. 9161–9171. Available at: https://doi.org/10.1074/jbc.M109.085779.

Zhou, Z., Corden, J.L. and Brown, T.R. (1997) 'Identification and characterization of a novel androgen response element composed of a direct repeat', *Journal of Biological Chemistry*, 272(13), pp. 8227–8235. Available at: https://doi.org/10.1074/jbc.272.13.8227.

Zwart, N. *et al.* (2017) 'Improved androgen specificity of AR-EcoScreen by CRISPR based glucocorticoid receptor knockout', *Toxicology in Vitro*, 45, pp. 1–9. Available at: https://doi.org/10.1016/j.tiv.2017.08.004.

Supplementary materials

1. Supplementary figures

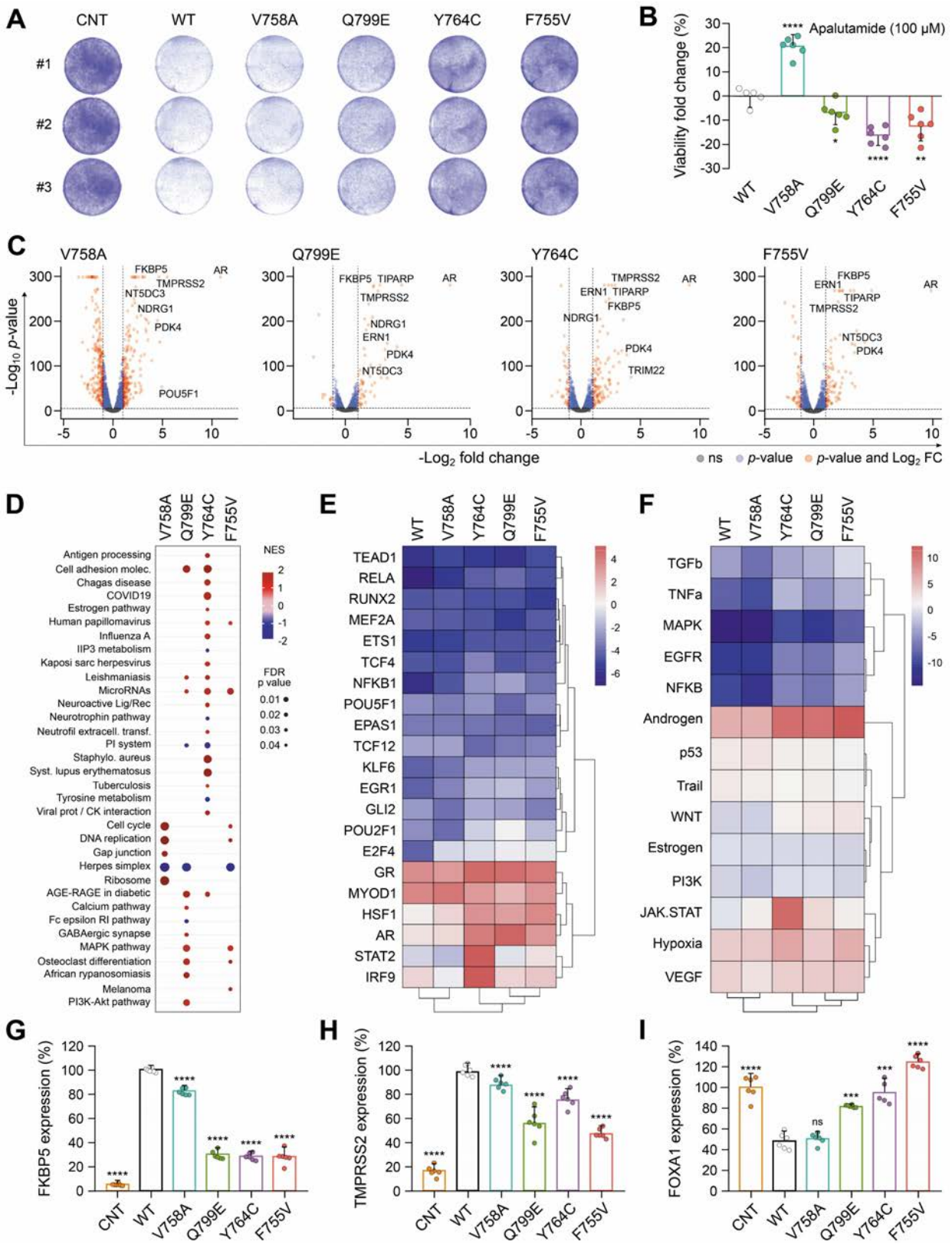

Fig. S1. The cellular phenotypes and the transcriptional profiles of AR mutants differ from that of the wild-type receptor.

(A) Representative crystal violet-stained cultures used to quantitate the colony formation capacity of PC3 cells expressing WT or mutant AR. *(B)* Relative viability fold change of CNT, WT, and mutant AR-transduced cells in response to the antiandrogen, apalutamide. *(C)* Volcano plots showing the differential expression analysis between PC3-CNT and PC3-mut AR cells (V758A, Q799E, Y764C and F755V as indicated), using DESeq2 data. Genes with an absolute log2(fold change) ≥ 1 and a p value ≤ 0.05 are labelled in red. *(D-F)* RT-qPCR validation of AR transcriptional activity using canonical targets FKBP5 (D) and TMPRSS2 (E). Also shown is the RT-qPCR validation for expression of the pioneer factor, FOXA1, in WT and mutant AR transduced cells (F). RT-qPCR measurements were conducted in triplicate (mean ± SD are shown) and differences against WT-AR cells were calculated using a t- test and considered significant at p values < 0.05. (*p < 0.05, ** p < 0.01, *** p < 0.001 and **** p < 0.0001).

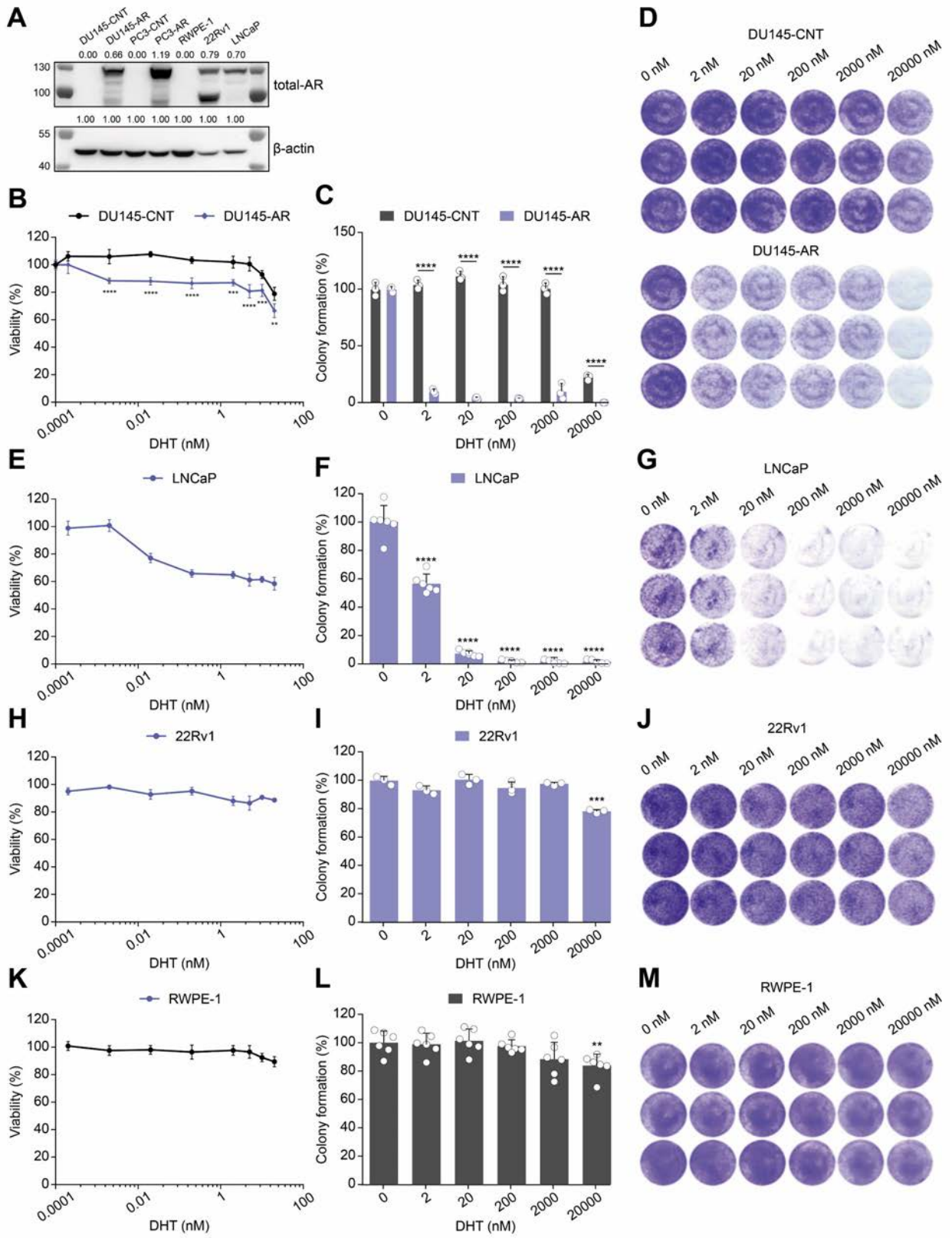

Fig. S2. Supraphysiological dihydrotestosterone concentrations suppress cell growth of AR-responsive cell lines.

(A) WB analysis of total AR in the cell lines and derivatives used in the current study. *(B-D)* Analysis of the effect of AR expression in DU145 cells. *(B)* Viability assays comparing parental and AR-expressing cells upon DHT treatment. *(C-D)* Quantification and representative images of colony formation assays in parental and AR-expressing DU145 cells. Note the significant reduction in viability and clonogenicity in AR-expressing cells upon DHT stimulation. *(E-G)* Analysis of the effect of AR expression in LNCaP cells. *(E)* Viability assay of LNCaP cells upon DHT treatment. *(F-G)* Quantification and representative images of colony formation assays in LNCaP cells. *(H-J)* Analysis of the effect of AR expression in CRPC 22Rv1 cells. *(H)* viability assays of 22Rv1 in response to DHT treatment. *(I-J)* Quantification and representative images of colony formation assays in 22Rv1 cells. Note that 22Rv1 cells express the truncated AR variant lacking the LBD and therefore do not respond to DHT. *(K-M)* Analysis of the effect of AR activation upon DHT treatment in AR-negative RWPE-1 cells. *(K)* Viability assays of RWPE-1 cells upon DHT treatment. *(L-M)* Quantification and representative images of colony formation assays in RWPE-1 cells. Note that in RWPE-1 cells do not express AR and similarly to parental PC3 and DU145 cells do not respond to DHT. Viability and clonogenic assays were conducted in n=3 or n=6 as indicated (mean ± SD are shown) and differences were calculated using a t-test and considered significant at p values < 0.05. (*p < 0.05, **p < 0.01, ***p < 0.001 and ****p < 0.0001).

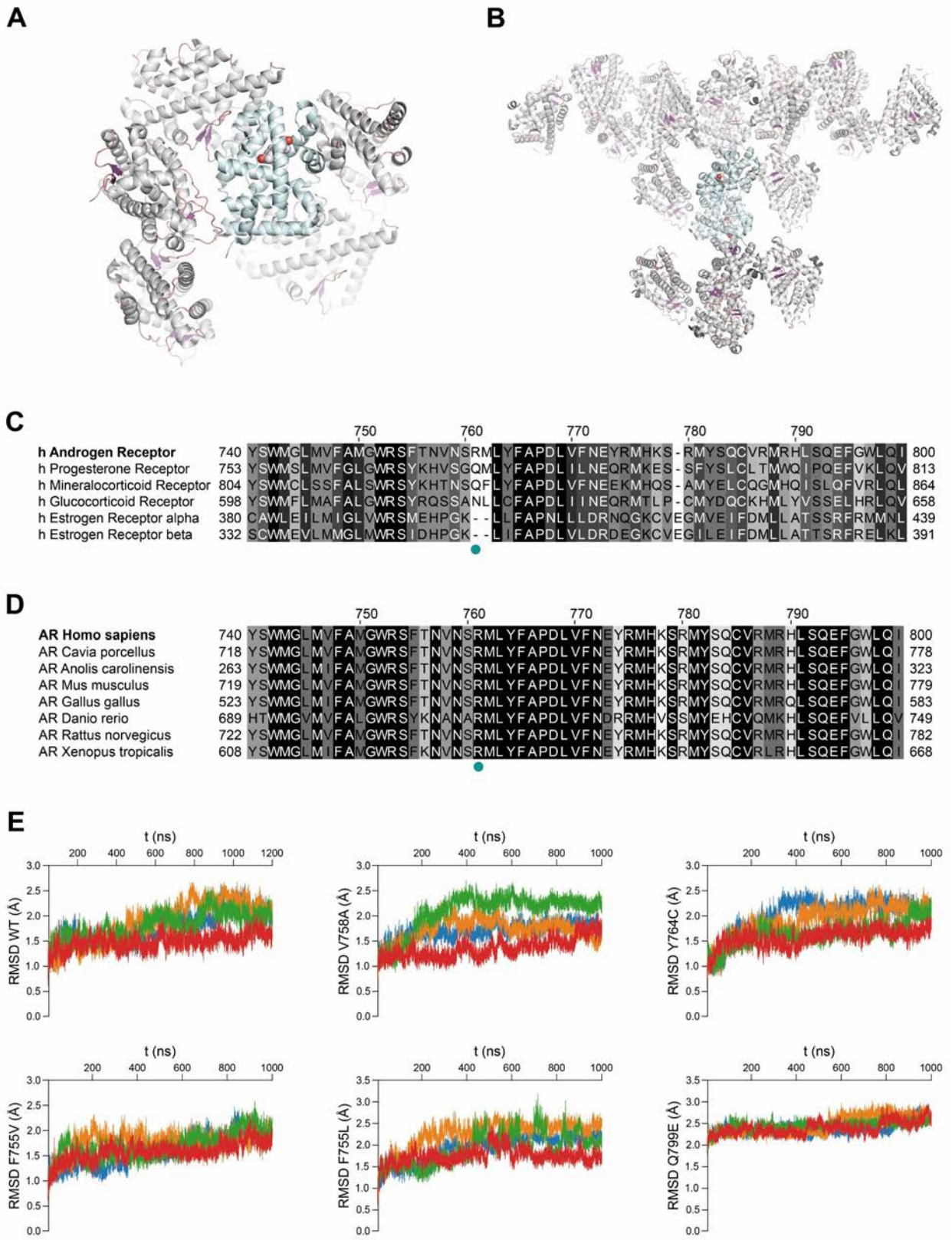

Fig. S3. In silico characterization of AR-LBD dimer interface mutants.

(A-B) Crystal packing in monomeric (A, PDB 1T7T) and tetrameric AR-LBD (B, PDB 5JJM). Only the closest crystal neighbours are shown. *(C-D)* Partial sequence alignments of the AR-LBD sequence around residue Arg761 (marked with a blue dot). Residues topologically equivalent to the Tyr740-Ile800 sequence of human AR are compared to other steroid receptors (C) and to AR sequences from different species (from fish to humans; D). Strictly conserved residues are white with black shading; other conservative mutations are coloured by conservation (the darker, the more conserved). Note that Arg761 is strictly conserved among the different species of AR, but not in other steroid receptors. *(E)* Evolution of the RMSD for WT AR- LBD and the studied mutants along four independent MD runs. All structures converge demonstrating global structural stability.

A

	Ele	Desolv	VdW	Bind E	BSA
5JJM	-12.1	-1.6	-81.9	**-21.8**	1592
V758A	-4.9	-11.5	-59.7	**-22.4**	1327
Y764C	-7.4	-10.6	-55.3	**-23.6**	1219
F755V	-5.9	-5.8	-53.3	**-17.0**	927
F755L	-2.8	-8.8	-41.1	**-15.7**	945
Q799E	-3.9	-9.98	-32.4	**-17.1**	1196

B

	Ele	Desolv	VDW	Total E	RMSD	Rank
5JJM	-24.2	-1.0	14.2	**-23.8**	5.59	1
V758A	-6.6	-14.2	-19.9	**-22.7**	5.10	39
Y764C	-12.7	-9.4	-3.4	**-22.4**	3.53	34
F755V	-26.7	-5.1	75.4	**-24.3**	6.54	16
F755L	-18.8	-15.2	9.6	**-33.4**	6.08	5
Q799E	-16.4	-6.1	-0.3	**-22.6**	8.33	107

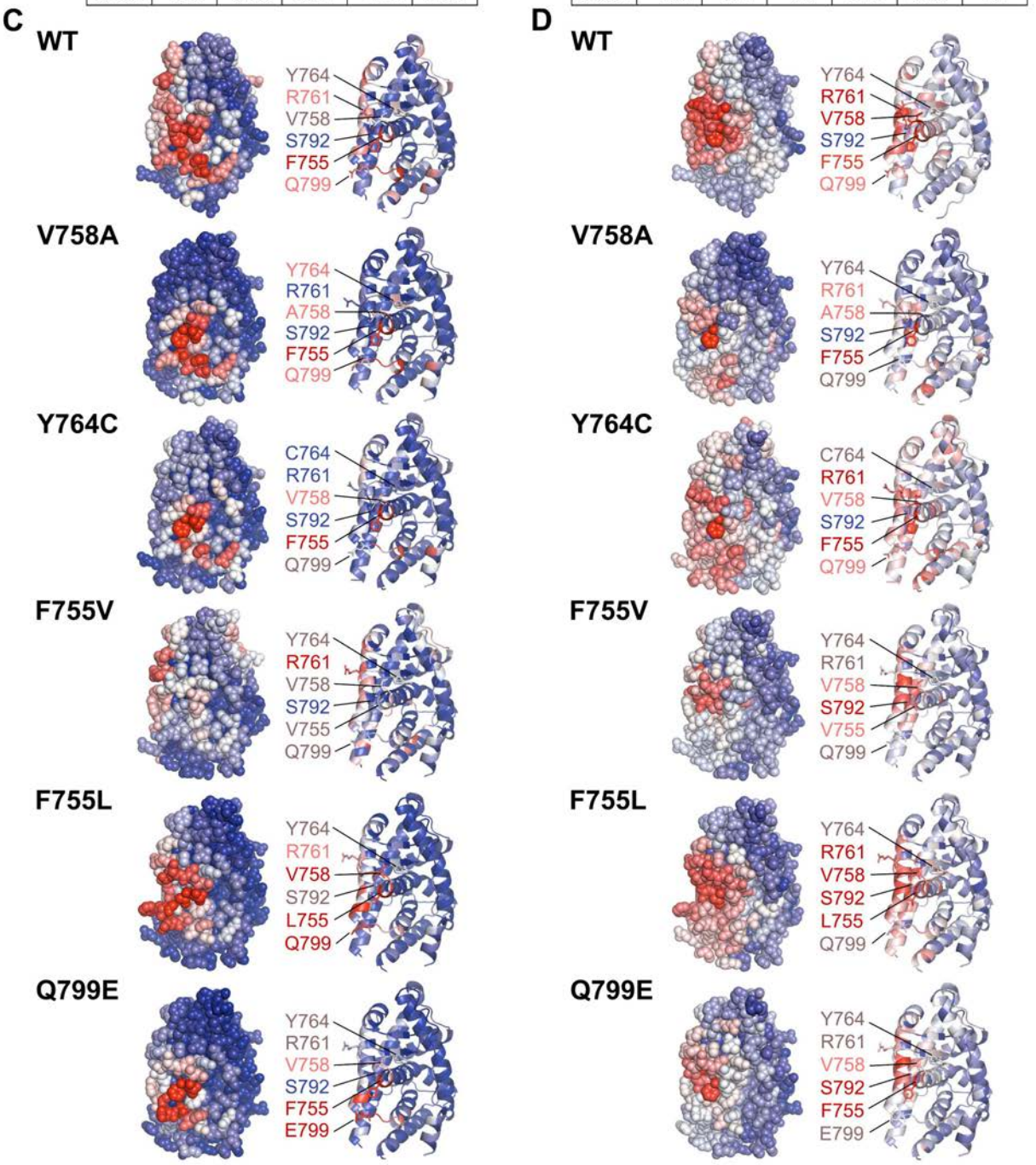

Fig. S4. AR-LBD interface mutants are predicted to dimerize essentially as non-canonical wild type AR-LBD.

(A) Buried surface area (BSA) and pyDock scoring (total binding energy, calculated as the sum of electrostatics (Ele), desolvation (Dslvt), and one-tenth of the VdW energy term) for dimeric AR-LBD. Values were calculated assuming that mutants dimerize as in the previously reported structure of WT AR-LBD (B:C chains of PDB entry 5JJM). *(B)* pyDock scoring of the best-ranked docking solutions. Docking experiments with WT AR-LBD (B chain from 5JJM) and the current structures of monomeric mutant with themselves were independently conducted. In all cases, arrangements close to the experimental dimer were identified among the top solutions (RMSD < 10 Å). *(C)* Hotspot interface residues in WT and mutant AR-LBD predicted from docking experiments. Surface residues are coloured according to their NIP, from lowest (blue) to highest (red) values; intermediate values are scaled accordingly (left panel). Residues of interest are labelled and coloured according to their relative NIP values in the right panel. *(D)* Predicted protein-protein interaction ODA. Residues are coloured according to their ODA values, from minimum (red) to maximum (blue), and intermediate values are scaled accordingly (left panel). Residues of interest are labelled and coloured according to their relative ODA values (right panel).

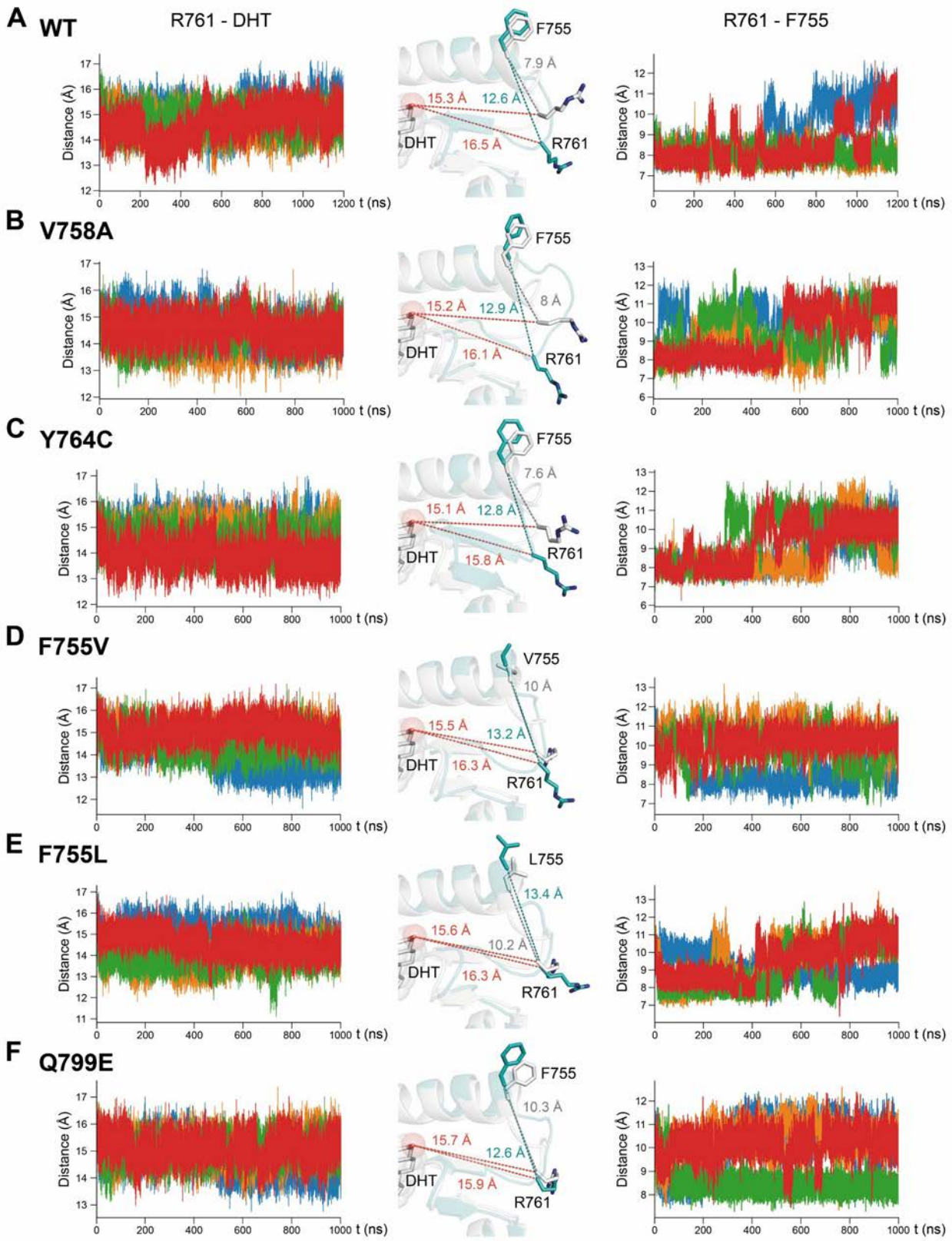

Fig. S5. Dynamics of R761-zone large conformational reorientations.

MD simulations were performed in quadruplicate. *(A-F)* Analysis of the displacements of the H5-S1 loop along the MD simulations, as assessed by the time evolution of the distances between the Cα atoms of some of the most significant pairwise interactions identified from the inter-residue distance calculations, represented in the left and right panels of each AR-LBD row, respectively (see Materials and Methods section 3.4). Figures in the central panels represent the calculated distances between Arg761 and DHT (in red) or mutated residues (Phe755, Val758 and Tyr764) for the AR-LBD WT structure and mutants. Minimum and maximum distances identified during the MD simulations are coloured grey and blue, respectively, to illustrate the dynamical changes of the H5-S1 loop.

2. Supplementary tables

	LBP			AF-2			BF-3			Dimer interface			R761-zone			Arginines		
	Res	PCa	AIS	Res	PCa	AIS	Res	PCa	AIS	Res	PCa	AIS	Res	PCa	AIS	Res	PCa	AIS
	L702	H	I	L713		F	I673	T		P672		H, S	W752	C	R	R711	G, I	T
	L705			V714			F674		C	L675	R, P		F755	L	V, L, S	R727	C, H, L	
	N706	S	S, Y, I	V717		F	P724	T	S, L	E679	K	G	T756	A		R753	Q	Q, P
	L708		R	K718			G725	D	S, A, V	A680	T, G		N757	D, S, K	S	R761	G	S
	G709		R	K721		L	R727	M		E682	K, V, D	K, D	V758	I, L, A		R775	C, H	C, H
	Q712		E	F726	C, H, L		N728		K	P683	S, L	T, A	N759		T	R780	G, Q	W
	W742	L, C	R	R727	M		F827	L	L	G684			S760	P	F, Y	R787	Q	
	M743		V	V731	H	H	E830	K, D		V685	A	I	R761		S	R789		S
	M746		T, I, L	Q734			L831	P	V	C687		R	Y764	C	C, H	R832	Q	Q, L
	V747		M	M735		F, T	N834			W752	C	R	R789		S	R841	C, H, L	C, G, H, S
	M750	T, K, I	V	I738		R	E838			R753			H790	Q		R847	G	
	R753	Q	Q, P	Q739	K		R841	C, H, L	C, H, G, S	F755	L	V, L, S	S792	P, F		R855		K
	F765		L	E894						T756	A		Q793			R856	C, H	C, H
	M781		I	M895	D	G				N757	D, S, K		W797			R872		G
	M788	I		E898		F, T				V758	I, L, A		Q799	E	E			
	L874			I899						N759		T						
	H875	Y, Q	R							R761		S						
	F877	L								M762		T						
	T878	A, S	I							Y764	C	H, C						
	L881	Q								P767	T	S, A						
	M896	L	T							D768	N	E, Y						
										G796	E, V							
										Q799	E	E						
										I800	T							
										T801		I						
										P802	L							
										Q803		R						
										L806								
										C845								
										K846								
										R847	G							
										K848	N							
										N849	H, K	K						
										S852								
Total residues	20			16			12			34			15			14		
Mutated residues	17	9	15	11	5	8	10	8	7	25	21	18	13	10	9	14	10	11
Unique mutations	32	14	20	16	7	10	21	11	13	51	32	27	24	15	13	28	18	18

Table S1. Reported mutations in the major functional areas of the AR-LBD.

Mutations that affect the LBP as well as the major protein-protein interaction sites, AF-2, BF-3 and the dimer interface are separately given. Within each subgroup, we also distinguish between those reported in PCa patients and in AIS cases. The total numbers of mutated residues and of unique mutations within each functional region are given at the bottom of the table. Note that several mutations have been linked to both PCa and AIS (e.g., R753Q, F755L).

AR mutant	Identified in	Protein stability	Ligand affinity	Intra- / intermolecular interactions	Transcriptional activity	Ref.
F755V	CAIS	Not studied	Five-fold lower affinity for mibolerone.	Reduced N/C interaction.	Largely impaired (5% of WT activity at 10 nM DHT).	1, 2
F755L	PCa, PAIS	Enhanced thermolability but as resistant to trypsinolysis as WT protein.	One-third of the affinity for DHT and mibolerone. 10-fold higher concentration of androgen needed to achieve same activity as WT.	Severely compromised N/C interactions. Reduced binding to Qia2.	Significantly impaired: high activity with mibolerone and methyltrienolone, 40-60% of WT with DHT, 30% of WT activity with testosterone.	2, 3, 4, 5, 6, 7
V758A	PCa	Not studied	PC3 transiently expressing AR V758A present sensitivity to darolutamide.	Increased binding to coactivators and impaired binding to corepressors. WT-like or increased N/C interaction.	Normal activity in response to DHT; weak activity with DHEA.	3, 8, 9, 10, 11
R761G	PCa	Not studied	Not studied	Not studied	Poor response to low concentrations of R1881 in CV-1 cells, but WT-like activity in PC3 cells. EPI-002 inhibitor blocks mutant activity similar to WT.	12, 13, 14
Y764C	PCa, PAIS	More thermolabile, especially in combination with a shorter polyQ stretch.	WT-like binding to DHT, but reduced binding to other androgens, non-androgens, and anti-androgens.	Abnormal or even complete loss of N/C interactions.	Conflicting results: reported to have complete, moderate, or no function at all in different studies.	3, 11, 15, 16, 17, 18, 19
Q799E	PCa, PAIS	Normal thermal stability.	Normal androgen binding. Sensitive to darolutamide in PC3 cells.	Mild reduction of N/C interaction. Reduced binding to Qia2. Impaired binding to NCoA.	Impaired at normal androgen doses but overcome with high doses of androgens. In other studies, full activity in the presence of DHT an partial activity DHEA.	3, 4, 11, 19, 20, 21, 22, 23

Table S2. Summary of clinical and biological information on AR-LBD dimer interface mutants.

References numbered in the last column are:

1) J. M. Lobaccaro, S. Lumbroso, R. Ktari, R. Dumas, C. Sultan. An exonic point mutation creates a MaeIll site in the androgen receptor gene of a family with complete androgen insensitivity syndrome. Hum. Mol. Genet. 2, 1041–1043 (1993).
2) R. Tadokoro-Cuccaro, T. I. Bunch, J. W. Schwabe, I. A. Hughes, J. C. Murphy. Comparison of the molecular consequences of different mutations at residue 754 and 690 of the androgen receptor (AR) and androgen insensitivity syndrome (AIS) phenotype. Clin. Endocrinol. 71, 253–260 (2009).
3) X. B. Shi, A. H. Ma, L. Xia, H. J. Kung, R. W. De Vere White. Functional analysis of 44 mutant androgen receptors from human prostate cancer. Cancer Res. 62, 1496–1502 (2002).
4) J. Qi, M. Tripathi, R. Mishra, N. Sahgal, L. Fazil, S. Ettinger, W. J. Placzek, G. Claps, L. W. Chung, D. Bowtell, M. Gleave, N. Bhowmick, Z. A. Ronai. The E3 ubiquitin ligase siah2 contributes to castration-resistant prostate cancer by regulation of androgen receptor transcriptional activity. Cancer Cell 23, 332–346 (2013).
5) H. Takahashi, M. Furusato, W. C. Allsbrook, H. Nishii, S. Wakui, J. C. Barrett, J. Boyd. Prevalence of androgen receptor gene mutations in latent prostatic carcinomas from Japanese men. Cancer Res. 55, 1621–1624 (1995).
6) W. Weidemann, B. Linck, H. Haupt, B. Mentrup, G. Romalo, K. Stockklauser, A. O. Brinkmann, H. U. Schweikert, K. D. Spindler. Clinical and biochemical investigations and molecular analysis of subjects with mutations in the androgen receptor gene. Clin. Endocrinol. 45, 733–739 (1996).
7) J. Thompson, F. Saatcioglu, O. A. Jänne, J. J. Palvimo. Disrupted amino- and carboxyl- terminal interactions of the androgen receptor are linked to androgen insensitivity. Mol. Endocrinol. 15, 923–935 (2001).
8) M. Marcelli, M. Ittmann, S. Mariani, R. Sutherland, R. Nigam, L. Murthy, Y. Zhao, D. Diconcini, E. Puxeddu, A. Esen, J. Eastham, N. L. Weigel, D. J. Lamb. Androgen receptor mutations in prostate cancer. Cancer Res. 60, 944–949 (2000).
9) X. E. Zhou, K. M. Suino-Powell, J. Li, Y. He, J. P. MacKeigan, K. Melcher, E. L. Yong, H. E. Xu. Identification of SRC3/AIB1 as a preferred coactivator for hormone-activated androgen receptor. J. Biol. Chem. 285, 9161–9171 (2010).
10) S. Grosdidier, L. R. Carbó, V. Buzón, G. Brooke, P. Nguyen, J. D. Baxter, C. L. Bevan, P. Webb, E. Estébanez-Perpiñá, J. Fernández-Recio. Allosteric conversation in the androgen receptor ligand-binding domain surfaces. Mol. Endocrinol. 26, 1078–1090 (2012).
11) C. W. Hay, I. J. McEwan, The impact of point mutations in the human androgen receptor: Classification of mutations on the basis of transcriptional activity. PLOS ONE 7, e32514 (2012).

12) O. A. O'Mahony, M. P. Steinkamp, M. A. Albertelli, M. Brogley, H. Rehman, D. M. Robins. Profiling human androgen receptor mutations reveals treatment effects in a mouse model of prostate cancer. Mol. Cancer Res. 6, 1691–1701 (2008).
13) Y. C. Yang, C. A. Banuelos, N. R. Mawji, J. Wang, M. Kato, S. Haile, I. J. McEwan, S. Plymate, M. D. Sadar. Targeting androgen receptor activation function-1 with EPI to overcome resistance mechanisms in castration-resistant prostate cancer. Clin. Cancer Res. 22, 4466–4477 (2016).
14) N. G. R. D. Elshan, M. B. Rettig, M. E. Jung. Molecules targeting the androgen receptor (AR) signaling axis beyond the AR-Ligand binding domain. Med. Res. Rev. 39, 910–960 (2019).
15) M. J. McPhaul, M. Marcelli, S. Zoppi, C. M. Wilson, J. E. Griffin, J. D. Wilson. Mutations in the ligand-binding domain of the androgen receptor gene cluster in two regions of the gene. J. Clin. Invest. 90, 2097–2101 (1992).
16) M. J. McPhaul, M. Marcelli, W. D. Tilley, J. E. Griffin, R. F. Isidro-Gutierrez, J. D. Wilson. Molecular basis of androgen resistance in a family with a qualitative abnormality of the androgen receptor and responsive to high-dose androgen therapy. J. Clin. Invest. 87, 1413–1421 (1991).
17) I. Murono, B. B. Mendonca, I. J. Arnhold, A. C. Rigon, C. J. Migeon, T. R. Brown. Human androgen insensitivity due to point mutations encoding amino acid substitutions in the androgen receptor steroid-binding domain. Hum. Mutat. 6, 152–162 (1995).
18) E. Langley, J. A. Kemppainen, E. M. Wilson. Intermolecular NH2−/carboxyl-terminal interactions in androgen receptor dimerization revealed by mutations that cause androgen insensitivity. J. Biol. Chem. 273, 92–101 (1998).
19) I. Jääskeläinen, A. Deeb, J. W. Schwabe, N. P. Mongan, H. Martin, I. A. Hughes. Human androgen receptor gene ligand-binding-domain mutations leading to disrupted interaction between the N- and C-terminal domains. J. Mol. Endocrinol. 36, 361–368 (2006).
20) J. Batch, D. Williams, H. Davies, B. Brown, B. A. Evans, I. A. Hughes, M. Patterson. Androgen receptor gene mutations identified by SSCP in fourteen subjects with androgen insensitivity syndrome. Hum. Mol. Genet. 1, 497–503 (1992).
21) C. L. Bevan, B. B. Brown, H. R. Davies, B. A. Evans, I. A. Hughes, M. N. Patterson. Functional analysis of six androgen receptor mutations identified in patients with partial androgen insensitivity syndrome. Hum. Mol. Genet. 5, 265–273 (1996).
22) Q. Wang, F. J. Ghadessy, A. Trounson, D. de Kretser, R. McLachlan, S. Ng, E. Yong. Azoospermia associated with a mutation in the ligand-binding domain of an androgen receptor displaying normal ligand binding, but defective trans-activation. J. Clin. Endocrinol. Metab. 83, 4303–4309 (1998).
23) O. Hiort, P.-M. Holterhus, T. Horter, W. Schulze, B. Kremke, M. Bals-Pratsch, G. H. G. Sinnecker, K. Kruse. Significance of Mutations in the Androgen Receptor Gene in Males with Idiopathic infertility. J. Clin. Endocrinol. Metab. 85, 2810–2815 (2000).

3. Publications

3.1. A hotspot for posttranslational modifications on the androgen receptor dimer interface drives pathology and anti-androgen resistance

Andrea Alegre-Martí*, Alba Jiménez-Panizo*, Adrián Martínez-Tébar*, Coralie Poulard, M. Núria Peralta-Moreno, Montserrat Abella, Rosa Antón, Marcos Chiñas, Ulrich Eckhard, Josep M. Piulats, Ana M. Rojas, Juan Fernández-Recio, Jaime Rubio-Martínez, Muriel Le Romancer, Álvaro Aytes‡, Pablo Fuentes-Prior‡, and Eva Estébanez-Perpiñá‡.

* These authors equally contributed to this work.
‡ These authors jointly supervised this work.

Published in: Science Advances, 2023
Impact factor: 14.136
Quartile: Q1
DOI: 10.1126/sciadv.ade2175

For this publication I conducted and analysed all the functional experiments with created stable PCa cell lines, including RNA-seq, transcriptional activity, anti-androgens response, and cell proliferation assays. These experiments unveiled the differential impact of FL-AR mutants on cellular phenotype and transcriptional profile. I performed site-directed mutagenesis, and conducted protein expression, purification, and crystallisation assays of the five AR-LBD mutants. I collected X-ray crystallisation data, solved, and analysed mutant structures, which revealed large structural rearrangements in four functional areas of the AR-LBD, being the R761 zone the most affected upon mutation. I characterised mutant proteins in solution by means of differential scanning fluorimetry, limited proteolysis and cross-linking experiments and interpreted mass spectrometry results. I also participated in the interpretation of MD simulations, docking, NIP and ODA calculations and FoldX estimations to further explore the mutational impact on AR-LBD structure. *In vitro* and *in silico* characterization showed that mutants do not alter protein folding and dimerization capacity of the AR-LBD but compromise its stability in solution by inducing local and distant changes in flexibility. This analysis further confirmed the significant dislodgement of R761, which I experimentally demonstrated that is differentially monomethylated *in vivo* upon mutation of the FL-AR, by means of protein immunoprecipitation and western blotting. I created all the figures, tables and article writing.

BIOCHEMISTRY

A hotspot for posttranslational modifications on the androgen receptor dimer interface drives pathology and anti-androgen resistance

Andrea Alegre-Martí[1,2]†, Alba Jiménez-Panizo[1,2]†, Adrián Martínez-Tébar[3]†, Coralie Poulard[4], M. Núria Peralta-Moreno[5], Montserrat Abella[1,2], Rosa Antón[6], Marcos Chiñas[3,7], Ulrich Eckhard[8], Josep M. Piulats[3], Ana M. Rojas[9], Juan Fernández-Recio[10], Jaime Rubio-Martínez[5], Muriel Le Romancer[4], Álvaro Aytes[3]‡*, Pablo Fuentes-Prior[6]‡*, Eva Estébanez-Perpiñá[1,2]‡*

Copyright © 2023 The Authors, some rights reserved; exclusive licensee American Association for the Advancement of Science. No claim to original U.S. Government Works. Distributed under a Creative Commons Attribution NonCommercial License 4.0 (CC BY-NC).

Mutations of the androgen receptor (AR) associated with prostate cancer and androgen insensitivity syndrome may profoundly influence its structure, protein interaction network, and binding to chromatin, resulting in altered transcription signatures and drug responses. Current structural information fails to explain the effect of pathological mutations on AR structure–function relationship. Here, we have thoroughly studied the effects of selected mutations that span the complete dimer interface of AR ligand–binding domain (AR-LBD) using x-ray crystallography in combination with in vitro, in silico, and cell-based assays. We show that these variants alter AR-dependent transcription and responses to anti-androgens by inducing a previously undescribed allosteric switch in the AR-LBD that increases exposure of a major methylation target, Arg^{761}. We also corroborate the relevance of residues Arg^{761} and Tyr^{764} for AR dimerization and function. Together, our results reveal allosteric coupling of AR dimerization and posttranslational modifications as a disease mechanism with implications for precision medicine.

INTRODUCTION

The androgen receptor (AR; *AR*/*NR3C4*) is a member of the steroid subfamily of nuclear receptors essential for male development and tissue homeostasis (*1*–*2*). The AR protein is composed of an intrinsically disordered N-terminal region (NTD) followed by a "core" that contains the actual DNA- and ligand-binding domains (DBD and LBD, respectively) (Fig. 1A) (*2*–*3*). The atomic details of full-length AR (FL AR) still remain elusive, but a low-resolution structure by cryo–electron microscopy (cryo-EM) complexed to DNA and a coregulator has provided a model of its overall architecture (*4*). This EM structure features a noncanonical head-to-head dimer (i.e., centered on H5 helices, in contrast to the canonical, H10-centered arrangement [see (*3*) for a detailed comparison of the dimerization modes], in line with previously reported x-ray structures of dimeric DBD (*5*) and LBD isolated moieties (*6*). Another EM structure of the AR core has recently been published in three distinctive configurations (*7*), further corroborating the noncanonical AR-LBD dimerization mode (*3*). These EM structures evidence that AR is a highly dynamic protein. AR physiological functions are inherently linked to not only the correct folding of DBD and LBD modules but also to their relative orientations (e.g., N-terminal and C-terminal (N/C) interaction), oligomerization, and coregulator binding to control transcription (*2*, *8*). Besides, AR protein structure and function relationship are regulated by posttranslational modifications (PTMs) such as methylation, phosphorylation, ubiquitination, acetylation, and sumoylation, adding an extra level of complexity that has only been scarcely studied (*9*–*19*). In particular, no structural data have been reported on the mechanistic consequences of these covalent modifications to date.

Tight spatial and temporal regulation of AR activity is critical for the proper functioning of tissue-specific signaling cascades. Therefore, dysfunctions of the AR-regulated pathways have profound pathophysiological consequences (*2*, *8*, *20*–*22*). Up-regulated receptor activity is the dominant driver in one of the leading cancers in adult men, prostate cancer (PCa; *1*–*2*, *8*, *21*–*22*), making AR a central therapeutic target for PCa treatment (*2*). On the other hand, impaired response to androgens leads to an X chromosome–linked disorder of sex development in genetic males termed androgen insensitivity syndrome (AIS) (*23*–*25*). Many point mutations in the *AR* gene associated with either resistance to PCa therapeutic drugs (anti-androgens; *26*–*28*) and/or with AIS have been reported (*29*) (table S1 and Fig. 1A). Knowledge of the structure of the wild-type (WT) protein does not allow to predict the structural and functional impact of point mutations and therefore their pathogenicity and clinical implications in patients (*3*, *6*–*7*). Whereas mutations causing AIS occur in the germ line, PCa-linked mutations are mostly somatic and occur before endocrine treatment or

[1]Structural Biology of Nuclear Receptors, Department of Biochemistry and Molecular Biomedicine, Faculty of Biology, University of Barcelona (UB), 08028 Barcelona, Spain. [2]Institute of Biomedicine of the University of Barcelona (IBUB), University of Barcelona (UB), 08028 Barcelona, Spain. [3]Programs of Molecular Mechanisms and Experimental Therapeutics in Oncology (ONCOBell) and Cancer Therapeutics Resistance (ProCURE), Catalan Institute of Oncology, Bellvitge Institute for Biomedical Research, 08908 Barcelona, Spain. [4]Cancer Research Center of Lyon, CNRS UMR5286, Inserm U1502, University of Lyon, 69000 Lyon, France. [5]Department of Materials Science and Physical Chemistry, Faculty of Chemistry and Institut de Recerca en Química Teorica i Computacional (IQTCUB), 08028 Barcelona, Spain. [6]Biomedical Research Institute Sant Pau (IIB Sant Pau), 08041 Barcelona, Spain. [7]Universidad Nacional Autónoma de México, Centro de Ciencias Genómicas, Cuernavaca, 61740 Morelos, Mexico. [8]Department of Structural and Molecular Biology, Molecular Biology Institute of Barcelona (IBMB-CSIC), 08028 Barcelona, Spain. [9]Computational Biology and Bioinformatics, Andalusian Center for Developmental Biology (CABD-CSIC), 41013 Sevilla, Spain. [10]Instituto de Ciencias de la Vid y del Vino (ICVV-CSIC), CSIC-UR-Gobierno de La Rioja, 26007 Logroño, Spain.
†These authors contributed equally to this work.
‡These authors contributed equally to this work.
*Corresponding author. Email: evaestebanez@ub.edu (E.E.-P.); fuentespriorpablo@gmail.com (P.F.-P.); aaytes@idibell.cat (A.A.)

Downloaded from https://www.science.org on April 26, 2023

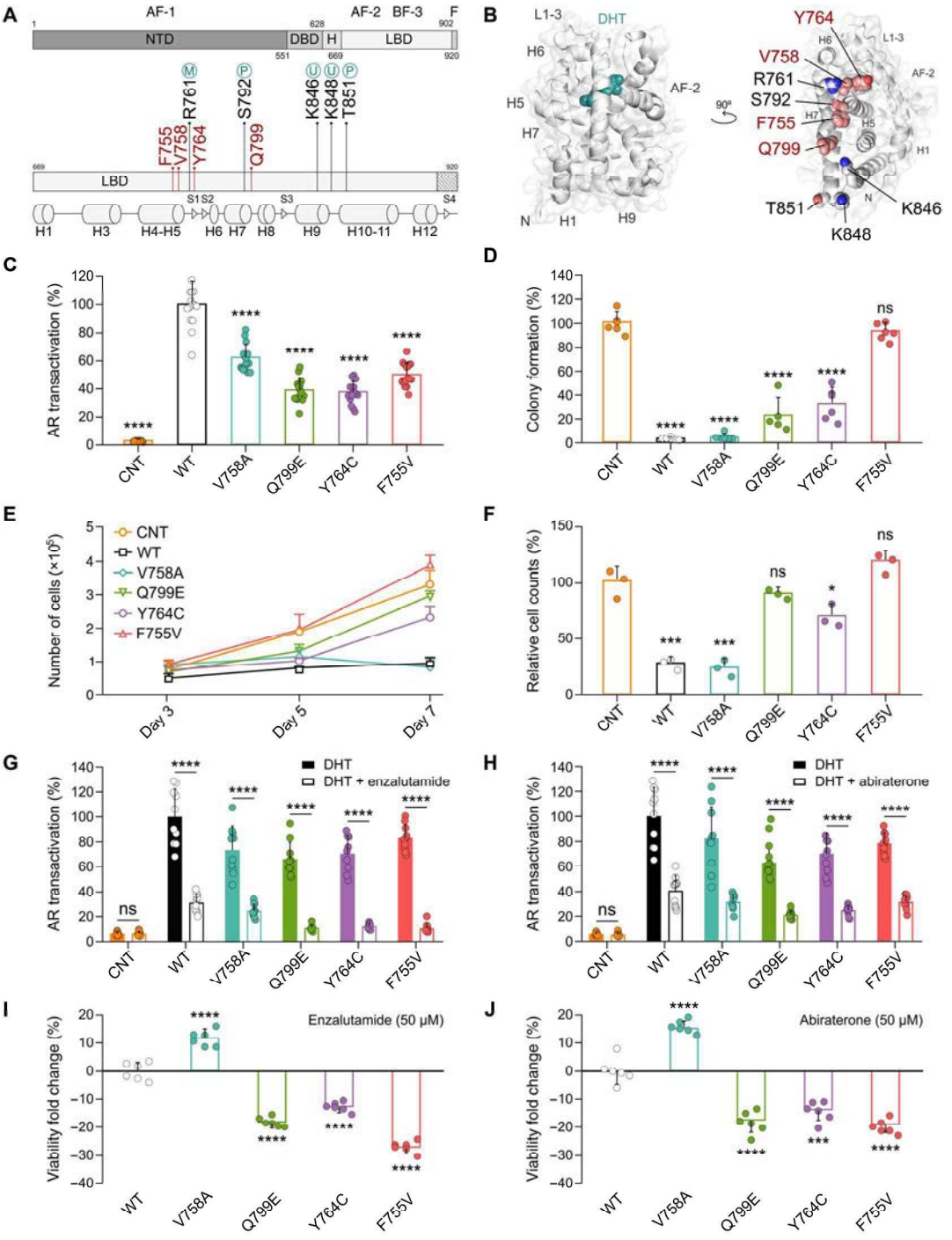

Fig. 1. Mutations at the AR-LBD dimer interface affect cellular phenotypes, transcriptional activity, and response to antiandrogens. (**A**) Cartoon of AR domain organization. Physiologically relevant interaction sites [top; activation function-1 (AF-1), AF-2 and binding function-3 (BF-3)], mutated AR-LBD residues (red; middle), and secondary structure elements [bottom; helices (H, cylinders) and β strands (S1 to S4, triangles)] are indicated. Neighboring residues of major PTM sites are shown [methylation (M), phosphorylation (P), and ubiquitination (U)]. (**B**) Three-dimensional structure of AR-LBD (gray). Note that disease-linked residues (red spheres) and PTM sites (gray spheres) highlighted in (A) form an extended path on the AR-LBD dimer interface. (**C**) Relative AR transcriptional activity in CNT, WT, and mutant AR-transduced PC3 cells (mean ± SD, $n = 3$). Differences against WT were calculated using a t test and considered significant at P values <0.1. (#$P < 0.1$ *$P < 0.05$, **$P < 0.01$, ***$P < 0.001$, and ****$P < 0.0001$). The same P value guidelines and asterisk significance will be used through this manuscript. (**D**) Clonogenicity assay quantification in transduced PC3 cells (mean ± SD, $n = 3$). Representative crystal violet–stained cultures are shown in fig. S1A. (**E**) Time course of transduced PC3 cells proliferation (mean ± SD, $n = 3$). Proliferation is completely suppressed with WT AR or V785A but no other mutants. (**F**) Relative cell counts at day 7 after transduction. (**G** and **H**) Effect of anti-androgens on the relative AR transcriptional activity of transduced PC3 cells (mean ± SD, $n = 5$). (**I** and **J**) Viability fold change in response to anti-androgens in transduced cells relative to the CNT cells (mean ± SD, $n = 3$). Differences against CNT (D and F) between anti-androgen treated and nontreated cells (G and H) or against WT (I and J) were calculated using t tests. ns, not significant.

are induced by the selective pressure of anti-androgen therapies (*2*–*3*). While few mutations in PCa have been described as oncogenic or drivers (causative of the disease), most are considered passenger or silent mutations, although a contribution to PCa development and/or progression cannot be excluded (*29*–*32*).

To date, only three point mutants of the AR-LBD have been structurally characterized out of the over 350 reported variants (table S1). These oncogenic mutations (W742L, H875Y, and T878A) map to the internal ligand-binding pocket (LBP) and are responsible for rendering the anti-androgens cyproterone acetate, flutamide, and bicalutamide ineffective, respectively. Comparison of the WT AR-LBD and these mutant structures did not reveal any overall conformational changes. However, these mutations change the volume and shape of the LBP allowing the receptor to

Downloaded from https://www.science.org on April 26, 2023

remain active even in the presence of antagonists, thus explaining tumor escape from therapeutic control (*2*, *26*–*28*). On the other hand, there are a wide variety of phenotypes associated with *AR* gene mutations in patient with AIS, ranging from mild symptoms (MAIS), to partial (PAIS) or completely feminized phenotypes (CAIS) (*23*–*25*, *33*–*34*). Expectedly, about half of the CAIS-linked mutations map to the AR-LBD, but only a few of them can be easily rationalized as directly affecting hormone binding (*3*, *29*).

AR-LBD pathogenic mutations outside the LBP may affect AR-dependent gene signatures through modulation of the monomer-oligomer equilibrium, accessibility of PTM sites, and/or by altering dynamic interactions with coregulators and chromatin. These processes are likely to be intricately intertwined and coupled via allosteric signaling transmission both within the AR monomer and across its dimerization interface (*3*–*7*). Here, we present a multidisciplinary investigation of the impact of several mutations of solvent-exposed AR-LBD residues identified in patients with PCa and/or AIS (Fig. 1A; see table S2 for major information on the studied mutations). Transcriptomic and in vitro cell–based assays demonstrate that these variants affect PCa proliferation and response to anti-androgens. Biochemical and biophysical investigations including high-resolution x-ray structures of mutant AR-LBD showed reduced thermal stability of the isolated domains as well as changes in the flexibility in functional sites of the receptor distal from the mutation site and unexpectedly revealed a previously unobserved rearrangement of the loop-featuring residue Arg^{761}. The structural reorganization of this loop increases the degree of Arg^{761} exposure, which correlated with an apparent increase in the extent of its methylation in cells. Together, our findings point to an intricate interplay between networks of local structural changes at and around the dimerization interface and global AR tertiary and quaternary structures that are coupled to PTM events. In turn, this network has a definite impact on AR transcriptional activity and gene programs that are affected by specific mutations. Our results may serve to predict the structural and functional impact of AR pathogenic mutations and open unexplored avenues for structure-guided modulation of its function in PCa tumors and patients with AIS.

RESULTS

We previously presented the crystal structure of the transcriptionally active, isolated dimeric AR-LBD (*6*) also corroborated in the multidomain protein (*4*, *7*). The structural analysis revealed that the dimerization interface is a hotspot for mutations identified in patients with PCa and/or AIS [see (*3*) and table S1]. There was no clear-cut separation between PCa- and AIS-linked mutations, and some of these variants were linked to both conditions, albeit occurring in different developmental stages. These observations prompted us to perform a thorough characterization of the structural changes and functional impact of AR point mutants at the dimerization interface (Fig. 1B).

Mutations at the AR-LBD dimer interface differently affect cell proliferation and response to anti-androgens

To assess the functional impact of point mutations that affect the AR-LBD dimer interface, we generated AR-null PC3 cell lines (CNT) stably expressing either WT AR or mutants $Phe^{755}Val$ (F755V) (*35*–*37*), $Val^{758}Ala$ (V758A) (*38*–*42*), $Tyr^{764}Cys$ (Y764C) (*36*, *39*, *42*–*48*), or $Gln^{799}Glu$ (Q799E) (*39*, *42*, *44*–*45*, *48*–*54*) (Fig. 1, A and B). As expected, WT expression resulted in a 24.5-fold increase in AR transactivation as measured by luciferase reporter expression under the control of a synthetic AR promoter. All four mutants displayed a significantly lower AR transactivation activity compared to WT (Fig. 1C). Further, expression of WT and V758A resulted in a nearly complete inhibition of colony formation (Fig. 1D and fig. S1A) and proliferation (Fig. 1, E and F) compared to CNT cells that were highly statistically significant. Dihydrotestosterone (DHT) treatment of AR-transduced DU145 (fig. S2, B to D) and of AR-sensitive lymph node carcinoma of the prostate (LNCaP) cells (fig. S2, E to G) resulted in comparable growth-suppressive effects that were not observed in AR-negative parental DU145 cells (fig. S2, B to D), in a castration-resistant PCa cell line, 22rv1 (fig. S2, H to J), or in AR-insensitive, nontumor human prostate epithelial cells,RWPE1 (fig. S2, K to M). These observations confirm previous reports on the growth-suppressive effect of AR stimulation in AR-responsive cells (*55*, *56*). In notable contrast, F755V and Q799E had proliferation rates not significantly different from those of the CNT cells, while proliferation was only modestly impaired by Y764C (Fig. 1, E and F). Similarly, colony forming capacity was unchanged for F755V and partially, albeit significantly, reduced in Glu^{799}- and Cys^{764}-expressing cells (Fig. 1D and fig. S1A).

Next, we asked whether the differences in proliferation and clonogenicity displayed by the AR variants would translate into distinct responses to anti-androgenic treatments. WT or mutant AR-expressing cells were treated with enzalutamide (Fig. 1, G and I), abiraterone (Fig. 1, H and J), or apalutamide (fig. S1B), and AR transactivation was measured. Transactivation was significantly inhibited by enzalutamide and abiraterone in both WT and mutant AR cells (Fig. 1, G and H). Reduction in AR transactivation was not a consequence of impaired cell viability upon anti-androgen treatment (Fig. 1, I and J, and fig. S1B). Specifically, V758A cells showed an 11.7, 20.6, and 16.1% increased viability compared to WT when treated with enzalutamide, apalutamide, or abiraterone, respectively. On the contrary, F755V, Y764C, and Q799E mutant cells displayed a significantly increased sensitivity to all three anti-androgens (Fig. 1, I and J, and fig. S1B).

Together, these results indicate that expression of ligand-bound WT AR in AR-null PCa cells induces a quiescent cell phenotype in AR-responsive cells without affecting the response to anti-androgen treatment. The data also demonstrate that, overall, point mutations at the AR dimerization surface negatively impact its ability to suppress proliferation and clonogenicity and mostly sensitize cells to anti-androgens (Fig. 1 and figs. S1, A and B, and S2).

Mutations at the AR-LBD dimer interface profoundly deregulate androgen-dependent transcription programs

Having demonstrated that dimerization surface mutations in the AR-LBD have an important impact on cellular functions, we next investigated whether these mutations alter gene expression patterns (Fig. 2 and fig. S1). Transcriptomic data were generated for WT and each mutant AR and compared to nontransduced cells as control. As expected, AR and canonical AR target genes such as *Transmembrane protease, serine 2* (*TMPRSS2*), *FK506-binding protein 5* (*FKBP5*), and *TCDD-inducible poly* [*ADP-ribose*] *polymerase* (*TIPARP*) were significantly up-regulated in both WT and mutant AR-expressing cells (Fig. 2A and fig. S1C), which was orthogonally

Downloaded from https://www.science.org on April 26, 2023

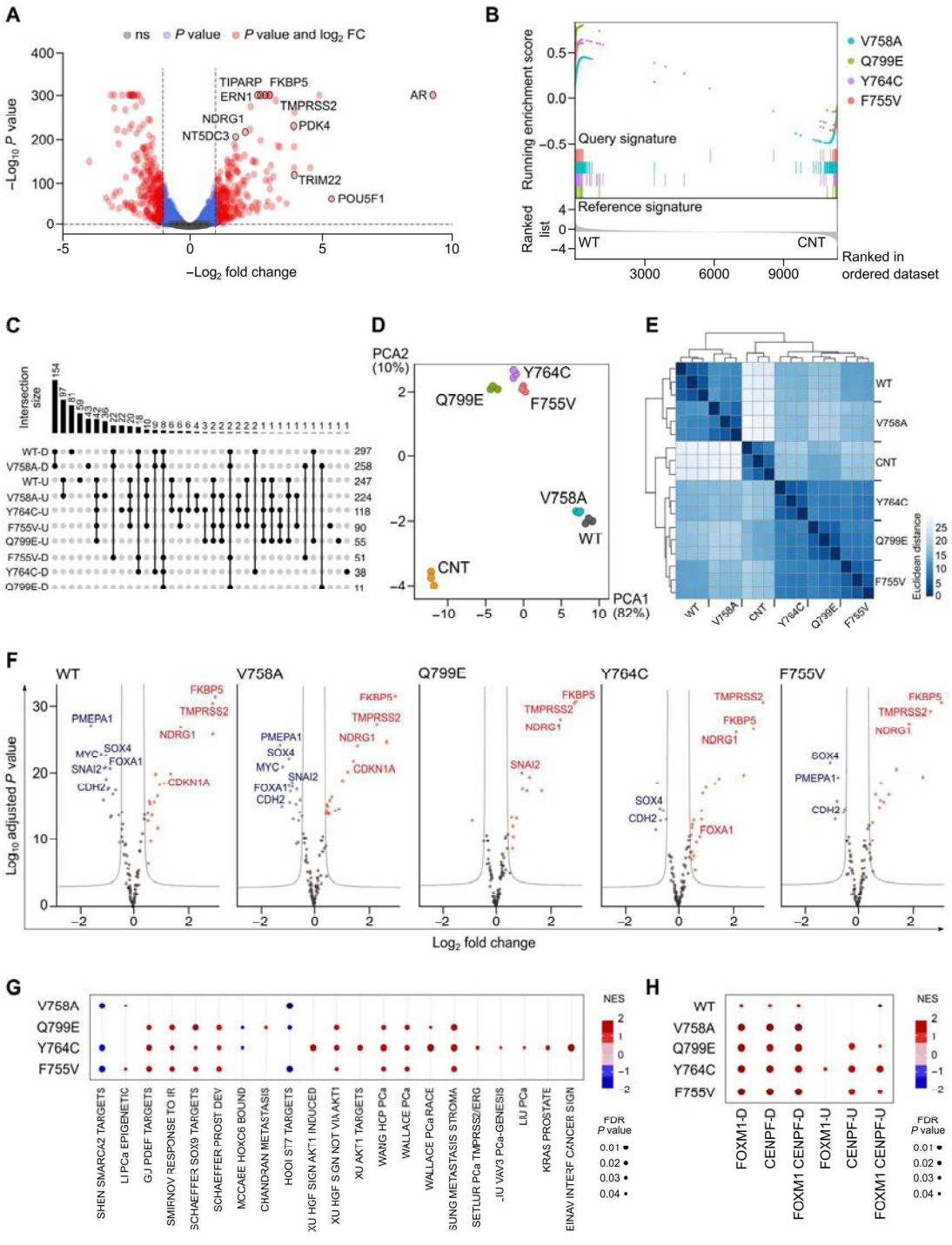

Fig. 2. The transcriptional profiles of AR-LBD dimerization surface mutants differ from that of the WT receptor. The results of RNA-seq experiments conducted in triplicate for each cell line are summarized. (**A**) Differential expression analysis between CNT and AR-transduced cells. Genes with $|\log_2(\text{fold change})| \geq 1$ and $P \leq 0.05$ are shown in red. (**B**) GSEA demonstrates similar signatures of WT and mutant AR. (**C**) Differentially expressed genes overlap between WT AR and its mutants. The bar plot (top) indicates the number of genes in the intersection between signatures. Vertical lines (bottom) connect the corresponding overlapping signatures. For each WT and mutant AR, signatures are separately given for up- (U) and down-regulated genes (D), and the size of the gene set is indicated (right). (**D** and **E**) Principal component analysis (PCA) and heatmap analysis of transcription profiles identifies three groups: (i) CNT, (ii) V785A and WT, and (iii) F755V, Y764C, and Q799E. (**F**) Volcano plots of AR target genes for WT and mutant AR. Canonical repressed (blue) and activated (red) AR targets are labeled. Note that repression of genes such as *MYC*, *SOX4*, *FOXA1*, and *CDH2* is lost in Q799E, Y764C, and F755V but not in V785A. (**G**) GSEA of the mutant AR signatures against WT AR on prostate cancer gene sets. Note that the V758A signature shows very limited overall enrichment indicating its strong similarity with WT. (**H**) GSEA of WT and mutant AR against a previously defined PCa malignancy signature (*58*). Enrichment for up- and down-regulated targets of the malignancy signature drivers *forkhead box protein M1* (*FOXM1*), *Centromere Protein F* (*CENPF*), or both are shown separately. Only the F755V, Y764C, and Q799E signatures are enriched in the *FOXM1* and/or *CENPF* regulons. Normalized enrichment score (NES) scale and false discovery rate (FDR) *P* value thresholds are indicated.

validated in quantitative polymerase chain reaction (qPCR) assays (fig. S1, G and H). In agreement with the functional evidence described above, the V758A mutant displayed AR target gene expression patterns most similar to WT AR (Fig. 2, C to E). Accordingly, gene set enrichment analysis (GSEA) showed that all four mutant AR signatures were similar to the WT signature (Fig. 2B). Although the AR regulon was conserved in all mutants, there were significant differences between the four variants. V758A showed a dynamic gene expression profile most similar to WT, while the differentially expressed gene (DEG) sets of F755V, Y764C, and Q799E were much smaller and shared fewer target genes compared to WT AR or V758A (Fig. 2C and fig. S1C). Variance assessment and clustering

Downloaded from https://www.science.org on April 26, 2023

of expression profiles further confirmed the similarity of WT and V758A transcriptomes, on the one hand, and those of F755V, Y764C, and Q799E, on the other. These two clusters were identified both by a principal components analysis (PCA) (Fig. 2D) and by clustering analysis computing sample-to-sample distances using variance-stabilizing transformation (VST) data (Fig. 2E). Further, gene expression in the AR regulon as defined by the DoRothEA collection of human regulons (*57*) showed that the set of activated AR target genes in WT and mutants remains largely conserved (Fig. 2F). However, only WT and V758A maintained a repressed gene set that included cancer drivers *Forkhead Box A1* (*FOXA1*) and *MYC proto-oncogen* (*MYC*) as well as epithelial-to-mesenchymal transition drivers *Snail Family Transcriptional Repressor 2* (*SNAI2*/*SLUG*), *Cadherin-2* (*CDH2*, encoding N-cadherin), and *SRY-Box Transcription Factor 4* (*SOX4*) (Fig. 2F and fig. S1I). This is consistent with the important reduction in proliferation and clonogenicity described above (Fig. 1, D to F, and fig. S1A). GSEA analysis of the four AR mutants versus WT signatures evidenced again that V758A was not enriched in any of the PCa signatures in the Molecular Signature Database (MSigDB), as opposed to the significant enrichment demonstrated for F755V, Y764C, and Q799E (Fig. 2G). Accordingly, only these three mutant signatures were found positively enriched in a previously defined up-regulated gene signature strongly associated with poorer outcome in patients with PCa (Fig. 2H) (*58*).

Last, querying the collection of manually drawn Kyoto Encyclopedia of Genes and Genomes (KEGG) database evidenced an unexpected enrichment for the Y764C mutant in biological pathways associated with pathogen infection and immune response including coronavirus disease 2019 (fig. S1D), which was supported by the significant regulon enrichment in the mediator of type I interferon signaling, *STAT2* (fig. S1E), and the activation of the *Janus kinase/signal transducers and activators of transcription* (*JAK/STAT*) pathway (fig. S1F) using the DoRothEA and the Pathway RespOnsive GENes (PROGENy) algorithms, respectively. Together, these data suggest that the observed differences in cellular phenotype between the different AR mutants are at least in part the result of a differentially reprogramed transcriptome in which WT and V758A show a less oncogenic and undifferentiated molecular phenotype compared to F755V, Y764C, and Q799E mutants.

AR-LBD interface residue mutations do not compromise domain folding but lead to reduced thermal stability and increased sensitivity to proteolysis

To study the possible structural impact of point mutants located at the AR-LBD dimerization interface, we produced and purified to homogeneity WT AR-LBD and its point mutants F755L, F755V, V758A, Y764C, and Q799E. Next, we characterized these recombinant proteins both biophysically using differential scanning fluorimetry (DSF) and biochemically through limited proteolysis assays (figs. S3 and S4). The results of these experiments demonstrated that all mutants are properly folded but have substantially lower thermal stability compared to the WT protein, as indicated by the reduced melting temperatures (T_m) (fig. S3, A and B). In line with the RNA sequencing (RNA-seq) results presented above, core dimer interface mutants F755V, F755L, and Y764C exhibited a remarkable drop in T_m compared to the WT protein (between 5° and 6°C), the latter being the most thermolabile of all the studied variants. By contrast, the T_m of mutants V758A and Q799E was only 1°C lower than the WT AR-LBD protein, demonstrating WT-like stability (fig. S3, A and B). Energy estimations using FoldX based on previously reported structures of monomeric and dimeric AR-LBD also suggested that the studied missense mutations have an important impact on the domain stability (fig. S3C), both in its monomeric and putative dimeric conformations. Mutations of the core interface, F755V/L and Y764C, are predicted to be particularly deleterious for homodimeric AR-LBD (fig. S3C).

AR-LBD is a highly basic protein domain (isoelectric point: 8.94) with 14 arginines (fig. S4A) and 14 lysines outbalancing 11 negatively charged aspartate or glutamate residues. To assess whether the decrease in thermal stability of AR-LBD point mutants also manifests as an increased sensitivity to proteolysis, we incubated highly purified samples of WT AR-LBD and its point mutants with the endoproteinase, Arg-C, which cleaves peptide bonds at the C-terminus of Arg residues (fig. S4, B to E).

Again, the resulting cleavage pattern of V758A is most similar to that of WT AR-LBD (fig. S4, B, C, E, and F). Although the thermal stabilities of the two mutants are similar (fig. S3, A and B), the proteolytic patterns of V758A and Q799E differ notably (fig. S4, C to F and H). Mutants F755L (fig. S4, B, E, and G), F755V (fig. S4, C, E, and I), and Y764C (fig. S4, D, E, and H) have enhanced proteolytic susceptibility. In summary, point mutations of residues at the AR-LBD homodimerization interface appear to have an unanticipated global impact on the overall domain stability, as evidenced by notably lower T_m and enhanced sensitivity to proteolytic attack (figs. S3 and S4).

AR-LBD dimer interface mutants exhibit enhanced flexibility and distinct structural rearrangements both locally and at distant AF-2 and BF-3 sites

The results of the experiments described above demonstrate a large impact of AR-LBD dimer interface mutants on AR transcriptional function, stability, and sensitivity to proteolytic attack. To assess whether these differences are reflected by noticeable structural rearrangements, we expressed crystallized and refined at high resolution the x-ray crystal structures of the V758A, Y764C, F755V, F755L, and Q799E AR-LBD variants (Figs. 3 and 4). All mutant proteins crystallized as monomers in the orthorhombic space group ($P2_12_12_1$) (Figs. 3A and 4A and fig. S3D; see fig. S3E and Fig. 4B for comparison; Table 1). The "helical sandwich" fold typical of the nuclear receptor superfamily is conserved (*3*), and the hormone (DHT) is bound inside the LBP essentially as in WT AR-LBD (Figs. 3A and 4A). The root mean square deviations (RMSDs) for the equivalent Cα atoms between the WT structure [Protein Data Bank (PDB) 1T7T] and the V758A, Y764C, F755V, Q799E, and F755L mutants are 0.29, 0.33, 0.47, 0.52, and 0.54 Å, respectively.

Despite this overall conservation of the global protein fold, superimposition of the current mutant structures on previously solved structures of WT AR-LBD reveals important local structural changes on four specific distant sites of the domain (see Fig. 3A for an overall representation of the domain with these sites highlighted and Fig. 3, B to E for close-ups of these areas): the H5-S1-H7 area (from now on termed "R761 zone," described in detail below) (Fig. 3B), the L1-3 loop, H6, and the C-t end of H11 (Fig. 3C), two major functional sites, the BF-3 pocket comprising H9 and L9-10 (Fig. 3D), and the AF-2 pocket featuring the L3-4 loop and H12 (chaperone and coactivator binding sites, respectively) (Fig. 3E). In particular, several side chains of charged AF-2 residues

Downloaded from https://www.science.org on April 26, 2023

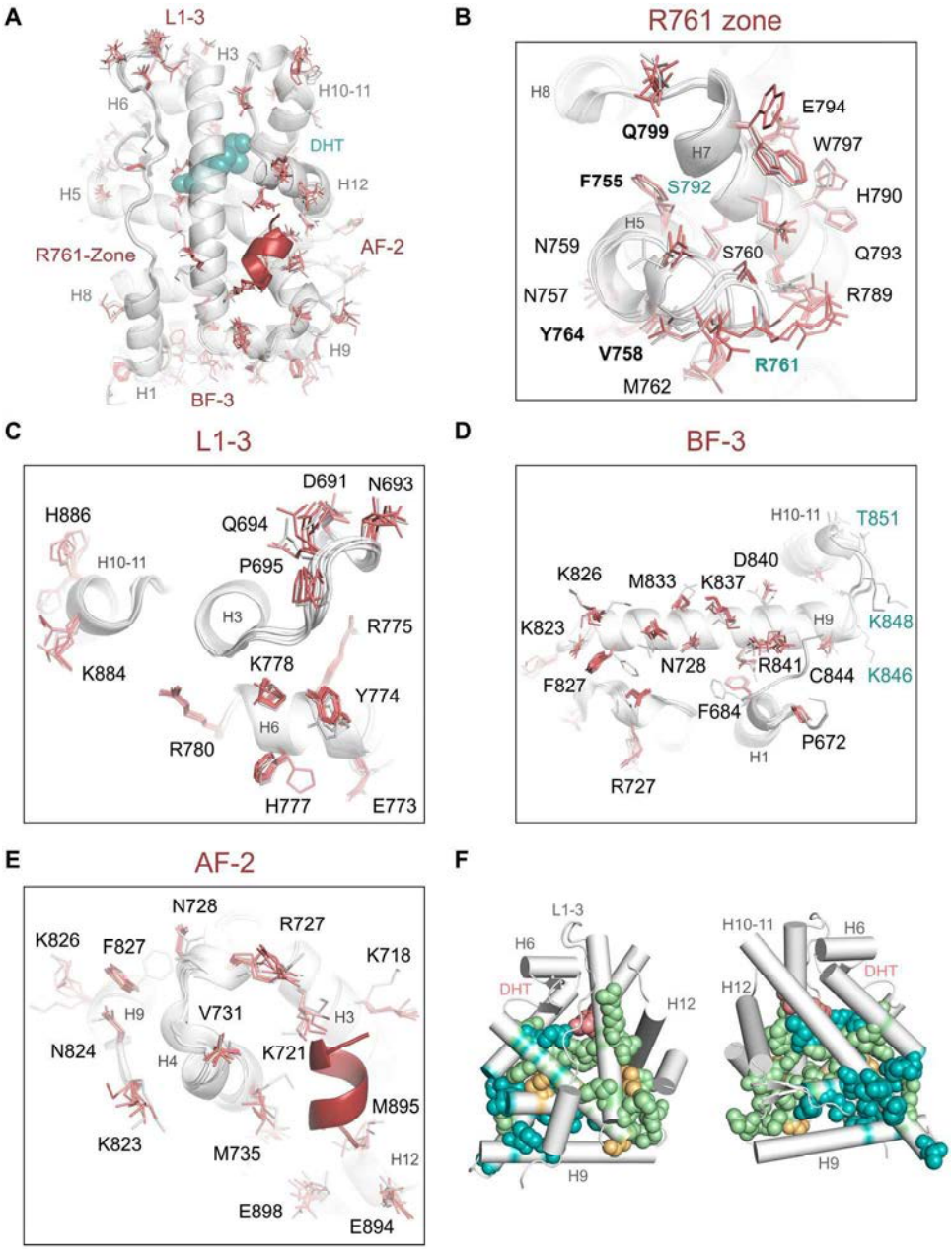

Fig. 3. High-resolution crystal structures of AR-LBD dimer interface mutants reveal local and long-range conformational changes. (**A**) Superimposition of current crystal structures of mutant AR-LBD on WT monomeric (1T7T) and dimeric (5JJM) forms of the domain. Secondary structure elements identical in all structures are depicted as a gray cartoon, with DHT as teal spheres and the AF-2–bound peptide (from 5JJM) in red. Large main- and/or side chain conformational changes cluster in four areas (B to E), highlighted by the major secondary structure elements (coral sticks). (**B**) Dimer interface core lined by H5 and H7, which, in addition to the studied point mutations [Phe^{755} and Val^{758} (H5), Tyr^{764} (S1), and Gln^{799} (H7)] features mostly residues with nonpolar/aromatic side chains, along with the positively charged Arg^{761}. (**C**) The more distal part of the dimer interface formed by H3 and L1-3 [Tyr^{774} and His^{777} from (B) are shown for orientation]. In this area, several polar residues exhibit noticeable conformational changes. (**D**) BF-3 pocket, where multiple residues exhibit conformational changes, most notably those from H9. (**E**) AF-2 pocket, where in addition to the charge-clamp residues, Lys^{721} and Glu^{894}, known to stabilize bound coregulators at this interaction site, the side chains of both charged (Lys^{718}, Arg^{727}, Lys^{823}, and Glu^{898}) and aliphatic residues (Met^{735} and Met^{895}) display conformational variability. (**F**) Sector 1 (teal) comprises 17 residues in and around H5, H7, H8, H9, and H10-11 (Met^{743}, Phe^{748}, Gly^{751}, Arg^{753}, Leu^{798}, Ile^{800}, Thr^{801}, Met^{808}, Leu^{811}, Phe^{814}, Glu^{838}, Ile^{842}, Thr^{851}, Tyr^{858}, Thre^{861}, Lys^{862}, and Leu^{864}), whereas sector 2 (green) features 20 residues mostly from H3, H5, H7, H8, S3, and H10-11 (Arg^{711}, Leu^{713}, Trp^{719}, Ala^{720}, Lys^{721}, Phe^{726}, Leu^{729}, Gln^{734}, Tyr^{739}, Trp^{742}, Gly^{744}, Met^{746}, Ala^{749}, Trp^{752}, Ser^{754}, Leu^{791}, Lys^{809}, Leu^{813}, Asp^{820}, and Arg^{856}). Last, three residues (Gly^{725} and Ile^{738} at the AF-2 groove and Phe^{805} at H7) belong to both sectors (yellow).

Downloaded from https://www.science.org on April 26, 2023

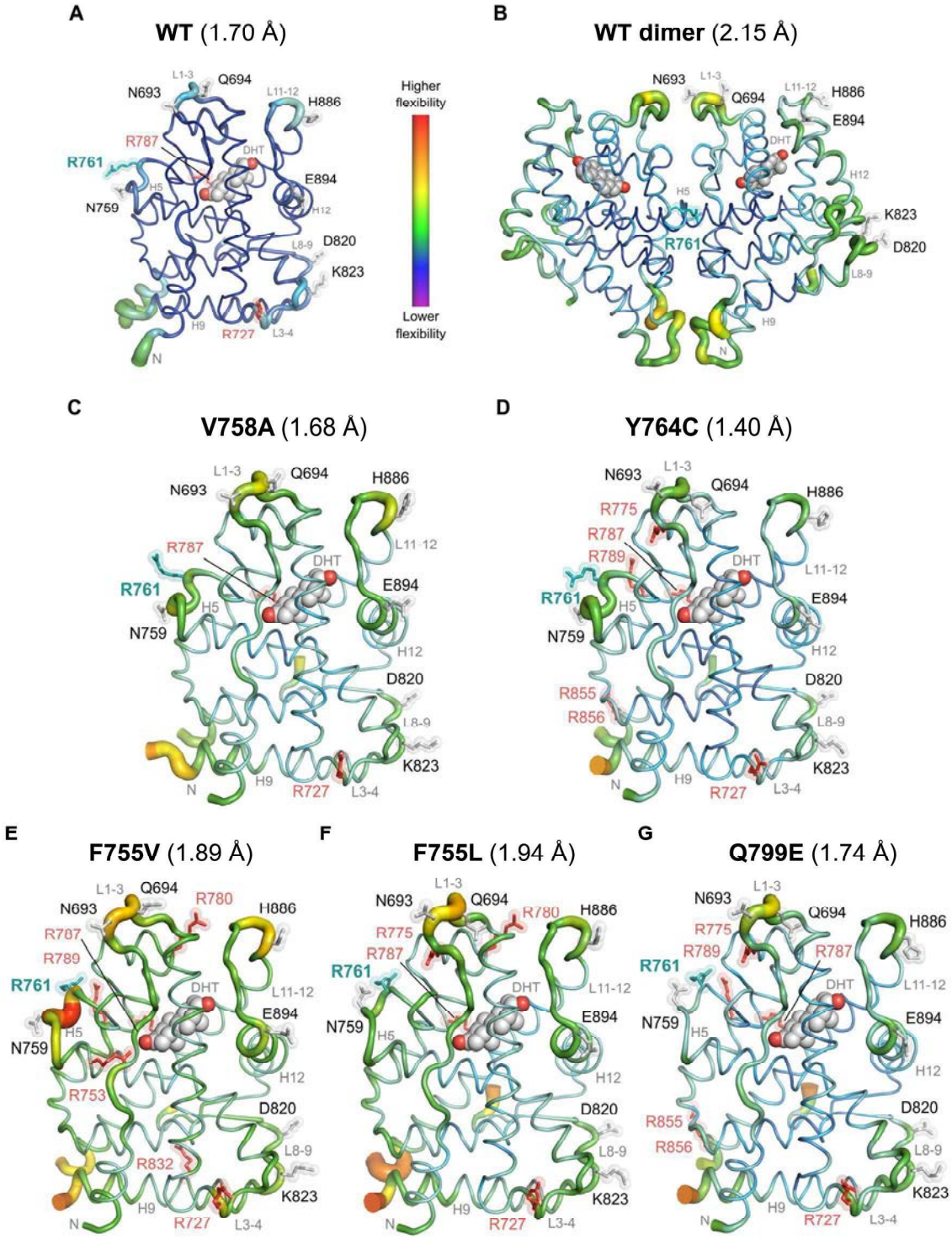

Fig. 4. AR-LBD dimer interface mutants display local flexibility differences. (**A** to **G**) Visualization of protein mobility for WT and AR-LBD mutant proteins. Proteins are represented as ribbons sized by temperature factors (B-factors) and colored according to the average B-factors of each residue (i.e., areas with larger atomic displacements appear thicker and are depicted with warmer colors (red, orange, and yellow), whereas those with lower thermal motion are shown thinner and with cold colors (green, blue, and violet). DHT molecules bound inside the LBP pockets are shown as gray spheres with oxygen atoms in red. WT AR-LBD·DHT monomer (A, PDB 1T7T) and dimer (B, PDB 5JJM) are shown for comparison. Note that all mutants exhibit a larger mobility than WT AR-LBD.

Downloaded from https://www.science.org on April 26, 2023

Table 1. X-ray crystallography data collection, refinement statistics, and model quality.

	V758A	Y764C	F755V	F755L	Q799E
PDB code	**7ZU1**	**7ZTZ**	**7ZTX**	**7ZTV**	**7ZU2**
Wavelength (Å)	0.979	0.979	0.979	0.979	0.979
Resolution range	66.17–1.68 (1.71–1.68)	65.84–1.40 (1.42–1.40)	65.82–1.89 (1.93–1.89)	56.2–1.94 (1.99–1.94)	44.55–1.74 (1.77–1.74)
Space group	$P2_12_12_1$	$P2_12_12_1$	$P2_12_12_1$	$P2_12_12_1$	$P2_12_12_1$
Cell constants a, b, c (Å) / α, β, γ (°)	55.62, 66.17, 70.95 / 90, 90, 90	56.39, 65.84, 72.82 / 90, 90, 90	54.57, 65.82, 70.37 / 90, 90, 90	56.18, 65.80, 72.31 / 90, 90, 90	56.51, 66.04, 72.42 / 90, 90, 90
Molecules in the ASU	1	1	1	1	1
Total reflections	176567 (4168)	247697 (9727)	143549 (9454)	84880 (3942)	147708 (8184)
Unique reflections	29533 (1229)	53810 (2576)	20910 (1309)	18026 (1027)	28510 (1559)
Multiplicity	6.0 (3.4)	4.6 (3.8)	6.9 (7.2)	4.7 (3.8)	5.2 (5.2)
Completeness (%)	96.6 (80.4)	99.6 (98.2)	99.9 (100.0)	88.1 (79.8)	100.0 (100.0)
Mean I/sigma(I)	10.3 (0.7)	18.8 (0.5)	8.8 (0.7)	10.4 (2.8)	12.3 (1.5)
Wilson B-factor	27.1	27.0	38.2	22.8	26.1
R-meas	0.084 (2.026)	0.030 (1.692)	0.116 (3.399)	0.093 (0.720)	0.089 (2.398)
R-pim	0.033 (1.015)	0.014 (0.841)	0.045 (1.257)	0.042 (0.363)	0.039 (1.042)
CC1/2	0.998 (0.364)	1.000 (0.395)	0.998 (0.364)	0.989 (0.854)	0.999 (0.337)
Reflections used in refinement	28174	51127	19842	17086	27029
Reflections used for R-free	1235 (4.2)	2619 (4.9)	1020 (4.9)	888 (4.9)	1433 (5.0)
R-work	0.21	0.19	0.20	0.22	0.18
R-free	0.25	0.22	0.25	0.26	0.22
Total number of atoms / Protein / DHT ligand / Water	2135 / 2008 / 21 / 81	2161 / 2010 / 21 / 120	2041 / 1973 / 21 / 32	2066 / 1997 / 21 / 44	2080 / 1985 / 21 / 64
RMS (bonds)	0.007	0.011	0.008	0.007	0.009
RMS (angles)	1.420	1.828	1.606	1.500	1.581
Ramachandran favored (%)	98.76	98.74	98.32	98.33	99.16
Ramachandran allowed (%)	1.24	1.26	1.26	1.25	0.84
Clashscore	5.32	1.23	3.47	2.47	3.7
Average B-factor / Protein (main, side chains) / DHT ligand / Water	40.4 / 40.0 (36.9, 42.8) / 29.1 / 44.4	35.6 / 35.1 (32.0, 38.1) / 25.4 / 42.8	48.2 / 48.1 (44.2, 51.9) / 34.3 / 47.3	37.5 / 37.6 (34.3, 40.8) / 25.3 / 36.3	37.3 / 37.2 (33.3, 40.9) / 26.0 / 41.9

exhibit conformational differences, most notably the so-called charge-clamp residues, Lys^{721} and Glu^{894}, which are known to stabilize bound coregulators at this protein-protein interaction site (Fig. 3E). Regarding the BF-3 pocket, and in addition to charged/polar residues such as Arg^{841} and Thr^{851}, also the aromatic Phe^{827} exhibits a large flexibility (Fig. 3D). Noteworthy, Phe^{827} and Arg^{841} undergo major conformational changes upon small-molecule binding to this surface-exposed pocket (*63*). Loop L1-3 also exhibits side-chain conformational differences in several residues (Tyr^{774}, His^{777}, and Lys^{778}), which we had previously identified as part of a secondary dimer interface in AR-LBD crystals to generate a tetrameric arrangement of the receptor (Fig. 3C) (*6*).

These structural variations are also reflected by an overall enhanced flexibility of all mutants compared to WT AR-LBD [average temperature factor (B-factor) of 21.2 for the monomeric AR-LBD; PDB 1T7T], as demonstrated by the higher B-factors of both main and side chain atoms in all variable regions (Fig. 4). Residues with particularly higher B-factors in the mutants are Asn^{693} and Gln^{694} (L1-3), Arg^{727} (L4-5), Asn^{759}, and Arg^{761}, a residue strictly conserved in AR from fish to humans, but not found in other steroidal receptors (H5 and loop H5-S1; fig. S3, F and G), Asp^{820} and Lys^{823} (L9-10), His^{886} (H6), and Glu^{894} (H12) (Fig. 4). Overall, mutants V758A and Y764C are most similar to the WT protein in this regard, while Q799E, F755L, and F755V exhibit increased flexibility in H5, L1-3, and L9-10 (Fig. 4, A to G).

Our previous statistical coupling analysis (SCA) (*64*) revealed that two groups of correlated residues or "sectors" define the internal circuits linking major interaction sites in the LBD of the related glucocorticoid receptor (GR). To analyze whether the AR-LBD dimerization surface is allosterically coupled to other functional regions, we also performed SCA analysis, which identified 40 residues grouped in two sectors in the upper half of the domain (Fig. 3, F and G). Sector 1 residues cluster around the domain N-terminus (except the DHT ligand, Arg^{752}), while sector 2 comprises LBP and

Downloaded from https://www.science.org on April 26, 2023

AF-2 residues. Further, three residues common to both sectors are strategically located to cross-connect the LBP, AF-2, and BF-3 and dimerization interface (Fig. 3, F and G). Together, our results suggest that both sectors link functionally relevant regions thus coupling, e.g., ligand binding to dimerization, coregulator binding, or chaperone docking/release.

To further explore the LBD dynamics and possible allosteric couplings between AR-LBD functional areas, we performed four 1-μs-long molecular dynamics (MD) simulations for both WT AR-LBD and all the mutants (Fig. 5). The analysis of the time evolution of the RMSD for all the Cα atoms using the experimental structure of WT AR-LBD as reference confirms that the overall fold of the domain is stable against these point mutations, and all structures show global structural stability. Moreover, global conformations do not vary remarkably for any of the mutants, and their final RMSDs oscillate at around 2 Å (Fig. 5A). To evaluate the flexibility of the mutants in more detail, we analyzed how a given residue fluctuates around a specific position with time. To this end, we quantified the fluctuations for all residues using the averaged root mean square fluctuation (RMSF) value, averaged for the four MD replicas (Fig. 5B). As expected, more flexible regions correspond to those with higher B-factors in the current structures (compare Figs. 4 and 5). To analyze how specific mutations affect the dynamics of the different regions, we calculate the RMSF differences between WT AR and the studied variants (Fig. 5B). The stretch Lys^{884}-Val^{888} (H10-H11) presents, for all the mutants, a markedly decreased flexibility compared to WT (Figs. 5B and 3C). On the other hand, the L1-3 loop (residues Cys^{687}-Asn^{693}) is notably more flexible in the V758A and F755L mutants. This behavior is also observed in the Q799E mutant, although less pronounced, but neither in Y764C nor in F755V mutants. These two regions are located far from the mutated residues, suggesting that mutations in the AR-LBD dimerization site induce conformational changes in the AF-2 pocket and thus that dimerization and coregulator binding are allosterically coupled.

Next, and to complement the dynamic description of the impact of the different mutations, we quantified local conformational changes by calculating the differences in the average Cα-Cα distances between spatially neighboring residue pairs [extended up to the second coordination shell (SCS); ~9.1 Å]. The results of these $\Delta\overline{R}_{ij}$ analyses are presented in Fig. 5C. Overall, all mutant structures tend to have larger inter-residue distances compared to the WT protein, and some specific groups of residues show remarkable changes in their average pair distances. This is particularly true for residues Lys^{884}-His^{886} and Val^{888}-Phe^{892} at the C-terminal end of H10-H11 and the L11-12 loop (box A in Fig. 5C). In line with the experimental findings, the R761 zone shows important changes in all the mutants (residues Asn^{759} to Tyr^{764}, L5-S1 loop). This region presents two different groups of moving residues, consisting of the stretch from Arg^{789} to Phe^{795} (H7) and Ser^{754}-Val^{758} of H4-H5 (boxes B1 and B2 in Fig. 5C, respectively). Furthermore, in all mutants, changes in average distances of residues Leu^{729}-Asp^{733} (L3-4 loop and N-terminal end of H4-H5) and Gly^{821}-Asn^{824} (S3-9 loop) are coupled (box C in Fig. 5C). However, in this case, changes are negative for mutations Q779E and F755V, both negative and positive for Y764C and V758A mutants, or positive for F755L. Last, residues Cys^{687} to Gln^{694} (L1-3) behave differently in each mutant. For F755L, this region shows negative changes in their average distances to residues Ala^{688}-Arg^{711} (L1-3 and H3) and the Phe^{765}-Leu^{769} stretch (boxes D1 and D2 in Fig. 5C, respectively). Mutant V758A presents fewer changes in the average distances in the same regions, some of which are positive in the first one (box D1 in Fig. 5C). For the Y764C mutant, the first group of distances becomes completely positive, while the second one practically disappears. No noticeable changes were detected for mutants F755V and Q799E. In summary, residue pair distance analysis shows that the different interface mutations induce local conformational changes in AR-LBD. These changes are located far from the mutated residues in line with an allosteric mechanism. Moreover, although some changes are common to all the mutations, markedly different local responses were observed in specific AR regions.

The noncanonical AR-LBD dimerization mode is conserved upon single point mutations of dimer interface residues

Because the studied AR mutations are located at the noncanonical dimerization interface, we next wondered whether they might impair homodimer formation (Fig. 6). We had previously shown that AR-LBD dimerization in solution could be demonstrated with the homo-bifunctional cross-linker, bis(maleimido)ethane (BMOE), which cross-links residue Cys^{687} from two monomers (*6*). To verify whether mutant proteins are able to dimerize as WT AR-LBD, we incubated purified samples of the recombinant proteins with either BMOE (spacer arm length: 8.0 Å) or a similar cross-linker with a slightly larger spacer arm, 1,4-bis(maleimido)-butane (BMB; 10.9 Å) and separated the reaction products by SDS–polyacrylamide gel electrophoresis (SDS-PAGE). The results of these experiments revealed similar patterns of AR-LBD homodimer formation in all cases, indicating that receptor homodimerization is not compromised by point mutations of interface residues (Fig. 6A).

Further, and to assess the possible impact of the studied mutants on the dimerization potential of AR-LBD mutants, we performed docking calculations using normalized interface propensity (NIP) (*65*) and optimal docking area (ODA) (*66*) (fig. S5). The computed binding energy of dimeric WT AR-LBD (PDB 5JJM; Fig. 4B; chains B and C, removing residues 845 to 851; Fig. 4B) was similar to that of V758A and Y764C mutants (assuming the same orientation as WT) and more favorable than that of the other mutants. Actually, the electrostatic energy contribution was much larger for WT than for any mutant, while the desolvation energy showed the opposite trend (fig. S5A). The size of the dimer interface as estimated from the buried surface area (BSA) was larger for WT than for the mutants, being V758A the one closest to WT (fig. S5A).

We also built alternative dimer arrangements by docking, based on WT (PDB 5JJM, chain B without residues 845 to 851) and current mutant monomeric structures (fig. S5B). The top ranked model in WT docking matched the x-ray dimer orientation (5.6 Å RMSD), with slightly better binding energy (fig. S5B). For all mutants, we also obtained similar orientations to the experimental dimer (RMSD < 10 Å), although not as the lowest-ranking models (fig. S5B). Binding energies for V758A and Y764C docking dimers were similar to those obtained by superimposition on the x-ray dimer, while in the rest of the mutants, the binding energy of the docking dimer was more favorable (although showing slightly higher RMSD). NIP-based interface hotspot residues predicted from docking (red residues in fig. S5C) were located at the x-ray dimer interface in WT and all mutants (except in F755V, which shows an additional NIP region around Asp^{829}, Arg^{832}, and

Downloaded from https://www.science.org on April 26, 2023

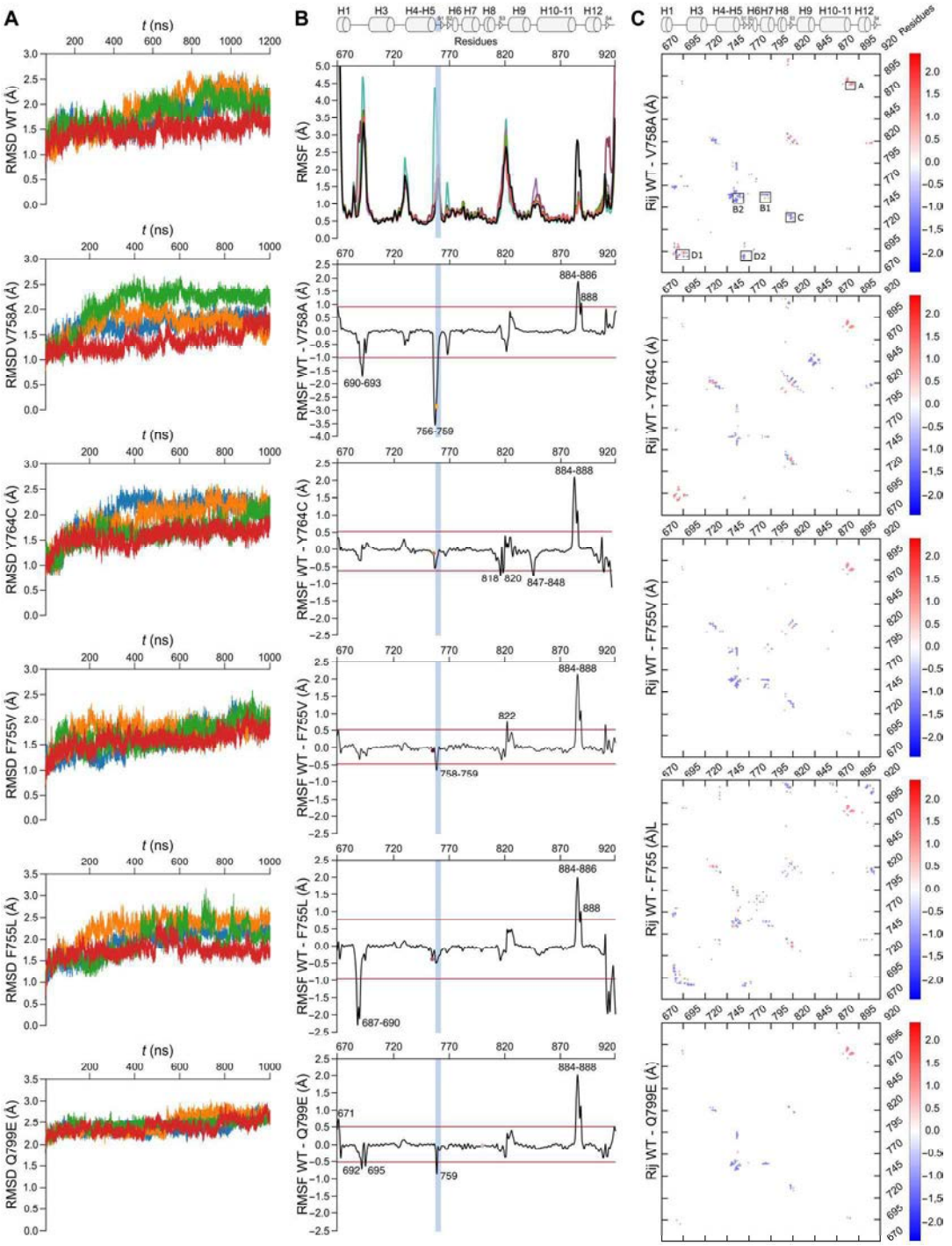

Fig. 5. Molecular dynamics study of the WT and mutant AR-LBD structures demonstrate overall domain stability coupled with local changes in flexibility. (**A**) Evolution of the RMSD for WT AR-LBD and the studied mutants along four independent MD runs. All structures converge demonstrating global structural stability. (**B**) Averaged RMSF of the four MD runs calculated for each structure: WT AR-LBD (black), V758A (blue), Y764C (purple), Q799E (green), F755L (violet), and F755V (red) (top plot). The remaining plots show the differences between the WT and mutant RMSF values. Residues with RMSF values higher than +2σ or lower than −2σ (indicating decreased or increased flexibility compared to WT, respectively) are labeled. Only changes with values greater than twice their SDs were considered significant (red lines). Major changes in flexibility around the mutation site were detected only for the V758A mutant. Mutant F755V only shows a small change in this region, while Q799E does not present any changes near the mutated residue but around Asn^{759} instead, in line with the experimental structure. Note that flexibility in the L5-S1 loop is remarkably higher in V758A, F755V, and Q799E compared to WT (blue). On the contrary, the C-terminal end of H10-11 shows lower relative flexibility in all the mutants. (**C**) Plots of the differences in average pairwise distances ($\Delta\overline{R}_{ij}$), with $\Delta\overline{R}_{ij} = \overline{R}_{ij,WT} - \overline{R}_{ij,mut}$, being $\overline{R}_{ij,WT}$ and $\overline{R}_{ij,mut}$ the average distances between Cα atoms of residues *i* and *j* along the MD trajectories of the WT and mutated structures, respectively. Red and blue represent positive and negative $\Delta\overline{R}_{ij}$ values, corresponding to residue pairs whose average distances decrease or increase due to the mutation, respectively. Only residue pairs with $\Delta\overline{R}_{ij} > 2.50$ or < -1.40, which represent the most significant distance changes, are shown.

Ile^{836}), with residue at position 755 appearing among the highest NIP values in all cases but in F755V. Desolvation areas predicted by ODA surface analysis were mostly located at the x-ray dimer interface in WT and all mutants (fig. S5D), indicating that a large part of the expected dimeric interface has favorable desolvation energy, especially the region around residue position 755. In general, predicted dimer interfaces from docking experiments and ODA are consistent with the x-ray dimer orientation (*6*).

Downloaded from https://www.science.org on April 26, 2023

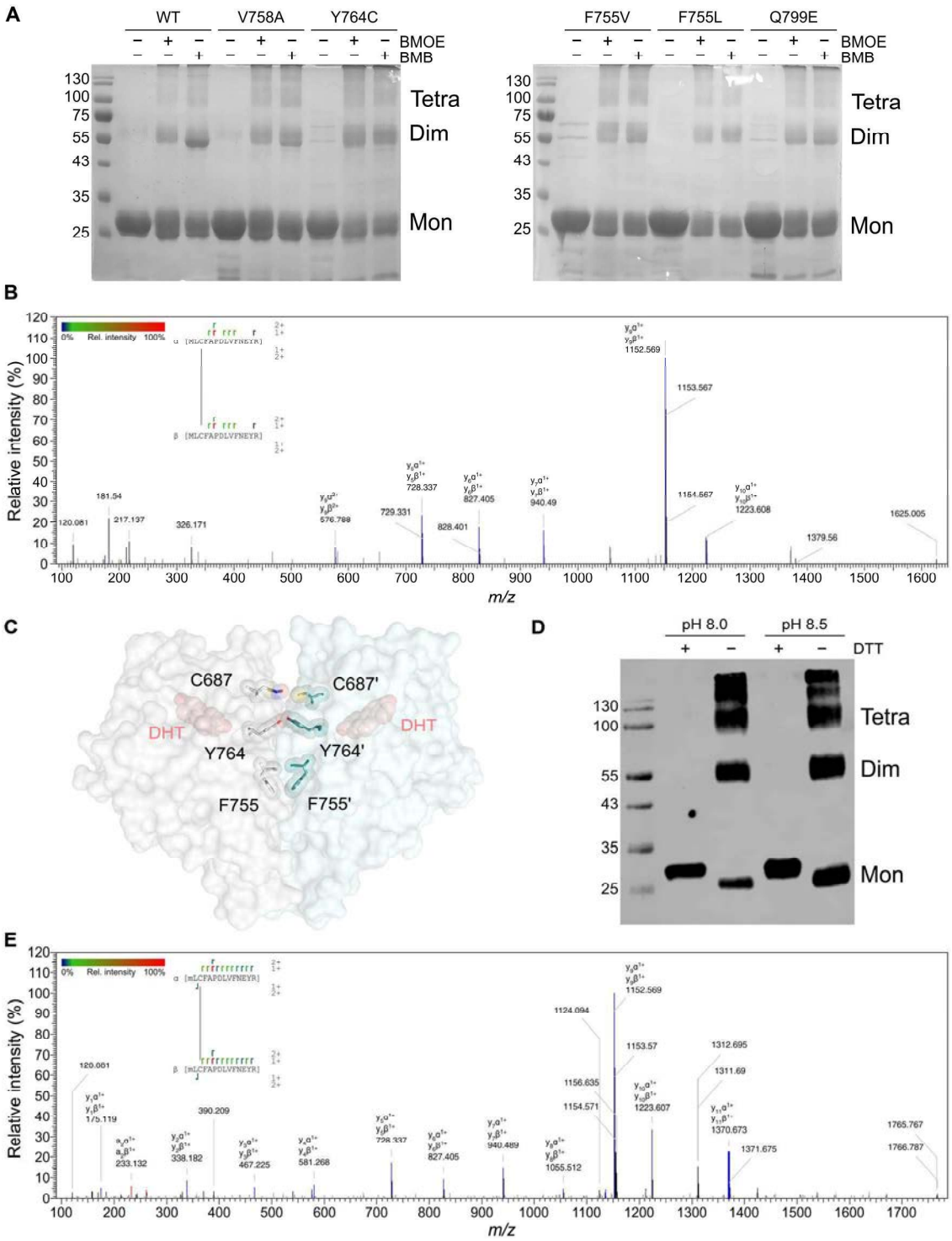

Fig. 6. Point mutations at the AR-LBD dimer interface do not impair homodimer formation, which is even enhanced in the Tyr^{764}Cys mutant. (**A**) SDS-PAGE analysis of WT and mutant AR-LBD samples treated with the bifunctional cross-linkers, BMOE or BMB. Note similar intensities of bands corresponding to dimeric AR-LBD in all cases, indicating that homodimer formation is not compromised by any of the studied point mutants. (**B**) Representative MS/MS spectra identifying BMB-cross-linked tryptic peptides between Cys^{764} residues from two LBD monomers. (**C**) Three-dimensional structure of the AR-LBD dimer (PDB 5JJM) in surface representation. Selected interface residues of both monomers [Cys^{687}, Tyr^{764}, and Phe^{755} (as reference)] are shown as sticks. The DHT molecule is depicted as salmon spheres. (**D**) SDS-PAGE analysis of AR-LBD(Y764C) behavior under reducing (lanes 2 and 4, +DTT) and nonreducing conditions (lanes 3 and 5, −DTT). Note the spontaneous dimerization in solution when the protein is incubated under nonreducing conditions. (**E**) Representative MS/MS spectra demonstrating formation of a disulfide bridge between mutant Cys^{764} residues from two LBD monomers. *m/z* stands for mass/charge ratio.

Downloaded from https://www.science.org on April 26, 2023

The recurrent point mutation Y764C highlights the ability of AR-LBD dimer interface to adopt different relative orientations in AR homodimers

AR variant Tyr^{764}Cys was first identified in a PAIS family and has since been repeatedly reported in AIS and PCa individuals worldwide (*36*, *39*, *42*–*48*). Because this recurrent mutation introduces a solvent-exposed cysteine at the AR-LBD dimerization interface (Fig. 6C), we reasoned that the mutant protein would be more reactive, favoring formation of disulfide-bridged homodimers in solution. Y764C but neither WT AR-LBD nor other mutants tested rapidly forms covalent dimers in solution at basic pH as assessed by nonreducing SDS-PAGE (Fig. 6D). To directly prove that residues Cys^{764}/Cys$^{764'}$ from each monomer are responsible for disulfide bridge-mediated dimerization in solution, bands corresponding to the AR-LBD(Y764C) dimer were excised from the gel and subjected to enzymatic digestion with endoproteinases trypsin and GluC. Tandem mass spectrometry (MS/MS) analysis of these digests allowed indeed the identification of peaks corresponding to Cys^{764}–cross-linked peptides (Fig. 6E and table S3). The dimeric AR-LBD conformation previously identified by x-ray crystallography (Fig. 4B) (*6*) would not support reaction of neighboring Cys^{764} residues (distance between Cβ atoms: 11 Å; Fig. 5C), but the recent structure of multidomain AR reveals the plasticity of this interface (*7*). Therefore, and to provide additional evidence of the plasticity of the AR-LBD homodimer, we analyzed by MS/MS the band corresponding to BMB–cross-linked, dimeric AR-LBD(Y764C) (Fig. 6B). The results corroborated the presence of a BMB-mediated linkage between Cys^{764} Sγ atoms from two monomers (Fig. 6B and table S4).

The R761 zone undergoes large conformational rearrangements in AR-LBD point mutants

In the AR-LBD homodimer, the major interface is formed by polar and hydrophobic residues from H5, β strand S1, and their connecting loop, with additional contributions made by residues from H1 and H7-H9 and L1-3 (Fig. 7, A and B). The core dimer interface features residues Val^{758}-Arg^{761}, along with the aromatic residues Trp^{752}, Phe^{755}, and Tyr^{764}, which are involved in an intricate network of hydrogen bond (H-bond) and van der Waals (VdW) interactions. Most notably, stacked residues Trp^{752} and Phe^{755} rigidify the H5-H5′ dimer interface, which is strengthened by strong VdW contacts of the latter with Pro^{802} as well as by H-bonds between the guanidinium group of Arg^{761} and the main chain carbonyl oxygen atoms of Glu6^{79}, Ala^{680}, and/or Glu^{682} from the neighboring monomer (Fig. 7B). Unexpectedly, point mutations F755V/L (Fig. 7, F and G) and Q799E (Fig. 7H) resulted in a fully different conformation of H5-S1 loop residues compared to WT (Fig. 7C). Although residues Val^{755}/Leu^{755} occupy essentially the same position as the WT Phe^{755}, loss of stabilizing interactions mediated by the Phe^{755} phenol ring ultimately result in the exposure of the downstream Asn^{758}-Arg^{761} sequence, which deviates by up to 4 Å from the more compact conformation commonly observed in structures of AR-LBD, and in which residue Ser^{760} is essentially buried (Fig. 7, C to H). Most notably, the side chain of Arg^{761} extends into bulk solvent and exhibits various degrees of freedom in the different mutants (Figs. 3B and 7, A to G). These residues are best defined by electron density in the F755L and Q799E crystals, in which the guanidinium group of Arg^{761} is sandwiched between the carboxylates of its "own" Glu^{773} and Asp^{829} from a crystal neighbor (Fig. 7, G and H). This extended conformation is stabilized by the side chain of Asn^{759}, which accepts an H-bond from the main chain N atom of Arg^{761}. The proline-like conformation adopted by the preceding residue, Ser^{760}, is also noteworthy (Fig. 7G). Important contacts with a crystal neighbor constrain H5-S1 residues from larger displacements (Fig. 7, C to H). We reasoned that, in solution, these rearrangements could lead to even more extensive unfolding of the R761 switch zone. Important residue movements in this region were identified in our current MD simulations, some of which are larger than the deviations between mutant and WT in experimental structures (Fig. 5B and fig. S6).

Full-length AR is preferentially monomethylated in vivo by the methyltransferase, PRMT5, and methylation of Arg^{761} is affected by AR-LBD dimer interface disease-linked mutations

Our structural analysis of AR-LBD point mutants that affect the dimer interface revealed important structural rearrangements, which parallel the differences in the transcription profiles of these variants (see above). These observations prompted us to explore possible functional consequences of the studied mutations. Residue Arg^{761} adopts a markedly different, more exposed conformation in several mutants (Fig. 8, A to G), and it has been previously reported as a substrate of a major type II arginine methyltransferase with both mono- and symmetrical dimethylation activity, Protein arginine methyltransferase 5 (PRMT5), with important functional implications (*18*). To assess direct physical interactions between FL AR and endogenous PRMT5 in living cells, we performed proximity-ligation assays (PLA). The results of these experiments demonstrated strong AR-PRMT5 interactions in PC3-WT and PC3-Q799E cells, which were significantly reduced in PRMT5-silenced cells (Fig. 9, A and B; note the 50% loss of AR-PRMT5 interactions for both WT and Q799E). Furthermore, PLA experiments demonstrated arginine monomethylation of FL AR, as well as weaker symmetric dimethylation, which was reduced 50% upon incubation with the PRMT5-specific inhibitor, GSK595 (Fig. 9, D to F). In all PLA experiments, we observed heterogeneous patterns, with some nuclei showing strong AR-PRMT5 or methylation signals while others were practically devoid of these signals (Fig. 9, A and C). We also note that levels of Q799E mutant were remarkably lower in these experiments.

Western blot analysis of immunoprecipitated AR samples verified that Arg residues of both WT and mutant AR proteins were monomethylated in PC3 cells (Fig. 8H). Similar to the results of PLA experiments for the Q799E variant (Fig. 9C), the concentrations of mutant proteins were lower, and comparison of the relative intensities of bands corresponding to total and methylated AR fractions revealed that mutants were methylated to a lower extent. This feature is probably due to enhanced degradation of the mutant proteins, compared to WT AR (figs. S3, A and B, and S4) rather than reduced expression. In this regard, recombinant WT AR-LBD and its mutants are produced at similar levels in a heterologous system (Fig. 8I). In light of the structural information presented above, these findings strongly suggest that residue Arg^{761} is preferentially monomethylated by PRMT5 in WT and AR-LBD mutants (Fig. 8H).

In the absence of structural information on the mechanism of recognition and processing of globular, macromolecular substrates by the methylosome (the hetero-octameric PRMT5·MEP50

Downloaded from https://www.science.org on April 26, 2023

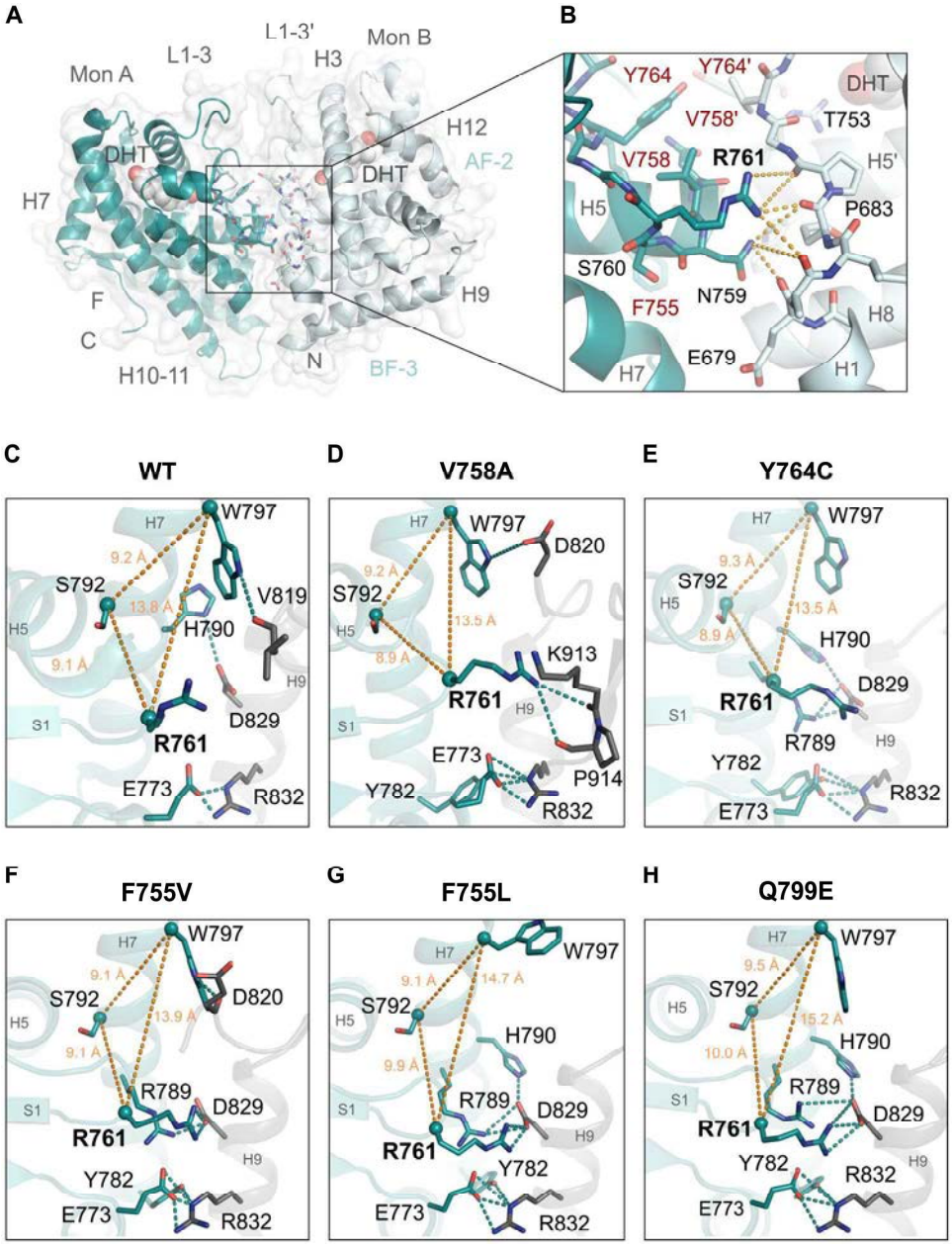

Fig. 7. The R761 zone undergoes large conformational rearrangements in AR-LBD point mutants. (**A**) Surface and cartoon representation of the AR-LBD·DHT dimer (PDB 5JJM). Residues comprising the core dimer interface are shown as color-coded sticks (oxygen, red; nitrogen, blue; carbon, teal or sky blue). (**B**) Close-up of the core dimer interface. Interface residues are shown as sticks and labeled. Major interdomain hydrogen bonds are represented as orange dotted lines. (**C** to **H**) Close-ups of the R761 zone in the crystal structures of mutant AR-LBD (teal-colored cartoons). The closest crystal neighbor is also shown in all cases (colored dark gray), to highlight major interactions due to the crystal packing. Residues involved in the crystal contacts are represented as color-coded sticks. Note the tighter contacts involving the Arg^{761} side chain in mutants F755V (F), F755L (G), and Q799E (H) compared to WT (C), V758A (D), and Y764C (E), most notably salt bridges with the Asp^{829} carboxylate from the neighboring monomer. Distances between the posttranslationally modifiable residues, Arg^{761} and Ser^{792}, and from both of them to the reference residue, Trp^{797}, are also given.

complex) and to explore possible binding modes of AR, we performed docking experiments using the current structure of AR-LBD Q799E mutant and previously reported structures of the PRMT5·MEP50 complex (Fig. 9, G and H) (*67*–*70*). Similar interactions could be expected for WT AR and other point mutants. The results of these docking experiments suggest how the extended H5-S1 loop in the AR-LBD would fit into the active site of the methyltransferase, supported by additional interactions of residues from the neighboring PRMT5 monomer (Fig. 9, G and H). Further, inspection of the docking solutions suggests that the AR-PRMT5 complex might be stabilized by additional interactions of AR-DBD with the N-terminal subunit of the transferase, while the

Downloaded from https://www.science.org on April 26, 2023

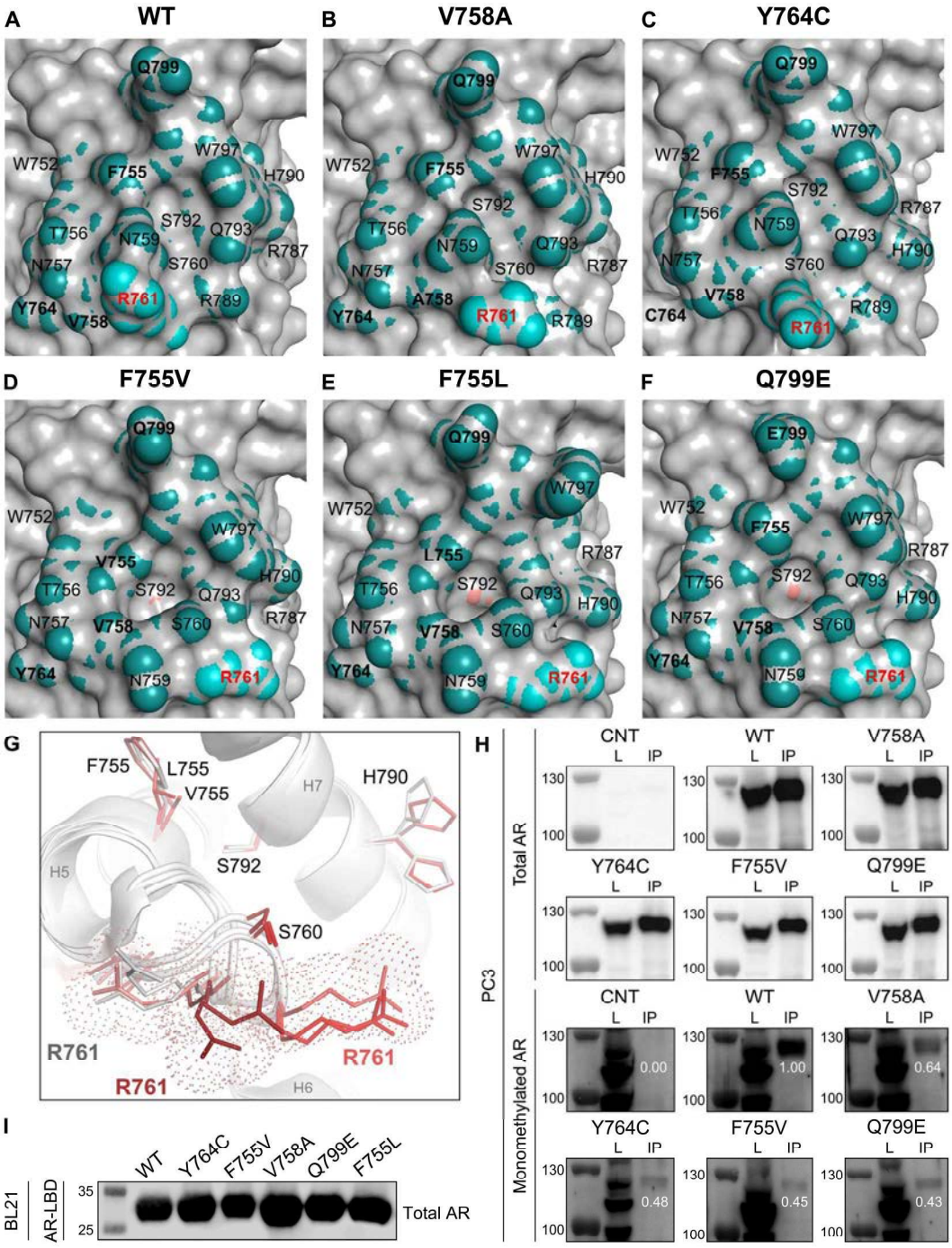

Fig. 8. Arg^{761} is more solvent exposed in pathological AR mutations affecting on arginine methylation of the full-length receptor. (**A** to **F**) Surface representation of the AR-LBD pocket spanned by residues Trp^{752} and Phe^{755}-Val^{758} (H5), Tyr^{764} (S1), Arg^{789}-Gln^{793}, Trp^{797}, and Gln^{799} (H7) and Asn^{759}-Arg^{761} (loop H5-S1). All residues are shown as teal spheres superimposed by a gray surface to highlight the pocket topography. Note that conformational changes of Arg^{761} (labeled in red) and surrounding residues remodel this pocket thus increasing solvent accessibility of Ser^{792} (salmon), a key phosphorylation site by AKT kinase nested at its bottom. (**G**) Simplified cartoon representation of the Arg^{761} zone depicting the major displacement of Arg^{761} triggered by the dimerization mutants (different shades of red) relative to the WT position (gray). The pathological mutations induce a dislodgement of loop H5-S1, best appreciated by the different conformations adopted by the Arg^{761} side chain: from an intermediate state in V758A and Y764C (dark red, facing the viewer) to a right-oriented, more solvent-exposed position in F755V, F755L and Q799E (in salmon). (**H**) Western blot analysis of total and monomethylated FL AR fractions in PC3 cell lines expressing transduced WT or point mutants of the receptor. L, total lysate; IP, immunoprecipitated fraction. A monoclonal antibody that specifically recognizes monomethylated arginine residues was used for WB. Monomethylated AR bands were double normalized against the total IP AR and against the monomethylated WT AR band (= 1.00), so that monomethylation levels of AR mutants are not biased by the amount of immunoprecipitated proteins. (**I**) Relative expression levels of WT and mutant AR-LBD recombinant domains in BL21 *Escherichia coli* cells.

Downloaded from https://www.science.org on April 26, 2023

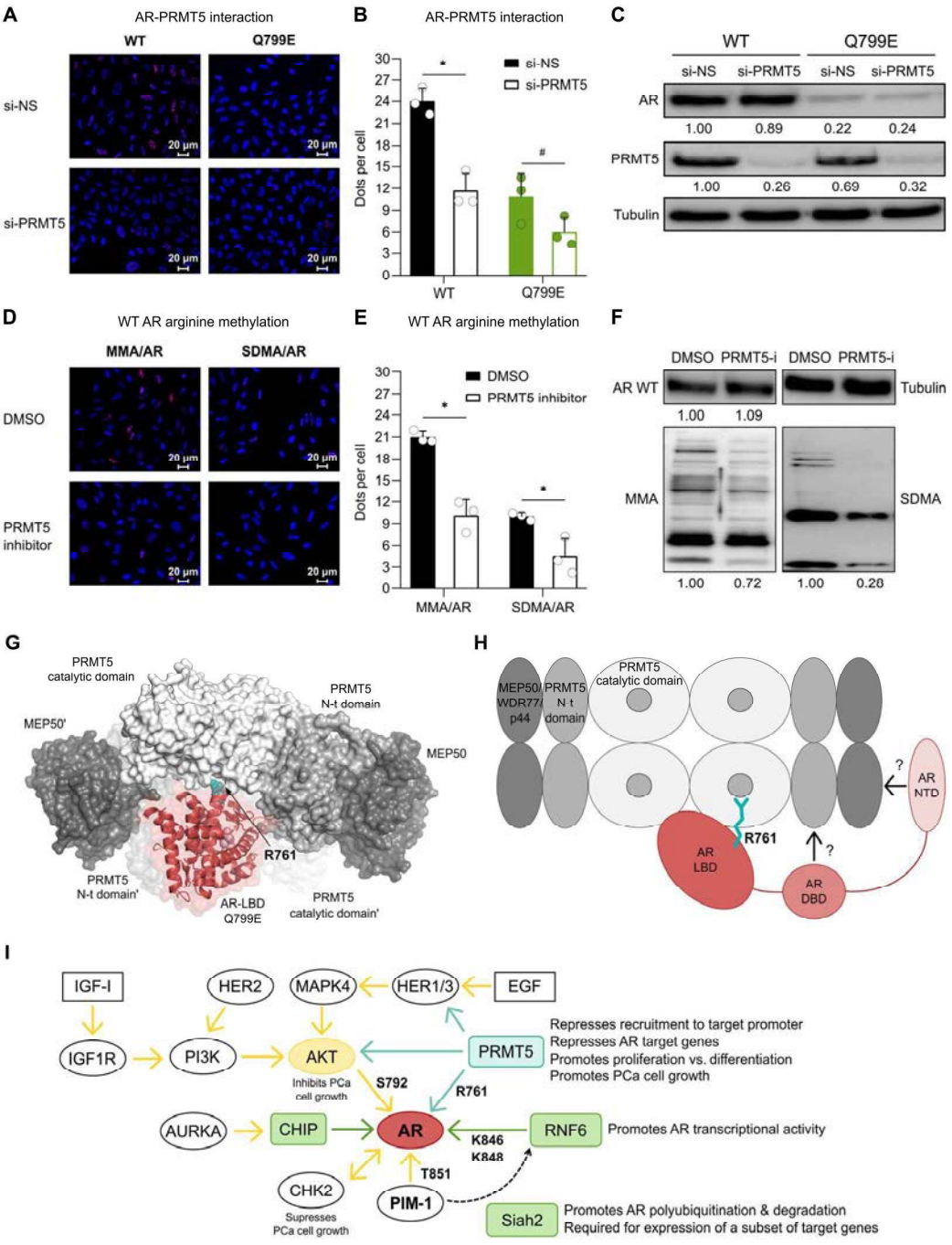

Fig. 9. AR is preferentially monomethylated in living cells by the PRMT5·MEP50 complex. (**A**) Representative PLA images demonstrating AR·PRMT5 physical interactions (red dots). Nuclei were counterstained with 4′,6-diamidino-2-phenylindole (DAPI; blue). PRMT5-silenced cells (si-PRMT5) were compared to nonsilenced cells (si-NS). (**B**) Quantified PRMT5-AR interactions are shown (mean ± SEM, $n = 3$). Differences between si-PRMT5 and si-NS cells were calculated using a t test. (**C**) Whole-cell extracts from (A) were analyzed and quantified for AR, PRMT5, and tubulin expression by immunoblot. (**D**) Representative images from AR methylation assessed using PLA with anti-AR and pan-methyl antibodies recognizing mono- (MMA) or symmetrically dimethylated arginine residues (SDMA). Red dots correspond to detected MMA and SDMA WT AR, and nuclei counterstained with DAPI (blue). A PRMT5-specific inhibitor was used to verify that the methylation signal was PRMT5-dependent. (**E**) The number of detected MMA/AR and SDMA/AR is shown (mean ± SEM, $n = 3$). Differences between catalytically active and inhibited PRMT5 cells were calculated using a t test. (**F**) Whole-cell extracts from (D) were analyzed and quantified for total AR, MMA-, and SDMA-protein patterns and tubulin expression by immunoblot. Note that, while SDMA can be mediated only by PRMT5 and PRMT9, MMA can be catalyzed by type I and II PRMTs. This explains the larger impact of the PRMT5-specific inhibitor on the SDMA fraction. (**G**) Model of AR-LBD(Q799E) approaching the active site of the PRMT5·MEP50 methylosome. For simplicity, only a heterotetrameric $(PRMT5)_2$·$(MEP50)_2$ complex is shown (PDB 4GQB). Note that folded substrates such as AR-LBD would interact with two neighboring catalytic subunits, in addition to NTD-MEP50 and DBD-PRMT5 contacts. (**H**) Diagram of putative interactions between AR domains and the methylosome. (**I**) Summary of PTMs affecting the AR-LBD. Note that PRMT5 regulates the cascade at different levels, including epidermal growth factor receptor (EGFR/HER1), protein kinase B (AKT), and AR. Phosphorylation (yellow), methylation (blue), and ubiquitination (green) pathways are shown: insulin-like growth factor 1 (IGF-I), insulin-like growth factor 1 receptor (IGF-1R), epidermal growth factor (EGF), epidermal growth factor receptor (HER1, 2 or 3), phosphoinositide 3-kinase (PI3K), mitogen-activated protein kinase 4 (MAPK4), aurora kinase A (AURKA), clonal hematopoiesis of indeterminate potential (CHIP), ring finger protein 6 (RNF6), checkpoint kinase 2 (CHK2), proto-oncogene serine/threonine-protein kinase (PIM-1) and E3 ubiquitin-protein ligase (Siah2).

Downloaded from https://www.science.org on April 26, 2023

MEP50/WDR77 component could recognize methylated Arg residues within the AR-NTD (Fig. 9, G and H). Synergy between these different interactions would ultimately provide the necessary energy to enforce structural rearrangements required to insert the nonglycine side chains of Ser^{760} and Met^{762} in the corresponding subsites of the enzyme, thus allowing methylation of residue Arg^{761}.

DISCUSSION

Although missense mutations of the *AR* gene have repeatedly been associated with conditions such as PCa and AIS (*29*), the molecular mechanisms of disease causation and the affected pathways remain poorly understood to date. Previous structural analyses of AR point mutants have been limited to internal residues that line the LBP, which are particularly relevant because of their association with resistance to anti-androgen therapy in patients with PCa (e.g., W742L, H875Y, and T878A) (*26*–*28*). Here, we present a thorough multidisciplinary analysis of the structural and functional impact of several mutations that are buried at the AR-LBD dimer interface (*6*) and which have been repeatedly linked to either AIS and/or PCa (F755L/V, V758A, Y764C, and Q799E). Although being essentially solvent-exposed residues in monomeric AR and thus unlikely to compromise the overall folding of the protein, we show that these disease-linked variants have significant structural and functional implications. Most notably, transcriptomic analysis demonstrated that, despite overall conservation of AR programs, notable differences exist at the transcriptional level between WT AR and most mutants, including key drivers of PCa progression such as *FOXA1* and *MYC*. In general, mutations at the AR-LBD dimer interface impaired AR's ability to halt proliferation and colony formation while retaining sensitivity to AR targeting drugs, consistent with a role for the nuclear factor as master regulator of differentiation (*58*). The growth-suppressive role for ligand-bound AR had previously been shown (*55*, *56*) and has been the basis for the proposed supraphysiologic testosterone treatment in patients with PCa that is being evaluated in clinical settings as part of the bipolar androgen therapy (*71*). Mechanistically, AR signaling has been shown to be dichotomous, promoting or repressing growth at low or high activity levels, respectively (*72*), and distinct transcriptional outputs have been identified for patients responding to supraphysiologic testosterone (*73*).

These large differences in transcriptional programs were paralleled by a largely reduced stability of the mutant AR-LBD modules, as indicated by notably lower T_m of up to 6°C and increased sensitivity to proteolysis in F755L/V and Y764C. Our current high-resolution crystal structures of the mutant domains reveal, in addition to changes in the targeted dimerization interface, an increased propensity to side chain movements of residues that cluster in previously described functional areas of the receptor: the exposed AF-2 and BF-3 pockets but also in the minor dimerization site identified in our previous crystal structure of multimeric AR-LBD and which evokes the tetrameric assemblies identified in living cells (*6*). Similar movements were also identified in MD simulations of mutant proteins (Fig. 5 and fig. S6). Structural rearrangements are particularly noteworthy in variants F755L/V and Q799E, in which residues of the R761 zone (H5-S1 loop) adopt a previously not observed, much more solvent-exposed conformation, which deviates by up to 4 Å from that observed in all previously reported structures of AR-LBD bound to both agonists and antagonists. On the other hand, introduction of a cysteine in a solvent-exposed position at the dimer interface (Y764C) increases the propensity to nonproductive dimer formation, particularly in the crowded nuclear environment and likely further conformational changes in the FL protein. In this regard, the recently presented low-resolution cryo-EM structures of the core AR have revealed, in addition to an "entrenched" arrangement, which would correspond to our previously presented structure of dimeric AR-LBD (*6*), a more open or "splayed" assembly of AR monomers (*7*).

Our previous MD simulations of the V758A mutant indicated allosterically transmitted conformational changes in the AR-LBD (*41*). The current crystal structures of AR-LBD point mutations that affect the dimerization interface confirm and extend these observations. These replacements induce conformational changes at areas located in the diametrically opposed pole of the domain, most notably the AF-2 binding pocket (Figs. 1B and 3E). This is the first time that a mutation in the AR-LBD dimerization site has been linked to conformational changes in the AF-2 pocket, suggesting that dimerization and coregulators binding are allosterically coupled. Careful inspection of the crystal structures supported by MD and SCA analyses suggests allosteric pathways connecting the dimer interface with the LBP and the AF-2 and BF-3 sites in AR-LBD.

Previous investigations have revealed several functional defects in the studied mutants, including a lower affinity for agonists, which, at least in the case of Y764C, was shown to result from a more rapid dissociation of ligands without significant changes in the LBP, a significant to near complete loss of NTD-LBD (N/C) interactions, and a largely reduced transcriptional activity, particularly at physiological DHT concentrations (summarized in table S2). Together, these functional findings are in line with our current structural observations of increased mobility of AR-LBD mutants and have important consequences for the structure-function relationship of the receptor. First, the overall decrease in domain stability together with subtle displacements of AF-2 residues might impair both intra- (N-/C-terminal) and intermolecular interactions (with coactivators and corepressors). Conversely, the presence of the NTD would seem to stabilize the LBD upon N-/C- interactions, as suggested by the lower thermostability of a double mutant with a shortened polyQ stretch in the NTD in addition to the Y764C point mutation (*43*). This is also in line with the cryo-EM structures of FL AR, which revealed a compact conformation with a central LBD surrounded by the NTD (*4*, *7*), and with our recent identification of NTD-LBD interactions (*74*–*75*). Second, even mutations that do not affect the LBP directly can have a profound impact on DHT affinity, by facilitating its dissociation from the internal binding site. In this regard, hormone trafficking in and out the LBP is likely to involve displacements of residues in the H5-S1 loop similar to the ones observed in our current crystal structures or perhaps of a larger magnitude. N/C interactions of the Q799E mutant were normal, however (*48*), highlighting the unique molecular fingerprint of each mutation.

The PCa-associated transcription factor, estrogen-responsive gene (ERG), was previously shown to recruit protein arginine methyltransferase PRMT5 to AR-target genes (*18*). PRMT5 then methylates AR at position 761, ultimately down-regulating AR transcriptional activity. Here, we corroborate and extend these findings by showing a direct physical interaction of endogenous PRMT5 with both WT and the Q799E mutant of FL AR in living cells.

Downloaded from https://www.science.org on April 26, 2023

Further, we verified that AR is both mono- and, to a lesser extent, symmetrically dimethylated in cells in a PRMT5-dependent manner (Fig. 9, A to F). The presence of nonglycine residues both before and after Arg^{761} would seem to make its methylation less favorable than canonical Gly-Arg-Gly motifs, in light of current structural evidence for PRMT5 (*68*–*69*) and other methylases (*76*). However, a recent systematic analysis of the human methylome has revealed a large number of substrates with bulky side chains preceding and/or following the modified arginine (*77*). Our docking experiments suggest that Arg^{761} processing by the octameric $(PRMT5)_4$·$(MEP50)_4$ heterocomplex known as methylosome would depend on secondary interactions of residues in the immediate vicinity of the methylated arginine, on the one side, and exposed residues of the PRMT5 catalytic domain and the N-terminal subunit of a neighboring molecule in the methylosome, on the other. Substrate recognition might be assisted by additional interactions with the highly acidic noncatalytic subunit of the methylosome, MEP50/WDR77, which have been shown to orient substrate histones toward the buried active site of PRMT5 (*78*). A summary of predicted AR interactions with the methylosome that might ultimately determine specific recognition and processing of Arg^{761} is schematically presented in Fig. 9 (G and H).

Although the more exposed, protruding conformation of Arg^{761} in AR-LBD mutants would favor recognition and processing by the methylosome, we have actually observed a decrease in the total and methylated fractions of the studied AR mutants in cells. Point mutants of the AR-LBD are unlikely to affect protein expression, and we have observed similar expression levels of recombinant WT AR-LBD and its mutants. Therefore, this apparent contradiction points to an enhanced degradation of mutant AR protein. AR is polyubiquitinated by several E3 ligases (Fig. 9I), followed by its degradation in the proteasome. The tumor suppressor, C terminus of Hsp70-interacting protein (CHIP), appears to be particularly relevant in this regard, as it couples the chaperone machinery to AR degradation, inducing mitotic arrest (*79*, *80*). Of particular clinical relevance, CHIP has been shown to modulate sensitivity to anti-androgen therapy in advanced PCa (*81*). These findings are also important with regard to the current development of proteolysis targeting chimeras as pharmacological alternatives for PCa treatment (*82*, *83*).

Multiple additional connections between the PRMT5·MEP50 methylosome, AR pathophysiological activity, and PCa etiology have been reported. PRMT5 functions as an epigenetic activator of AR transcription in PCa (*84*), while the noncatalytic methylosome component, MEP50 (also termed androgen coactivator p44), has been previously identified as an AR interactor linked to PCa progression, which enhances AR-driven gene expression independently of PRMT5 catalytic activity. Accordingly, MEP50 expression levels are higher in PCa tissue than in adjacent, normal prostate tissue (*85*), and it has been associated with androgen-independent PCa (*86*). Further, MEP50 is required for homeostasis of prostate epithelial cells by controlling the proper expression of AR-target genes, and its translocation from the nucleus into the cytoplasm in PCa cells results in exacerbated proliferation of prostate epithelial cells (*87*). Together, the close relationship between methylosome and AR activity at the light of our current observations provokes a systematic analysis of AR methylation in patients with PCa and suggests avenues for therapeutic intervention, in particular in *TMPRSS2:ERG*-positive PCa (*18*).

Another important PRMT5 substrate, AKT kinase, is also methylated at a noncanonical sequence that resembles the AR-LBD modification site (Gln-Arg-Leu) (*88*). The side chain of the methylated arginine residue, Arg^{391}, is fully buried in the AKT protein core, indicating that large conformational changes are not uncommon in PRMT5 substrates. This finding is also relevant because AKT has been shown to phosphorylate AR at two canonical RXRXX(S/T) sites, Ser^{213} in the NTD and Ser^{792} in the LBD (*12*–*15*). Noteworthy, Ser^{792} is located close to Arg^{761}, and it is more exposed in the mutants with an open H5-S1 loop. However, we have not detected significant differences in the degree of phosphorylation between WT and mutant AR.

Inspection of the AR-LBD 3D structure reveals that the dimerization interface comprises, in addition to Arg^{761} and the nearby Ser^{792}, several residues that have been previously reported as targets of PTMs (Figs. 1A and 9I). This extended patch includes in particular the pair of lysine residues at positions 846 and 848, which are ubiquitinated by RNF6 to modulate coactivator recruitment and AR transcriptional activity (*16*). Last, residue Thr^{851} is phosphorylated by the PIM-1L isoform of this Ser/Thr kinase, which stabilizes AR by recruiting RNF6 (*17*). The phosphomimetic $Thr^{851}Asp$ mutation resulted in increased transcriptional activity due to enhanced recruitment of coactivators at AF-2 (*89*), mirroring the impact of several point mutations at the dimer interface characterized in the current work. Together, this AR surface emerges as a major hotspot for PTMs (a summary of AR-LBD PTMs and their functional consequences is given in Fig. 9I). These findings underscore the realization that PTMs regulating DNA accessibility and transcription not only are not limited to histones but also affect also other elements of the transcription machinery (extended histone code) (*90*). Future investigations should depend on the cross-talk between PTMs and AR quaternary structure including interdomain motions and allosteric pathways connecting the different functional areas of the nuclear factor and their impact on its interactions with specific coregulatory proteins and its proteasome-mediated degradation.

In summary, the results of our multidisciplinary approach reveal a complex landscape of structure and function alterations induced by mostly conservative mutations that affect the dimerization interface of the AR-LBD, which opens various avenues for structure-guided modulation of AR function. The characterization of AR mutations presented here through a combination of complementary structural (x-ray crystallography coupled with docking experiments and MD simulations) and functional assays including transcriptome analysis could be straightforwardly extended to other pathological AR mutants including other oncogenic forms of the receptor. Early prognosis and precision pharmacology of AR-linked diseases would benefit from this integration of structural and cell biology studies under consideration of the interplay between AR mutations and PTM-driven pathology. Eventually, it might be possible to comprehensibly link all AR mutations to specific PCa subtypes, as has been achieved for the related estrogen receptor in breast cancer (*21*–*22*), as an important step toward truly personalized treatment of patients with PCa.

Our results open various avenues for structure-guided modulation of AR function. The future of precision pharmacology to tackle AR-linked diseases and also for the prognosis and treatment of patients with PCa needs to integrate structural biology with studies of cellular effects of mutations and PTM-driven pathology.

Downloaded from https://www.science.org on April 26, 2023

MATERIALS AND METHODS

Cell lines and plasmids

PC3, DU145, LNCaP, 22rv1, and RWPE-1 cell lines were purchased from and authenticated by ATCC (American Type Culture Collection). For maintenance, cells were cultured in RPMI 1640 or Dulbecco's modified Eagle's medium (DMEM), respectively, supplemented with 10% fetal bovine serum (FBS). For functional assay, cells were depleted of androgens using 10% charcoal-stripped serum (CSS; Thermo Fisher Scientific). Site-directed mutagenesis of a commercial lentiviral AR plasmid (pLENTI6.3/AR-GC-E2325, plasmid #85128, Addgene) was conducted to generate variants AR-F755V, AR-V758A, AR-Y764C, and AR-Q799E. For lentivirus production, human embryonic kidney 293FT (HEK293-FT) cells were cultured in DMEM (Thermo Fisher Scientific), and the lentiviral packaging vectors psPAX2 and pCMV-VSV-G were co-transfected in polyethylenimine (1 mg/ml) containing Opti-MEM (Thermo Fisher Scientific). After viral transduction using supernatants supplemented with polybrene (8 μg/ml), PC3 cells were incubated for 48 hours and selected with blasticidin (5 μg/ml) to generate control, WT AR, and mutants cell lines.

Luciferase reporter assay

To assess AR transcriptional activity, a luciferase-based assay was performed in PC3 cells, which were seeded (15,000 cells per well) in white with clear flat-bottom 96-well plates (RPMI 1640 media supplemented with 10% CSS). After 24 hours, 50% confluent cells were transfected using a Lipofectamine 2000 transfection reagent (Thermo Fisher Scientific), following the manufacturer's instructions. Renilla luciferase expression is controlled by a constitutive promoter for normalization (pRL-TK Renilla luciferase, Promega). On the other hand, Firefly luciferase plasmid (pARE-4X-Luciferase) contains four androgen response elements (AREs) cloned in tandem into pGL3 (Promega) (*91*). Transfection was performed using 100 ng of pARE-4X-Luciferase and 10 ng of pRL-TK Renilla luciferase. Both luciferases are monomeric and neither requires posttranslational processing, so they can function as genetic coreporters immediately upon translation.

Transfection mixes were prepared in Opti-MEM I (Thermo Fisher Scientific). Six hours after transfection, the medium was aspirated and replaced with RPMI 1640 media supplemented with 10% CSS. For the assay testing the transactivation level of AR mutants, cells were stimulated 24 hours after transfection for 4 hours with vehicle or 20 nM DHT. For luciferase assay testing AR mutants' resistance to PCa treatment drugs, cells were treated for 30 min with abiraterone (40 or 80 μM) or enzalutamide (50 or 200 μM) before 20-nM DHT stimulation for 4 hours. Luciferase activity was measured after cell incubation with the corresponding compounds with the Dual-Glo Luciferase Assay System (Promega) using an EnSpire Alpha plate reader (PerkinElmer). After background subtraction, the ratio of firefly to Renilla luciferase activity was calculated. Assays were performed in three independent experiments with five internal replicates each. GraphPad Prism 8.0 software was used to perform the statistical analyses using *t* test, once confirmed the normal distribution of the values.

Functional cell assays

Colony formation and proliferation assays

Approximately 30,000 PC3 cells were seeded in six-well plates and grown in RPMI 1640 media supplemented with 10% CSS, in two independent replicates for each experiment. The next day (day 1), cells were stimulated with 20 nM DHT. The stimulation was repeated every 2 days. Colonies were grown until day 9 and stained with crystal violet [0.5% (w/v) in 10% ethanol and 90% formaldehyde]. After 30 min of incubation and several washes with water, colonies were scanned and quantified using ImageJ software (https://imagej.nih.gov/ij/). Colony formation capacity was normalized to control cells. Statistical analysis was performed using *t* test, showing the differences with respect to PC3 WT AR. For colony formation assays in other cell lines, cells were seeded on the basis of their proliferation rate (DU145: 8000 cells per well; RWPE-1: 20,000 cells per well; 22Rv1: 30,000 cells per well; LNCaP: 80,000 cells per well). While DU145 and RWPE cells were cultured in CSS for this assay, 22Rv1 and LNCaP were cultured in FBS to prevent them from stopping proliferation. In all cases, media were supplemented with increasing concentrations of DHT.

Proliferation assays

Cells were trypsinized and counted (with trypan blue stain to discriminate living cells) every 2 days, starting at day 3 and finishing at day 7, to follow the time course growth. To compare proliferation at day 7, the number of cells of each PC3 variant was normalized to their corresponding nonstimulated control (without DHT). Statistical analysis was performed using *t* test, showing the differences with respect to PC3 WT AR.

MTT cell viability assays

Approximately 4000 cells ($n = 6$) were seeded in 96-well plates in RPMI 1640 media containing 10% CSS. Cells were supplemented the next day with DHT combined with abiraterone acetate (Memorial Sloan Kettering Cancer Center), enzalutamide (MDV3100; Sigma-Aldrich), or apalutamide (Janssen) at different concentrations. After 72 hours, cells were treated for 3 hours with 10 μl per well of MTT [3-(4,5-dimethylthiazol-2-yl)-2,5-diphenyltetrazolium bromide; 5 mg/ml], a yellow tetrazole that is reduced to purple formazan crystals by living cells. Formazan crystals were dissolved with 100 μl of solubilization buffer (10% SDS and 10 mM HCl) for 3 hours. Plates were read at optical density = 560 nm in a spectrophotometer, and then the percentage of viable cells compared to the untreated wells was determined. In the case of abiraterone, the inhibitory concentration was calculated using nonlinear regression fit in GraphPad Prism 8.0 software, normalizing to untreated cells. Statistical analysis was performed using parametric paired *t* test comparing each PC3 AR-mutant regression curve versus PC3 WT AR. Because of drug resistance of PC3 cells against enzalutamide and apalutamide, data did not fit nonlinear regression models. To compare enzalutamide and apalutamide resistance, normalized cell viability (at 50 μM enzalutamide or 100 μM apalutamide) was expressed as a fold change percentage with respect to WT AR. Statistical analysis was performed using a *t* test, showing the differences between the PC3 WT AR and its mutants. For viability assays of other cell lines, cells were seeded to reach confluence (90%) at the end of the experiment (DU145: 2500 cells per well; LNCaP, 22Rv1, and RWPE-1: 5000 cells per well). While DU145 and RWPE were cultured in CSS for this assay, 22Rv1 and LNCaP were cultured in FBS to prevent them from stopping proliferation. In both cases, media were supplemented with increasing concentrations of DHT.

Downloaded from https://www.science.org on April 26, 2023

Immunoprecipitation and Western blotting

For immunoprecipitation (IP) of FL AR, PC3 cells were scraped off the plate and transferred to a microcentrifuge tube using lysis buffer (LyB) containing 50 mM tris, 150 mM NaCl, 0.2% NP-40, and 10% glycerol supplemented with protease inhibitor cocktail (Roche), 1% phosphatase inhibitor cocktail 3 (Sigma-Aldrich), and 0.5% phenylmethylsulfonyl fluoride (Sigma-Aldrich) (in following, inhibitor mix). Samples were sonicated on ice three times for 5 s each, 30% amplitude, and centrifuged. IP of the collected supernatant was performed using magnetic beads (Protein G and Protein A Mag Sepharose beads, Thermo Fisher Scientific). AR XP (1:50; Cell Signaling, 5153) and immunoglobulin G (IgG; 1:50; rabbit IgG polyclonal–isotype control, Abcam) antibodies were preincubated for 1 hour with 25 μl of A + G beads (1:1) at 4°C, and cell lysates (1.6 mg) were precleared with 5 μl of A + G beads (1:1). Beads were removed from the precleared lysates and then transferred into AR or IgG tubes for IP at 4°C overnight in a rotating wheel. Afterward, beads from the negative control (IgG tubes) and the immunoprecipitated samples were washed twice with LyB and five times with LyB lacking NaCl. Last, beads were eluted with 70 μl of Laemmli buffer containing 10% β-mercaptoethanol for 5 min at 98°C, and samples were analyzed by Western blotting.

For Western blot analysis of total protein extracts, PC3 cells were lysed with 1× radioimmunoprecipitation assay (RIPA) buffer [10 mM tris-HCl (pH 7.5), 0.1% SDS, 1% deoxycholate sodium salt, 1% triton X-100, 0.15 M NaCl, and 1 mM EDTA] supplemented with inhibitor mix. Proteins (30 μg per lane) were resolved by SDS-PAGE and transferred onto a polyvinylidene difluoride membrane (GE Healthcare, Amersham), which was blocked with PBS-T (phosphate-buffered saline and 0.1× Tween 20) containing 5% bovine serum albumin (Sigma-Aldrich). Primary antibodies for Western blot were incubated at 4°C overnight: anti-AR (1:500; Abcam), anti-mono methyl arginine (R*GG) (1:500; Cell Signaling), and anti-rabbit IgG horseradish peroxidase–linked antibodies (1:10,000; Cell Signaling). HRP-conjugated secondary antibody was incubated for 1 hour at room temperature. The ECL Plus Western Blotting Detection Kit (Thermo Fisher Scientific) was used for detection in a ChemiDoc MP Imaging System (Bio-Rad).

Transcriptomic analysis

For transcriptomic analysis, approximately 500,000 PC3 cells were seeded in 10-cm plates in RPMI 1640 media supplemented with 10% CSS (hormone depletion conditions) (n = 3). After 48 hours, cells were stimulated with 20 nM DHT for 4 hours and collected. RNA was purified using the Maxwell RSC simplyRNA Tissue Kit (Promega), following the manufacturer's instructions. RNA quality control, library preparation, 2 × 100 bp, >25 M paired-end reads, and stranded mRNA sequencing (RNA-seq) were performed using an Illumina HiSeq2500 platform. RNA-seq lanes were joined and reads were mapped with STAR (*92*) to the primary assembly of the human reference genome (GRCh38) in conjunction with the complete gene annotation file available in GENCODE (*93*). The gene read count was performed with the STAR parameter - quantMode GeneCounts. Results indicate, on average, 90% of reads uniquely mapped in all samples; around 80% of the reads are overlapping genes.

We used the IDEAmex service (*94*) to perform differential expression analysis using DESeq2 (*95*) and limma methods (*96*). The count matrix was filtered considering 5 counts per million (CPM). To define DEGs, we considered an absolute $\log_2$ fold change ≥ 1 and an adjusted P value or false discovery rate (FDR) ≤ 0.05. The following DE analyses were performed: PC3 control versus WT AR and point mutants F755V, V758A, Y764C, and Q799E, as well as WT AR versus PC3, F755V, V758A, Y764C, and Q799E. To identify the intersection of genes differentially expressed between contrasts, we used the function UpSet from the package Complex heatmaps (*97*). Volcano plots were generated using the Enhanced Volcano R package on DESeq2. AR targets were recovered from DoRothEA (*57*).

For PCA, raw counts were filtered to have at least three samples with a CPM ≥ 5. Counts were transformed using the VST function (*98*). The PCA was calculated with the plotPCA function in DESeq2 and visualized with the ggplot2 package. For the VST data, we calculated the Euclidean distances between samples using the R function dist. We plotted the sample distance matrix with the rows/columns arranged by the distances, manually providing sampleDists to the clustering distance argument of the pheatmap function.

Enrichment analysis

GSEA (*99*) was performed to assess the enrichment of the different mutant AR signatures against a reference signature of DEGs between control versus WT AR ranked according to the $\log_2$ fold change value and the clusterProfiler R package (*100*) on DESeq2 results. GSEA was also used to ascertain the enrichment in selected gene sets that match against the search for "prostate cancer" in MSigDB or the entire Biological Pathways collection in the KEGG database. We performed GSEA against PCa malignant signatures FOXM1, CENPF, and FOXM1 + CENPF for each DESeq2 result between PC3 control versus WT AR, F755V, V758A, Y764C, or Q799E. Signatures recovered are defined as top 200 up- and down-regulated DEGs (*58*).

Transcription factor activity was estimated with the DoRothEA R package (*57*) using results from the limma package (*96*) between PC3 versus WT AR or F755V, V758A, Y764C, or Q799E mutants. We estimated activity for pathways involved in cancer with PROGENy (*101*). DEG results between PC3 control versus WT AR, F755V, V758A, Y764C, or Q799E using as input the list of genes ranked by the $\log_2$ fold change.

AR target genes expression analysis by RT-qPCR

For qPCR, approximately 300,000 PC3 cells were seeded in six-well plates in duplicates in RPMI 1640 media supplemented with 10% FBS. After 48 hours, 70% confluent cells were hormone-depleted by using RPMI 1640 media supplemented with 10% CSS. After 24 hours, cells were stimulated with 20 nM DHT for 4 hours and collected. RNA was extracted using a TRIzol reagent according to the manufacturer's instructions. After DNA digestion (deoxyribonuclease, Amplification Grade, Invitrogen), cDNA was obtained using the High-Capacity cDNA Reverse Transcription Kit (Applied Biosystems). Total cDNA was diluted 1:10, qPCR was performed using PowerUp SYBR Green Master Mix (Applied Biosystems), and plates were read with a LightCycler 480 (Roche). The following reverse transcription (RT)–qPCR primers were used to amplify glyceraldehyde phosphate dehydrogenase (GAPDH; 5′-CATCTTCCAGGAGCGAGATC; 5′-GCTGTTGTCATACTTCTCATGG), TMPRSS2 (5′-CCTGACGCAGGCTTCCAAC; 5′-GGTCAAGGTGATGCACAGTG), FKBP5 (5′-GCGAAGGAGAAGACCACGACAT; 5′-TAGGCTTCCCTGCCTCTCCAAA), and

Downloaded from https://www.science.org on April 26, 2023

FOXA1 (5′-GCAATACTCGCCTTACGGCT; 5′-TACACACCTTGGTAGTACGCC). Results were normalized to GADPH expression level, and each sample was quantified in triplicate. Relative quantification considers GAPDH internal standard and control conditions (PC3-CNT without DHT) to normalize and compare samples. GraphPad Prism 8.0 software was used to perform the statistical analyses using *t* test, which confirmed the normal distribution of the values.

Proximity ligation assay

PLA experiments were performed using reagents from the Naveniflex MR Kit (Navinci) essentially as previously described (*102*). Briefly, cells were seeded onto coverslips in 12-well plates, fixed in methanol for 2 min, and then washed twice in 1× phosphate-buffered saline. Fixed cells were stored at 4°C for subsequent staining or saturated with the blocking solution for 1 hour at 37°C. All further steps were performed at this temperature. Cells were then incubated with different pairs of primary antibodies: (i) anti-AR (Cell Signaling, #5153) and anti-PRMT5 (Santa Cruz Biotechnology, sc-376937), (ii) anti-AR (Santa Cruz, sc-7305) and anti-MMA (Cell Signaling, #8711), or (iii) anti-AR (Santa Cruz, sc-7305) and anti-SDMA (Cell Signaling, #13222) for 1 hour. After three washes in tris-buffered saline with 0.1% Tween® 20 detergent (TBS-T), mouse and rabbit secondary antibodies conjugated with complementary oligonucleotides ("Navenibodies") were added and incubated for 1 hour. Again, cells were washed three times in TBS-T and subsequently incubated with reaction reagents A, B, and C to activate the oligonucleotides, to allow the interaction of Navenibodies that are in close proximity and the DNA hybridization and amplification of the proximity fluorescent probes (ATTO647), respectively. Last, cells were washed 2 min in 1× tris-buffered saline (TBS) and incubated for 15 min with 0.1× TBS at room temperature. The samples were mounted using Duolink in situ mounting medium containing 4′,6-diamidino-2-phenylindole (DAPI; Sigma-Aldrich, #DUO82040). The edges of the coverslips were sealed using nail polish. Slides were then stored in the dark at 4°C for a short term or visualized under a Zeiss fluorescence microscope, and interactions were counted for at least 300 cells using ImageJ software (*103*). In some experiments, PRMT5 was downregulated using ON-TARGETplus Human SMARTpool small interfering RNA (siRNAs; Dharmacon, #L-015817-00-0005). The unrelated siRNA ON-TARGETplus Non-targeting Control Pool (Dharmacon, #D-001810-10-05) was used as control in these siRNA experiments. Alternatively, PRMT5 activity was blocked by preincubating the cells for 48 hours with the specific inhibitor, GSK595 (0.5 μM; Sigma-Aldrich). Cells incubated with the same volume of dimethyl sulfoxide were used as reference in these experiments.

Cloning and mutagenesis of the hAR-LBD construct

Recombinant human AR-LBD (hAR-LBD; amino acids 641 to 920) was cloned into a modified pGEX vector as previously published (*63*). The resulting fusion protein consists of a histidine tag sequence followed by a glutathione *S*-transferase and a *Tobacco etch* virus (TEV) cleavage site before the corresponding sequence of the hAR-LBD. The pGEX vector template encoding WT hAR-LBD was mutated using the Q5 Site-Directed Mutagenesis Kit (New England Biolabs) to generate AR-LBD mutant vectors with the following primers (Y764C: 5′-CAGGATGCTCTgGCTTCGC, 5′-GAGTTGACATTGGTGAAGGATCG; V758A: 5′- TTCACCAATGcCAACTCCAGGATGCTC, 5′- GGATCGCCAGCCCATGGC; F755V: 5′- CTGGCGATCCgTCACCAATGT, 5′-CCCATGGCAAACACCATGAGC; F755L: 5′- CTGGCGATCCTTaACCAATGT, 5′- CCCATGGCAAACACCATGAGC; and Q799E: 5′- TGGATGGCTCgAAATCACCCC, 5′-AACTCTTGAGAGAGGTGC).

Differential scanning fluorimetry

Thermofluor experiments were performed in an iQ5 Multicolor Real-Time PCR Detection System (Bio-Rad) using 96-well plates (Hard-Shell High-Profile Semi-Skirted PCR Plate, Bio-Rad) and a 25-μl total volume for each reaction essentially as described in *104*. Melting curves were acquired from eight replicates to determine the average T_m. AR samples (0.5 mg/ml) were prepared in 20 mM Hepes (pH 8.0), 150 mM Li_2SO_4, 10% glycerol, 50 mM imidazole, 1 mM dithiothreitol (DTT), and 50 μM DHT and centrifuged 5 min at 14,000 rpm. SYPRO Orange dye (Sigma-Aldrich) was first prepared at 80× in the protein buffer, starting from a 5000× commercial dilution. The final concentration of SYPRO Orange dye in each 25-μl reaction was 5×. The plates were sealed with optical quality sealing film (Microseal B Seals, Bio-Rad) and centrifuged at 2000*g* for 30 s. Samples were equilibrated for 60 s and analyzed using a linear gradient from 16° to 95°C in increments of 1°C/min, recording the SYPRO orange fluorescence throughout the gradient in the iQ5 Optical System Software 2.0. Values were fitted using the online tool JTSA with the Boltzmann four-parameter logistic equation, and the calculated fluorescence shift midpoints were compared via unpaired *t* test for equal variances in GraphPad Prism 8.

Proteolytic digestion

Samples of recombinant WT AR-LBD and all studied mutants were buffered-exchanged into 25 mM tris (pH 7.6), 10 mM $CaCl_2$, and 1 mM DTT using a PD-10 column and concentrated to 0.5 mg/ml using a centrifugal filter device. Sequencing-grade Arg-C protease (Clostripain, P5214 Abnova) was added [50/1 (w/w), protein/protease], and mixtures were incubated at 37°C with shaking. Aliquots of the proteolytic reactions were taken at indicated times, immediately mixed with reducing Laemmli buffer, and heated at 95°C for 5 min. Reaction products were separated on SDS-polyacrylamide gels and stained with Coomassie Brilliant Blue.

Crystallization and structure determination

Purified, concentrated DHT-bound AR-LBD mutants (F755L, F755V, V758A, Y764C, and Q799E) were combined with a twofold molar excess of UBA3 peptide and incubated for 1 hour at room temperature. Drops of the AR-LBD mixture were equilibrated against 0.1 M tris-HCl (pH 8.0) containing either 0.2 M sodium chloride, 2.0 M ammonium sulfate, 0.1 M ammonium acetate, or 2.5 M sodium formate using the sitting drop vapor-diffusion method. Diffraction data were collected at 100 K at the XALOC beamline of the ALBA-CELLS synchrotron (www.cells.es/en/beamlines/bl13-xaloc) and processed using MOSFLM (www.mrc-lmb.cam.ac.uk/harry/mosflm/) and CCP4 (www.ccp4.ac.uk/). The crystal structures were solved and refined using MOLREP (www.ccp4.ac.uk/html/molrep.html#references), REFMAC5 (www2.mrc-lmb.cam.ac.uk/groups/murshudov/content/refmac/refmac.html), and COOT (www2.mrc-lmb.cam.ac.

Downloaded from https://www.science.org on April 26, 2023

uk/personal/pemsley/coot/) from the CCP4 package. Crystal packing was analyzed using PISA (www.ebi.ac.uk/), model quality was assessed with MolProbity (http://molprobity.biochem.duke.edu/), and structure figures were prepared with PyMOL (www.pymol.org).

Cross-linking experiments

Purified recombinant WT and mutant AR-LBD proteins were incubated with fourfold molar excess of BMOE or BMB cross-linkers for 2 hours at 37°C following the manufacturer's instructions. Samples of the reaction mixtures were boiled in the presence of reducing Laemmli sample buffer and resolved by SDS-PAGE.

Y764C covalent dimerization in solution

Purified recombinant Y764C (3 mg/ml) was incubated in 20 mM Hepes (pH 8.0), 150 mM Li_2SO_4, 10% glycerol, 50 mM imidazole, 1 mM DTT, 50 μM DHT, or in the same buffer without DTT after desalting using a PD-10 column (GE Healthcare). Y764C samples incubated under reducing and nonreducing conditions were boiled in the presence of reducing Laemmli sample buffer and resolved in a 10% SDS-polyacrylamide gel.

Nano–liquid chromatography–MS/MS experiments

Bands corresponding to dimeric, BMB–cross-linked Y764C were excised from the gels and subjected to in-gel digestion following the standard protocols. Briefly, excised bands were reduced (10 mM DTT) in 50 mM bicarbonate buffer (pH 8.0) for 45 min at 56°C, alkylated (50 mM iodoacetamide in 50 mM ammonium bicarbonate buffer for 30 min at 25°C), and digested with trypsin overnight at 37°C in 100 mM ammonium acetate buffer (pH 8). (Sequencing-grade endoproteases were from Promega).

The following procedures have been performed as previously published (*64*). Tryptic peptides were diluted in 1% formic acid (FA) and loaded onto a 180 μm by 20 mm C18 Symmetry trap column (Waters) at a flow rate of 15 μl/min using a nanoAcquity Ultra Performance LCTM chromatographic system (Waters). Peptides were separated using a C18 analytical column (BEH130 C18, 75 mm by 25 cm, 1.7 μm; Waters) with a 120-min run, comprising three consecutive linear gradients: from 1 to 35% B in 100 min, from 35 to 50% B in 10 min, and from 50 to 85% B in 10 min (A = 0.1% FA in water, B = 0.1% FA in CH_3CN). The column outlet was directly connected to an Advion TriVersa NanoMate fitted on an Linear trap quadrupole furier transform (LTQ-FT) Ultra mass spectrometer (Thermo Fisher Scientific), which was operated in positive mode using the data-dependent acquisition mode. Survey MS scans were acquired in the Fourier transform ion cyclotron resonance (FT-ICR) cell with the resolution (defined at 400 mass/charge ratio) set to 100,000. Up to six of the most intense ions per scan were fragmented and detected in the linear ion trap. The ion count target value was 1,000,000 for the survey scan and 50,000 for the MS/MS scan. Target ions already selected for MS/MS were dynamically excluded for 30 s. Spray voltage in the NanoMate source was set to 1.70 kV. Capillary voltage and tube lens on the LTQ-FT were tuned to 40 and 120 V, respectively. The minimum signal required to trigger MS to MS/MS switch was set to 1000, and activation *Q* value was set at 0.25. Singly charged precursors were rejected for fragmentation.

Docking experiments and dimeric interface analysis

The dimerization energy of the AR-LBD dimeric conformation found in the x-ray structure (PDB 5JJM, chains B:C) as well as that of the modeled mutant dimers (built by superimposition of the mutant monomeric structures onto the corresponding subunits of the crystallographic dimer) was computed with the pyDock bindEy module (*105*) based on energy terms previously optimized for rigid-body docking. The pyDock binding energy is basically composed of Lennard-Jones VdW, Coulombic electrostatics, and implicit desolvation based on accessible surface area (ASA) with atomic solvation parameters optimized for protein-protein interactions (*106*). To avoid excessive penalization from possible clashes derived from the rigid-body approach, VdW total contribution was weighed by a factor of 0.1. For the same reason, VdW and electrostatic values per intermolecular atom pair were restricted to a maximum of +1.0 kcal/mol or to a range between −1.0 and +1.0 kcal/mol, respectively. BSA values of WT and mutant dimers were computed as the difference in ASA between the dimer and the unbound molecules, using ICM-Browser (www.molsoft.com). In addition, homodimeric docking models of WT AR-LBD and its mutants were built using the pyDock docking and scoring method (*105*). First, protein models were prepared by removing all cofactors and heteroatoms, and missing side chains were modeled with SCWRL 3.0 (*105*). Then, the fast Fourier transform–based docking programs FTDock (with electrostatics and 0.7 Å grid resolution) (www.sbg.bio.ic.ac.uk/docking/ftdock.html) and ZDOCK 2.1 (https://zdock.umassmed.edu/) were used to generate 10,000 and 2000 rigid-body docking poses, respectively. These were merged in a single pool for subsequent pyDock scoring, as detailed above. From the resulting docking poses, NIP values were obtained for each residue with the built-in patch module of pyDock, implementing the pyDockNIP algorithm (*65*). An NIP value of 1 indicates that the corresponding residue is involved in all predicted interfaces of the 100 lowest energy docking solutions, while a value of 0 means that it appears as expected by random chance. Last, a negative NIP value implies that the residue appears at the low-energy docking interfaces less often than random. Usually, residues with NIP $\geq$ 0.2 are considered as hotspot residues. In addition, ODA was obtained by computing surface patches with optimal desolvation energy generated from each surface residue (*66*). Residues with low ODA values, usually less than −10.0 kcal/mol, indicate regions with favorable desolvation energy upon interaction with a partner protein. Residues from Lys^{845} to Ser^{851} were removed from WT for all energy and docking calculations, for consistency in the comparative analysis, since these residues are missing in all mutant structures. Additional docking experiments were performed using the LZerD protein docking web server (https://lzerd.kiharalab.org/) with the structure of a hetero-tetrameric $(PRMT5)_2$·$(MEP50)_2$ complex as receptor (PDB 7L1G) and the current structure of AR-LBD(Q799E) as ligand. Solutions that satisfied the constraints (distance of Arg^{761}-flanking residues to the PRMNT5 catalytic machinery, <6 Å) were visually inspected.

Computational analysis of the estimated energetic impact of AR point mutations

We estimated the impact of the studied mutations on the overall protein stability with the FoldX empirical force (https://foldxsuite.crg.eu/) (*107*). Ten iterations were conducted for each mutation and later averaged. Computed free energy differences between mutant

Downloaded from https://www.science.org on April 26, 2023

and WT proteins (estimated $\Delta\Delta G$) < 1 kcal/mol were considered not significant, those between 1 and 2, 2 and 4, and >4 kcal/mol as slightly, mildly, and strongly destabilizing, respectively. (FoldX has an estimated error of ~0.7 kcal/mol).

Statistical coupling analysis

Following previously published protocol [(*64*), DOI: 10.5281/zenodo.7274365], we identified two different sectors by using the SCA5 8/2011 version (*108*) and the updated version pySCA (*109*–*110*) with an alignment of 880 sequences. The stability of the identified sectors was assessed with a statistical test based on hypergeometric calculations of the groups of residues belonging to given sectors between pairs of alignments. *P* values were adjusted using FDR. Next, specific residues from the significant sectors were extracted and selected according to their rank.

Molecular dynamic simulations

System preparation

The crystal structure of monomeric AR-LDB·DHT (PDB 1T7T) was used to represent the WT receptor, while the x-ray mutant structures used were those determined in this work. In a first step, hydrogens were added to all protein residues in their corresponding protonation states at pH 7.0, and side chain orientations were adjusted using the Protein Preparation Wizard workflow included in Maestro v.10.0 software package (www.schrodinger.com/products/maestro). Missing residues in all the mutant structures (Lys^{845} to Ser^{851}) were obtained from the WT structure by superposition. The parameters for DHT were obtained using the general amber force field (gaff2) (*111*), and charges were generated with the restrained electrostatic potential (*112*) at the HF/6-31G(d,p) level using the Antechamber module of AMBER18 (https://ambermd.org/). Next, each system was placed in a cubic periodic box filled with Optimal Point Charge water molecules (*113*), setting a minimum distance of 15 Å between the solute and the box walls. Water molecules closer than 1.0 Å to any complex atom were removed. Then, counter ions were added to neutralize the system following a grid-shaped procedure for mapping the electrostatic potential surface. All calculations were done using the ff19SB force field (*114*) with a cutoff of 10 Å for noncovalent interactions, applying the PME (Particle Mesh Ewald) method (*115*) for the treatment of the electrostatic interactions.

Molecular dynamics

Before starting the MD calculations, the structures were first relaxed to eliminate possible steric clashes with a 5000-step minimization procedure using the steepest descent method. Then, the systems were stepwise heated to 300 K at a rate of 30 K every 20 ps, fixing the main atoms of the proteins with a harmonic positional restriction of 5 kcal/mol $Å^{-2}$, using the Langevin thermostat algorithm with a collision frequency of 3 ps^{-1} under the NVT ensemble (heating). Subsequently, 100-ps simulations were performed at constant pressure (NPT ensemble) keeping fixed the main atoms with the same harmonic positional restrictions for density equilibration (density equilibration). Last, conventional MD of 1 μs for all the mutants and 1.2 μs for the WT protein were carried out within the NVT ensemble in quadruplicate to increase the conformational sampling of the system (*116*). The ParmEd program (https://parmed.github.io/ParmEd/html/index.html) was used to introduce hydrogen mass repartitioning to allow integration times of 4 fs (*117*), and the SHAKE algorithm (*118*) was used to constrain the bonds involving the hydrogen atoms.

RMSD and RMSF

RMSD along the simulation time was computed using the CPPTRAJ module from AMBER18 (https://amber-md.github.io/cpptraj/CPPTRAJ.xhtml) for all the MD trajectories to assess the structural stability of the systems along time. RMSD was computed with respect to all the Cα atoms, using the not minimized x-ray structure of the WT as reference for all the systems. The resulting superimposed trajectories were used to calculate the RMSF for each of the residues of the protein to obtain information about their conformational flexibility.

Residue pair distance

To quantify the effect of the different mutations on the distances between AR residue pairs, we implemented the algorithm described by Vatansever and coworkers (*119*). This algorithm is based on the concept of first coordination shell defined in the Gaussian network model but extended to a SCS with a radius of ~9.1 Å to better account for the contribution of nonbonded pairs (*120*). Briefly, for each Cα,i atom, the time-averaged distance to any other Cα,j atom that belongs to its SCS was obtained for the WT ($\overline{R}_{ij,\mathrm{WT}}$) and the studied mutants ($\overline{R}_{ij,\mathrm{mut}}$). Then, the difference ($\Delta\overline{R}_{ij}$) between $\overline{R}_{ij,\mathrm{WT}}$ and $\overline{R}_{ij,\mathrm{mut}}$ was calculated, where $\Delta\overline{R}_{ij} = \overline{R}_{ij,\mathrm{WT}} - \overline{R}_{ij,\mathrm{mut}}$. To this end, we first calculated for all residues the changes in the time-averaged distance between residue *i* and all *j* residues that belong to its SCS for the WT structure ($\overline{R}_{ij,\mathrm{WT}}$) and for all mutants ($\overline{R}_{ij,\mathrm{mut}}$). The obtained $\Delta\overline{R}_{ij}$ differences indicate the degree of distortion introduced by a specific mutation. Residue pairs (*i* and *j*) that have the largest positive ($\Delta\overline{R}_{ij} > 2.50$ Å) and negative distances ($\Delta\overline{R}_{ij} < -1.40$ Å) between WT and each mutant were highlighted.

Supplementary Materials

This PDF file includes:

Figs. S1 to S6
Tables S1 to S4
References

View/request a protocol for this paper from *Bio-protocol*.

References and Notes

1. W. D. Tilley, C. M. Wilson, M. Marcelli, M. J. McPhaul, Androgen receptor gene expression in human prostate carcinoma cell lines. *Cancer Res.* **17**, 5382–5386 (1990).
2. E. Estébanez-Perpiñá, C. L. Bevan, I. J. McEwan, Eighty years of targeting androgen receptor activity in prostate cancer: The fight goes on. *Cancers* **13**, 509 (2021).
3. A. Jiménez-Panizo, P. Pérez, A. M. Rojas, P. Fuentes-Prior, E. Estébanez-Perpiñá, Non-canonical dimerization of the androgen receptor and other nuclear receptors: Implications for human disease. *Endocr. Relat. Cancer* **26**, R479–R497 (2019).
4. X. Yu, P. Yi, R. A. Hamilton, H. Shen, M. Chen, C. E. Foulds, M. A. Mancini, S. J. Ludtke, Z. Wang, B. W. O'Malley, Structural insights of transcriptionally active, full-length androgen receptor coactivator complexes. *Mol. Cell* **79**, 812–823.e4 (2020).
5. P. L. Shaffer, A. Jivan, D. E. Dollins, F. Claessens, D. T. Gewirth, Structural basis of androgen receptor binding to selective androgen response elements. *Proc. Natl. Acad. Sci. U.S.A.* **101**, 4758–4763 (2004).
6. M. Nadal, S. Prekovic, N. Gallastegui, C. Helsen, M. Abella, K. Zielinska, M. Gay, M. Vilaseca, M. Taulès, A. B. Houtsmuller, M. E. van Royen, F. Claessens, P. Fuentes-Prior, E. Estébanez-Perpiñá, Structure of the homodimeric androgen receptor ligand-binding domain. *Nat. Commun.* **8**, 14388 (2017).

Downloaded from https://www.science.org on April 26, 2023

7. E. V. Wasmuth, A. Vanden Broeck, J. R. LaClair, E. A. Hoover, K. E. Lawrence, N. Paknejad, K. Pappas, D. Matthies, B. Wang, W. Feng, P. A. Watson, J. C. Zinder, W. R. Karthaus, M. J. de la Cruz, R. K. Hite, K. Manova-Todorova, Z. Yu, S. T. Weintraub, S. Klinge, C. L. Sawyers, Allosteric interactions prime androgen receptor dimerization and activation. *Mol. Cell.* **82**, 2021–2031 (2022).
8. K. E. Knudsen, T. M. Penning, Partners in crime: Deregulation of AR activity and androgen synthesis in prostate cancer. *Trends Endocrinol. Metab.* **21**, 315–324 (2010).
9. Y. Wen, M. C.-T. Hu, K. Makino, B. Spohn, G. Bartholomeusz, D. H. Yan, M. C. Hung, HER-2/neu promotes androgen-independent survival and growth of prostate cancer cells through the Akt pathway. *Cancer Res.* **60**, 6841–6845 (2000).
10. H. K. Lin, S. Yeh, H. Y. Kang, C. Chang, Akt suppresses androgen-induced apoptosis by phosphorylating and inhibiting androgen receptor. *Proc. Natl. Acad. Sci. U.S.A.* **98**, 7200–7205 (2001).
11. H. K. Lin, Y. C. Hu, L. Yang, S. Altuwaijri, Y. T. Chen, H. Y. Kang, C. Chang, Suppression versus induction of androgen receptor functions by the phosphatidylinositol 3-Kinase/Akt pathway in prostate cancer LNCaP cells with different passage numbers. *J. Biol. Chem.* **278**, 50902–50907 (2003).
12. S. S. Taneja, S. Ha, N. K. Swenson, H. Y. Huang, P. Lee, J. Melamed, E. Shapiro, M. J. Garabedian, S. K. Logan, Cell-specific regulation of androgen receptor phosphorylation in vivo. *J. Biol. Chem.* **280**, 40916–40924 (2005).
13. K. Xu, H. Shimelis, D. E. Linn, R. Jiang, X. Yang, F. Sun, Z. Guo, H. Chen, W. Li, H. Chen, X. Kong, J. Melamed, S. Fang, Z. Xiao, T. D. Veenstra, Y. Qiu, Regulation of androgen receptor transcriptional activity and specificity by RNF6-induced ubiquitination. *Cancer Cell* **15**, 270–282 (2009).
14. D. E. Linn, X. Yang, Y. Xie, A. Alfano, D. Deshmukh, X. Wang, H. Shimelis, H. Chen, W. Li, K. Xu, M. Chen, Y. Qiu, Differential regulation of androgen receptor by PIM-1 kinases via phosphorylation-dependent recruitment of distinct ubiquitin E3 ligases. *J. Biol. Chem.* **287**, 22959–22968 (2012).
15. D. Gioeli, B. M. Paschal, Post-translational modification of the androgen receptor. *Mol. Cell. Endocrinol.* **352**, 70–78 (2012).
16. T. van der Steen, D. J. Tindall, H. Huang, Posttranslational modification of the androgen receptor in prostate cancer. *Int. J. Mol. Sci.* **14**, 14833–14859 (2013).
17. Y. Koryakina, H. Q. Ta, D. Gioeli, Androgen receptor phosphorylation: Biological context and functional consequences. *Endocr. Relat. Cancer* **21**, T131–T145 (2014).
18. Z. Mounir, J. M. Korn, T. Westerling, F. Lin, C. A. Kirby, M. Schirle, G. McAllister, G. Hoffman, N. Ramadan, A. Hartung, Y. Feng, D. R. Kipp, C. Quinn, M. Fodor, J. Baird, M. Schoumacher, R. Meyer, J. Deeds, G. Buchwalter, T. Stams, N. Keen, W. R. Sellers, M. Brown, R. A. Pagliarini, ERG signaling in prostate cancer is driven through PRMT5-dependent methylation of the androgen receptor. *eLife* **5**, e13964 (2016).
19. L. Malbeteau, H. T. Pham, L. Eve, M. R. Stallcup, C. Poulard, M. Le Romancer, How protein methylation regulates steroid receptor function. *Endocr. Rev.* **43**, 160–197 (2022).
20. Q. Wang, W. Li, X. S. Liu, J. S. Carroll, O. A. Jänne, E. K. Keeton, A. M. Chinnaiyan, K. J. Pienta, M. Brown, A hierarchical network of transcription factors governs androgen receptor-dependent prostate cancer growth. *Mol. Cell* **27**, 380–392 (2007).
21. D. Robinson, E. M. Van Allen, Y. M. Wu, N. Schultz, R. J. Lonigro, J. M. Mosquera, B. Montgomery, M. E. Taplin, C. C. Pritchard, G. Attard, H. Beltran, W. Abida, R. K. Bradley, J. Vinson, X. Cao, P. Vats, L. P. Kunju, M. Hussain, F. Y. Feng, S. A. Tomlins, K. A. Cooney, D. C. Smith, C. Brennan, J. Siddiqui, R. Mehra, Y. Chen, D. E. Rathkopf, M. J. Morris, S. B. Solomon, J. C. Durack, V. E. Reuter, A. Gopalan, J. Gao, M. Loda, R. T. Lis, M. Bowden, S. P. Balk, G. Gaviola, C. Sougnez, M. Gupta, E. Y. Yu, E. A. Mostaghel, H. H. Cheng, H. Mulcahy, L. D. True, S. R. Plymate, H. Dvinge, R. Ferraldeschi, P. Flohr, S. Miranda, Z. Zafeiriou, N. Tunariu, J. Mateo, R. Perez-Lopez, F. Demichelis, B. D. Robinson, M. Schiffman, D. M. Nanus, S. T. Tagawa, A. Sigaras, K. W. Eng, O. Elemento, A. Sboner, E. I. Heath, H. I. Scher, K. J. Pienta, P. Kantoff, J. S. De Bono, M. A. Rubin, P. S. Nelson, L. A. Garraway, C. L. Sawyers, A. M. Chinnaiyan, Integrative clinical genomics of advanced prostate cancer. *Cell* **161**, 1215–1228 (2015).
22. D. A. Quigley, H. X. Dang, S. G. Zhao, P. Lloyd, R. Aggarwal, J. J. Alumkal, A. Foye, V. Kothari, M. D. Perry, A. M. Bailey, D. Playdle, T. J. Barnard, L. Zhang, J. Zhang, J. F. Youngren, M. P. Cieslik, A. Parolia, T. M. Beer, G. Thomas, K. N. Chi, M. Gleave, N. A. Lack, A. Zoubeidi, R. E. Reiter, M. B. Rettig, O. Witte, C. J. Ryan, L. Fong, W. Kim, T. Friedlander, J. Chou, H. Li, R. Das, H. Li, R. Moussavi-Baygi, H. Goodarzi, L. A. Gilbert, P. N. Lara, C. P. Evans, T. C. Goldstein, J. M. Stuart, S. A. Tomlins, D. E. Spratt, R. K. Cheetham, D. T. Cheng, K. Farh, J. S. Gehring, J. Hakenberg, A. Liao, P. G. Febbo, Genomic hallmarks and structural variation in metastatic prostate cancer. *Cell* **174**, 758–769.e9 (2018).
23. D. B. Lubahn, T. R. Brown, J. A. Simental, H. N. Higgs, C. J. Migeon, E. M. Wilson, F. S. French, Sequence of the intron/exon junctions of the coding region of the human androgen receptor gene and identification of a point mutation in a family with complete androgen insensitivity. *Proc. Natl. Acad. Sci. U.S.A.* **86**, 9534–9538 (1989).
24. O. Hiort, G. H. Sinnecker, P. M. Holterhus, E. M. Nitsche, K. Kruse, The clinical and molecular spectrum of androgen insensitivity syndromes. *Am. J. Med. Genet.* **63**, 218–222 (1996).
25. I. A. Hughes, J. D. Davies, T. I. Bunch, V. Pasterski, K. Mastroyannopoulou, J. Macdougall, Androgen insensitivity syndrome. *Lancet* **380**, 1419–1428 (2012).
26. C. E. Bohl, W. Gao, D. D. Miller, C. E. Bell, J. T. Dalton, Structural basis for antagonism and resistance of bicalutamide in prostate cancer. *Proc. Natl. Acad. Sci. U.S.A.* **102**, 6201–6206 (2005).
27. C. E. Bohl, Z. Wu, D. D. Miller, C. E. Bell, J. T. Dalton, Crystal structure of the T877A human androgen receptor ligand-binding domain complexed to cyproterone acetate provides insight for ligand-induced conformational changes and structure-based drug design. *J. Biol. Chem.* **282**, 13648–13655 (2007).
28. J. S. Sack, K. F. Kish, C. Wang, R. M. Attar, S. E. Kiefer, Y. An, G. Y. Wu, J. E. Scheffler, M. E. Salvati, J. Krystek, R. Weinmann, H. M. Einspahr, Crystallographic structures of the ligand-binding domains of the androgen receptor and its T877A mutant complexed with the natural agonist dihydrotestosterone. *Proc. Natl. Acad. Sci. U.S.A.* **98**, 4904–4909 (2001).
29. B. Gottlieb, L. K. Beitel, A. Nadarajah, M. Paliouras, M. Trifiro, The androgen receptor gene mutations database: 2012 update. *Hum. Mutat.* **33**, 887–894 (2012).
30. Z. Culig, A. Hobisch, M. Erdel, G. Bartsch, H. Klocker, Studies on androgen receptor mutations and amplification in human prostate cancer. *Methods Mol. Med.* **81**, 267–275 (2003).
31. E. R. Hyytinen, K. Haapala, J. Thompson, I. Lappalainen, M. Roiha, I. Rantala, H. J. Helin, O. A. Jänne, M. Vihinen, J. J. Palvimo, P. A. Koivisto, Pattern of somatic androgen receptor gene mutations in patients with hormone-refractory prostate cancer. *Lab. Invest.* **82**, 1591–1598 (2002).
32. M. J. McPhaul, M. Marcelli, S. Zoppi, C. M. Wilson, J. E. Griffin, J. D. Wilson, Mutations in the ligand-binding domain of theandrogen receptor gene cluster in two regions of the gene. *J. Clin. Invest.* **90**, 2097–2101 (1992).
33. C. Radmayr, Z. Culig, A. Hobisch, S. Corvin, G. Bartsch, H. Klocker, Analysis of a mutant androgen receptor offers a treatment modality in a patient with partial androgen insensitivity syndrome. *Eur. Urol.* **33**, 222–226 (1998).
34. T. R. Brown, D. B. Lubahn, E. M. Wilson, F. S. French, C. J. Migeon, J. L. Corden, Functional characterization of naturally occurring mutant androgen receptors from subjects with complete androgen insensitivity. *Mol. Endocrinol.* **4**, 1759–1772 (1990).
35. J. M. Lobaccaro, S. Lumbroso, R. Ktari, R. Dumas, C. Sultan, An exonic point mutation creates a *Mae*III site in the androgen receptor gene of a family with complete androgen insensitivity syndrome. *Hum. Mol. Genet.* **2**, 1041–1043 (1993).
36. Y.-H. Liu, C. Li, S.-F. Zhou, Prediction of deleterious functional effects of non-synonymous single nucleotide polymorphisms in human nuclear receptor genes using a bioinformatics approach. *Drug Metab. Lett.* **3**, 242–286 (2009).
37. R. Tadokoro-Cuccaro, T. I. Bunch, J. W. Schwabe, I. A. Hughes, J. C. Murphy, Comparison of the molecular consequences of different mutations at residue 754 and 690 of the androgen receptor (AR) and androgen insensitivity syndrome (AIS) phenotype. *Clin. Endocrinol.* **71**, 253–260 (2009).
38. M. Marcelli, M. Ittmann, S. Mariani, R. Sutherland, R. Nigam, L. Murthy, Y. Zhao, D. Diconcini, E. Puxeddu, A. Esen, J. Eastham, N. L. Weigel, D. J. Lamb, Androgen receptor mutations in prostate cancer. *Cancer Res.* **60**, 944–949 (2000).
39. X. B. Shi, A. H. Ma, L. Xia, H. J. Kung, R. W. De Vere White, Functional analysis of 44 mutant androgen receptors from human prostate cancer. *Cancer Res.* **62**, 1496–1502 (2002).
40. X. E. Zhou, K. M. Suino-Powell, J. Li, Y. He, J. P. MacKeigan, K. Melcher, E. L. Yong, H. E. Xu, Identification of SRC3/AIB1 as a preferred coactivator for hormone-activated androgen receptor. *J. Biol. Chem.* **285**, 9161–9171 (2010).
41. S. Grosdidier, L. R. Carbó, V. Buzón, G. Brooke, P. Nguyen, J. D. Baxter, C. L. Bevan, P. Webb, E. Estébanez-Perpiñá, J. Fernández-Recio, Allosteric conversation in the androgen receptor ligand-binding domain surfaces. *Mol. Endocrinol.* **26**, 1078–1090 (2012).
42. C. W. Hay, I. J. McEwan, The impact of point mutations in the human androgen receptor: Classification of mutations on the basis of transcriptional activity. *PLOS ONE* **7**, e32514 (2012).
43. M. J. McPhaul, M. Marcelli, W. D. Tilley, J. E. Griffin, R. F. Isidro-Gutierrez, J. D. Wilson, Molecular basis of androgen resistance in a family with a qualitative abnormality of the androgen receptor and responsive to high-dose androgen therapy. *J. Clin. Invest.* **87**, 1413–1421 (1991).
44. I. Murono, B. B. Mendonca, I. J. Arnhold, A. C. Rigon, C. J. Migeon, T. R. Brown, Human androgen insensitivity due to point mutations encoding amino acid substitutions in the androgen receptor steroid-binding domain. *Hum. Mutat.* **6**, 152–162 (1995).
45. C. A. Quigley, A. De Bellis, K. B. Marschke, M. K. El-Awady, E. M. Wilson, F. S. French, Androgen receptor defects: Historical, clinical, and molecular perspectives. *Endocr. Rev.* **16**, 271–321 (1995).
46. E. Langley, J. A. Kemppainen, E. M. Wilson, Intermolecular NH2–/carboxyl-terminal interactions in androgen receptor dimerization revealed by mutations that cause androgen insensitivity. *J. Biol. Chem.* **273**, 92–101 (1998).

Downloaded from https://www.science.org on April 26, 2023

47. K. F. Melo, B. B. Mendonca, A. E. C. Billerbeck, E. M. Costa, M. Inácio, F. A. Silva, A. M. Leal, A. C. Latronico, I. J. Arnhold, Clinical, hormonal, behavioral, and genetic characteristics of androgen insensitivity syndrome in a Brazilian cohort: Five novel mutations in the androgen receptor gene. *J. Clin. Endocrinol. Metab.* **88**, 3241–3250 (2003).
48. I. Jääskeläinen, A. Deeb, J. W. Schwabe, N. P. Mongan, H. Martin, I. A. Hughes, Human androgen receptor gene ligand-binding-domain mutations leading to disrupted interaction between the N- and C-terminal domains. *J. Mol. Endocrinol.* **36**, 361–368 (2006).
49. J. Batch, D. Williams, H. Davies, B. Brown, B. A. Evans, I. A. Hughes, M. Patterson, Androgen receptor gene mutations identified by SSCP in fourteen subjects with androgen insensitivity syndrome. *Hum. Mol. Genet.* **1**, 497–503 (1992).
50. C. L. Bevan, B. B. Brown, H. R. Davies, B. A. Evans, I. A. Hughes, M. N. Patterson, Functional analysis of six androgen receptor mutations identified in patients with partial androgen insensitivity syndrome. *Hum. Mol. Genet.* **5**, 265–273 (1996).
51. Q. Wang, F. J. Ghadessy, A. Trounson, D. de Kretser, R. McLachlan, S. Ng, E. Yong, Azoospermia associated with a mutation in the ligand-binding domain of an androgen receptor displaying normal ligand binding, but defective trans-activation. *J. Clin. Endocrinol. Metab.* **83**, 4303–4309 (1998).
52. O. Hiort, P.-M. Holterhus, T. Horter, W. Schulze, B. Kremke, M. Bals-Pratsch, G. H. G. Sinnecker, K. Kruse, Significance of Mutations in the Androgen Receptor Gene in Males with Idiopathic infertility. *J. Clin. Endocrinol. Metab.* **85**, 2810–2815 (2000).
53. N. Kalfa, P. Philibert, R. Werner, F. Audran, A. Bashamboo, H. Lehors, M. Haddad, J. M. Guys, R. Reynaud, P. Alessandrini, K. Wagner, J. Y. Kurzenne, F. Bastiani, J. Bréaud, J. S. Valla, G. M. Lacombe, M. Orsini, J. P. Daures, O. Hiort, F. Paris, K. McElreavey, C. Sultan, Minor hypospadias: The "Tip of the Iceberg" of the partial androgen insensitivity syndrome. *PLOS ONE* **8**, e61824 (2013).
54. J. Qi, M. Tripathi, R. Mishra, N. Sahgal, L. Fazil, S. Ettinger, W. J. Placzek, G. Claps, L. W. Chung, D. Bowtell, M. Gleave, N. Bhowmick, Z. A. Ronai, The E3 ubiquitin ligase siah2 contributes to castration-resistant prostate cancer by regulation of androgen receptor transcriptional activity. *Cancer Cell* **23**, 332–346 (2013).
55. R. Kumar, J. Mendonca, O. Owoyemi, K. Boyapati, N. Thomas, S. Kanacharoen, M. Coffey, D. Topiwala, C. Gomes, B. Ozbek, T. Jones, M. Rosen, L. Dong, S. Wiens, W. N. Brennen, J. T. Isaacs, A. M. D. Marzo, M. C. Markowski, E. S. Antonarakis, D. Z. Qian, K. J. Pienta, D. M. Pardoll, M. A. Carducci, S. R. Denmeade, S. K. Kachhap, Supraphysiologic testosterone induces ferroptosis and activates immune pathways through nucleophagy in prostate cancer. *Cancer Res.* **81**, 5948–5962 (2021).
56. H. M. Lam, H. M. Nguyen, M. P. Labrecque, L. G. Brown, I. M. Coleman, R. Gulati, B. Lakely, D. Sondheim, P. Chatterjee, B. T. Marck, A. M. Matsumoto, E. A. Mostaghel, M. T. Schweizer, P. S. Nelson, E. Corey, Durable response of enzalutamide-resistant prostate cancer to supraphysiological testosterone is associated with a multifaceted growth suppression and impaired DNA damage response transcriptomic program in patient-derived xenografts. *Eur. Urol.* **77**, 144–155 (2020).
57. L. Garcia-Alonso, C. H. Holland, M. M. Ibrahim, D. Turei, J. Saez-Rodriguez, Benchmark and integration of resources for the estimation of human transcription factor activities. *Genome Res.* **29**, 1363–1375 (2019).
58. A. Aytes, A. Mitrofanova, C. Lefebvre, M. J. Alvarez, M. Castillo-Martin, T. Zheng, J. A. Eastham, A. Gopalan, K. J. Pienta, M. M. Shen, A. Califano, C. Abate-Shen, Cross-species regulatory Network Analysis identifies a synergistic interaction between FOXM1 and CENPF that drives prostate cancer malignancy. *Cancer Cell* **25**, 638–651 (2014).
59. H. Takahashi, M. Furusato, W. C. Allsbrook, H. Nishii, S. Wakui, J. C. Barrett, J. Boyd, Prevalence of androgen receptor gene mutations in latent prostatic carcinomas from japanese men. *Cancer Res.* **55**, 1621–1624 (1995).
60. W. Weidemann, B. Linck, H. Haupt, B. Mentrup, G. Romalo, K. Stockklauser, A. O. Brinkmann, H. U. Schweikert, K. D. Spindler, Clinical and biochemical investigations and molecular analysis of subjects with mutations in the androgen receptor gene. *Clin. Endocrinol.* **45**, 733–739 (1996).
61. J. Thompson, F. Saatcioglu, O. A. Jänne, J. J. Palvimo, Disrupted amino- and carboxyl-terminal interactions of the androgen receptor are linked to androgen insensitivity. *Mol. Endocrinol.* **15**, 923–935 (2001).
62. O. A. O'Mahony, M. P. Steinkamp, M. A. Albertelli, M. Brogley, H. Rehman, D. M. Robins, Profiling human androgen receptor mutations reveals treatment effects in a mouse model of prostate cancer. *Mol. Cancer Res.* **6**, 1691–1701 (2008).
63. E. Estébanez-Perpiñá, L. A. Arnold, P. Nguyen, E. D. Rodrigues, E. Mar, R. Bateman, P. Pallai, K. M. Shokat, J. D. Baxter, R. K. Guy, P. Webb, R. J. Fletterick, A surface on the androgen receptor that allosterically regulates coactivator binding. *Proc. Natl. Acad. Sci. U.S.A.* **104**, 16074–16079 (2007).
64. A. Jiménez-Panizo, A. Alegre-Martí, T. T. Tettey, G. Fettweis, M. Abella, R. Antón, T. A. Johnson, S. Kim, R. L. Schiltz, I. Núñez-Barrios, J. Font-Díaz, C. Caelles, A. F. Valledor, P. Pérez, A. M. Rojas, J. Fernández-Recio, D. M. Presman, G. L. Hager, P. Fuentes-Prior, E. Estébanez-Perpiñá, The multivalency of the glucocorticoid receptor ligand-binding domain explains its manifold physiological activities. *Nucleic Acids Res.* **50**, gkac1119 (2022).
65. S. Grosdidier, J. Fernández-Recio, Identification of hot-spot residues in protein-protein interactions by computational docking. *BMC Bioinformatics* **9**, 447 (2008).
66. J. Fernandez-Recio, M. Totrov, C. Skorodumov, R. Abagyan, Optimal docking area: A new method for predicting protein-protein interaction sites. *Proteins* **58**, 134–143 (2005).
67. L. Sun, M. Wang, Z. Lv, N. Yang, Y. Liu, S. Bao, W. Gong, R. M. Xu, Structural insights into protein arginine symmetric dimethylation by PRMT5. *Proc. Natl. Acad. Sci. U.S.A.* **108**, 20538–20543 (2011).
68. S. Antonysamy, Z. Bonday, R. M. Campbell, B. Doyle, Z. Druzina, T. Gheyi, B. Han, L. N. Jungheim, Y. Qian, C. Rauch, M. Russell, J. M. Sauder, S. R. Wasserman, K. Weichert, F. S. Willard, A. Zhang, S. Emtage, Crystal structure of the human PRMT5:MEP50 complex. *Proc. Natl. Acad. Sci. U.S.A.* **109**, 17960–17965 (2012).
69. M. C. Ho, C. Wilczek, J. B. Bonanno, L. Xing, J. Seznec, T. Matsui, L. G. Carter, T. Onikubo, P. R. Kumar, M. K. Chan, M. Brenowitz, R. H. Cheng, U. Reimer, S. C. Almo, D. Shechter, Structure of the arginine methyltransferase PRMT5-MEP50 reveals a mechanism for substrate specificity. *PLOS ONE* **8**, e57008 (2013).
70. K. M. Mulvaney, C. Blomquist, N. Acharya, R. Li, M. J. Ranaghan, M. O'Keefe, D. J. Rodriguez, M. J. Young, D. Kesar, D. Pal, M. Stokes, A. J. Nelson, S. S. Jain, A. Yang, Z. Mullin-Bernstein, J. Columbus, F. K. Bozal, A. Skepner, D. Raymond, S. LaRussa, D. C. McKinney, Y. Freyzon, Y. Baidi, D. Porter, A. J. Aguirre, A. Ianari, B. McMillan, W. R. Sellers, Molecular basis for substrate recruitment to the PRMT5 methylosome. *Mol. Cell* **81**, 3481–3495.e7 (2021).
71. M. T. Schweizer, E. S. Antonarakis, H. Wang, A. Seun Ajiboye, A. Spitz, H. Cao, J. Luo, M. C. Haffner, S. Yegnasubramanian, M. A. Carducci, M. A. Eisenberger, J. T. Isaacs, S. R. Denmeade, Effect of bipolar androgen therapy for asymptomatic men with castration-resistant prostate cancer: Results from a pilot clinical study. *Sci. Transl. Med.* **7**, 269ra2 (2015).
72. M. D. Nyquist, L. S. Ang, A. Corella, I. M. Coleman, M. P. Meers, A. J. Christiani, C. Pierce, D. H. Janssens, H. E. Meade, A. Bose, L. Brady, T. Howard, N. De Sarkar, S. B. Frank, R. F. Dumpit, J. T. Dalton, E. Corey, S. R. Plymate, M. C. Haffner, E. A. Mostaghel, P. S. Nelson, Selective androgen receptor modulators activate the canonical prostate cancer androgen receptor program and repress cancer growth. *J. Clin. Invest.* **131**, e146777 (2021).
73. X. Qiu, L. G. Brown, J. L. Conner, H. M. Nguyen, N. Boufaied, S. A. Alaiwi, J. H. Seo, T. El Zarif, C. Bell, E. O'Connor, B. Hanratty, M. Pomerantz, M. L. Freedman, M. Brown, M. C. Haffner, P. S. Nelson, F. Y. Feng, D. P. Labbé, H. W. Long, E. Corey, Response to supraphysiological testosterone is predicted by a distinct androgen receptor cistrome. *JCI Insight* **7**, e157164 (2022).
74. V. Sheikhhassani, B. Scalvini, J. Ng, L. W. H. J. Heling, Y. Ayache, T. M. J. Evers, E. Estébanez-Perpiñá, I. J. McEwan, A. Mashaghi, Topological dynamics of an intrinsically disordered N-terminal domain of the human androgen receptor. *Protein Sci.* **31**, e4334 (2022).
75. S. A. Mosure, P. Munoz-Tello, K.-T. Kuo, B. M. Tavish, X. Yu, D. Scholl, C. C. Williams, T. S. Strutzenberg, J. Bass, R. Brust, A. A. Deniz, P. R. Griffin, D. J. Kojetin, Structural basis of interdomain communication in PPARγ (2022); www.biorxiv.org/content/10.1101/2022.07.13.499031v1.abstract.
76. X. Zhang, X. Cheng, Structure of the predominant protein arginine methyltransferase PRMT1 and analysis of its binding to substrate Peptides. *Structure* **11**, 509–520 (2003).
77. D. Musiani, J. Bok, E. Massignani, L. Wu, T. Tabaglio, M. R. Ippolito, A. Cuomo, U. Ozbek, H. Zorgati, U. Ghoshdastider, R. C. Robinson, E. Guccione, T. Bonaldi, Proteomics profiling of arginine methylation defines PRMT5 substrate specificity. *Sci. Signal.* **12**, eaat8388 (2019).
78. E. S. Burgos, C. Wilczek, T. Onikubo, J. B. Bonanno, J. Jansong, U. Reimer, D. Shechter, Histone H2A and H4 N-terminal tails are positioned by the MEP50 WD repeat protein for efficient methylation by the PRMT5 arginine methyltransferase. *J. Biol. Chem.* **290**, 9674–9689 (2015).
79. P. Chymkowitch, N. Le May, P. Charneau, E. Compe, J. M. Egly, The phosphorylation of the androgen receptor by TFIIH directs the ubiquitin/proteasome process. *EMBO J.* **30**, 468–479 (2011).
80. S. Sarkar, D. L. Brautigan, S. J. Parsons, J. M. Larner, Androgen receptor degradation by the E3 ligase CHIP modulates mitotic arrest in prostate cancer cells. *Oncogene* **33**, 26–33 (2014).
81. C. Liu, W. Lou, J. C. Yang, L. Liu, C. M. Armstrong, A. P. Lombard, R. Zhao, O. D. V. Noel, C. G. Tepper, H. W. Chen, M. Dall'Era, C. P. Evans, A. C. Gao, Proteostasis by STUB1/HSP70 complex controls sensitivity to androgen receptor targeted therapy in advanced prostate cancer. *Nat. Commun.* **9**, 4700 (2018).
82. M. L. Mohler, A. Sikdar, S. Ponnusamy, D. J. Hwang, Y. He, D. D. Miller, R. Narayanan, An overview of next-generation androgen receptor-targeted therapeutics in development for the treatment of prostate cancer. *Int. J. Mol. Sci.* **22**, 2124 (2021).
83. S. Ha, G. Luo, H. Xiang, A comprehensive overview of small-molecule androgen receptor degraders: Recent progress and future perspectives. *J. Med. Chem.* **65**, 16128–16154 (2022).

Downloaded from https://www.science.org on April 26, 2023

84. X. Deng, G. Shao, H. T. Zhang, C. Li, D. Zhang, L. Cheng, B. D. Elzey, R. Pili, T. L. Ratliff, J. Huang, C. D. Hu, Protein arginine methyltransferase 5 functions as an epigenetic activator of the androgen receptor to promote prostate cancer cell growth. *Oncogene* **36**, 1223–1231 (2017).
85. K. Hosohata, P. Li, Y. Hosohata, J. Qin, R. G. Roeder, Z. Wang, Purification and identification of a novel complex which is involved in androgen receptor-dependent transcription. *Mol. Cell. Biol.* **23**, 7019–7029 (2003).
86. Y. Peng, F. Chen, J. Melamed, L. Chiriboga, J. Wei, X. Kong, M. Mcleod, Y. Li, C. X. Li, A. Feng, M. J. Garabedian, Z. Wang, R. G. Roeder, P. Lee, Distinct nuclear and cytoplasmic functions of androgen receptor cofactor p44 and association with androgen-independent prostate cancer. *Proc. Natl. Acad. Sci. U.S.A.* **105**, 5236–5241 (2008).
87. L. Zhou, H. Wu, P. Lee, Z. Wang, Roles of the androgen receptor cofactor p44 in the growth of prostate epithelial cells. *J. Mol. Endocrinol.* **37**, 283–300 (2006).
88. S. Yin, L. Liu, C. Brobbey, V. Palanisamy, LE. Ball, S. K. Olsen, M. C. Ostrowski, W. Gan, PRMT5-mediated arginine methylation activates AKT kinase to govern tumorigenesis. *Nat. Commun* **12**, 1–13 (2021).
89. C. Helsen, T. Nguyen, T. Vercruysse, S. Wouters, D. Daelemans, A. Voet, F. Claessens, The T850D phosphomimetic mutation in the androgen receptor ligand binding domain enhances recruitment at activation function 2. *Int. J. Mol. Sci.* **23**, 1557 (2022).
90. I. Maksimovic, Y. David, Non-enzymatic covalent modifications as a new chapter in the histone code. *Trends Biochem. Sci.* **46**, 718–730 (2021).
91. H. S. Soifer, N. Souleimanian, S. Wu, A. M. Voskresenskiy, F. K. Collak, B. Cinar, C. A. Stein, Direct regulation of androgen receptor activity by potent CYP17 inhibitors in prostate cancer cells. *J. Biol. Chem.* **287**, 3777–3787 (2012).
92. A. Dobin, C. A. Davis, F. Schlesinger, J. Drenkow, C. Zaleski, S. Jha, P. Batut, M. Chaisson, T. R. Gingeras, STAR: Ultrafast universal RNA-seq aligner. *Bioinformatics* **29**, 15–21 (2013).
93. A. Frankish, M. Diekhans, A. M. Ferreira, R. Johnson, I. Jungreis, J. Loveland, J. M. Mudge, C. Sisu, J. Wright, J. Armstrong, I. Barnes, A. Berry, A. Bignell, S. Carbonell Sala, J. Chrast, F. Cunningham, T. Di Domenico, S. Donaldson, I. T. Fiddes, C. García Girón, J. M. Gonzalez, T. Grego, M. Hardy, T. Hourlier, T. Hunt, O. G. Izuogu, J. Lagarde, F. J. Martin, L. Martínez, S. Mohanan, P. Muir, F. C. P. Navarro, A. Parker, B. Pei, F. Pozo, M. Ruffier, B. M. Schmitt, E. Stapleton, M. M. Suner, I. Sycheva, B. Uszczynska-Ratajczak, J. Xu, A. Yates, D. Zerbino, Y. Zhang, B. Aken, J. S. Choudhary, M. Gerstein, R. Guigó, T. J. P. Hubbard, M. Kellis, B. Paten, A. Reymond, M. L. Tress, P. Flicek, GENCODE reference annotation for the human and mouse genomes. *Nucleic Acids Res.* **47**, D766–D773 (2019).
94. V. Jimenez-Jacinto, A. Sanchez-Flores, L. Vega-Alvarado, Integrative differential expression analysis for multiple experiments (IDEAMEX): a web server tool for integrated RNA-seq data analysis. *Front. Genet.* **10**, 279 (2019).
95. M. I. Love, W. Huber, S. Anders, Moderated estimation of fold change and dispersion for RNA-seq data with DESeq2. *Genome Biol.* **15**, 550 (2014).
96. M. E. Ritchie, B. Phipson, D. Wu, Y. Hu, C. W. Law, W. Shi, G. K. Smyth, *limma* powers differential expression analyses for RNA-sequencing and microarray studies. *Nucleic Acids Res.* **43**, e47 (2015).
97. Z. Gu, R. Eils, M. Schlesner, Complex heatmaps reveal patterns and correlations in multidimensional genomic data. *Bioinformatics* **32**, 2847–2849 (2016).
98. S. Anders, W. Huber, Differential expression analysis for sequence count data. *Genome Biol.* **11**, R106 (2010).
99. A. Subramanian, P. Tamayo, V. K. Mootha, S. Mukherjee, B. L. Ebert, M. A. Gillette, A. Paulovich, S. L. Pomeroy, T. R. Golub, E. S. Lander, J. P. Mesirov, Gene set enrichment analysis: A knowledge-based approach for interpreting genome-wide expression profiles. *Proc. Natl. Acad. Sci. U.S.A.* **102**, 15545–15550 (2005).
100. T. Wu, E. Hu, S. Xu, M. Chen, P. Guo, Z. Dai, T. Feng, L. Zhou, W. Tang, L. Zhan, X. Fu, S. Liu, X. Bo, G. Yu, clusterProfiler 4.0: A universal enrichment tool for interpreting omics data. *Innovation* **2**, 100141 (2021).
101. M. Schubert, B. Klinger, M. Klünemann, A. Sieber, F. Uhlitz, S. Sauer, M. J. Garnett, N. Blüthgen, J. Saez-Rodriguez, Perturbation-response genes reveal signaling footprints in cancer gene expression. *Nat. Commun.* **9**, 20 (2018).
102. C. Poulard, J. Jacquemetton, T. H. Pham, M. Le Romancer, Using proximity ligation assay to detect protein arginine methylation. *Methods* **175**, 66–71 (2020).
103. J. Schindelin, I. Arganda-Carreras, E. Frise, V. Kaynig, M. Longair, T. Pietzsch, S. Preibisch, C. Rueden, S. Saalfeld, B. Schmid, J. Y. Tinevez, D. J. White, V. Hartenstein, K. Eliceiri, P. Tomancak, A. Cardona, Fiji: An open-source platform for biological-image analysis. *Nat. Methods* **9**, 676–682 (2012).
104. R. Gustafsson, U. Eckhard, W. Ye, E. D. Enbody, M. Pettersson, P. Jemth, L. Andersson, M. Selmer, Structure and characterization of phosphoglucomutase 5 from atlantic and baltic herring—An inactive enzyme with intact substrate binding. *Biomolecules.* **10**, 1631 (2020).
105. T. M. K. Cheng, T. L. Blundell, J. Fernandez-Recio, PyDock: Electrostatics and desolvation for effective scoring of rigid-body protein-protein docking. *Proteins Struct. Funct. Genet.* **68**, 503–515 (2007).
106. J. Fernández-Recio, M. Totrov, R. Abagyan, Identification of protein-protein interaction sites from docking energy landscapes. *J. Mol. Biol.* **335**, 843–865 (2004).
107. R. Guerois, J. E. Nielsen, L. Serrano, Predicting changes in the stability of proteins and protein complexes: A study of more than 1000 mutations. *J. Mol. Biol.* **320**, 369–387 (2002).
108. N. Halabi, O. Rivoire, S. Leibler, R. Ranganathan, Protein sectors: evolutionary units of three-dimensional structure. *Cell* **138**, 774–786 (2009).
109. S. W. Lockless, R. Ranganathan, Evolutionarily conserved pathways of energetic connectivity in protein families. *Science* **286**, 295–299 (1999).
110. O. Rivoire, K. A. Reynolds, R. Ranganathan, Evolution-based functional decomposition of proteins. *PLOS Comput. Biol.* **12**, e1004817 (2016).
111. J. Wang, R. M. Wolf, J. W. Caldwell, P. A. Kollman, D. A. Case, Development and testing of a general Amber force field. *J. Comput. Chem.* **25**, 1157–1174 (2004).
112. C. I. Bayly, P. Cieplak, W. D. Cornell, P. A. Kollman, A well-behaved electrostatic potential based method using charge restraints for deriving atomic charges: The RESP model. *J. Phys. Chem.* **97**, 10269–10280 (1993).
113. S. Izadi, R. Anandakrishnan, A. V. Onufriev, Building water models: A different approach. *J. Phys. Chem. Lett.* **5**, 3863–3871 (2014).
114. C. Tian, K. Kasavajhala, K. A. A. Belfon, L. Raguette, H. Huang, A. N. Migues, J. Bickel, Y. Wang, J. Pincay, Q. Wu, C. Simmerling, Ff19SB: Amino-acid-specific protein backbone parameters trained against quantum mechanics energy surfaces in solution. *J. Chem. Theory Comput.* **16**, 528–552 (2020).
115. T. Darden, D. York, L. Pedersen, Particle mesh Ewald: An *N*·log(*N*) method for Ewald sums in large systems. *J. Chem. Phys.* **98**, 10089–10092 (1993).
116. J. J. Perez, M. S. Tomas, J. Rubio-Martinez, Assessment of the sampling performance of multiple-copy dynamics versus a unique trajectory. *J. Chem. Inf. Model.* **56**, 1950–1962 (2016).
117. C. W. Hopkins, S. Le Grand, R. C. Walker, A. E. Roitberg, Long-time-step molecular dynamics through hydrogen mass repartitioning. *J. Chem. Theory Comput.* **11**, 1864–1874 (2015).
118. J. P. Ryckaert, G. Ciccotti, H. J. C. Berendsen, Numerical integration of the cartesian equations of motion of a system with constraints: Molecular dynamics of n-alkanes. *J. Comput. Phys.* **23**, 327–341 (1977).
119. S. Vatansever, B. Erman, Z. H. Gümüş, Oncogenic G12D mutation alters local conformations and dynamics of K-Ras. *Sci. Rep.* **9**, 11730 (2019).
120. A. R. Atilgan, P. Akan, C. Baysal, Small-world communication of residues and significance for protein dynamics. *Biophys. J.* **86**, 85–91 (2004).
121. Y. C. Yang, C. A. Banuelos, N. R. Mawji, J. Wang, M. Kato, S. Haile, I. J. McEwan, S. Plymate, M. D. Sadar, Targeting androgen receptor activation function-1 with EPI to overcome resistance mechanisms in castration-resistant prostate cancer. *Clin. Cancer Res.* **22**, 4466–4477 (2016).
122. N. G. R. D. Elshan, M. B. Rettig, M. E. Jung, Molecules targeting the androgen receptor (AR) signaling axis beyond the AR-Ligand binding domain. *Med. Res. Rev.* **39**, 910–960 (2019).

Acknowledgments: We thank J. Lüders (IRB) for critical comments and suggestions on the manuscript. We thank M. Taulès (CCiTUB), M. Vilaseca (MS facility), R. El Bizri, L. Franco (Idibell), and K. Kahlem (CNAG) for technical support. We thank ALBA-Cells synchrotron Xaloc team for beamline support. **Funding:** E.E.-P. thanks G. E. Carretero and A. T. Hagler for sponsorships, CaixaImpulse 2018-00018 La Caixa, and 2018-LLavor with 2017SGR1089 (to P.F.-P.; Generalitat de Catalunya). E.E.-P. thanks 2021SGR01433, BFU-Retos2017-86906-R, PDC2021-121688-100, and SAF2017-71878-REDT (Red Nacional de Receptores Nucleares, NurCaMeln) with SAF2019-REDT-Uroncomol (to A.A.; Red Nacional de Mecanismos Moleculares del Cáncer Urológico, Uroncomol), RTI2018-101500-B-I00 (to P.F.-P.), PID2019-110167RB-I00/AEI/10.13039/501100011033 (to J.F.-R.), and RTI2018-096735-B-100 (to A.R.; MINECO). A.A. thanks PI19/00342 and CPII20/00024 (Instituto de Salud Carlos III), W81XWH-18-1-0193 (Department of Defense), and 2017SGR448 (Generalitat de Catalunya). U.E. acknowledges support from the Spanish Ministry of Science and Innovation (RYC2020-029773-I and PID2021-128682OA-I00). M.N.P.-M. thanks Predocs-UB2020 5760700. J.R.-M. thanks grants 2021SGR00350 and CEX2021-001202-M. C.P. and M.L.R. were supported by financial support from ITMO Cancer of Aviesan within the framework of the 2021-2030 Cancer Control Strategy, on funds administered by Inserm. **Author contributions:** E.E.-P., P.F.-P., and A.A conceived and designed the initial project and supervised its overall execution, provided financial support, and share overall responsibility for the presented results and final approval of the article. A.A.-M., A.J.-P., M.A., and R.A. expressed and purified recombinant proteins. A.A.-M., A.J.-P., and M.A. performed crystallization trials. A.A.-M., A.J.-P., R.A., and E.E.-P. performed site-directed mutagenesis and protein analyses. A.A.-M. and U.E. conducted and analyzed DSF experiments. A.M.R. performed sequence and SCA analyses with A.J.-P. P.F.-P. and E.E.-P. interpreted sequence and SCA analyses. J.F.-R. performed docking,

Downloaded from https://www.science.org on April 26, 2023

NIP, and ODA calculations. J.F.-R., A.A.-M., P.F.-P., and E.E.-P. interpreted docking, NIP, and ODA calculations. A.A.-M., A.J.-P., R.A., P.F.-P., and E.E.-P. performed MS experiments and interpreted results. A.A.-M., A.J.-P., P.F.-P., and E.E.-P. collected x-ray crystallography diffraction data, P.F.-P. interpreted diffraction data and solved and refined 3D structures. P.F.-P., A.A.-M., A.J.-P., and E.E.-P. analyzed and interpreted the structures. A.A.-M., A.M.-T., M.C., and A.A. performed and supervised RNA-seq experiments with created stable PCa cell lines and performed transcription activity, anti-androgens, and cell proliferation assays. C.P. and M.L.R. performed analysis of AR-PRMT5 interactions and AR methylation in living cells using PLA assays. A.A. and J.M.P. advised on anti-androgen treatments and discussions on prostate cancer implications. J.R.-M. and M.N.P.-M. performed MD simulations and interpreted results with A.A.-M., J.F.-R., E.E.-P., and P.F.-P. E.E.-P., P.F.-P., and A.A. drafted the article. A.A.-M., A.J.-P., A.A., P.F.-P., and E.E.-P. critically reviewed the manuscript. All authors discussed the results and commented on the manuscript. **Competing interests:** The authors declare that they have no competing interests. **Data and materials availability:** All data needed to evaluate the conclusions in the paper are present in the paper and/or the Supplementary Materials. The atomic coordinates and structure factors reported here have been deposited in the PDB with the accession codes 7ZTZ (Y764C), 7ZU2 (Q799E), 7ZU1 (V758A), 7ZTX (F755V), and 7ZTV (F755L). The PDB accessibility has been designed "for immediate release on publication." The MS proteomics data have been deposited to the ProteomeXchange Consortium via the PRIDE partner repository with the dataset identifier PXD028039. The transcriptomic data have been deposited at the NCBI Gene Expression Omnibus (GEO) repository under the accession code GSE210393. Bioinformatics data and code for the clustering and sector analyses are available at Zenodo (DOI: 10.5281/zenodo.7274365).

Submitted 2 August 2022
Accepted 15 February 2023
Published 15 March 2023
10.1126/sciadv.ade2175

Downloaded from https://www.science.org on April 26, 2023

ScienceAdvances

A hotspot for posttranslational modifications on the androgen receptor dimer interface drives pathology and anti-androgen resistance

Andrea Alegre-Mart, Alba Jimnez-Panizo, Adrin Martnez-Tbar, Coralie Poulard, M. Nria Peralta-Moreno, Montserrat Abella, Rosa Antn, Marcos Chias, Ulrich Eckhard, Josep M. Piulats, Ana M. Rojas, Juan Fernndez-Recio, Jaime Rubio-Martnez, Muriel Le Romancer, Ivaro Aytes, Pablo Fuentes-Prior, and Eva Estbanez-Perpi

Sci. Adv., **9** (11), eade2175.
DOI: 10.1126/sciadv.ade2175

View the article online
https://www.science.org/doi/10.1126/sciadv.ade2175
Permissions
https://www.science.org/help/reprints-and-permissions

Downloaded from https://www.science.org on April 26, 2023

Use of this article is subject to the Terms of service

Science Advances (ISSN) is published by the American Association for the Advancement of Science. 1200 New York Avenue NW, Washington, DC 20005. The title *Science Advances* is a registered trademark of AAAS.
Copyright © 2023 The Authors, some rights reserved; exclusive licensee American Association for the Advancement of Science. No claim to original U.S. Government Works. Distributed under a Creative Commons Attribution NonCommercial License 4.0 (CC BY-NC).

Science Advances
AAAS

Supplementary Materials for

A hotspot for posttranslational modifications on the androgen receptor dimer interface drives pathology and resistance to antiandrogens

Andrea Alegre-Martí *et al.*

Corresponding author: Eva Estébanez-Perpiñá, evaestebanez@ub.edu;
Pablo Fuentes-Prior, fuentespriorpablo@gmail.com; Álvaro Aytes, aaytes@idibell.cat

Sci. Adv. **9**, eade2175 (2023)
DOI: 10.1126/sciadv.ade2175

This PDF file includes:

Figs. S1 to S6
Tables S1 to S4
References

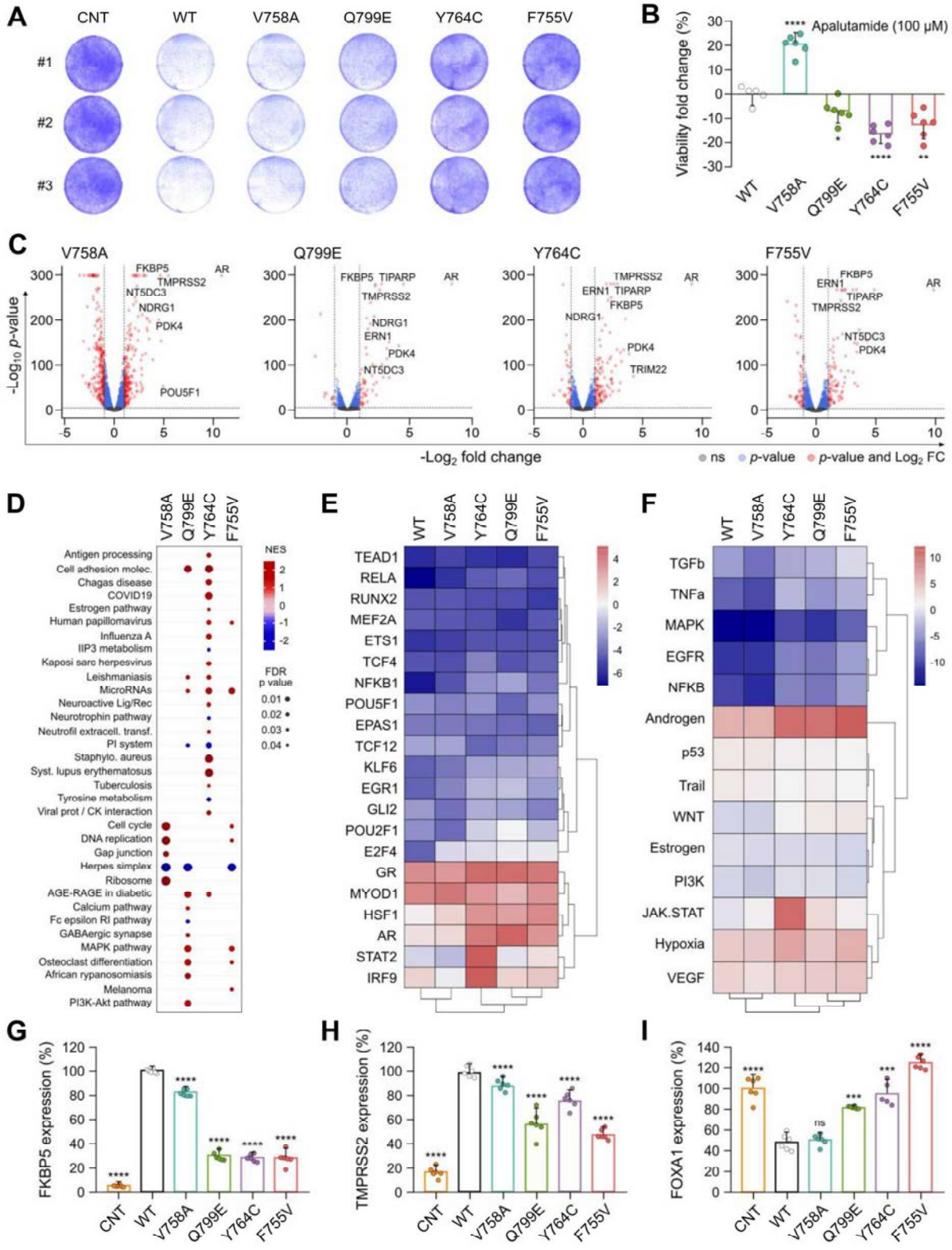

Fig. S1. The transcriptional profiles of AR-LBD dimerization surface mutants differ from that of the WT receptor.

Fig. S1 Legend. Summary of RNAseq experiments performed in triplicate for each cell line. **A,** Representative crystal violet-stained cultures used to quantitate the colony formation capacity of PC3 cells expressing WT or mutant AR. **B,** Relative viability fold change of CNT, WT, and mutant AR-transduced cells in response to the antiandrogen, apalutamide. **C,** Volcano plots showing the differential expression analysis between PC3-CNT and PC3-mut AR cells (V758A, Q799E, Y764C and F755V as indicated), using DESeq2 data. Genes with an absolute log2(fold change) ≥ 1 and a *p* value ≤ 0.05 are labeled in red. **D,** Analysis of the mutant AR signatures against WT AR on the KEEG Pathway database using GSEA. Note that the Y764C mutant is significantly enriched in pathways related to pathogen infection and immune response activation. Normalized Enrichment Score (NES) scale and False Discovery Rate (FDR) *p* value thresholds are indicated. **E,** Transcription factor regulon enrichment heatmap using DoRothEA. Regulons with an adjusted FDR *p* value ≤ 0.05 on the NES are shown. Note the strong enrichment of the STAT2 transcription factor in line with activation of the pathogen infection and inflammatory response pathways shown in (D). **F,** Pathway activity heatmap using the Pathway RespOnsive GENes for activity Inference (PROGENy) algorithm. In line with data shown in (D) and (E), the JAK/STAT pathway is significantly enriched in the Y764C mutant AR cells compared to both WT and other AR mutants. **G-H,** RT-qPCR validation of AR transcriptional activity using canonical targets FKBP5 (**G**) and TMPRSS2 (**H**). Also shown is the RT-qPCR validation for expression of the pioneer factor, FOXA1, in WT and mutant AR transduced cells (**I**). RT-qPCR measurements were conducted in triplicate (mean ± SD are shown) and differences against WT-AR cells were calculated using a t-test and considered significant at p values < 0.05. (*$p < 0.05$, ** $p < 0.01$, *** $p < 0.001$ and **** $p < 0.0001$).

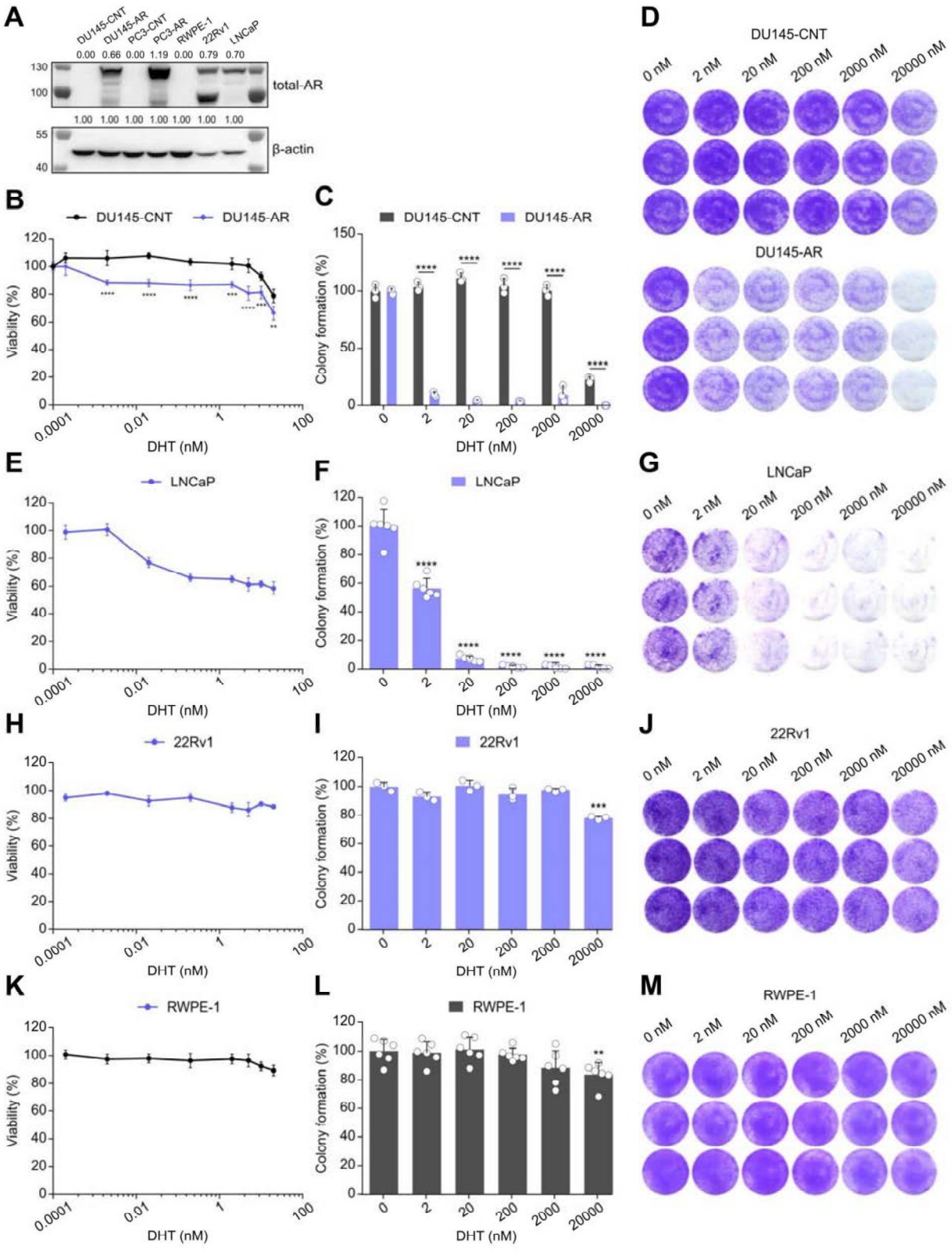

Fig. S2. Supraphysiological DHT concentrations suppress cell growth of AR-responsive cell lines.

Fig. S2 Legend. A, Western blot analysis of total AR in the cell lines and derivatives used in the current study. **B to D,** Analysis of the effect of AR expression in DU145 cells. **B,** Viability assays comparing parental and AR-expressing cells upon DHT treatment. **C and D**, Quantification and representative images of colony formation assays in parental and AR-expressing DU145 cells. Note the significant reduction in viability and clonogenicity in AR-expressing cells upon DHT stimulation. **E to G**, Analysis of the effect of AR expression in LNCaP cells. **E**, Viability assay of LNCaP cells upon DHT treatment. **F and G,** Quantification and representative images of colony formation assays in LNCaP cells. **H to J,** Analysis of the effect of AR expression in CRPC 22Rv1 cells**. H,** viability assays of 22Rv1 in response to DHT treatment. **I and J**, Quantification and representative images of colony formation assays in 22Rv1 cells. Note that 22Rv1 cells express the truncated AR variant lacking the LBD and therefore do not respond to DHT. **K to M,** Analysis of the effect of AR activation upon DHT treatment in AR-negative RWPE-1 cells. **K,** Viability assays of RWPE-1 cells upon DHT treatment. **L and M**, Quantification and representative images of colony formation assays in RWPE-1 cells. Note that in RWPE-1 cells do not express AR and similarly to parental PC3 and DU145 cells do not respond to DHT. Viability and clonogenic assays were conducted in n=3 or n=6 as indicated (mean ± SD are shown) and differences were calculated using a t-test and considered significant at p values < 0.05. (*$p < 0.05$, **$p < 0.01$, ***$p < 0.001$ and ****$p < 0.0001$).

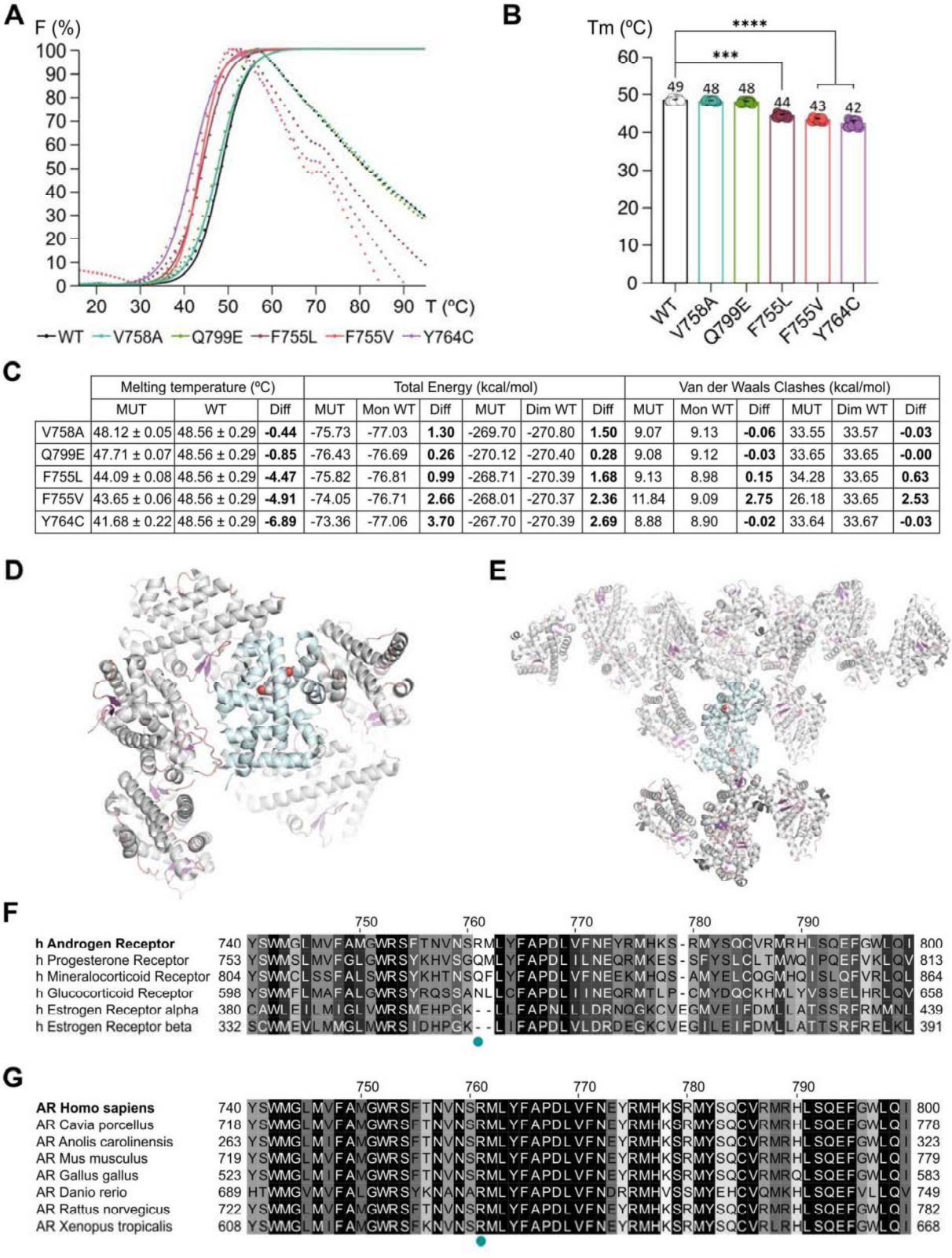

C

	Melting temperature (°C)			Total Energy (kcal/mol)						Van der Waals Clashes (kcal/mol)					
	MUT	WT	Diff	MUT	Mon WT	Diff	MUT	Dim WT	Diff	MUT	Mon WT	Diff	MUT	Dim WT	Diff
V758A	48.12 ± 0.05	48.56 ± 0.29	**-0.44**	-75.73	-77.03	**1.30**	-269.70	-270.80	**1.50**	9.07	9.13	**-0.06**	33.55	33.57	**-0.03**
Q799E	47.71 ± 0.07	48.56 ± 0.29	**-0.85**	-76.43	-76.69	**0.26**	-270.12	-270.40	**0.28**	9.08	9.12	**-0.03**	33.65	33.65	**-0.00**
F755L	44.09 ± 0.08	48.56 ± 0.29	**-4.47**	-75.82	-76.81	**0.99**	-268.71	-270.39	**1.68**	9.13	8.98	**0.15**	34.28	33.65	**0.63**
F755V	43.65 ± 0.06	48.56 ± 0.29	**-4.91**	-74.05	-76.71	**2.66**	-268.01	-270.37	**2.36**	11.84	9.09	**2.75**	26.18	33.65	**2.53**
Y764C	41.68 ± 0.22	48.56 ± 0.29	**-6.89**	-73.36	-77.06	**3.70**	-267.70	-270.39	**2.69**	8.88	8.90	**-0.02**	33.64	33.67	**-0.03**

Fig. S3. In solution and *in silico* characterization of AR-LBD dimer interface mutants.

Fig. S3 Legend. A and B, Thermal shift assay of purified WT and mutant AR-LBDs. The melting curves of each sample **(A)** were analyzed to calculate their melting temperatures **(B)** (mean ± SD, n = 4). Differences against WT AR-LBD were calculated using the t-test and considered significant at p values < 0.05. (*$p < 0.05$, ** $p < 0.01$, *** $p < 0.001$ and **** $p < 0.0001$). **C,** Comparison between the experimentally determined melting temperatures (B) and the *in silico* calculated free energies of unfolding and Van der Waals clashes with FoldX. **D and E,** Crystal packing in monomeric (**D**, PDB 1T7T) and tetrameric AR-LBD (**E**, PDB 5JJM). Only the closest crystal neighbors are shown. **F and G,** Partial sequence alignments of the AR-LBD sequence around residue Arg761 (marked with a blue dot). Residues topologically equivalent to the Tyr740-Ile800 sequence of human AR are compared to other steroid receptors (**F**) and to AR sequences from different species (from fish to humans; **G**). Strictly conserved residues are white with black shading; other conservative mutations are colored by conservation (the darker, the more conserved). Note that Arg761 is strictly conserved among the different species of AR, but not in other steroid receptors.

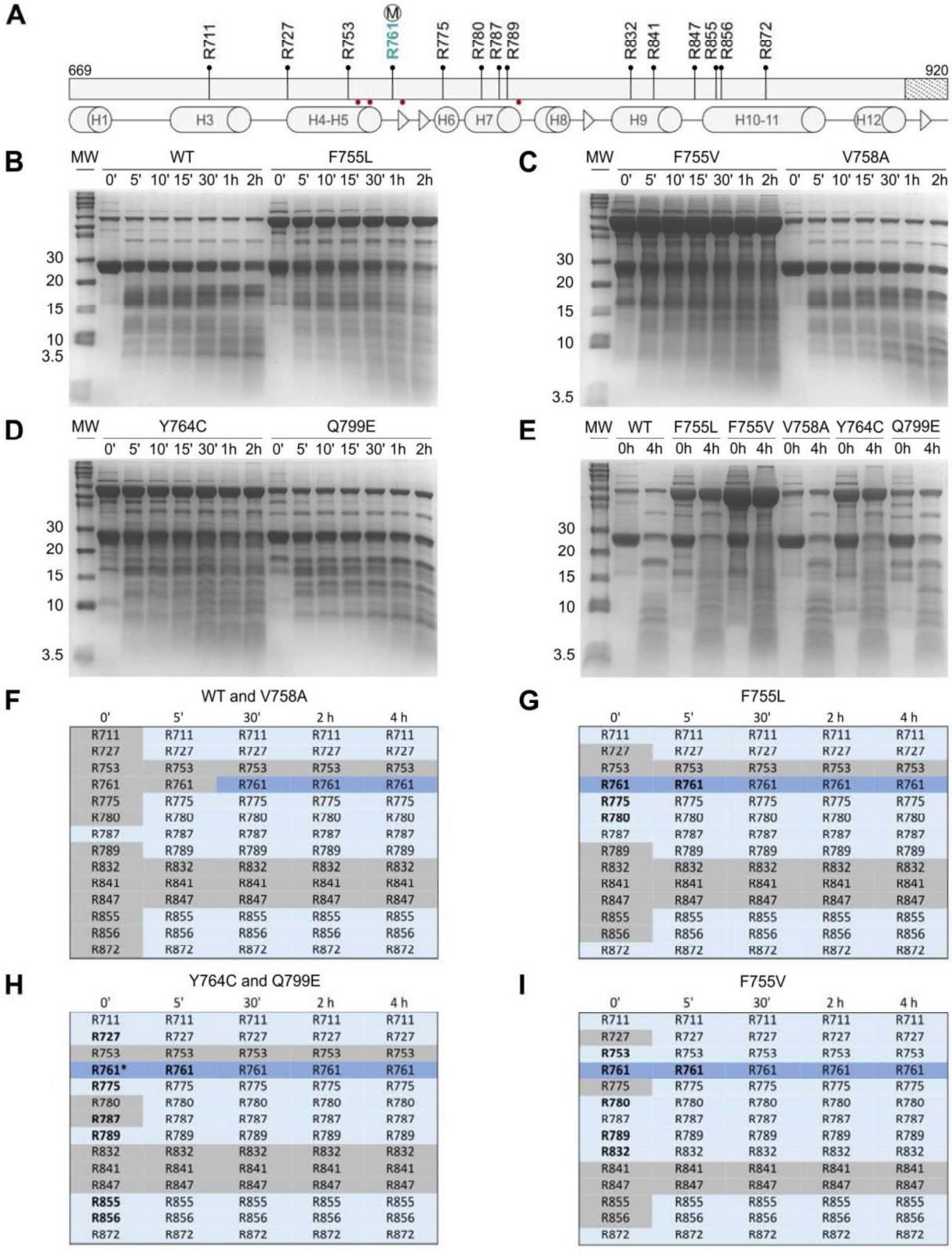

Fig. S4. AR-LBD interface residue mutations alter sensitivity to proteolysis of the domain.

Fig. S4 Legend. A, Schematic representation of the AR-LBD secondary structure. The positions of the 14 arginine residues within the domain are indicated; the methylated Arg761 is labeled in blue (M). Red dots mark the position of the mutated residues in the current investigation. **B to D,** Representative SDS-polyacrylamide gels showing the time course of proteolytic cleavage of WT and mutant AR-LBDs with Arg-C. **E,** SDS-PAGE analysis of initial and end time points (limited proteolysis with Arg-C for 4 h). **F to I,** Inferred proteolysis patterns for each mutant. Uncleaved arginines are shown in gray, cleaved Arg761 is colored dark blue, and other cleaved arginines in sky blue. Bold-labeled arginines are cleaved with different kinetics compared to WT AR-LBD. Note that four different proteolysis patterns can be observed, corresponding to (F) WT and V758A, (G) F755L, (H) Y764C and Q799E, and (I) F755V.

A

	Ele	Desolv	VdW	Bind E	BSA
5JJM	-12.1	-1.6	-81.9	**-21.8**	1592
V758A	-4.9	-11.5	-59.7	**-22.4**	1327
Y764C	-7.4	-10.6	-55.3	**-23.6**	1219
F755V	-5.9	-5.8	-53.3	**-17.0**	927
F755L	-2.8	-8.8	-41.1	**-15.7**	945
Q799E	-3.9	-9.98	-32.4	**-17.1**	1196

B

	Ele	Desolv	VDW	Total E	RMSD	Rank
5JJM	-24.2	-1.0	14.2	**-23.8**	5.59	1
V758A	-6.6	-14.2	-19.9	**-22.7**	5.10	39
Y764C	-12.7	-9.4	-3.4	**-22.4**	3.53	34
F755V	-26.7	-5.1	75.4	**-24.3**	6.54	16
F755L	-18.8	-15.2	9.6	**-33.4**	6.08	5
Q799E	-16.4	-6.1	-0.3	**-22.6**	8.33	107

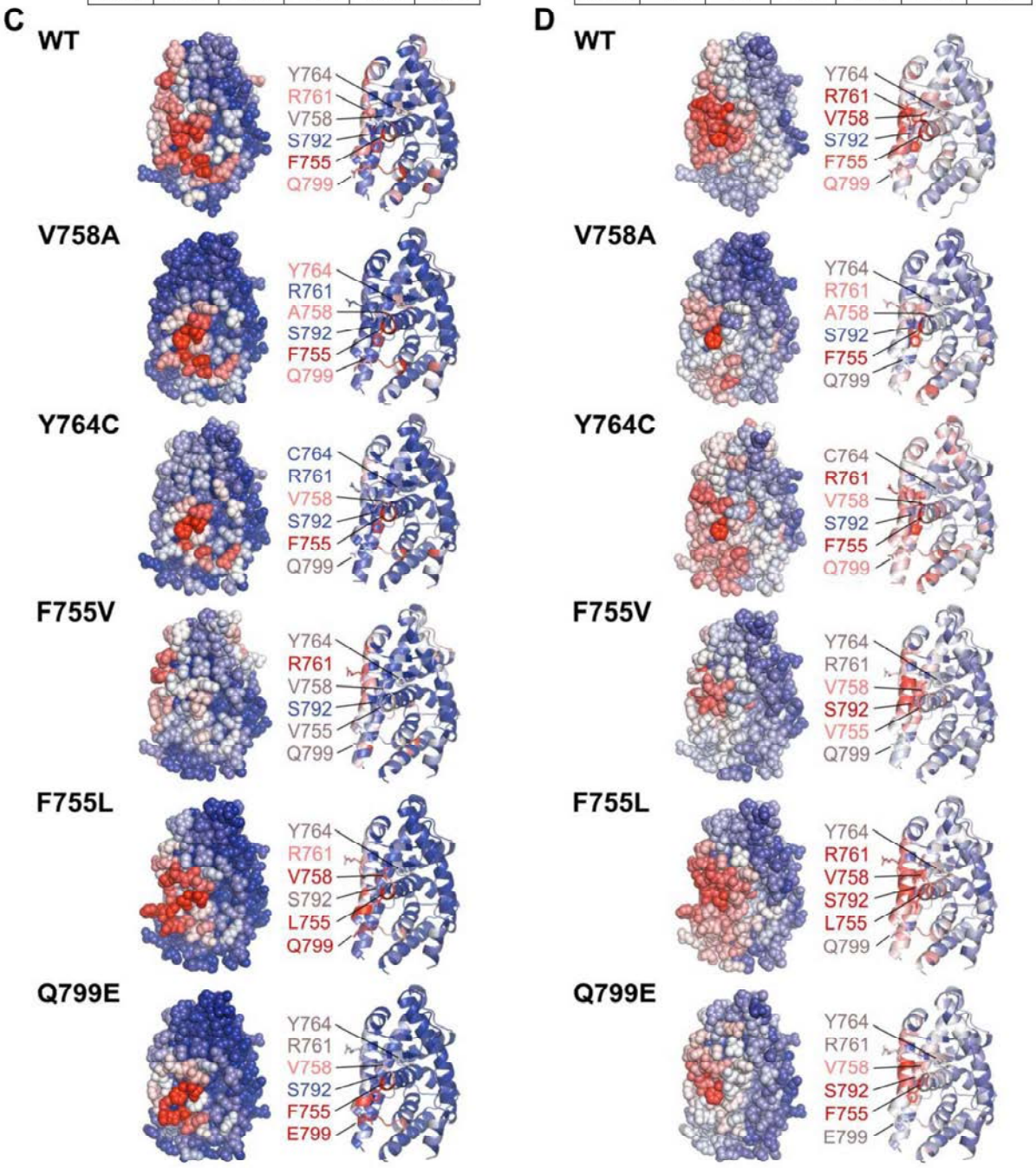

Fig. S5. AR-LBD interface mutants are predicted to dimerize essentially as non-canonical WT AR-LBD.

Fig. S5 Legend. A, Buried surface area (BSA) and pyDock scoring (total binding energy, calculated as the sum of electrostatics (Ele), desolvation (Dslvt), and one-tenth of the VdW energy term) for dimeric AR-LBD. Values were calculated assuming that mutants dimerize as in the previously reported structure of WT AR-LBD (B:C chains of PDB entry 5JJM). **B,** pyDock scoring of the best-ranked docking solutions. Docking experiments with WT AR-LBD (B chain from 5JJM) and the current structures of monomeric mutant with themselves were independently conducted. In all cases, arrangements close to the experimental dimer were identified among the top solutions (RMSD < 10 Å). **C,** Hotspot interface residues in WT and mutant AR-LBD predicted from docking experiments. Surface residues are colored according to their normalized interface propensity (NIP), from lowest (blue) to highest (red) values; intermediate values are scaled accordingly (left panel). Residues of interest are labeled and colored according to their relative NIP values in the right panel. **D,** Predicted protein-protein interaction optimal docking areas (ODA). Residues are colored according to their ODA values, from minimum (red) to maximum (blue), and intermediate values are scaled accordingly (left panel). Residues of interest are labeled and colored according to their relative ODA values (right panel).

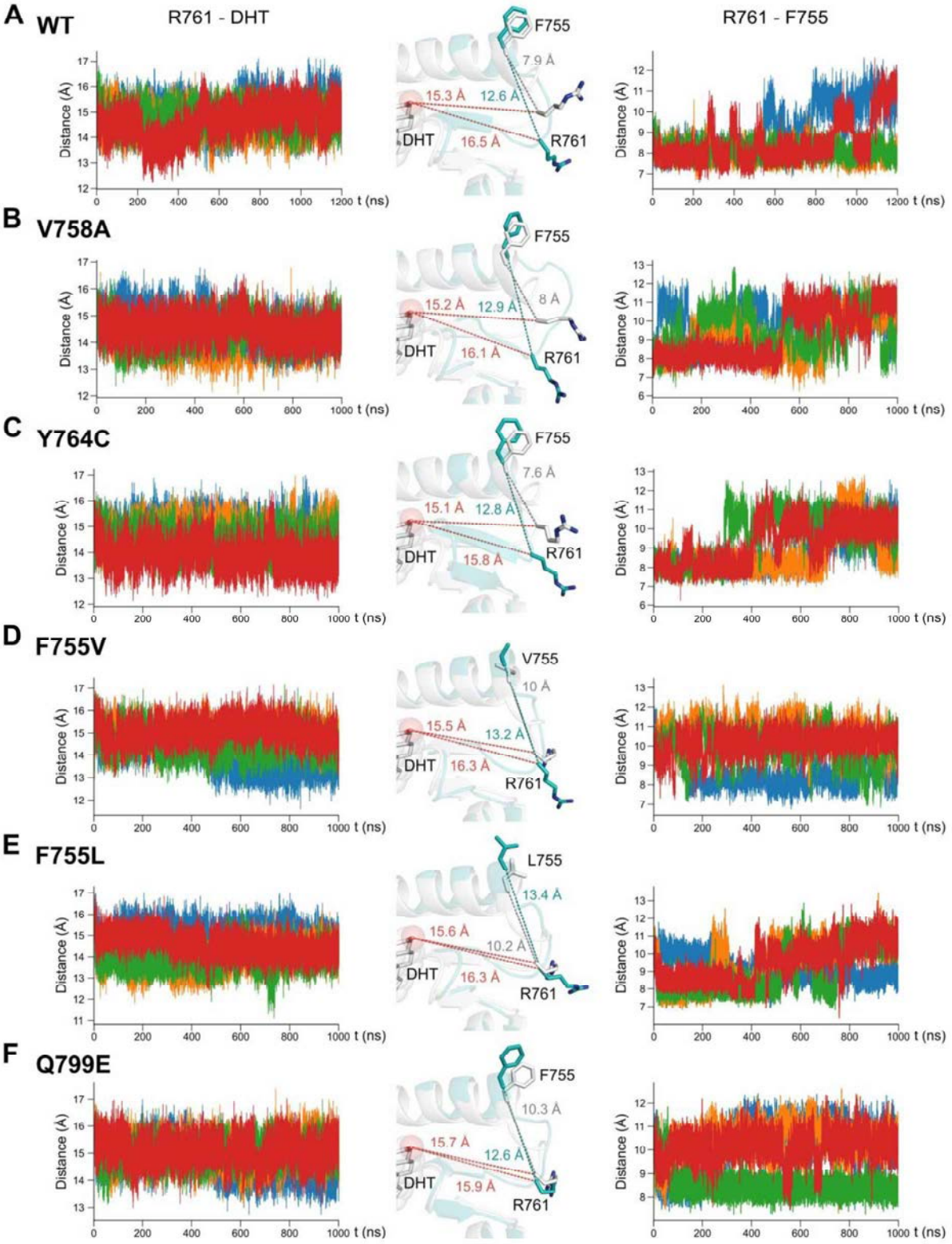

Fig. S6. Dynamics of R761-zone large conformational reorientations.

Fig. S6 Legend. Molecular dynamics were performed in quadruplicate. **A-F,** Analysis of the displacements of the H5-S1 loop along the MD simulations, as assessed by the time evolution of the distances between the Cα atoms of some of the most significant pairwise interactions identified from the inter-residue distance calculations, represented in the left and right panels of each AR-LBD row, respectively (see Materials and Methods section for details). Figures in the central panels represent the calculated distances between Arg761 and DHT (in red) or mutated residues (Phe755, Val758 and Tyr764) for the AR-LBD WT structure and mutants. Minimum and maximum distances identified during the MD simulations are colored gray and blue, respectively, to illustrate the dynamical changes of the H5-S1 loop.

	LBP			AF-2			BF-3			Dimer interface			R761-zone			Arginines		
	Res	PCa	AIS	Res	PCa	AIS	Res	PCa	AIS	Res	PCa	AIS	Res	PCa	AIS	Res	PCa	AIS
	L702	H	I	**L713**		F	**I673**	T		**P672**		H, S	**W752**	C	R	**R711**	G, I	T
	L705			**V714**			**F674**		C	**L675**	R, P		**F755**	L	V, L, S	**R727**	C, H, L	
	N706	S	S, Y, I	**V717**		F	**P724**	T	S, L	**E679**	K	G	**T756**	A		**R753**	Q	Q, P
	L708		R	**K718**			**G725**	D	S, A, V	**A680**	T, G		**N757**	D, S, K	S	**R761**	G	S
	G709		R	**K721**		L	**R727**	M		**E682**	K, V, D	K, D	**V758**	I, L, A		**R775**	C, H	C, H
	Q712		E	**F726**	C, H, L		**N728**		K	**P683**	S, L	T, A	**N759**		T	**R780**	G, Q	W
	W742	L, C	R	**R727**	M		**F827**	L	L	**G684**			**S760**	P	F, Y	**R787**	Q	
	M743		V	**V731**	H	H	**E830**	K, D		**V685**	A	I	**R761**		S	**R789**		S
	M746		T, I, L	**Q734**			**L831**	P	V	**C687**		R	**Y764**	C	C, H	**R832**	Q	Q, L
	V747		M	**M735**		F, T	**N834**			**W752**	C	R	**R789**		S	**R841**	C, H, L	C, G, H, S
	M750	T, K, I	V	**I738**		R	**E838**			**R753**			**H790**	Q		**R847**	G	
	R753	Q	Q, P	**Q739**	K		**R841**	C, H, L	C, H, G, S	**F755**	L	V, L, S	**S792**	P, F		**R855**		K
	F765		L	**E894**						**T756**	A		**Q793**			**R856**	C, H	C, H
	M781		I	**M895**	D	G				**N757**	D, S, K		**W797**			**R872**		G
	M788	I		**E898**		F, T				**V758**	I, L, A		**Q799**	E	E			
	L874			**I899**						**N759**		T						
	H875	Y, Q	R							**R761**		S						
	F877	L								**M762**		T						
	T878	A, S	I							**Y764**	C	H, C						
	L881	Q								**P767**	T	S, A						
	M896	L	T							**D768**	N	E, Y						
										G796	E, V							
										Q799	E	E						
										I800	T							
										T801		I						
										P802	L							
										Q803		R						
										L806								
										C845								
										K846								
										R847	G							
										K848	N							
										N849	H, K	K						
										S852								
Total residues	21			16			12			34			15			14		
Mutated residues	19	11	16	11	5	8	10	8	7	25	21	18	13	10	9	14	10	11
Unique mutations	35	16	21	16	7	10	21	11	13	51	32	27	24	15	13	28	18	18

Table S1. Reported mutations in the major functional areas of the AR-LBD.

Mutations that affect the ligand-binding pocket (LBP) as well as the major protein-protein interaction sites, AF-2, BF-3 and the dimer interface are separately given. Within each subgroup, we also distinguish between those reported in PCa patients and in AIS cases. The total numbers of mutated residues and of unique mutations within each functional region are given at the bottom of the table. Note that several mutations have been linked to both PCa and AIS (e.g., R753Q, F755L).

Mutant	Identified in	Protein stability	Ligand affinity	Intra- and intermolecular interactions	Transcriptional activity	Ref.
F755V	CAIS	Not studied	Five-fold lower affinity for mibolerone.	Reduced N/C interaction.	Largely impaired (5% of WT activity at 10 nM DHT).	(*35, 37*)
F755L	PCa, PAIS	Enhanced thermolability but as resistant to trypsinolysis as WT protein.	One-third of the affinity for DHT and mibolerone. 10-fold higher concentration of androgen needed to achieve same activity as WT.	Severely compromised N/C interactions. Reduced binding to Qia2.	Significantly impaired: high activity with mibolerone and methyltrienolone, 40-60% of WT with DHT, 30% of WT activity with testosterone.	(*37, 39, 54, 59, 60, 61*)
V758A	PCa	Not studied	PC3 transiently expressing AR V758A present sensitivity to darolutamide.	Increased binding to coactivators and impaired binding to corepressors. WT-like or increased N/C interaction.	Normal activity in response to DHT; weak activity with DHEA.	(*38, 39, 40, 41, 42*)
R761G	PCa	Not studied	Not studied	Not studied	Poor response to low concentrations of R1881 in CV-1 cells, but WT-like activity in PC3 cells. EPI-002 inhibitor blocks mutant activity similar to WT.	(*62, 121, 122*)
Y764C	PCa, PAIS	More thermolabile, especially in combination with a shorter polyQ stretch.	WT-like binding to DHT, but reduced binding to other androgens, non-androgens, and anti-androgens.	Abnormal or even complete loss of N/C interactions.	Conflicting results: reported to have complete, moderate, or no function at all in different studies.	(*32, 39, 42, 43, 44, 46, 48*)
Q799E	PCa, PAIS	Normal thermal stability.	Normal androgen binding. Sensitive to darolutamide in PC3 cells.	Mild reduction of N/C interaction. Reduced binding to Qia2. Impaired binding to NCoA.	Impaired at normal androgen doses but overcome with high doses. In other studies, full activity in the presence of DHT an partial activity DHEA.	(*39, 42, 48, 49, 50, 51, 52, 54*)

Table S2. Summary of clinical and biological information on point mutants that affect the AR-LBD dimerization interface.

AR-LBD(Y764C) Cys-Cys covalent bound peptides								
Site A	Site B	Sequence A	Sequence B	MeroX	XlinkX	Xi SEARCH	Max among Nodes	Stars
C-687	C-764	^{680}AIEPGVVCAGHDNNQPDSFAALLSSLNE^{707}	^{762}MLCFAPDLVFNE^{773}	5	3	2	5	***
			^{762}MLCFAPDLVFNEYR^{773}	1	9	4	9	***
	C-785	^{680}AIEPGVVCAGHDNNQPDSFAALLSSLNE^{707}	^{781}MYSQCVR^{787}			1	1	*
	C-807	^{680}AIEPGVVCAGHDNNQPDSFAALLSSLNE^{707}	^{795}FGWLQITPQEFLCMK^{809}	2	2	2	2	***
	C-853	^{680}AIEPGVVCAGHDNNQPD^{696}	^{849}NPTSCSR^{855}			1	1	*
		^{680}AIEPGVVCAGHDNNQPDSFAALLSSLNE^{707}	^{849}KNPTSCSR^{855}			1	1	*
			^{849}NPTSCSR^{855}			1	1	*
C-764	C-764	^{762}MLCFAPDLVFNE^{773}	^{762}MLCFAPDLVFNEYR^{775}			2	2	*
		^{762}MLCFAPDLVFNEYR^{775}	^{762}MLCFAPDLVFNE^{733}		1		1	*
			^{762}MLCFAPDLVFNEYR^{775}	7		4	7	**
	C-785	^{762}MLCFAPDLVFNE^{773}	^{781}MYSQCVR^{787}		2	3	3	**
		^{762}MLCFAPDLVFNEYR^{775}	^{781}MYSQCVR^{787}		14	6	14	**
	C-807	^{762}MLCFAPDLVFNE^{773}	^{795}FGWLQITPQEFLCMK^{809}			1	1	*
		^{762}MLCFAPDLVFNEYR^{775}	^{795}FGWLQITPQEFLCMK^{809}	3	7	4	7	***
	C-845	^{762}MLCFAPD^{768}	^{842}IIACK^{846}		1		1	*
		^{762}MLCFAPDLVFNE^{773}	^{842}IIACK^{846}	1	1		1	**
		^{762}MLCFAPDLVFNEYR^{775}	^{842}IIACK^{846}		8		8	*
	C-853	^{762}MLCFAPD^{768}	^{849}NPTSCSR^{855}		1	2	2	**
		^{762}MLCFAPDLVFNE^{773}	^{849}NPTSCSR^{855}			1	1	*
		^{762}MLCFAPDLVFNEYR^{775}	^{848}KNPTSCSR^{855}		1	1	1	**
			^{849}NPTSCSR^{855}		5	4	5	**

Table S3. Summary of Cys-Cys' covalently linked peptides in the covalent AR-LBD(Y764C) dimer identified by mass spectrometry.

The sequences of disulfide-bridged tryptic peptides identified in samples of dimeric Y764C are given along with the number of counts each peptide pair was detected with different software.

AR-LBD(Y764C) Cys-Cys crosslinked with BMB								
Site A	Site B	Sequence A	Sequence B	MeroX	XlinkX	Xi SEARCH	Unique CSM	Stars
C-764	C-764	^{762}MLCFAPDLVFNEYR^{775}	^{762}MLCFAPDLVFNEYR^{775}	5		5	8	**
	C-785	^{762}MLCFAPDLVFNEYR^{775}	^{781}MYSQCVR^{787}		6	5	9	**
	C-853	^{762}MLCFAPDLVFNEYR^{775}	^{849}NPTSCSR^{855}		1	2	3	**

Table S4. Summary of BMB-crosslinked peptides in the covalent AR-LBD(Y764C) dimer identified by mass spectrometry. The number of counts each peptide pair was detected with different search tools is indicated. The only BMB-crosslinked tryptic peptides identified by MS involve the mutant Cys764, demonstrating its higher reactivity in solution.

REFERENCES AND NOTES

1. W. D. Tilley, C. M. Wilson, M. Marcelli, M. J. McPhaul, Androgen receptor gene expression in human prostate carcinoma cell lines. *Cancer Res.* **17**, 5382–5386 (1990).

2. E. Estébanez-Perpiñá, C. L. Bevan, I. J. McEwan, Eighty years of targeting androgen receptor activity in prostate cancer: The fight goes on. *Cancers* **13**, 509 (2021).

3. A. Jiménez-Panizo, P. Pérez, A. M. Rojas, P. Fuentes-Prior, E. Estébanez-Perpiñá, Non-canonical dimerization of the androgen receptor and other nuclear receptors: Implications for human disease. *Endocr. Relat. Cancer* **26**, R479–R497 (2019).

4. X. Yu, P. Yi, R. A. Hamilton, H. Shen, M. Chen, C. E. Foulds, M. A. Mancini, S. J. Ludtke, Z. Wang, B. W. O'Malley, Structural insights of transcriptionally active, full-length androgen receptor coactivator complexes. *Mol. Cell* **79**, 812–823.e4 (2020).

5. P. L. Shaffer, A. Jivan, D. E. Dollins, F. Claessens, D. T. Gewirth, Structural basis of androgen receptor binding to selective androgen response elements. *Proc. Natl. Acad. Sci. U.S.A.* **101**, 4758–4763 (2004).

6. M. Nadal, S. Prekovic, N. Gallastegui, C. Helsen, M. Abella, K. Zielinska, M. Gay, M. Vilaseca, M. Taulès, A. B. Houtsmuller, M. E. van Royen, F. Claessens, P. Fuentes-Prior, E. Estébanez-Perpiñá, Structure of the homodimeric androgen receptor ligand-binding domain. *Nat. Commun.* **8**, 14388 (2017).

7. E. V. Wasmuth, A. Vanden Broeck, J. R. LaClair, E. A. Hoover, K. E. Lawrence, N. Paknejad, K. Pappas, D. Matthies, B. Wang, W. Feng, P. A. Watson, J. C. Zinder, W. R. Karthaus, M. J. de la Cruz, R. K. Hite, K. Manova-Todorova, Z. Yu, S. T. Weintraub, S. Klinge, C. L. Sawyers, Allosteric interactions prime androgen receptor dimerization and activation. *Mol. Cell.* **82**, 2021–2031 (2022).

8. K. E. Knudsen, T. M. Penning, Partners in crime: Deregulation of AR activity and androgen synthesis in prostate cancer. *Trends Endocrinol. Metab.* **21**, 315–324 (2010).

9. Y. Wen, M. C.-T. Hu, K. Makino, B. Spohn, G. Bartholomeusz, D. H. Yan, M. C. Hung, HER-2/neu promotes androgen-independent survival and growth of prostate cancer cells through the Akt pathway. *Cancer Res.* **60**, 6841–6845 (2000).

10. H. K. Lin, S. Yeh, H. Y. Kang, C. Chang, Akt suppresses androgen-induced apoptosis by phosphorylating and inhibiting androgen receptor. *Proc. Natl. Acad. Sci. U.S.A.* **98**, 7200–7205 (2001).

11. H. K. Lin, Y. C. Hu, L. Yang, S. Altuwaijri, Y. T. Chen, H. Y. Kang, C. Chang, Suppression Versus Induction of androgen receptor functions by the phosphatidylinositol 3-Kinase/Akt pathway in prostate cancer LNCaP cells with different passage numbers. *J. Biol. Chem.* **278**, 50902–50907 (2003).

12. S. S. Taneja, S. Ha, N. K. Swenson, H. Y. Huang, P. Lee, J. Melamed, E. Shapiro, M. J. Garabedian, S. K. Logan, Cell-specific regulation of androgen receptor phosphorylation in vivo. *J. Biol. Chem.* **280**, 40916–40924 (2005).

13. K. Xu, H. Shimelis, D. E. Linn, R. Jiang, X. Yang, F. Sun, Z. Guo, H. Chen, W. Li, H. Chen, X. Kong, J. Melamed, S. Fang, Z. Xiao, T. D. Veenstra, Y. Qiu, Regulation of Androgen Receptor Transcriptional Activity and Specificity by RNF6-Induced Ubiquitination. *Cancer Cell* **15**, 270–282 (2009).

14. D. E. Linn, X. Yang, Y. Xie, A. Alfano, D. Deshmukh, X. Wang, H. Shimelis, H. Chen, W. Li, K. Xu, M. Chen, Y. Qiu, Differential regulation of androgen receptor by PIM-1 kinases via phosphorylation-dependent recruitment of distinct ubiquitin E3 ligases. *J. Biol. Chem.* **287**, 22959–22968 (2012).

15. D. Gioeli, B. M. Paschal, Post-translational modification of the androgen receptor. *Mol. Cell. Endocrinol.* **352,** 70–78 (2012).

16. T. van der Steen, D. J. Tindall, H. Huang, Posttranslational modification of the androgen receptor in prostate cancer. *Int. J. Mol. Sci.* **14**, 14833–14859 (2013).

17. Y. Koryakina, H. Q. Ta, D. Gioeli, Androgen receptor phosphorylation: Biological context and functional consequences. *Endocr. Relat. Cancer* **21**, T131–T145 (2014).

18. Z. Mounir, J. M. Korn, T. Westerling, F. Lin, C. A. Kirby, M. Schirle, G. McAllister, G. Hoffman, N. Ramadan, A. Hartung, Y. Feng, D. R. Kipp, C. Quinn, M. Fodor, J. Baird, M. Schoumacher, R. Meyer, J. Deeds, G. Buchwalter, T. Stams, N. Keen, W. R. Sellers, M. Brown, R. A. Pagliarini, ERG signaling in prostate cancer is driven through PRMT5-dependent methylation of the androgen receptor. *eLife* **5**, e13964 (2016).

19. L. Malbeteau, H. T. Pham, L. Eve, M. R. Stallcup, C. Poulard, M. Le Romancer, How protein methylation regulates steroid receptor function. *Endocr. Rev.* **43**, 160–197 (2022).

20. Q. Wang, W. Li, X. S. Liu, J. S. Carroll, O. A. Jänne, E. K. Keeton, A. M. Chinnaiyan, K. J. Pienta, M. Brown, A hierarchical network of transcription factors governs androgen receptor-dependent prostate cancer growth. *Mol. Cell* **27**, 380–392 (2007).

21. D. Robinson, E. M. Van Allen, Y. M. Wu, N. Schultz, R. J. Lonigro, J. M. Mosquera, B. Montgomery, M. E. Taplin, C. C. Pritchard, G. Attard, H. Beltran, W. Abida, R. K. Bradley, J. Vinson, X. Cao, P. Vats, L. P. Kunju, M. Hussain, F. Y. Feng, S. A. Tomlins, K. A. Cooney, D. C. Smith, C. Brennan, J. Siddiqui, R. Mehra, Y. Chen, D. E. Rathkopf, M. J. Morris, S. B. Solomon, J. C. Durack, V. E. Reuter, A. Gopalan, J. Gao, M. Loda, R. T. Lis, M. Bowden, S. P. Balk, G. Gaviola, C. Sougnez, M. Gupta, E. Y. Yu, E. A. Mostaghel, H. H. Cheng, H. Mulcahy, L. D. True, S. R. Plymate, H. Dvinge, R. Ferraldeschi, P. Flohr, S. Miranda, Z. Zafeiriou, N. Tunariu, J. Mateo, R. Perez-Lopez, F. Demichelis, B. D. Robinson, M. Schiffman, D. M. Nanus, S. T. Tagawa, A. Sigaras, K. W. Eng, O. Elemento, A. Sboner, E. I. Heath, H. I. Scher, K. J. Pienta, P. Kantoff, J. S. De Bono, M. A. Rubin, P. S. Nelson, L. A. Garraway, C. L. Sawyers, A. M. Chinnaiyan, Integrative clinical genomics of advanced prostate cancer. *Cell* **161**, 1215–1228 (2015).

22. D. A. Quigley, H. X. Dang, S. G. Zhao, P. Lloyd, R. Aggarwal, J. J. Alumkal, A. Foye, V. Kothari, M. D. Perry, A. M. Bailey, D. Playdle, T. J. Barnard, L. Zhang, J. Zhang, J. F. Youngren, M. P. Cieslik, A. Parolia, T. M. Beer, G. Thomas, K. N. Chi, M. Gleave, N. A. Lack, A. Zoubeidi, R. E. Reiter, M. B. Rettig, O. Witte, C. J. Ryan, L. Fong, W. Kim, T. Friedlander, J. Chou, H. Li, R. Das, H. Li, R. Moussavi-Baygi, H. Goodarzi, L. A. Gilbert, P. N. Lara, C. P. Evans, T. C. Goldstein, J.

M. Stuart, S. A. Tomlins, D. E. Spratt, R. K. Cheetham, D. T. Cheng, K. Farh, J. S. Gehring, J. Hakenberg, A. Liao, P. G. Febbo, J. Shon, B. Sickler, S. Batzoglou, K. E. Knudsen, H. H. He, J. Huang, A. W. Wyatt, S. M. Dehm, A. Ashworth, A. M. Chinnaiyan, C. A. Maher, E. J. Small, F. Y. Feng, Genomic Hallmarks and Structural Variation in Metastatic Prostate Cancer. *Cell*. **174**, 758–769.e9 (2018).

23. D. B. Lubahn, T. R. Brown, J. A. Simental, H. N. Higgs, C. J. Migeon, E. M. Wilson, F. S. French, Sequence of the intron/exon junctions of the coding region of the human androgen receptor gene and identification of a point mutation in a family with complete androgen insensitivity. *Proc. Natl. Acad. Sci. U.S.A.* **86**, 9534–9538 (1989).

24. O. Hiort, G. H. Sinnecker, P. M. Holterhus, E. M. Nitsche, K. Kruse, The clinical and molecular spectrum of androgen insensitivity syndromes. *Am. J. Med. Genet.* **63**, 218–222 (1996).

25. I. A. Hughes, J. D. Davies, T. I. Bunch, V. Pasterski, K. Mastroyannopoulou, J. Macdougall, Androgen insensitivity syndrome. *Lancet* **380**, 1419–1428 (2012).

26. C. E. Bohl, W. Gao, D. D. Miller, C. E. Bell, J. T. Dalton, Structural basis for antagonism and resistance of bicalutamide in prostate cancer. *Proc. Natl. Acad. Sci. U.S.A.* **102**, 6201–6206 (2005).

27. C. E. Bohl, Z. Wu, D. D. Miller, C. E. Bell, J. T. Dalton, Crystal structure of the T877A human androgen receptor ligand-binding domain complexed to cyproterone acetate provides insight for ligand-induced conformational changes and structure-based drug design. *J. Biol. Chem.* **282**, 13648–13655 (2007).

28. J. S. Sack, K. F. Kish, C. Wang, R. M. Attar, S. E. Kiefer, Y. An, G. Y. Wu, J. E. Scheffler, M. E. Salvati, J. Krystek, R. Weinmann, H. M. Einspahr, Crystallographic structures of the ligand-binding domains of the androgen receptor and its T877A mutant complexed with the natural agonist dihydrotestosterone. *Proc. Natl. Acad. Sci. U.S.A.* **98**, 4904–4909 (2001).

29. B. Gottlieb, L. K. Beitel, A. Nadarajah, M. Paliouras, M. Trifiro, The androgen receptor gene mutations database: 2012 update. *Hum. Mutat.* **33**, 887–894 (2012).

30. Z. Culig, A. Hobisch, M. Erdel, G. Bartsch, H. Klocker, Studies on androgen receptor mutations and amplification in human prostate cancer. *Methods Mol. Med.* **81**, 267–275 (2003).

31. E. R. Hyytinen, K. Haapala, J. Thompson, I. Lappalainen, M. Roiha, I. Rantala, H. J. Helin, O. A. Jänne, M. Vihinen, J. J. Palvimo, P. A. Koivisto, Pattern of somatic androgen receptor gene mutations in patients with hormone-refractory prostate cancer. *Lab. Invest.* **82**, 1591–1598 (2002).

32. M. J. McPhaul, M. Marcelli, W. D. Tilley, J. E. Griffin, R. F. Isidro-Gutierrez, J. D. Wilson, Molecular basis of androgen resistance in a family with a qualitative abnormality of the androgen receptor and responsive to high-dose androgen therapy. *J. Clin. Invest.* **87**, 1413–1421 (1991).

33. C. Radmayr, Z. Culig, A. Hobisch, S. Corvin, G. Bartsch, H. Klocker, Analysis of a mutant androgen receptor offers a treatment modality in a patient with partial androgen insensitivity syndrome. *Eur. Urol.* **33**, 222–226 (1998).

34. T. R. Brown, D. B. Lubahn, E. M. Wilson, F. S. French, C. J. Migeon, J. L. Corden, Functional characterization of naturally occurring mutant androgen receptors from subjects with complete androgen insensitivity. *Mol. Endocrinol.* **4**, 1759–1772 (1990).

35. J. M. Lobaccaro, S. Lumbroso, R. Ktari, R. Dumas, C. Sultan, An exonic point mutation creates a *Mae*Ill site in the androgen receptor gene of a family with complete androgen insensitivity syndrome. *Hum. Mol. Genet.* **2** (1993), pp. 1041–1043.

36. Y.-H. Liu, C. Li, S.-F. Zhou, Prediction of Deleterious Functional Effects of Non-Synonymous Single Nucleotide Polymorphisms in Human Nuclear Receptor Genes Using a Bioinformatics Approach. *Drug Metab. Lett.* **3**, 242–286 (2009).

37. R. Tadokoro-Cuccaro, T. I. Bunch, J. W. Schwabe, I. A. Hughes, J. C. Murphy, Comparison of the molecular consequences of different mutations at residue 754 and 690 of the androgen receptor (AR) and androgen insensitivity syndrome (AIS) phenotype. *Clin. Endocrinol.* **71**, 253–260 (2009).

38. M. Marcelli, M. Ittmann, S. Mariani, R. Sutherland, R. Nigam, L. Murthy, Y. Zhao, D. Diconcini, E. Puxeddu, A. Esen, J. Eastham, N. L. Weigel, D. J. Lamb, Androgen receptor mutations in prostate cancer. *Cancer Res.* **60**, 944–949 (2000).

39. X. B. Shi, A. H. Ma, L. Xia, H. J. Kung, R. W. De Vere White, Functional analysis of 44 mutant androgen receptors from human prostate cancer. *Cancer Res.* **62**, 1496–1502 (2002).

40. X. E. Zhou, K. M. Suino-Powell, J. Li, Y. He, J. P. MacKeigan, K. Melcher, E. L. Yong, H. E. Xu, Identification of SRC3/AIB1 as a preferred coactivator for hormone-activated androgen receptor. *J. Biol. Chem.* **285**, 9161–9171 (2010).

41. S. Grosdidier, L. R. Carbó, V. Buzón, G. Brooke, P. Nguyen, J. D. Baxter, C. L. Bevan, P. Webb, E. Estébanez-Perpiñá, J. Fernández-Recio, Allosteric conversation in the androgen receptor ligand-binding domain surfaces. *Mol. Endocrinol.* **26**, 1078–1090 (2012).

42. C. W. Hay, I. J. McEwan, The impact of point mutations in the human androgen receptor: Classification of mutations on the basis of transcriptional activity. *PLOS ONE* **7**, e32514 (2012).

43. M. J. McPhaul, M. Marcelli, W. D. Tilley, J. E. Griffin, R. F. Isidro-Gutierrez, J. D. Wilson, Molecular basis of androgen resistance in a family with a qualitative abnormality of the androgen receptor and responsive to high-dose androgen therapy. *J. Clin. Invest.* **87**, 1413–1421 (1991).

44. I. Murono, B. B. Mendonca, I. J. Arnhold, A. C. Rigon, C. J. Migeon, T. R. Brown, Human androgen insensitivity due to point mutations encoding amino acid substitutions in the androgen receptor steroid-binding domain. *Hum. Mutat.* **6**, 152–162 (1995).

45. C. A. Quigley, A. De Bellis, K. B. Marschke, M. K. El-Awady, E. M. Wilson, F. S. French, Androgen receptor defects: Historical, clinical, and molecular perspectives. *Endocr. Rev.* **16**, 271–321 (1995).

46. E. Langley, J. A. Kemppainen, E. M. Wilson, Intermolecular NH2−/carboxyl-terminal interactions in androgen receptor dimerization revealed by mutations that cause androgen insensitivity. *J. Biol. Chem.* **273**, 92–101 (1998).

47. K. F. Melo, B. B. Mendonca, A. E. C. Billerbeck, E. M. Costa, M. Inácio, F. A. Silva, A. M. Leal, A. C. Latronico, I. J. Arnhold, Clinical, hormonal, behavioral, and genetic characteristics of androgen insensitivity syndrome in a Brazilian cohort: Five novel mutations in the androgen receptor gene. *J. Clin. Endocrinol. Metab.* **88**, 3241–3250 (2003).

48. I. Jääskeläinen, A. Deeb, J. W. Schwabe, N. P. Mongan, H. Martin, I. A. Hughes, Human androgen receptor gene ligand-binding-domain mutations leading to disrupted interaction between the N- and C-terminal domains. *J. Mol. Endocrinol.* **36**, 361–368 (2006).

49. J. Batch, D. Williams, H. Davies, B. Brown, B. A. Evans, I. A. Hughes, M. Patterson, Androgen receptor gene mutations identified by SSCP in fourteen subjects with androgen insensitivity syndrome. *Hum. Mol. Genet.* **1**, 497–503 (1992).

50. C. L. Bevan, B. B. Brown, H. R. Davies, B. A. Evans, I. A. Hughes, M. N. Patterson, Functional analysis of six androgen receptor mutations identified in patients with partial androgen insensitivity syndrome. *Hum. Mol. Genet.* **5**, 265–273 (1996).

51. Q. Wang, F. J. Ghadessy, A. Trounson, D. de Kretser, R. McLachlan, S. Ng, E. Yong, Azoospermia associated with a mutation in the ligand-binding domain of an androgen receptor displaying normal ligand binding, but defective trans-activation. *J. Clin. Endocrinol. Metab.* **83**, 4303–4309 (1998).

52. O. Hiort, P.-M. Holterhus, T. Horter, W. Schulze, B. Kremke, M. Bals-Pratsch, G. H. G. Sinnecker, K. Kruse, Significance of Mutations in the Androgen Receptor Gene in Males with Idiopathic infertility. *J. Clin. Endocrinol. Metab.* **85**, 2810–2815 (2000).

53. N. Kalfa, P. Philibert, R. Werner, F. Audran, A. Bashamboo, H. Lehors, M. Haddad, J. M. Guys, R. Reynaud, P. Alessandrini, K. Wagner, J. Y. Kurzenne, F. Bastiani, J. Bréaud, J. S. Valla, G. M. Lacombe, M. Orsini, J. P. Daures, O. Hiort, F. Paris, K. McElreavey, C. Sultan, Minor hypospadias: The "Tip of the Iceberg" of the partial androgen insensitivity syndrome. *PLOS ONE* **8**, e61824 (2013).

54. J. Qi, M. Tripathi, R. Mishra, N. Sahgal, L. Fazil, S. Ettinger, W. J. Placzek, G. Claps, L. W. Chung, D. Bowtell, M. Gleave, N. Bhowmick, Z. A. Ronai, The E3 ubiquitin ligase siah2 contributes to castration-resistant prostate cancer by regulation of androgen receptor transcriptional activity. *Cancer Cell* **23**, 332–346 (2013).

55. R. Kumar, J. Mendonca, O. Owoyemi, K. Boyapati, N. Thomas, S. Kanacharoen, M. Coffey, D. Topiwala, C. Gomes, B. Ozbek, T. Jones, M. Rosen, L. Dong, S. Wiens, W. N. Brennen, J. T.

Isaacs, A. M. D. Marzo, M. C. Markowski, E. S. Antonarakis, D. Z. Qian, K. J. Pienta, D. M. Pardoll, M. A. Carducci, S. R. Denmeade, S. K. Kachhap, Supraphysiologic testosterone induces ferroptosis and activates immune pathways through nucleophagy in prostate cancer. *Cancer Res.* **81**, 5948–5962 (2021).

56. H. M. Lam, H. M. Nguyen, M. P. Labrecque, L. G. Brown, I. M. Coleman, R. Gulati, B. Lakely, D. Sondheim, P. Chatterjee, B. T. Marck, A. M. Matsumoto, E. A. Mostaghel, M. T. Schweizer, P. S. Nelson, E. Corey, Durable response of enzalutamide-resistant prostate cancer to supraphysiological testosterone is associated with a multifaceted growth suppression and impaired DNA damage response transcriptomic program in patient-derived xenografts. *Eur. Urol.* **77**, 144–155 (2020).

57. L. Garcia-Alonso, C. H. Holland, M. M. Ibrahim, D. Turei, J. Saez-Rodriguez, Benchmark and integration of resources for the estimation of human transcription factor activities. *Genome Res.* **29**, 1363–1375 (2019).

58. A. Aytes, A. Mitrofanova, C. Lefebvre, M. J. Alvarez, M. Castillo-Martin, T. Zheng, J. A. Eastham, A. Gopalan, K. J. Pienta, M. M. Shen, A. Califano, C. Abate-Shen, Cross-species regulatory Network Analysis identifies a synergistic interaction between FOXM1 and CENPF that drives prostate cancer malignancy. *Cancer Cell* **25**, 638 (2014), 651.

59. H. Takahashi, M. Furusato, W. C. Allsbrook, H. Nishii, S. Wakui, J. C. Barrett, J. Boyd, Prevalence of androgen receptor gene mutations in latent prostatic carcinomas from japanese men. *Cancer Res.* **55**, 1621–1624 (1995).

60. W. Weidemann, B. Linck, H. Haupt, B. Mentrup, G. Romalo, K. Stockklauser, A. O. Brinkmann, H. U. Schweikert, K. D. Spindler, Clinical and biochemical investigations and molecular analysis of subjects with mutations in the androgen receptor gene. *Clin. Endocrinol.* **45**, 733–739 (1996).

61. J. Thompson, F. Saatcioglu, O. A. Jänne, J. J. Palvimo, Disrupted amino- and carboxyl- terminal interactions of the androgen receptor are linked to androgen insensitivity. *Mol. Endocrinol.* **15**, 923–935 (2001).

62. O. A. O'Mahony, M. P. Steinkamp, M. A. Albertelli, M. Brogley, H. Rehman, D. M. Robins, Profiling human androgen receptor mutations reveals treatment effects in a mouse model of prostate cancer. *Mol. Cancer Res.* **6**, 1691–1701 (2008).

63. E. Estébanez-Perpiñá, L. A. Arnold, P. Nguyen, E. D. Rodrigues, E. Mar, R. Bateman, P. Pallai, K. M. Shokat, J. D. Baxter, R. K. Guy, P. Webb, R. J. Fletterick, A surface on the androgen receptor that allosterically regulates coactivator binding. *Proc. Natl. Acad. Sci. U.S.A.* **104**, 16074–16079 (2007).

64. A. Jiménez-Panizo, A. Alegre-Martí, T. T. Tettey, G. Fettweis, M. Abella, R. Antón, T. A. Johnson, S. Kim, R. L. Schiltz, I. Núñez-Barrios, J. Font-Díaz, C. Caelles, A. F. Valledor, P. Pérez, A. M. Rojas, J. Fernández-Recio, D. M. Presman, G. L. Hager, P. Fuentes-Prior, E. Estébanez-Perpiñá, The multivalency of the glucocorticoid receptor ligand-binding domain explains its manifold physiological activities. *Nucleic Acids Res.* **50**, gkac1119 (2022).

65. S. Grosdidier, J. Fernández-Recio, Identification of hot-spot residues in protein-protein interactions by computational docking. *BMC Bioinformatics* **9**, 447 (2008).

66. J. Fernandez-Recio, M. Totrov, C. Skorodumov, R. Abagyan, Optimal docking area: A new method for predicting protein-protein interaction sites. *Proteins* **58**, 134–143 (2005).

67. L. Sun, M. Wang, Z. Lv, N. Yang, Y. Liu, S. Bao, W. Gong, R. M. Xu, Structural insights into protein arginine symmetric dimethylation by PRMT5. *Proc. Natl. Acad. Sci. U.S.A.* **108**, 20538–20543 (2011).

68. S. Antonysamy, Z. Bonday, R. M. Campbell, B. Doyle, Z. Druzina, T. Gheyi, B. Han, L. N. Jungheim, Y. Qian, C. Rauch, M. Russell, J. M. Sauder, S. R. Wasserman, K. Weichert, F. S. Willard, A. Zhang, S. Emtage, Crystal structure of the human PRMT5:MEP50 complex. *Proc. Natl. Acad. Sci. U.S.A.* **109**, 17960–17965 (2012).

69. M. C. Ho, C. Wilczek, J. B. Bonanno, L. Xing, J. Seznec, T. Matsui, L. G. Carter, T. Onikubo, P. R. Kumar, M. K. Chan, M. Brenowitz, R. H. Cheng, U. Reimer, S. C. Almo, D. Shechter, Structure of

the arginine methyltransferase PRMT5-MEP50 reveals a mechanism for substrate specificity. *PLOS ONE* **8**, e57008 (2013).

70. K. M. Mulvaney, C. Blomquist, N. Acharya, R. Li, M. J. Ranaghan, M. O'Keefe, D. J. Rodriguez, M. J. Young, D. Kesar, D. Pal, M. Stokes, A. J. Nelson, S. S. Jain, A. Yang, Z. Mullin-Bernstein, J. Columbus, F. K. Bozal, A. Skepner, D. Raymond, S. LaRussa, D. C. McKinney, Y. Freyzon, Y. Baidi, D. Porter, A. J. Aguirre, A. Ianari, B. McMillan, W. R. Sellers, Molecular basis for substrate recruitment to the PRMT5 methylosome. *Mol. Cell* **81**, 3481–3495.e7 (2021).

71. M. T. Schweizer, E. S. Antonarakis, H. Wang, A. Seun Ajiboye, A. Spitz, H. Cao, J. Luo, M. C. Haffner, S. Yegnasubramanian, M. A. Carducci, M. A. Eisenberger, J. T. Isaacs, S. R. Denmeade, Effect of bipolar androgen therapy for asymptomatic men with castration-resistant prostate cancer: Results from a pilot clinical study. *Sci. Transl. Med.* **7**, 269ra2 (2015).

72. M. D. Nyquist, L. S. Ang, A. Corella, I. M. Coleman, M. P. Meers, A. J. Christiani, C. Pierce, D. H. Janssens, H. E. Meade, A. Bose, L. Brady, T. Howard, N. De Sarkar, S. B. Frank, R. F. Dumpit, J. T. Dalton, E. Corey, S. R. Plymate, M. C. Haffner, E. A. Mostaghel, P. S. Nelson, Selective androgen receptor modulators activate the canonical prostate cancer androgen receptor program and repress cancer growth. *J. Clin. Invest.* **131**, e146777 (2021).

73. X. Qiu, L. G. Brown, J. L. Conner, H. M. Nguyen, N. Boufaied, S. A. Alaiwi, J. H. Seo, T. El Zarif, C. Bell, E. O'Connor, B. Hanratty, M. Pomerantz, M. L. Freedman, M. Brown, M. C. Haffner, P. S. Nelson, F. Y. Feng, D. P. Labbé, H. W. Long, E. Corey, Response to supraphysiological testosterone is predicted by a distinct androgen receptor cistrome. *JCI Insight* **7**, e157164 (2022).

74. V. Sheikhhassani, B. Scalvini, J. Ng, L. W. H. J. Heling, Y. Ayache, T. M. J. Evers, E. Estébanez-Perpiñá, I. J. McEwan, A. Mashaghi, Topological dynamics of an intrinsically disordered N-terminal domain of the human androgen receptor. *Protein Sci.* **31**, e4334 (2022).

75. S. A. Mosure, P. Munoz-Tello, K.-T. Kuo, B. M. Tavish, X. Yu, D. Scholl, C. C. Williams, T. S. Strutzenberg, J. Bass, R. Brust, A. A. Deniz, P. R. Griffin, D. J. Kojetin, Structural basis of interdomain communication in PPARγ (2022); www.biorxiv.org/content/10.1101/2022.07.13.499031v1.abstract.

76. X. Zhang, X. Cheng, Structure of the Predominant Protein Arginine Methyltransferase PRMT1 and Analysis of Its Binding to Substrate Peptides. *Structure* **11**, 509–520 (2003).

77. D. Musiani, J. Bok, E. Massignani, L. Wu, T. Tabaglio, M. R. Ippolito, A. Cuomo, U. Ozbek, H. Zorgati, U. Ghoshdastider, R. C. Robinson, E. Guccione, T. Bonaldi, Proteomics profiling of arginine methylation defines PRMT5 substrate specificity. *Sci. Signal.* **12**, eaat8388 (2019).

78. E. S. Burgos, C. Wilczek, T. Onikubo, J. B. Bonanno, J. Jansong, U. Reimer, D. Shechter, Histone H2A and H4 N-terminal tails are positioned by the MEP50 WD repeat protein for efficient methylation by the PRMT5 arginine methyltransferase. *J. Biol. Chem.* **290**, 9674–9689 (2015).

79. P. Chymkowitch, N. Le May, P. Charneau, E. Compe, J. M. Egly, The phosphorylation of the androgen receptor by TFIIH directs the ubiquitin/proteasome process. *EMBO J.* **30**, 468–479 (2011).

80. S. Sarkar, D. L. Brautigan, S. J. Parsons, J. M. Larner, Androgen receptor degradation by the E3 ligase CHIP modulates mitotic arrest in prostate cancer cells. *Oncogene* **33**, 26–33 (2014).

81. C. Liu, W. Lou, J. C. Yang, L. Liu, C. M. Armstrong, A. P. Lombard, R. Zhao, O. D. V. Noel, C. G. Tepper, H. W. Chen, M. Dall'Era, C. P. Evans, A. C. Gao, Proteostasis by STUB1/HSP70 complex controls sensitivity to androgen receptor targeted therapy in advanced prostate cancer. *Nat. Commun.* **9**, 4700 (2018).

82. M. L. Mohler, A. Sikdar, S. Ponnusamy, D. J. Hwang, Y. He, D. D. Miller, R. Narayanan, An overview of next-generation androgen receptor-targeted therapeutics in development for the treatment of prostate cancer. *Int. J. Mol. Sci.* **22**, 2124 (2021).

83. S. Ha, G. Luo, H. Xiang, A comprehensive overview of small-molecule androgen receptor degraders: Recent progress and future perspectives. *J. Med. Chem.* **65**, 16128–16154 (2022).

84. X. Deng, G. Shao, H. T. Zhang, C. Li, D. Zhang, L. Cheng, B. D. Elzey, R. Pili, T. L. Ratliff, J. Huang, C. D. Hu, Protein arginine methyltransferase 5 functions as an epigenetic activator of the androgen receptor to promote prostate cancer cell growth. *Oncogene* **36**, 1223–1231 (2017).

85. K. Hosohata, P. Li, Y. Hosohata, J. Qin, R. G. Roeder, Z. Wang, Purification and identification of a novel complex which is involved in androgen receptor-dependent transcription. *Mol. Cell. Biol.* **23**, 7019–7029 (2003).

86. Y. Peng, F. Chen, J. Melamed, L. Chiriboga, J. Wei, X. Kong, M. Mcleod, Y. Li, C. X. Li, A. Feng, M. J. Garabedian, Z. Wang, R. G. Roeder, P. Lee, Distinct nuclear and cytoplasmic functions of androgen receptor cofactor p44 and association with androgen-independent prostate cancer. *Proc. Natl. Acad. Sci. U.S.A.* **105**, 5236–5241 (2008).

87. L. Zhou, H. Wu, P. Lee, Z. Wang, Roles of the androgen receptor cofactor p44 in the growth of prostate epithelial cells. *J. Mol. Endocrinol.* **37**, 283–300 (2006).

88. S. Yin, L. Liu, C. Brobbey, V. Palanisamy, L. E. Ball, S. K. Olsen, M. C. Ostrowski, W. Gan, PRMT5-mediated arginine methylation activates AKT kinase to govern tumorigenesis. *Nat. Commun.* **12**, 3444 (2021).

89. C. Helsen, T. Nguyen, T. Vercruysse, S. Wouters, D. Daelemans, A. Voet, F. Claessens, The T850D phosphomimetic mutation in the androgen receptor ligand binding domain enhances recruitment at activation function 2. *Int. J. Mol. Sci.* **23**, 1557 (2022).

90. I. Maksimovic, Y. David, Non-enzymatic covalent modifications as a new chapter in the histone code. *Trends Biochem. Sci.* **46**, 718–730 (2021).

91. H. S. Soifer, N. Souleimanian, S. Wu, A. M. Voskresenskiy, F. K. Collak, B. Cinar, C. A. Stein, Direct regulation of androgen receptor activity by potent CYP17 inhibitors in prostate cancer cells. *J. Biol. Chem.* **287**, 3777–3787 (2012).

92. A. Dobin, C. A. Davis, F. Schlesinger, J. Drenkow, C. Zaleski, S. Jha, P. Batut, M. Chaisson, T. R. Gingeras, STAR: Ultrafast universal RNA-seq aligner. *Bioinformatics* **29**, 15–21 (2013).

93. A. Frankish, M. Diekhans, A. M. Ferreira, R. Johnson, I. Jungreis, J. Loveland, J. M. Mudge, C. Sisu, J. Wright, J. Armstrong, I. Barnes, A. Berry, A. Bignell, S. Carbonell Sala, J. Chrast, F. Cunningham, T. Di Domenico, S. Donaldson, I. T. Fiddes, C. García Girón, J. M. Gonzalez, T. Grego, M. Hardy, T. Hourlier, T. Hunt, O. G. Izuogu, J. Lagarde, F. J. Martin, L. Martínez, S.

Mohanan, P. Muir, F. C. P. Navarro, A. Parker, B. Pei, F. Pozo, M. Ruffier, B. M. Schmitt, E. Stapleton, M. M. Suner, I. Sycheva, B. Uszczynska-Ratajczak, J. Xu, A. Yates, D. Zerbino, Y. Zhang, B. Aken, J. S. Choudhary, M. Gerstein, R. Guigó, T. J. P. Hubbard, M. Kellis, B. Paten, A. Reymond, M. L. Tress, P. Flicek, GENCODE reference annotation for the human and mouse genomes. *Nucleic Acids Res.* **47**, D766–D773 (2019).

94. V. Jimenez-Jacinto, A. Sanchez-Flores, L. Vega-Alvarado, Integrative Differential expression analysis for multiple experiments (IDEAMEX): A web server tool for integrated RNA-seq data analysis. *Front. Genet.* **10**, 279 (2019).

95. M. I. Love, W. Huber, S. Anders, Moderated estimation of fold change and dispersion for RNA-seq data with DESeq2. *Genome Biol.* **15**, 550 (2014).

96. M. E. Ritchie, B. Phipson, D. Wu, Y. Hu, C. W. Law, W. Shi, G. K. Smyth, *limma* powers differential expression analyses for RNA-sequencing and microarray studies. *Nucleic Acids Res.* **43**, e47 (2015).

97. Z. Gu, R. Eils, M. Schlesner, Complex heatmaps reveal patterns and correlations in multidimensional genomic data. *Bioinformatics* **32**, 2847–2849 (2016).

98. S. Anders, W. Huber, Differential expression analysis for sequence count data. *Genome Biol.* **11**, R106 (2010).

99. A. Subramanian, P. Tamayo, V. K. Mootha, S. Mukherjee, B. L. Ebert, M. A. Gillette, A. Paulovich, S. L. Pomeroy, T. R. Golub, E. S. Lander, J. P. Mesirov, Gene set enrichment analysis: A knowledge-based approach for interpreting genome-wide expression profiles. *Proc. Natl. Acad. Sci. U.S.A.* **102**, 15545–15550 (2005).

100. T. Wu, E. Hu, S. Xu, M. Chen, P. Guo, Z. Dai, T. Feng, L. Zhou, W. Tang, L. Zhan, X. Fu, S. Liu, X. Bo, G. Yu, clusterProfiler 4.0: A universal enrichment tool for interpreting omics data. *Innovation* **2**, 100141 (2021).

101. M. Schubert, B. Klinger, M. Klünemann, A. Sieber, F. Uhlitz, S. Sauer, M. J. Garnett, N. Blüthgen, J. Saez-Rodriguez, Perturbation-response genes reveal signaling footprints in cancer gene expression. *Nat. Commun.* **9**, 20 (2018).

102. C. Poulard, J. Jacquemetton, T. H. Pham, M. Le Romancer, Using proximity ligation assay to detect protein arginine methylation. *Methods* **175**, 66–71 (2020).

103. J. Schindelin, I. Arganda-Carreras, E. Frise, V. Kaynig, M. Longair, T. Pietzsch, S. Preibisch, C. Rueden, S. Saalfeld, B. Schmid, J. Y. Tinevez, D. J. White, V. Hartenstein, K. Eliceiri, P. Tomancak, A. Cardona, Fiji: An open-source platform for biological-image analysis. *Nat. Methods* **9**, 676–682 (2012).

104. R. Gustafsson, U. Eckhard, W. Ye, E. D. Enbody, M. Pettersson, P. Jemth, L. Andersson, M. Selmer, Structure and characterization of phosphoglucomutase 5 from atlantic and baltic herring—An inactive enzyme with intact substrate binding. *Biomolecules.* **10**, 1631 (2020).

105. T. M. K. Cheng, T. L. Blundell, J. Fernandez-Recio, PyDock: Electrostatics and desolvation for effective scoring of rigid-body protein-protein docking. *Proteins Struct. Funct. Genet.* **68**, 503–515 (2007).

106. J. Fernández-Recio, M. Totrov, R. Abagyan, Identification of protein-protein interaction sites from docking energy landscapes. *J. Mol. Biol.* **335**, 843–865 (2004).

107. R. Guerois, J. E. Nielsen, L. Serrano, Predicting changes in the stability of proteins and protein complexes: A study of more than 1000 mutations. *J. Mol. Biol.* **320**, 369–387 (2002).

108. N. Halabi, O. Rivoire, S. Leibler, R. Ranganathan, Protein sectors: Evolutionary units of three-dimensional structure. *Cell* **138**, 774–786 (2009).

109. S. W. Lockless, R. Ranganathan, Evolutionarily conserved pathways of energetic connectivity in protein families. *Science* **286**, 295–299 (1999).

110. O. Rivoire, K. A. Reynolds, R. Ranganathan, Evolution-Based Functional Decomposition of Proteins. *PLOS Comput. Biol.* **12**, e1004817 (2016).

111. J. Wang, R. M. Wolf, J. W. Caldwell, P. A. Kollman, D. A. Case, Development and testing of a general Amber force field. *J. Comput. Chem.* **25**, 1157–1174 (2004).

112. C. I. Bayly, P. Cieplak, W. D. Cornell, P. A. Kollman, A well-behaved electrostatic potential based method using charge restraints for deriving atomic charges: The RESP model. *J. Phys. Chem.* **97**, 10269–10280 (1993).

113. S. Izadi, R. Anandakrishnan, A. V. Onufriev, Building water models: A different approach. *J. Phys. Chem. Lett.* **5**, 3863–3871 (2014).

114. C. Tian, K. Kasavajhala, K. A. A. Belfon, L. Raguette, H. Huang, A. N. Migues, J. Bickel, Y. Wang, J. Pincay, Q. Wu, C. Simmerling, Ff19SB: Amino-acid-specific protein backbone parameters trained against quantum mechanics energy surfaces in solution. *J. Chem. Theory Comput.* **16**, 528–552 (2020).

115. T. Darden, D. York, L. Pedersen, Particle mesh Ewald: An $N\cdot\log(N)$ method for Ewald sums in large systems. *J. Chem. Phys.* **98**, 10089–10092 (1993).

116. J. J. Perez, M. S. Tomas, J. Rubio-Martinez, Assessment of the sampling performance of multiple-copy dynamics versus a unique trajectory. *J. Chem. Inf. Model.* **56**, 1950–1962 (2016).

117. C. W. Hopkins, S. Le Grand, R. C. Walker, A. E. Roitberg, Long-time-step molecular dynamics through hydrogen mass repartitioning. *J. Chem. Theory Comput.* **11**, 1864–1874 (2015).

118. J. P. Ryckaert, G. Ciccotti, H. J. C. Berendsen, Numerical integration of the cartesian equations of motion of a system with constraints: Molecular dynamics of n-alkanes. *J. Comput. Phys.* **23**, 327–341 (1977).

119. S. Vatansever, B. Erman, Z. H. Gümüş, Oncogenic G12D mutation alters local conformations and dynamics of K-Ras. *Sci. Rep.* **9**, 11730 (2019).

120. A. R. Atilgan, P. Akan, C. Baysal, Small-world communication of residues and significance for protein dynamics. *Biophys. J.* **86**, 85–91 (2004).

121. Y. C. Yang, C. A. Banuelos, N. R. Mawji, J. Wang, M. Kato, S. Haile, I. J. McEwan, S. Plymate, M. D. Sadar, Targeting androgen receptor activation function-1 with EPI to overcome resistance mechanisms in castration-resistant prostate cancer. *Clin. Cancer Res.* **22**, 4466–4477 (2016).

122. N. G. R. D. Elshan, M. B. Rettig, M. E. Jung, Molecules targeting the androgen receptor (AR) signaling axis beyond the AR-Ligand binding domain. *Med. Res. Rev.* **39**, 910–960 (2019).

3.2. The multivalency of the glucocorticoid receptor ligand-binding domain explains its manifold physiological activities

Alba Jiménez-Panizo*, **Andrea Alegre-Martí***, Theophilus T. Tettey*, Gregory Fettweis, Montserrat Abella, Rosa Antón, Thomas A. Johnson, Sohyoung Kim, R. Louis Schiltz, Israel Núñez-Barrios, Joan Font-Díaz, Carme Caelles, Annabel F. Valledor, Paloma Pérez, Ana M. Rojas, Juan Fernández-Recio, Diego M. Presman, Gordon L. Hager‡, Pablo Fuentes-Prior‡, and Eva Estébanez-Perpiñá‡.

* These authors equally contributed to this work.
‡ These authors jointly supervised this work.

Published in: Nucleic Acids Research, 2022
Impact factor: 19.16
Quartile: Q1
DOI: 10.1093/nar/gkac1119

For this study I performed GR-LBD site-directed mutagenesis, protein expression, purification, and crystallisation assays. We tried to crystallize several GR-LBD mutants and managed to successfully solve the structure of Y545A (PDB: 7YXR). I performed and interpreted surface plasmon resonance experiments with the GR-LBD Y545C and Y545A variants to assess the contribution of Tyr545 to GR-LBD homodimerization in solution. The results confirmed that this residue plays a key role for GR-LBD homodimer formation, as evidenced by the decrease in homodimer affinity when Tyr545 is truncated to Ala and the increase in the complex affinity and lifetime due to mutant Cys545-Cys545' disulfide bond formation. I produced the Supplementary Figure 2 to show the results of this experiment.

Published online 5 December 2022

Nucleic Acids Research, 2022, Vol. 50, No. 22 ***13063–13082***
https://doi.org/10.1093/nar/gkac1119

The multivalency of the glucocorticoid receptor ligand-binding domain explains its manifold physiological activities

Alba Jiménez-Panizo[1,2,3,†], Andrea Alegre-Martí[1,2,†], Theophilus T. Tettey[3,†], Gregory Fettweis[3], Montserrat Abella[1,2], Rosa Antón[4], Thomas A. Johnson[3], Sohyoung Kim[3], R. Louis Schiltz[3], Israel Núñez-Barrios[5], Joan Font-Díaz[2,6], Carme Caelles[2,7], Annabel F. Valledor[2,6], Paloma Pérez[8], Ana M. Rojas[5], Juan Fernández-Recio[9], Diego M. Presman[10], Gordon L. Hager[3,*], Pablo Fuentes-Prior[4,*] and Eva Estébanez-Perpiñá[1,2,*]

[1]Department of Biochemistry and Molecular Biomedicine, Faculty of Biology, University of Barcelona (UB), 08028 Barcelona, Spain, [2]Institute of Biomedicine of the University of Barcelona (IBUB), University of Barcelona (UB), 08028 Barcelona, Spain, [3]National Cancer Institute, National Institutes of Health, Bethesda, MD 20892-5055, USA, [4]Biomedical Research Institute Sant Pau (IIB Sant Pau), 08041 Barcelona, Spain, [5]Andalusian Center for Developmental Biology (CABD-CSIC). Campus Universitario Pablo de Olavide, 41013 Sevilla, Spain, [6]Department of Cell Biology, Physiology and Immunology, Faculty of Biology, University of Barcelona, 08028 Barcelona, Spain, [7]Department of Biochemistry and Physiology, Faculty of Pharmacy and Food Sciences, University of Barcelona, Barcelona 08028, Spain, [8]Instituto de Biomedicina de Valencia (IBV)-CSIC, 46010, Valencia, Spain, [9]Instituto de Ciencias de la Vid y del Vino (ICVV), CSIC - Universidad de La Rioja - Gobierno de La Rioja, 26007 Logroño, Spain and [10]IFIBYNE, UBA-CONICET, Universidad de Buenos Aires, Facultad de Ciencias Exactas y Naturales, Buenos Aires C1428EGA, Argentina.

Received May 03, 2022; Revised October 28, 2022; Editorial Decision October 28, 2022; Accepted November 08, 2022

ABSTRACT

The glucocorticoid receptor (GR) is a ubiquitously expressed transcription factor that controls metabolic and homeostatic processes essential for life. Although numerous crystal structures of the GR ligand-binding domain (GR-LBD) have been reported, the functional oligomeric state of the full-length receptor, which is essential for its transcriptional activity, remains disputed. Here we present five new crystal structures of agonist-bound GR-LBD, along with a thorough analysis of previous structural work. We identify four distinct homodimerization interfaces on the GR-LBD surface, which can associate into 20 topologically different homodimers. Biologically relevant homodimers were identified by studying a battery of GR point mutants including crosslinking assays in solution, quantitative fluorescence microscopy in living cells, and transcriptomic analyses. Our results highlight the relevance of non-canonical dimerization modes for GR, especially of contacts made by loop L1–3 residues such as Tyr545. Our work illustrates the unique flexibility of GR's LBD and suggests different dimeric conformations within cells. In addition, we unveil pathophysiologically relevant quaternary assemblies of the receptor with important implications for glucocorticoid action and drug design.

INTRODUCTION

Nuclear receptors (NRs) are transcription factors that control central physiological processes ranging from reproduction and development to metabolism, homeostasis, and ultradian rhythms (1,2). Steroid receptors are a NR subclass that includes the glucocorticoid receptor (GR/NR3C1) (Figure 1A), the androgen receptor (AR/NR3C4), the progesterone receptor (PR/NR3C3), the mineralocorticoid receptor (MR/NR3C2), as well as estrogen receptors α and

*To whom correspondence should be addressed. Tel: +34 93 403 11 19; Email: evaestebanez@ub.edu
Correspondence may also be addressed to Pablo Fuentes-Prior. Email: fuentespriorpablo@gmail.com
Correspondence may also be addressed to Gordon L. Hager. Tel: +1 240 760 6618; Email: hagerg@dce41.nci.nih.gov
†The authors wish it to be known that, in their opinion, the first three authors should be regarded as Joint First Authors.

Published by Oxford University Press on behalf of Nucleic Acids Research 2022.
This work is written by (a) US Government employee(s) and is in the public domain in the US.

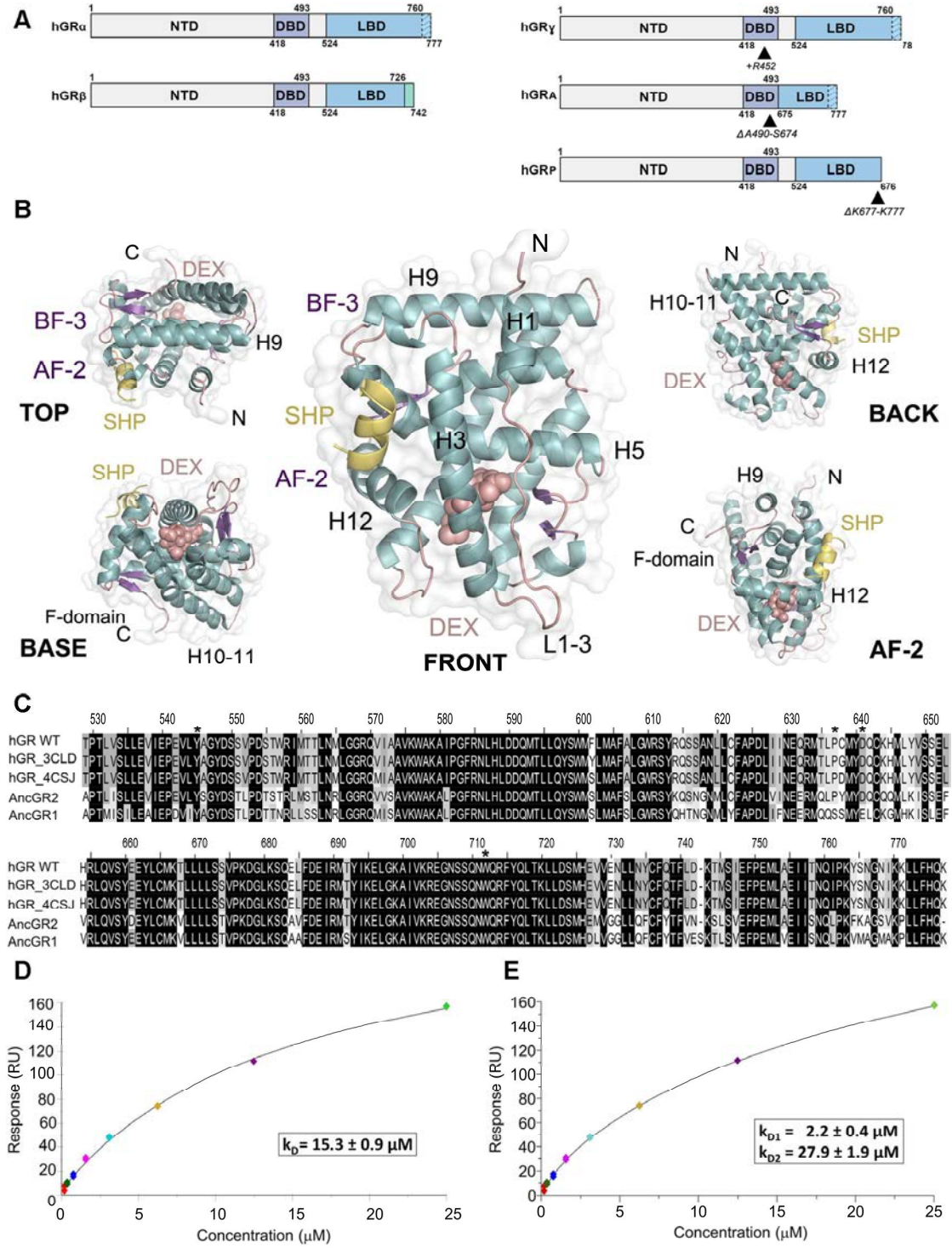

Figure 1. The ligand-binding domain of GR self-associates in solution. (**A**) Schematic representation of GR domain organization. GRα and GRβ are identical up to residue 727 (H10/11), but the last 50 (in GRα) and 15 residues (in GRβ, green box) are unrelated. Other GR isoforms are shown (right). (**B**) Overall structure of the GR-LBD monomer. The module is shown in standard orientation in the middle of the panel (i.e. with H1 and H3 displayed facing the viewer and the AF-2 pocket on the left). Four additional views are shown to present other LBD areas. Models are depicted as cartoons with helices (blue), loops (pink) and beta-sheets (purple). DEX (salmon spheres) and SHP peptide (yellow cartoon) are shown. The BF-3 pocket is also labeled. (**C**) Sequence alignment of LBDs between WT human GR, two engineered variants used in several structures (PDBs 3CLD and 4CSJ), and the ancGR1 and 2 forms. Strictly conserved residues are white with black shading; other conservatively replaced residues are shaded gray. Residues mutated in the current study are marked with asterisks. (D, E) SPR analysis of GR-LBD self-association according to (**D**) 1:1 or (**E**) multisite models. The results of experiments conducted in duplicate are shown along with the calculated affinity constants (k_D). Data were fitted to the 1:1 and multisite models with χ^2 values of 4.52 and 1.25, respectively.

β (ERα/NR3A1 and ERβ/NR3A2) (3–5). NRs display a modular architecture with an unstructured N-terminal domain (NTD) followed by a 'core' formed by a highly conserved DNA-binding domain (DBD), an interdomain linker or hinge, and a C-terminal ligand-binding domain (LBD) (Figures 1A and Supplementary Figure S1) (6–8). GR binds glucocorticoids (GCs; either endogenous such as cortisol, or synthetic, e.g. dexamethasone (DEX)) in an internal cavity of the LBD. This ligand-binding pocket (LBP) is allosterically coupled to activation function 2 (AF-2), a pocket that binds coregulators (9,10). A nearby cavity, topologically equivalent to AR binding function-3 (BF-3) interacts with cochaperones (11,12). Finally, the LBDs of GR and the related oxosteroid receptors (AR, PR and MR) feature a unique C-terminal extension termed F-domain (5,13) (Figure 1B).

NR3C1 is constitutively expressed in nearly all vertebrate cells. Upon ligand binding, GR translocates to the nucleus (14) where it binds to chromatin (15) and integrates signals ranging from available ligands to chromatin remodeling complexes (16) to control cognate target genes (up to 17% of the human transcriptome (17)) to regulate inflammation, cell proliferation, and differentiation in a tissue-specific manner (18–20). GR also antagonizes the activity of other transcription factors such as activator protein 1 (AP-1) and nuclear factor kappaB (NF-κB) (21). Even though monomeric GR is believed to play a DNA-independent role in modulating inflammation (22), more recent work suggests the relevance also of both direct DNA binding of GR dimers/tetramers (23–28). In line with these manifold activities, alterations in GR signaling pathways due to mutations in *NR3C1* lead to impaired sensitivity to GCs, which may manifest as either GC resistance (Chrousos syndrome) or hypersensitivity (29). GR is thus an important pharmacological target to treat inflammatory diseases, but chronic GC use results in drug resistance and side effects (16).

Structures of the DBD dimer, both free and DNA-bound have been solved (30–33), and the LBD has been extensively studied in complex with agonists or antagonists (3,15,34–37). To date, however, no structure of full-length (FL) GR has been solved. Thus, several key issues regarding GR tertiary and quaternary structure remain unresolved: what is the conformation adopted by dimeric GR and DNA-bound tetramers *in vivo*, and how do LBDs associate in these multimers? Are topologically distinct GR conformations possible, and are they linked to specific biological functions (e.g. activation vs. repression of transcription)? Knowledge of the oligomeric conformations of oxosteroid receptors would aid in the design of novel selective, potent GR modulators that may lessen side effects of current drugs.

Here we present a systematic structure-and-function investigation of GR multimerization using X-ray crystallography, state-of-the-art bioinformatics tools, surface plasmon resonance (SPR) and crosslinking experiments in solution, quantitative fluorescence microscopy in live cells, and RNA-seq analysis of relevant GR variants. We report five new structures of DEX-bound GR-LBD (GR-LBD·DEX) and integrate this information into the wealth of previous structural data to generate the most thorough catalog to date of possible GR homodimers. Four distinct interfaces have been observed to participate in 20 topologically different GR-LBD homodimers. We have identified the most favored GR homodimers and suggest how they can combine into pathophysiologically relevant oligomeric assemblies in cells.

MATERIALS AND METHODS

Peptides and proteins

A peptide corresponding to residues Gln18-Lys27 of the small heterodimer partner (SHP/NR0B2, box 1 motif; NH2-Q^{18}GAASRPAILYALLSSSLK^{27}-OH) was custom-synthesized at Pepmic. Recombinant ancGR2-LBD (corresponding to residues 529–777 of the human receptor) cloned into a pMALCH10T vector was expressed as fusion protein with an N-terminal maltose-binding protein (MBP) and a hexahistidine tag and purified to homogeneity using standard chromatographic procedures (38).

Crystallization and structure determination

Purified, concentrated DEX-bound ancGR2-LBD was combined with a 3-fold molar excess of SHP peptide and incubated for one hour at RT. Drops of the ancGR2-LBD-SHP mixture were equilibrated against 0.1 M Tris–HCl, pH 8.0, 0.2 M sodium chloride, 2.0 M ammonium sulfate ($P3_1$, $I4_122$ and $I4_132$ crystals); 0.1 M PIPES, pH 7.0, 0.1 M ammonium acetate, 2.5 M sodium formate ($P6_1$ crystals); or 85 mM sodium cacodylate trihydrate, pH 6.5, 0.17 M sodium acetate trihydrate, 25.5% (w/v) PEG8000, 15% (v/v) glycerol (C2 crystals) using the sitting drop vapor-diffusion method. Diffraction data were collected at 100 K at the ALBA-CELLS synchrotron and processed using MOSFLM (http://www.mrc-lmb.cam.ac.uk/harry/mosflm/) and CCP4 (http://www.ccp4.ac.uk/). The crystal structures were solved and refined using MOLREP, REFMAC5 and COOT from the CCP4 package. Crystal packing was analyzed using PISA (http://www.ebi.ac.uk/), model quality was assessed with MolProbity (http://molprobity.biochem.duke.edu/), and figures were prepared with PyMOL (http://www.pymol.org).

Surface plasmon resonance (SPR) analyses

SPR analyses were performed at 25°C in a BIAcore T200 instrument (GE Healthcare). Highly purified, DEX-bound recombinant WT ancGR2-LBD and its Y545C and Y545A mutants were diluted in 10 mM sodium acetate, pH 5.0, and directly immobilized on CM5 chips (GE Healthcare) by amine coupling at densities between 300 and 400 resonance units (RU). As a reference, one of the channels was also amine-activated and blocked in the absence of protein. The running buffer was 50 mM HEPES, pH 7.2, 50 mM Li_2SO_4, 5% glycerol, 5 μM DEX, supplemented with various concentrations of dithiothreitol (DTT). Sensorgrams were analyzed with the BIAcore T200 Evaluation software 3.0 and fitted according to the Langmuir 1:1 and multisite models.

Crosslinking experiments

Purified recombinant ancGR2-LBD (33 μM) was incubated with 100-fold molar excess of crosslinkers 1-

ethyl-3-(3-dimethylaminopropyl)carbodiimide hydrochloride (EDC, Pierce) or disuccinimidyl dibutyric acid (DSBU) for 1–2 h at 37°C following the manufacturer's instructions. In some experiments the Y545C variant was incubated after affinity purification for 30 min at room temperature without further treatment. Samples of the reaction mixtures were boiled in the presence of Laemmli sample buffer, either reducing (EDC- and DSBU-crosslinked proteins) or non-reducing (in the case of the Y545C variant) and resolved by SDS-PAGE.

Nano-LC–MS/MS mass spectrometry

CBB-stained bands corresponding to monomeric, dimeric and tetrameric GR-LBD after crosslinking with EDC or DSBU were excised from the gels and subjected to in-gel digestion following standard protocols. Briefly, excised bands were reduced (10 mM DTT) in 50 mM bicarbonate buffer, pH 8.0, for 45 min at 56°C, alkylated (50 mM iodoacetamide in 50 mM ammonium bicarbonate buffer for 30 min at 25°C) and digested with either trypsin alone or followed by GluC treatment, or with chymotrypsin overnight at 37°C in 100 mM ammonium acetate buffer, pH 8.0 (sequencing-grade endoproteases were from Promega). In the case of the Y545C mutant, proteins in the excised bands were directly alkylated without previous DTT treatment to prevent reduction of the Cys545–Cys545' disulfide bridge.

Tryptic peptides were diluted in 1% formic acid and loaded onto a 180 μm × 20 mm C18 Symmetry trap column (Waters) at a flow rate of 15 μl/min using a nanoAcquity Ultra Performance LCTM chromatographic system (Waters). Peptides were separated using a C18 analytical column (BEH130 C18, 75 mm × 25 cm, 1.7 μm; Waters) with a 120-min run, comprising three consecutive linear gradients: from 1 to 35% B in 100 min, from 35 to 50% B in 10 min, and from 50 to 85% B in 10 min (A = 0.1% formic acid in water, B = 0.1% formic acid in CH_3CN). The column outlet was directly connected to an Advion TriVersa NanoMate (Advion) fitted on an LTQ-FT Ultra mass spectrometer (Thermo), which was operated in positive mode using the data-dependent acquisition mode. Survey MS scans were acquired in the FT-ICR cell with the resolution (defined at 400 m/z) set to 100,000. Up to six of the most intense ions per scan were fragmented and detected in the linear ion trap. The ion count target value was 1,000,000 for the survey scan and 50,000 for the MS/MS scan. Target ions already selected for MS/MS were dynamically excluded for 30 s. Spray voltage in the NanoMate source was set to 1.70 kV. Capillary voltage and tube lens on the LTQ-FT were tuned to 40 and 120 V, respectively. The minimum signal required to trigger MS to MS/MS switch was set to 1,000 and activation Q value was set at 0.25. Singly charged precursors were rejected for fragmentation.

Differential scanning fluorimetry

Thermofluor experiments were performed in an iQ5 Multicolor Real Time PCR Detection System (BIO-RAD) using 96-well plates (Hard-Shell® High-Profile Semi-Skirted PCR Plate, BIO-RAD) and a 25 μl total volume for each reaction. Melting curves were acquired from eight replicates to determine the average melting temperature (Tm). GR-LBD samples (0.5 mg/mL) were prepared in 20 mM HEPES, pH 8.0, 200 mM NaCl, 10% glycerol, 50 mM imidazole, 1 mM DTT, 50 μM DEX, and centrifuged 5 min. at 14,000 rpm immediately before measurements. SYPRO Orange dye (Sigma-Aldrich) was firstly prepared at 80× in the same buffer, starting from a 5,000× commercial dilution. The final concentration of the dye in each well was 5×. The plates were sealed with optical-quality sealing film (Microseal® B Seals, BIO-RAD) and centrifuged at 2,000 × g for 30 s. Samples were equilibrated for 60 s and analyzed using a linear gradient from 16 to 95°C with increments of 1°C/min, recording the SYPRO orange fluorescence throughout the gradient using the iQ5 Optical System Software 2.0. Values were fitted using the online tool JTSA with the four-parameter logistic equation, and the calculated fluorescence midpoints were compared with an unpaired t-test for equal variances using GraphPad Prism 8.

Cell line generation and culture

Mammary adenocarcinoma 3617-derived GRKO cells for number and brightness assays (N&B) were transiently transfected with the various forms of mouse GR (WT, W718A, Y551A, Y551A-Dim, P643A, D647V, P643A-Tetra, D647V-Tetra) using jetOPTIMUS™ reagent (Poly-Plus) according to the manufacturer's instructions. The cell lines used for total RNA-sequencing (RNA-Seq) experiments were developed in the same GRKO cell line (25,39). Briefly, GFP-tagged versions of mouse GR (WT, Y551A, Y551A-Dim, D647V, D647V-Tetra) were stably integrated into the GT-Rosa26 locus via Crispr Cas9/homology directed repair with puromycin selection and FACS sorting. Cells for the RNA-Seq and N&B assays were grown in Dulbecco's modified Eagle's medium (DMEM, Invitrogen) supplemented with 5 μg/ml tetracycline (Sigma), 10% fetal bovine serum (Sigma), sodium pyruvate, non-essential amino acids, and 2 mM L-glutamine maintained in a humidifier at 37°C. The FBS-supplemented media was replaced with media supplemented with charcoal/dextran-treated FBS (CSS) to remove glucocorticoids from cells for 24 h prior to hormone treatment (100 nM DEX). All variants of GFP-GR for RNA-Seq and N&B were generated with the QuikChange II XL Site-Directed Mutagenesis Kit (Stratagene).

Number and brightness (N&B) analysis

Images were taken at the CCR, LRBGE Optical Microscopy Core facility in a LSM 780 laser scanning microscope (Carl Zeiss, Inc.) equipped with an environmental chamber. Cells were imaged from 20 min up to a maximum of 2 h after DEX addition. We used a 63× oil immersion objective (NA = 1.4). The excitation source was a multi-line Ar laser tuned at 488 nm. Fluorescence was detected with a GaAsP detector in photon-counting mode.

N&B measurements were done as previously described (24). For each studied cell, a single-plane stack of 150 images (256 × 256 pixels) were taken with a pixel size of 80 nm and the pixel dwell time of 6.3 μs. In all stacks, we

discarded the first 10 images to reduce the effect of image bleaching on the results. The frame time under these conditions is 0.97 s, which guarantees independent sampling of molecules according to previously reported FCS measurements (40). Each stack was further analyzed using the N&B routine of the SIMFCS 2.0 software (Global Dynamics). In this routine, the average fluorescence intensity ($<I>$) and its variance (σ^2) at each pixel of an image are determined from the intensity values obtained at the given pixel along the image stack. The apparent brightness (B) is calculated as the ratio of σ^2 to $<I>$ while the apparent number of moving particles (N) corresponds to the ratio of $<I>$ to B (41). We used SIMFCS 2.0 software to classify pixels as occurring in the nucleus or the MMTV array (42) according to their intensity values. Selection of cells for analysis followed these criteria. (i) In the case of stimulated cells, an accumulation of signal at the MMTV array must be visible. (ii) The average apparent number of molecules (N) in the nuclear compartment must have a range of 3–30 units in all cases, (iii) no saturation of the detector at any pixel ($N < 60$), and (iv) bleaching cannot exceed 5–10%. In a previous work it has been demonstrated that B is equal to the real brightness ε of the particles plus one (41). Therefore, ε at every pixel of images can be easily extracted from B measurements. Importantly, this analysis only provides information regarding the moving or fluctuating fluorescent molecules since fixed molecules (relative to our frame time) will give B values equal to 1. The experiments were independently repeated two times for each treatment/condition.

Total RNA collection and sequencing

RNA isolations were performed using the PureLink RNA kit (Thermo Fisher Scientific 12183018A) as per the manufacturer's instructions. We collected three biological replicates of each condition and sample quality was assessed using the Agilent Bioanalyzer. Strand-specific sequencing libraries were generated from rRNA-depleted (Illumina RS-122-2301) total-RNA samples, using Illumina stranded total RNA (Illumina20020596) according to the manufacturer's instructions. Raw reads were demultiplexed into Fastq format allowing up to one mismatch using Illumina Bcl2fastq v2.17. Reads of the samples were trimmed for adapters and low-quality bases using Cutadapt1.18. RNA-Seq alignment to the mouse mm10 genome was performed by STAR (43). DESEQ2 (44) was used to normalize the data by read depth, identify differentially expressed genes for each form of GR (DEX/vehicle) and calculate $\log_2$ fold changes and false discovery rates (FDR) for each gene. RNA-Seq analyses was performed in two batches that were sequenced and analyzed separately: (i) GFP-GR WT (batch1), GFP-GR-Y551A, GFP-GRdim-Y551A; (ii) GFP-GR WT (batch2), GFP-GR-D647V, GFP-GRtetra-D647V. The two sets of GR WT RNA-Seq data are biological replicates collected and sequenced separately with each batch.

Impact of GR point mutations on protein folding/stability

We estimated the impact of the generated mutations on the overall protein stability with the FoldX empirical force (http://foldxsuite.crg.eu/), which has an estimated error of ∼0.7 kcal/mol. Ten iterations were conducted for each mutation, and later averaged. Free energy differences between mutant and WT proteins ($\Delta\Delta G$) < 1 kcal/mol were considered not significant, those between 1 and 2, 2 and 4, and >4 kcal/mol as slightly, mildly, and strongly destabilizing, respectively.

Sequence conservation analyses

The sequence of human GR-LBD was used as query against the whole NR database, from which we selected ∼880 sequences and included the ancestral GR (38). We also downloaded the sequences corresponding to the LBD regions from a representative fraction of proteomes at PFAM rp55 (PF00104_rp55). (Note that the sequences included in the PFAM alignment are truncated, as they lack for instance the non-conserved F-domain). We followed three different approaches to ensure sequence and alignment diversity and thus stability of the analyses. First, we aligned the ∼880 sequences to a structure-based profile from entries 5UFS (GR-LBD) and 5JJM (AR-LBD). The resulting alignment, 880_aln, was used to run pySCA in addition to the original SCA5 method. Secondly, we aligned our ∼880 sequences to a profile generated from the PF00104_rp55 removing fragments to generate the 840_aln. Finally, we used the PFAM alignment as retrieved from the PFAM database, which contains ∼13,000 sequences (PF00104_rp55).

Multiple correspondence analysis (MCA): identifying specificity-determining positions. We have performed both supervised and unsupervised runs of the S3DET method (http://csbg.cnb.csic.es/JDet/) on 840_aln using default parameters to maintain a large sequence diversity.

Statistical coupling analysis (SCA). We have used the SCA5 8/2011 version with the three different alignment versions given above, and the updated version pySCA with 880_aln. Each alignment produced unique sets of residues termed Sca5_880, Sca5_840 and Sca5_onPFAMrp55, respectively. Next, we labeled residues in the three different sectors that emerged as outputs of the program with letters A, B and C, following their order of appearance. The stability of the identified sectors was assessed with a statistical test based on hypergeometric calculations of the groups of residues belonging to given sectors between pairs of alignments. P-values were adjusted using FDR. Next, specific residues from the significant sectors were extracted and selected according to their rank. For instance, if a particular residue appears only in one sector on a low-ranking pair of alignments (e.g. rank 19, with a borderline P-value) this residue will not be selected as part of a sector. On the contrary, if a residue appears in high-ranking pairs, it will be retained. Residues termed as 'A' and 'B' appeared to be equivalent in different pairs of alignments, so they were assigned to the class sector 2, while residues belonging to the 'C' group were stable, and thus assigned to class sector 1.

Clustering of interaction surfaces in GR-LBD dimers

We grouped the interaction surfaces observed in the 20 topologically different GR-LBD homodimers by a hier-

archical clustering analysis, using *ad-hoc* R scripts. For each dimer, the interaction surface was defined as the set of solvent-exposed residues in the monomers (i.e. residues with >25% relative accessible surface area, ASA) that became buried (<25% relative ASA) in the corresponding dimer. Relative ASA were calculated using ICM (Molsoft LLC). Then, we calculated the center of coordinates of the residues forming each interaction interface. To compare two pairs of homodimers, we computed the Euclidean distances between the centers of their interaction surfaces after superimposition on a common monomer. The 40 × 40 distance matrix representing the distances between all pairs of interaction surfaces was used to perform hierarchical clustering with Ward's method. Finally, the dendrogram generated from this analysis was sorted in order of increasing distance.

Docking experiments and analysis

Homodimeric models of GR-LBD were built using pyDock docking and scoring method (45). First, protein models were prepared by removing all cofactors and heteroatoms, and missing side chains were modeled with SCWRL 3.0 (46). Then, the Fast Fourier Transform (FFT)-based docking programs FTDock (47) (with electrostatics and 0.7-Å grid resolution) and ZDOCK 2.1 (48) were used to generate 10,000 and 2,000 rigid-body docking poses, respectively. These were merged in a single pool for subsequent pyDock scoring, based on energy terms previously optimized for rigid-body docking. The pyDock binding energy is basically composed of ASA-based desolvation, Coulombic electrostatics, and Van der Waals (VdW) energy terms. Electrostatics and VdW contributions were limited to –1.0/+1.0 and 1.0 kcal/mol for each inter-atomic energy value, respectively, to avoid excessive penalization from possible clashes derived from the rigid-body approach.

Predicted dimer interfaces. Optimal docking areas (ODA) per surface-exposed protein residues were obtained by computing surface patches with optimal desolvation energy based on the selection of low-energy docking regions generated from each surface residue (49). ODA hot spots (residues with low ODA values, usually less than –10.0 kcal/mol) indicate regions with favorable desolvation energy upon interaction with a partner protein.

From the resulting docking poses, normalized interface propensity (NIP) values were obtained for each residue with the built-in patch module of pyDock, implementing the pyDockNIP algorithm (50). A NIP value of 1 indicates that the corresponding residue is involved in all predicted interfaces of the 100 lowest energy docking solutions, while a value of 0 means that it appears as expected by random chance. Finally, a negative NIP value implies that the residue appears at the low-energy docking interfaces less often than expected by random chance. Usually, residues with NIP ≥ 0.2 are considered as hot-spot residues when using FTDock.

Energetic characterization of GR dimers. The binding energy of the different crystal dimers was computed with the pyDock bindEy module, using the same scoring function as in docking.

RESULTS

GR-LBD self-associates in solution

To characterize GR-LBD behavior in solution, we performed SPR experiments with the ancient variant of the human GR (ancGR2; Figure 1C). This construct has been repeatedly used in GR structure-function studies because of its higher solubility and stability *in vitro* (7). For simplicity, we will refer to all variants of the receptor as GR-LBD, unless otherwise specified. Briefly, purified GR-LBD·DEX was expressed and purified, immobilized on CM5 chips using amine coupling and increasing concentrations of the same agonist-bound protein (between 0.2 and 25 μM) were run over as analyte. Although GR-LBD immobilization to the CM5 chip might occlude some interaction surfaces, SPR experiments clearly demonstrate interactions between soluble and immobilized GR. Several affinity models were used to interpret SPR data (Figure 1D, E and Supplementary Figure S2A, B). GR-LBD self-association behavior could be fitted to a non-covalent, 1:1 Langmuir model with an affinity constant (k_D) of 15.3 ± 0.9 μM (Figure 1D). Interestingly, we obtained a statistically significant (*F*-test, *P*-value = 0.001) better fit of the data by using a model with non-covalent multisite interactions, with two independent binding sites (k_{D1} = 2.2 ± 0.4 μM and k_{D2} = 27.9 ± 1.9 μM, respectively; Figure 1E). These results are consistent with GR-LBD tetramer formation, as previously reported for FL-GR in living cells (24).

Novel crystal structures of agonist-bound GR-LBD highlight its versatility for self-association

Next, we performed crystallization trials with GR-LBD·DEX in the presence of the AF-2 targeting peptide Gln12-Lys30 from SHP. Coregulator peptides are usually added to induce the active conformation of H12 forming the AF-2 pocket (38). We conducted solubility screens using all commercially available kits (over 4,800 conditions) to identify several unreported crystallization conditions. Diffraction data from crystals that belong to five different space groups (C2, $P3_1$, $P6_1$, $I4_122$ and $I4_132$, from lower to higher symmetry) were collected using synchrotron radiation. The major features of the inter-monomer contacts observed in these new GR-LBD structures are shown in Figure 2 and Supplementary Table S1.

C2 crystals contain a single molecule of GR-LBD·DEX complexed with the SHP peptide, which is well defined by electron density. Two different inter-monomer contacts were identified: the larger, symmetric interaction surface is centered on the L1–3 loops of both monomers and is stabilized by aromatic π-stacking interactions between opposite Tyr545/Tyr545' residues (Figure 2A; residues from the second monomer are primed). Further stability is provided by a network of hydrogen bonds (H-bonds), involving most notably Asp549 (L1–3), Arg569 (H3), and Asp626 (β-strand S1). A significantly smaller, asymmetric interface features Glu688 (H9), whose carboxylate engages in strong H-bonds with the main chain N atom and the hydroxyl of Ser556' (L1–3). Additional interactions involve H1 (Leu532) and H9 residues (Lys695, Lys699) from one LBD molecule facing H6 (Glu632') from the neighbor.

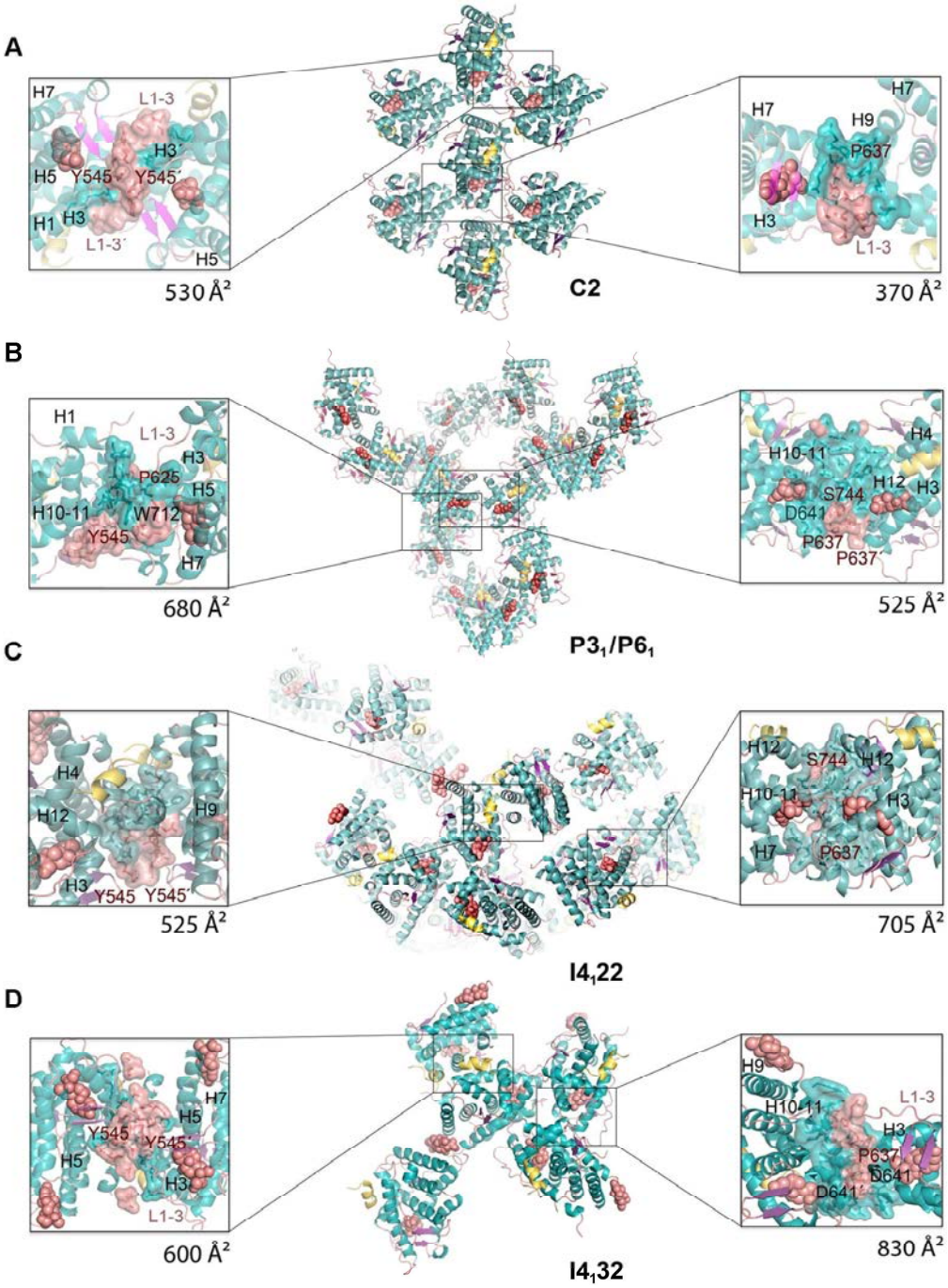

Figure 2. New crystal structures of GR-LBD·DEX reveal a variety of quaternary assemblies. For all structures, the overall crystal packing is shown in the central panels. Monomers are depicted as cartoons with helices colored blue and loops colored salmon. DEX molecules are represented as salmon spheres and SHP peptides as yellow ribbons. Details of intermonomer interfaces are given in the lateral panels, in which the side chains of interacting residues are shown as sticks. (**A**) C2 crystals. Note that major contacts are centered on L1–3 with stacked Tyr545 phenol rings from two neighboring molecules. A monoclinic structure of ancGR2-LBD bound to another synthetic GC, triamcinolone acetonide, and complexed to a shorter SHP peptide had been previously reported (5UFS; (38)). Interestingly, 5UFS features a Tyr545-centered parallel dimer almost identical to the topologically equivalent arrangement in our current C2 crystals. (**B**) Related $P3_1$ and $P6_1$ crystals. Tyr545 engages in heterologous contacts with a neighboring molecule in these crystals (see the position of the Trp712' side chain). Structures of ancGR2-LBD bound to either DEX or a different GC (mometasone furoate) and complexed to a TIF-2 peptide had been previously reported in a similar hexagonal crystal form (3GN8 and 4E2J; a and b axes are ~5% longer in our crystals, while the c axis is ~4% shorter). These relatively small differences in the cell constants compared to the current $P6_1$ structure result in a markedly different small intermonomer interface, however, which is asymmetric in 3GN8/4E2J. (**C, D**) Common packing of $I4_122$ and $I4_132$ crystals. Note that the phenol rings of two Tyr545 residues stack as in the C2 crystals, although the two interacting monomers are fully differently oriented relative to each other. Note also that the largest interface in these crystals features abutting Asp641 side chains from three monomers organized around a local ($I4_122$) or exact 3-fold axis ($I4_132$; right side panel in D).

Residue Pro637' (L5–6) is part of this interface, making strong VdW interactions with Glu688.

Two additional, related structures were solved in the enantiomorphic trigonal and hexagonal space groups, $P3_1$ and $P6_1$ (Figure 2B and Supplementary Table S1). In the GR-LBD·DEX homodimer with the larger interface, the cleft between H9 and H10–11 is filled with side chains from neighboring L1–3' and L5–6' loops. In particular, the aromatic side chains of Trp712 and Phe715 dock into a shallow groove formed by residues at the C-terminal end of H5 and the following loop. This arrangement is thus topologically unrelated to the canonical dimerization mode, in which H10–11 helices from two monomers run parallel to each other, resulting in much larger interaction areas of ∼1,000 Å^2. This interface is strengthened by salt bridges between residues Arg690 and Asp549' and by several H-bonds (e.g. between the carbonyl oxygen of Phe774 and the hydroxyl of Ser550'). Noteworthy, the side chain of Tyr545' engages also in important contacts at this interface, docking on H9 from a neighboring monomer. A second, symmetric homodimer is centered on the aromatic Tyr638 (L6–7) and Phe735/Tyr738 (C-terminal end of H11) facing each other. However, since positions 638 and 738 are occupied by smaller polar residues in WT GR (Cys and Gln, respectively; Figure 1C), this arrangement is unlikely to be significant *in vivo*.

Finally, two related, medium-resolution structures of GR-LBD·DEX·SHP were obtained in the tetragonal and cubic space groups ($I4_122$ and $I4_132$, respectively; Figure 2C, D). Also in this case, we observe a symmetric homodimer in which the Tyr545/Tyr545' aromatic rings are stacked, although the overall arrangement of LBD modules differs strongly from the Tyr545-directed dimer found in C2 crystals. Additional H1-H3' contacts result in a more compact conformation, which is stabilized by H-bonds between both main- and side-chain atoms of the two monomers, including a Glu542–Arg569' salt bridge. The largest interaction interface in these forms features a trimeric arrangement in which loops L1–3'/H3', S2-L6' and L11–12' dock perpendicularly onto H10–11. The large, buried surface area in this trimer appears to compensate the electrostatic repulsion of abutting Asp641 carboxylates from the three monomers around a pseudo (in the tetragonal form) or exact 3-fold axis (in the cubic cell).

A thorough catalog of homodimeric arrangements illustrates the multivalent potential of the GR-LBD

The fact that even minor changes in protein complexes and crystallization conditions result in different GR-LBD arrangements, as demonstrated by the variety of crystal contacts described above (Figure 2A–D), prompted us to systematically analyze protein-protein contacts in all crystal structures of the domain previously deposited in the PDB (Figure 3A, B; Supplementary Tables S2 and S3). GR-LBD residues involved in homodimer formation cluster in four areas on the surface, the 'front', 'back', 'top' and 'base' of the domain (Figure 3B–D), in the standard view of NRs (Figure 1B).

Next, we analyzed which combinations of these four homodimerization interfaces have been encountered in crystal structures. This analysis revealed 20 topologically distinct homodimers (see Supplementary Table S3 for interacting residues in all monomer pairs) numbered #1–20 throughout the manuscript. These homodimeric arrangements appear to cover the whole GR-LBD self-association landscape. Along with 11 symmetric (isologous) dimeric arrangements (i.e. between the same secondary structure elements / residues, such as in the Tyr545-mediated dimers described above), asymmetric or heterotypic homodimers (i.e. where the contacting GR-LBDs engage in interactions using different elements) are also common (nine arrangements).

We further explored the homodimerization potential of GR-LBD with a state-of-the-art protein-protein docking procedure and a total of 12,000 generated docking dimers. This analysis revealed the existence of at least one docking orientation close to 16 of the 20 representative 'crystal homodimers' (with a root-mean-square deviation (RMSD) ≤ 10 Å) (Supplementary Figure S3). Interestingly, the 2nd best-scoring docking orientation was close (7.3 Å RMSD) to one of the dimers (#20). In two further cases (#8, #10), there were docking orientations within 5 Å from the crystal structures, although with no optimal docking scoring.

For an unbiased estimate of the similarity between different homodimers, we first considered the overlapping of shared contact residues. To this end, we mapped these sets of residues into a multiple sequence alignment and calculated distances between the resulting vectors using different metrics (Figure 4A). This Jaccard analysis confirmed e.g. the topological similarity between two front-to-front homodimers: the first described non-canonical conformation (#1, 1M2Z (3)) and #2, an arrangement observed in 4P6W (51) (Supplementary Tables S2 and S3). On the other hand, front-to-front homodimer pairs #6 and #11, although sharing interface residues, differ strongly in that the two monomers are arranged parallel and antiparallel to each other, respectively. Similarly, homodimers #9 and #10 share the important residue Ile628 at the center of their intermonomer interfaces, but the two modules are quite differently oriented relative to each other. The way the four distinct areas on the GR-LBD surface assemble to generate the 20 topologically different homodimers is schematically presented in Figure 4B.

Alternatively, GR-LBD homodimers were superimposed on a common origin and classified by mapping the centers of coordinates of their interaction surfaces (Supplementary Figure S3A). Supplementary Figure S3B shows the orientations of these surfaces, represented by vectors between the common center of coordinates and each interaction surface. A hierarchical clustering analysis based on the Euclidean distance between these vectors grouped all homodimers into six clusters (Supplementary Figure S3C). From the spherical coordinates of the vectors representing the orientations of the interaction surfaces (Supplementary Figure S3E), we found that these clusters can be associated with combinations of the previously defined surfaces: cluster 1 (top-front), cluster 2 (top-back), cluster 3 (base-back), cluster 4 (base-front), cluster 5 (front), and cluster 6 (base). While each cluster may contain surfaces with different binding energy values (Supplementary Figure S3D), arrangements corresponding to top and back interaction

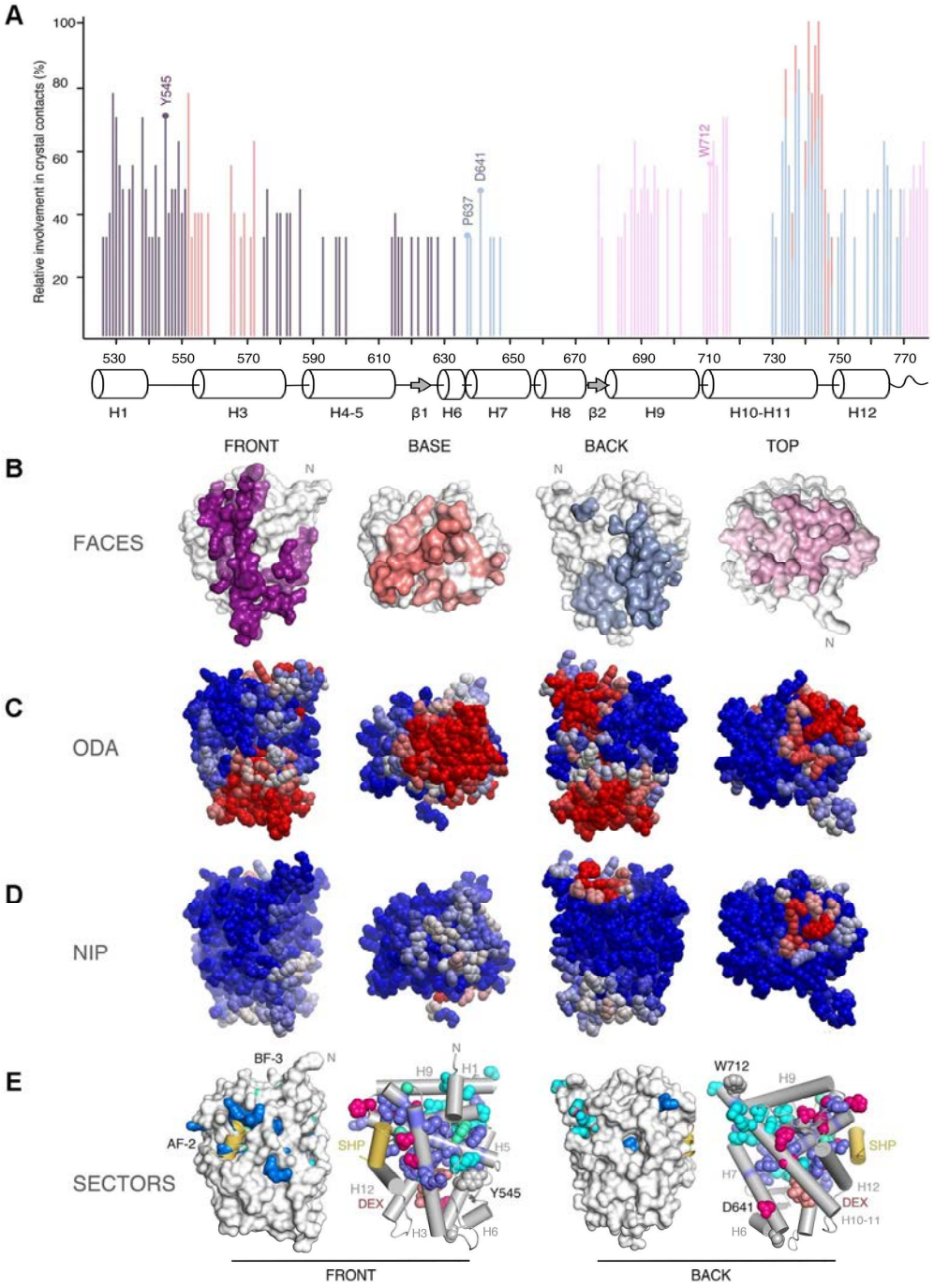

Figure 3. Experimental structures and bioinformatics analyses unveil four major homodimerization surfaces on GR-LBD. (**A**) Relative frequencies of residue involvement in GR-LBD homodimer formation. Bar height indicates how often a given residue engages in crystal contacts in all available structures of GR-LBD, normalized to the residue most frequently found in homodimer interfaces, Leu741. Secondary structure elements given below the plot correspond to the crystal structure of human GR-LBD resolved at the highest resolution, 6NWL. (**B**) Residues involved in GR-LBD homodimerization cluster in continuous patches on its front (colored purple), base (coral), back (blue) and top (pink) faces. The association of these four faces yields the catalog of GR-LBD dimers represented in Figure 4. Models are shown in the same orientation and at the same magnification in panels (C)–(E). (**C**) Predicted protein-protein interaction ODA. ODA 'hotspots' (residues with favorable docking energy; ODA < -10.0 kcal/mol) are colored red, residues with ODA $>$ 0 kcal/mol are shown in blue, and intermediate values are scaled accordingly. ODA hotspots form continuous surface patches that essentially overlap with the four protein-protein interaction interfaces shown in panel (B). (**D**) Hotspot interface residues predicted from docking experiments. Surface residues are colored according to their NIP. Residues with NIP > 0.4 and < 0 are colored red and blue, respectively; intermediate values are scaled accordingly. (**E**) SCA identifies two sectors of clustered, physically connected residues in GR-LBD. The front and back orientations of GR-LBD are depicted, and in both cases the module is represented as a solid surface and as a cartoon, with helices shown as rods and labeled. Residues belonging to sectors I and II are shown with their side chains atoms as spheres, colored cyan and dark blue, respectively. Residues belonging to both sectors are colored pink. SHP peptide is colored yellow, and DEX is shown as salmon spheres.

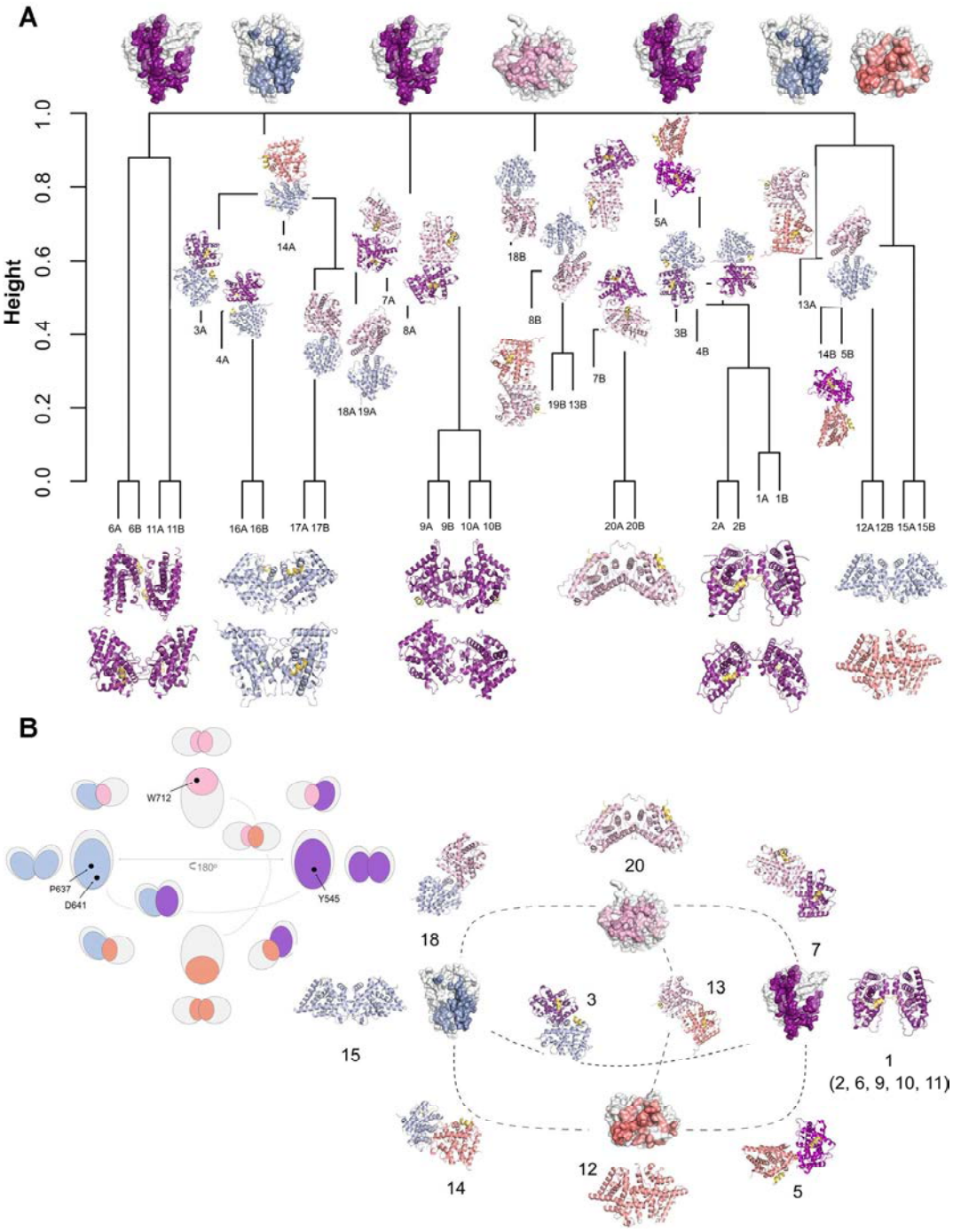

Figure 4. An integrated catalog of GR-LBD homodimers. The four distinct GR-LBD protein-protein interfaces associate to generate 20 topologically different homodimers. (**A**) A dendrogram based on a hierarchical analysis of protein-protein contacts using Jaccard's index groups the 20 unique GR-LBD assemblies into six different clusters. (**B**) Relationships between the different GR-LBD homodimers. For orientation, monomers highlighting the four interacting surfaces are placed at the cardinal points in this panel (top, nord; front, east; base, south; and back, west), colored-coded as in Figure 3. Monomers in 10 representative homodimers are depicted as cartoons; each monomer is colored according to the face used to associate with its partner. Dimers are placed closest to the generating monomers. An equivalent schematic representation of GR-LBD homodimerization potential is shown at the upper left corner, with the position of major interacting residues indicated.

surfaces have in general more favorable binding energy. The distribution of interfaces in the top 1,000 docking models also shows significant clustering around regions with favorable binding energy (Supplementary Figure S3F). However, docking solutions also clustered in other regions with less optimal energy, such as front and base surfaces.

Two sectors define the internal circuits linking key GR-LBD interaction sites

Positions differentially conserved within protein subfamilies (termed 'specificity determining positions', SDPs) are related to functional specificity (e.g. binding of different cofactors). Recent bioinformatics methods based on MCA have allowed identification of the subtle patterns of conservation of SDPs within large protein families (52). Our initial MCA run did not replicate the previously reported family classification (38), and only identified three residues that divide the NR superfamily into two clusters. This prompted us to use more sophisticated statistical tools to search for evolutionary conserved units in GR-LBD. To analyze if self-association surfaces may be allosterically coupled to other functional regions, we performed a SCA, which entirely relies on correlated amino acid variations across the domain without considering its 3D structure (53,54). Indeed, this analysis identified 40 residues that decompose the GR-LBD sequence into two quasi-independent groups of correlated residues or 'sectors' (Figure 3E). Sector 1 comprises 17 residues in and around H1 and H10, most notably LBP residues Met601 and Arg611 along with the nearby Phe606, whereas sector 2 features 20 residues mostly from H3 and H5 (e.g. Met604 in the LBP, Lys579, Phe584, Gln597 of AF-2 and Trp577 in an internal path connecting AF-2 to the LBP). Finally, Gly583 (BF-3), Leu596 (AF-2) and the internal Tyr663 belong to both sectors. Interestingly, all residues cluster in the upper half of the LBD, where both sectors are physically interconnected (Figure 3E). Sector 1 residues cluster around the N-terminus of the LBD and are thus likely candidates to interact with the hinge and DBD. Perhaps more relevantly, sector 2 comprising residues profusely innervate the LBP and AF-2 regions while Arg611 from sector 1 is essential to position the hormone. The three residues that belong to both sectors are strategically located to link the LBP with AF-2 and BF-3. Taken together, our results suggest that both sectors couple functionally relevant regions (e.g. ligand and coregulator binding or chaperone docking/release).

In vitro crosslinking experiments corroborate non-canonical GR-LBD dimerization

The results presented above suggest that many surface-exposed residues of GR-LBD engage in a variety of crystal contacts. To clarify their role in homodimer formation in solution, we took advantage of intermolecular H-bonds between Glu/Asp and Lys at some of the crystal interfaces, which can be 'frozen' upon incubation with the zero-length crosslinker, EDC.

Indeed, we observed rapid formation of a covalent dimer upon incubation of GR-LBD with EDC, as well as a fainter band corresponding to a tetrameric arrangement(s) (Figure 5A). To identify crosslinked Asp/Glu-Lys pairs, gel bands corresponding to oligomeric GR-LBD were excised, enzymatically digested with either trypsin or chymotrypsin, and analyzed by MS (Supplementary Figure S4A, Supplementary Tables S4 and S5). Most notably, we found that elements essential for top-to-top (#20) and front-to-front (#1, #2, #6, #9, #10 and #11), non-canonical dimerization are overrepresented among EDC-linked peptides, with the most common contacts involving (i) residues of H1 and L1–3, on the one side, and from H3, on the other, which would correspond to front-to-front interactions, as well as (ii) H9 and the L9-10 linker from two monomers, which is compatible with homodimer #20 (Figure 5B, C and Supplementary Figure S4B, Supplementary Table S4). Similar results were obtained with the MS-cleavable, urea-based crosslinker, DSBU (Supplementary Table S6).

Mutant Y545C exhibits GR-LBD non-canonical homodimerization in solution

Inspection of homodimer interfaces in GR-LBD revealed several symmetric arrangements in which the side chain of a solvent-exposed residue from one monomer is located within VdW distance of the same residue from a crystal neighbor (Figure 2A and Figure 5D). To verify whether some of these conformations are present in solution, we have generated several Cys mutants of the GR-LBD. All studied mutants were properly folded, as indicated by only minor decreases in melting temperatures in DSF analysis, in line with the results of a systematic bioinformatics analysis of mutant stability performed using Fold-X (not shown). Incubation of purified Y545C in low-reducing conditions resulted in the rapid formation of covalent dimers (Figure 5E). By contrast, neither the WT protein nor other Cys mutants tested (e.g. D641C, S744C) dimerized under the same conditions (Figure 5E). These findings strongly suggest that the side chains of Tyr545 from two monomers are close enough in solution, at least in a subset of GR-LBD molecules.

To directly confirm that residues Cys545/Cys545' are responsible for disulfide bridge-mediated dimerization in solution, bands corresponding to the dimer were excised from the gel, treated with iodoacetamide to block free Cys residues, and subjected to enzymatic digestion with trypsin and GluC. MS analysis of these digests allowed indeed the identification of peaks corresponding to peptide V^{543}LCSGYD^{549} crosslinked to either V^{543}'LCSGYD^{549}' or V^{543}'LCSGYDSTLPDTSTR^{558}', thus confirming Cys545-mediated covalent bond formation (Supplementary Figure S4C and Supplementary Table S7).

To further assess the contribution of Tyr545 to GR homodimerization in solution, we performed SPR assays with its Y545C and Y545A mutants. Indeed, experiments conducted with the Cys mutant revealed significant increases in affinity. The increase was the highest when the mutant was used as both ligand (i.e. chip-immobilized) and analyte, as indicated by dramatic increases in affinity (k_D = 0.85 vs. 13.5 μM for the WT-WT association at 100 μM DTT; Supplementary Figure S2C, D) as well as in complex lifetime, with a 4-fold increase at 10 μM DTT ($t_{1/2}$ = 1,130 vs. 270 s). By contrast, truncation to Ala at position 545 led to a

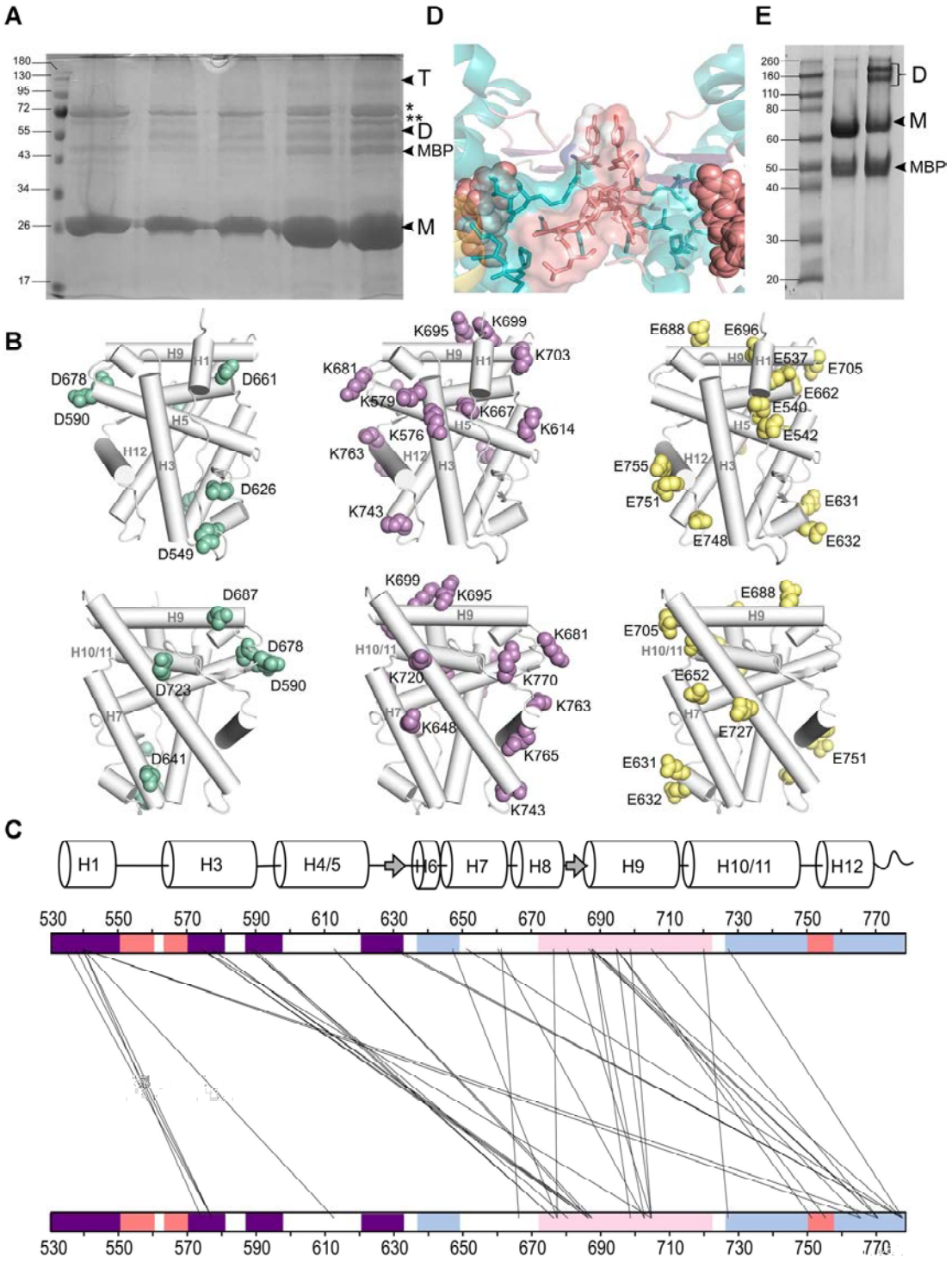

Figure 5. Several GR-LBD homodimers are populated in solution. (**A**) SDS-PAGE analysis of GR-LBD after incubation with EDC. Notice bands with relative molecular masses corresponding to GR-LBD dimers (D) and tetramers (T) in all the lanes except control lane 1 (no EDC added). Lanes 2 and 3, protein incubated at about 0.37 mg/ml; lanes 4 and 5, protein incubated at about 1.5 mg/ml. Samples in lanes 2 and 4 were treated at RT; those in lanes 3 and 5 at 30°C. Bands corresponding to co-purified DnaK and GroEL *E. coli* chaperones are marked with (*) and (**), respectively. (**B**) Schematic representation of GR-LBD structure, with side side chains of residues identified using EDC shown as spheres (Asp in green, Lys in lilac, and Glu in yellow). (**C**) Crosslink map of EDC-treated GR-LBD showing all intermonomer crosslinks identified by MS analysis. Regions corresponding to the top, front, base, and back surfaces are colored as in Figures 3 and 4. A secondary structure plot is shown above the map. (**D**) Closeup of the major homodimerization interface in C2 crystals (front-to-front homodimer #11), dominated by stacked Tyr545/Tyr545' residues. (**E**) Non-reducing SDS-PAGE analysis of purified GR-LBD(Y545C) (lane 3) shows spontaneous dimerization in solution. Note that the WT protein does not form dimers when incubated at the same concentration (lane 2).

slightly less tight association (Supplementary Figure S2E). We also crystallized and solved the structure of the Y545A variant, thus confirming proper folding of the generated point mutants. Noteworthy, Y545A crystallized in the $P6_1$ space group, which does not involve symmetric contacts between the side chains of residues at position 545 (Figure 2B). Altogether, our results confirm that residue Tyr545 plays an important role in GR-LBD homodimerization in solution.

Residues Tyr545 and Asp641 modulate multimerization of FL-GR

Quantitative fluorescence microscopy in living cells (the number and brightness method, N&B) allows to estimate the average oligomeric state of a fluorescent protein from its molecular brightness (ε; (41)). For N&B experiments we use mouse adenocarcinoma cells, which possess a tandem array of DNA binding sites for GR, the MMTV array (42). We have knocked out expressed GR protein in these cells, thus designated GRKO (25). These cells are transiently transfected with GFP-tagged full length mouse GR (GFP-mGR) or mutants thereof, and the oligomeric state of fluorescently tagged GR molecules is quantified by comparing to a constitutively monomeric GR variant (N525*) (24). The mutated residues of the mouse GR variants correspond to the human versions discussed above and are noted in the figure legends. Further, presence of the MMTV array in the GRKO cells allows us to differentially assess GR oligomerization not only in the entire nucleoplasm but also in a region highly enriched in GR binding sites that is visible under the microscope as a bright spot (Figure 6B, arrowheads).

To test the relevance for the full-length receptor (FL-GR) of key surface-exposed residues identified in GR-LBD homodimer interfaces *in vitro*, we generated Ala mutants of mouse GR at positions topologically equivalent to human residues Tyr545, Pro637, Asp641 and Trp712, all of which are conserved in ancGR2 (Figure 1C). Further, all residues but Asp641 are strictly conserved from fish to humans, and Asp641 is conservatively replaced by a glutamate in non-mammals (Supplementary Figure S1). To study the impact of the Tyr545→Ala exchange in the background of two other variants previously shown to be important for GR homodimerization (23), we also generated the double mutant (Ala458Thr, Tyr545Ala) (in following termed $GR^{dim/Y545A}$) and the triple mutant (Ala458Thr, Tyr545Ala, Ile628Ala), or $GR^{mon/Y545A}$. Finally, we also generated double mutants in which a GR variant that tetramerizes both in the nucleus and at the array (Pro474Arg, (24)) was combined with either P637A or D641V (These variants, (Pro474Arg, Pro637Ala) and (Pro474Arg, Asp641Val), are in following termed $GR^{tetra/P637A}$ and $GR^{tetra/D641V}$, respectively; Figure 6A).

Next, we transiently transfected GFP-mGR and the generated mutants into GRKO cells and performed N&B experiments as previously described (23,24,55). All mutants translocate to the nucleus upon hormone stimulation (Figure 6B), indicating the mutants can bind ligand at the tested hormone concentration of 100 nM DEX. Further, all variants except those carrying the GR^{mon} double mutant (Ala458Thr, Ile628Ala) were visible at the MMTV array, suggesting that DNA binding was possible (Figure 6B, arrowheads). Of note, reduced genome-wide chromatin binding for GR^{mon} has recently been shown (39), and only a very small percentage of GR^{mon} cells form visible arrays (23,24). Interestingly, we did not detect any arrays in cells with $GR^{mon/Y545A}$ (Figure 6B), suggesting an even more drastic phenotype for this triple mutant.

While W712A oligomerizes as the WT receptor both in the nucleoplasm and at the array (Figure 6C, D), Tyr545Ala substitution appears to slightly decrease dimerization in the nucleoplasm ($\varepsilon = 1.83$). By contrast, Pro637Ala produces a slight increase in oligomerization ($\varepsilon = 2.46$), even though neither difference achieves statistical significance. Since FL-GR dimerizes at least through both DBD and LBD (Figure 6A), we tested the effect of the Tyr545Ala mutation in the GR^{dim} background, which has impaired DBD-DBD contacts yet mostly dimerizes in the nucleoplasm (Figure 6C, (23,24)). Indeed, the $GR^{dim/Y545A}$ double mutant shows significant tendency to remain monomeric in the nucleus ($\varepsilon = 1.16$), like the previously characterized GR^{mon} (Figure 6C, (23,24,56)). Taken together, these results confirm the important role of Tyr545 in the dimerization of GR in live cells.

On the other hand, the Asp641Val mutation, linked to a GC resistance phenotype known as Chrousos syndrome (57), and Pro637Ala promoted higher-order oligomerization at the array (Figure 6D), possibly hexamers or a mixture of tetra- and octamers. These findings prompted us to analyze the impact of these two mutants when combined with a DBD mutation that enforces GR tetramerization, Pro474Arg. Unexpectedly, instead of a synergistic effect, the combined mutations reversed to GR^{tetra} oligomerization in the nucleus (Figure 6C). By contrast, the GR^{tetra} mutation abrogated the ability of P637A and D641V variants to form higher-order oligomers at the array level (Figure 6D). These observations highlight a complex relationship between the different structural domains of the NR.

Role of residues Tyr545 and Asp641 on GR transcriptional activity

Having demonstrated that residues Tyr545 and Asp641 play essential roles in FL-GR oligomerization, both in solution and in live cells, we wondered if they would modulate the activity of the receptor. To this end, we generated stable cell lines expressing GFP-tagged mouse versions of the GR^{Y545A} and $GR^{dim/Y545A}$ variants (see methods), and compared their transcriptional programs to that of mouse GR WT by RNA-seq, after 2h of 100 nM Dex stimulation (Supplementary Table S8 and Supplementary Figure S5A–F). As summarized in Figure 7A, GR^{Y545A} upregulates only 56% of the genes compared to WT GR, and only three out of the 21 genes downregulated by the WT receptor. In line with the more significant impact of the $GR^{dim/Y545A}$ double mutant on receptor homodimerization, its transcriptional activity was more compromised than GR^{Y545A} single mutant, with only 28% of the number of genes being modulated respect to WT GR (Figure 7A). Of the 17 common genes between the three GR types, all but 2 have only modestly lower fold change with Dex between GR WT and GR^{Y545A}, while most of the same common genes exhibit a more severe impact upon hormone treatment in the $GR^{dim/Y545A}$ cells (Figure 7B).

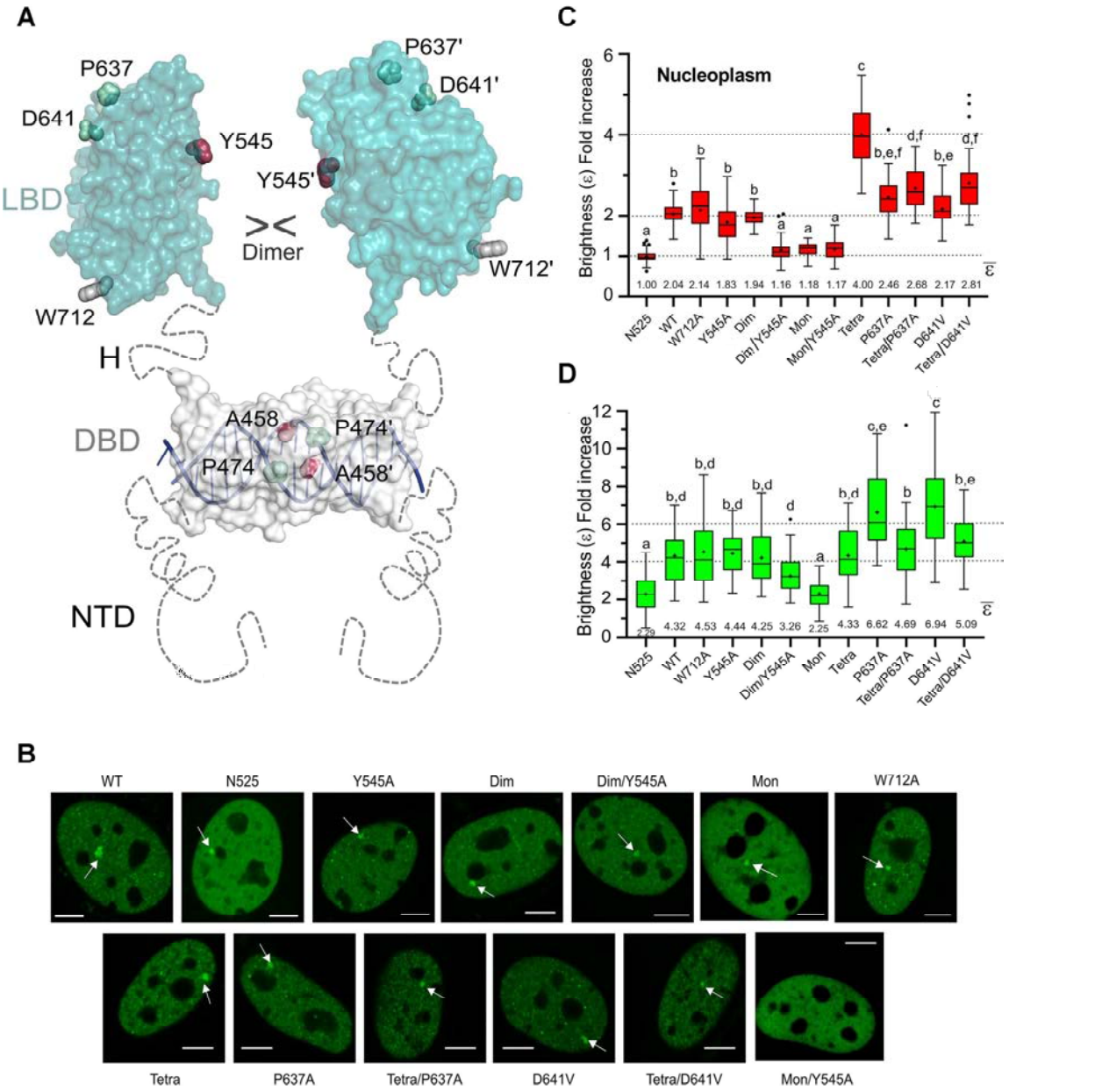

Figure 6. Mutation of LBD–LBD interface residues profoundly affects the multimerization behavior of FL-GR. (**A**) Schematic 3D model of FL-GR. The NTD is highly disordered and is followed by the globular DBD (DNA-bound conformation is shown) and the LBD. Note that the length and flexibility of the hinge (H) allows for the formation of various homodimers. The side chains of all residues mutated to assess the multimerization behavior of GR are shown as spheres. (**B**) Subcellular localization of WT GFP-mGR and indicated mutants in 3617-GRKO cells, as assessed by fluorescence microscopy. Variant N525* lacks the entire LBD and remains monomeric, irrespective of DEX treatment (23). White arrowheads point to the MMTV arrays. Scale bar: 5 μm. Data for WT_GR, GR^{dim}, GR^{mon} and GR^{tetra} were taken from (24) and are shown for comparison purposes. All N&B experiments have been performed with mouse GR as in (23). However, residue numbers correspond to the human protein to facilitate comparisons. (**C**) GR oligomerization in the nucleus, as determined in N&B assays. The fold increase in molecular brightness (ε) relative to the N525* monomeric control is shown ($N = 428$ total cells with $21 < N < 37$ between treatments). (**D**) Quaternary structure of DNA-bound GR. The results of N&B assays at the MMTV arrays are represented as in panel C ($N = 338$ total cells with $17 < N < 35$ between treatments). Note that simultaneous disruption of intermonomer interactions mediated by the DBD (Ala458Thr) and the LBD (Tyr545Ala) in the $GR^{dim/Y545A}$ double mutant results in a variant that is monomeric in the nucleus, while at the array it formed mostly trimers. In panels (C) and (D), centered lines show the medians and crosses represent sample means (average numbers below each box-plot). Box limits indicate the 25th and 75th percentiles; whiskers extend 1.5-fold the interquartile range from the 25th and 75th percentiles, with outliers represented by dots. Boxes with different superscript letters are significantly different from each other ($P < 0.05$; one-way ANOVA followed by Tukey's multiple comparison test).

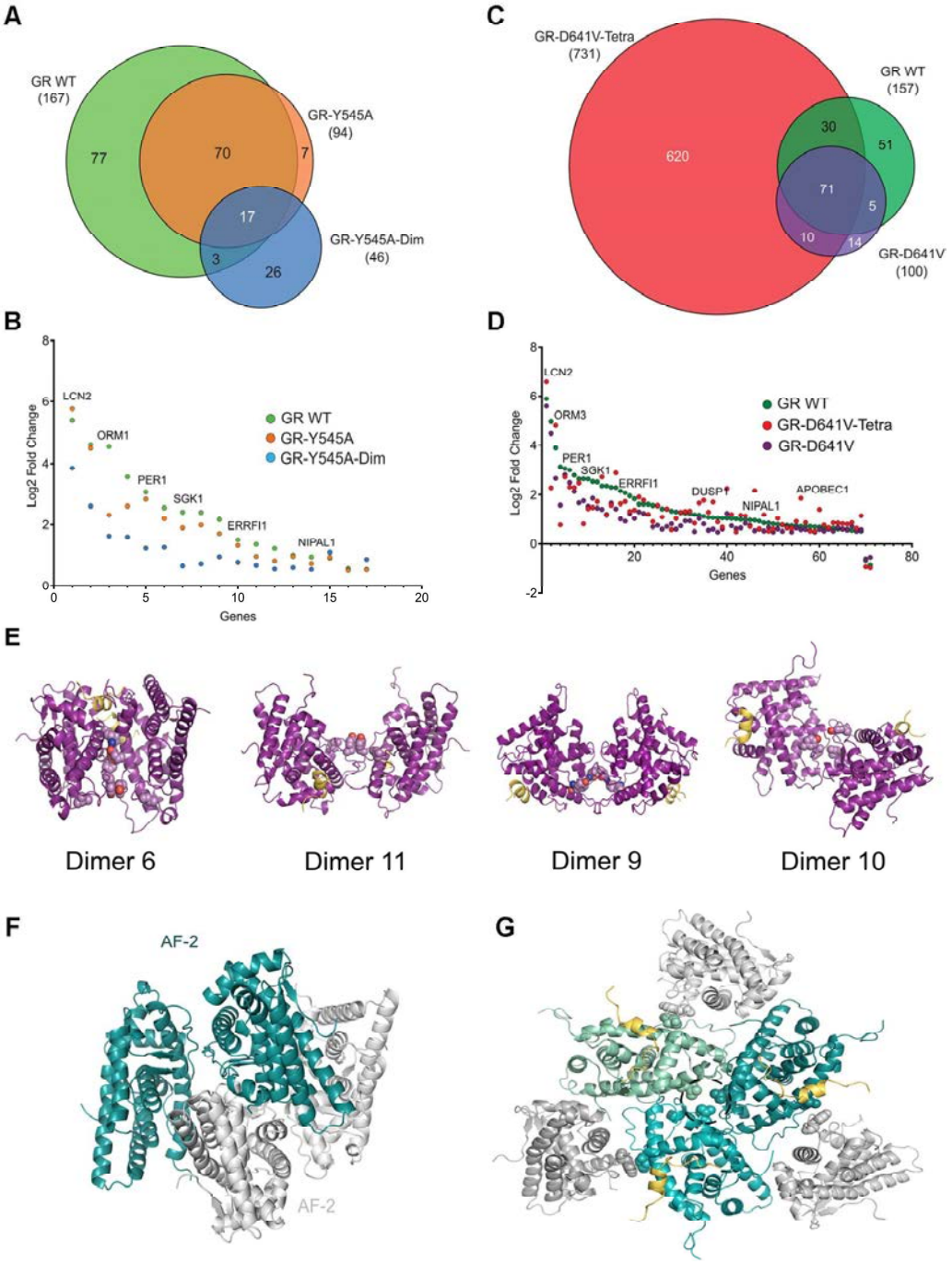

Figure 7. Residues Tyr545 and Asp641 have major roles in GR quaternary structures and transcriptional activity. Stable cell lines expressing GFP-tagged variants of the indicated mouse GR mutants were treated with 100 nM DEX for 2 h (note than numbers correspond to hGR, as in Figure 6). (**A**, **C**) Venn diagrams of differentially expressed genes from RNA-Seq (|log2 Fold change| > 0.5, False-discovery-rate < 0.01). The two WT GR sets (b1, b2) are biological replicates collected and sequenced separately for each batch. (**B**, **D**) Scatter plots of shared hormone-regulated genes (17 and 71 common genes, respectively) between GR mutants, compared and plotted against their respective WT GR control. (**E**) Models of human GR-LBD homodimers based on the observed assemblies #10, #6, #9 and #11. The critical homodimerization residues, Tyr545 and Ile628, are shown as color-coded spheres in all cases. (**F**) Model of GR-LBD tetramer generated by docking dimer #11 onto itself. The model is compatible with the results obtained with the Y545C mutant and EDC-crosslinking. (**G**) Putative GR-LBD hexamer favored by the Asp641Val mutation. The central trimer corresponds to an arrangement observed in tetragonal and cubic crystal forms (#14; Figures 2C, D and 4), while the peripheral monomers dock according to conformation #4. Asp641 residues from the central trimer are encircled. This generates a closed hexamer by additional interactions between the N-terminal end of H10 and H12' at the third interface. In addition to D641V, other GR mutants associated with Chrousos disease might favor multimeric forms that are incompatible with active GR tetramers on DNA. For instance, replacement of Thr556 by an aliphatic Ile would stabilize this arrangement through contacts with e.g. residues Met560 and Pro637 from its 'own' monomer and/or His645'/Asn731' from a neighboring molecule. Similar considerations apply to mutations such as Arg714Gln, Phe737Leu, Ile747Met and Leu773Pro as well as to variant Pro637Ala, which also forms higher-order oligomers at the array (Figure 6D).

RNA-Seq analysis of cells expressing the higher oligomeric variant, D641V, revealed that the mutant modulated only two thirds of the hormone-responsive genes compared to WT GR (Figure 7C), consistent with the *in vivo* phenotype described as Chrousos syndrome (GC resistance) (57). The double mutant $GR^{tetra/D641V}$ shows a much larger number of hormone responsive genes with respect to GR WT, similar to the GR^{tetra} single mutation reported elsewhere (25). This suggests that the constitutively tetrameric conformation exhibited by this DBD mutant can exert a strong effect on gene response even in tandem with the D641V variant of the LBD. However, the tetramer mutation cannot completely rescue the relative fold change of many common DEX-responsive genes, especially genes with the highest response (Figure 7D). These observations reinforce the importance of both DBD and LBD modules of the GR in transcription regulation, and underscore the functional relevance of two surface-exposed LBD residues, Tyr545 and Asp641.

DISCUSSION

Although many structures of GR-LBD have been reported (Supplementary Table S2), the physiologically relevant conformation(s) of GR and other oxosteroid NRs remain controversial. The new structures presented here highlight the ability of different GR-LBD surfaces to engage in various quaternary arrangements depending on the bound agonists/antagonists, cofactors, and other biochemical parameters. These observations prompted us to dissect the oligomerization capability of GR-LBD. Since the ancient LBD structure may not accurately mimic the multimerization behavior of modern, wild-type GR, our structural predictions were experimentally verified by characterizing several key mutations of exposed residues in the background of mouse FL-GR in live cells. The results of these experiments demonstrate that the multimerization landscape of ancGR2 reproduces that of modern GR, in the context of the full-length receptor. Careful inspection of intermonomer contacts in all available 3D structures, irrespective of the variant used for the structural analysis, allowed us to identify 20 topologically different homodimeric architectures (Figure 4, Supplementary Table S3). These experimental GR conformations could be grouped into six different clusters considering relationships between the interacting residues (Figure 4A, Supplementary Figures S3C and S3E), which correspond to three topologically distinct front-to-front homodimers (#1, #2, #6, #9, #10 and #11), along with base-to-base (#12), top-to-top (#20), and back-to-back arrangements (#15, #16 and #17). SPR and XL-MS experiments in solution coupled with quantitative fluorescence microscopy of FL-GR WT and several mutants in live cells along with RNA-seq analyses of most relevant variants allow us to postulate the more likely quaternary arrangements of GR-LBD associated with its different genetic variants (Supplementary Table S9).

It has long been accepted that the 'canonical', H10-mediated homodimeric conformation adopted by ERα-LBD (Supplementary Figure S6B) is hindered by the F-domain in oxosteroid receptors (5,13). Several observations suggested that the non-canonical dimer reported for AR (Supplementary Figure S6A), (5,13,58) could be adopted by other NRs. However, none of the 20 GR-LBD homodimers can be considered as topologically equivalent to the one observed in the crystal structure of AR-LBD, illustrating a more complex multimerization behavior than previously anticipated. Replacement of AR interface residues such as Thr656 by positively charged Lys/Arg residues and of the following Asn657 by bulkier Gln/His residues in all other members of the subfamily might preclude the formation of AR-like homodimers in GR/MR/PR. This highlights the difficulty to extrapolate the quaternary structure of one NR to other, even closely related NRs, and the need for experimental evidence to identify physiologically relevant conformations (13). A related arrangement had been previously observed in some structures of agonist- or antagonist-bound GR-LBD (3), but its biological relevance has been repeatedly questioned (59,60). Here we identify and discuss several unrelated multimeric assemblies of GR-LBD that might illuminate different structural arrangements of the chromatin-bound full-length protein.

GR can adopt several topologically distinct dimeric conformations

Our data indicates that 'non-canonical' GR homodimers centered on the Tyr545 phenol ring are critical for GR homodimerization. In live cells, variant Y545A is mostly monomeric when combined with an exchange that also disrupts DBD-DBD contacts (Ala458Thr, GRdim). Consistently, the transcriptional program of the Y545A variant is significantly affected, and the double mutant $GR^{dim/Y545A}$ is practically inactive (Figure 7A). Further, an important fraction of GR-LBD Y545C molecules rapidly and spontaneously forms covalent homodimers in vitro mediated by the Cys545–Cys545' disulfide bond (Figures 5C, D). Finally, Ala replacement of Try545 led to a reduced monomer-monomer affinity in SPR experiments (Supplementary Figure S2E).

Taken together, we propose four agonist-bound plausible GR dimers (Figure 7E). Formation of the Cys545–Cys545' disulfide bridge in the Y545C variant is compatible with two topologically different, roughly parallel and antiparallel symmetric homodimers (#6 and #11; Figure 7E). Incomplete dimerization of GR-LBD(Y545C) suggests that other dimeric states are also populated in solution. Indeed, in a third, also antiparallel GR-LBD homodimer the Tyr545 side chains are located at the borders of the protein-protein interface (#9, Figure 7E). This arrangement is centered on residues Ile628/Ile628', which are important for receptor dimerization (23). Indeed, the I628A mutant decreased GR multimerization of FL-GR in living cells to a larger extent than the Y545A variant, both in the nucleoplasm and DNA-bound (24). The most likely explanation for these differences is that Tyr545 and Ile628 affect two topologically distinct although interconnected dimerization interfaces of GR-LBD, in line with our structural analysis (Figures 3 and 4). In this regard, it is noteworthy that this side chain is less exposed than the Tyr545 phenolic ring, engaging in close VdW contacts with Leu620, Cys622 and Pro625. Thus, the larger impact of the I628A mutant might simply reflect disruption of an extended protein-protein interface

area centered on the Ile628 side chain. Finally, a second Ile628-centered, parallel conformation is found in crystals of ancGR1 (homodimer #10; Figure 7E, (56)). Therefore, both parallel and antiparallel arrangements of LBD modules with different involvement of the Tyr545 and Ile628 valences are compatible with current data and are equally possible. Some of these quaternary arrangements in solution could be verified in our XL-MS experiments (Figure 5A, Supplementary Table S6). GR-LBD features several strictly conserved Tyr/Trp residues, two of which, Tyr545 and Trp712, are repeatedly found at monomer-monomer interfaces (Figure 2 and Supplementary Table S3). Against expectations, elimination of the bulky indole ring at position 712 had no effect on the oligomerization properties of FL-GR in live cells, as the W712A variant behaved as WT both in the nucleoplasm and DNA-bound (Figures 6C and D). These findings strongly suggest that Trp712 is not important for GR multimerization in vivo. This would exclude, among others, the symmetric homodimer #20, which had been proposed as the most likely conformation of dimeric GR-LBD (61). Nevertheless, the fact that Trp712 participates in six topologically different homodimeric arrangements suggests an enhanced propensity for protein-protein interactions. Indeed, the recently reported cryo-EM structure of GR-LBD bound to the 'client-maturation complex' Hsp90-p23 has revealed that Trp712 occupies the central position in a major binding epitope for the p23 co-chaperone (62).

Interestingly, antagonist binding appears to result in completely unrelated GR-LBD assemblies: the symmetric back-to-back (#15) and base-to-base homodimers (#12), which have much larger interface areas and much lower energies than all other GR-LBD conformations (Supplementary Table S3). These dimers are indeed only observed in GR-LBD bound to the antagonist, mifepristone/RU-486 (1NHZ and 5UC3, respectively, (59)), and share several important features. First, the bound antagonist displaces H12, which partially disrupts the LBP. More importantly, in both cases the AF-2 of one monomer is partially covered by either H12 (#15) or H3 (#12) from a neighboring molecule, thus interfering with coregulator binding (Supplementary Figures S5G, H). Further, essentially the same arrangements are found in crystals of the dominant negative GRβ, which is known to bind only antagonists (63). Even though tetrameric assemblies in 1NHZ/5UC3 and in a third structure of mifepristone-bound GR (3H52; (64)) have been reported, these are not compatible with the results of our XL experiments with EDC (Figure 5A and Supplementary Figure S4B) or DSBU (Supplementary Tables S4 and S6). Inactive RXRα also adopts a disc-like tetrameric conformation, in which H12 from one molecule protrudes away and docks on the AF-2 of an adjacent monomer (Supplementary Figure S5I; (65)). Although the overall arrangement differs from the ones adopted by agonist-bound GR-LBD, the fact that AF-2 is occluded in both cases points to a general feature of self-repressed or inactive conformations in NRs. Altogether, these findings strongly suggest that the most stable, back-to-back (#15) and base-to-base conformations (#12) of GR-LBD are associated with inactive, self-repressed states, which are induced or stabilized by antagonist binding. Previous experiments had demonstrated that FL-GR bound to mifepristone is fully dimeric in the nucleus, but its ability to form tetramers on DNA is compromised (24). Thus, impaired tetramerization of RU486-bound GR might account for its transcriptional deficiency.

Towards a model for FL-GR quaternary arrangements and their role in physiology and disease

Our earlier live-cell imaging studies have revealed that dimeric GR might be an intermediate state towards transcriptionally active tetramers bound to target DNA sequences (24,25,39) also in line with the current SPR results (Figure 1D, E). Although more speculative, it is possible to generate tentative models of DNA-bound GR tetramers that satisfy the constraints derived from current structure-function information (Figure 7F). First, we reasoned that since tetramers but not higher order multimers are detected on chromatin, none of the known intermonomer 'anchors', Tyr545 and Ile628, would be available for protein-protein interactions in active tetramers. In other words, all GR-LBD valences should be satisfied in bona fide GR tetramers. Since the Ile628 side chain is exposed in both conformations with opposing Tyr545 rings (#6 and #11), different combinations with homodimers #9 and #10 are conceivable (Supplementary Figures S6E-J). These hypothetical multimeric arrangements reconcile the role of residues Tyr545 and Ile628 for GR multimerization. The additional interactions predicted in these multimeric arrangements, in addition to DBD-DBD interactions (23) and condensation provided by the NTD (27) would overcome the energy loss due to Tyr545→Ala or Ile628→Ala exchanges, explaining why variants Y545A and I628A are still tetrameric on chromatin (Figure 6D). However, the triple mutant (A458T, Y545A, I628A) did not bind the array, indicating that simultaneous elimination of the Tyr545 and Ile628 valences would generate a well folded, but fully inactive variant.

On the other hand, our results suggest that formation of non-physiological multimers might underlie the deleterious effect of glucocorticoid resistance mutants. Unexpectedly, we observed that a GR mutant linked to Chrousos syndrome, D641V (57), preferentially formed higher-order oligomers when bound to DNA (Figure 6D), which was accompanied by a significant reduction in its transcriptional activity (Figure 7C). A three-fold reduced affinity of the Val641 mutant for DEX was previously proposed as the underlying molecular defect in the D641V variant. However, since Asp641 is exposed on the GR surface and is located 8 Å away from the closest DEX atom, it is unlikely to play any relevant role in hormone recognition. This non-conservative mutation has a particularly strong stabilizing impact of 3.4 kcal/mol for each dimer pair on the GR-LBD trimer observed in current tetragonal and cubic crystals (#14; see Figure 2D, Supplementary Table S3). Therefore, these structures provide a plausible model for a trimeric arrangement in which the three Asp641 side chains face each other around a three-fold axis. The positive effect of the mutation results from the relief of strong electrostatic repulsion between the three abutting negatively charged Asp641 residues, coupled with favorable VdW contacts made by the aliphatic Val641 side chains with each other and with Cys638 from a neighboring molecule. Notably, conformation #4 is fully compatible with this trimer

and generates a closed hexamer (Figure 7G). This conformation would occlude the AF-2 pockets of the 'external' monomers and is thus incompatible with coregulator binding, impeding GR transcription. Several additional residues linked to Chrousos disease are located at or close to one of the three monomer-monomer interfaces, and their mutations might promote local conformations that also stabilize this hexamer (Figure 7G). This is, to the best of our knowledge, the first time in which non-productive multimers of a NR are postulated as the molecular basis of a human disease.

In conclusion, our results suggest that GR multimerization needs to be reconsidered from the perspective of multiple, energetically roughly equivalent homodimers. It is therefore conceivable that several different GR dimers coexist within a cell, all of which, in principle, recruit different cofactors and thus activate different transcription pathways. 'Selection' of a given conformation might be determined not only by the availability of GR-specific agonist/antagonist but also by many other parameters, including cell state. Current structure-function information suggests that at least four different GR-LBD homodimers have roughly equal probabilities to be formed *in vivo*, which would in turn generate different tetrameric arrangements on DNA. We are tempted to speculate that these individual conformations of tetrameric GR are associated with specific transcriptional programs. Future investigations should verify the validity of this hypothesis and establish whether specific GR conformations result in unique expression patterns. The high plasticity of GR-LBD for self-association and its potential modulation by different agonists and/or antagonists opens new venues for the potential treatment of GR-related diseases. The ability to promote or stabilize these specific GR multimeric states might be an essential step towards the development of novel GCs with reduced side effects.

DATA AVAILABILITY

The atomic coordinates and structure factors have been deposited in the PDB with accession codes 7YXC (C2), 7YXD ($P3_1$), 7YXN ($P6_1$), 7YXO ($I4_122$), 7YXP ($I4_132$) and 7YXR ($P6_1$, Y545A). The PDB data has been designed 'for immediate release on publication'. MS data have been deposited to the ProteomeXchange Consortium (PRIDE partner repository: dataset identifier PXD028039). Bioinformatics data and code for the clustering and SCA are available at https://github.com/ibn90/GRPROJECT2021. The Gene Expression profiles are deposited in the Gene Expression Omnibus (GEO) database and the code assigned is GSE212973. All relevant data are available upon request.

ACCESSION NUMBERS

The atomic coordinates and structure factors have been deposited in the Protein Data Bank (PDB) with accession codes 7YXC (C2), 7YXD ($P3_1$), 7YXN ($P6_1$), 7YXO ($I4_122$), 7YXP ($I4_132$) and 7YXR ($P6_1$, Y545A). The Gene Expression profiles are deposited in the Gene Expression Omnibus (GEO) database and the code assigned is GSE212973.

SUPPLEMENTARY DATA

Supplementary Data are available at NAR Online.

ACKNOWLEDGEMENTS

We thank Erick Ortlund (Emory University) for providing the plasmid for ancGR2-LBD, Arnold T. Hagler for his comments on the manuscript, and Ildefonso Cases (CABD) for his help with code. We thank ALBA-Cells synchrotron XALOC team for beamline support.

Author contributions: P.F.-P. and E.E.-P. designed and supervised the project, obtained financial support, and share overall responsibility. A.J.P., A.A.M., M.A.M. and R.A. obtained recombinant proteins. M.A.M., A.A.M. and A.J.P. performed crystallization trials. A.A.M, J.F.D. and R.A. generated mutants and analyzed proteins. I.N.B. and A.R.M. performed and interpreted SCA analyses. J.F.R. performed and interpreted docking, NIP, and ODA calculations. T.T., R.L.S. and T.A.J. generated FL-GR mutants. G.F. and D.M.P. performed and analyzed N&B experiments. A.J.P., A.A.M., R.A., P.F.-P. and E.E.-P. performed and interpreted MS SPR. A.J.P., P.F.-P. and E.E.-P. collected and interpreted X-ray diffraction data, P.F.-P. solved and refined structures. T.T., R.L.S., T.A.J., A.V.F., C.C. and P.P. contributed tools. T.T., T.A.J. and SK performed and analyzed the genomics data. D.M.P., and G.L.H. supervised cell experiments. A.J.P., P.F.-P. and E.E.-P. drafted the article. A.R.M, T.A.J., J.F.R., D.M.P., G.L.H., P.F.-P. and E.E.-P. critically reviewed the manuscript. All authors approved the manuscript.

FUNDING

E.E.-P. thanks the generosity of the Gemma E. Carretero Fund; MINECO [BFU2017-86906-R, SAF2017-71878-REDT, SAF2015-71878-REDT to E.E.-P., RTI2018-101500-B-I00 to P.F.-P., RTI2018-096735-B-100 to A.R.M., PID2019-110167RB-I00 to J.F.-R., SAF2017-89510-R to A.V.F. and C.C.]; G.L.H thanks the NIH Intramural Research Program; D.M.P was supported by CONICET. Funding for open access charge: Spanish Ministry of Science (MINECO).

Conflict of interest statement. None declared.

REFERENCES

1. Conway-Campbell,B.L., Pooley,J.R., Hager,G.L. and Lightman,S.L. (2011) Molecular dynamics of ultradian glucocorticoid receptor action. *Mol. Cell Endocrinol.*, **348**, 383–393.
2. Busada,J.T. and Cidlowski,J.A. (2017) Mechanisms of glucocorticoid action during development. *Curr. Top Dev. Biol.*, **125**, 147–170.
3. Bledsoe,R.K., Montana,V.G., Stanley,T.B., Delves,C.J., Apolito,C.J., McKee,D.D., Consler,T.G., Parks,D.J., Stewart,E.L., Willson,T.M. *et al.* (2002) Crystal structure of the glucocorticoid receptor ligand binding domain reveals a novel mode of receptor dimerization and coactivator recognition. *Cell*, **110**, 93–105.
4. Evans,R.M. and Mangelsdorf,D.J. (2014) Nuclear receptors, RXR, and the big bang. *Cell*, **157**, 255–266.
5. Jimenez-Panizo,A., Perez,P., Rojas,A., Fuentes-Prior,P. and Estebanez-Perpina,E. (2019) Non-canonical dimerization of the androgen receptor and other nuclear receptors: implications for human disease. *Endocr. Relat. Cancer*, **26**, R479–R497.
6. Housley,P.R., Sanchez,E.R., Danielsen,M., Ringold,G.M. and Pratt,W.B. (1990) Evidence that the conserved region in the steroid

binding domain of the glucocorticoid receptor is required for both optimal binding of hsp90 and protection from proteolytic cleavage. A two-site model for hsp90 binding to the steroid binding domain. *J. Biol. Chem.*, **265**, 12778–12781.
7. Ortlund,E.A., Bridgham,J.T., Redinbo,M.R. and Thornton,J.W. (2007) Crystal structure of an ancient protein: evolution by conformational epistasis. *Science*, **317**, 1544–1548.
8. Meijsing,S.H., Pufall,M.A., So,A.Y., Bates,D.L., Chen,L. and Yamamoto,K.R. (2009) DNA binding site sequence directs glucocorticoid receptor structure and activity. *Science*, **324**, 407–410.
9. Rogatsky,I., Wang,J.C., Derynck,M.K., Nonaka,D.F., Khodabakhsh,D.B., Haqq,C.M., Darimont,B.D., Garabedian,M.J. and Yamamoto,K.R. (2003) Target-specific utilization of transcriptional regulatory surfaces by the glucocorticoid receptor. *Proc. Natl. Acad. Sci. U.S.A.*, **100**, 13845–13850.
10. Pfaff,S.J. and Fletterick,R.J. (2010) Hormone binding and co-regulator binding to the glucocorticoid receptor are allosterically coupled. *J. Biol. Chem.*, **285**, 15256–15267.
11. Estebanez-Perpina,E., Arnold,L.A., Nguyen,P., Rodrigues,E.D., Mar,E., Bateman,R., Pallai,P., Shokat,K.M., Baxter,J.D., Guy,R.K. *et al.* (2007) A surface on the androgen receptor that allosterically regulates coactivator binding. *Proc. Natl. Acad. Sci. U.S.A.*, **104**, 16074–16079.
12. Jehle,K., Cato,L., Neeb,A., Muhle-Goll,C., Jung,N., Smith,E.W., Buzon,V., Carbo,L.R., Estebanez-Perpina,E., Schmitz,K. *et al.* (2014) Coregulator control of androgen receptor action by a novel nuclear receptor-binding motif. *J. Biol. Chem.*, **289**, 8839–8851.
13. Fuentes-Prior,P., Rojas,A., Hagler,A.T. and Estebanez-Perpina,E. (2019) Diversity of quaternary structures regulates nuclear receptor activities. *Trends Biochem. Sci.*, **44**, 2–6.
14. Vandevyver,S., Dejager,L. and Libert,C. (2012) On the trail of the glucocorticoid receptor: into the nucleus and back. *Traffic*, **13**, 364–374.
15. Weikum,E.R., Knuesel,M.T., Ortlund,E.A. and Yamamoto,K.R. (2017) Glucocorticoid receptor control of transcription: precision and plasticity via allostery. *Nat. Rev. Mol. Cell. Biol.*, **18**, 159–174.
16. Clark,A.R. and Belvisi,M.G. (2012) Maps and legends: the quest for dissociated ligands of the glucocorticoid receptor. *Pharmacol Ther.*, **134**, 54–67.
17. Franco,L.M., Gadkari,M., Howe,K.N., Sun,J., Kardava,L., Kumar,P., Kumari,S., Hu,Z., Fraser,I.D.C., Moir,S. *et al.* (2019) Immune regulation by glucocorticoids can be linked to cell type-dependent transcriptional responses. *J. Exp. Med.*, **216**, 384–406.
18. Sevilla,L.M., Bayo,P., Latorre,V., Sanchis,A. and Perez,P. (2010) Glucocorticoid receptor regulates overlapping and differential gene subsets in developing and adult skin. *Mol. Endocrinol.*, **24**, 2166–2178.
19. Cain,D.W. and Cidlowski,J.A. (2017) Immune regulation by glucocorticoids. *Nat. Rev. Immunol.*, **17**, 233–247.
20. Oh,K.S., Patel,H., Gottschalk,R.A., Lee,W.S., Baek,S., Fraser,I.D.C., Hager,G.L. and Sung,M.H. (2017) Anti-inflammatory chromatinscape suggests alternative mechanisms of glucocorticoid receptor action. *Immunity*, **47**, 298–309.
21. De Bosscher,K., Desmet,S.J., Clarisse,D., Estebanez-Perpina,E. and Brunsveld,L. (2020) Nuclear receptor crosstalk - defining the mechanisms for therapeutic innovation. *Nat. Rev. Endocrinol.*, **16**, 363–377.
22. Louw,A. (2019) GR dimerization and the impact of GR dimerization on GR protein stability and half-life. *Front. Immunol.*, **10**, 1693.
23. Presman,D.M., Ogara,M.F., Stortz,M., Alvarez,L.D., Pooley,J.R., Schiltz,R.L., Grontved,L., Johnson,T.A., Mittelstadt,P.R., Ashwell,J.D. *et al.* (2014) Live cell imaging unveils multiple domain requirements for in vivo dimerization of the glucocorticoid receptor. *PLoS Biol.*, **12**, e1001813.
24. Presman,D.M., Ganguly,S., Schiltz,R.L., Johnson,T.A., Karpova,T.S. and Hager,G.L. (2016) DNA binding triggers tetramerization of the glucocorticoid receptor in live cells. *Proc. Natl. Acad. Sci. U.S.A.*, **113**, 8236–8241.
25. Paakinaho,V., Johnson,T.A., Presman,D.M. and Hager,G.L. (2019) Glucocorticoid receptor quaternary structure drives chromatin occupancy and transcriptional outcome. *Genome Res.*, **29**, 1223–1234.
26. Escoter-Torres,L., Greulich,F., Quagliarini,F., Wierer,M. and Uhlenhaut,N.H. (2020) Anti-inflammatory functions of the glucocorticoid receptor require DNA binding. *Nucleic Acids Res.*, **48**, 8393–8407.
27. Garcia,D.A., Johnson,T.A., Presman,D.M., Fettweis,G., Wagh,K., Rinaldi,L., Stavreva,D.A., Paakinaho,V., Jensen,R.A.M., Mandrup,S. *et al.* (2021) An intrinsically disordered region-mediated confinement state contributes to the dynamics and function of transcription factors. *Mol. Cell*, **81**, 1484–1498
28. Weikum,E.R., de Vera,I.M.S., Nwachukwu,J.C., Hudson,W.H., Nettles,K.W., Kojetin,D.J. and Ortlund,E.A. (2017) Tethering not required: the glucocorticoid receptor binds directly to activator protein-1 recognition motifs to repress inflammatory genes. *Nucleic Acids Res.*, **45**, 8596–8608.
29. Chrousos,G.P., Loriaux,D.L., Tomita,M., Brandon,D.D., Renquist,D., Albertson,B. and Lipsett,M.B. (1986) The new world primates as animal models of glucocorticoid resistance. *Adv. Exp. Med. Biol.*, **196**, 129–144.
30. Luisi,B.F., Xu,W.X., Otwinowski,Z., Freedman,L.P., Yamamoto,K.R. and Sigler,P.B. (1991) Crystallographic Analysis of the Interaction of the Glucocorticoid Receptor with DNA. *Nature*, **352**, 497–505.
31. Hudson,W.H., Youn,C. and Ortlund,E.A. (2013) The structural basis of direct glucocorticoid-mediated transrepression. *Nat. Struct. Mol. Biol.*, **20**, 53–58.
32. Frank,F., Okafor,C.D. and Ortlund,E.A. (2018) The first crystal structure of a DNA-free nuclear receptor DNA binding domain sheds light on DNA-driven allostery in the glucocorticoid receptor. *Sci. Rep.*, **8**, 13497.
33. Hard,T., Kellenbach,E., Boelens,R., Maler,B.A., Dahlman,K., Freedman,L.P., Carlstedt-Duke,J., Yamamoto,K.R., Gustafsson,J.A. and Kaptein,R. (1990) Solution structure of the glucocorticoid receptor DNA-binding domain. *Science*, **249**, 157–160.
34. Schacke,H., Berger,M., Rehwinkel,H. and Asadullah,K. (2007) Selective glucocorticoid receptor agonists (SEGRAs): novel ligands with an improved therapeutic index. *Mol. Cell Endocrinol.*, **275**, 109–117.
35. Biggadike,K., Bledsoe,R.K., Coe,D.M., Cooper,T.W., House,D., Iannone,M.A., Macdonald,S.J., Madauss,K.P., McLay,I.M., Shipley,T.J. *et al.* (2009) Design and x-ray crystal structures of high-potency nonsteroidal glucocorticoid agonists exploiting a novel binding site on the receptor. *Proc. Natl. Acad. Sci. U.S.A.*, **106**, 18114–18119.
36. Hurt,D.E., Suzuki,S., Mayama,T., Charmandari,E. and Kino,T. (2016) Structural analysis on the pathologic mutant glucocorticoid receptor ligand-binding domains. *Mol. Endocrinol.*, **30**, 173–188.
37. Liu,X., Wang,Y. and Ortlund,E.A. (2019) First high-resolution crystal structures of the glucocorticoid receptor ligand-binding domain-peroxisome proliferator-activated gamma coactivator 1-alpha complex with endogenous and synthetic glucocorticoids. *Mol. Pharmacol.*, **96**, 408–417.
38. Weikum,E.R., Okafor,C.D., D'Agostino,E.H., Colucci,J.K. and Ortlund,E.A. (2017) Structural analysis of the glucocorticoid receptor ligand-binding domain in complex with triamcinolone acetonide and a fragment of the atypical coregulator, small heterodimer partner. *Mol. Pharmacol.*, **92**, 12–21.
39. Johnson,T.A., Paakinaho,V., Kim,S., Hager,G.L. and Presman,D.M. (2021) Genome-wide binding potential and regulatory activity of the glucocorticoid receptor's monomeric and dimeric forms. *Nat. Commun.*, **12**, 1987.
40. Mikuni,S., Tamura,M. and Kinjo,M. (2007) Analysis of intranuclear binding process of glucocorticoid receptor using fluorescence correlation spectroscopy. *FEBS Lett.*, **581**, 389–393.
41. Digman,M.A., Dalal,R., Horwitz,A.F. and Gratton,E. (2008) Mapping the number of molecules and brightness in the laser scanning microscope. *Biophys. J.*, **94**, 2320–2332.
42. McNally,J.G., Mueller,W.G., Walker,D., Wolford,R.G. and Hager,G.L. (2000) The glucocorticoid receptor: rapid exchange with regulatory sites in living cells. *Science*, **287**, 1262–1265.
43. Dobin,A. and Gingeras,T.R. (2015) Mapping RNA-seq reads with STAR. *Curr. Protoc. Bioinformatics*, **51**, 11.14.1–11.14.19.
44. Love,M.I., Huber,W. and Anders,S. (2014) Moderated estimation of fold change and dispersion for RNA-seq data with DESeq2. *Genome Biol.*, **15**, 550.

45. Cheng,T.M., Blundell,T.L. and Fernandez-Recio,J. (2007) pyDock: electrostatics and desolvation for effective scoring of rigid-body protein-protein docking. *Proteins*, **68**, 503–515.
46. Canutescu,A.A., Shelenkov,A.A. and Dunbrack,R.L. Jr (2003) A graph-theory algorithm for rapid protein side-chain prediction. *Protein. Sci.*, **12**, 2001–2014.
47. Gabb,H.A., Jackson,R.M. and Sternberg,M.J. (1997) Modelling protein docking using shape complementarity, electrostatics and biochemical information. *J. Mol. Biol.*, **272**, 106–120.
48. Chen,R., Li,L. and Weng,Z. (2003) ZDOCK: an initial-stage protein-docking algorithm. *Proteins*, **52**, 80–87.
49. Fernandez-Recio,J., Totrov,M., Skorodumov,C. and Abagyan,R. (2005) Optimal docking area: a new method for predicting protein-protein interaction sites. *Proteins*, **58**, 134–143.
50. Grosdidier,S. and Fernandez-Recio,J. (2008) Identification of hot-spot residues in protein-protein interactions by computational docking. *BMC Bioinformatics*, **9**, 447.
51. He,Y., Yi,W., Suino-Powell,K., Zhou,X.E., Tolbert,W.D., Tang,X., Yang,J., Yang,H., Shi,J., Hou,L. *et al.* (2014) Structures and mechanism for the design of highly potent glucocorticoids. *Cell Res.*, **24**, 713–726.
52. Chagoyen,M., Garcia-Martin,J.A. and Pazos,F. (2016) Practical analysis of specificity-determining residues in protein families. *Brief Bioinform.*, **17**, 255–261.
53. Halabi,N., Rivoire,O., Leibler,S. and Ranganathan,R. (2009) Protein sectors: evolutionary units of three-dimensional structure. *Cell*, **138**, 774–786.
54. Lockless,S.W. and Ranganathan,R. (1999) Evolutionarily conserved pathways of energetic connectivity in protein families. *Science*, **286**, 295–299.
55. Presman,D.M., Ball,D.A., Paakinaho,V., Grimm,J.B., Lavis,L.D., Karpova,T.A. and Hager,G.L. (2017) Quantifying transcription factor dynamics at the single-molecule level in live cells. *Methods*, **123**, 76–88.
56. Liu,X., Wang,Y., Gutierrez,J.S., Damsker,J.M., Nagaraju,K., Hoffman,E.P. and Ortlund,E.A. (2020) Disruption of a key ligand-H-bond network drives dissociative properties in vamorolone for duchenne muscular dystrophy treatment. *Proc. Natl. Acad. Sci. U.S.A.*, **117**, 24285–24293.
57. Hurley,D.M., Accili,D., Stratakis,C.A., Karl,M., Vamvakopoulos,N., Rorer,E., Constantine,K., Taylor,S.I. and Chrousos,G.P. (1991) Point mutation causing a single amino acid substitution in the hormone binding domain of the glucocorticoid receptor in familial glucocorticoid resistance. *J. Clin. Invest.*, **87**, 680–686.
58. Nadal,M., Prekovic,S., Gallastegui,N., Helsen,C., Abella,M., Zielinska,K., Gay,M., Vilaseca,M., Taules,M., Houtsmuller,A.B. *et al.* (2017) Structure of the homodimeric androgen receptor ligand-binding domain. *Nat. Commun.*, **8**, 14388.
59. Kauppi,B., Jakob,C., Farnegardh,M., Yang,J., Ahola,H., Alarcon,M., Calles,K., Engstrom,O., Harlan,J., Muchmore,S. *et al.* (2003) The three-dimensional structures of antagonistic and agonistic forms of the glucocorticoid receptor ligand-binding domain: RU-486 induces a transconformation that leads to active antagonism. *J. Biol. Chem.*, **278**, 22748–22754.
60. Helsen,C. and Claessens,F. (2014) Looking at nuclear receptors from a new angle. *Mol. Cell Endocrinol.*, **382**, 97–106.
61. Bianchetti,L., Wassmer,B., Defosset,A., Smertina,A., Tiberti,M.L., Stote,R.H. and Dejaegere,A. (2018) Alternative dimerization interfaces in the glucocorticoid receptor-alpha ligand binding domain. *Biochim. Biophys. Acta. Gen. Subj.*, **1862**, 1810–1825.
62. Noddings,C.M., Wang,R.Y., Johnson,J.L. and Agard,D.A. (2022) Structure of Hsp90-p23-GR reveals the hsp90 client-remodelling mechanism. *Nature*, **601**, 465–469.
63. Min,J., Perera,L., Krahn,J.M., Jewell,C.M., Moon,A.F., Cidlowski,J.A. and Pedersen,L.C. (2018) Probing dominant negative behavior of glucocorticoid receptor beta through a hybrid structural and biochemical approach. *Mol. Cell Biol.*, **38** , e00453-17.
64. Schoch,G.A., D'Arcy,B., Stihle,M., Burger,D., Bar,D., Benz,J., Thoma,R. and Ruf,A. (2010) Molecular switch in the glucocorticoid receptor: active and passive antagonist conformations. *J. Mol. Biol.*, **395**, 568–577.
65. Gampe,R.T. Jr, Montana,V.G., Lambert,M.H., Wisely,G.B., Milburn,M.V. and Xu,H.E. (2000) Structural basis for autorepression of retinoid x receptor by tetramer formation and the AF-2 helix. *Genes Dev.*, **14**, 2229–2241.

Figure S1

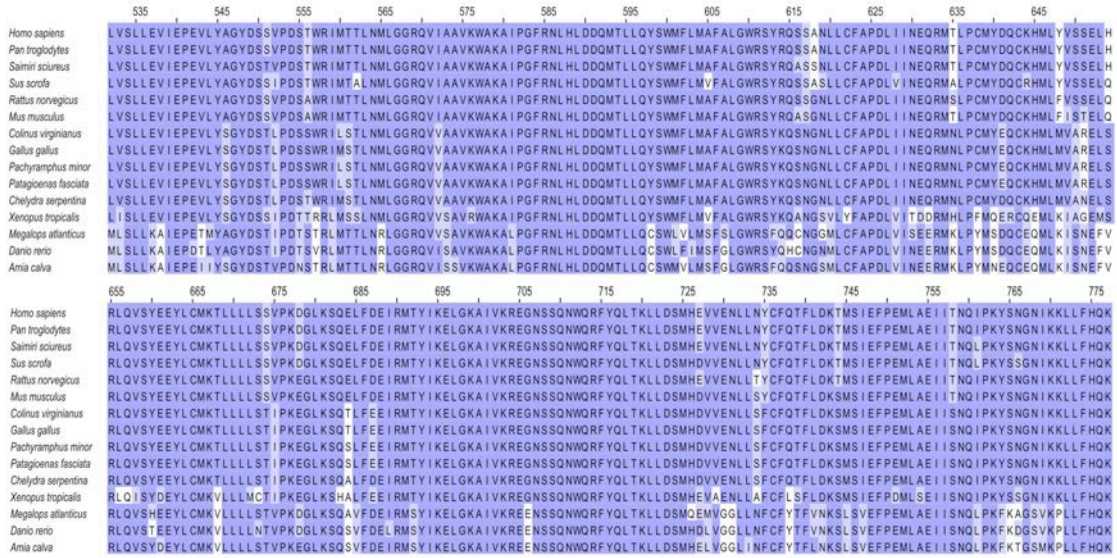

Figure S1 legend. Partial sequence alignment of GR-LBD from selected species.

GR homologs were identified and aligned using PSI-BLAST (https://blast.ncbi.nlm.nih.gov/Blast.cgi?PAGE_TYPE=BlastSearch&PROGRAM=blastp&BLAST_PROGRAMS=psiBlast). To provide a representative view of LBD conservation across vertebrates, sequences of mammalian (human, chimpanzee, squirrel monkey, pig, rat, and mouse), avian (chicken, quail, becard, and pigeon), reptile (turtle), amphibian (frog) and fish GR (tarpon, zebrafish, and dogfish) were included in the alignment. Residues conserved in hGR and other homologs are shaded purple, and conservative replacements are shaded light violet.

Figure S2

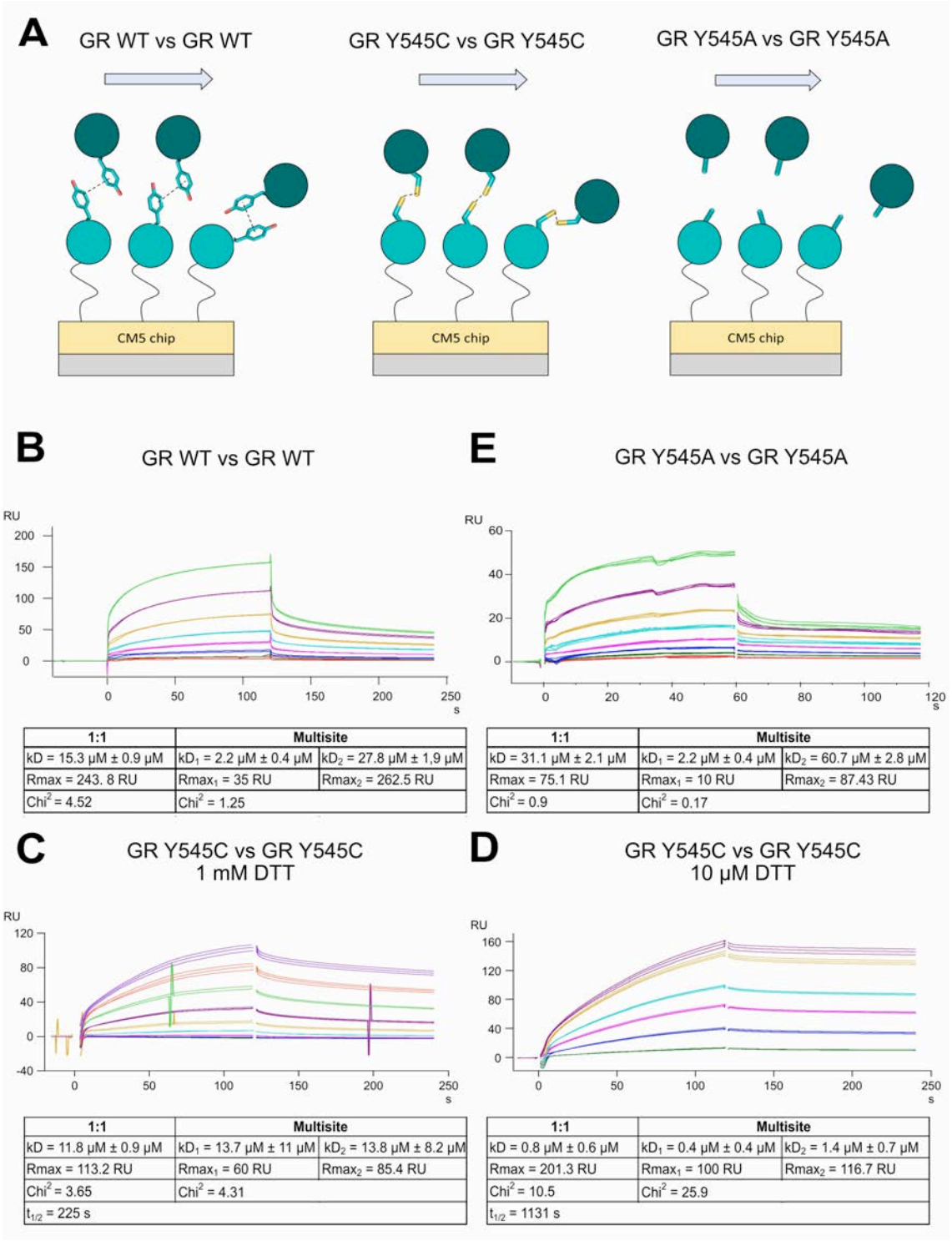

1:1	Multisite	
kD = 15.3 µM ± 0.9 µM	kD_1 = 2.2 µM ± 0.4 µM	kD_2 = 27.8 µM ± 1,9 µM
Rmax = 243. 8 RU	$Rmax_1$ = 35 RU	$Rmax_2$ = 262.5 RU
Chi^2 = 4.52	Chi^2 = 1.25	

1:1	Multisite	
kD = 31.1 µM ± 2.1 µM	kD_1 = 2.2 µM ± 0.4 µM	kD_2 = 60.7 µM ± 2.8 µM
Rmax = 75.1 RU	$Rmax_1$ = 10 RU	$Rmax_2$ = 87.43 RU
Chi^2 = 0.9	Chi^2 = 0.17	

1:1	Multisite	
kD = 11.8 µM ± 0.9 µM	kD_1 = 13.7 µM ± 11 µM	kD_2 = 13.8 µM ± 8.2 µM
Rmax = 113.2 RU	$Rmax_1$ = 60 RU	$Rmax_2$ = 85.4 RU
Chi^2 = 3.65	Chi^2 = 4.31	
$t_{1/2}$ = 225 s		

1:1	Multisite	
kD = 0.8 µM ± 0.6 µM	kD_1 = 0.4 µM ± 0.4 µM	kD_2 = 1.4 µM ± 0.7 µM
Rmax = 201.3 RU	$Rmax_1$ = 100 RU	$Rmax_2$ = 116.7 RU
Chi^2 = 10.5	Chi^2 = 25.9	
$t_{1/2}$ = 1131 s		

Figure S2 legend. SPR analysis of protein-protein interactions between wild-type GR-LBD and its Tyr545 mutants.

A, Schematic representation of the interactions between soluble analyte and chip-immobilized GR-LBD molecules. Panels **B-E** summarize SPR experiments performed by running increasing concentrations (0.2, 0.4, 0.8, 1.6, 3.12, 6.25, 12.5 and 25 μM) of WT GR-LBD·DEX (**B**), GR-LBD Y545C mutant (**C, D**), or GR-LBD Y545A mutant (**E**) over the same immobilized protein. SPR sensorgrams corresponding to experiments conducted in duplicate are shown in all cases. Tables below panels **B, C, D** and **E** summarize major parameters (maximum response (R_{max}), dissociation constant (k_D), and fitting error (χ^2)) derived from the fitting of self-association sensorgrams according to either 1:1 or multisite models.

Figure S3

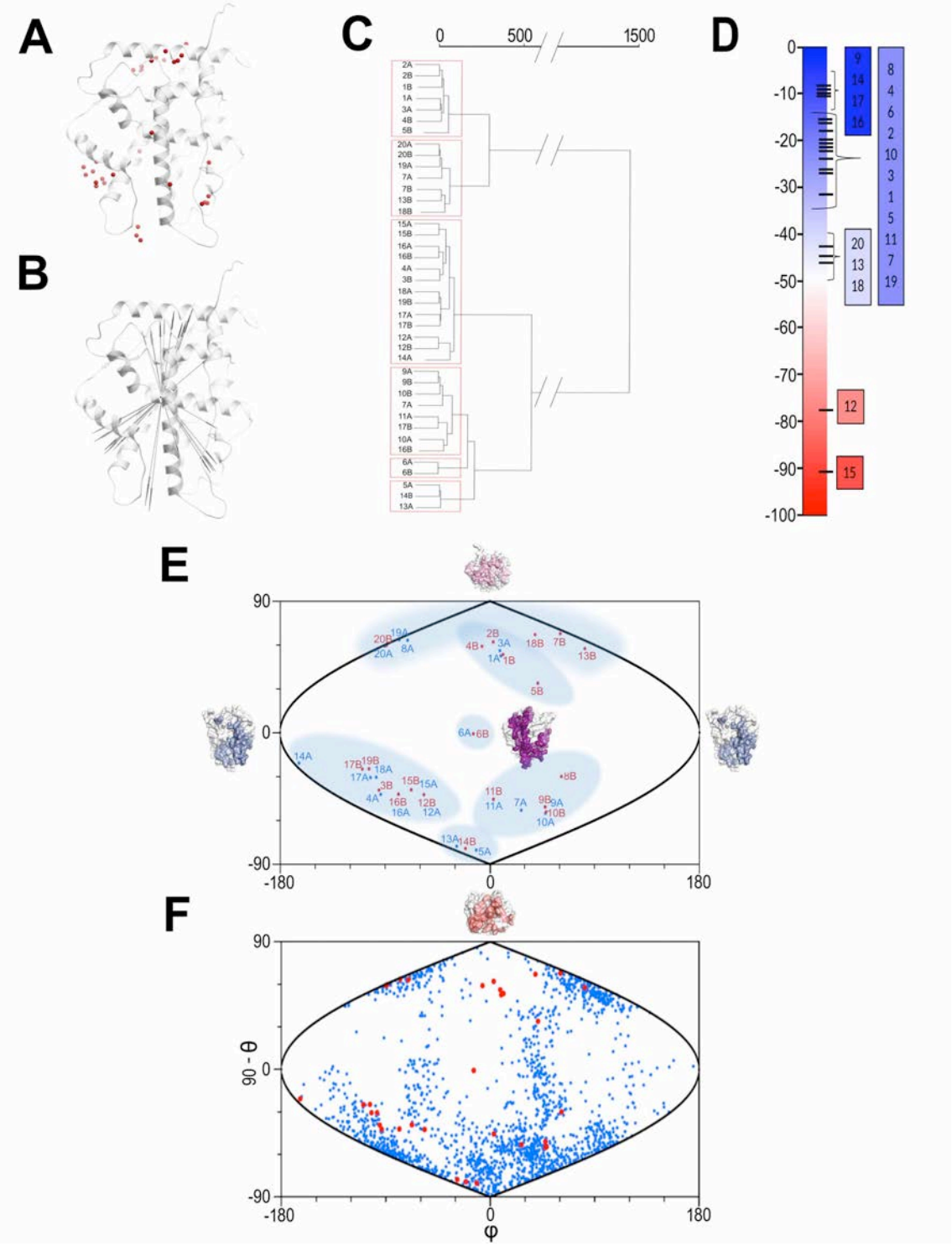
A
B
C
0
500
1500
D
0
-10
-20
-30
-40
-50
-60
-70
-80
-90
-100
E
90
0
-90
-180
0
180
F
90
0
-90
-180
0
180
90 - θ
φ

Figure S3 legend. Distribution and clustering of homodimerization interfaces in GR-LBD.

The centers of coordinates of the interaction surfaces in the 20 topologically distinct GR-LBD homodimers are schematically represented as dots (**A**) or as vectors drawn from the center of coordinates of a common monomer to the given interface (**B**). **C**, Dendrogram generated from the hierarchical clustering of all GR-LBD homodimers, based on the Euclidean distances between the centers of coordinates of the interaction surfaces. Each interaction surface is named according to the dimer number (#1-#20) and the chain ID of the monomer. Note that the clustering analysis separates the interaction surfaces in six clusters. **D**, Binding energy of the GR-LBD homodimers, as calculated with pyDock. **E**, A sinusoidal equal-area projection of the interaction surfaces in the 20 GR-LBD dimers, represented as spherical coordinates from the vectors defined in panel B. Clusters obtained as described above are shaded blue. **F**, Representation in spherical coordinates of the interaction surfaces in the top 1,000 docking solutions of monomeric GR-LBD on itself (blue dots, results obtained using coordinates form PDB entry 5UFS). For comparison, the interaction surfaces for the 20 topologically distinct crystal homodimers are shown as red dots.

Figure S4

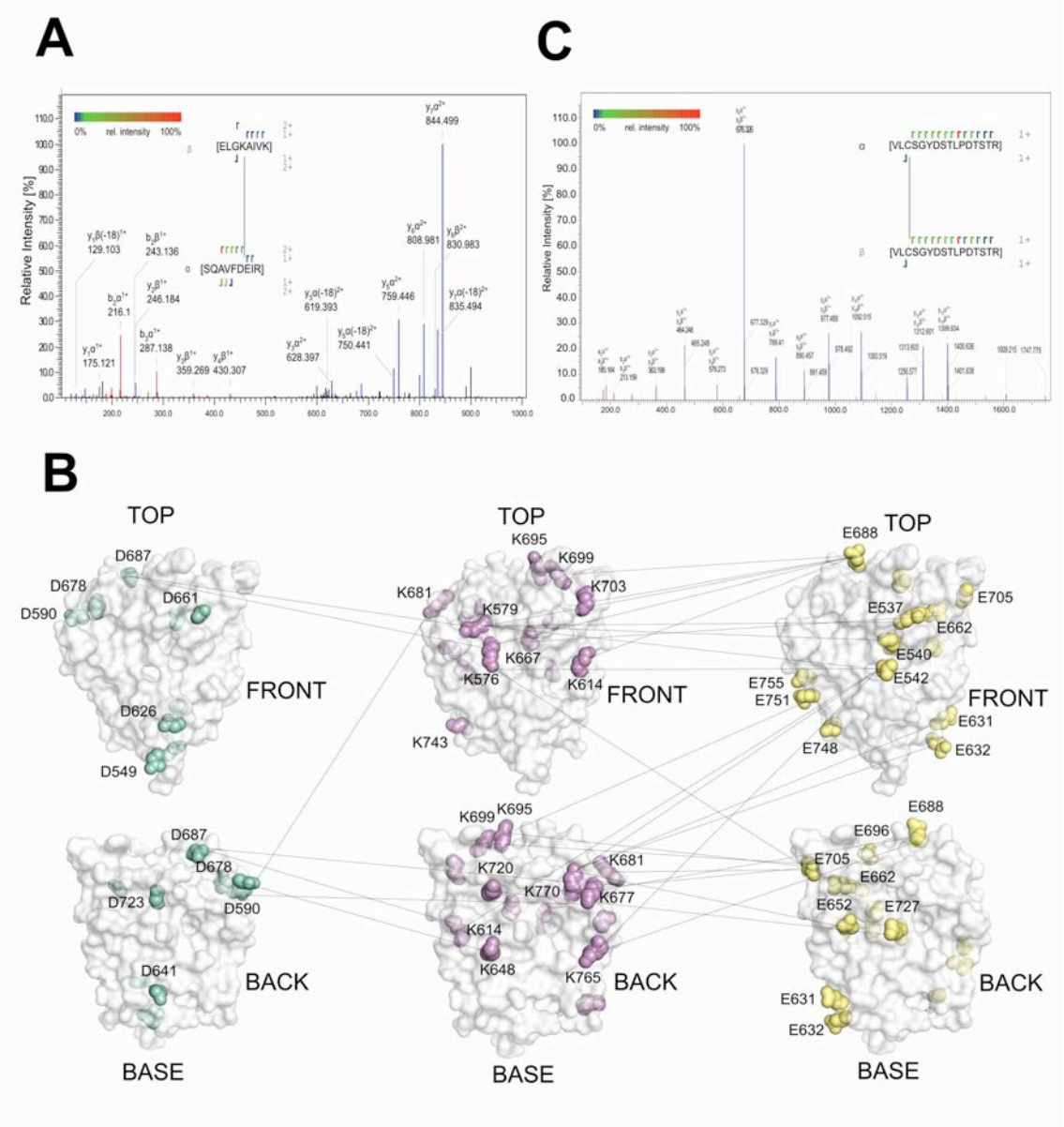
A
C
B
Relative Intensity [%]
0% rel. intensity 100%
[ELGKAIVK]
[SQAVFDEIR]
[VLCSGYDSTLPDTSTR]
TOP
FRONT
BACK
BASE
D687
D678
D661
D590
D626
D549
D723
D641
K695
K699
K703
K681
K579
K667
K576
K614
K743
K720
K770
K677
K648
K765
E688
E537
E705
E662
E540
E542
E755
E751
E631
E748
E632
E696
E652
E727

Figure S4 legend. Mass spectrometric verification of cross-links between GR-LBD molecules in solution.

A, Representative MS/MS spectra identifying EDC-crosslinked peptides between Glu688 and Lys699, corresponding to the top-to-top conformation (#20). **B,** Summary of all EDC-crosslinks identified between Lys-Asp and Lys-Glu residue pairs, mapped on the 3D structure of GR-LBD. The central panels show the surface-exposed lysines, while aspartate and glutamate residues are highlighted in the left and right panels, respectively. Note that the uneven distribution of charged residues across the domain surface, in particular of lysines, only allows demonstration of a subset of possible homodimeric conformations populated in solution. **C**, Representative MS/MS spectra identifying crosslinked peptides formed by disulfide bridges between Cys545-Cys545' residues in the Y545C variant of GR-LBD.

Figure S5

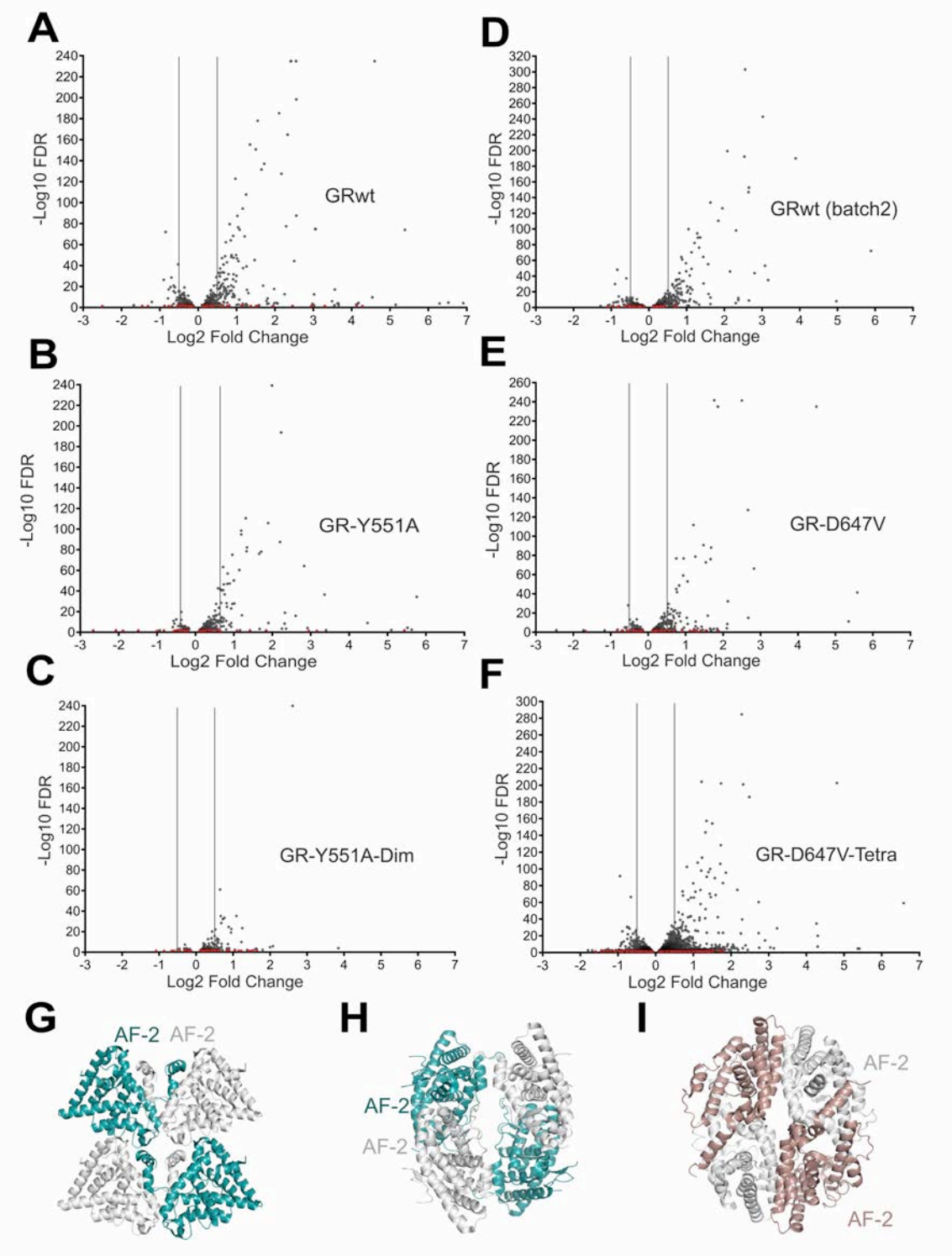
A
GRwt
-Log10 FDR
Log2 Fold Change
D
GRwt (batch2)
-Log10 FDR
Log2 Fold Change
B
GR-Y551A
-Log10 FDR
Log2 Fold Change
E
GR-D647V
-Log10 FDR
Log2 Fold Change
C
GR-Y551A-Dim
-Log10 FDR
Log2 Fold Change
F
GR-D647V-Tetra
-Log10 FDR
Log2 Fold Change
G
AF-2
AF-2
H
AF-2
AF-2
I
AF-2
AF-2

Figure S5 legend: Residues Tyr545 and Asp641 play a major role on GR transcriptional activity and GR quaternary structures. (**A-F**) Volcano-plot representation from RNA-Seq data after 2h DEX treatment for each indicated mutant. The vertical lines delineate a Log2 |FC| $\geq$ 0.5. Gray dots represent genes with an FDR $\leq$ 0.01) and red dots represent genes with an FDR of 0.05. **G-I**, Tetrameric arrangements found in the crystal structures of GR-LBD bound to the antagonist RU-486 (1NHZ (**G**) and 5UC3 (**H**), respectively) compared to (**I)** the inactive RXR-LBD tetramer (1G1U). Two-fold axes generating the dimers-of-dimers run roughly perpendicular to the page plane.

Figure S6

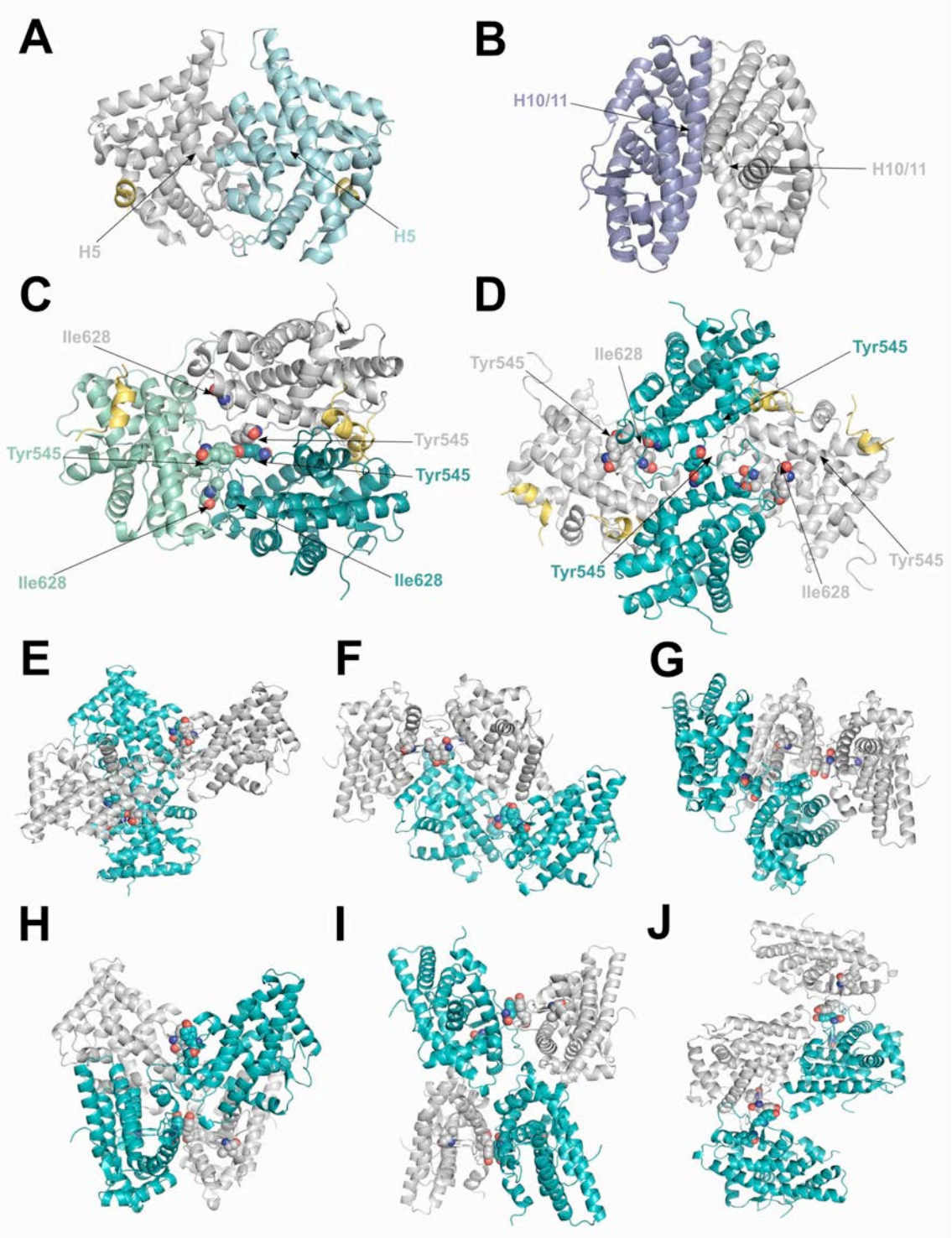
A
H5
H5
B
H10/11
H10/11
C
Ile628
Tyr545
Tyr545
Tyr545
Ile628
Ile628
D
Tyr545
Ile628
Tyr545
Tyr545
Tyr545
Ile628
E
F
G
H
I
J

Figure S6 legend. **Possible conformations of multimeric GR-LBD.**

A, Three-dimensional structure of dimeric AR-LBD (5JJM), a prototype of non-canonical NR dimerization. The two monomers are shown as cartoons, colored gray and light cyan, respectively. The interacting H5 from both monomers are labeled. **B**, Three-dimensional structure of ERα-LBD dimer (1ERE), representing the canonical conformation observed in NR homo- and heterodimers. The two monomers are shown as cartoons, colored slate blue and gray, respectively. The interacting H10/11 from both monomers are labeled. Different combinations with homodimers #9 and #10 are compatible with several **C**, trimeric and tetrameric arrangements, eventually upon replacing the "true" crystal monomer by a close docking solution to avoid intermonomer clashes. GR-LBD trimer generated by docking dimers #6 and #10. **D**, GR-LBD tetramer generated by combining dimers #11 and #14. **E-J**, Putative alternative conformations of tetrameric GR-LBD generated by docking dimer #11 onto itself. The major interface residues Tyr545 and Ile628 are given as spheres in panels **C** - **J**. Note that there are no free valences (exposed Tyr545 / Ile628 side chains) in these multimeric arrangements.

TABLES

Table S1 legend. Summary of X-ray diffraction data, refinement statistics and model quality.

	GR WT 1	GR WT 2	GR WT 3	GR WT 4	GR WT 5	GR Y545A
PDB code	7YXC	7YXD	7YXN	7YXO	7YXP	7YXR
Wavelength (Å)	0.9	0.9	0.9	0.9	0.9	0.9
Resolution range	43.42-2.25 (2.32-2.25)	76.81-2.30 (2.42-2.30)	94.81-2.46 (2.56-2.46)	90.10-2.99 (3.18-2.99)	72.80-3.36 (3.63-3.36)	93.44-2.50 (2.60-2.50)
Space group	C121	P31	P61	$I4_122$	$I4_132$	$P6_1$
Cell dimensions a, b, c (Å) α, β, γ (°)	86.61, 52.44, 69.60 90.0, 116.62, 90.0	107.60, 107.60, 135.64 90.0, 90.0, 120.0	109.36,109.36, 137.77 90.0, 90.0, 120.0	180.20, 180.20, 169.18, 90.0, 90.0, 90.0	178.05, 178.05, 178.05 90.00, 90.00, 90.00	107.90, 107.90 134.01 90.0, 90.0, 120.0,
Total reflections	34,022 (1,954)	156,013 (22,547)	94,861 (11,087)	223,344 (40,285)	82,328 (16,909)	87,676 (9,859)
Unique reflections	12,530 (907)	73,686 (10,882)	33,009 (3,799)	23,704 (4,229)	7,178 (1,431)	30,280 (9,859)
Multiplicity	2.7 (2.2)	2.1 (2.1)	2.9 (2.9)	9.4 (9.5)	11.5 (11.8)	2.9 (2.9)
Completeness (%)	93.8 (75.5)	94.4 (95.6)	96.8 (98.5)	100.0 (100.0)	100.0 (100.0)	99.0 (99.5)
Mean I/sigma(I)	11.1 (1.8)	5.9 (1.4)	7.4 (0.7)	6.6 (2.2)	10.8 (1.7)	6.5 (1.9)
Wilson B-factor	44.7	45.0	57.5	73.5	141.0	39.5
R-meas	0.069 (0.697)	0.125 (0.987)	0.074 (1.050)	0.307 (1.701)	0.108 (1.762)	0.121 (0.582)
R-pim	0.039 (0.439)	0.079 (0.641)	0.051 (0.725)	0.149 (0.815)	0.031 (0.505)	0.081 (0.390)
CC1/2	0.997 (0.654)	0.986 (0.314)	0.994 (0.317)	0.982 (0.386)	1.000 (0.561)	0.993 (0.621)
Reflections used in refinement	12,018	69,901	31,272	22,492	6,809	28,706
Reflections used for R-free	510 (4.1%)	3,765 (5.1%)	1,692 (5.1%)	1,194 (5.0%)	344 (4.8%)	1,517 (5.0%)
R-work	0.192	0.177	0.216	0.242	0.199	0.187
R-free	0.245	0.220	0.247	0.280	0.288	0.224
Total number of atoms	2,146	8280	4,190	6,109	2,111	4,234
RMS (bonds)	0.007	0.010	0.007	0.006	0.006	0.007
RMS (angles)	1.565	2.016	1.655	1.555	1.727	1.564
Ramachandran favored (%)	96.00	95.93	93.16	89.38%	84.55	97
Ramachandran allowed (%)	100.0	99.3	99.0	98.9%	95.9	99.8
Clashscore	12.86	13.16	9.36	27.61	29.6	4.84
Average B-factor	54.0	50.0	68.0	67.0	142.0	43.0

Table S2 legend. Summary of GR-LBD structures reported to date.

PDB entries are ordered from lowest (monoclinic, C2) to highest (cubic, $I4_132$) space group symmetry. Major crystal parameters are given, along with the identity of LBP-bound compounds, peptides occupying the AF2 site, and other co-crystallized small-molecule compounds. The sequences of ancGR1 and 2 are given in Fig. 1C. Other engineered variants of human GR (hGR; UniProt entry P04150) are named according to the first deposited structure. The mutations introduced in these variants are: hGR_1M2Z: F602S; hGR_3CLD: F602Y, C638G; hGR_1NHZ: F602S, C638D; hGR_3H52: F602S, C638D, E684A, E688A, W712S; hGR_4CSJ: V571M, F602S, C638D; hGR_5NFT: V571M, F602S, C638D, E684A, W712S; hGR_4P6X: F602A, C622Y, T668V, S674T, V675I, E684A, E688A; and hGR_4P6W: F602A, C622Y, T668V, S674T, V675I, K699A, K703A. PDB entry 5UC3 features a dominant negative hGR variant (L733K, N734P). The reported PDB of mouse GR-LBD contain either the F602S mutation (3MNE), the double mutant (F602S, A605V) in 3MNO, or the triplet (A605V, V702A, E705G) in 3MNP. HetgaGRb refers to the GRb variant from the naked mole-rat, *Heterocephalus glaber*, with residues topologically equivalent to Phe602 and Val728 replaced by Ser and Asn, respectively.

Other abbreviations: 1CA / 1TA, triamcinolone acetonide; 29M, non-steroidal GR antagonist; 8W5, budesonide; 8W8, indazole ether-based GR modulator AZD5423; ACE, acetyl group; B9Q, B9T, and B9W, oral GR modulators; BOG, b-octyl glucopyranoside; CL, chloride ion; CHAPS, 3-[(3-cholamidopropyl)dimethylammonio]-1-propanesulfonate; CV7, desisobuytyryl ciclesonide; DAY, deacylcortivazol; DEX, dexamethasone; DMS, dimethyl sulfoxide; DOC, desoxycorticosterone; E7T, GR agonist; EDO, 1,2-ethylenediol; FMT, formic acid; GOL, glycerol; GSK866, non-steroidal GR agonist; GW6, fluticasone furoate; HCY, cortisol; HEPES, 4-(2-hydroxyethyl)-1-piperazine ethanesulfonic acid; HEX, hexane 1,6-diol; HYC, hydrocortisone; JZN, D-prolinamide 11; JZS, alanine amide derivative; JZR, hexyl b-D-glucopyranoside; LSJ, dibenzoxepane sulfonamide; MOF, mometasone furoate; MPD,

(4*S*)-2-methyl-2,4-pentanediol; NN7, non-steroidal GR modulator, suitable for inhalation; R8C, indazole ether-based non-steroidal GR modulator; RU-468, mifepristone; SCN, thiocyanate ion; TLA, tartaric acid.

PDB code	Space group	Res. (Å)	Cell constants	Protein	Ligands		
					LBP	AF-2	Dimer interfaces (Dis) and other pockets
5UFS	C2	2.12	a = 87.0, b = 52.8, c = 126.0 Å, β = 101.8°	ancGR2	1TA	SHP (17-27), R17A	–
3K23	C2	3	a = 184.9, b = 66.0, c = 71.5 Å, β = 103.6°	hGR_3CLD	JZN	SRC2 (740-751)	–
3RY9	C2	1.95	a = 139.4, b = 49.1, c = 100.4 Å, β = 105.8°	ancGR1[1]	DOC	–	GOL (DI)
5UC3	C2	2	a = 136.7, b = 88.3, c = 64.7 Å, β = 110.8°	hGR_5UC3	RU-486	–	EDO (DI), HEPES, MPD
This work	C2	2.15	a = 91.1, b = 90.8, c = 157.2 Å, β = 116.6º	ancGR2	DEX	SHP (12-30)	–
1NHZ	$P2_12_12$	2.3	a = 74.9, b = 109.8, c = 39.3 Å	hGR_1NHZ	RU-486	–	HEX (3 molecules, two at two different DIs)
4LSJ	$P2_12_12$	2.35	a = 39.0, b = 139.4, c = 48.1 Å	hGR_3CLD	LSJ	Synthetic peptide[2]	LSJ (DI)
6NWK	$C222_1$	1.65	a = 71.7, b = 96.4, c = 107.9 Å	ancGR2	DEX	PGC1a (141-152)	ACE, FMT (DI #1), DMS (one at DI #2), GOL
6NWL	$C222_1$	1.59	a = 71.7, b = 96.4, c = 108.2 Å	ancGR2	HYC	PGC1a (141-152)	GOL (one at DI #1), HEPES, SCN (one at DI #2), TLA
1P93[3]	$P3_1$	2.7	a = b = 127.4,	hGR_1NHZ	DEX	SRC2 (939-950)	–

			c = 91.8 Å, γ = 120°				
This work	$P3_1$	2.7	a = b = 107.75, c = 135.8 Å, γ = 120°	ancGR2	DEX	SHP (12-30)	–
3GN8	$P6_1$	2.5	a = b = 104.2, c = 144.2 Å, γ = 120°	ancGR2	DEX	SRC2 (734-754) [4]	–
4E2J	$P6_1$	2.5	a = b = 104.4, c = 143.9 Å, γ = 120°	ancGR2	MOF	SRC2 (741-752), GOL	FMT, GOL (DI)
1M2Z	$P6_1$	2.5	a = b = 125.8, c = 86.0 Å, γ = 120°	hGR_1M2Z	DEX	SRC2 (734-754)	BOG (3 molecules at the DI)
3CLD	$P6_1$	2.84	a = b = 127.3, c = 77.8 Å, γ = 120°	hGR_3CLD	GW6	SRC2 (740-751)	–
3E7C	$P6_1$	2.15	a = b = 126.6, c = 79.0 Å, γ = 120°	hGR_3CLD	GSK866	SRC2 (741-751)	GOL (3 molecules, one at DI)
3K22	$P6_1$	2.1	a = b = 127,6, c = 78.2 Å, γ = 120°	hGR_3CLD	JZS	SRC2 (740-751)	JZR (fully embedded in DI)
4P6X	$P6_1$	2.5	a = b = 220.8, c = 74.2 Å, γ = 120°	hGR_4P6X	HCY	SRC2 (740-753)	–
5UC1	$P6_1$	2.35	a = b = 48.4, c = 385.8 Å, γ = 120°	HetgaGRβ	RU-486	–	RU-486 (two molecules fully embedded in DI #1), CHAPS (two molecules in DI #1, 3rd molecule in DI #2), CL (DI #2), EDO, MPD
This work	$P6_1$	2.7	a = b = 190.6, c = 137.9 Å, γ = 120°	ancGR2	DEX	SHP (12-30)	–
3BQD	$P6_2$	2.5	a = b = 93.8, c = 130.0 Å, γ = 120°	hGR_1M2Z	DAY	SRC1 (739-751)	–

3MNE	$P6_5$	1.96	a = b = 71.8, c = 128.6 Å, γ = 120°	mGR	DEX	SRC2 (740-752)	GOL (2 molecules, one at the DI)
3MNP	$P6_5$	1.5	a = b = 72.1, c = 128.8 Å, γ = 120°	mGR	DEX	SRC2 (740-752)	GOL (2 molecules, one at DI #1), SCN (2 molecules, one at DI #2)
3MNO	$P6_5$	1.55	a = b = 71.4, c = 127.9 Å, γ = 120°	mGR	DEX	SRC2 (740-752)	SCN (2 molecules at DIs #1 and #2), GOL (at a 3rd DI)
3H52	$P3_221$	2.8	a = b = 99.5, c = 252.4 Å, γ = 120°	hGR_3H52	RU-486	NCOR1 (2260-2274)	GOL
4MDD	$P3_221$	2.4	a = b = 72.5, c = 229.5 Å, γ = 120°	hGR_3H52	29M	NCOR1 (1-14)	–
4CSJ	$P3_221$	2.3	a = b = 84.4, c = 105.7 Å, γ = 120°	hGR_4CSJ	NN7	SRC2 (741-753)	EDO
4UDC	$P3_221$	2.5	a = b = 84.7, c = 105.9 Å, γ = 120°	hGR_1NHZ	DEX	SRC2 (741-753)	CHAPS (at DI)
4UDD	$P3_221$	1.8	a = b = 87.2, c = 102.9 Å, γ = 120°	hGR_4CSJ	CV7	SRC2 (741-753)	CHAPS (at DI)
5G3J	$P3_221$	2.4	a = b = 84.3, c = 106.7 Å, γ = 120°	hGR_4CSJ	E7T	SRC2 (741-753)	CHAPS (at DI), EDO
5G5W	$P3_221$	2.2	a = b = 83.9, c = 105.7 Å, γ = 120°	hGR_4CSJ	R8C	SRC2 (741-753)	EDO
5NFP	$P3_221$	2.1	a = b = 84.0, c = 106.1 Å, γ = 120°	hGR_4CSJ	8W5	SRC2 (741-753)	CHAPS (at DI), EDO, GOL
5NFT	$P3_221$	2.3	a = b = 84.4, c = 106.1 Å, γ = 120°	hGR_5NFT	8W8	SRC2 (741-753)	EDO
6EL6	$P3_221$	2.4	a = b = 85.0, c = 106.4 Å, γ = 120°	hGR_4CSJ	B9Q	SRC2 (740-753)	EDO
6EL7	$P3_221$	2.18	a = b = 83.8, c = 106.0 Å, γ = 120°	hGR_5NFT	B9T	SRC2 (740-753)	EDO
6EL9	$P3_221$	2.19	a = b = 84.5, c = 105.7 Å	hGR_5NFT	B9W	SRC2 (740-753)	EDO

This work	$I4_122$	3.18	a = b = 180.3, c = 169.2 Å	ancGR2	DEX	SHP (12-30)	DEX (embedded in DI)
4P6W	P23	1.95	a = b = c = 130.2 Å	hGR_4P6W	MOF	SRC2 (741-752)	–
This work	$I4_132$	3.36	a = b = c = 178.05 Å	ancGR2	DEX	SHP (12-30)	DEX (embedded in DI)

[1] Sequence not identical to ancGR1 – rather an intermediate between ancGR1 and ancGR2.
[1] His-Ser-Ser-Arg-Leu-Trp-Glu-Leu-Leu-Met-Glu-Ala-Thr. (Leucines of the LXXLL motif are underlined).
[1] Structure not refined. (R 34.5%, R_{free} 36.3%, and worrisome MolProbity statistics).
[1] Only residues Asn742-Asp752 defined by electron density.

Table S3 legend. Heatmap representation of the 20 topologically distinct GR-LBD homodimers. Interface residues in all pairs of GR-LBD monomers identified by PISA are marked (X).

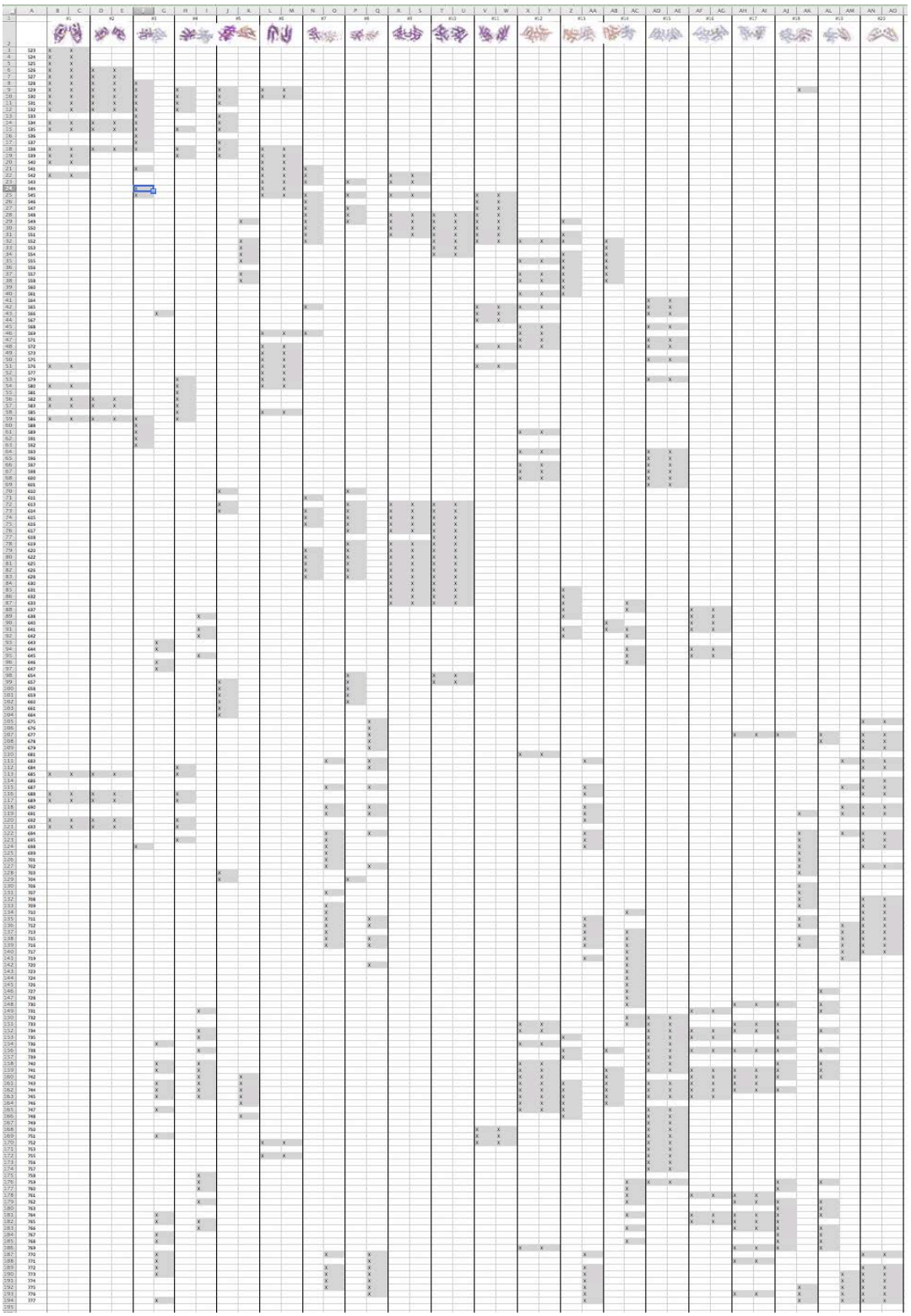

Table S4 legend. Summary of EDC-crosslinked peptides of ancGR2-LBD identified by mass spectrometry.

					Count		Average MH+ (exp)		Average δm	
				Oligomer	Dim	Tetra	Dimer	Tetramer	Dimer	Tetramer
Peptide 1	**A site**	**Peptide 2**	**B site**	**MH+ (theo)**						
E^{537}VIEPEVLY^{545}	Glu537 / H1	A^{578}KALPGF^{584}	Lys579 / H3	1774.96	1		1774.96228		0	
E^{537}VIEPEVLY^{545}	Glu537 / H1	A^{578}KALPGFRNL^{587}	Lys579 / H3	2158.19	1		2158.18928		-0.46335139	
E^{537}VIEPEVL^{544}	Glu540 / L1-3	A^{578}KALPGF^{584}	Lys579 / H3	1611.9	1		1611.89828		-0.62038654	
E^{537}VIEPEVLY^{545}	Glu540 / L1-3	A^{578}KALPGF^{584}	Lys579 / H3	1774.96	1		1774.96228		0	
E^{537}VIEPEVLY^{545}	Glu540 / L1-3	A^{578}KALPGFRNL^{587}	Lys579 / H3	2158.19	1		2158.18828		-0.92670321	
E^{537}VIEPEVL^{544}	Glu542 / L1-3	G^{567}GRQVVSAVKW^{577}	Lys576 / H3	2095.15	2		2095.15378		-0.23864602	
E^{537}VIEPEVLY^{545}	Glu542 / L1-3	G^{567}GRQVVSAVKW^{577}	Lys576 / H3	2258.22	2		2258.21778		-0.22141359	
E^{537}VIEPEVLY^{545}	Glu542 / L1-3	N^{564}RLGGRQVVSAVKW^{577}	Lys576 / H3	2641.45	1		2641.45228		2.27147772	
P^{530}TLISLLEVIEPEVLYS GYDSTLPDTSTR^{558}	Glu542 / L1-3	Q^{570}VVSAVKWAK^{579}	Lys576 / H3	4305.29	2		4305.27978		-2.43886623	
E^{537}VIEPEVL^{544}	Glu542 / L1-3	A^{578}KALPGF^{584}	Lys579 / H3	1611.9	1		1611.90028		0.62038577	
E^{537}VIEPEVL^{544}	Glu542 / L1-3	A^{578}KALPGFRNL^{587}	Lys579 / H3	1995.13	1		1995.12728		0	
E^{537}VIEPEVLY^{545}	Glu542 / L1-3	A^{578}KALPGF^{584}	Lys579 / H3	1774.96		1		1774.96228		0
E^{537}VIEPEVLY^{545}	Glu542 / L1-3	A^{578}KALPGFRNL^{587}	Lys579 / H3	2158.19	2		2158.18993		-0.22277314	
E^{537}VIEPEVLY^{545}	Glu542 / L1-3	K^{614}QSNGNML^{621}	Lys614 / H5	1978.98	1		1978.97828		-0.50531126	
E^{537}VIEPEVLY^{545}	Glu542 / L1-3	K^{765}AGSVKPL^{772}	Lys765 / H12	1871.05	1		1871.05128		-0.5344589	
E^{537}VIEPEVL^{544}	Glu542 / L1-3	K^{765}AGSVKPL^{772}	Lys770 / S4	1707.99	1		1707.98828		-0.58548411	
E^{537}VIEPEVLY^{545}	Glu542 / L1-3	K^{765}AGSVKPL^{772}	Lys770 / S4	1871.05	2		1871.05178		-0.26722945	
H^{588}LDDQMTL^{595}	Asp590 / H4-5	S^{672}TVPKDGLKSQAVF^{686}	Lys681 / L8-9	2446.23	3		2446.23094		1.09011135	
H^{588}LDDQMTLL^{596}	Asp590 / H4-5	S^{672}TVPKDGLKSQAVF^{686}	Lys681 / L8-9	2559.31	2		2559.31028		-0.7814607	
H^{588}LDDQMTLL^{596}	Asp590 / H4-5	L^{671}STVPKDGLKSQAVF^{686}	Lys677 / L8-9	2672.4	1		2672.39628		0	
Q^{615}SNGNMLCFAPDLVINEER^{633}	Glu631 / H6	A^{766}GSVKPLLFHQK^{777}	Lys777 / C-t	3512.78	5		3512.73379		-12.5019153	
Q^{615}SNGNMLCFAPDLVINEER^{633}	Glu631 / H6	A^{766}GSVKPLLFHQK^{777}	Lys777 / C-t	3528.77	1		3528.76428		-2.26708257	
Q^{615}SNGNMLCFAPDLVINEER^{633}	Glu632 / H6	A^{766}GSVKPLLFHQK^{777}	Lys777 / C-t	3512.78	2		3512.73745		-11.4588416	
Q^{615}SNGNMLCFAPDLVINEER^{633}	Glu632 / H6	A^{766}GSVKPLLFHQK^{777}	Lys777 / C-t	3528.77	1		3528.75828		-3.96740125	
K^{648}ISSEF^{653}	Glu652 / H7	L^{773}FHQK^{777}	Lys777 / C-t	1363.74	1		1363.73516		-1.24503646	

V[654]RLQVSYDEY[663]	Glu662 / H8	C[665]MKVLL[670]	Lys667 / H8	2032.02	1		2032.02228		-0.98424118	
S[673]TVPKDGL[680]	Asp678 / L8-9	K[648]ISSEF[653]	Lys648 / H7	1507.8	1		1507.80235		1.38418009	
S[682]QAVFDEIR[690]	Asp687 / H9	Q[570]VVSAVKWAK[579]	Lys576 / H3	2161.18	2		2161.16389		-5.77495063	
S[682]QAVFDEIR[690]	Asp687 / H9	W[577]AKALPGFR[585]	Lys579 / H3	2091.11	1		2091.11328		0	
D[687]EIRMTY[693]	Asp687 / H9	K[614]QSNGNML[621]	Lys614 / H5	1831.83	1		1831.83028		-0.5459021	
S[682]QAVFDEIR[690]	Asp687 / H9	S[612]YKQSNGNMLC FAPDLVINEER[633]	Lys614 / H5	3630.73	2		3630.73453		0.82367906	
S[682]QAVFDEIR[690]	Asp687 / H9	S[612]YKQSNGNMLC FAPDLVINEER[633]	Lys614 / H5	3646.73	2		3646.73477		2.2803852	
S[682]QAVFDEIR[690]	Asp687 / H9	A[766]GSVKPLLFHQK[777]	Lys770 / S4	2370.29		1		2370.29328		0
S[682]QAVFDEIR[690]	Glu688 / H9	Q[570]VVSAVKWAK[579]	Lys576 / H3	2161.18	6	1	2161.17542	2161.17571	-0.44174584	-0.32651209
S[682]QAVFDEIR[690]	Glu688 / H9	W[577]AKALPGFR[585]	Lys579 / H3	2091.11	1		2091.11428		0.47821394	
D[687]EIRMTY[693]	Glu688 / H9	K[614]QSNGNML[621]	Lys614 / H5	1831.83	2		1831.82678		-2.45656781	
S[682]QAVFDEIR[690]	Glu688 / H9	S[612]YKQSNGNMLC FAPDLVINEER[633]	Lys614 / H5	3630.73	3		3630.72128		-2.75427374	
S[682]QAVFDEIR[690]	Glu688 / H9	S[612]YKQSNGNMLC FAPDLVINEER[633]	Lys614 / H5	3646.73	3		3646.70528		-5.75862276	
S[682]QAVFDEIR[690]	Glu688 / H9	E[696]LGKAIVK[703]	Lys699 / H9	1903.06	11	2	1903.06413	1903.06472	-0.28240761	-0.00789802
S[682]QAVFDEIR[690]	Glu688 / H9	A[700]IVKR[704]	Lys703 / L9-10	1631.92	4		1631.9221		-0.40437143	
D[687]EIRMTY[693]	Glu688 / H9	K[765]AGSVKPL[772]	Lys765 / H12	1723.9	1		1723.90264		-1.21469737	
D[687]EIRMTY[693]	Glu688 / H9	K[765]AGSVKPL[772]	Lys770 / S4	1723.9		1		1723.90728		1.74023281
S[682]QAVFDEIR[690]	Glu688 / H9	A[766]GSVKPLLFHQK[777]	Lys770 / S4	2370.29		2		2370.28728		-2.53133945
S[682]QAVFDEIR[690]	Glu688 / H9	A[766]GSVKPLLFHQK[777]	Lys777 / C-t	2370.29	1		2370.29628		1.26566456	
E[705]GNSSQNWQR[714]	Glu705 / H9	Q[570]VVSAVKWAK[579]	Lys576 / H3	2302.17	2		2302.16954		0.45512975	
E[705]GNSSQNWQR[714]	Glu705 / H9	D[678]GLKSQAVFDEIR[690]	Lys681 / L8-9	2664.28		1		2664.27733		0.43307053
E[705]GNSSQNWQR[714]	Glu705 / H9	M[691]TYIKELGK[699]	Lys695 / H9	2269.1	9		2269.1015		-0.71892555	
E[705]GNSSQNWQR[714]	Glu705 / H9	M[691]TYIKELGK[699]	Lys695 / H9	2285.1	9	2	2285.09668	2285.09782	-0.57981458	-0.03817383
E[705]GNSSQNWQR[714]	Glu705 / H9	E[696]LGKAIVK[703]	Lys699 / H9	2044.06	1		2044.05828		0.48922284	
E[705]GNSSQNWQR[714]	Glu705 / H9	A[766]GSVKPLLFHQK[777]	Lys770 / S4	2511.29	16		2511.28502		-0.04776769	
L[722]DSMHEMVGGL[732]	Glu727 / H10-11	Q[717]LTKLL[722]	Lys720 / H10-11	1916.98	1		1916.98128		-0.5216535	
L[722]DSMHEMVGGL[732]	Glu727 / H10-11	Q[717]LTKLL[722]	Lys720 / H10-11	2030.07	1		2030.06528		-0.492595	
Q[717]LTKLLDSMHEM[728]	Glu727 / H10-11	T[719]KLL[722]	Lys720 / H10-11	1901.02	5		1900.98772		-18.802073	
Q[717]LTKLLDSMHEM[728]	Glu727 / H10-11	T[719]KLL[722]	Lys720 / H10-11	1917.02	5	2	1916.98137	1916.98124	-19.306 6265	-19.372 7039
Q[717]LTKLLDSMHEM[728]	Glu727 / H10-11	T[719]KLL[722]	Lys720 / H10-11	1933.01	5		1932.976		-19.292 3812	
Y[716]QLTKLLDSMHEM[728]	Glu727 / H10-11	T[719]KLL[722]	Lys720 / H10-11	2080.08	1		2080.04398		-18.136	

									9146	
Y^{716}QLTKLLDSMHEM^{728}	Glu727 / H10-11	Y^{716}QLTKL^{721}	Lys720 / H10-11	2355.21	5		2355.17114		-15.9482651	
D^{723}SMHEMVGGLL^{733}	Glu727 / H10-11	H^{775}QK^{777}	Lys777 / C-t	1613.74	1		1613.74016		-0.54110322	
S^{744}LSVEFPEMLAEIISNQLPK^{763}	Glu751 / H12	M^{691}TYIKELGK^{699}	Lys695 / H9	3340.74	2		3340.74336		0.36453942	
S^{744}LSVEFPEMLAEIISNQLPK^{763}	Glu755 / H12	M^{691}TYIKELGK^{699}	Lys695 / H9	3340.74	1		3340.74185		-0.00793237	

Table S5 legend. MS/MS verification of EDC-mediated crosslink between residues Glu688 and Lys699

The masses of generated a, b and y ions are indicated.

Peptide: α	SQAVFDEIR						Peptide: α	SQAVFDEIR		
Charge: +1							Charge: +1			
b	b-H2O	b-NH3	AA	y	y-H2O	y-NH3	a	a-H2O	a-NH3	AA
88.039	70.029	71.013	S				60.044	42.034	43.018	S
216.098	198.087	199.071	Q	1816.033	1798.022	1799.006	188.103	170.092	171.076	Q
287.135	269.124	270.108	A	1687.974	1669.964	1670.948	259.14	241.13	242.114	A
386.203	368.193	369.177	V	1616.937	1598.926	1599.91	358.208	340.198	341.182	V
533.272	515.26	516.245	F	1517.869	1499.858	1500.842	505.277	487.266	488.25	F
648.299	630.288	631.272	D	1370.8	1352.79	1353.774	620.304	602.293	603.277	D
1615.869	1597.858	1598.842	E	1255.773	1237.763	1238.747	1587.874	1569.864	1570.848	E
1728.953	1710.942	1711.927	I	288.203	270.192	271.176	1700.958	1682.948	1683.932	I
			R	175.119	157.108	158.092				R
Charge: +2							Charge: +2			
b	b-H2O	b-NH3	AA	y	y-H2O	y-NH3	a	a-H2O	a-NH3	AA
44.523	35.518	36.01	S				30.526	21.521	22.013	S
108.553	99.547	100.039	Q	908.52	899.515	900.007	94.555	85.55	86.042	Q
144.071	135.066	135.558	A	844.491	835.485	835.977	130.074	121.068	121.56	A
193.605	184.6	185.092	V	808.972	799.967	800.459	179.608	170.603	171.095	V
267.14	258.134	258.625	F	759.438	750.433	750.925	253.142	244.137	244.629	F
324.653	315.648	316.14	D	685.904	676.898	677.39	310.656	301.65	302.142	D
808.438	799.433	799.925	E	628.39	619.385	619.877	794.441	785.435	785.927	E
864.98	855.975	856.467	I	144.605	135.6	136.092	850.983	841.977	842.469	I
			R	88.063	79.058	79.55				R
Charge: +3							Charge: +3			
b	b-H2O	b-NH3	AA	y	y-H2O	y-NH3	a	a-H2O	a-NH3	AA
30.018	24.014	24.342	S				20.686	14.683	15.011	S
72.704	66.701	67.029	Q	606.016	600.012	600.34	63.373	57.369	57.697	Q
96.383	90.38	90.708	A	563.33	557.326	557.654	87.052	81.048	81.376	A
129.406	123.402	123.73	V	539.651	533.647	533.975	120.074	114.071	114.399	V

178.429	172.425	172.753	F	506.628	500.624	500.952	169.097	163.094	163.422	F
216.771	210.768	211.096	D	457.605	451.601	451.929	207.439	201.436	201.764	D
539.295	533.291	533.619	E	419.263	413.259	413.587	529.963	523.958	524.287	E
576.989	570.986	571.314	I	96.739	90.736	91.064	567.658	561.654	561.982	I
			R	59.045	53.041	53.369				R
Peptide: β	ELGKAIVK						Peptide: β	ELGKAIVK		
Charge: +1							Charge: +1			
b	b-H2O	b-NH3	AA	y	y-H2O	y-NH3	a	a-H2O	a-NH3	AA
130.05	112.039	113.023	E				102.055	84.044	85.028	E
243.134	225.123	226.107	L	1774.022	1756.012	1756.996	215.139	197.128	198.112	L
300.155	282.145	283.129	G	1660.938	1642.928	1643.912	272.16	254.15	255.134	G
1473.77	1455.759	1456.743	K	1603.917	1585.906	1586.89	1445.775	1427.764	1428.748	K
1544.807	1526.796	1527.78	A	430.302	412.292	413.276	1516.812	1498.801	1499.785	A
1657.891	1639.88	1640.864	I	359.265	341.255	342.239	1629.896	1611.885	1612.869	I
1756.959	1738.949	1739.933	V	246.181	228.171	229.155	1728.964	1710.954	1711.938	V
			K	147.113	129.102	130.086				K
Charge: +2							Charge: +2			
b	b-H2O	b-NH3	AA	y	y-H2O	y-NH3	a	a-H2O	a-NH3	AA
65.529	56.523	57.015	E				51.531	42.526	43.018	E
122.071	113.065	113.557	L	887.515	878.509	879.001	108.073	99.068	99.56	L
150.581	141.576	142.068	G	830.973	821.967	822.459	136.584	127.579	128.071	G
737.388	728.383	728.875	K	802.462	793.457	793.949	723.391	714.386	714.878	K
772.907	763.902	764.394	A	215.655	206.65	207.142	758.91	749.904	750.396	A
829.449	820.444	820.936	I	180.136	171.131	171.623	815.452	806.446	806.938	I
878.983	869.978	870.47	V	123.594	114.589	115.081	864.986	855.981	856.473	V
			K	74.06	65.055	65.547				K
Charge: +3							Charge: +3			
b	b-H2O	b-NH3	AA	y	y-H2O	y-NH3	a	a-H2O	a-NH3	AA
44.021	38.018	38.346	E				34.69	28.686	29.014	E
81.716	75.713	76.041	L	592.012	586.009	586.337	72.385	66.381	66.709	L
100.723	94.72	95.048	G	554.318	548.314	548.642	91.392	85.388	85.716	G
491.928	485.925	486.253	K	535.31	529.307	529.635	482.596	476.593	476.921	K
515.607	509.604	509.932	A	144.106	138.102	138.43	506.275	500.272	500.6	A
553.302	547.298	547.626	I	120.427	114.423	114.751	543.97	537.967	538.295	I

586.325	580.321	580.649	V	82.732	76.728	77.056	576.993	570.989	571.317	V
										K

Table S6 legend. Summary of DSBU-crosslinked peptides of ancGR2-LBD identified by mass spectrometry.

Site A	Site B	Seq A	Start A	Stop A	Seq B	Start B	Stop B	Intra-molecular Distance*
Y-545	K-579	PEVLYSGYDSTLPDTSTR	541	558	LGGRQVVSAVKWAKALPGFR	566	585	26,6 Å
	Y-738	PEVLYSGYDSTLPDTSTR	541	558	MVGGLLQFCFYTFVNKSLSVE	728	748	33,9 Å
S-546	K-579	PEVLYSGYDSTLPDTSTR	541	558	LGGRQVVSAVKWAKALPGFR	566	585	25,1 Å
K-576	K-579	QVVSAVKWAK	570	579	WAKALPGFR	577	585	11,5 Å
	K-695	QVVSAVKWAK	570	579	MTYIKELGK	691	699	30,3 Å
K-579	K-614	WAKALPGFR	577	585	SYKQSNGNMLCFAPDLVINEER	612	633	30,9 Å
	K-677	WAKALPGFR	577	585	VLLLLSTVPKDGLK	668	681	30,8 Å
	K-681	WAKALPGFR	577	585	DGLKSQAVFDEIR	678	690	18,9 Å
	K-695	WAKALPGFR	577	585	MTYIKELGK	691	699	26,3 Å
	K-703	WAKALPGFR	577	585	AIVKR	700	704	29,2 Å
	K-770	WAKALPGFR	577	585	AGSVKPLLFHQK	766	777	27,2 Å
	K-777	WAKALPGFR	577	585	PLLFHQK	771	777	36,6 Å
K-614	K-703	SYKQSNGNMLCFAPDLVINEER	612	633	AIVKR	700	704	10,5 Å
S-659	K-667	LQVSYDEYLCMKVLLLLSTVPK	656	677	LQVSYDEYLCMKVLLLLSTVPK	656	677	13,0 Å
K-677	K-695	VLLLLSTVPKDGLK	668	681	MTYIKELGK	691	699	31,1 Å
	K-765	VLLLLSTVPKDGLK	668	681	FKAGSVK	764	770	18,4 Å
					FKAGSVKPLLFHQK	764	777	18,4 Å
	K-770	VLLLLSTVPKD	668	678	AGSVKPLLFHQK	766	777	8,9 Å
		VLLLLSTVPKDGLK	668	681	AGSVKPLLFHQK	766	777	8,9 Å
	K-777	VLLLLSTVPKD	668	678	PLLFHQK	771	777	12,4 Å
		VLLLLSTVPKDGLK	668	681	AGSVKPLLFHQK	766	777	12,4 Å
					PLLFHQK	771	777	12,4 Å
K-681	K-763	DGLKSQAVFDEIR	678	690	SLSVEFPEMLAEIISNQLPKFK	744	765	10,7 Å
K-695	K-695	MTYIKELGK	691	699	MTYIKELGK	691	699	0 Å
	K-699	MTYIKELGK	691	699	ELGKAIVK	696	703	5,4 Å
	S-708	MTYIKELGK	691	699	EGNSSQNWQR	705	714	17,9 Å
	S-709	MTYIKELGK	691	699	EGNSSQNWQR	705	714	18,6 Å
	T-719	MTYIKELGK	691	699	FYQLTK	715	720	15,8 Å
	K-765	MTYIKELGK	691	699	FKAGSVK	764	770	39,3 Å
					FKAGSVKPLLFHQK	764	777	39,3 Å
	K-770	MTYIKELGK	691	699	AGSVKPLLFHQK	766	777	22,9 Å

	K-777	MTYIKELGK	691	699	AGSVKPLLFHQK	766	777	25,2 Å
					PLLFHQK	771	777	25,2 Å
K-699	K-765	ELGKAIVK	696	703	FKAGSVK	764	770	40,7 Å
	K-770	ELGKAIVK	696	703	AGSVKPLLFHQK	766	777	26,4 Å
	K-777	ELGKAIVK	696	703	PLLFHQK	771	777	29,8 Å
K-703	K-765	AIVKR	700	704	FKAGSVK	764	770	37,9 Å
	K-770	AIVKR	700	704	AGSVKPLLFHQK	766	777	29,8 Å
	K-777	AIVKR	700	704	AGSVKPLLFHQK	766	777	29,4 Å
					PLLFHQK	771	777	29,4 Å
S-709	K-777	EGNSSQNWQR	705	714	PLLFHQK	771	777	28,4 Å
T-719	K-777	FYQLTK	715	720	PLLFHQK	771	777	15,8 Å
K-720	K-777	FYQLTKLLD	715	723	PLLFHQK	771	777	11,0 Å
S-744	K-770	SLSVEFPEMLAEIISNQLPK	744	763	AGSVKPLLFHQK	766	777	40,6 Å
K-765	K-765	FKAGSVK	764	770	FKAGSVK	764	770	0 Å
	K-770	FKAGSVK	764	770	AGSVKPLLFHQK	766	777	20,8 Å
K-777	K-777	PLLFHQK	771	777	PLLFHQK	771	777	0 Å

Table S7 legend. MS/MS verification of disulfide bridge formation between Cys545 residues from two GR-LBD(Y545C) monomers.

The masses of generated a, b and y ions are given.

Peptide: β	VLCSGYDSTLPDTSTR						Peptide: β	VLCSGYDSTLPDTSTR		
Peptide: α	VLCSGYDSTLPDTSTR						Peptide: α	VLCSGYDSTLPDTSTR		
Charge: +1							Charge: +1			
b	b-H2O	b-NH3	AA	y	y-H2O	y-NH3	a	a-H2O	a-NH3	AA
100.076	82.065	83.049	V				72.081	54.07	55.054	V
213.16	195.149	196.133	L	3327.499	3309.489	3310.473	185.165	167.154	168.138	L
2027.941	2009.931	2010.915	C	3214.415	3196.405	3197.389	1999.946	1981.936	1982.92	C
2114.973	2096.963	2097.947	S	1399.634	1381.623	1382.607	2086.978	2068.968	2069.952	S
2171.995	2153.984	2154.968	G	1312.602	1294.591	1295.575	2144	2125.989	2126.973	G
2335.058	2317.048	2318.032	Y	1255.58	1237.57	1238.554	2307.063	2289.053	2290.037	Y
2450.085	2432.074	2433.058	D	1092.517	1074.506	1075.49	2422.09	2404.08	2405.064	D
2537.117	2519.106	2520.09	S	977.49	959.479	960.463	2509.122	2491.112	2492.096	S
2638.165	2620.154	2621.138	T	890.458	872.447	873.431	2610.17	2592.159	2593.143	T
2751.249	2733.238	2734.222	L	789.41	771.4	772.384	2723.254	2705.243	2706.227	L
2848.302	2830.291	2831.275	P	676.326	658.315	659.299	2820.307	2802.296	2803.28	P
2963.328	2945.318	2946.302	D	579.273	561.263	562.247	2935.334	2917.323	2918.307	D
3064.376	3046.366	3047.35	T	464.246	446.236	447.22	3036.381	3018.371	3019.355	T
3151.408	3133.398	3134.382	S	363.199	345.188	346.172	3123.413	3105.403	3106.387	S
3252.456	3234.445	3235.429	T	276.167	258.156	259.14	3224.461	3206.45	3207.434	T
			R	175.119	157.108	158.092				R
Charge: +2							Charge: +2			
b	b-H2O	b-NH3	AA	y	y-H2O	y-NH3	a	a-H2O	a-NH3	AA
50.541	41.536	42.028	V				36.544	27.539	28.031	V
107.084	98.078	98.57	L	1664.253	1655.248	1655.74	93.086	84.081	84.573	L
1014.474	1005.469	1005.961	C	1607.711	1598.706	1599.198	1000.477	991.472	991.964	C
1057.99	1048.985	1049.477	S	700.32	691.315	691.807	1043.993	1034.988	1035.48	S
1086.501	1077.496	1077.988	G	656.804	647.799	648.291	1072.504	1063.498	1063.99	

1168.033	1159.027	1159.519	Y	628.294	619.288	619.78	1154.035	1145.03	1145.522	
1225.546	1216.541	1217.033	D	546.762	537.757	538.249	1211.549	1202.543	1203.035	
1269.062	1260.057	1260.549	S	489.249	480.243	480.735	1255.065	1246.059	1246.551	
1319.586	1310.581	1311.073	T	445.733	436.727	437.219	1305.589	1296.583	1297.075	
1376.128	1367.123	1367.615	L	395.209	386.203	386.695	1362.131	1353.125	1353.617	
1424.654	1415.649	1416.141	P	338.667	329.661	330.153	1410.657	1401.652	1402.144	
1482.168	1473.163	1473.655	D	290.14	281.135	281.627	1468.17	1459.165	1459.657	
1532.692	1523.686	1524.178	T	232.627	223.622	224.114	1518.694	1509.689	1510.181	
1576.208	1567.202	1567.694	S	182.103	173.098	173.59	1562.21	1553.205	1553.697	
1626.732	1617.726	1618.218	T	138.587	129.582	130.074	1612.734	1603.729	1604.221	
			R	88.063	79.058	79.55				
Charge: +3							Charge: +3			
b	b-H2O	b-NH3	AA	y	y-H2O	y-NH3	a	a-H2O	a-NH3	
34.03	28.027	28.355	V				24.698	18.695	19.023	
71.725	65.721	66.049	L	1109.838	1103.834	1104.162	62.393	56.39	56.718	
676.652	670.648	670.976	C	1072.143	1066.14	1066.468	667.32	661.317	661.645	
705.663	699.659	699.987	S	467.216	461.213	461.541	696.331	690.327	690.655	
724.67	718.666	718.994	G	438.205	432.202	432.53	715.338	709.335	709.663	
779.024	773.021	773.349	Y	419.198	413.195	413.523	769.693	763.689	764.017	
817.367	811.363	811.691	D	364.844	358.84	359.168	808.035	802.031	802.359	
846.377	840.374	840.702	S	326.501	320.498	320.826	837.046	831.042	831.37	
880.06	874.056	874.384	T	297.491	291.487	291.815	870.728	864.725	865.053	
917.754	911.751	912.079	L	263.808	257.805	258.133	908.423	902.419	902.747	
950.105	944.102	944.43	P	226.114	220.11	220.438	940.774	934.77	935.098	
988.448	982.444	982.772	D	193.763	187.759	188.087	979.116	973.113	973.441	
1022.13	1016.127	1016.455	T	155.42	149.417	149.745	1012.799	1006.795	1007.123	
1051.141	1045.137	1045.465	S	121.738	115.734	116.062	1041.809	1035.806	1036.134	
1084.823	1078.82	1079.148	T	92.727	86.724	87.052	1075.492	1069.488	1069.816	

Supplementary S8. Differentially expressed genes after hormone treatment between WT GR and mutants Y545A, Y545A/Dim, D641V and D641V/Tetra

	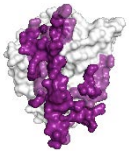	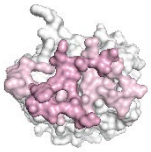		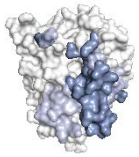
X-ray crystallography	1M2Z, 1P93, 3BQD, 3CLD, 3E7C, 3GN8 3K22, 3K23, 3RY9, 4E2J, 4P6W, 4P6X, 5UC3, 5UFS, 6NWL, 7YXC, 7YXD, 7YXN, 7YXO, 7YXP	1M2Z, 1P93, 3RY9, 3BQD, 3CLD, 3E7C, 3GN8, 3K22, 3MNE, 3MNO, 3MNP, 4E2J, 4P6W, 4P6X, 6NWL, 7YXD, 7YXN, 7YXO	3BQD, 3GN8, 3K23 3MNE, 3MNO, 3MNP, 5UC1, 5UC3, 7YXO, 7YXP	1NHZ, 3GN8, 3H52 3RY9, 4E2J, 4LSJ, 4MMD, 4P6X, 7YXD, 7YXN
Docking simulations	ODA	ODA/NIP	ODA/NIP	ODA
Cross-linking/MS	EDC/DSBU	EDC/DSBU	-	EDC/DSBU
N&B / RNAseq	Y545A	-	-	P637A / D641V
Literature	I634A (23, 24)	-	-	-

Supplementary Table 9. Summary of experimental and bioinformatic support for each of the four intermonomer interfaces of GR-LBD.

3.3. γ-Linolenic acid in maternal milk drives cardiac metabolic maturation

Ana Paredes, Raquel Justo-Méndez, Daniel Jiménez-Blasco, Vanessa Núñez, Irene Calero, María Villalba-Orero, **Andrea Alegre-Martí**, Thierry Fischer, Ana Gradillas, Viviane Aparecida Rodrigues Sant'Anna, Felipe Were, Zhiqiang Huang, Pablo Hernansanz-Agustín, Carmen Contreras, Fernando Martínez, Emilio Camafeita, Jesús Vázquez, Jesús Ruiz-Cabello, Estela Area-Gómez, Fátima Sánchez-Cabo, Eckardt Treuter, Juan Pedro Bolaños, Eva Estébanez-Perpiñá, Francisco Javier Rupérez, Coral Barbas, José Antonio Enríquez, and Mercedes Ricote.

Published in: Nature, 2023
Impact factor: 69.504
Quartile: Q1
DOI: 10.1038/s41586-023-06068-7

For this publication I conducted protein expression and purification assays of the retinoic X receptor LBD (RXR-LBD). I performed and interpreted surface plasmon resonance experiments to contribute to the validation of γ-linolenic acid (GLA) as an endogenous ligand of RXR. The results showed that GLA binds to RXR-LBD with micromolar affinity and further induced the RXR-LBD binding to a steroid receptor coactivator-derived peptide (SRC2-3), which was unable to bind to in the absence of GLA. This result, in combination with other experimental data, indicates that in the presence of GLA, the AF-2 coactivator-binding surface had acquired the active conformation capable of recruiting coactivators. I designed panels A to C of Figure 5 to illustrate the results of these experiments.

Article

γ-Linolenic acid in maternal milk drives cardiac metabolic maturation

https://doi.org/10.1038/s41586-023-06068-7

Received: 3 January 2022

Accepted: 11 April 2023

Published online: 24 May 2023

Check for updates

Ana Paredes[1], Raquel Justo-Méndez[1], Daniel Jiménez-Blasco[2,3,4], Vanessa Núñez[1], Irene Calero[1], María Villalba-Orero[1,5], Andrea Alegre-Martí[6], Thierry Fischer[7], Ana Gradillas[8], Viviane Aparecida Rodrigues Sant'Anna[8], Felipe Were[9], Zhiqiang Huang[10], Pablo Hernansanz-Agustín[1], Carmen Contreras[1], Fernando Martínez[9,11], Emilio Camafeita[11,12], Jesús Vázquez[11,12], Jesús Ruiz-Cabello[13,14,15,16], Estela Area-Gómez[17,18], Fátima Sánchez-Cabo[9], Eckardt Treuter[10], Juan Pedro Bolaños[2,3,4], Eva Estébanez-Perpiñá[6], Francisco Javier Rupérez[8], Coral Barbas[8], José Antonio Enríquez[1,4] & Mercedes Ricote[1]✉

Birth presents a metabolic challenge to cardiomyocytes as they reshape fuel preference from glucose to fatty acids for postnatal energy production[1,2]. This adaptation is triggered in part by post-partum environmental changes[3], but the molecules orchestrating cardiomyocyte maturation remain unknown. Here we show that this transition is coordinated by maternally supplied γ-linolenic acid (GLA), an 18:3 omega-6 fatty acid enriched in the maternal milk. GLA binds and activates retinoid X receptors[4] (RXRs), ligand-regulated transcription factors that are expressed in cardiomyocytes from embryonic stages. Multifaceted genome-wide analysis revealed that the lack of RXR in embryonic cardiomyocytes caused an aberrant chromatin landscape that prevented the induction of an RXR-dependent gene expression signature controlling mitochondrial fatty acid homeostasis. The ensuing defective metabolic transition featured blunted mitochondrial lipid-derived energy production and enhanced glucose consumption, leading to perinatal cardiac dysfunction and death. Finally, GLA supplementation induced RXR-dependent expression of the mitochondrial fatty acid homeostasis signature in cardiomyocytes, both in vitro and in vivo. Thus, our study identifies the GLA–RXR axis as a key transcriptional regulatory mechanism underlying the maternal control of perinatal cardiac metabolism.

The mammalian heart requires a continuous supply of energy to maintain cardiac contraction. The highly flexible metabolism of cardiomyocytes enables them to meet their ATP needs by consuming a broad spectrum of substrates including glucose, lipids, lactate, amino acids and ketone bodies, depending on physiological context and age[5]. Fetal cardiomyocytes rely primarily on glucose and lactate oxidation, but the main ATP source after birth is mitochondrial lipid oxidation[1,2,5,6]. However, although the importance of mitochondria in the adult heart is well-established, their contribution to fetal and perinatal heart function has been less explored. The cardiac fetal-to-neonatal switch is believed to occur progressively during the first two weeks of life, culminating in a functional mitochondrial compartment in which fatty acids are efficiently oxidized by β-oxidation[7] (FAO). This adaptive step is crucial for the maintenance of heartbeat and survival, yet very little is known about the molecular mechanisms and upstream signals that instruct this metabolic transition.

RXRs are a nuclear receptor subfamily of ligand-regulated transcription factors that specifically respond to 9-*cis*-retinoic acid and various endogenous fatty acids[8]. Because RXRs operate as both permissive homo- and heterodimers, their ability to be activated by dietary compounds defines them as molecular master sensors that transduce external cues into transcriptional programmes[4]. RXR subtypes are encoded by three genes (in mouse they are *Rxra* (also known as *Nr2b1*), *Rxrb* (*Nr2b2*) and *Rxrg* (*Nr2b3*)), which exhibit time-specific and tissue-dependent differential expression. Whole-body knockout mice lacking RXRα show impaired myocardial growth and die between embryonic day (E)13.5 and E16.5[9,10]. However, specific RXRα depletion in ventricular cardiomyocytes does not result in cardiac

[1]Cardiovascular Regeneration Program, Centro Nacional de Investigaciones Cardiovasculares (CNIC), Madrid, Spain. [2]Institute of Functional Biology and Genomics (IBFG), University of Salamanca, CSIC, Salamanca, Spain. [3]Institute for Biomedical Research of Salamanca (IBSAL), Salamanca, Spain. [4]CIBER de Fragilidad y Envejecimiento Saludable (CIBERFES), Madrid, Spain. [5]Departamento de Medicina y Cirugía Animal, Universidad Complutense de Madrid (UCM), Madrid, Spain. [6]Department of Biochemistry and Molecular Biomedicine, Institute of Biomedicine (IBUB) of the University of Barcelona (UB), Barcelona, Spain. [7]Department of Immunology and Oncology, Centro Nacional de Biotecnología-Consejo Superior de Investigaciones Científicas (CNB/CSIC), Campus Universidad Autónoma de Madrid (UAM), Madrid, Spain. [8]Centro de Metabolómica y Bioanálisis (CEMBIO), Facultad de Farmacia, Universidad San Pablo-CEU, CEU Universities, Madrid, Spain. [9]Bioinformatics Unit, Centro Nacional de Investigaciones Cardiovasculares (CNIC), Madrid, Spain. [10]Department of Biosciences and Nutrition, Karolinska Institutet, Huddinge, Sweden. [11]CIBER de Enfermedades Cardiovasculares (CIBERCV), Madrid, Spain. [12]Proteomics Unit, Centro Nacional de Investigaciones Cardiovasculares (CNIC), Madrid, Spain. [13]CIC biomaGUNE, Basque Research and Technology Alliance (BRTA), San Sebastian, Spain. [14]Ikerbasque, Basque Foundation for Science, Bilbao, Spain. [15]CIBER de Enfermedades Respiratorias (CIBERES), Madrid, Spain. [16]Departamento de Ciencias Farmacéuticas, Facultad de Farmacia, Universidad Complutense Madrid (UCM), Madrid, Spain. [17]Departament of Cellular and Molecular Biology, Centro de Investigaciones Biológicas Margarita Salas-CSIC, Madrid, Spain. [18]Department of Neurology, Columbia University Medical Campus, New York, NY, USA. ✉e-mail: mricote@cnic.es

morphological defects, thus excluding a cell-autonomous role of RXRα expressed in cardiomyocytes[11]. We and others have reported that RXR subtypes show redundancy in several contexts[9,12,13]; however, previous studies have not addressed RXR redundancy in the heart, and the physiological role of RXRs in cardiomyocyte homeostasis remains unknown.

RXR deletion causes lethal cardiac dysfunction

Analysis of RXR subtypes in embryonic and adult hearts revealed progressive increases in *Rxra* and *Rxrb* expression from developmental stages to adulthood, whereas *Rxrg* expression was restricted to postnatal cardiomyocytes (Extended Data Fig. 1a). To dissect RXR function in cardiomyocytes during development, we generated an RXR loss-of-function mouse model by crossing *Nkx2.5-cre* mice, in which the embryonic myocardium is specifically targeted[14], with *Rxra* and *Rxrb* floxed mice[12] (*Rxra*$^{f/f}$*Rxrb*$^{f/f}$). This approach enabled us to avoid compensatory effects between RXR subtypes during cardiac development.

Rxra and *Rxrb* were efficiently deleted in the hearts of embryonic double-knockout (*Nkx2.5-cre*$^{+/-}$*Rxra*$^{f/f}$*Rxrb*$^{f/f}$ (hereafter EDKO)) mice from E11.5 onwards (Extended Data Fig. 1b). Although EDKO newborns were born at Mendelian frequency (data not shown), 80% of EDKO pups died during the first 24 h of life, and no EDKO newborn survived beyond day 7 after birth (Fig. 1a). Extensive echocardiography assessment revealed that EDKO mice progressively underwent severe contractile dysfunction, as shown by gradually decreased ejection fraction (LVEF) within the first 24 h (Fig. 1b, Extended Data Fig. 1c and Supplementary Videos 1 and 2). This change was accompanied by pathological alterations in stroke volume, cardiac output and left ventricle end systolic volume over time. Despite these alterations, the left ventricle diastolic dimension did not change, presumably owing to the rapid onset of death (Extended Data Fig. 1c). The cardiac impairment preceded morbidity of the newborns, suggesting that these heart abnormalities probably contributed to neonatal death. In line with this, EDKO hearts also showed increased expression of the cardiac stress markers *Anf* and *Bnp* (Fig. 1c). These results demonstrate that RXRs expressed in cardiomyocytes exert a cell-autonomous function in the myocardium.

Histological analysis of EDKO hearts revealed no morphological myocardial abnormalities preceeding the cardiac malfunction (Extended Data Fig. 1d–f). Myocardial thickness and the ratio of non-compacted to compacted myocardium were normal (Extended Data Fig. 1d). EDKO pups were slightly smaller than controls but showed no evidence of cardiac hypertrophy or differences in cardiac diameter (Extended Data Fig. 1f,g).

Electrocardiogram (ECG) analysis of postnatal day (P)0 newborns revealed typical ECG traces, with no differences from controls in QRS complex duration or PR, QTc and P intervals (Extended Data Fig. 1h), thus ruling out a contribution to the functional defects from altered rhythmic patterns. We also ruled out leaky expression of the *Nkx2.5-Cre* driver in the brain, liver, stomach, thymus, diaphragm and spleen (Extended Data Fig. 1i). Although subtle gene deletion was observed in the tongue, as previously reported[15], EDKO mice displayed visible milk spots but to a lesser extent than in control pups (Extended Data Fig. 1j), probably owing to a competing disadvantage against wild-type littermates. Further analysis excluded functional irregularities of the lungs (Extended Data Fig. 1k–m) or alternative systemic alterations such as thermogenesis (Extended Data Fig. 1n). These data thus reveal the existence of a physiological mechanism through which RXRs expressed in cardiomyocytes sustain cardiac function and neonatal survival.

RXR drives the switch to neonatal metabolism

Gene expression profiling of P0 hearts (Fig. 1d–f) identified 145 significantly upregulated genes (adjusted P value ≤ 0.05, fold change ≥ 1.5) and 192 significantly downregulated genes (adjusted P value ≤ 0.05, fold change ≤ −1.5) in the EDKO model. Gene ontology analysis highlighted strong downregulation of essential lipid homeostasis-related processes, such as FAO, cholesterol biosynthesis and the L-carnitine mitochondrial shuttle (Fig. 1d). Dysregulated lipid metabolism was further evidenced by transcriptional dampening of the fatty acid homeostasis signature in EDKO hearts (Fig. 1e). Notably, 26.05% of the downregulated genes (50 out of 192) encode mitochondrial proteins related to lipid-derived energy production (Fig. 1f). We called this gene subset the mitochondrial fatty acid homeostasis (mtFAH) cluster. Quantitative PCR with reverse transcription (RT–qPCR) analysis of the mtFAH gene expression signature at gestational and perinatal stages revealed a sharp induction of mtFAH genes from E18.5 to P0 in control hearts. By contrast, mtFAH cluster expression was curtailed in EDKO mice at P0, coinciding with the time of death (Fig. 1g). Prominent cardiomyocyte-intrinsic RXR-controlled genes detected in this analysis included those encoding critical components of lipid droplet homeostasis (*Plin5*), fatty acid activation (*Acsl1* and *Acot1*), fatty acid import to the mitochondrial matrix (*Cpt1a*, *Cpt1b*, *Cpt2* and *Slc25a20*), β-oxidation (*Acadvl*, *Hadha* and *Hadhb*), glucose and fatty acid catabolism balance (*Pdk4* and *Fbp2*), lipid-derived energy dissipation (*Ucp3*), ketogenesis (*Hmgcs2*) and lipogenesis (*Scd4* and *Dgat2*) (Extended Data Fig. 2a). This finding challenges the view that cardiomyocytes acquire the capacity for ATP generation from mitochondrial FAO progressively over the first 15 days of life[5], suggesting instead that cardiomyocytes require mitochondria equipped with the FAO machinery immediately after birth.

To investigate the mechanisms through which transcriptional dysregulation in the EDKO heart might lead to defective lipid-derived energy generation in perinatal cardiomyocytes, we measured ATP production by cardiac P0 mitochondria fed with pyruvate, glutamate, succinate or palmitate (Fig. 2a). No significant differences in ATP production were detected between the genotypes when the substrate was pyruvate, glutamate or succinate, indicating that entry to the electron transport chain by NADH (pyruvate and glutamate) and $FADH_2$ (succinate) was not significantly altered in EDKO mitochondria. By contrast, ATP generation by β-oxidation from palmitate was significantly reduced in EDKO mitochondria. EDKO hearts also showed a significantly decreased rate of palmitate oxidation (Fig. 2b) and decreased fatty acid mitochondrial respiration (Fig. 2c), overall indicating impaired fatty acid import or use. In agreement with these results, an unbiased lipidomics approach highlighted that the depletion of RXRs resulted in significantly lower levels of typical metabolites of FAO such as long-chain acyl-carnitines[16,17] (C14 to C18), and fatty acid esters of hydroxy fatty acids (FAHFAs) (Fig. 2d and Supplementary Table 1). Proteomics analysis of EDKO hearts further confirmed that RXR deletion reduced the abundance of proteins involved in lipid handling (Fig. 2e). Moreover, the hearts of EDKO mice showed altered expression of several proteins related to mitochondrial dynamics and homeostatic pathways, such as reactive oxygen species production, the degradome and the mitochondrial unfolded protein response (Extended Data Fig. 2b). These findings suggest that cardiomyocyte-specific RXR deletion blunts cardiac mitochondrial remodelling towards lipid consumption and synthesis.

This effect was not linked to any alterations to the morphology (Extended Data Fig. 2c,d) or number (Extended Data Fig. 2e) of EDKO mitochondria. Defective lipid-derived ATP production in the absence of RXR suggested that EDKO hearts might commit their metabolism towards anaerobic glucose use. Significantly increased activity of glycolytic flux and lactate production was confirmed by ex vivo quantification (Fig. 2f,g). In parallel, EDKO mice displayed hypoglycaemia and hyperlactaemia (Fig. 2h,i), supporting the idea that RXRs are needed to initiate the fetal-to-neonatal transition. Hence, in their absence, cardiomyocytes remain metabolically immature and unable to establish bioenergetic fitness.

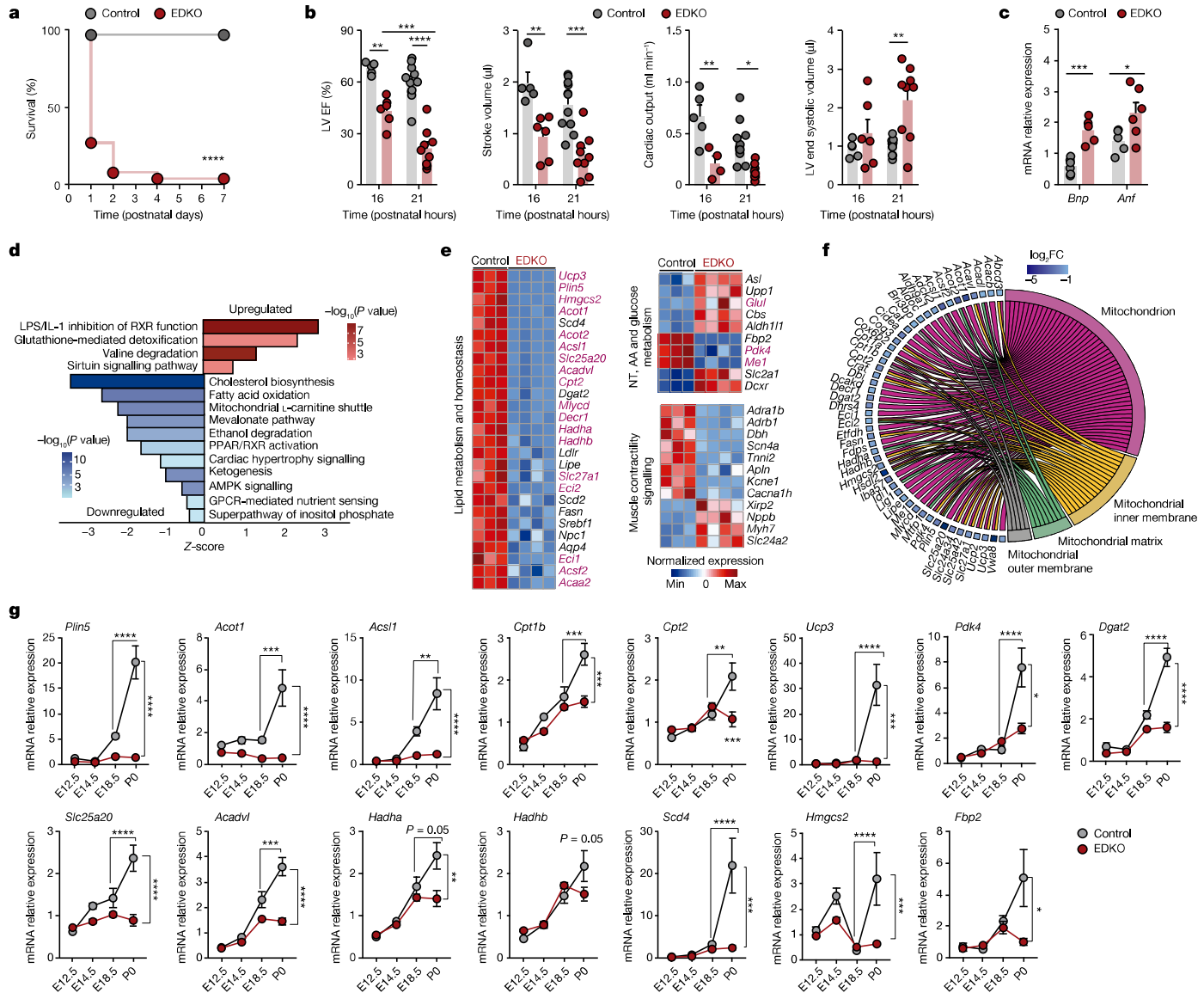

Fig. 1 | EDKO mice undergo lethal cardiac dysfunction and transcriptional alteration of lipid metabolism. a, Kaplan–Meier curves for EDKO and control mice ($n = 27–32$ mice per genotype). Log-rank test ($P < 0.0001$). **b**, Echocardiographic acquisition of EDKO ($n = 6–9$ mice per time point) and control ($n = 5–11$ mice per stage) mice (16 h and 21 h after birth). LVEF, stroke volume, cardiac output and left ventricle (LV) end-systolic volume are shown. Data are mean ± s.e.m. Two-way ANOVA with Tukey post-test. **c**, RT–qPCR quantification of *Bnp* and *Anf* genes in P0 EDKO ($n = 5–6$ mice) and control ($n = 5–6$ mice) hearts. Independent biological replicates. Data are mean ± s.e.m. Two-tailed Student's *t*-test. **d**, Ingenuity pathway analysis biological processes that are changed in P0 EDKO hearts. GPCR, G-protein-coupled receptor; LPS, lipopolysaccharide. **e**, Heat map of normalized RNA-seq expression data for the top differentially expressed genes (DEGs) ($n = 3–4$ mice per genotype, independent biological replicates). Genes are clustered according to biological processes, with genes encoding mitochondrial proteins shaded red. AA, amino acid; NT, nucleotide. **f**, Chord diagram representing cellular component analysis of downregulated mitochondrial protein-encoding genes in EDKO P0 hearts. Shading of squares adjacent to gene symbols indicates the $\log_2$fold change (FC) for EDKO versus control. **g**, Relative quantification by RT–qPCR of FAO gene expression in developmental (E12.5, E14.5 and E18.5) and perinatal (P0) stages of hearts from EDKO ($n = 3–6$) and control ($n = 4–6$) mice. Data are mean ± s.e.m. Two-way ANOVA. Independent biological replicates. $^*P < 0.05$, $^{**}P < 0.01$, $^{***}P < 0.001$, $^{****}P < 0.0001$; NS, not significant. Exact *P* values are provided in Source Data.

Metabolomics profiling of the metabolic status of EDKO hearts using gas chromatography with mass spectrometry revealed a significant decrease in glycerol relative to controls, whereas the amounts of uracil, creatinine and aspartate were increased (Extended Data Fig. 2f). Uracil abundance correlated with the relative mRNA expression of *Upp1*, which encodes the uracil biosynthetic uridine phosphorylase (Extended Data Fig. 2g). The generation of creatinine through the non-enzymatic cyclization of creatine is favoured at low pH[18], and the rise in creatinine could be due to a more acidic cellular environment resulting from the increased lactate production in EDKO hearts. In the case of aspartate, enhanced glucose oxidation is known to promote its biosynthesis in failing cardiomyocytes[19]. Aspartate is also intimately linked to α-ketoglutarate, as both are end-products of glutamate and oxaloacetate transamination[20]. These findings prompted us to explore whether amino acids might contribute to energy homeostasis in EDKO hearts by replenishing Krebs cycle intermediates. Although the amino acid oxidation rate was unaltered (Extended Data Fig. 2h), α-ketoglutarate levels were higher in EDKO hearts (Extended Data Fig. 2i), suggesting that they exhibit imbalanced Krebs cycle activity. These results suggest that RXRs expressed in cardiomyocytes are critical integrators of energy production and mitochondrial maturation immediately after birth.

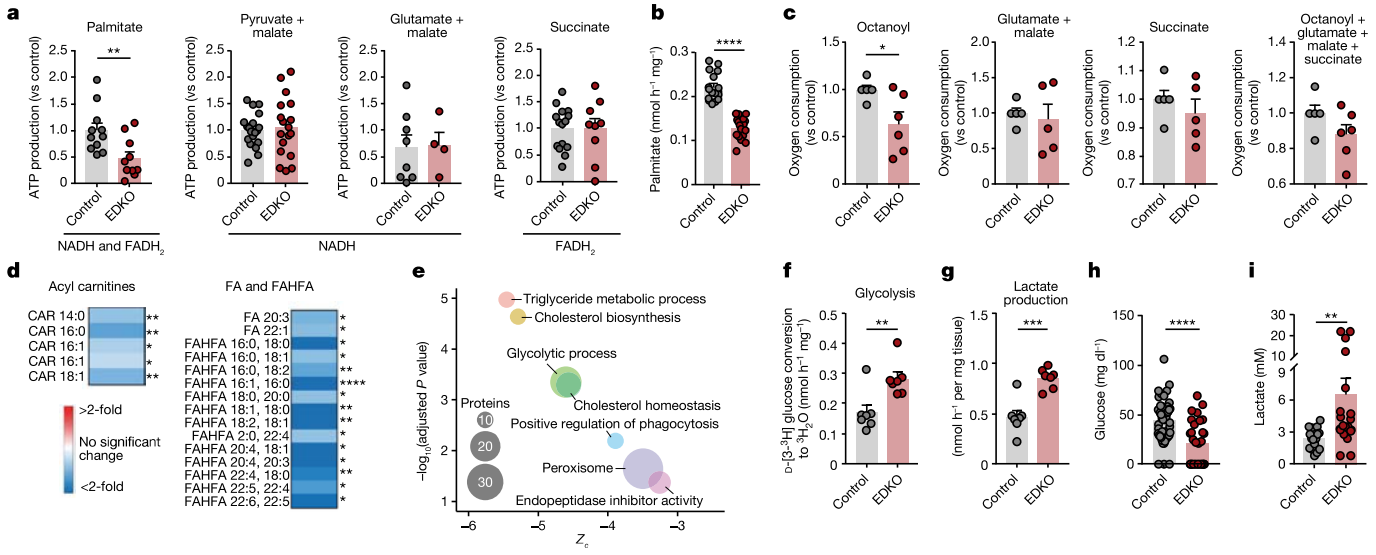

Fig. 2 | Lack of RXR in perinatal cardiomyocytes blocks fetal-to-neonatal metabolic switch. a, Ex vivo ATP production assay in control ($n = 8$–19) and EDKO ($n = 4$–18) P0 cardiac mitochondria supplied with pyruvate (pyruvate + malate), glutamate (glutamate + malate), succinate or palmitate (palmitate + carnitine). In the case of pyruvate or glutamate, malate was added to reach detectable amounts of complex I-dependent ATP synthesis. Individual biological replicates. Data are mean ± s.e.m. Two-tailed Student's *t*-test. Data are normalized as the change versus the change in the control. **b**, Ex vivo β-oxidation flux in control ($n = 17$) and EDKO ($n = 18$) P0 hearts. Individual biological replicates. Data are mean ± s.e.m. Two-tailed Student's *t*-test. **c**, Ex vivo oxygen consumption assay in control ($n = 5$) and EDKO ($n = 5$–6) P0 cardiac mitochondria supplied with octanoyl-carnitine (fatty acid oxidation), glutamate plus malate, succinate and a combination of all substrates. Individual biological replicates. Data are mean ± s.e.m., normalized to the control. Two-tailed Student's *t*-test. **d**, Unbiased lipidomics analysis in control ($n = 4$) and EDKO ($n = 4$) P0 hearts. Acyl-carnitines (CAR), fatty acids (FA) and fatty acid esters of hydroxyl fatty acid (FAHFA) are shown. Data are presented as fold change (EDKO versus control). Independent biological replicates. Two-tailed Student's *t*-test. **e**, Protein function enrichment plot for hearts from P0 EDKO mice ($n = 5$) versus P0 controls ($n = 5$). Independent biological replicates. Dot size indicates the number of proteins in each term. The *x*-axis shows Zc, the standardized variable at the functional category level (EDKO versus control), and the *y*-axis indicates $-\log_{10}$FDRc, the false discovery rate indicating which values stand out as outliers at the functional category level (EDKO versus control). **f**,**g**, Ex vivo glycolytic flux (**f**) and lactate generation (**g**) in control ($n = 7$) and EDKO ($n = 7$) P0 hearts. Independent biological replicates. Data are mean ± s.e.m. Two-tailed Student's *t*-test. **h**, Blood glucose in control ($n = 48$) and EDKO ($n = 30$) (P0) newborn mice. Individual biological replicates. Data are mean ± s.e.m. Mann–Whitney test. **i**, Blood lactate in control ($n = 16$) and EDKO ($n = 20$) (P0) newborn mice. Individual biological replicates. Data are mean ± s.e.m. Mann–Whitney test. *$P < 0.05$, **$P < 0.01$, ***$P < 0.001$, ****$P < 0.0001$; NS, not significant. Exact *P* values are provided in Source Data.

RXR remodels cardiac transcription

To determine the molecular basis of the altered metabolic status in P0 EDKO hearts, we conducted a multifaceted genome-wide characterization by assay for transposase-accessible chromatin regions using sequencing[21] (ATAC–seq) and by chromatin immunoprecipitation with sequencing (ChIP–seq) for acytlation of histone 3 lysine 27 (H3K27ac), a histone modification that marks active enhancers and promoters (Fig. 3a). The combination of these techniques allowed us to delineate dynamic changes in chromatin accessibility and activation upon RXR depletion (Fig. 3). ATAC–seq captured 326 differentially open chromatin regions (adjusted *P* value < 0.05, $\log_2$FC > 0.6) and 629 closed regions (adjusted *P* value < 0.05, $\log_2$FC < −0.6) in EDKO versus control P0 hearts, whereas H3K27ac ChIP–seq identified 42 differentially active peaks (adjusted *P* value < 0.05, $\log_2$FC > 0.6) and 650 inactive peaks (adjusted *P* value < 0.05, $\log_2$FC < −0.6) (Fig. 3b and Extended Data Fig. 3a). The relative loss of open and active genomic regions in EDKO hearts suggests that loss of RXRs has an effect on the epigenetic landscape of activated genes in perinatal cardiomyocytes. Moreover, annotation analysis identified similar distributions of ATAC–seq and H3K27ac ChIP–seq differential peaks (Fig. 3c and Extended Data Fig. 3b), with closed and inactive peaks both predominantly annotated as introns (40.22% and 42.62%, respectively) or intergenic regions (36.72% and 31.08%, respectively). This suggests that in perinatal cardiomyocytes, RXRs might have a major role in the distal regulation of chromatin access and transcription via enhancers (Fig. 3c). In line with this idea, transcription factor motif enrichment analysis of these peaks revealed that one of the most frequently found binding motifs was the conventional RXR homodimer response element with 1 nucleotide spacing (DR1), together with motifs for other cardiac-related transcription factors (MEF2 family and GATA4) (Fig. 3d). DR1 motifs are also bound by peroxisome proliferator-activated receptor (PPAR), suggesting that they are plausible heterodimeric partners for cardiac RXRs. Supporting this idea, we found that depletion of RXRs or PPARα result in a similar mtFAH gene expression signature in neonatal hearts (Extended Data Fig. 3c). Notably, the intersection of closed and inactive loci upon RXR depletion demarked the mtFAH signature (Fig. 3e and Extended Data Fig. 3d), indicating that RXRs are specifically required for adaptive epigenetic changes within the regulatory regions of the fatty acid homeostasis gene cluster.

To determine whether the cardiac RXR cistrome included the mtFAH signature, we performed RXR ChIP–seq experiments in control and EDKO neonatal cardiomyocytes. Differential occupancy analysis detected 6,896 loci that contained RXR peaks (10,829 peaks, adjusted *P* value < 0.05, $\log_2$FC > 0.6), defining its cistrome. Transcription factor enrichment analysis revealed the highest enrichment in DR1 and DR4 elements, known motifs for diverse RXR dimers (Extended Data Fig. 3e). Notably, mtFAH signature genes were annotated to the 185 overlapping loci between RXR ChIP–seq, closed ATAC–seq peaks and inactive H3K27ac ChIP–seq peaks (Fig. 3f,g), marking the functional RXR-regulated enhancers and promoters among all RXR-occupied candidate regions (Extended Data Fig. 3f). Furthermore, gene ontology

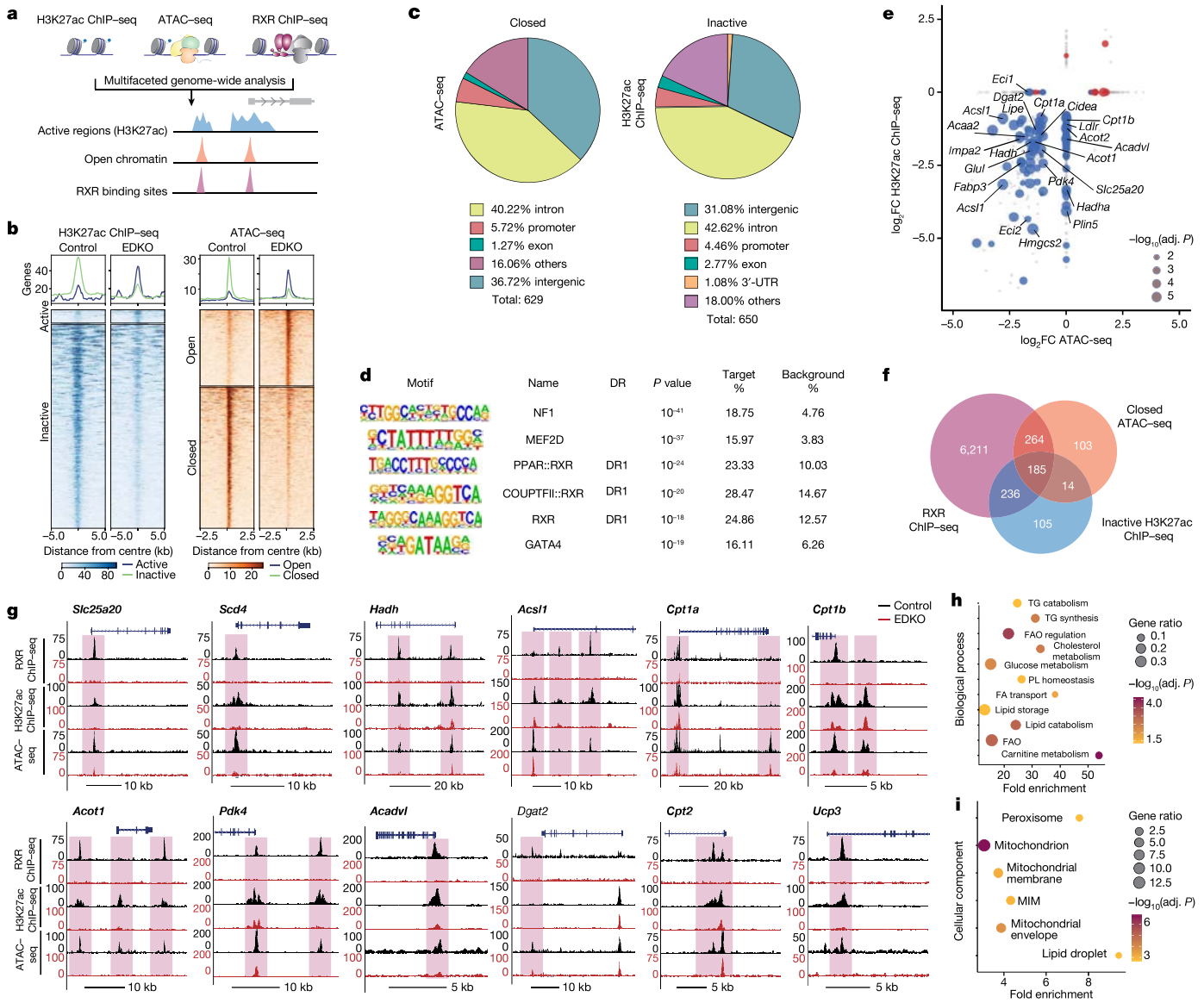

Fig. 3 | RXR transactivates the expression of mtFAH genes. a, Schematic outlining the genome-wide analysis. **b**, Left, H3K27ac ChIP–seq heat map illustrating differentially active or inactive peaks in EDKO hearts. Right, ATAC–seq heat map showing differentially open or closed peaks in EDKO hearts. Adjusted *P* value < 0.05, $\log_2$FC = 0.6; *n* = 2–3 per genotype or experiment, independent biological replicates. Colour bars depict peak intensity. **c**, Annotation distribution of differentially closed peaks (ATAC–seq) and differentially inactive peaks (H3K27ac ChIP–seq) in EDKO P0 hearts. UTR, untranslated region. **d**, HOMER motif enrichment analysis in EDKO P0 hearts. Top-scoring motifs, *P* values, best-match transcription factors, type of nuclear receptor binding DR element, and percentage of target and background sequences are shown. **e**, Intersection of RNA-seq, H3K27ac ChIP–seq and ATAC–seq experiments. For peaks found in only one experiment, a value of 0 was specified for the other axis. Blue and red dots indicate genes significantly downregulated or upregulated according to the $\log_2$FC (RNA-seq). Size indicates $-\log_{10}$(adjusted *P* value) (RNA-seq). Two-tailed Student's *t*-test (Benjamini–Hochberg). For loci absent in the RNA-seq experiment, a size of 1 was specified. **f**, Venn diagram of the RXR cistrome (RXR ChIP–seq), differentially closed annotated loci (closed ATAC–seq), and differentially inactive annotated loci (inactive H3K27ac ChIP–seq) in EDKO hearts. Numbers indicate the number of loci that contained annotated peaks in each experiment. The overlapping section (185 loci) contains the mtFAH signature. **g**, mtFAH loci UCSC tracks identified in the RXR ChIP–seq (*n* = 2 hearts per genotype, independent biological replicates), H3K27ac ChIP–seq and ATAC–seq experiments. Black, control; red, EDKO. Genes encoding mitochondrial proteins are in bold. **h**,**i**, Gene Ontology (GO) enrichment of the 185 annotated mtFAH loci for biological process (**h**) and cellular component (**i**) analysis. Two-tailed Student's *t*-test with Benjamini–Hochberg post-test. MIM, mitochondrial inner membrane; PL, phospholipids; TG, triglycerides.

analysis of the overlapping RXR loci identified lipid homeostasis-related pathways as the most significantly enriched biological process (Fig. 3h) and mitochondria-related compartments as the most enriched cellular compartment (Fig. 3i). We therefore conclude that RXRs operate directly at enhancers and promoters to activate the transcription of mtFAH signature genes and control the surrounding epigenetic landscape in perinatal cardiomyocytes.

Milk fatty acids drive cardiac RXR functions

To confirm that RXR activity directly controls the mtFAH signature and other lipid metabolism-related genes, we administered the selective RXR agonist bexarotene to eight-week-old mice (C57Bl6/J)[12]. RT–qPCR analysis of cardiac tissue from these mice showed that bexarotene significantly induced expression of the mtFAH signature and other

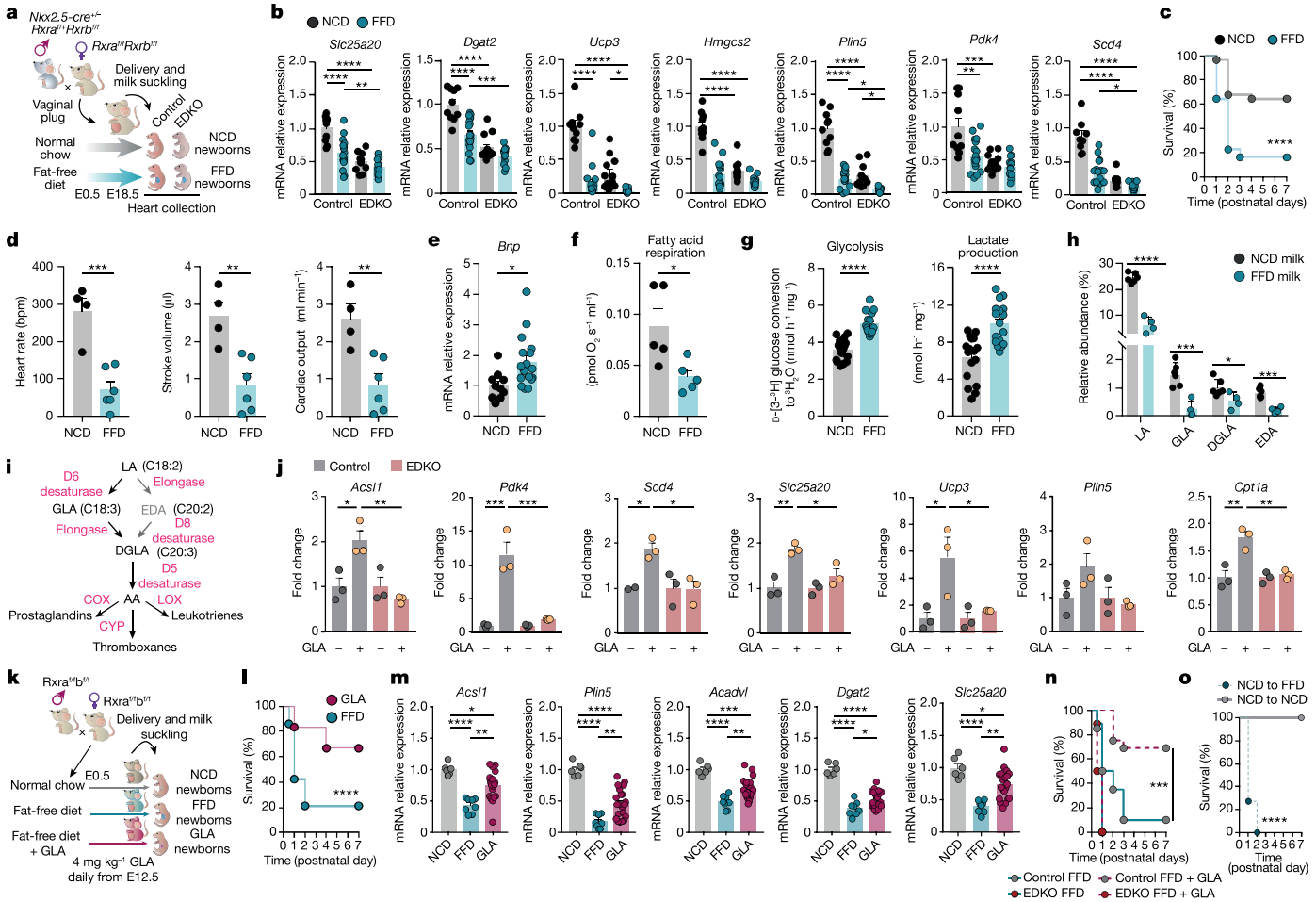

Fig. 4 | Maternal milk-borne GLA activates the RXR-dependent gene signature. a, Experimental outline. **b**, Cardiac expression of mtFAH signature from control ($n = 10–17$) and EDKO ($n = 11–14$) mice (P0) suckled with milk from dams fed a NCD or FFD. Data are mean ± s.e.m. Two-way ANOVA with Tukey's corrections. **c**, Kaplan–Meier curve of control mice fed NCD ($n = 58$) or FFD ($n = 33$) milk. Log-rank test ($P < 0.0001$). **d**, Echocardiography analysis from control newborns (P1) suckling NCD ($n = 4$) or FFD ($n = 6$) milk. Data are mean ± s.e.m. Two-tailed Student's *t*-test. **e**, Cardiac *Bnp* expression in newborn (P1) mice fed NCD (n = 10) or FFD (n = 17) milk. Data are mean ± s.e.m. Two-tailed Student's *t*-test. **f**, β-oxidation oxygen consumption assay in cardiac mitochondria from P1 mice fed NCD ($n = 5$) or FFD ($n = 5$) milk. Data are mean ± s.e.m. Two-tailed Student's *t*-test. **g**, Glycolytic flux and lactate generation in hearts of P1 mice fed NCD ($n = 17$) or FFD ($n = 17$) milk. Data are mean ± s.e.m. Two-tailed Student's *t*-test. **h**, Relative abundance of omega-6 fatty acids in NCD ($n = 6$) and FFD ($n = 4$) milk. LA, linoleic acid; GLA, γ-linolenic acid; DGLA, dihomo-γ-linolenic acid; EDA, eicosadienoic acid. Data are mean ± s.e.m. Two-tailed Student's *t*-test. **i**, The omega-6 fatty acid biosynthesis pathway. AA, arachidonic acid. COX, cyclooxigenase. LOX, lypoxigenase. CYP, CYP450. **j**, In vitro mtFAH gene signature expression in control or EDKO cardiomyocytes treated with GLA–bovine serum albumin (BSA) (500 µM). Data are mean ± s.e.m. ($n = 3$ replicates per condition). Two-way ANOVA. **k**, Outline for rescue of the FFD milk-fed neonatal phenotype. **l**, Kaplan–Meier curve of control mice fed FFD milk (FFD, $n = 64$) or FFD + GLA milk (GLA, $n = 18$). Log-rank test ($P = 0.0003$). **m**, Cardiac mtFAH gene expression in perinatal mice fed NCD milk ($n = 6$), FFD milk (n = 8) or FFD + GLA milk (GLA, $n = 21$) mice. Data are mean ± s.e.m. One-way ANOVA Tukey and Benjamini–Hochberg correction. **n**, Kaplan–Meier curve of control and EDKO mice fed FFD or FFD + GLA milk. Log-rank test ($n = 8–20$ mice per condition), $P = 0.0002$. **o**, Kaplan–Meier curve of control newborns born from NCD-fed mothers but exposed to NCD or FFD milk. Log-rank test, $P < 0.0001$ ($n = 15–22$ mice per group). Independent biological samples in **b**–**h**,**l**–**o**. $^*P < 0.05$, $^{**}P < 0.01$, $^{***}P < 0.001$, $^{****}P < 0.0001$. Exact *P* values in Source Data.

lipid-metabolism genes (Extended Data Fig. 4a), validating the use of this synthetic ligand to modulate RXR-dependent transcriptional circuits in myocardial cells.

The identity of endogenous RXR ligands is a long-standing question, given the central role of RXRs in controlling metabolic homeostasis across the lifespan[22]. In newborns, maternal milk is a powerful source of signalling molecules that can trigger metabolic adaptions by increasing blood lipid content[3,7]. To investigate the effect of lactation on the RXR-dependent mtFAH signature, we analysed relative mRNA expression in control and EDKO hearts from maternal milk-fed or fasted P0 newborns (Extended Data Fig. 4b). *Rxra* and *Rxrb* transcripts were unaltered in milk-fed and fasted control hearts, indicating that maternal milk does not influence RXR abundance (Extended Data Fig. 4c). However, the expression of mtFAH genes (*Slc25a20*, *Ucp3*, *Hmgcs2*, *Plin5* and *Pdk4*) and other lipid homeostasis genes (*Dgat2* and *Scd4*) was significantly reduced in fasted control mice, resembling the EDKO transcriptional phenotype (Extended Data Fig. 4d). Maternal milk deprivation had no effect on lipid homeostasis gene expression in EDKO hearts, suggesting that RXRs are important receptors for milk-derived inducers of the mtFAH transcriptional programme.

Maternal milk is highly enriched in vitamin A and lipids[23,24], the metabolic precursors of RXR ligands[25]. Moreover, nutritional intervention in pregnant mice efficiently modulates maternal milk composition[26]. We therefore investigated whether a lack of fatty acids or vitamin A compounds in milk would prevent RXR-dependent mtFAH transcriptional induction in offspring (Fig. 4a and Extended Data Fig. 4e–g). For these

experiments, we crossed *Nkx2.5-cre*$^{+/-}$*Rxra*$^{f/+}$*Rxrb*$^{f/f}$ male mice with *Rxra*$^{f/f}$ *Rxrb*$^{f/f}$ females, and fed *Rxra*$^{f/f}$*Rxrb*$^{f/f}$ dams with a normal chow diet (NCD), a fat-free diet (FFD) or a vitamin A-deficient (VAD) diet from E0.5 onwards. Lactation was monitored, and control and EDKO hearts were collected from pups 4 h after birth (Fig. 4a). Hearts from neonates fed milk from dams on the VAD (VAD milk) had a normal mtFAH gene expression profile, indicating that 9-*cis*-retinoic acid is not the relevant RXR ligand in perinatal cardiomyocytes (Extended Data Fig. 4e). By contrast, hearts from pups fed milk from dams on a FFD (FFD milk) showed a pronounced reduction in the expression of mtFAH signature genes and other lipid metabolism-related genes (Fig. 4b), matching the effect observed in milk-deprived neonates (Extended Data Fig. 4d). Other key metabolic genes involved in glycolysis, Krebs cycle or mitochondrial oxidative phosphorylation complexes were not changed in hearts from pup fed FFD milk (Extended Data Fig. 4f). The residual mtFAH signature in EDKO hearts was largely insensitive to the FFD milk, with only mild decreases in *Ucp3* and *Plin5* gene expression (Fig. 4b). Because expression of *Rxra* and *Rxrb* was insensitive to FFD milk (Extended Data Fig. 4g), these data support the conclusion that RXRs expressed in cardiomyocytes relay signals from maternal milk-derived fatty acids (milk-FA) to enable mitochondrial maturation and metabolic adaptation in neonatal hearts.

To determine whether a lack of milk-FA reproduces the RXR-deficient phenotype, we examined control newborns suckled with either milk from dams fed a NCD (NCD milk) or FFD milk upon delivery. Whereas neonates fed NCD milk thrived, control mice fed FFD milk died within 48 h of birth (Fig. 4c) and showed a significant reduction in body weight at P1 (Extended Data Fig. 4h). Echocardiography analysis showed that feeding on FFD milk severely impaired cardiac function in the pups (Fig. 4d, Extended Data Fig. 4i and Supplementary Videos 3 and 4). Cardiac defects in control pups fed FFD milk included significantly decreased heart rate, stroke volume, cardiac output and LVEF compared to pups fed NCD milk (Fig. 4d and Supplementary Videos 3 and 4). Moreover, the hearts of pups fed FFD milk showed reduced LV telediastolic volume (Extended Data Fig. 4i). Consistent with these findings, neonates fed FFD milk exhibited significantly increased cardiac expression of *Bnp* mRNA (Fig. 4e). We excluded other causes of death for the pups fed FFD milk, such as thermogenesis or lung oedema (Extended Data Fig. 4j,k). In addition, control hearts from pups fed FFD milk showed reduced fatty acid mitochondrial respiration and enhanced glycolysis and lactate production (Fig. 4f,g). Together, these results indicate that milk-FA support metabolic adaptation in the neonatal heart and suggest that activation of a milk-FA–RXR axis is a relevant mechanism for sustaining perinatal life.

GLA–RXR drives mitochondrial maturation

We next aimed to identify the endogenous RXR ligand in maternal milk. To precisely dissect the contribution of each milk-FA, we performed an unbiased lipidomics analysis comparing the milk-FA profiles in NCD milk and FFD milk (Supplementary Table 2). Milk-FAs that were significantly diminished in milk from dams fed the FFD would be candidate RXR ligands. We detected 45 free fatty acids and estimated their abundance as the relative proportion within their fatty acid class: saturated (SAFA), monounsaturated (MUFA), di-unsaturated (DUFA) and polyunsaturated (PUFA) fatty acids. The family of omega-6 fatty acids exhibited the most significant decrease in FFD milk compared with NCD milk (P value < 0.05, $\log_2$FC < 0, mean content in NCD milk > 0.5%). Specifically, LA (C18:2n-6), GLA (C18:3n-6), DGLA (C20:3n-6) and EDA (C20:2n-6) (Fig. 4h and Extended Data Fig. 4l,m). Omega-6 fatty acids are a family of important bioactive PUFAs that is generated through an elongation cascade from LA, an essential fatty acid that is provided only by dietary intake and therefore cannot be compensated by endogenous maternal synthesis[27] (Fig. 4i). The presence of LA, GLA, DGLA and EDA has been widely reported in human breast milk, which provides the required physiological source of omega-6 fatty acids to the human newborn[27–30].

LA and GLA bind the ligand-binding domain of RXRα and stabilize RXRα heterodimerization, respectively[31,32]. To assess whether these omega-6 fatty acids induce the mtFAH signature, we analysed gene expression in C57B6/J primary neonatal cardiomyocytes and the HL-1 cardiac muscle cell line treated with LA or GLA (Extended Data Fig. 5a–d). The synthetic RXR agonist LG268[12] was used as an additional pharmacological approach and served as a control. GLA and LG268 both strongly increased mtFAH gene expression, whereas LA had no effect (Extended Data Fig. 5a–d). We further demonstrated that GLA-induced mtFAH gene expression is RXR-dependent, as the GLA effect was lost in EDKO primary cardiomyocytes (Fig. 4j) as well as in C57B6/J primary neonatal cardiomyocytes pretreated with UVI3003 (UVI), an RXR antagonist[33] (Extended Data Fig. 5e). We further determined the absolute concentration of GLA (from all lipid forms) in cardiac tissue (30.4 μmol kg^{-1}) as well as in NCD milk (1,066.3 ± 167.4 μM) and FFD milk (335.9 μM ± 165.4 μM), showing a substantial decrease in FFD milk compared with NCD.

Additionally, to validate the physiological role of GLA derived from maternal milk in metabolic cardiac maturation, we aimed to rescue the FFD phenotype by selectively restoring GLA levels in FFD milk (Fig. 4k). Neonates that were fed milk from dams on a FFD supplemented with GLA (FFD + GLA milk) thrived and had normal body weight, glycaemia and ability to feed compared to neonates fed FFD milk (Fig. 4l and Extended Data Fig. 5f–h). Moreover, mtFAH gene expression in perinatal hearts of mice fed FFD + GLA milk was significantly increased (Fig. 4m and Extended Data Fig. 5i), suggesting that GLA is a critical signal to ensure neonatal cardiac transcriptional energetics. Rescue of survival in neonates fed FFD + GLA milk was RXR-dependent, supporting the existence of a GLA–RXR transcriptional axis in perinatal cardiomyocytes (Fig. 4n). In alternative approaches, customized FFD diets supplemented with LA and GLA or GLA alone rescued lethality in neonates fed FFD milk (Extended Data Fig. 5j). Notably, pups delivered by NCD mothers and exposed to FFD milk died, supporting the role of maternal milk, and not lipid deposits during pregnancy, as the relevant GLA source for ensuring perinatal survival (Fig. 4o).

To provide more direct evidence that GLA binds to RXR, we first confirmed the interaction of GLA with recombinant RXRα ligand-binding domain (RXRα-LBD) in vitro using surface plasmon resonance (Fig. 5a), showing that unliganded RXRα-LBD bound GLA with a dissociation constant (K_d) of 10.9 ± 7.1 μM. Moreover, GLA binding to the RXRα-LBD induced the recruitment of a steroid receptor coactivator-derived LxxLL peptide with a K_d of 80.9 ± 3.6 μM (Fig. 5b,c). This result indicates that in the presence of RXR ligand, the AF2 coactivator-binding surface had acquired the active conformation capable of recruiting coactivators[34]. We further used a GAL4-UAS-driven luciferase reporter to monitor the activity of the wild-type RXRα-LBD fused to a GAL4 DNA-binding domain (RXRα-LBD–GAL4-DBD) or RXRα-LBD(ΔAF2)–GAL4-DBD, which lacks the AF2 helix 12 that is required for ligand-dependent transcriptional activation[9,35], in the presence of GLA (Fig. 5d). GLA treatment significantly induced luciferase activity in cells expressing RXRα-LBD–GAL4-DBD but not in cells expressing RXRα-LBD(ΔAF2)–GAL4-DBD (Fig. 5d). Notably, blockade of RXRα–GAL4 binding by the RXR antagonist UVI3003 abolished the GLA-mediated luciferase induction (Fig. 5d). In addition, we corroborated the ability of GLA to stabilize the RXRα–SRC1 coactivator complex in a ligand-dependent manner (Fig. 5e). These assays were reproduced in an alternative system where RXRα or RXRα-ΔAF2 plasmids were cotransfected with a reporter plasmid containing three copies of the $(AOX)_3$ response element (RXR response element-specific binding sites) (Extended Data Fig. 5k–m). Finally, in silico modelling revealed structural docking of GLA in the RXRα ligand-binding pocket, generating a stable GLA–RXRα complex (Fig. 5f and Supplementary Table 3). Overall, these data demonstrate that GLA is a potential ligand for RXR.

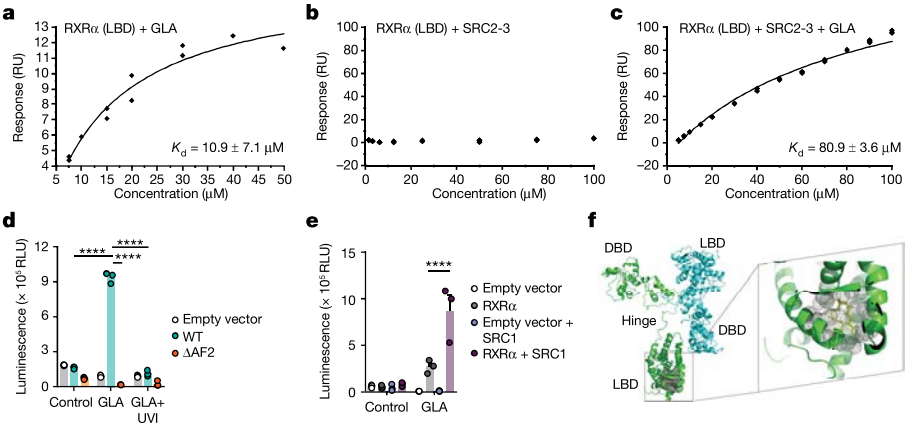

Fig. 5 | GLA is a potential ligand for RXR. a–**c**, Surface plasmon resonance analysis of the interaction of unliganded RXRα-LBD with increasing concentrations of GLA (**a**), SRC2-3 coactivator (**b**) or SRC2-3 coactivator in the presence of a saturating concentration of 120 μM GLA (**c**). The results of experiments conducted in duplicate are shown along with the calculated K_d. The maximum binding signal (R_{max}) and chi-squared calculated from the 1:1 Langmuir fitting were 19.82 resonance units (RU) and 0.510 RU^2 (**a**) and 30.00 RU and 1.66 RU^2 (**c**), respectively. **d**, Representative experiment (out of three) with the GAL4-UAS-driven luciferase reporter assay in HEK293T cells. Cells were transfected with empty vector (control), wild-type RXRα-LBD–GAL4-DBD (WT) or mutated RXRα-LBD(ΔAF2)–GAL4-DBD (ΔAF2) for 6 h ($n = 3$ technical replicates per condition). Then, cells were treated with 500 μM GLA–BSA (GLA) or 500 μM GLA–BSA with 1 μM UVI3003 (UVI) for 24 h. Data are mean ± s.e.m. Two-way ANOVA with Tukey post-test. RLU, relative light units. **e**, Representative experiment (out of 3) of GAL4-UAS-driven luciferase reporter assay to monitor ligand-dependent coactivator recruitment in HEK293T cells. Transient transfections were performed with a limiting amount of wild-type RXRα-LBD–GAL4-DBD and/or SRC1 coactivator for 6 h. Then, cells were treated with 500 μM GLA–BSA for 24 h ($n = 3$ technical replicates per condition). Data are mean ± s.e.m. Two-way ANOVA with Tukey post-test. **f**, In silico model of GLA docking in the ligand-binding domain of the mouse RXRα dimer. Left, 3D view (cartoon representation) illustrating RXRα chain A in green and chain B in cyan. The ligand cavity is represented as grey dots. Right, zoomed view of GLA docking in the ligand cavity of chain A. The ligand cavity is represented as grey dots and GLA as a yellow stick model. ****$P < 0.0001$. Exact P values are provided in Source Data.

Discussion

The neonatal cardiac dysfunction and death of mice lacking cardiomyocyte RXRα and RXRβ demonstrates that myocardial-specific RXRs have a cell-autonomous role in cardiac physiology. Furthermore, given the absence of cardiac abnormalities in ventricle-restricted RXRα-deficient mice[11] and the full RXRβ-deficient mice[36], our results show that RXR subtypes can compensate for each other's absence in myocardial cells. In agreement with previous reports[37,38], we have excluded myocardial RXRs as transcriptional controllers of cardiac morphogenesis. In this setting, the structural abnormalities observed in the myocardium of full RXRα-deficient mice[10] may be owing to the loss of epicardial-specific RXRα action, which has been proposed to regulate cardiomyocyte growth via WNT signalling in a paracrine fashion[39].

Although our study identifies RXRs as the key transcription factors controlling the fetal-to-neonatal metabolic transition, the extent to which this activity relies on RXR homodimers or heterodimers with other nuclear receptors is currently difficult to estimate. Transcription factor motif analysis indicates that the DR1 motif is enriched at RXR target gene loci, including the mtFAH signature. Of note, the DR1 motif is recognized by both RXR homodimers and heterodimers with PPARs, which are expressed in embryonic cardiomyocytes. Indeed, we show that PPARα-deficient neonatal hearts also display a downregulated mtFAH gene signature. However, unlike RXRs, PPARα is not essential in the heart, since PPARα-knockout mice have a milder phenotype that does not compromise neonatal survival[40]. This could be a consequence of functional redundancy among the PPAR subtypes [9,12,13]. Alternatively, the cooperation of RXR with other transcription factors or nuclear receptors could contribute to the lethality in EDKO mice. Along with the EDKO phenotype, the induction of the mtFAH signature by the endogenous ligand GLA and the RXR-selective agonist LG268 strongly supports the active role of RXRs, irrespective of the distinct RXR dimer states.

Our results identify the essential omega-6 PUFA GLA as a critical maternal milk nutrient for proper cardiac adaptation and survival in newborn mice, demonstrating that GLA is a potential RXR ligand in perinatal cardiomyocytes. The obligate dietary intake of GLA could establish a checkpoint in newborns, as only dams that are not nutritionally deprived will be able to provide their progeny with GLA and thus support proper nutritional health and growth. We also found that non-essential fatty acids were dispensable for cardiac mitochondrial maturation, in line with a report that offspring survival is unaffected by conditional deletion of the key lipogenic enzyme PERK[41]. The death of EDKO neonates makes it difficult to dissect the functional implications of GLA–RXR signalling on postnatal cardiac physiology. An intriguing question for future research is whether the GLA–RXR axis has a conserved role in the perinatal adaptation of other organs.

A technical limitation of our study was the inability to specifically quantify the absolute amount of GLA in the FFD + GLA milk, and therefore we cannot exclude the possibility of other metabolites being involved in this context. Moreover, the potential relevance of our findings for human physiology should be investigated further. Carnitine-acylcarnitine translocase deficiency (CACTD) is a life-threatening metabolic disease that provokes heart failure and neonatal death in humans. CACTD is caused by mutations in the RXR-controlled gene *SLC25A20*[42]. Therefore, it would be interesting to explore whether modulation of RXR transcriptional pathways would be an effective therapeutic approach for CACTD. From a nutritional standpoint, low GLA abundance in human maternal milk has been linked to growth deficits in newborns[43], suggesting a potential role of this fatty acid in human neonatal physiology. Our results reinforce the emerging idea that mother–infant interactions in early life are major drivers of organismal physiology and highlight the importance of maternal milk ingestion for mitochondrial maturation of perinatal hearts, a finding with major implications for cardiac health.

Online content

Any methods, additional references, Nature Portfolio reporting summaries, source data, extended data, supplementary information, acknowledgements, peer review information; details of author contributions and competing interests; and statements of data and code availability are available at https://doi.org/10.1038/s41586-023-06068-7.

1. Itoi, T. & Lopaschuk, G. D. The contribution of glycolysis, glucose oxidation, lactate oxidation, and fatty acid oxidation to ATP production in isolated biventricular working hearts from 2-week-old rabbits. *Pediatr. Res.* **34**, 735–741 (1993).
2. Lopaschuk, G. D. & Spafford, M. A. Energy substrate utilization by isolated working hearts from newborn rabbits. *Am. J. Physiol.* **258**, H1274–H1280 (1990).
3. Girard, J., Ferré, P., Pégorier, J. P. & Duée, P. H. Adaptations of glucose and fatty acid metabolism during perinatal period and suckling-weaning transition. *Physiol. Rev.* **72**, 507–562 (1992).
4. Rőszer, T., Menéndez-Gutiérrez, M. P., Cedenilla, M. & Ricote, M. Retinoid X receptors in macrophage biology. *Trends Endocrinol. Metab.* **24**, 460–468 (2013).
5. Lopaschuk, G. D., Ussher, J. R., Folmes, C. D., Jaswal, J. S. & Stanley, W. C. Myocardial fatty acid metabolism in health and disease. *Physiol. Rev.* **90**, 207–258 (2010).
6. Lopaschuk, G. D., Spafford, M. A. & Marsh, D. R. Glycolysis is predominant source of myocardial ATP production immediately after birth. *Am. J. Physiol.* **261**, H1698–H1705 (1991).
7. Piquereau, J. & Ventura-Clapier, R. Maturation of cardiac energy metabolism during perinatal development. *Front. Physiol.* **9**, 959 (2018).
8. Krężel, W., Rühl, R. & de Lera, A. R. Alternative retinoid X receptor (RXR) ligands. *Mol. Cell. Endocrinol.* **491**, 110436 (2019).
9. Mascrez, B. et al. The RXRα ligand-dependent activation function 2 (AF-2) is important for mouse development. *Development* **125**, 4691–4707 (1998).
10. Sucov, H. M. et al. RXR alpha mutant mice establish a genetic basis for vitamin A signaling in heart morphogenesis. *Genes Dev.* **8**, 1007–1018 (1994).
11. Chen, J., Kubalak, S. W. & Chien, K. R. Ventricular muscle-restricted targeting of the RXRα gene reveals a non-cell-autonomous requirement in cardiac chamber morphogenesis. *Development* **125**, 1943–1949 (1998).
12. Menendez-Gutierrez, M. P. et al. Retinoid X receptors orchestrate osteoclast differentiation and postnatal bone remodeling. *J. Clin. Invest.* **125**, 809–823 (2015).
13. Ricote, M. et al. Normal hematopoiesis after conditional targeting of RXRα in murine hematopoietic stem/progenitor cells. *J. Leukocyte Biol.* **80**, 850–861 (2006).
14. Stanley, E. G. et al. Efficient Cre-mediated deletion in cardiac progenitor cells conferred by a 3′ UTR-ires-Cre allele of the homeobox gene Nkx2-5. *Int. J. Dev. Biol.* **46**, 431–439 (2002).
15. Moses, K. A., DeMayo, F., Braun, R. M., Reecy, J. L. & Schwartz, R. J. Embryonic expression of an Nkx2-5/Cre gene using ROSA26 reporter mice. *Genesis* **31**, 176–180 (2001).
16. Schooneman, M. G., Vaz, F. M., Houten, S. M. & Soeters, M. R. Acylcarnitines: reflecting or inflicting insulin resistance? *Diabetes* **62**, 1–8 (2013).
17. Koves, T. R. et al. Mitochondrial overload and incomplete fatty acid oxidation contribute to skeletal muscle insulin resistance. *Cell Metab.* **7**, 45–56 (2008).
18. Wyss, M. & Kaddurah-Daouk, R. Creatine and creatinine metabolism. *Physiol. Rev.* **80**, 1107–1213 (2000).
19. Ritterhoff, J. et al. Metabolic remodeling promotes cardiac hypertrophy by directing glucose to aspartate biosynthesis. *Circ. Res.* **126**, 182–196 (2020).
20. Zdzisińska, B., Żurek, A. & Kandefer-Szerszeń, M. α-Ketoglutarate as a molecule with pleiotropic activity: well-known and novel possibilities of therapeutic use. *Arch. Immunol. Ther. Exp.* **65**, 21–36 (2017).
21. Buenrostro, J. D., Wu, B., Chang, H. Y. & Greenleaf, W. J. ATAC-seq: a method for assaying chromatin accessibility genome-wide. *Curr. Protoc. Mol. Biol.* **109**, 21.29.21–21.29.29 (2015).
22. Szanto, A. et al. Retinoid X receptors: X-ploring their (patho)physiological functions. *Cell Death Differ.* **11**, S126–S143 (2004).
23. Silverman, J., Stone, D. W. & Powers, J. D. The lipid composition of milk from mice fed high or low fat diets. *Lab. Anim.* **26**, 127–131 (1992).
24. Vries, J. Y. D., Pundir, S., McKenzie, E., Keijer, J. & Kussmann, M. Maternal circulating vitamin status and colostrum vitamin composition in healthy lactating women–a systematic approach. *Nutrients* **10**, 687 (2018).
25. Dawson, M. I. & Xia, Z. The retinoid X receptors and their ligands. *Biochim. Biophys. Acta* **1821**, 21–56 (2012).
26. Oosting, A., Verkade, H. J., Kegler, D., van de Heijning, B. J. & van der Beek, E. M. Rapid and selective manipulation of milk fatty acid composition in mice through the maternal diet during lactation. *J. Nutr. Sci.* **4**, e19 (2015).
27. Sergeant, S., Rahbar, E. & Chilton, F. H. Gamma-linolenic acid, dihommo-gamma linolenic, eicosanoids and inflammatory processes. *Eur. J. Pharmacol.* **785**, 77–86 (2016).
28. Wright, S. & Bolton, C. Breast milk fatty acids in mothers of children with atopic eczema. *Br. J. Nutr.* **62**, 693–697 (1989).
29. Vaidya, H. & Cheema, S. K. Breastmilk with a high omega-6 to omega-3 fatty acid ratio induced cellular events similar to insulin resistance and obesity in 3T3-L1 adipocytes. *Pediatr. Obes.* **13**, 285–291 (2018).
30. Okolska, G., Ziemlański, S., Kowalska, M. & Ostojska, J. The levels of essential unsaturated fatty acids in human milk on the 3rd, 4th, 5th, and 6th days after labour. *Acta Physiol. Pol.* **34**, 239–248 (1983).
31. Lengqvist, J. et al. Polyunsaturated fatty acids including docosahexaenoic and arachidonic acid bind to the retinoid X receptor alpha ligand-binding domain. *Mol. Cell Proteomics* **3**, 692–703 (2004).
32. Forman, B. M., Chen, J. & Evans, R. M. Hypolipidemic drugs, polyunsaturated fatty acids, and eicosanoids are ligands for peroxisome proliferator-activated receptors alpha and delta. *Proc. Natl Acad. Sci. USA* **94**, 4312–4317 (1997).
33. Watanabe, M. & Kakuta, H. Retinoid X receptor antagonists. *Int. J. Mol. Sci.* **19**, 2354 (2018).
34. Henttu, P. M., Kalkhoven, E. & Parker, M. G. AF-2 activity and recruitment of steroid receptor coactivator 1 to the estrogen receptor depend on a lysine residue conserved in nuclear receptors. *Mol. Cell. Biol.* **17**, 1832–1839 (1997).
35. Niu, H. et al. Endogenous retinoid X receptor ligands in mouse hematopoietic cells. *Sci. Signal.* **10**, eaan1011 (2017).
36. Kastner, P. et al. Abnormal spermatogenesis in RXR beta mutant mice. *Genes Dev.* **10**, 80–92 (1996).
37. Mascrez, B., Ghyselinck, N. B., Chambon, P. & Mark, M. A transcriptionally silent RXRα supports early embryonic morphogenesis and heart development. *Proc. Natl Acad. Sci. USA* **106**, 4272–4277 (2009).
38. Subbarayan, V. et al. RXRα overexpression in cardiomyocytes causes dilated cardiomyopathy but fails to rescue myocardial hypoplasia in RXRα-null fetuses. *J. Clin. Invest.* **105**, 387–394 (2000).
39. Merki, E. et al. Epicardial retinoid X receptor alpha is required for myocardial growth and coronary artery formation. *Proc. Natl Acad. Sci. USA* **102**, 18455–18460 (2005).
40. Leone, T. C., Weinheimer, C. J. & Kelly, D. P. A critical role for the peroxisome proliferator-activated receptor alpha (PPARα) in the cellular fasting response: the PPARα-null mouse as a model of fatty acid oxidation disorders. *Proc. Natl Acad. Sci. USA* **96**, 7473–7478 (1999).
41. Cardoso, A. C. et al. Mitochondrial substrate utilization regulates cardiomyocyte cell-cycle progression. *Nat. Metab.* **2**, 167–178 (2020).
42. Chinen, Y. et al. A novel homozygous missense *SLC25A20* mutation in three CACT-deficient patients: clinical and autopsy data. *Hum. Genome Var.* **7**, 11 (2020).
43. Mychaleckyj, J. C. et al. Association of breast milk gamma-linolenic acid with infant anthropometric outcomes in urban, low-income Bangladeshi families: a prospective, birth cohort study. *Eur. J. Clin. Nutr.* **74**, 698–707 (2020).

Publisher's note Springer Nature remains neutral with regard to jurisdictional claims in published maps and institutional affiliations.

Springer Nature or its licensor (e.g. a society or other partner) holds exclusive rights to this article under a publishing agreement with the author(s) or other rightsholder(s); author self-archiving of the accepted manuscript version of this article is solely governed by the terms of such publishing agreement and applicable law.

© The Author(s), under exclusive licence to Springer Nature Limited 2023

Methods

Mice

All experiments were performed according to local ethical guidelines and were approved by the Animal Subjects Committee of the Instituto de Salud Carlos III (Madrid, Spain) in accordance with EU Directive 86/609/EEC and Madrid Community Organs in the PROEX 188/26. All mice used in this study were generated on a C57BL/6J background. Mice were housed at 2–5 animals per cage with a 12 h light/dark cycle (lights on from 07:00 to 19:00) at constant temperature (23 °C) with ad libitum access to food and water, and 45–65% relative humidity. Mice were fed a NCD (LASQCdiet Rod18-A), FFD (TD.03314-160, Ssniff), VAD (TD.86143, Ssniff), FFD + 3% safflower oil + 3% borage oil (GLA+LA, TD.03314-162, Ssniff) and FFD + 6% borage oil (GLA, TD.03314-163, Ssniff). In order to conditionally ablate *Rxra* and *Rxrb* in the developing heart, we crossed *Nkx2.5-cre*$^{+/-}$ heterozygous males[14] with females bearing *Rxra*$^{f/f}$ (ref. 13) and *Rxrb*$^{f/f}$ (ref. 44) alleles. We finally obtained EDKO mice: *Nkx2.5-cre*$^{+/-}$*Rxra*$^{f/f}$*Rxrb*$^{f/f}$ after an additional crossing of heterozygous offspring *Nkx2.5-cre*$^{+/-}$*Rxrab*$^{f/+}$ with *Rxrab*$^{f/f}$ females. *Rxra*$^{f/f}$*Rxrb*$^{f/f}$ littermates were used as controls. PPARα-null mice were kindly provided by G. Sabio. Genotyping was performed by PCR of genomic DNA extracted from tail snips. Total DNA was obtained using REDExtract-N-Amp Tissue PCR Kit (R4775, Sigma). PCR conditions and primers are described in Supplementary Table 4. Male and female mice were studied during the whole study. In studies using P0 mice, pregnant females were monitored according to vaginal plug. Before tissue collection, neonates were euthanized by decapitation. Adult animals were killed either by cervical dislocation or carbon dioxide (CO_2) asphyxiation. For in vitro experiments samples were allocated randomly in each experiment. Randomization was produced by blindly collecting tissues prior genotyping. In vivo experiments were reproduced 2–3 independent times.

Echocardiography analysis

Transthoracic echocardiography was performed on P0 newborns. Neonatal mice were not anaesthetized. Mice were placed in a biofeedback warming station that control core body temperature. Warm ultrasound gel was applied to the chest of the animals, and echocardiography measurements were obtained using the VEVO 2100 high frequency ultrasound system with a linear transducer MS400 18-38 MHz (Visual Sonics). Parasternal short- and long-axis views at 3 levels (base, middle and apex) in two-dimensional and M-mode were obtained as described previously[45]. The LV end-systolic and end-diastolic volume (LV Vol;s and LV Vol;d, respectively) were acquired from the parasternal two-dimensional short-axis view, and LVEF was calculated using the area-length method[46]. Wall thickness at the end of the systole and diastole was measured from the M-mode short-axis. Analysis was performed offline by two blinded echocardiography experts. Ultrasounds were performed in collaboration with M.V.-O.

Body temperature quantification

Whole-body temperature of P0 newborns was quantified by thermographic images using a FLIR T430sc Infrared Camera (FLIR Systems) and analysed with FlirIR software.

Wet/dry lung ratio

Lung tissue (P0 newborns) was weighed immediately after collection (wet) and then, after dessication (dry) at 95 °C overnight. The wet/dry ratio was calculated by dividing wet weight/dry weight of each corresponding sample.

Blood glucose and lactate determination

After decapitation, blood drops were collected and glucose and lactate levels were measured by a glucose tester (Hoffmann-La Roche) and lactate tester (Accutrend Plus, Roche diagnostics), respectively.

Effects of fasting and nutritional milk intervention on cardiac gene expression

In fasting experiments, 2 mg progesterone (Sigma, P0130) was injected intraperitoneally in pregnant females at E17.5 and E18.5. At E19.5, pregnant dams were euthanized by cervical dislocation and caesarean sections were performed. After 4 h, neonates were euthanized by decapitation and hearts were collected. For milk intervention experiments, pregnant dams were fed a NCD, FFD or VAD diet from E0.5. After natural delivery, pups were allowed to suckle for 4 h and then newborns were euthanized and hearts were collected.

In vivo GLA supplementation

Dams were fed a FFD (TD.03314, Ssniff) from E0.5 and then gavaged with GLA (4 mg kg^{-1}, L2378 Sigma) daily from E12.5.

Bexarotene

Eight-week-old C57BL6/J mice were treated with 1 dose of 10 mg kg^{-1} bexarotene (200499, Sigma) by oral gavage. Five days after the treatment, mice were euthanized and hearts were collected for gene expression analysis.

Lipidomic profiling of milk samples

For maternal milk extraction at day 1 post-partum, dams were intraperitoneally treated with 4UI oxytocin (Sigma, O325) and separated from their pups for 4 h. Then, 50 µl of milk per female was obtained by manual stimulation.

Solutions containing 1,000 ppm of the internal standards deuterated palmitic acid-d31 and C17 sphinganine (Merck/Sigma-Aldrich) were prepared in methanol, and diluted in a MMC solvent mixture (methanol:methyl tert-butyl ether:chloroform (4:3:3 v/v/v) (all MS-grade from Honeywell)), so the final concentration of both internal standards was 15 ppm. Then, 10 µl of each milk sample was mixed in 0.5 ml microtubes with 70 µl of MMC including the internal standard, vortex-mixed for 20 min and centrifuged (10,800*g*) at room temperature for 5 min. Finally, the supernatant was transferred to a chromatographic vial with insert, and 1 µl was injected onto the LC–MS system (approximately equivalent to 10 nl of milk).

Lipidomics data from milk samples were acquired using an Agilent 1290 Infinity II Ultrahigh Performance Liquid Chromatography (UHPLC) system coupled to an Agilent 6545 quadrupole time-of-flight (QTOF) mass spectrometer. The Agilent 1290 Infinity II Multisampler system, equipped with a multiwash option, was used to uptake 1 µl of extracted samples. The multisampler temperature was maintained at 15 °C to preserve compounds in a stable environment and avoid lipid precipitation. An Agilent InfinityLab Poroshell 120 EC-C18 (3.0 × 100 mm, 2.7 µm) (Agilent Technologies) column and a compatible guard column (Agilent InfinityLab Poroshell 120 EC-C18, 3.0 × 5 mm, 2.7 µm) were used and maintained at 50 °C. The chromatography gradient started at 70% of B at 0–1 min, 86% of B at 3.5–10 min, 100% of B at 11–17 min. The starting conditions were recovered by minute 17, followed by a 2 min re-equilibration time; the total running time was 19 min. The mobile phases used for both positive and negative ionization modes consisted of (A) 10 mM ammonium acetate, 0.2 mM ammonium fluoride in water/methanol (9:1, v/v) and (B) 10 mM ammonium acetate, 0.2 mM ammonium fluoride in acetonitrile:methanol:isopropanol (2:3:5, v/v/v). The flow rate was held constant, set at 0.6 ml min^{-1}. The multiwash strategy consisted of a mixture of methanol:isopropanol (50:50, v/v) with the wash time set at 15 s, and aqueous phase:organic phase (30:70, v/v) mixture to assist in the starting conditions.

The Agilent 6545 QTOF mass spectrometer equipped with a dual AJS Electrospray (ESI) ion source was set with the following parameters: 150 V fragmentor, 65 V skimmer, 3,500 V (positive), 3,000 V (negative) capillary voltage, 750 V octopole radio frequency voltage, 10 l min^{-1} nebulizer gas flow, 200 °C gas temperature, 50 psi nebulizer

gas pressure, 12 l min^{-1} sheath gas flow, and 300 °C sheath gas temperature. Data were collected in positive and negative ESI modes in separate runs, operated in full scan mode from 50 to 1,800 *m/z* with a scan rate of 3 spectra per s. A solution consisting of two reference mass compounds were used throughout the whole analysis: purine (C5H4N4) at *m/z* 121.0509 for the positive and *m/z* 119.0363 for the negative ionization modes; and HP-0921 (C18H18O6N3P3F24) at *m/z* 922.0098 for the positive and *m/z* 980.0163 (HP-0921 + acetate) for the negative ionization modes. These masses were continuously infused into the system through an Agilent 1260 Iso Pump at a 1 ml min^{-1} (split ratio 1:100) to provide a constant mass correction. For both ionization modes, 10 iterative MS/MS runs were performed. They were operated with an MS and MS/MS scan rates of 3 spectra per s, 40–1,800 *m/z* mass window, a narrow (~1.3 amu) MS/MS isolation width, 3 precursors per cycle, and a MS/MS threshold of 5,000 counts and 0.001%. Five iterative MS/MS runs were set with a collision energy of 20 eV, and the next five runs were performed at 40 eV. References masses and contaminants detected in blank samples were excluded from the analysis to avoid their inclusion in the iterative MS/MS.

Workflow for lipid identification. All the iterative MS/MS spectra datasets collected after the LC–MS analyses, from data-dependent acquisition (DDA) in positive and negative ionization modes, were used for lipid molecular species identification using a strategy relied on two independent software tools: Agilent MassHunter LipidAnnotator[47] (Agilent Technologies), and the open-source software MS-DIAL 4[48] (RIKEN Center for Integrative Medical Sciences) to ensure high-confidence accurate lipid identification.

The annotation process was carried out in four steps: (1) The raw iterative MS/MS data obtained was imported to both software to build a fragmentation-based (MS/MS) library comprising the *m/z* of all the precursors identified as lipids by the software, together with their corresponding retention time (RT). The method parameters were set as follows: Lipid Annotator vendor software: ion species $[M+H]^+$, $[M+Na]^+$, and $[M+NH_4]^+$ for positive; and $[M-H]^-$, and $[M+CH_3COOH-H]^-$ for negative ionization mode. Then, for both ion modes, the Q-score was set at ≥50; all the lipid classes were selected, mass deviation was established as ≤20 ppm, fragment score threshold was fixed as ≥30, and total score was set at ≥60. MS-DIAL 4 open-source software. MS1 centroid data, MS/MS centroid data, positive ion mode, lipidomics as a target omics, MS1 tolerance and MS2 tolerance set at 0.01 Da and 0.025 Da, respectively. Retention time from 0 to 23 min, minimum peak height 1.000; mass slice width, 0.1 Da; smoothing level 3 scans, minimum peak width 5 scans and sigma window value, 0.5. Results from the two software were merged and filtered in an Excel file following the inclusion criteria: candidate matches at least in two software, within ΔRT < 0.3 min; in the case that the compound is found just by one tool and the other tool does not yield any compound for that molecular feature, the total score is going to be a crucial point, it is higher than 80% is considered annotated and if it is not, a manual inspection of the MS/MS spectrum using MassHunter Qualitative 10.0 must be done; or candidate with the highest spectral matching. (2) The principal aim of this step is to remove false positives from the putative list obtained previously. Here, a manual MS/MS spectral interpretation was carried out using Agilent MassHunter Qualitative Analysis software (B.10.00). Specific fragments ions helped to resolve interferences on isobaric and isomeric peaks as well as the information available in databases such as Lipid Maps (https://www.lipidmaps.org). Then, an additional manual MS1 inspection is done to complete the series of fatty acid chain composition based on literature, retention time behaviours of each molecule backbone (chromatographic RT mapping: mass-to-charge ratio (*m/z*) versus RT) and using our online tool CEU Mass Mediator (https://ceumass.eps.uspceu.es/). At the end of this step, an in-house library containing molecular formulas, isotopic mass and retention times is generated. (3) Then, the in-house library is used to perform data mining by the Batch Targeted Feature Extraction (TFE) algorithm of Agilent MassHunter Profinder software (B.10.00). Finally, all peak area values of every molecular feature extracted was exported to an Excel file for a comparison of the major lipid classes and their fatty acid composition present in the milk from dams fed the FFD versus those fed the NCD. Changes observed (Supplementary Table 2) are expressed as a fold change and percentage of change.

Absolute quantification of GLA in milk and hearts

NCD milk ($n = 6$ biological replicates), FFD milk ($n = 5$ biological replicates) and control hearts ($n = 4$ biological replicates) were used for the determination of total GLA by GC-FID as described[49]. In brief, lipids were extracted in chloroform:methanol (2:1), and the extracts were evaporated to dryness under vacuum, resuspended in toluene and subjected to methanolysis for 2.5 h at 80 °C in methanol:toluene (4:1) containing acetyl chloride. The FAME (fatty acid methyl esters) were separated and quantified on a Perkin Elmer gas chromatograph (Autosystem), with a flame ionization detector and a 30 m × 0.25 mm Omegawax (Sigma) capillary column. Nitrogen was used as carrier gas. Purified standards of FAME were analysed for the calculation of the amount of GLA based on the comparison of the peak areas.

Lipidomic profiling of heart samples

Mouse hearts were transferred to a sealed microtube and weighed. Then, 350 µl of methanol:water 1:1 v/v and 2 beads (stainless steel, 2 mm) were added. All samples were shaken at 50 Hz in a QIAGEN TissuLyser LT for 60 min, and then centrifuged at 15,000g for 5 min. Chloroform:methanol 6:1 (350 µl) were added and the tubes were vortex-mixed (VXHDAL Ohaus, Nänikon) 60 min at maximum speed. The tubes were centrifuged at 400*g* for 10 min at room temperature. 100 µl of the lower phase were taken with a glass syringe and transferred to a vial with glass insert, and the solvent evaporated to dryness in a Gyrozen HyperVac VC2124 coupled to a LVS 110Z (Gardner Denver Thomas GmbH Welch Vacuum). Samples were resuspended in 100 µl methanol and directly transferred to the UHPLC system.

Lipidomics data from heart samples were acquired using an Agilent 1290 Infinity II UHPLC system coupled to an Agilent 6545 QTOF mass spectrometer. The Agilent 1290 Infinity II Multisampler system, equipped with a multiwash option, was used to uptake 1 µl of extracted samples. The multisampler temperature was maintained at 15 °C to preserve compounds in a stable environment and avoid lipid precipitation. An Agilent InfinityLab Poroshell 120 EC-C18 (3.0 × 100 mm, 2.7 µm) (Agilent Technologies) column and a compatible guard column (Agilent InfinityLab Poroshell 120 EC-C18, 3.0 × 5 mm, 2.7 µm) were used and maintained at 50 °C. The chromatography gradient started at 70% of B at 0–1 min, 86% of B at 3.5–10 min, 100% of B at 11–17 min. The starting conditions were recovered by minute 17, followed by a 2 min re-equilibration time; the total running time was 19 min. The mobile phases used for both positive and negative ionization modes consisted of (1) 10 mM ammonium acetate, 0.2 mM ammonium fluoride in water/methanol (9:1, v/v) and (2) 10 mM ammonium acetate, 0.2 mM ammonium fluoride in acetonitrile/methanol/isopropanol (2:3:5, v/v/v). The flow rate was held constant, set at 0.6 ml min^{-1}. The multiwash strategy consisted of a mixture of methanol:isopropanol (50:50, v/v) with the wash time set at 15 s, and aqueous phase:organic phase (30:70, v/v) mixture to assist in the starting conditions.

The Agilent 6545 QTOF mass spectrometer equipped with a dual AJS Electrospray (ESI) ion source was set with the following parameters: 150 V fragmentor, 65 V skimmer, 3,500 V (positive), 3,000 V (negative) capillary voltage, 750 V octopole radio frequency voltage, 10 l min^{-1} nebulizer gas flow, 200 °C gas temperature, 50 psi nebulizer gas pressure, 12 l min^{-1} sheath gas flow, and 300 °C sheath gas temperature. Data were collected in positive and negative ESI modes in separate runs, operated in full scan mode from 50 to 1,800 *m/z* with a scan rate of 3 spectra per s. A solution consisting of two reference mass compounds were used throughout the whole analysis: purine (C5H4N4) at *m/z*

121.0509 for the positive and *m/z* 119.0363 for the negative ionization modes; and HP-0921 (C18H18O6N3P3F24) at *m/z* 922.0098 for the positive and m/z 980.0163 (HP-0921 + acetate) for the negative ionization modes. These masses were continuously infused into the system through an Agilent 1260 Iso Pump at a 1 ml min^{-1} (split ratio 1:100) to provide a constant mass correction. For both ionization modes, 10 iterative MS/MS runs were performed. They were operated with an MS and MS/MS scan rates of 3 spectra per s, 40–1,800 *m/z* mass window, a narrow (~1.3 amu) MS/MS isolation width, 3 precursors per cycle, and a MS/MS threshold of 5,000 counts and 0.001%. Five iterative MS/MS runs were set with a collision energy of 20 eV, and the next five runs were performed at 40 eV. References masses and contaminants detected in blank samples were excluded from the analysis to avoid their inclusion in the iterative MS/MS.

All the iterative MS/MS spectra datasets collected after the LC–MS analyses, from data-dependent acquisition (DDA) in positive and negative ionization modes, were used for lipid molecular species identification using a strategy relied on Agilent MassHunter LipidAnnotator (Agilent Technologies).

The raw iterative MS/MS data obtained were imported to the LipidAnnotator to build a fragmentation-based (MS/MS) library comprising the *m/z* of all the precursors identified as lipids by the software, together with their corresponding RT. The method parameters were set as follows: ion species [M+H]+, [M+Na]+, and [M+NH4]+ for positive; and $[M-H]^-$, and $[M+CH3COOH-H]^-$ for negative ionization mode. Then, for both ion modes, the Q-Score was set at ≥50; all the lipid classes were selected, mass deviation was established as ≤20 ppm, fragment score threshold was fixed as ≥ 30, and total score was set at ≥60.

Cell culture and omega-6 fatty acid treatments

Neonatal cardiomyocytes were isolated from P1–P3 C57Bl/6J, control or EDKO pups and cultured as previously described[50,51]. HL-1 cell line was cultured in Claycomb medium (51800C, Sigma) supplemented with 1% penicillin-streptomycin, 2 mM glutmaine and 10% FBS. Dishes were pre-coated with 1 mg ml^{-1} human fibronectin (F2006, Sigma). For omega-6 fatty acid supplementation, 500.000 cells were seeded in p24 plates and treated with: 500 µM BSA-conjugated LA (L9530 Sigma), 500 µM BSA-conjugated GLA (L2378, Sigma) or 1 µM LG268 (SML0279, Sigma) for 6 h. For RXR antagonist assays, neonatal cardiomyocytes were pretreated for 2 h with 0.5 µM UVI3003 (3303, Tocris). Then, 500 µM GLA–BSA was added for 6 h and RT–qPCR gene expression analysis was performed. For dose-response assays, GLA was serially diluted and neonatal CMs were treated for 6 h which was followed by RT–qPCR gene expression analysis.

ECG and data analysis

P0 mice were acquired. Four-lead surface ECGs were recorded, for a period of 5 min, from subcutaneous 23-gauge needle electrodes attached to each limb using the MP36R amplifier unit (BIOPAC Systems). During offline analysis, lead II was used for QRS duration using AcqKnowledge 4.1 analysis software. A representative 30 s segment of the recording was averaged to obtain the signal-averaged ECG. Then, ECG intervals duration was measured as the time interval between the earliest moment of deviation from baseline and the moment when the S-wave returned to the isoelectric line.

Histology

E18.5 embryonic hearts were extracted, washed twice in cold phosphate-buffered saline (PBS 1×) and fixed in 4% paraformaldehyde (50-980-487, Fisher Scientific) overnight. After alcohol dehydration, tissues were embedded in paraffin and cut using a semi-automatic microtome. Transverse or longitudinal sections (7 µm) were with haematoxylin and eosin (H&E) according to standard procedures. Whole slide images were digitalized with a digital slide scanner (Hamamatsu, Nanozoomer-RS C110730) and visualized and exported to TIFF images using NDP.view2 software (Hamamatsu Photonics). For quantification, Fiji ImageJ software (NIH, https://imagej.nih.gov/ij/) was used.

RT–qPCR

Total RNA from neonatal tissues was isolated using Trizol (T9424, Sigma-Aldrich) and MaXtract High Density tubes (129056, Qiagen) followed by standard chloroform-isopropanol extraction. For neonatal hearts/spleen/thymus/diaphragm, RNA carrier (1068337, Qiagen) was added according to manufacturer´s information. RNA was measured using a Nanodrop UV Visible Spectrophotomer (Thermo Fisher Scientific) and cDNA was prepared with High-Capacity cDNA Reverse Transcription Kit (4374966, Thermo Fisher Scientific). Transcripts were quantified with SYBR Green PCR Master Mix (4309155, Applied biosystems) using the system AB7900-FAST-384 with the following programme: 95 °C × 15 min, (95 °C × 10 s, 60 °C × 20 s, 72 °C × 30 s) × 40 cycles, 95 °C × 15 s, 60 °C × 15 s, 95 °C × 15 s. Gene expression values were normalized to housekeeping genes *36b4* and cyclophilin. For mRNA relative expression experiments, values were expressed as relative mRNA levels or fold changes compared to littermate controls. Data were analysed using qBASE (Biogazelle). For absolute expression quantification, C_t values were extrapolated into standard curves for *Rxra*, *Rxrb*, *Rxrg* and cyclophilin. Primer sequences are listed in Supplementary Table 4.

Transmission electron microscopy

For transmission electron microscopy images, the whole neonatal heart was processed. Tissues were fixed overnight 4 °C in 1 ml of Karnovsky's solution (5% glutaraldehyde (G5882, Sigma), 4% paraformaldehyde [50-980-487, Fisher Scientific], 0.1 M cacodylate buffer (C4945, Sigma) and 0.5 mg ml^{-1} $CaCl_2$) followed by 3 PBS 1× washes. Samples were post-fixed using 1% osmium tetroxide (in distilled water) for 1 h at room temperature, washed twice with distilled water and stained with 0.5% uranyl acetate for 10 min (in distilled water). Samples dehydration consisted of ascending alcohol solutions (30%, 50%, 70%, 95% and 100%) and acetone. For embedding step, samples were included in Durcupan resin at incubated for 48 h at 60 °C. Ultra-thin sections (60 nm) were obtained with a Leica Ultracut S Ultramicrotome (Leica), placed in copper grids (200 mesh) and contrasted with uranyl acetate and lead citrate. Images were acquired with Jeol Jem1010 de 100 Kv electron microscope coupled with Gatan Orius SC200 digital camera. For quantification, Fiji ImageJ software was used. Adobe Photoshop CC 19.1.5 and Adobe Illustrator CC v22.1 were used for downstream image analysis and illustration.

Mitochondrial and nuclear DNA quantification

Copy number of mitochondrial DNA measurement was performed as described[52]. In brief, genomic DNA was extracted from neonatal hearts using phenol:chloroform:isoamyl alcohol standard protocol. Nuclear DNA (nDNA) and mitochondrial DNA (mtDNA) were quantifying by *Hk2* and *Nd1* transcripts levels, respectively, by quantitative PCR. Primer sequences are provided in Supplementary Table 4. Each neonatal heart was considered as individual biological replicates. mtDNA/nDNA quantification was calculated as follows:

$$\Delta C_t = C_t(\text{nDNA gene}) - C_t(\text{mtDNA genes})$$

$$\frac{\text{mtDNA}}{\text{nDNA}}\text{copy number} = 2 \times 2^{\Delta C_t}$$

ATP synthesis assay

Each neonatal heart was processed separately and considered as individual biological samples. Cardiac mitochondria were isolated as described[53]. In brief, hearts were removed and immediately cooled at 4 °C in medium A (320 mM sucrose, 10 mM Tris-HCl, 1 mM EDTA pH 7.4)

with 1 mg ml^{-1} fatty acid-free BSA (A8806, Sigma). Tissue homogenization was performed with a glass tissue grinder using a motor-driven Teflon pestle (Heidolph RZR 2041) with 10–15 strokes at 600 rpm followed by a centrifugation at 1,000*g* for 5 min at 4 °C. Supernatant was sequentially centrifuged at 10,000*g* for 5 min at 4 °C to spin down mitochondrial fraction. Mitochondria-containing pellets were resuspended in medium A and quantified using Bradford's method[54]. ATP synthesis was performed as described previously[55]. In brief, 25–50 µg of mitochondrial protein was resuspended in buffer A (150 mM KCl, 25 mM Tris-HCl, 2 mM EDTA, 0.1% fatty acid-free BSA, 10 mM KPO_4, 0.1 mM $MgCl_2$ pH 7.4) at room temperature and dispensed into the wells of a 96-well luminescence reading plate (Costar). Substrate cocktail and buffer B (0.5 M Tris-acetate pH 7.75, 0.4 mM luciferine (E1601, Promega), 10 µg ml^{-1} luciferase (from *Photinus pyralis*, 10411523001, Roche)) were added and luminescence was measured over 2 min in a plate luminometer (Orion Microplate Luminometer, Simplicity 4.2). Substrate cocktails were composed of 6 mM of diadenosine pentaphosphate (D4022, Sigma) and 6 mM ADP (A2754, Sigma) supplemented with 0.1 M glutamate + malate (G1626 and M9138, Sigma), 0.1 M pyruvate + malate (P5280, Sigma), 0.1 M succinate (398055, Sigma), 0.1 M palmitate + L-carnitine (P9716, Sigma) or pyruvate + malate + palmitate + L-carnitine. An ATP standard curve (0–10 mM final concentration of ATP) and the consequent regression curve was performed to correlate ATP concentration and luminescence in cardiac samples. ATP production rate was expressed as nmol ATP min^{-1} (mg protein)$^{-1}$ normalized versus control.

Oxygen consumption

Cardiac mitochondria or tissue homogenate (0.02 mg ml^{-1}) were resuspended in 2 ml of mir05 medium (https://www.bioblast.at/index.php/MiPNet22.10_MiR05-Kit) and analysed using a Clark-type electrode (Oxygraph O2k, Oroboros Instruments). In order to permeabilize the cells. Fatty acids oxidation was measured with 0.2 mM octanoylcarnitine (Sigma, 50892), 2.5 mM ADP (Sigma, 09015) and 0.1 mM malate (Sigma, M1000). Next, CI-dependent oxygen consumption was measured by adding 10 mM glutamate (Sigma, G1626) and 0.4 mM malate. Finally, CII-dependent oxygen consumption was measured by adding 10 mM succinate (Sigma, S2378). 2.5 µM antimycin A (Sigma, A8674) and 0.5 µM rotenone (Sigma, R8875) were added in order to discard the non-mitochondrial respiration for all the above-mention calculations. For normalization purpose, CIV-dependent oxygen consumption was measured with 0.5 mM TMPD and 2 mM ascorbate were added as well as 100 mM azide after stabilization.

Determination of the β-oxidation flux ex vivo

The β-oxidation flux was measured by assessing the rate of conversion of [9,10-^{3}H(N)] palmitic acid into ^3H_2O. In essence, heart slices (5–10 mg) were pre-incubated for 30 min in 2 ml of a Krebs–Henseleit buffer (11 mM Na_2HPO_4, 122 mM NaCl, 3.1 mM KCl, 0.4 mM KH_2PO_4, 1.2 mM $MgSO_4$, 1.3 mM $CaCl_2$; pH 7.4), supplemented with 30 µM BSA-conjugated palmitic acid and 0.5 mg ml^{-1} BSA fatty acid free at 37 °C, followed by incubation in the presence of 1 µCi ml^{-1} of [9,10-^{3}H (N)] palmitic acid in fresh Krebs–Henseleit buffer (2 ml) in glass 25-ml Erlenmeyer flasks equipped with a central well containing a tube with 0.5 ml of water. The flask atmosphere was gassed with a O_2/CO_2 (95/5) mixture for 20 s and stopped with a rubber cap, and the flasks were incubated in a thermostatic orbital shaker (Forma Benchtop Orbital Shaker, Model 420, Thermo Fisher) for 3 h at 37 °C. In preliminary experiments (data not shown), we observed that ^3H_2O collected in the tube placed in the central well was linear with time at least up to 4 h. Incubations were finished by injecting 0.2 ml of 20 % (v/v) $HClO_4$ (Merck Millipore) through the rubber cap, and flasks were further incubated for 72 h to allow the equilibration of ^3H_2O between the incubation medium and the water of the central well. The rate of β-oxidation was expressed as nmol of [9,10-^{3}H] palmitic acid converted into ^3H_2O per hour and per mg of heart.

Glycolytic flux

The glycolytic flux was measured by assessing the rate of conversion of D-[3-^{3}H] glucose into ^3H_2O, as previously described[56]. In essence, heart slices (5–10 mg) were pre-incubated for 30 min in 2 ml of a Krebs–Henseleit buffer (11 mM Na_2HPO_4, 122 mM NaCl, 3.1 mM KCl, 0.4 mM KH_2PO_4, 1.2 mM $MgSO_4$, 1.3 mM $CaCl_2$; pH 7.4), supplemented with 5.5 mM D-glucose at 37 °C, followed by incubation in the presence of 5 µCi ml^{-1} of D-[3-^{3}H] glucose in fresh Krebs–Henseleit buffer (2 ml) in glass 25-ml Erlenmeyer flasks equipped with a central well containing a tube with 0.5 ml of water. The flask atmosphere was gassed with a O_2/CO_2 (95/5) mixture for 20 s and stopped with a rubber cap, and the flasks were incubated in a thermostatic orbital shaker (Forma Benchtop Orbital Shaker, Model 420, Thermo Fisher) for 4 h at 37 °C. In preliminary experiments (data not shown), we observed that ^3H_2O collected in the tube placed in the central well was linear with time at least up to 4 h. Incubations were finished by injecting 0.2 ml of 20% (v/v) $HClO_4$ (Merck Millipore) through the rubber cap, and flasks were further incubated for 72 h to allow the equilibration of ^3H_2O between the incubation medium and the water of the central well. The rate of glycolysis was expressed as nmol of D-[3-^{3}H] glucose converted into ^3H_2O per hour and per mg tissue.

Lactate concentration

Lactate concentrations were measured in the buffer after the 4 h incubation period spectrophotometrically by determining the increments in absorbance at 340 nm in a mixture containing 1 mM NAD^+ and 22.5 U/ml lactate dehydrogenase in 0.25 M glycine/0.5 M hydrazine/1 mM EDTA buffer at pH 9.5.

Amino acid decarboxylation rate

Amino acid oxidation rate was measured by assessing the rate of conversion of L-[^{14}C(U)] amino acid mixture (NEC850E050UC, Perkin Elmer) into $^{14}CO_2$. In brief, heart slices (5–10 mg) were pre-incubated for 30 min in 2 ml of a Krebs–Henseleit buffer (11 mM Na_2HPO_4, 122 mM NaCl, 3.1 mM KCl, 0.4 mM KH_2PO_4, 1.2 mM $MgSO_4$, 1.3 mM $CaCl_2$; pH 7.4), supplemented with 5.5 mM D-glucose at 37 °C, followed by incubation in the presence of 0.25 µCi ml^{-1} of amino acid mixture L-[^{14}C(U)] in fresh Krebs–Henseleit buffer (2 ml) in glass 25-ml Erlenmeyer flasks equipped with a central well containing a tube with 0.5 ml of benzethonium hydroxide (Sigma) for $^{14}CO_2$ equilibration. The flask atmosphere was gassed with a O_2/CO_2 (95/5) mixture for 20 s and stopped with a rubber cap, and the flasks were incubated in a thermostatic orbital shaker (Forma Benchtop Orbital Shaker, Model 420, Thermo Fisher) for 3 h at 37 °C. In preliminary experiments (data not shown), we observed that $^{14}CO_2$ collected in the tube placed in the central well was linear with time at least up to 3 h. Incubations were then terminated by the addition of 0.2 ml 20% (v/v) perchloric acid (Merck Millipore) for 30 min before the benzethonium hydroxide (containing $^{14}CO_2$) was removed, and the radioactivity was measured with a liquid scintillation analyser (Tri-Carb 4810 TR, Perkin Elmer). Amino acid oxidation rate was expressed as nmol of L-[14C(U)] amino acid mixture converted into $^{14}CO_2$ per hour per mg tissue.

Protein digestion of mouse heart samples

Neonatal mouse heart samples were homogenized using a FastPrep-24 instrument (MP Biomedicals), following manufacturer's instructions, in the presence of 50 mM Tris-HCl pH 6.8, 2% SDS and 50 mM DTT, and the resulting solution was boiled for 5 min at 95 °C. The tissue lysates were centrifuged at 13,000*g* for 15 min to remove debris, and protein concentration in the supernatant was determined using the RCDC Protein Assay Kit (Bio-Rad). Protein samples (100 µg) were mixed with denaturing buffer (8 M urea in 100 mM Tris-HCl pH 8.5) and concentrated on 30 K FASP filters (Expedeon). After washing with denaturing buffer at 10,000 rpm for 15 min, free thiol groups were alkylated by

incubation with 50 mM iodoacetamide 30 min at room temperature in the dark. Then the filters were washed with denaturing buffer followed by washing with trypsin digestion buffer (50 mM ammonium bicarbonate pH 8.8). Protein samples were digested overnight at 37 °C with sequencing grade trypsin (Promega) at 1:40 (w/w) trypsin:protein ratio in digestion buffer. The resulting tryptic peptides from each sample were recovered by centrifugation at 10,000 rpm for 5 min after addition of 40 µl of trypsin digestion buffer, after which 50 µl of 500 mM NaCl were added and the filters centrifuged for 15 min at 10,000 rpm. Trifluoroacetic acid was added to a final concentration of 1% and the peptides were desalted on C18 Oasis HLB extraction cartridges (Waters Corporation) and dried-down.

Isobaric labelling of peptides using tandem mass tags

The dried peptides were dissolved in triethylammonium bicarbonate buffer, and their concentration was determined using a Direct Detect IR spectrometer (Millipore). Equal amounts of each peptide sample were labelled with isobaric 10-plex Tandem Mass Tags (TMT, Thermo Scientific) according to the manufacturer's instructions and mixed together. Samples were desalted using C18 Oasis HLB extraction cartridges (Waters) and dried-down for later LC–MS/MS analysis.

LC–MS/MS analysis

Peptide samples were taken up in 0.1% formic acid and applied to an EASY-nLC 1000 nano-flow HPLC system (Thermo Fisher Scientific) coupled online with an Orbitrap Fusion mass spectrometer (Thermo Fisher Scientific). C18-based reverse phase separation was used with a 2-cm trap column and a 50-cm analytical column (EASY-Spray, Thermo Fisher Scientific). Peptides were loaded in buffer A (0.1% formic acid (v/v)) and eluted with a 300-min linear gradient of buffer B (90% acetonitrile, 0.1% formic acid (v/v)) at 200 nl min^{-1} flow. Mass spectra were acquired in a data-dependent manner, with an automatic switch between MS and MS/MS, using a top-speed method and 30 s dynamic exclusion. MS spectra were acquired in the 400–1,500 m/z range at 120,000 resolution, while HCD MS/MS were performed at 33 normalized collision energy and analysed with 35,000 resolution in the orbitrap.

Peptide identification

LC–MS/MS data were analysed with Proteome Discoverer (version 2.1, Thermo Fisher Scientific) using SEQUEST-HT (Thermo Fisher Scientific) against a Uniprot database containing all sequences from Mus musculus (January 2021; 63,700 entries). Database search parameters were selected as follows: trypsin digestion with two maximum missed cleavage sites, precursor mass tolerance of 800 ppm, fragment mass tolerance of 0.02 Da. Met oxidation was considered a variable modification, while Cys carbamidomethylation and Lys and peptide N-terminal modification of +229.163 were set as fixed modifications. The corresponding inverted protein sequences were incorporated to the database for false discovery rate (FDR) calculation. Peptide identification from MS/MS data was performed using the probability ratio method[57], and the FDR of peptide identifications was calculated using the refined method after precursor mass tolerance post filtering at 15 ppm[58,59], taking 1% FDR as a threshold for peptide identification. Peptides were assigned only to the best protein proposed by the Proteome Discoverer algorithm.

Peptide and protein quantification

The quantitative information extracted from the MS/MS spectra by Proteome Discoverer was integrated from the spectrum level to the peptide level and then to the protein level on the basis of the WSPP model[60] and the systems biology triangle algorithm[61] using the SanXoT software package[62]. In brief, in every scan the $x_{qps} = \log_2 A/B$ was calculated using the TMT reporter ion intensities coming from samples A and B. The statistical weight w_{qps} of each scan was calculated as described[60]. The $\log_2$-ratio of every peptide (x_{qp}) was calculated as the weighted average of its scans, whereas the quantification of each protein (x_p) was the weighted average of its peptides, and the grand mean ($\bar{x}$) was the weighted average of all the protein values[60]. Peptide and protein quantification weights (w_{qp} and w_q, respectively) were calculated from the corresponding scan weights and the peptide variance (σ_p^2) or the peptide weights and the protein variance (σ_Q^2), respectively[60]. The standardized variable at the peptide level, z_{pq}, was calculated as:

$$z_{pq} = (x_{pq} - x_q) \times \sqrt{w_{pq}} \times \sqrt{\frac{n_p}{n_p - 1}}, n_p > 1 \quad (1)$$

expressing the deviation between the $\log_2$-ratio quantifications of the peptide p coming from the protein q, quantified with n_p peptides. Similarly, the standardized variable at the protein level, z_q, was calculated as:

$$z_q = (x_q - \bar{x}) \times \sqrt{w_q} \times \sqrt{\frac{n_q}{n_q - 1}}, n_q > 1 \quad (2)$$

where n_q is the number of quantified proteins in the whole experiment. The validity of the null hypothesis was carefully checked at every level (spectrum, peptide and protein) by plotting the cumulative distributions with zero mean and unit variance[60]. Outliers at the peptide and protein levels were detected at 1% FDR as described in[60].

Quantification of protein function

The proteins quantified were functionally annotated using the Gene Ontology[63] database. Quantitative assessment of protein function between samples was carried out using SanXoT as described[62].

RNA sequencing and analysis

In brief, total RNA was prepared with RNeasy Mini kit (Qiagen) by standard protocols (74104, Qiagen RNeasy mini Kit) from 4 biological replicates. cDNA was synthesized and amplified from total RNA (1–10 ng) using the Ovation RNA-seq System v2 (NuGEN Technologies). Sequencing was performed using the Illumina HiSeq-2500 system (1×50 8M reads). Transcript abundances were quantified with the Ensembl GRCh38 cDNA reference using RSEM. The expression matrix was filtered for only transcripts with greater than 5 TPM in replicates. Only genes with at least 1 count per million in the 3 or 4 replicates were considered for statistical analysis. Differential expression statistics between knockout and control were generated using limma with TMM normalization. Genes with a Benjamini–Hochberg adjusted P value < 0.05 and a cut-off of 0.6 in logFC were considered DEGs. GO term enrichment was performed using Panther (http://pantherdb.org) applying Bonferroni and Ingenuity analysis (IPA, Qiagen). Heat maps and volcano plots were built using RStudio (version 1.2.5033). These experiments were performed at the CNIC Genomics and Bioinformatics Units (Supplementary File 1).

ChIP–seq

ChIP–seq was performed in individual P0 hearts. Each heart was extracted, washed twice in cold 1× PBS and resuspended in 10 ml 1× PBS supplemented with cOmplete EDTA-free protease inhibitor (05056489001, Roche). The whole tissue was fixed with 1% formaldehyde (28906, Thermo Fisher Scientific) for 15 min at room temperature and gently balance. The reaction was quenched with 125 mM glycine for 5 min at room temperature followed by two washes with 1× PBS. Fixed heart was resuspended in 1 ml heart buffer (10 mM Tris-HCl pH 7.5, 1 mM EDTA, 0.5% SDS, 0.2% Triton X-100), minced and incubated in a rotator for 30 min at room temperature. The mixture was next transferred to pre-chilled 1 ml AFA tube (Covaris) and sheared in a S220 Focused-ultrasonicator (Covaris) for 20 min (duty 10%, cycle 200, PIP 140 and one cycle/ per 20 s). After sonication, chromatin was diluted 1:1 in ChIP dilution buffer (0.01% SDS, 1.1% Triton X-100, 1.2 mM EDTA,

16.7 mM Tris-HCl pH 8, 167 mM NaCl, cOmplete EDTA-free protease inhibitor) and 20 µl was removed and kept as input. For immunoprecipitation, the remaining chromatin volume was incubated with either 5 µl H3K27ac antibody (39135, ActiveMotif, 1:400) or 5 µl pan-RXR antibody (21218-1-AP, ProteinTech, 1:400) in a rotator at 4 °C overnight. The next day, 50 µl of Dynabeads A (10001D, Thermo Fisher Scientific) were washed twice with 2 volumes of cold ChIP dilution buffer, resuspended in the initial volume added to chromatin+antibody mixture. After 2 h, beads were washed 5 times with RIPA buffer (50 mM HEPES-KOH pH 7.5, 500 mM LiCl, 1 mM EDTA, 1% NP-40, 0.7% sodium deoxycholate) and 1 time with final wash buffer (1× Tris-EDTA, 50 mM NaCl). Each wash consisted of 1 ml of buffer for 2 min in the cold-room rotator. Next, beads were resuspended in 205 µl of fresh elution buffer (50 mM Tris-HCl pH 8, 10 mM EDTA, 1% SDS) and incubated at 55 °C 30 min. Two-hundred microlitres of eluate were moved to a DNA lo-bind tube and 32 µl of reverse crosslinking buffer (250 mM Tris-HCl pH 7.5, 32.5 mM EDTA pH 8, 1.25 M NaCl, 5 mg ml^{-1} proteinase K) were added and incubated at 65 °C overnight. Input was completed with 180 µl molecular biology water and treated in the same way. DNA was purified using ChIP Clean and Concetrator Zymo kit (D5201, Zymo Research). DNA concentration and size distribution were checked with Qbit dsDNA HS Assay kit (Thermo Fisher Scientific) and Bioanalyzer DNA High Sensitivity Kit (Agilent), respectively. Libraries were prepared according standard protocols and sequenced in HiSeq 3000 (Illumina) with an average of 20 million single-end reads per sample.

ChIP–seq processing and analysis

Sequencing reads were pre-processed with Cutadapt v1.7.1[64] to remove adapter remains. Pre-processed reads were mapped against reference genome mm10 with a pipeline that used BWA 0.7.10 as aligner[65], Piccard to mark duplicate alignments (http://picard.sourceforge.net), and samtools v0.1.18[66] to eliminate multi-mapped alignments. Only mapped reads were kept. Alignments against the mitochondrial genome or chromosomes X and Y were also removed. Once filtered alignments had been obtained, ChIP peaks were called with MACS2 v2.1.1[67], using parameter "-q 0.05" as the FDR cut-off, using ChIP and control files as input. Next, filtered alignments and peaks were processed with the R package DiffBind[68,69] to define a consensus set of peaks, to calculate and normalize their coverage in all samples, and to identify differentially occupied regions, using EdgeR[70] as analysis method. UCSC genome browser was used for visualization of ChIP–seq reads in selected genomic regions. The overlap between ATAC–seq and ChIP–seq peaks was tested with bedtools v2.24.0[71], and motif enrichment analyses were performed with HOMER v4.10.3[72] (Supplementary File 1).

ATAC–seq in neonatal hearts

Chromatin accessibility experiments were performed according B.Ren ENCODE ATAC–seq protocol (https://www.encodeproject.org/experiments/ENCSR451NAE/) with minor modifications. In brief, P0 hearts from EDKO and Control mice were processed individually. Cardiac tissue was pulverized with liquid N_2. 10 mg pulverized tissue was resuspended in 1 ml NPB buffer (5% BSA, (A7906, Sigma); 0.2% IGEPAL (I8896, Sigma), 1 mM DTT (D9779, Sigma), 1×cOmplete EDTA-free protease inhibitor (05056489001, Roche) in 1× PBS) and rotated for 10 min at 4 °C. Nuclei suspension was filtered using a 30 µm CellTrics (25004-0042-2316, Sysmex) and spin down for 5 min at 500*g* at 4 °C. Nuclei were resuspended in TB buffer (33 mM Tris-acetate pH 7.8 (BP-152, Thermo Fisher Scientific), 66 mM potassium acetate (P5708, Sigma), 11 mM magnesium acetate (M2545, Sigma), 16% DMF (DX1730, EMD Millipore) in molecular biology water) and nuclei concentration was quantified using and haemocytometer and Trypan Blue stain (15250061, Thermo Fisher Scientific). Nucleus concentration was adjusted to 50,000 nuclei per µl with TB buffer. Transposase reaction was performed by mixing 10 µl nuclei solution (50,000 total nuclei) and 0.5 µl Tagment DNA Enzyme 1 (FC-121-1030, Illumina) and incubated 30 min with 500 rpm at 37 °C. Tagmented DNA was purified using MinElute PCR Purification Kit (28004,Qiagen) and eluted in 10 µl EB. For library preparation, barcodes were added by mixing 10 µl tagmented DNA, 11 µl NEBNext 2× PCR Master mix (M0541), 0.2 µl primer Ad1_noMx 100 µM (forward), 0.2 µl Ad2.X 100 µM (reverse, different for each sample), 0.6 µl molecular biology water and with the following PCR programme: 72 °C 5 min, 98 °C 30 s, 8 cycles (98 °C × 10 s, 63 °C × 30 s, 72 °C 1 min). Primers were made as described elsewhere[21]. PCR product was again purified with MinElute PCR Purification Kit (28004, Qiagen) and eluted in 50 µl EB. We next performed 0.65× size selection followed by 1.5× clean-up with AMPure XP beads (A63880, Beckman Coulter). Depending on library concentration, additional PCRs cycles (98 °C × 30 s, (98 °C × 10 s, 63 °C × 30 s, 72 °C × 1 min) for 5–8 cycles depending on the sample) were performed. Libraries were purified with AMPure XP beads, and concentration was measured by the Qbit dsDNA HS Assay kit (Thermo Fisher Scientific) and fragment profiles were analysed with the Bioanalyzer DNA High Sensitivity Kit (Agilent). Libraries were sequenced on 2×50 HiSeq 3000 (Illumina) and with an average of 25 million paired-end reads per sample.

ATAC–seq processing and analysis

Cutadapt v1.7.1 was used to trim adapters (http://journal.embnet.org/index.php/embnetjournal/article/view/200). Trimmed paired-end reads were aligned to the mm10 mouse reference genome using Bowtie2 v4.1.2[73] with settings -X 2000 -very-sensitive in paired-end mode. Duplicates were marked with PICARD tools (http://picard.sourceforge.net). Reads were subsequently filtered for alignment quality (>Q30) and were required to be properly paired.Duplicates and reads mapping to the mitochondria, unmapped contigs or chromosomes X and Y were removed. Secondary alignments were not considered. ATAC–seq peaks were called using MACS2 v2.1.1[67] with parameters -nomodel -shift 100 -extsize 200 -keep-dup all -pval 0.001. Peaks falling within mouse mm10 ENCODE blacklisted regions (http://mitra.stanford.edu/kundaje/akundaje/release/blacklists/mm10-mouse) were discarded using bedtools v2.24.0 intersect. A consensus peak set of peaks detected in at least two samples was generated using function dba.counts from DiffBind R package v2.6.6 (http://bioconductor.org/packages/release/bioc/htmL/DiffBind.htmL). EdgeR v3.20.9[70] was used to perform a differential accessibility analysis on the set of consensus peaks using Diffbind functions (dba.analyze). Control-increased chromatin accesibility regions were defined by log2 fold change in read density > 1 and adjusted *P* value < 0.05. Conversely, EDKO-increased chromatin accessibility regions were defined by log2 fold change < −1 and adjusted *P* value < 0.05. Differentially accessible peaks were associated to the gene with the nearest TSS using command annotatePeaks.pl from the HOMER v4.10.3[72]. UCSC genome browser was used for visualization of ATAC–seq reads in selected genomic regions. Transcription factor motif enrichment analyses for genomic regions showing differential accessibility were performed using HOMER command findMotifsGenome.pl. EDKO peaks with increased accessibility were compared to control peaks and vice versa (Supplementary File 1).

GC–MS metabolomics

Neonatal hearts were excised and frozen in liquid N_2. Similar amounts were added to 100 µl of cold 100% methanol and homogenated using a TissueLyser (Qiagen) −3.8 (1 ball) 50 Hz speed for 5 min. Metabolite extraction, derivatization, instrumental analysis and data analysis were performed as recently described[74]. For metabolite extraction, 50 µl homogenate were mixed with 100 µl 100% methanol in a vortex for 20 min at room temperature and centrifuged at 4,000*g* for 20 min at room temperature. Fifty microlitres of supernatant were taken and dried in Speedvac. For derivatization first step, 20 µl of O-methoxyamine HCL in pyridine was added, ultrasonicated (2 min, 3 cycles), vortexed for 5 min and incubated in darkness at room temperature for 16 h. Derivatization step 2 consisted of vortexing for 5 min with 20 µl of BSTFA, 1 h incubation at 70 °C and cool-down in the darkness for

30 min. Next, 100 µl of 10 ppm internal standard was incorporated and centrifuged for 15 min at 700*g* at room temperature. The analysis was performed with an GC instrument (7890 A) coupled to an inert mass spectrometer with Triple-Axis Detector (5975C), both from Agilent Technologies. Data were acquired using the Agilent MSD ChemStation software. Deconvolution and metabolite identification of raw data collected by GC–MS analysis were performed by Agilent MassHunter Unknowns Analysis Tool 7.0. A chemical identity was assigned to the compounds by the software by searching in two target libraries: Fiehn library and NIST (National Institute of Standards and Technology) B09.0 2017. Data were aligned using Agilent MassProfiler Professional 13.1 and integration was performed with Agilent MassHunter Quantitative. The raw data collected by GC–MS was cleaned of background noise with Microsoft Excel. To keep only metabolites with a good repeatability only features with RSD <25% in QC were evaluated as relevant. Data was normalized by Total Useful Signal (TUS). For univariate analysis, differences between groups (EDKO versus control) for GC–MS analysis were evaluated for individual metabolites using univariate statistical analysis after $\log_2$ transformation of the data and normalization by TUS. Unpaired *t*-test with Bonferroni FWER were performed with Mass Profiler Professional 13.1.

In silico ligand-docking analysis

Fasta sequences of mouse RXRa (Uniprot ID P28700) was aligned to Uniclust·30 (release 08-2018) and pdb70 (release 09-2019) databases using the hhblits/hhsearch tools of the HH-suite3[75] to obtain a multisequence alignment (MSA) and pdb templates for comparative modelling. For docking the monomer, a comparative modelling was made using de RosettaCM[76] tool of the of Rosetta suite v3.12 (https://www.rosettacommons.org) with the fasta sequence, the alignment and templates obtained before. The models obtained were clustered using the cluster tool of Rosetta suite v3.12 and the bigger clusters were selected. A multi structural alignment (MSTA) of the models selected with the templates was made using the mTMAlign tool[77,78]. The model with best structural alignment to the templates was selected as final candidate. A final cycle of refinement for minimize clashes and energy was made with the relax tool[79,80] of Rosetta suite v3.12. At least 100 independent models were calculated. The model with correct topology and minimal score was selected as final model. To model the dimer form of RXRα, a MSTA of the model obtained before and 4nqaAH.pdb structure to generate a template and a symmetric restrictions file (order 2) for docking the dimer using the symmetric docking protocol of Rosetta suite v3.12. Models with positive energy were cut-off and filtered models were clustered as before and the bigger cluster was MSTA using the MMAlign tool[81]. The model with best MSTA to template was selected as final model. To evaluate energy of the complex and the interface, the model was analysed with the InterfaceAnalyzer tool of Rosetta suite v3.12. To compare the effect of different ligands GLA and DGLA, the complex of each one with the models of RXRα homodimer modelled before were docked with the ligand-docking tool using the Rosetta script[82,83] of the Rosetta software suite v3.12. In brief, a representative conformer of the ligand was located close to the ligand pocket in chain A of the receptor complex RXRα dimer (MSTA to 1fm9). The protocol compute combinations of atomic coordinates for conformers of ligand and rearrangement of the sidechain (rotamers) of the residues of the receptor to explore the conformational space to find interactions between ligand and protein. In all cases, at least 1,000 models were computed and the model with correct interface topology (ligand inside the pocket without clashes between ligand and protein) and best energy interface (minor ΔG, more stability and interactions between protein and ligand like electrostatic, hydrophobic/hydrophilic, van der Waals and hydrogen bonds or salt bridges) was selected. A final cycle of refinement for minimize clashes and energy was made with the relax tool. At least, 100 independent models were calculated for each one. As before, the model with correct topology and minimal score was selected as final model candidate. The protocol before was repeated with a new ligand residue in the second pocket in chain B for each model candidate to obtain final models.

Luciferase assays

For transient transfection, 80,000 cells HEK293T cells were seeded and transfected with jetPEI transfection reagent (Polyplus) following the manufacturer's instructions. We transfected $(AOX)_3$-TK or UAS-TK luciferase reporters together with expression plasmids for human RXRα, human RXRα(ΔAF2), GAL4-RXRα, GAL4-RXRα(ΔAF2), coactivator SRC1 or pCMX empty vector, as a negative control. GAL4 constructs were provided by J. S. Welch[35]. After a transient transfection of 6 h, cells were treated with LG268 (1 µM), GLA–BSA (500 µM) or UVI3003 (1 µM) together with 500 µM GLA–BSA for 24 h hours. Luciferase activity was measured with Luciferase Assay System (Promega).

Protein expression and purification

Non-liganded recombinant human RXRα-LBD (residues 223–462) cloned into a pET15b expression vector was expressed in BL21 (DE3) bacterial strain as fusion proteins with an N-terminal hexahistidine (His) tag and purified to homogeneity using standard chromatographic procedures[84]. Cells were grown in LB medium and induced overnight with 1 mM isopropyl-β-D-thiogalactopyranoside (IPTG) at 16 °C. The purification procedure included two sequential affinity chromatography steps using a nickel chelating column. His tag was removed using thrombin digestion overnight during dialysis. Protein samples contained 20 mM HEPES, 500 mM NaCl, 10% glycerol, 75 mM imidazole, 1 mM DTT at pH 8.0. SDS–PAGE was used to assess purity and homogeneity of protein samples.

Surface plasmon resonance analysis

Surface plasmon resonance analyses were performed at 25 °C in a BIAcore T200 instrument (GE Healthcare). Highly purified, recombinant and unliganded RXRα-LBD protein was diluted in 10 mM sodium acetate pH 5.0, and directly immobilized as ligand on CM5 chips (GE Healthcare) by amine coupling at a density of 4,000 RU. As a reference, one of the channels was also amine-activated and blocked in the absence of protein. The running buffer was 1x PBS, 5% DMSO and 0.05% Tween. The compound GLA and an SRC3-2 coactivator derived-peptided were used as analyte and injected in solution over the immobilized protein sample. Sensorgrams were analysed with the BIAcore T200 Evaluation software 3.0 and fitted according to the Langmuir 1:1 model.

Statistical analysis

Data are presented as mean ± s.e.m. Unpaired *t*-test was used when two groups were compared, and comparison of more than two datasets was done using one-way analysis of variance (ANOVA) with Tukey's post-test. When indicated, Benjamini–Hochberg correction was applied to correct multiple-testing per genes. Comparisons of two-time curves or datasets were performed using two-way ANOVA followed by Tukey's post-test. For blood lactate and glucose determinations, non-parametric Kruskal–Wallis (Dun´s correction) was applied. All statistical analyses were performed using Prism v7 (GraphPad Software). Differences were considered significant when $P < 0.05$, and represented as $^{*}P < 0.05$, $^{**}P < 0.01$, $^{***}P < 0.001$, and $^{****}P < 0.0001$. Sample exclusion was not performed unless statistically significant outliers were identified using Grubb's test (ESD method).

Reporting summary

Further information on research design is available in the Nature Portfolio Reporting Summary linked to this article.

Data availability

Data generated from RNA-seq, ATAC–seq and ChIP–seq have been deposited in the Gene Expression Omnibus with the accession number

GSE18899. Source data for main and extended data figures are available online as separate Excel files for each figure. Lipidomics raw data from cardiac tissue (Fig. 2d) and milk (Fig. 4h) can be found in Supplementary Table 1 and Supplementary Table 2, respectively. Source data are provided with this paper.

44. Li, M. et al. Retinoid X receptor ablation in adult mouse keratinocytes generates an atopic dermatitis triggered by thymic stromal lymphopoietin. *Proc. Natl Acad. Sci. USA* **102**, 14795–14800 (2005).
45. Cruz-Adalia, A. et al. CD69 limits the severity of cardiomyopathy after autoimmune myocarditis. *Circulation* **122**, 1396–1404 (2010).
46. Ram, R., Mickelsen, D. M., Theodoropoulos, C. & Blaxall, B. C. New approaches in small animal echocardiography: imaging the sounds of silence. *Am. J. Physiol.* **301**, H1765–H1780 (2011).
47. Koelmel, J. P. et al. Lipid annotator: towards accurate annotation in non-targeted liquid chromatography high-resolution tandem mass spectrometry (LC–HRMS/MS) lipidomics using a rapid and user-friendly software. *Metabolites* **10**, 101 (2020).
48. Tsugawa, H. et al. A lipidome atlas in MS-DIAL 4. *Nat. Biotechnol.* **38**, 1159–1163 (2020).
49. Ortega-Senovilla, H., Schaefer-Graf, U. & Herrera, E. Pregnant women with gestational diabetes and with well controlled glucose levels have decreased concentrations of individual fatty acids in maternal and cord serum. *Diabetologia* **63**, 864–874 (2020).
50. Alonso-Herranz, L. et al. Macrophages promote endothelial-to-mesenchymal transition via MT1-MMP/TGFβ1 after myocardial infarction. *eLife* **9**, e57920 (2020).
51. Li, Z., Ross Stewart, K. M., Bruton, F. A., Denvir, M. A. & Brittan, M. in *Angiogenesis: Methods and Protocols* (ed. Benest, A. V.) 297–309 (Springer, 2022).
52. Quiros, P. M., Goyal, A., Jha, P. & Auwerx, J. Analysis of mtDNA/nDNA ratio in mice. *Curr. Protoc. Mouse Biol.* **7**, 47–54 (2017).
53. Fernandez-Vizarra, E., Lopez-Perez, M. J. & Enriquez, J. A. Isolation of biogenetically competent mitochondria from mammalian tissues and cultured cells. *Methods* **26**, 292–297 (2002).
54. Bradford, M. M. A rapid and sensitive method for the quantitation of microgram quantities of protein utilizing the principle of protein-dye binding. *Anal. Biochem.* **72**, 248–254 (1976).
55. Vives-Bauza, C., Yang, L. & Manfredi, G. Assay of mitochondrial ATP synthesis in animal cells and tissues. *Methods Cell. Biol.* **80**, 155–171 (2007).
56. Herrero-Mendez, A. et al. The bioenergetic and antioxidant status of neurons is controlled by continuous degradation of a key glycolytic enzyme by APC/C-Cdh1. *Nat. Cell Biol.* **11**, 747–752 (2009).
57. Martinez-Bartolome, S. et al. Properties of average score distributions of SEQUEST: the probability ratio method. *Mol. Cell. Proteomics* **7**, 1135–1145 (2008).
58. Navarro, P. & Vazquez, J. A refined method to calculate false discovery rates for peptide identification using decoy databases. *J. Proteome Res.* **8**, 1792–1796 (2009).
59. Bonzon-Kulichenko, E., Garcia-Marques, F., Trevisan-Herraz, M. & Vazquez, J. Revisiting peptide identification by high-accuracy mass spectrometry: problems associated with the use of narrow mass precursor windows. *J. Proteome Res.* **14**, 700–710 (2015).
60. Navarro, P. et al. General statistical framework for quantitative proteomics by stable isotope labeling. *J. Proteome Res.* **13**, 1234–1247 (2014).
61. Garcia-Marques, F. et al. A novel systems-biology algorithm for the analysis of coordinated protein responses using quantitative proteomics. *Mol. Cell. Proteomics* **15**, 1740–1760 (2016).
62. Trevisan-Herraz, M. et al. SanXoT: a modular and versatile package for the quantitative analysis of high-throughput proteomics experiments. *Bioinformatics* **35**, 1594–1596 (2018).
63. The Gene Ontology Consortium. The Gene Ontology Resource: 20 years and still GOing strong. *Nucleic Acids Res.* **47**, D330–D338 (2019).
64. Martin, M. Cutadapt removes adapter sequences from high-throughput sequencing reads. *EMBnet.journal* **17**, 10–12 (2011).
65. Li, H. & Durbin, R. Fast and accurate short read alignment with Burrows–Wheeler transform. *Bioinformatics* **25**, 1754–1760 (2009).
66. Li, H. et al. The Sequence Alignment/Map format and SAMtools. *Bioinformatics* **25**, 2078–2079 (2009).
67. Zhang, Y. et al. Model-based analysis of ChIP–seq (MACS). *Genome Biol.* **9**, R137 (2008).
68. Ross-Innes, C. S. et al. Differential oestrogen receptor binding is associated with clinical outcome in breast cancer. *Nature* **481**, 389–393 (2012).
69. Stark, R. & Brown, G. DiffBind: differential binding analysis of ChIP–seq peak data. https://bioconductor.org/packages/devel/bioc/vignettes/DiffBind/inst/doc/DiffBind.pdf (2011).
70. Robinson, M. D., McCarthy, D. J. & Smyth, G. K. edgeR: a Bioconductor package for differential expression analysis of digital gene expression data. *Bioinformatics* **26**, 139–140 (2010).
71. Quinlan, A. R. & Hall, I. M. BEDTools: a flexible suite of utilities for comparing genomic features. *Bioinformatics* **26**, 841–842 (2010).
72. Heinz, S. et al. Simple combinations of lineage-determining transcription factors prime *cis*-regulatory elements required for macrophage and B cell identities. *Mol. Cell* **38**, 576–589 (2010).
73. Langmead, B. & Salzberg, S. L. Fast gapped-read alignment with Bowtie 2. *Nat. Methods* **9**, 357–359 (2012).
74. Rey-Stolle, F. et al. Low and high resolution gas chromatography-mass spectrometry for untargeted metabolomics: a tutorial. *Anal. Chim. Acta* **1210**, 339043 (2021).
75. Steinegger, M. et al. HH-suite3 for fast remote homology detection and deep protein annotation. *BMC Bioinformatics* **20**, 473 (2019).
76. Song, Y. et al. High-resolution comparative modeling with RosettaCM. *Structure* **21**, 1735–1742 (2013).
77. Dong, R., Pan, S., Peng, Z., Zhang, Y. & Yang, J. mTM-align: a server for fast protein structure database search and multiple protein structure alignment. *Nucleic Acids Res.* **46**, W380–w386 (2018).
78. Dong, R., Peng, Z., Zhang, Y. & Yang, J. mTM-align: an algorithm for fast and accurate multiple protein structure alignment. *Bioinformatics* **34**, 1719–1725 (2018).
79. Conway, P., Tyka, M. D., DiMaio, F., Konerding, D. E. & Baker, D. Relaxation of backbone bond geometry improves protein energy landscape modeling. *Protein Sci.* **23**, 47–55 (2014).
80. Nivón, L. G., Moretti, R. & Baker, D. A Pareto-optimal refinement method for protein design scaffolds. *PLoS ONE* **8**, e59004 (2013).
81. Mukherjee, S. & Zhang, Y. MM-align: a quick algorithm for aligning multiple-chain protein complex structures using iterative dynamic programming. *Nucleic Acids Res.* **37**, e83 (2009).
82. Capra, J. A., Laskowski, R. A., Thornton, J. M., Singh, M. & Funkhouser, T. A. Predicting protein ligand binding sites by combining evolutionary sequence conservation and 3D structure. *PLoS Comput. Biol.* **5**, e1000585 (2009).
83. Fleishman, S. J. et al. RosettaScripts: a scripting language interface to the Rosetta macromolecular modeling suite. *PLoS ONE* **6**, e20161 (2011).
84. Egea, P. F. et al. Crystal structure of the human RXRα ligand-binding domain bound to its natural ligand: 9-*cis* retinoic acid. *EMBO J.* **19**, 2592–2601 (2000).

Acknowledgements The authors thank the members of the M.R. and J.A.E laboratories, A. Hidalgo and M. Torres for extensive discussions of the paper; G. Sabio, N. Rochel and D. Metzger for mice and reagents; CNIC and CRG Genomics Units for sequencing; S. Bartlett for editorial assistance; and A.V. Alonso, L. Flores, R. Baeza, R. Santos-Clemente, C. Gifford and N. Spann for technical assistance. J.P.B. is funded by the NextGenerationEU/PRTR and Agencia Estatal de Investigación (10.13039/501100011033; PID2019-105699RB-I00; PDC2021-121013-I00, RED2018-102576-T), Instituto de Salud Carlos III (CB16/10/00282), and Junta de Castilla y León (Apoyo Regional a la Competitividad Empresarial, ICE 04/18/LE/0017 and Escalera de Excelencia CLU-2017-03). D.J.-B. And P.H.A. are recipients of a Juan de la Cierva-Incorporación contracts (IJC2020-044230-I and IJC2020-042679-I, respectively). F.J.R. is funded by the Ministerio de Ciencia e Innovación (MCIN) and European Regional Development Fund FEDER (PID2021-122490NB-I00). V.A.R.S. received funding from Airbus Defense and Space through the CLX-2 programme in partnership with Comando da Aeronautica (COMAER) and the Coordenação de Aperfeiçoamento de Pessoal de Nível Superior-Brasil (CAPES). E.T. received funding from the Swedish Research Council (2020-01150), the Swedish Cancer Society (211582), and the Novo Nordisk Foundation (NNF20OC0063672). J.A.E. was supported by RTI2018-099357-B-I00, MCIU/AEI/ ERDF/UE; RTI2018-099357-B-I00 MCIU/AEI; PID2021-127988OB-100 MCIN/AEI/ 10.13039/501100011033/ERDF,UE; CB16/10/00282 CIBERFES and 17CVD04 Foundation Leducq. This work was supported by grants to M.R.: SAF2017-90604-REDT-NurCaMeIn MINECO/AEI; RTI2018-095928-BI00, MCIU/AEI/ ERDF/UE; PID2021-122552OB-I00 MCIN/AEI/ 10.13039/501100011033/ERDF,UE; 201605-32 Fundació La Marató de TV3; and S2017/BMD-3684 Comunidad de Madrid/ESF/EU, S2022/BMD-7227 Comunidad de Madrid; and an MINECO fellowship to A.P. (BES-2016-076632/AEI/ESF) and to R.J.-M. (PRE2019-087462). The CNIC is supported by the Instituto de Salud Carlos III (ISCIII), the Ministerio de Ciencia e Innovación (MCIN), and the Pro CNIC Foundation, and is a Severo Ochoa Center of Excellence (grant CEX2020-001041-S funded by MICIN/ AEI/ 10.13039/501100011033).

Author contributions Conceptualization: A.P. and M.R. Performed research: A.P., R.J.-M., D.J.-B., V.N., I.C., M.V.-O., A.A., T.F., A.G., V.A.R.S., Z.H., P.H.-A., C.C. and E.C. Software: F.W., F.M. and F.S.-C. Data interpretation and analysis: A.P., R.J.-M, M.V.-O., J.V., J.R.-C., E.A.-G., E.T., J.P.B., E.E.-P., F.J.R., C.B., J.A.E. and M.R. Writing, reviewing and manuscript editing: A.P., J.A.E. and M.R. Project supervision: A.P., J.A.E. and M.R. Funding: M.R.

Competing interests The authors declare no competing interests.

Additional information

Supplementary information The online version contains supplementary material available at https://doi.org/10.1038/s41586-023-06068-7.

Correspondence and requests for materials should be addressed to Mercedes Ricote.

Peer review information *Nature* thanks Christoph Thiele and the other, anonymous, reviewer(s) for their contribution to the peer review of this work.

Reprints and permissions information is available at http://www.nature.com/reprints.

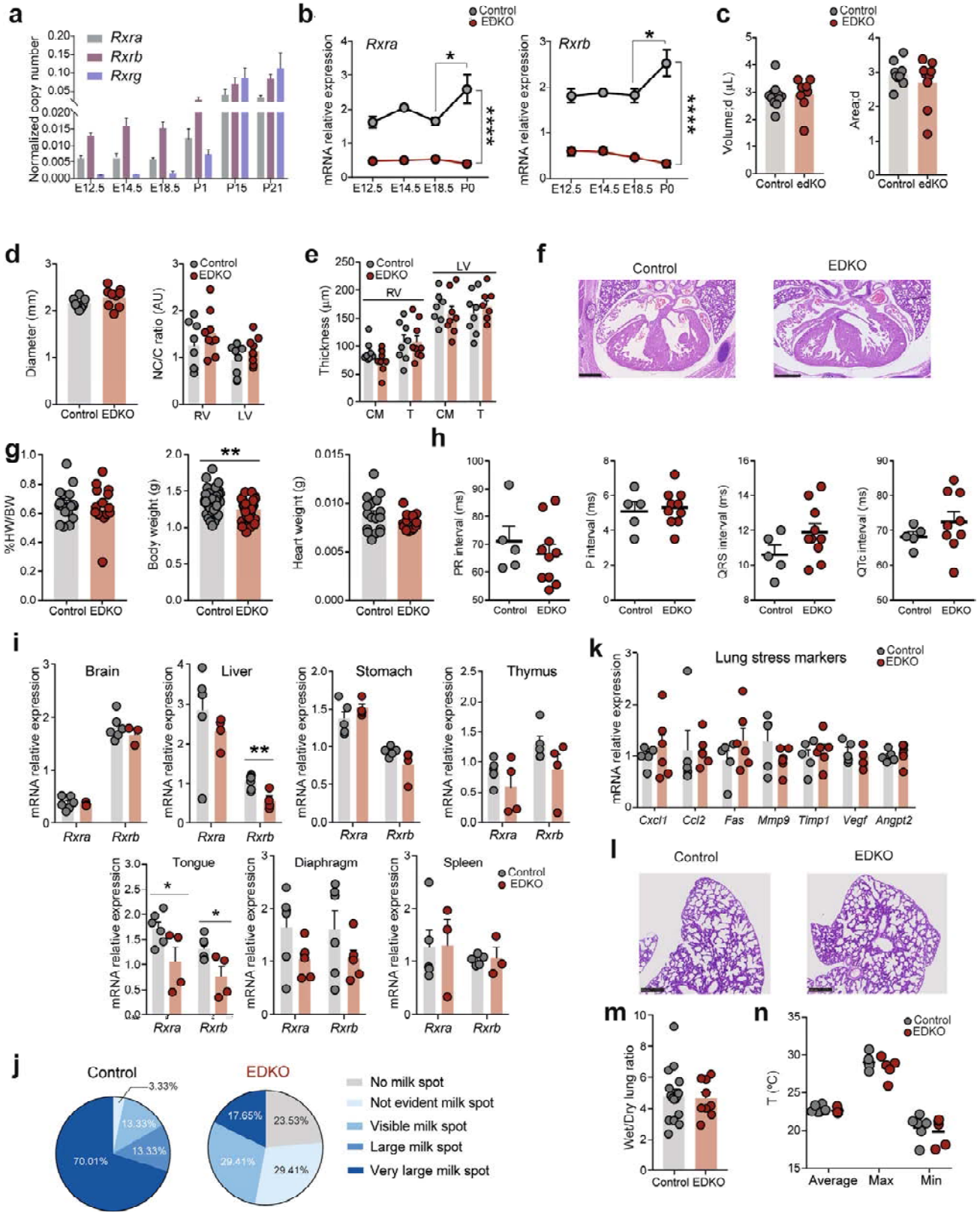

Extended Data Fig. 1 | See next page for caption.

Extended Data Fig. 1 | Functional features of EDKO mice after birth. (a) RXRs gene expression (E12.5 (n = 5), E14.5 (n = 4), E18.5 (n = 5), P1 (n = 4), P15 (n = 4) and P21 (n = 3)) in C57Bl6/J hearts. Data as means±s.e.m. **(b)** *Rxra* and *Rxrb* cardiac expression in EDKO (n = 3-6) and Control (n = 4-6) mice. Data as means±s.e.m. Two-way ANOVA. **(c)** Echocardiography parameters in EDKO (n = 9) and control (n = 11) mice (P0). Data as means±s.e.m. Two-tailed Student t test. **(d)** Left, Heart diameter (mm) and right, non-compacted (NC) and compacted (C) myocardial width in E18.5 EDKO (n = 9) and control (n = 8) mice. Data as means±s.e.m. Two-tailed Student t test. **(e)** Thickness (µm) of trabeculae (T) and compact myocardium (CM) in E18.5 EDKO (n = 9) and control (n = 8) mice. Data as means ± s.e.m. Paired Two-tailed Student t test. **(f)** Hematoxylin-eosin staining of EDKO and control hearts (E18.5). Scale bar = 500 µm. **(g)** Heart weight/body weight ratio (%HWBW) (control = 17, EDKO = 15), body weight (g) (control = 48, EDKO = 33), and heart weight (g) (control = 17, EDKO = 14). Data as means±s.e.m. Two-tailed Student t test. **(h)** Electrocardiography parameters in P0 EDKO (n = 10) and control (n = 5) mice. Data as means±s.e.m. Two-tailed Student t test. **(i)** *Rxra* and *Rxrb* expression in tissues from EDKO (n = 3-6) and control (n = 5-6) mice (P0). Data as means±s.e.m. Two-tailed Student t test. **(j)** Suckling score piecharts for 30 control and 15 EDKO mice. **(k)** Stress markers expression in control (n = 5) and EDKO (n = 6) lungs (P0). Data as means±s.e.m. Two-tailed Student t test. **(l)** Hematoxylin-eosin staining of EDKO and control lungs (P0). Scale bar = 500 µm. **(m)** Wet/Dry lung ratio from control (n = 16) and EDKO (n = 9) (P0) mice. Data as means±s.e.m. Two-tailed Student t test. **(n)** Mean, maximum, and minimum body temperature (°C) in EDKO (n = 5) and control (n = 5) mice at P0. Data as means±s.e.m. Two-tailed Student t test. Exact *P* values in Source Data.

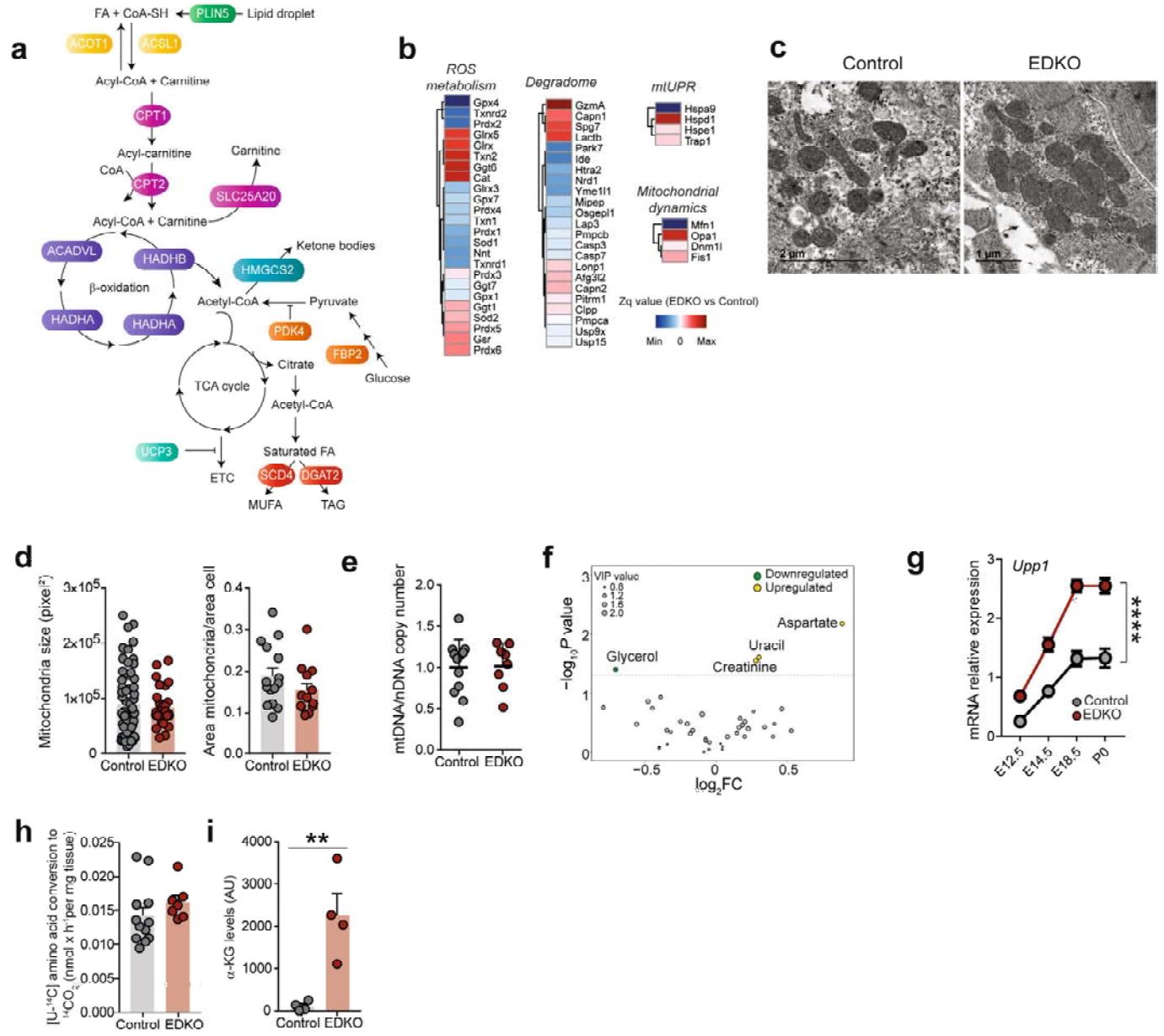

Extended Data Fig. 2 | Cardiac mitochondrial morphology or quantity is not altered in EDKO hearts. (a) Fatty acid-derived energy homeostasis pathway. **(b)** Heatmaps and hierarchical clustering of proteomics enrichment data (Zq value EDKO vs control hearts) for proteins involved in ROS metabolism, the degradome, mitochondrial dynamics, and the mitochondrial unfolded protein response (mtUPR). **(c)** TEM acquisition of cardiac mitochondria at P0 in control and EDKO hearts. **(d)** Left, Mitochondrial area normalized to the cell area in EDKO (n = 3) and control (n = 3) hearts (P0) (arbitrary units). Dots are technical replicates from 3 individual biological replicates/group. Right. Mitochondrial area in EDKO (n = 3) and control (n = 3) hearts (P0). Each dot is one mitochondrion (mean = 25-65 mitochondria/3 mice per condition). Data as means±s.e.m. Two-tailed Student t test. **(e)** Mitochondrial copy number (mtDNA/nDNA) in P0 EDKO (n = 8) and control (n = 12) hearts. Data as means±s.e.m. Two-tailed Student t test. **(f)** GC-MS volcano plot in EDKO and control hearts (P0). $P_{\text{Aspartic acid}} = 0.00669$, $P_{\text{Uracil}} = 0.0249$, $P_{\text{Creatinine}} = 0.02812$, $P_{\text{Glycerol}} = 0.03959$. Log_2FC, log2 fold-change EDKO vs control. The dotted line indicates P value < 0.05. Dot size represents the variable importance parameter (VIP) value. Green and yellow dots represent downregulated and upregulated metabolites, respectively. **(g)** RT-qPCR quantification of *Upp1* in cardiac tissue in EDKO (n = 3-6) and Control (n = 4-6) mice. Data as means±s.e.m. Two-way ANOVA. **(h)** *Ex vivo* rate of amino acid decarboxilation in P0 EDKO (n = 7) and control (n = 12) hearts, measured as [U-^{14}C] amino acid conversion to $^{14}CO_2$ (nmol x h^{-1} per mg tissue). Data as means ± s.e.m. Two-tailed Student t test. **(i)** a-ketoglutarate (α-KG) quantification (area corrected/signal quantification, arbitrary units) in EDKO (n = 4) and control (n = 4) P0 hearts. Data were presented as means±s.e.m. Two-tailed Student t test. *P < 0.05, **P < 0.01, ***P < 0.001, ****P < 0.0001. Exact P values in Source Data.

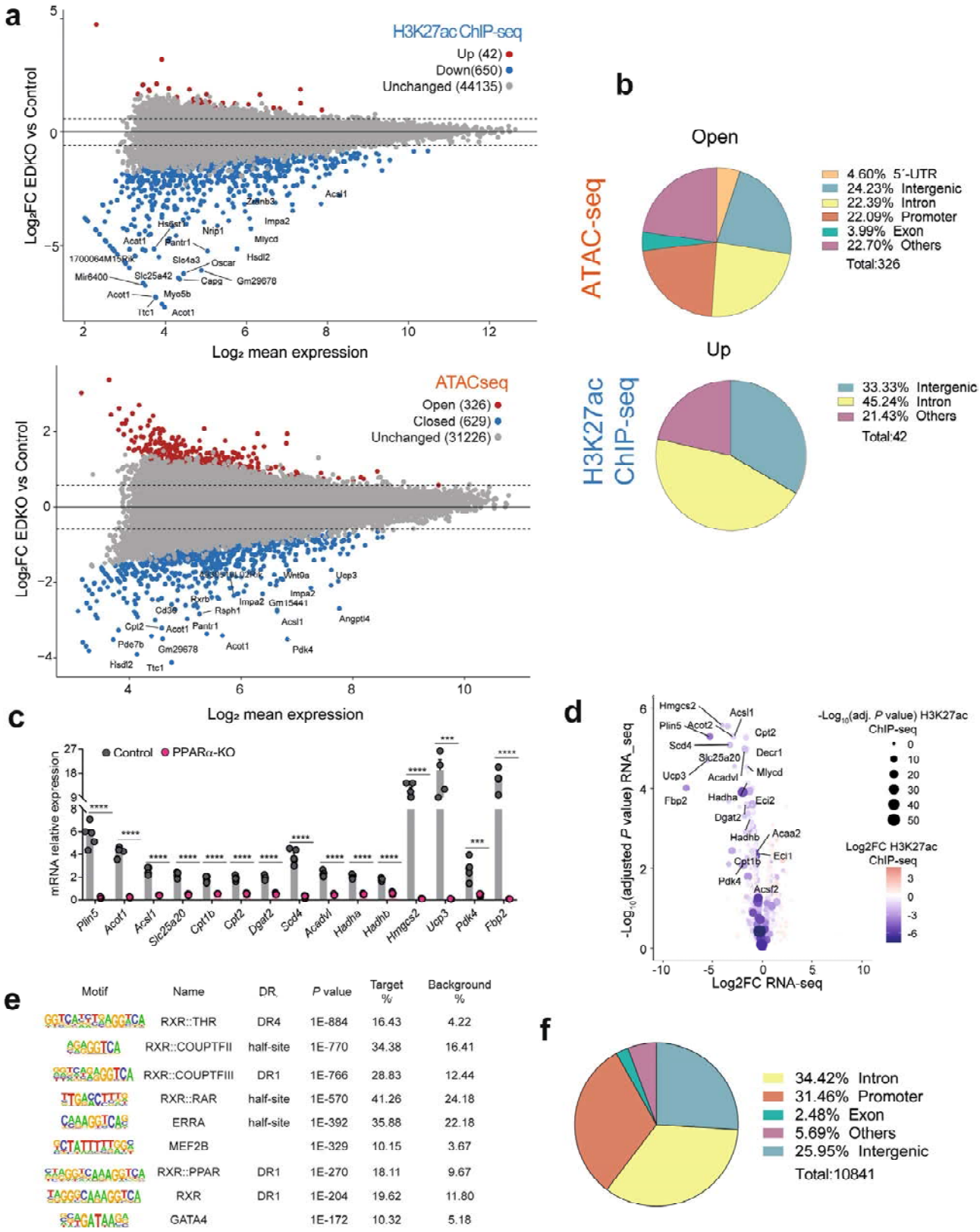

Extended Data Fig. 3 | See next page for caption.

Extended Data Fig. 3 | RXR drives chromatin openness and histone activation of mtFAH signature genes. (a) MA plots representing the H3K27ac ChIP-seq data (left) and ATAC-seq data (right) of changes in chromatin activation and openness in EDKO perinatal hearts, respectively. *x*-axis denotes the log_2mean expression for each peak and *y*-axis indicates Log_2FC EDKO vs control for each peak. Significant (adjusted *P* value < 0.05, Log_2FC = 0.6) active/open and inactive/closed annotated genes are colored in red and blue, respectively. Two-tailed Student t test (Benjamini-Hochberg correction per gene). Top 20 genes are highlighted in each case. **(b)** Annotation distribution of differentially open peaks (ATAC-seq) and differentially active *loci* (H3K27ac ChIP-seq) in EDKO P0 hearts. Total peaks are indicated as well as the percentage of each annotation. **(c)** Relative RT-qPCR quantification of mtFAH genes in cardiac tissue from control (n = 5) and PPARα-null (n = 5) P0 newborns. Independent biological replicates. Data were presented as means ± s.e.m. Two-tailed Student t test. **(d)** Volcano plot depicting the intersection between RNA-seq and H3K27ac ChIP-seq experiments in EDKO P0 hearts. Points are plot according Log_2FC and $-log_{10}$(adjusted *P* value) in RNA-seq experiment. Two-tailed Student t test (Benjamini-Hochberg correction per gene). Color and size are plot according Log_2FC and $-log_{10}$(adjusted *P* value) in H3K27ac ChIP-seq experiment, respectively. **(e)** HOMER motif enrichment analysis. Top-scoring motifs in RXR ChIP-seq peaks are shown, together with *P* values, best-match transcription factors, type of direct repeat sequence (DR) and % of target and background sequences. **(f)** Annotation distribution of RXR cistrome in P0 hearts. Total peaks are indicated as well as the percentage of each annotation. $^{*}P < 0.05$, $^{**}P < 0.01$, $^{***}P < 0.001$, $^{****}P < 0.0001$. Exact *P* values are provided in Source Data.

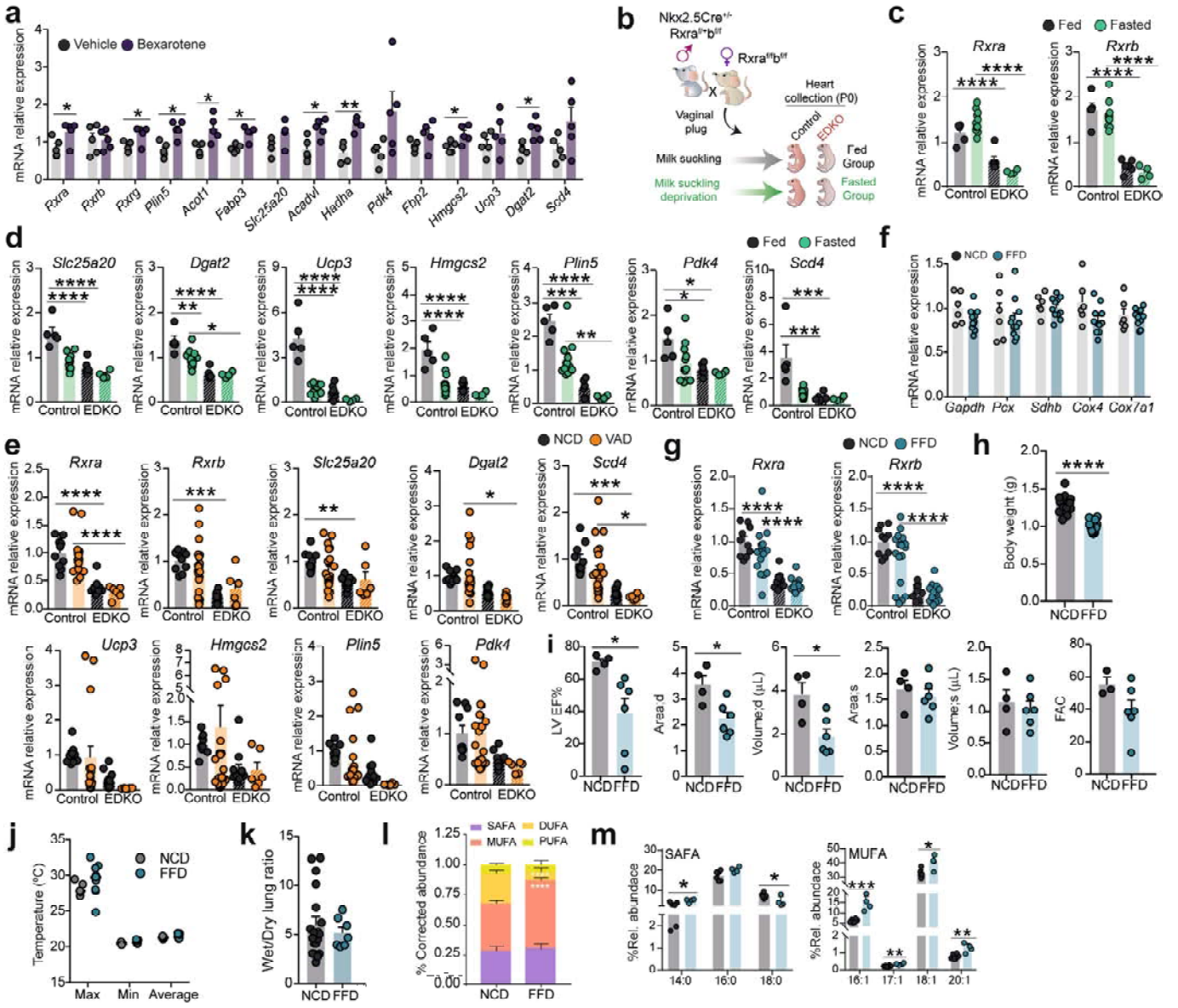

Extended Data Fig. 4 | Fasting and milk-borne vitamin A effects on the mtFAH gene signature. (a) RXR and mtFAH gene expression in C57Bl6/J hearts treated with vehicle (n = 5) or bexarotene (n = 5). Data as means ± s.e.m. Two-tailed Student t test (Benjamini-Hochberg). **(b)** Experimental outline for studying the contribution of milk suckling. **(c)** RXR expression from fed (black) or fasted (green) control (n = 5-12) and EDKO (n = 4-6) hearts. Data as means±s.e.m. Two-way ANOVA (Tukey's) **(d)** mtFAH gene expression from fed or fasted control (n = 5-12) and EDKO (n = 4-6) hearts (P0). Data as mean ± s.e.m. Two-way ANOVA (Tukey's). **(e)** RXR and mtFAH gene expression from control (n = 10-22) and EDKO (n = 6-12) newborns (P0) suckled with NCD or vitamin-A-deficient (VAD) milk. Data as means±s.e.m. Two-way ANOVA (Tukey's). **(f)** Metabolic gene expression from NCD (n = 6) or FFD (n = 11) hearts (P0). Data as mean ± s.e.m. Two-tailed Student t test. **(g)** RXRs gene cardiac expression from control (n = 10-17) and EDKO (n = 12-13) NCD or FFD pups. Data as means±s.e.m. Two-way ANOVA (Tukey). **(h)** Body weight (g) of NCD (n = 12) or FFD (n = 16) newborns (P1). Data as means±s.e.m. Two-tailed Student t test. **(i)** Echocardiography parameters in NCD (n = 4) and FFD (n = 6) newborns. Fractional area change (FAC, %). Data as means±s.e.m. Two-tailed Student t test. **(j)** Body temperature (°C) in FFD (n = 9) and NCD (n = 5) mice (P0). Data as means±s.e.m. Two-tailed Student t test. **(k)** Wet/Dry lung ratio from NCD (n = 19) and FFD (n = 7) (P0) mice. Data as means±s.e.m. Two-tailed Student t test (n = 7-19 mice/condition). **(l)** Corrected abundance of total free FAs in NCD (n = 6) or FFD (n = 4) milk. SAFA, saturated FAs. MUFA, monounsaturated FAs. DUFA, di-unsaturated FAs. PUFA, polyunsaturated FAs. Data as means±s.e.m. Two-tailed Student t test. **(m)** Relative abundance of predominant SAFAs and MUFAs in NCD (n = 6) and FFD (n = 4) milk. Data as means±s.e.m. Two-tailed Student t test. Exact *P* values in Source Data.

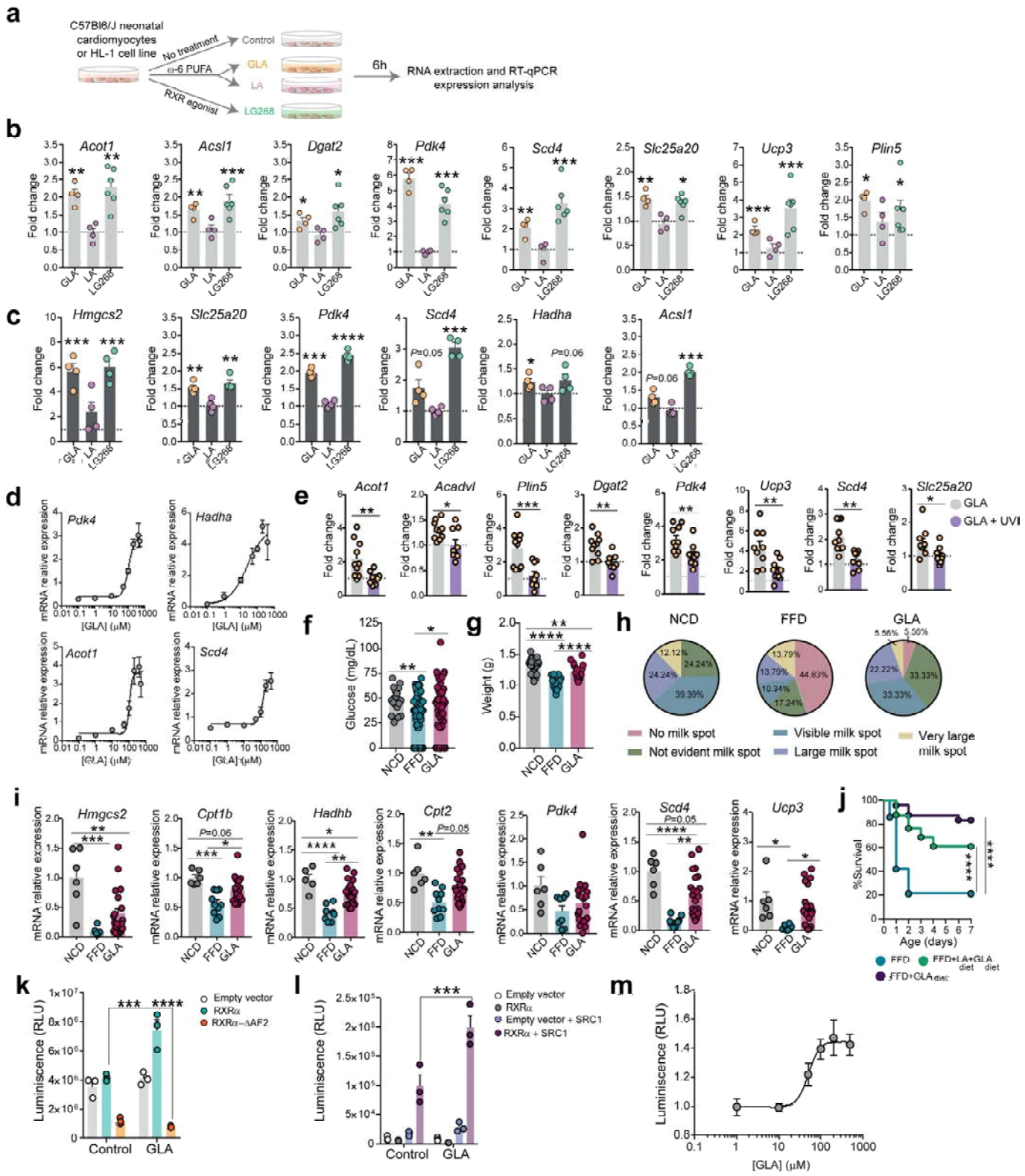

Extended Data Fig. 5 | See next page for caption.

Extended Data Fig. 5 | GLA-RXR activates the expression of mtFAH gene signature. (a) ω-6 fatty acids in vitro stimulation approach. **(b-c)** mtFAH gene expression (% of control) resulting from GLA-BSA (n = 4), LA-BSA (n = 4), and LG268 (n = 4-6) stimulation in primary neonatal cardiomyocytes (nCM) **(b)** or HL1 cell line **(c)**. Data as means±s.e.m. Two-tailed Student t-test (ligand vs baseline, Benjamini-Hochberg). Representative experiment (n = 3). **(d)** Dose-response curves of GLA-BSA stimulation in nCM (n = 3 technical replicates). Representative experiment (n = 3). Data as means±s.e.m. Non-linear regression. **(e)** mtFAH gene signature expression in nCM with GLA-BSA (n = 10) and GLA-BSA +UVI3003 (n = 9). GLA as a %Control, and GLA+UVI as a %Control+UVI. Data as means±s.e.m. Two-way ANOVA (Tukey&Benjamini-Hochberg). **(f)** Blood glucose in NCD (n = 21), FFD (n = 56) or GLA+fat-free-diet (GLA, n = 55) newborns (P0). Data as means±s.e.m. Kruskal-Wallis test (Dunn's). **(g)** Body weight of NCD (n = 34), FFD (n = 17) or GLA (n = 17) newborns. Data as means±s.e.m. One-way ANOVA (Tukey). **(h)** Suckling score piecharts (%) for 33 NCD, 29 FFD, 18 GLA neonates. **(i)** Cardiac mtFAH gene signature expression from NCD (n = 6), FFD (n = 8) or GLA (n = 21) newborns. Data as means±s.e.m. One-way ANOVA (Tukey&Benjamini-Hochberg). **(j)** Kaplan-Meier curve of FFD (n = 64), GLA+LA+fat-free diet milk (n = 33), GLA+fat-free-diet milk (n = 24) mice. Log-Rank test. ($P < 0.00001$). **(k)** $(AOX)_3$-TK-driven luciferase reporter assay in HEK293.T cells. Cells transfected with: empty vector, wild-type RXRα(LBD) (n = 3) or mutated RXRα(LBD)-ΔAF2 (n = 3) and stimulated with GLA-BSA. Data as means±s.e.m. Two-way ANOVA (Tukey's). Representative experiment (n = 3). **(l)** $(AOX)_3$-TK-driven luciferase reporter assay to assess SRC1 coactivator recruitment (HEK293.T cells). Cells transfected with wild-type RXRα(LBD) (n = 3) and/or SRC1 coactivator (n = 3), and treated with GLA-BSA. Data as means±s.e.m. Two-way ANOVA (Tukey). Representative experiment (n = 3). **(m)** Dose-response curves of GLA-BSA in $(AOX)_3$-TK-driven luciferase assay. HEK293.T cells were transfected with wild-type RXRα(LBD) (n = 3). Representative experiment (n = 3). Data as means±s.e.m. Non-linear regression. Exact *P* values in Source Data.

nature portfolio

Corresponding author(s): Mercedes Ricote

Last updated by author(s): 02/03/2023

Reporting Summary

Nature Portfolio wishes to improve the reproducibility of the work that we publish. This form provides structure for consistency and transparency in reporting. For further information on Nature Portfolio policies, see our Editorial Policies and the Editorial Policy Checklist.

Statistics

For all statistical analyses, confirm that the following items are present in the figure legend, table legend, main text, or Methods section.

n/a	Confirmed	
☐	☒	The exact sample size (*n*) for each experimental group/condition, given as a discrete number and unit of measurement
☐	☒	A statement on whether measurements were taken from distinct samples or whether the same sample was measured repeatedly
☐	☒	The statistical test(s) used AND whether they are one- or two-sided *Only common tests should be described solely by name; describe more complex techniques in the Methods section.*
☒	☐	A description of all covariates tested
☐	☒	A description of any assumptions or corrections, such as tests of normality and adjustment for multiple comparisons
☐	☒	A full description of the statistical parameters including central tendency (e.g. means) or other basic estimates (e.g. regression coefficient) AND variation (e.g. standard deviation) or associated estimates of uncertainty (e.g. confidence intervals)
☐	☒	For null hypothesis testing, the test statistic (e.g. *F*, *t*, *r*) with confidence intervals, effect sizes, degrees of freedom and *P* value noted *Give P values as exact values whenever suitable.*
☒	☐	For Bayesian analysis, information on the choice of priors and Markov chain Monte Carlo settings
☒	☐	For hierarchical and complex designs, identification of the appropriate level for tests and full reporting of outcomes
☒	☐	Estimates of effect sizes (e.g. Cohen's *d*, Pearson's *r*), indicating how they were calculated

Our web collection on statistics for biologists contains articles on many of the points above.

Software and code

Policy information about availability of computer code

Data collection	RNA-seq, ChIP-seq and ATAC-seq data were collected with Illumina software. qRT-PCR data was collected with AB7900 thermocycler software (Applied Biosystems). TEM were acquired with Jeol Jem1010 de 100Kv (Tokyo-Japan) electron microscope coupled with Gatan Orius SC200 (Pleasanton CA) digital camera. Echocardiography measurements were obtained using the VEVO 2100 high frequency ultrasound system with a linear transducer MS400 18-38 MHz (Visual Sonics, Toronto, Canada). Thermographic images were acquiered using a FLIR T430sc Infrared Camera (FLIR Systems, Inc., Wilsonville, OR, version 3.4.13235.2002). Chromatographic analysis and detection were carried out in the Agilent Technologies 1290 Infinity II system and Agilent Technologies 6545 Q-TOF (Santa Clara CA, USA). Electrocardiograms were acquired with MP36R amplificator unit (BIOPAC Systems). Proteomics was performed in EASY-nLC 1000 nano-flow HPLC system (Thermo Fisher Scientific) coupled on-line with an orbitrap Fusion mass spectrometer (Thermo Fisher Scientific). GC/MS metabolomics was perfomed in an GC instrument (7890 A) coupled to an inert mass spectrometer with Triple-Axis Detector (5975C), both from Agilent Technologies (Santa Clara CA, USA).
Data analysis	Numerical data was first processed with Microsoft Excel 2016 and after analysed and plotted with Graphpad Prism v7.03. RNA-seq data was analysed following standard software: FastQC v0.11.5 for QC of bulk RNA-seq data, RSEM v1.2.30 for quantification of gene level counts for bulk RNA-seq data, limma v3.32.10 for differential gene expression analysis of bulk RNA-seq data. ATAC-seq and ChIP-seq data was analysed following standard software: FastQC v0.11.5 for QC, reads alignment were performed with BWA 0.7.10 and samtools v0.1.18, peak calling was performed with MACS2 v2.1.1, differential occupancy analysis was performed with EdgeR (edgeR_3.28.1) and motif enrichment analysis was performed with HOMER v4.10.3. Microscope images were processed and analysed/quantified with ImageJ/FIJI v1.53c. Adobe Photoshop CC 19.1.5 and Adobe Illustrator CC v22.1 were used for downstream image analysis and illustration.

For manuscripts utilizing custom algorithms or software that are central to the research but not yet described in published literature, software must be made available to editors and reviewers. We strongly encourage code deposition in a community repository (e.g. GitHub). See the Nature Portfolio guidelines for submitting code & software for further information.

Data

Policy information about availability of data

All manuscripts must include a data availability statement. This statement should provide the following information, where applicable:

- Accession codes, unique identifiers, or web links for publicly available datasets
- A description of any restrictions on data availability
- For clinical datasets or third party data, please ensure that the statement adheres to our policy

RNA-seq, ATA-seq and RXR/H3K27ac ChIP-seqs datasets generated during the current study are available in the GEO repository, under SuperSeries accession number: GSE188998. Mus musculus mm10 genome was used for annotation. For more details, please see "Data analysis" section above.

Field-specific reporting

Please select the one below that is the best fit for your research. If you are not sure, read the appropriate sections before making your selection.

☒ Life sciences ☐ Behavioural & social sciences ☐ Ecological, evolutionary & environmental sciences

For a reference copy of the document with all sections, see nature.com/documents/nr-reporting-summary-flat.pdf

Life sciences study design

All studies must disclose on these points even when the disclosure is negative.

Sample size	Sample size was calculated taking into account the expected experimental variability (based on published and our own protocols) or a posteriori based on the statistical analysis of the data. Statistical analysis was performed as following: unpaired t-test was used when two groups were compared, and comparison of more than two datasets was done using one-way analysis of variance (ANOVA) with Tukey's post-test. For blood glycemia and lactate Mann Whitney test has been used. Comparisons of two-time curves or datasets were performed using two-way ANOVA followed by Tukey's post-test. Graphs represent mean +/- SEM as indicated, and differences were considered significant at $p < 0.05$ as indicated. All calculations were done and represented with GraphPad Prism.
Data exclusions	Data was excluded only if technical problems were detected. Moreover, sample exclusion was performed when statistically significant outliers were identified using Grubb's test (ESD method).
Replication	We repeated the in vivo and in vitro experiments at least 2 or 3 times (we confirmed that all attempts at replication were successful) to guarantee reproducibility. In addition, the main conclusions are supported by several different approaches using mouse models (transgenic models and diet-based nutritional intervention mice model), gene expression profiling and genome-wide techniques.
Randomization	For in vitro experiments samples were allocated randomly in each experiment. For in vivo experiments: i) given that edKO-Control subjects were littermates, randomization was produced by collecting tissues prior genotyping; ii) in FFD/VAD/GLA vs NCD experiments, purely randomization was not possible, as dams where subjected to distinct diets during pregnancy and each litter had to suckle specific intervened maternal milks. To control covariates, dams were individualized and feeding behaviour was monitored. Moreover, when possible, tissues were collected and processed at the same time.
Blinding	Investigators were blinded during data collection. Given the fact that RXR-KO phenotype was indistinguishable from RXR-WT, newborn hearts were collected randomly. For survival curves experiments of RXR-KO mice, mice genotype was performed once the experiment was concluded. For survival curves experiments of FFD (and GLA) control mice, the blinding was not possible due to the utilization of different cages for each diet. For gene expression profiling, hearts were collected and RNA was extracted without prior genotype knowledge. For metabolic assays (ATP synthesis, glycolytic flux and lactate production rate), hearts were collected and analyzed without prior genotype knowledge. Despite metabolic studies, RT-qPCR, omics (ChIP-seq, ATAC-seq), oxygen consumption assays, ATP synthesis, mitochondrial structure assessment were conducted blindly.

Reporting for specific materials, systems and methods

We require information from authors about some types of materials, experimental systems and methods used in many studies. Here, indicate whether each material, system or method listed is relevant to your study. If you are not sure if a list item applies to your research, read the appropriate section before selecting a response.

Materials & experimental systems

n/a	Involved in the study
☐	☒ Antibodies
☐	☒ Eukaryotic cell lines
☒	☐ Palaeontology and archaeology
☐	☒ Animals and other organisms
☒	☐ Human research participants
☒	☐ Clinical data
☒	☐ Dual use research of concern

Methods

n/a	Involved in the study
☐	☒ ChIP-seq
☒	☐ Flow cytometry
☒	☐ MRI-based neuroimaging

Antibodies

Antibodies used: For RXR ChIP-sequencing , RXR antibody #21218-1-AP (ProteinTech) was used.
For H3K27ac ChIP-sequencing, H3K27ac antibody #39135 (ActiveMotif) was used.

Validation: All antibodies used are commercially available and have been pre-validated by the companies and us. Both ChIP antibodies were first validated by ChIP-qPCR assays, where we designed specific primer sets of already known H3K27ac and RXR peaks (obtained from ENCODE). Moreover, H3K27ac peak distribution resulted according to what was expected from previous reports (https://pubmed.ncbi.nlm.nih.gov/22504884/). RXR peak distribution resulted according to what was expected from our previous experiments.

Eukaryotic cell lines

Policy information about cell lines

Cell line source(s): We used HL-1 cells from Pura Muñoz (CNIC), and HEK293.T cells (ATCC) provided by Thierry Fischer.

Authentication: Cells lines were not formally authenticated, but they had the reported phenotype and biology.

Mycoplasma contamination: Cells were routinely checked for mycoplasma contamination and were found to be negative.

Commonly misidentified lines (See ICLAC register): No commonly misidentified cell lines were used.

Animals and other organisms

Policy information about studies involving animals; ARRIVE guidelines recommended for reporting animal research

Laboratory animals: All experiments were performed according to local ethical guidelines and were approved by the Animal Subjects Committee of the Instituto de Salud Carlos III (Madrid, Spain) in accordance with EU Directive 86/609/EEC and Madrid Community Organs in the PROEX 188/26 and PROEX 018.5/21. The CNIC mouse colony (mus musculus) is mantained in racks with individual ventilation cages according to current Spanish and European legislation (RD 53/2013 and EU Directive 63/2010, respectively). Rodents have a dust/pathogen-free bedding, sufficient nesting and environmental enrichment material for the development of species-specific behavior. All the animals have food and water "ad libitum" in environmental conditions of 45-65% of relative humidity, temperature of 21-24ºC and a light/dark cycle of 12:12 hours. In addition and in order to preserve animal welfare, an animal health surveillance program is applied for health monitoring, which follows FELASA recommendations for Specific Pathogen Free facilities.
We used Mus musculus with C57Bl6/J backgrounds. To generate newborns for analysis we intercrossed mice with a age range between 7 and 30 weeks. We do not expect our data to be influenced by animal sex. In this study, we used C57Bl6/J mice, edKO mice and PPARa-null mice (kindly provided by G. Sabio, CNIC).Details about the transgenic are provided in the paper text.

Wild animals: No wild animals were used in the study.

Field-collected samples: No field collected samples were used in the study.

Ethics oversight: All experiments were performed according to local ethical guidelines and were approved by the Animal Subjects Committee of the Instituto de Salud Carlos III (Madrid, Spain) in accordance with EU Directive 86/609/EEC and Madrid Community Organs in the PROEX 188/26 and PROEX 018.5/21.

Note that full information on the approval of the study protocol must also be provided in the manuscript.

ChIP-seq

Data deposition

☒ Confirm that both raw and final processed data have been deposited in a public database such as GEO.

☒ Confirm that you have deposited or provided access to graph files (e.g. BED files) for the called peaks.

Data access links *May remain private before publication.*	GSE188998
Files in database submission	For each sample, raw fastq file and processed file (narrow peak) are available.
Genome browser session (e.g. UCSC)	https://genome.ucsc.edu/s/aparedes/eDKO_RXR_ATAC_K27ac

Methodology

Replicates	In the case of H3K27ac ChIP-seq, 3 biological replicates (including the corresponding input and immunoprecipitation) per genotype were performed. In the case of RXR ChIP-seq, 2 biological replicates per genotype (including the corresponding input and immunoprecipitation) were included in the analysis.
Sequencing depth	Libraries were prepared according standard protocols and sequenced in HiSeq 3000 (Illumina) with an average of 20 million single-end total reads per sample.
Antibodies	For RXR ChIP-sequencing , RXR antibody #21218-1-AP (ProteinTech) was used. For H3K27ac ChIP-sequencing, H3K27ac antibody #39135 (ActiveMotif) was used.
Peak calling parameters	Once filtered alignments had been obtained, ChIP peaks were called with MACS2 v2.1.174, using parameter "-q 0.05" as the false discovery rate cut-off, using ChIP and control files as input.
Data quality	Alignments were filtered with samtools to retain only properly mapped, non duplicate reads, with mapping quality above 0, not aligning to unlocalized or unassembled contigs, the mitochondrial genome, or chromosome Y.
Software	Sequencing reads were pre-processed with Cutadapt v1.7.171 to remove adaptor remains. Pre-processed reads were mapped against reference genome mm10 with a pipeline that used BWA 0.7.10 as aligner72, Piccard to mark duplicate alignments (http://picard.sourceforge.net), and samtools v0.1.1873 to eliminate multi-mapped alignments. Only mapped reads were kept. Alignments against the mitochondrial genome or chromosomes X and Y were also removed. Once filtered alignments had been obtained, ChIP peaks were called with MACS2 v2.1.174, using parameter "-q 0.05" as the false discovery rate cut-off, using ChIP and control files as input. Next, filtered alignments and peaks were processed with the R package DiffBind75,76 to define a consensus set of peaks, to calculate and normalize their coverage in all samples, and to identify differentially occupied regions, using EdgeR77 as analysis method. UCSC genome browser was used for visualization of ChIP-seq reads in selected genomic regions. The overlap between ATACseq and ChIPseq peaks was tested with bedtools v2.24.0,78and motif enrichment analyses were performed with HOMER v4.10.379.

3.4. The mineralocorticoid receptor modulates timing and location of genomic binding by glucocorticoid receptor in response to synthetic glucocorticoids in keratinocytes

Elena Carceller-Zazo, Lisa M. Sevilla, Omar Pons-Alonso, Álvaro Chiner-Oms, Larbi Amazit, Thi An Vu, Géraldine Vitellius, Say Viengchareun, Iñaki Comas, Yan Jaszczyszyn, Montserrat Abella, **Andrea Alegre-Martí**, Eva Estébanez-Perpiñá, Marc Lombès and Paloma Pérez.

Published in: The FASEB Journal, 2022
Impact factor: 5.834
Quartile: Q1
DOI: 10.1096/fj.202201199RR

For this paper I conducted protein expression and purification assays of GR and MR LBDs, as well as the core module of GR. I performed and interpreted surface plasmon resonance assays to investigate the GR and MR homo- and hetero-dimerization. Complexes affinities and lifetimes showed that the preferred dimer formation in solution ranks as MR-MR > GR-MR ~ GR-GR. I also tested the GR core binding capacity to the GR response elements of Nr3c1, Nfil3, and Tsc22d3, three GR-target genes previously identified in CHIP-seq to validate these results. Since MR dimers likely represent a minor fraction due to low protein abundance, these results indicate that MR mainly acts as modulator of GR-dependent transcription through their heterodimerization, as a key player in response to synthetic GCs. I produced Figure 4 and Supplementary Figure 5 to show the results of the protein-protein and protein-DNA assays, respectively.

Received: 31 July 2022 | Revised: 29 November 2022 | Accepted: 2 December 2022

DOI: 10.1096/fj.202201199RR

RESEARCH ARTICLE

The mineralocorticoid receptor modulates timing and location of genomic binding by glucocorticoid receptor in response to synthetic glucocorticoids in keratinocytes

Elena Carceller-Zazo[1] | Lisa M. Sevilla[2] | Omar Pons-Alonso[2] | Álvaro Chiner-Oms[3] | Larbi Amazit[1,4] | Thi An Vu[1] | Géraldine Vitellius[1] | Say Viengchareun[1] | Iñaki Comas[3] | Yan Jaszczyszyn[5] | Montserrat Abella[6,7] | Andrea Alegre-Martí[6,7] | Eva Estébanez-Perpiñá[6,7] | Marc Lombès[1] | Paloma Pérez[2]

[1]Inserm, Physiologie et Physiopathologie Endocriniennes, Université Paris-Saclay, Le Kremlin-Bicêtre, France

[2]Department of Pathology and Molecular and Cell Therapy, Instituto de Biomedicina de Valencia (IBV-CSIC), Valencia, Spain

[3]Department of Genomics and Proteomics, Instituto de Biomedicina de Valencia (IBV-CSIC), Valencia, Spain

[4]Unité Mixte de Service UMS-44, Le Kremlin Bicêtre, France

[5]CEA, CNRS, Institute for Integrative Biology of the Cell, Université Paris-Saclay, Gif-sur-Yvette, France

[6]Structural Biology of Nuclear Receptors, Department of Biochemistry and Molecular Biomedicine, Faculty of Biology, University of Barcelona, Barcelona, Spain

[7]Institute of Biomedicine of the University of Barcelona (IBUB), University of Barcelona, Barcelona, Spain

Correspondence
Paloma Pérez, Instituto de Biomedicina de Valencia (IBV-CSIC), Jaume Roig 11, Valencia 46010, Spain.
Email: pperez@ibv.csic.es

Marc Lombès, Inserm U1185, Faculté de Médecine Paris-Saclay, 63 Rue Gabriel Péri, Le Kremlin-Bicêtre Cedex 94276, France.
Email: marc.lombes@universite-paris-saclay.fr

Funding information
Institut National de la Santé et de la Recherche Médicale (Inserm); Ministerio de Ciencia e Innovación (MICINN), Grant/Award Number: PID2020-114652RB-I00 and PDC2021-121688-I00

Abstract

Glucocorticoids (GCs) exert potent antiproliferative and anti-inflammatory properties, explaining their therapeutic efficacy for skin diseases. GCs act by binding to the GC receptor (GR) and the mineralocorticoid receptor (MR), co-expressed in classical and non-classical targets including keratinocytes. Using knockout mice, we previously demonstrated that GR and MR exert essential nonoverlapping functions in skin homeostasis. These closely related receptors may homo- or heterodimerize to regulate transcription, and theoretically bind identical GC-response elements (GRE). We assessed the contribution of MR to GR genomic binding and the transcriptional response to the synthetic GC dexamethasone (Dex) using control (CO) and MR knockout (MR^{EKO}) keratinocytes. GR chromatin immunoprecipitation (ChIP)-seq identified peaks common and unique to both genotypes upon Dex treatment (1 h). GREs, AP-1, TEAD, and p53 motifs were enriched in CO and MR^{EKO} peaks. However, GR genomic binding was 35% reduced in MR^{EKO}, with

Abbreviations: ChIP-seq, Chromatin immunoprecipitation sequencing; CO, control; CORT, corticosterone; DBD, DNA-binding domain; Dex, dexamethasone; GCs, glucocorticoids; GR, glucocorticoid receptor; GRE, GC-response element; LBD, ligand-binding domain; MR, mineralocorticoid receptor; MREKO, MR epidermal knockout,; SPR, surface plasmon resonance.

Elena Carceller-Zazo and Lisa M. Sevilla contributed equally to this work as first authors.

Marc Lombès and Paloma Pérez contributed equally to this work as senior authors.

This is an open access article under the terms of the Creative Commons Attribution-NonCommercial-NoDerivs License, which permits use and distribution in any medium, provided the original work is properly cited, the use is non-commercial and no modifications or adaptations are made.
© 2022 The Authors. *The FASEB Journal* published by Wiley Periodicals LLC on behalf of Federation of American Societies for Experimental Biology.

significantly decreased GRE enrichment, and reduced nuclear GR. Surface plasmon resonance determined steady state affinity constants, suggesting preferred dimer formation as MR-MR > GR-MR ~ GR-GR; however, kinetic studies demonstrated that GR-containing dimers had the longest lifetimes. Despite GR-binding differences, RNA-seq identified largely similar subsets of differentially expressed genes in both genotypes upon Dex treatment (3 h). However, time-course experiments showed gene-dependent differences in the magnitude of expression, which correlated with earlier and more pronounced GR binding to GRE sites unique to CO including near *Nr3c1*. Our data show that endogenous MR has an impact on the kinetics and differential genomic binding of GR, affecting the time-course, specificity, and magnitude of GC transcriptional responses in keratinocytes.

KEYWORDS

epidermal keratinocytes, genomic binding, glucocorticoid and mineralocorticoid receptors, glucocorticoids, transcription

1 | INTRODUCTION

Glucocorticoids (GCs) have been prescribed to treat chronic inflammatory conditions, including the prevalent skin diseases atopic dermatitis (AD) and psoriasis, for more than 60 years due to their potent anti-inflammatory properties. However, continuous treatment or high doses of GCs often lead to unwanted systemic side effects, including hypertension, osteoporosis, adrenal insufficiency, cataracts, glaucoma, diabetes, skin atrophy, and delayed wound healing.[1–5] Also, GC treatments elicit highly variable outcomes among patients due to differences in sensitivity to these ligands,[6] underscoring the need to understand the cell type- and context-specific actions to optimize current therapies.[2,3]

GCs act through a dual system formed by the corticosteroid receptors GC receptor (GR/*NR3C1*) and mineralocorticoid receptor (MR/*NR3C2*), members of the steroid subclass of nuclear receptors that, upon hormone binding, act as ligand-activated transcription factors (TFs).[5,7,8] GR and MR comprise four structural and functional domains: an N-terminal domain, a DNA-binding domain (DBD), a flexible hinge region, and a ligand-binding domain (LBD). Upon GC binding, GR and MR dissociate from multimeric cytoplasmic chaperone complexes, undergo posttranslational modifications, and translocate to the nuclear compartment, where they regulate gene expression through DNA-binding-dependent and -independent mechanisms.[3,9,10]

GR and MR are highly similar in structure and function, with 94% amino acid identity in their DBDs, implying that, theoretically, both can recognize identical consensus DNA sequences known as GC response elements (GRE; AGAACAnnnTGTTCT). While this would result in transcriptional regulation of the same target genes, GR and MR differ in the cell-type expression pattern and affinity for endogenous ligands. GR expression is ubiquitous and activated only by GCs; in turn, MR shows a more restricted expression pattern and can bind GCs and the mineralocorticoid aldosterone with similar affinity. Also, the differential expression of 11β-hydroxysteroid dehydrogenase (HSD11B) type I and II enzymes, which catalyze the interconversion between active and inactive GCs, respectively, modulates the tissue-specific availability of active hormone, and therefore, the specific activation of these corticosteroid receptors.[8]

GR and MR can also promote or suppress gene transcription indirectly by interfering with other TFs (typically AP-1 or NF-κB) bound to their respective DNA-binding sites.[3,5,11,12] GR but not MR can also repress inflammatory genes by binding to negative (n)GREs preventing the assembly of an active transcription complex, or to unrelated sequences called inverted repeat (IR)nGREs, to which it is recruited along with corepressors.[5,13] Also, both GR and MR can interfere with signal transduction components such as MAPKs or PI3 kinases. However, and in contrast to GR, typically anti-inflammatory, MR can act as pro- or anti-inflammatory depending on the cell type and the ligand.[14]

The role of MR in mediating GC effects has been long disregarded despite the fact that endogenous GCs bind to MR with 10-fold higher affinity than GR. However, in recent years, there is accumulating evidence that GR-MR cross-talk and heterodimer formation modulate the specificity and magnitude of the GC-regulated transcriptional responses.[15–29]

In cells with co-expression of both receptors, transcriptional outcome will depend on ligand availability, the GR:MR relative ratio, formation of homo- or heterodimers, patterns and kinetics of GR- and MR- genomic binding, and selective GR-MR interactions with cell type-specific

15306860, 2023, 1, Downloaded from https://faseb.onlinelibrary.wiley.com/doi/10.1096/fj.202201199RR by Readcube (Labtiva Inc.), Wiley Online Library on [02/06/2023]. See the Terms and Conditions (https://onlinelibrary.wiley.com/terms-and-conditions) on Wiley Online Library for rules of use; OA articles are governed by the applicable Creative Commons License

TFs and co-regulators.[15,23,24,30,31] Recently, MR was shown to tether to genomic DNA by GR in neuroblastoma cells, contributing to an augmented GC transcriptional response.[16] Moreover, studies revealed that genomic binding of distinct MR- and GR- homo- and heterodimers in response to GCs or aldosterone in a human renal cell line followed different kinetics.[23]

The skin, given its anatomical location and continuous exposure to chemical and mechanical injuries, such as UV radiation, microorganisms, and wounding, is a frequent target of inflammatory diseases.[32] Among the different cutaneous compartments, the epidermis is mainly formed by keratinocytes and constitutes the outer epithelial barrier, crucial to modulate cutaneous immunity and host defense and to protect the organism from external damage.[32] Keratinocytes only proliferate in the epidermal basal layer, then migrate outward and differentiate forming squames that together with cross-linked lipids form the outmost layer, the stratum corneum. Perturbations of the skin barrier favor alterations in symbiotic host–microbiota relationship and associated immune responses, and are the bases of many inflammatory cutaneous disorders.[33,34]

In previous studies, we demonstrated that epidermal GR and MR play key roles in the development, aging, and homeostasis of skin via nonoverlapping functions, suggesting biologically relevant cross-talk.[35] By proximity ligation assays, we identified GR-MR heterodimers in mouse keratinocytes, both in the cytoplasm (in the absence of the synthetic ligand dexamethasone, Dex), and in the nucleus upon Dex treatment.[24] These interactions were functionally relevant as keratinocyte-specific loss of GR, MR, or both, decreased Dex-induced GRE-luciferase activity to different extents.[24,36] While Dex response was absolutely dependent on the presence of GR, it decreased around 40% in MR epidermal KO keratinocytes (MR^{EKO}) relative to controls (CO) despite the fact that overall GR levels were similar in both genotypes.[36] However, the role of MR in modulating GR genomic binding and on transcriptional responses to GCs in keratinocytes is unknown.

To address these questions, we performed ChIP-seq and RNA-seq studies in CO and MR^{EKO} keratinocytes upon Dex treatment, and identified genomic targets of GR and associated changes in the transcriptome. MR-deficient keratinocytes showed a significant reduction of GR peaks relative to CO (35%). While AP-1, GRE, TEAD, and p53 motifs were found to be overrepresented in both CO and MR^{EKO} ChIP-seq datasets, there were statistically significant differences in signal intensity between genotypes. Along these lines, there was a decrease in GRE motifs in GR-bound sequences (GBS) in MR^{EKO} versus CO cells. Immunofluorescence and nuclear fractionation experiments indicated that GR showed a decreased nuclear localization in response to Dex in MR^{EKO} versus CO. Also, using surface plasmon resonance (SPR), we assessed GR- and MR- protein–protein interactions and estimated the affinity and kinetics of their physical associations. Data suggest that MR homodimers have the highest affinity but the shortest lifetime, while GR homodimers and GR/MR heterodimers show similar intermediate affinity and extended dimer half-life.

Despite differential patterns in GR nuclear localization and DNA recruitment in the presence or absence of MR, the gene expression profiles in response to 3 h of Dex treatment were very similar in CO and MR^{EKO}. However, kinetics studies demonstrated good correlation between earlier and more pronounced GR binding to GBS with GRE sites unique to CO near *Nfil3* and *Nr3c1*, and transcript levels.

2 | MATERIAL AND METHODS

2.1 | Cell culture

Immortalized mouse control (CO) and MR epidermal KO (MR^{EKO}) keratinocyte cell lines were generated as described from 8-week-old female mouse dorsal skin.[37] Keratinocytes were isolated following overnight incubation of skin with 0.25% trypsin-PBS at 4°C and cultured on mitomycin C-treated J2-3T3 feeders in type I collagen (Gibco)-coated flasks with DMEM (Gibco)-Ham's F12 (Biowest) (3:1) medium supplemented with 0.18 mM adenine, 0.35 mM calcium, 7.5% FBS (Biowest), 100 U/ml penicillin/100 µg/ml streptomycin (Biowest), 2 mM glutamine (Biowest), 0.25 µg/ml amphotericin B (Biowest), 5 µg/mL insulin (Sigma), 0.1 nM cholera toxin (Sigma), and 10 ng/ml EGF (Peprotech). Following eight passages, spontaneously immortalized lines arose.[36] The MR^{EKO} cell line showed no significant differences in GR protein or mRNA expression, relative to CO.[24,36]

To evaluate response to dexamethasone (Dex, 100 nM; Sigma) or corticosterone (CORT, 100 nM; Sigma) treatment, keratinocytes were cultured in type I collagen-coated dishes in the absence of feeders. The MR antagonist eplerenone was used at 10 µM (Sigma). Forty-eight hours prior to experimentation, cells were washed twice with PBS and incubated with the medium described above, with FBS replaced by 7.5% dextran-coated charcoal (Sigma)-stripped serum for steroid starvation.

2.2 | ChIP-sequencing

Steroid-starved CO and MR^{EKO} keratinocytes were treated with vehicle (EtOH) or 100 nM Dex for 1 h prior to processing. The iDeal ChIP-Seq kit for Transcription Factors (Diagenode, Seraing, Belgium), was used for

15306860, 2023, 1, Downloaded from https://faseb.onlinelibrary.wiley.com/doi/10.1096/fj.202201199RR by Readcube (Labtiva Inc.), Wiley Online Library on [02/06/2023]. See the Terms and Conditions (https://onlinelibrary.wiley.com/terms-and-conditions) on Wiley Online Library for rules of use; OA articles are governed by the applicable Creative Commons License

sample preparation. Chromatin shearing was performed by sonication with Bioruptor Pico (Diagenode) for 10 min (30"ON/30"OFF cycles). A total of 5 μg of GR-specific antibody (sc-393 232X, Santa Cruz Biotechnology) were used for immunoprecipitation. Input controls were 1% chromatin used for ChIP. ChIP-qPCR experiments were performed as previously described,[38] with 3 μg of antibody and Dynabeads™ Protein A or G magnetic beads (Invitrogen). For MR ChIP, 4 μg of MR-specific antibody (21854-1-AP, Proteintech) was used.

ChIP samples and respective input controls (inputs for CO or MR^{EKO} Vehicle were used to normalize both treatment conditions within respective genotype) were processed for library construction and Illumina sequencing in the NGS Core Facility of the Institute for Integrative Biology of the Cell (http://www.i2bc.paris-saclay.fr/). DNA fragments were end repaired and dA-tailed with the NEBNext® Ultra™ II End Repair/dA-Tailing Module and Illumina TruSeq adapters were ligated with the NEBNext® Quick Ligation Module (New England Biolabs Inc.). Libraries were amplified with Kapa Biosystems Hifi polymerase (Sigma). Library quality was verified on an Agilent Bioanalyzer 2100, using an Agilent High Sensitivity DNA Kit. Libraries were pooled in equimolar proportions and sequenced on a Paired-End 2×43 bp run, on the Illumina NextSeq500.

Raw sequence reads were quality checked, adapter trimmed, and filtered using Cutadapt1.15 and FastQC v0.11.5 and only reads longer than 10 bp were kept for analysis. Trimmed sequences were mapped to the *Mus musculus* genome (assembly: GRCm38/mm10) using the bwa-mem algorithm. Only reads mapped with a mapping quality of 60 (maximum) were kept for further analyses. Peak calling and search for enrichment of TF-binding motifs in identified GR-bound sequences (GBS) were performed using HOMER,[39] with the findPeaks and findMotifsGenome functions, using respective input controls for each genotype. Peaks were assigned an identification code based on genomic location for comparative purposes. Overlapping intervals were grouped into "active regions," defined by the start coordinate of the most upstream interval and the end coordinate of the most downstream interval.[40] The criterion for overlapping represents at least 50% coincidence among peak sequences. Peaks were visualized using Integrated Genomics Viewer (version 2.11.9) Software.[41] We used CREMA (Cis-Regulatory Element Motif Activities; https://crema.unibas.ch/cumara/) to identify statistically significant differences in TF motif enrichment in identified CO and MR^{EKO} GBS. Comprehensive motif analysis with XTREME[42] determined consensus GRE sequences and the positional distribution in GBS, as well as the percentage of GBS in datasets containing one or more identified motifs (parameters: motif width between 6 and 30 bp and any number of repetitions of motif within peaks). Gene ontology was determined using DAVID functional clustering with an EASE score less than 0.05 and medium stringency.[43,44]

2.3 | RNA isolation, cDNA preparation, and qPCR

Total RNA was isolated using TRI reagent (Molecular Research Center, Inc., Euromedex, Mundolsheim, France). The RevertAid H Minus Reverse Transcriptase kit (ThermoFisher) was used to generate cDNA.

qPCR was performed with gene-specific oligonucleotides (0.3 μM each; Sigma) and the FastStart Universal SYBR Green Master mix ROX (Roche) with the Quant Studio 5 Real-Time PCR System (Applied Biosystems, Foster City, California, USA). In the case of cDNA amplification, Ct values were normalized to those of the housekeeping gene *Hprt1*. In the case of ChIP-qPCR, Ct values of each ChIP were normalized to those of respective inputs. Technical triplicates were used; and a minimum of three biological replicates per experimental group were assessed to calculate the mean value ± SD. Primer sequences are in Table S1 and unless otherwise indicated were designed using Primer-BLAST (NIH, https://www.ncbi.nlm.nih.gov/tools/primer-blast/). Primers from PrimerBank (https://pga.mgh.harvard.edu/primerbank/) are indicated with corresponding IDs.

2.4 | RNA sequencing

Steroid starved CO and MR^{EKO} keratinocytes were treated with vehicle (EtOH) or 100 nM Dex for 3 h prior to RNA isolation. This experiment was performed with two biological replicates per genotype and condition, which were subsequently pooled for library preparation and Illumina sequencing in the NGS Core Facility of the Institute for Integrative Biology of the Cell. Total RNA quality was assessed on an Agilent Bioanalyzer 2100, using RNA 6000 pico kit (Agilent Technologies). Directional RNA-Seq Libraries were constructed using the TruSeq total RNA Stranded library prep kit, with H/M/R Ribo-Zero reagents (Illumina). Quality of libraries was assessed on an Agilent Bioanalyzer 2100, using an Agilent High Sensitivity DNA Kit. Libraries were pooled in equimolar proportions and sequenced on a paired-end 51–35 bp run, with the Illumina NextSeq500.

FASTQ files were obtained from applying the bcl2fastq2 Conversion Software (V2.18.12) to the BCL files generated by the sequencer. Adapters were removed with Cutadapt 1.15; only reads longer than 10 bp were kept for analysis.

15306860, 2023, 1, Downloaded from https://faseb.onlinelibrary.wiley.com/doi/10.1096/fj.202201199RR by Readcube (Labtiva Inc.), Wiley Online Library on [02/06/2023]. See the Terms and Conditions (https://onlinelibrary.wiley.com/terms-and-conditions) on Wiley Online Library for rules of use; OA articles are governed by the applicable Creative Commons License

Filtered FASTQ files were mapped against the *Mus musculus* reference genome (assembly: GRCm38/mm10) with HISAT2, with the –rna-strandness RF argument. Absolute values ranging from 117 to 151 million paired-end 51–35 bp reads were obtained from samples.

Reads mapping on each feature were counted with the HTSeq-count script, with the "union" mode of overlapping and with the—stranded option for detecting reads falling in the reverse strand. A count table was created with the information derived from HTSeq-count for each sample. Later, the DESeq2 package in R was used to analyze differential gene expression using this count table as an input. The log2 fold-change between the expression (normalized counts) of each gene in the Dex versus vehicle samples was calculated. With these values, we generated a distribution and identified outliers as Q3 + 1.5*IQR and Q2 − 1.5*IQR. In addition, for each gene, we performed a Fisher test comparing the expression of both conditions, using the housekeeping gene *Hprt* as a normalization factor. The p-values obtained were adjusted using the Benjamini–Hochberg method.

2.5 | Nuclear fractionation

Steroid-starved CO and MR^{EKO} keratinocytes were treated with vehicle (EtOH) or 100 nM Dex for 1 h. Cells were lysed with hypotonic lysis buffer (10 mM HEPES pH 7.9, 10 mM KCl, 1 mM EDTA, 1 mM EGTA, 0.5 mM DTT, protease and phosphatase inhibitors). After incubation for 20 min on ice, IGEPAL was added to a final concentration of 0.05%. Cell lysates were centrifuged at 1000*g* for 10 min at 4°C to pellet nuclei. The supernatant (cytoplasmic fraction) was removed and nuclear proteins were extracted by incubating on ice for 45 min with lysis buffer (10 mM HEPES pH 7.9, 200 mM NaCl, 0.2 mM EDTA, 2 mM $MgCl_2$, 20% glycerol, 0.5 mM DTT, 0.1% IGEPAL, protease and phosphatase inhibitors), and centrifuged for 10 min at 16 000*g*. The supernatant was the nuclear fraction. Protein concentrations were determined using Bradford reagent (Fisher).

2.6 | Immunoprecipitation and Immunoblotting

For immunoprecipitation of GR, equivalent quantities of nuclear extracts were diluted in IP buffer (50 mM Tris pH 7.6, 150 mM NaCl, 5 mM EDTA, 0.1% IGEPAL, protease and phosphatase inhibitors), precleared, and then incubated overnight at 4°C with 3 μg GR antibody (sc-393232). Protein G Dynabeads were added for 2 h at 4°C and then washed 3x with IP buffer; bound proteins were then eluted in Laemmli buffer.

Total nuclear extracts and immunoprecipitated proteins were separated on denaturing SDS-polyacrylamide gels and transferred to nitrocellulose (Amersham). Filters were probed overnight at 4°C using the following antibodies specific for: actin (A2066, Sigma), Pan-TEAD (13295, Cell Signaling), p63 (sc-8431, Santa Cruz), and GR (sc-1004, Santa Cruz). Following washing with TBS-Tween and incubation with anti-mouse or anti-rabbit HRP-linked secondary antibodies (NA931 and NA934, respectively, Cytiva, Merck), proteins were visualized using Pierce™ ECL Plus Western Blotting Substrate (Pierce, ThermoFisher) and the ImageQuant LAS 4000 mini Biomolecular Imager (GE Healthcare). Band intensities were quantitated using ImageJ software and normalized to Lamin A/C as loading control. Data (at least three biological replicates per group) are presented as mean ± SD.

2.7 | Immunofluorescence and high-throughput microscopy

After Dex treatment (100 nM) for indicated times, keratinocytes were fixed with 4% paraformaldehyde for 15 min at room temperature. After 15 min of permeabilization with 0.5% Triton X-100, cells were washed and incubated in blocking buffer (5% nonfat dry milk, 0.1% Tween20 in PBS) for 1 h. Then, the cells were incubated with GR-specific antibody (sc-393232X) overnight at 4°C. The next day, cells were washed five times and incubated with Alexa Fluor 555 conjugated anti-mouse secondary antibody (ThermoFisher). DAPI (Invitrogen) was used to stain nuclei. High-throughput microscopy was performed with an Arrayscan VTI micro-scope (Thermofisher). For the quantification of the ratio of nuclear/cytoplasmic immunofluorescence (500–1500 individual cells per data group), we used the Molecular Translocation V4 BioApplication algorithm (vHCS Scan, version 6.3.1, Build 6586). Statistical significance was calculated using the nonparametric Kruskal–Wallis and the post hoc Dunn test (GraphPad software).

2.8 | Protein expression and surface plasmon resonance (SPR) analyses

Recombinant ancGR2-LBD cloned into a pMALCH10T vector was expressed as fusion protein with an N-terminal maltose-binding protein (MBP) and a hexahistidine (His) tag and purified to homogeneity using standard chromatographic procedures after cleavage with TEV protease.[45] Recombinant MR-LBD cloned into a pSMT3 vector was expressed as fusion protein with an N-terminal His-SUMO-tagged fusion protein and purified to homogeneity

15306860, 2023, 1, Downloaded from https://faseb.onlinelibrary.wiley.com/doi/10.1096/fj.202201199RR by Readcube (Labtiva Inc.), Wiley Online Library on [02/06/2023]. See the Terms and Conditions (https://onlinelibrary.wiley.com/terms-and-conditions) on Wiley Online Library for rules of use; OA articles are governed by the applicable Creative Commons License

using standard chromatographic procedures after cleavage with Ulp1 protease.[46]

SPR analyses were performed at 25°C in a BIAcore T200 instrument (GE Healthcare). Highly purified, Dex-bound recombinant WT ancGR2-DBD-LBD, ancGR2-LBD, and MR-LBD were diluted in 10 mM sodium acetate, pH 5.0, and directly immobilized on CM5 chips (GE Healthcare) by amine coupling at densities between 100 and 150 resonance units (RU). As a reference, one of the channels was also amine-activated and blocked in the absence of protein. The same protein samples were run over the ancGR2-LBD and MR-LBD immobilized partners in a running buffer including 50 mM HEPES, pH 7.2, 50 mM NaCl, 3% glycerol, 1 mM dithiothreitol (DTT), 50 µM Dex. *Nr3c1* (5′-GGATACACTGTGTACT-3′; 5′-AGTACACAGTGTATCC-3′), *Nfil3* (5′-TAGAACATTCT GTACT-3′; 5′-AGTACAGAATGTTCTA-3′), and *Tsc22d3* (5′-AAAAACAGAATGTTCA-3′; 5′-TGAACATTCTGTTT TT-3′) oligonucleotides were run over the ancGR2-DBA-LBD immobilized partner in a pH 3 buffer consisting of 10 mM HEPES, 150 mM NaCl, 0.005% Tween-20, 10 mM Na molybdate, and 5 mM Zn citrate. Sensorgrams were analyzed with the BIAcore T200 Evaluation software 3.0 and fitted according to the Langmuir 1:1 model.

2.9 | Statistics and data analysis

Unless otherwise mentioned, statistical significance of experimental data was calculated using the GraphPad Prism software (version 5.2; GraphPad Software Inc., San Diego, CA) and IBM SPSS software. Data were obtained in at least three independent experiments. Data with normal distribution are presented as mean ± SD; non-normal data were reported as median ± interquartile range (Figure 2D) or mean ± SEM (Figure 3D). Means of two and three or more groups of normally distributed variables were compared by Student's t test or ANOVA with a Tukey post hoc test, respectively. The Mann–Whitney U test or the Kruskal–Wallis with a post hoc Dunn test was used to compare means of two and three or more groups, respectively, of non-normally distributed data. p-values <.05 were considered statistically significant. Biovenn was used to generate Venn diagrams.[47]

3 | RESULTS

3.1 | Keratinocyte loss of MR reduces genomic GR recruitment in response to Dex

To assess whether GC-induced genomic GR binding could be altered by the absence of MR, CO, and MR^{EKO} keratinocytes were treated with Dex (100 nM) for 1 h followed by ChIP-seq. GR chromatin occupancy was mapped in the presence and absence of MR (Table S2). While identified GR-bound sequences (GBS) were only marginal in vehicle-treated CO and MR^{EKO} cells, Dex treatment dramatically increased GR chromatin occupancy in both genotypes (Table S2; Figure 1A). Importantly, the absence of MR correlated with an approximately 35% reduction in the number of GBS relative to CO (Figure 1A; 2761 vs 1829 peaks corresponding to 1804 vs 1242 genes, in CO and MR^{EKO}, respectively). Furthermore, in comparing the 1533 GBS common to both genotypes, an overall 10% decrease in tag counts was observed in MR^{EKO} versus CO ($p < .0001$).

To compare peaks and analyze overlap between CO and MR^{EKO} GBS, all peaks were assigned an identifier (Table S2). Then, overlapping intervals were grouped into "active regions," defined by the start coordinate of the most upstream interval and the end coordinate of the most downstream interval.[40] The criterion for overlapping represents at least 50% coincidence among peak sequences. Almost half (45%) of GBS identified in CO were not present in MR^{EKO}, indicating a striking dependence on MR for GR genomic binding (Figure 1B). In contrast, the majority of GBS (84%) identified in MR^{EKO} overlapped with those identified in CO (Figure 1B). However, multiple GBS were often detected *per* gene, some of which were common to both genotypes while others were unique for CO or MR^{EKO} (Table S2).

The identification of GBS in genes (nearest TSS) common to both genotypes (*Tsc22d3/Gilz* and *Per1*), unique to CO (*Nfil3*, *Nr3c1* and *Dusp10*), or unique to MR^{EKO} (*Hlf1* and *Lmnb2*) indicate context-dependent consequences of the loss of MR on GR binding (Figure 1C). Data were validated by ChIP-qPCR in independent experiments, showing reduction in GR binding to regulatory sequences of common (*Tsc22d3*/*Gilz1* and *Per1*) and unique (*Nfil3* and *Dusp10*) GBSs in MR^{EKO} versus CO (Figure 1D). Likewise, peaks unique to MR^{EKO} were also validated confirming increased GR binding relative to CO cells (Figure 1D; *Hlf* and *Lmnb2*). Moreover, treatment of CO cells with the MR antagonist eplerenone resulted in a reduction of GR recruitment to *Tsc22d3* and *Per1* of more than eightfold (Figure S1). Altogether, these data indicate that MR plays a role in the Dex-induced GR genomic binding in keratinocytes.

Consistent with previous reports,[48–50] after Dex treatment, most GBS in CO and MR^{EKO} keratinocytes were found in introns (46%–49%) and intergenic (36%–39%) regions while only 7%–8% of the peaks were found near promoters (Figure S2). Therefore, the absence of MR did not alter the genomic distribution of GR DNA-binding sites.

15306860, 2023, 1, Downloaded from https://faseb.onlinelibrary.wiley.com/doi/10.1096/fj.202201199RR by Readcube (Labtiva Inc.), Wiley Online Library on [02/06/2023]. See the Terms and Conditions (https://onlinelibrary.wiley.com/terms-and-conditions) on Wiley Online Library for rules of use; OA articles are governed by the applicable Creative Commons License

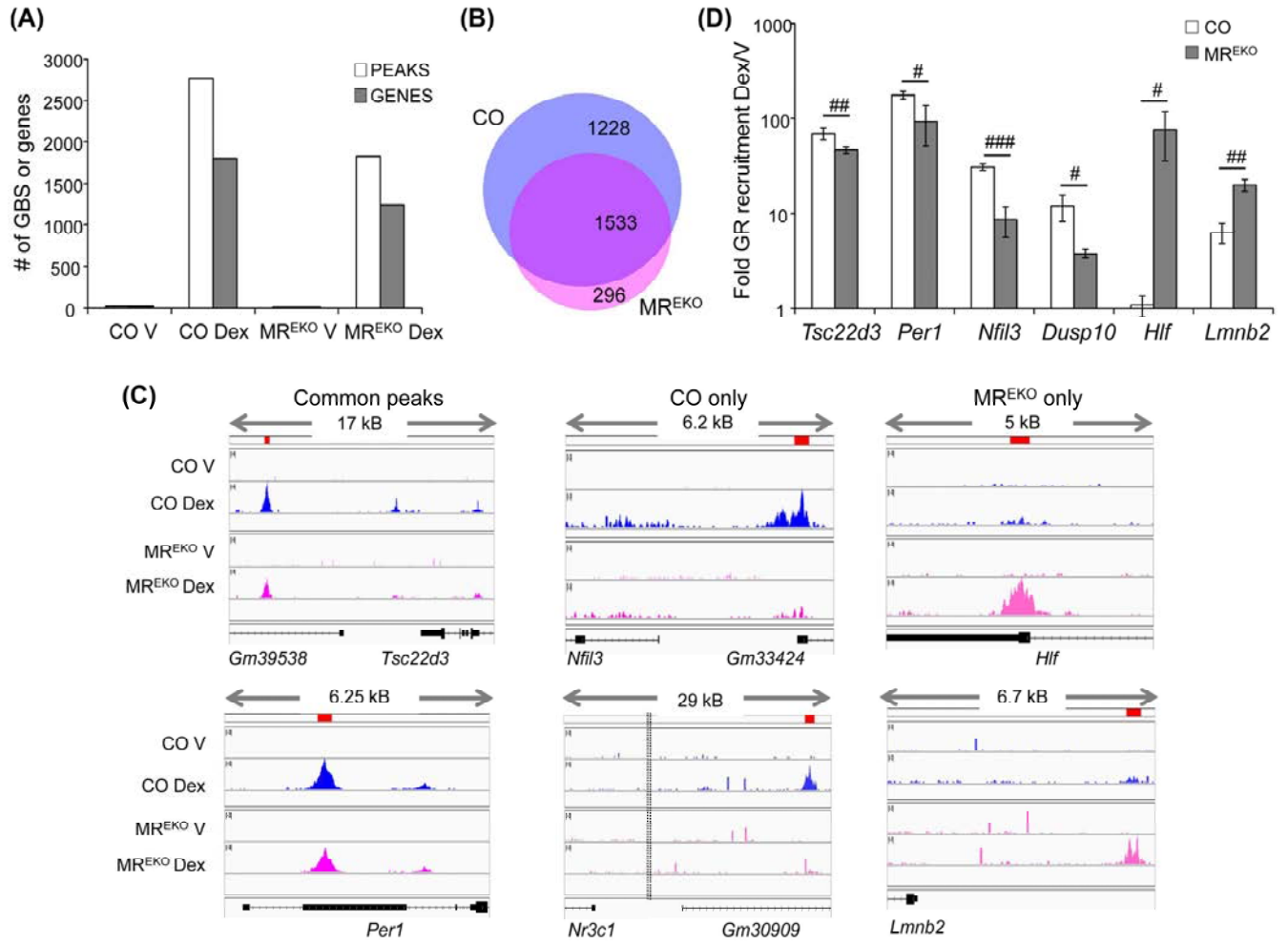

FIGURE 1 The lack of MR in keratinocytes correlates with an overall reduction in Dex-induced GR genomic recruitment. (A) GR genomic binding in control (CO) versus MR^{EKO} keratinocytes treated 1 h with either vehicle (V) or 100 nM Dex. The number of GR-bound sequences (GBS) and associated genes is indicated. (B) Venn diagram showing overlap of GBS identified in Dex-treated CO and MR^{EKO} cells. (C) Screenshots from IGV browser showing peaks common to both genotypes (*Tsc22d3/Gilz* and *Per1*), unique to CO (*Nfil3* and *Nr3c1*), and unique to MR^{EKO} (*Hlf* and *Lmnb2*). Genomic regions corresponding to peaks are indicated by red bars. Dotted lines in screenshot of *Nr3c1* indicate break in X-axis genomic coordinates. (D) Validation by independent experiments of GR ChIP-qPCR for indicated genes; mean values and SD are shown. Hash symbols indicate statistically significant differences in recruitment between genotypes ($n = 3$; $^{\#}p < .05$; $^{\#\#}p < .01$; $^{\#\#\#}p < .001$).

To have direct evidence of MR binding to the identified GR-bound fragments, we performed MR-ChIP after treatment with Dex or the physiological ligand corticosterone (CORT) for 1 h. While Dex did not induce detectable MR binding to regulatory sequences such as *Nfil3, Nr3c1*, and *Dusp10* (not shown), CORT elicited robust MR binding to these sites as well as *Tsc22d3* and *Per1* (Figure S3). The fact that CORT also induced strong GR binding to the same regulatory sequences (Figure S3) indicate that, upon ligand binding, MR and GR can co-occupy DNA in these cells. However, the different magnitude of GR recruitment to distinct genomic sequences suggests that formation of GR/MR oligomers depends on genomic context.

3.2 | The absence of MR alters enrichment of GR-binding motifs, with significant decrease in GREs, and reduces GR nuclear localization

To determine the specific DNA sequences enriched within CO and MR^{EKO} GBS, we searched for TF-binding motifs in an unbiased manner using HOMER (Figure 2A). The top overrepresented motifs, common to both genotypes, included AP-1, GRE, TEAD, and p53. We used CREMA to determine whether there were statistically significant differences in TF motif enrichment between genotypes and found that importantly, GRE motifs were infra-represented in MR^{EKO} relative to

15306860, 2023, 1, Downloaded from https://faseb.onlinelibrary.wiley.com/doi/10.1096/fj.202201199RR by Readcube (Labtiva Inc.), Wiley Online Library on [02/06/2023]. See the Terms and Conditions (https://onlinelibrary.wiley.com/terms-and-conditions) on Wiley Online Library for rules of use; OA articles are governed by the applicable Creative Commons License

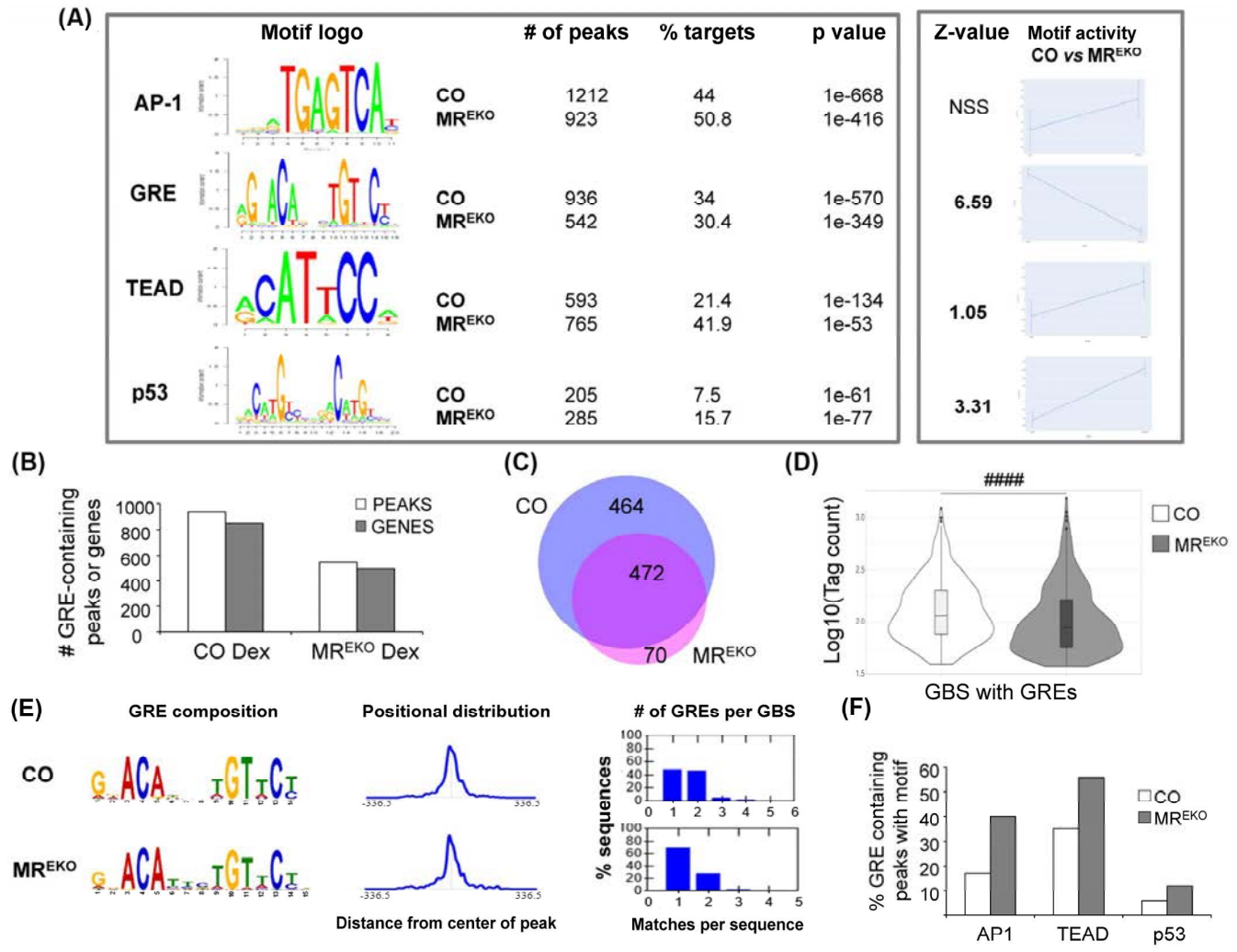

FIGURE 2 MR absence affects motif composition of GR-bound genomic regions and decreases GR binding to GRE-containing sequences. (A) Left panel: Transcription factor binding motif enrichment analysis was performed by HOMER. Motif logo of the top overrepresented motifs, number of peaks and percentage of targets containing motifs, and p-values, are indicated for each genotype. Right panel: Statistically significant differences in motif enrichment in CO versus MR^{EKO} (Z-value) determined by CREMA. Graphs represent changes in motif activity between genotypes. (B) Number of GRE-containing peaks and associated genes in CO versus MR^{EKO} Dex-treated cells. (C) Venn diagram depicting the overlap between GRE-containing GBS in CO and MR^{EKO}. (D) The plot shows the distribution of GRE tag counts for both genotypes represented by median values and interquartile range; $n = 472$; $^{\#\#\#\#}p < 10^{-8}$. (E) XTREME results for palindromic GRE motifs identified in CO and MR^{EKO} datasets; left to right: sequence logo, positional distribution of motifs in GBS, and bar graphs showing percentage of GBS containing indicated number of GREs. (F) Percentages of indicated enriched TF motifs in the subsets of GRE-containing GBS in MR^{EKO} relative to CO cells.

CO, while TEAD and p53 motifs were overrepresented (Figure 2A).

The decreased number of peaks containing GREs in MR-deficient versus CO cells indicated that the GR affinity and/or specificity toward a subset of GRE motifs depend on the presence of MR (Figure 2B; 542 vs 936 peaks, respectively). Indeed, 47% of GRE-containing peaks were unique to CO (Figure 2C). Moreover, GBS with GREs identified in both genotypes showed a 14% decrease in tag count in MR^{EKO} versus CO (Figure 2D; p-value $<10^{-8}$). Ontological analysis of GRE-containing peak-associated genes unique to CO showed enrichment in transcriptional regulation and cell differentiation annotation clusters (Figure S4); notable genes within these categories included *Nfil3*, *Nr3c1*, *Dusp10*, *Nfkb1*, and *Pparg*. Comprehensive motif analysis of GBS by XTREME showed that the composition and positional distribution of palindromic GREs did not vary between genotypes. However, the number of GREs present in GR-bound genomic regions was decreased in MR^{EKO} versus CO datasets (Figure 2E). This suggests that MR is involved in cooperative interactions between multiple GRE within a GBS.

We evaluated the presence of identified enriched TF motifs (AP-1, TEAD, and p53) in the subsets of

15306860, 2023, 1, Downloaded from https://faseb.onlinelibrary.wiley.com/doi/10.1096/fj.202201199RR by Readcube (Labtiva Inc.), Wiley Online Library on [02/06/2023]. See the Terms and Conditions (https://onlinelibrary.wiley.com/terms-and-conditions) on Wiley Online Library for rules of use; OA articles are governed by the applicable Creative Commons License

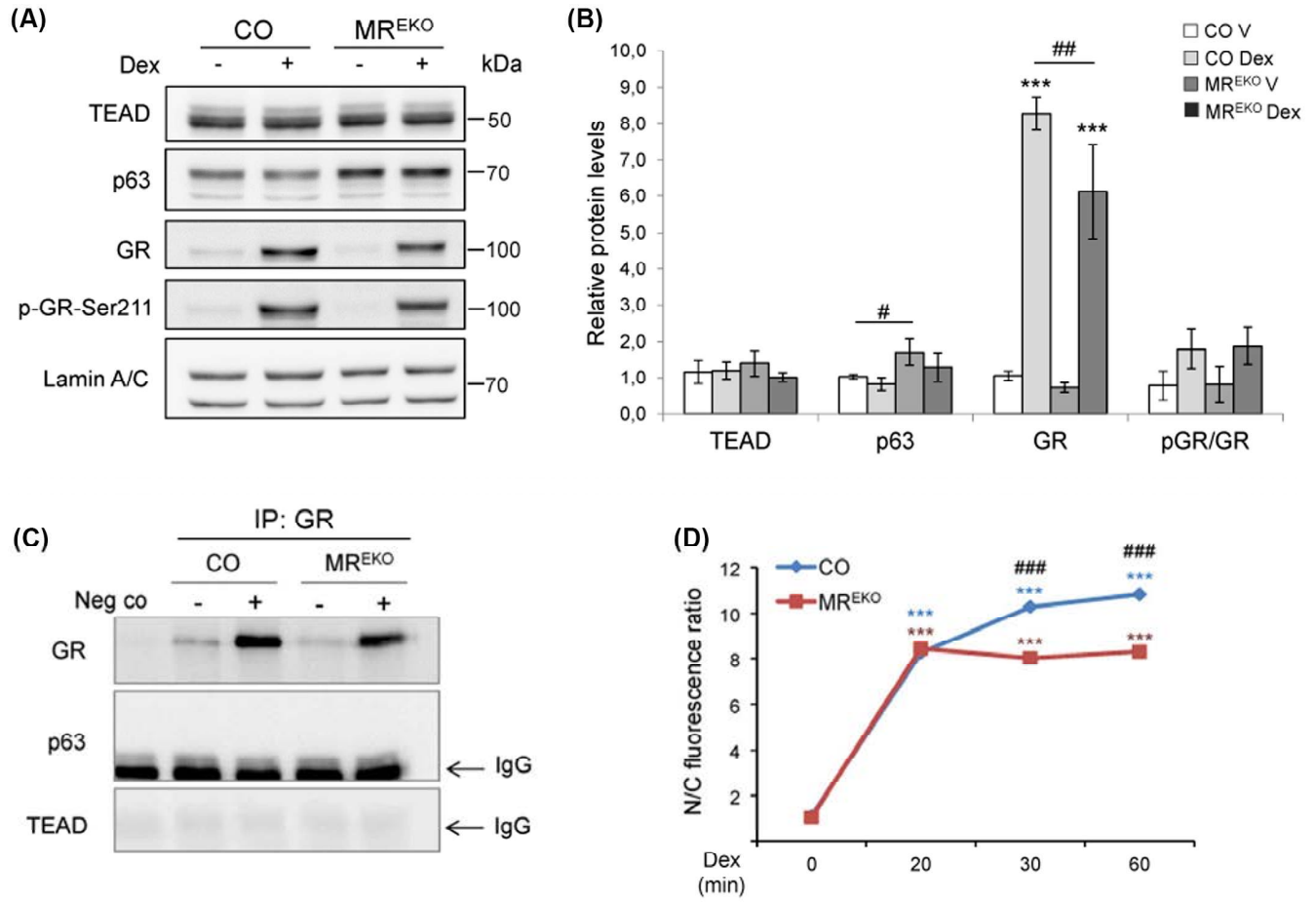

FIGURE 3 Nuclear GR, p63, and TEAD in CO and MR^{EKO} keratinocytes upon treatment with Dex. CO and MR^{EKO} keratinocytes were treated with vehicle or 100 nM Dex to evaluate the following parameters. (A) Expression and (B) quantitation of TEAD, p63, GR, and phospho(p)-GR, in CO and MR^{EKO} cells; Lamin A/C was used as reference for loading control. Mean values and SD are shown ($n = 4$; $^{\#}p < .05$; $^{\#\#}p < .01$; $^{***}p < .001$). (C) Immunoprecipitation studies to assess GR interaction with indicated TFs. (D) Nuclear/cytoplasmic (N/C) ratio of immunofluorescence for GR at indicated time points following treatment. Mean values and SEM are shown (a minimum of 500 individual cells per condition were quantitated; $n = 3$; ***, $^{\#\#\#}p < .001$). Statistically significant differences relative to t = 0 are denoted by asterisks and those between genotypes by hash symbols.

GRE-containing GBS, and found increased co-occurrence with other motifs in MR^{EKO} relative to CO cells: TEAD (56% vs 35%), AP-1 (40% vs 17%), and p53 (12% vs 6%). These data suggest that these GBS may be maintained in the absence of MR due to interactions of GR with these TFs (Figure 2F).

While we did not detect any changes in the expression of TEAD between genotypes, the overrepresentation of p53 motifs correlated with constitutively increased expression of the epithelial-specific homolog of p53, p63 (Figure 3A,B). However, co-immunoprecipitation studies did not identify protein–protein interactions between GR and these TFs in the nucleus (Figure 3C).

To understand the mechanisms behind the decreased number of GRE-containing peaks in MR^{EKO} versus CO cells, we also assessed the expression and activity of GR. Following 1 h of Dex treatment, the levels of nuclear GR were significantly decreased in MR^{EKO} relative to CO (by 25%), without changes in the ratio of phospho (p)-GRS211/total GR (Figure 3A,B). Next, we investigated the GR nuclear/cytoplasmic ratio at several time points following Dex treatment using immunofluorescence and high-throughput microscopy (Figure 3D). While at 20 min following treatment, CO and MR^{EKO} showed identical GR nuclear/cytoplasmic ratios, this ratio was significantly reduced in MR^{EKO} at 30 min (by 22%) and 1 h (by 23%).

3.3 | Dex-bound GR-LBD, MR-LBD self-associate, and GR-MR LBDs heterodimerize in solution

In cells that co-express GR and MR, the combinatorial of distinct homo- and heterodimers represents an important mechanism to modulate gene expression.[22] After

15306860, 2023, 1, Downloaded from https://faseb.onlinelibrary.wiley.com/doi/10.1096/fj.202201199RR by Readcube (Labtiva Inc.), Wiley Online Library on [02/06/2023]. See the Terms and Conditions (https://onlinelibrary.wiley.com/terms-and-conditions) on Wiley Online Library for rules of use; OA articles are governed by the applicable Creative Commons License

expression and purification of GR-LBD and MR-LBD bound to Dex, we used surface plasmon resonance (SPR) to analyze the physical protein–protein interactions of the GR and MR homodimers as well as the suggested GR/MR heterodimers. The respective ligand-bound receptors were immobilized on sensor chips, and increasing concentrations of either ligand-bound protein were run over as analyte (Figure 4).

The analyses of SPR data demonstrated MR-LBD and GR-LBD self-association, showing steady state affinities (K_D) of 1.49 ± 0.41 μM and 17.4 ± 1.5 μM, respectively (Figure 4A,C). Interestingly, the resulting K_D for MR homodimer was one order of magnitude lower than that obtained for GR homodimer. Also, the K_D of GR-LBD over MR-LBD was 11.6 ± 1.5 μM (Figure 4B), suggesting that the order of preferred dimer formation ranks as MR-MR > GR-MR ~ GR-GR. However, kinetic studies demonstrated very different life time of respective dimers, with MR homodimers showing the shortest $t_{1/2}$, followed by GR homodimers and GR/MR (Figure 4D–G).

Importantly, upon expression of GR multidomain (GR-DBD-LBD) protein, there was binding to specific regulatory sequences identified by ChIP-seq such as *Nr3c1*, *Nfil3*, and *Tsc22d3* (Figure S5). Note that the K_D for GR protein–DNA interactions was higher for the peaks unique to CO, *Nr3c1*, and *Nfil3*, relative to the common peack *Tsc22d3*, suggesting that MR contributes to GR binding to DNA.

3.4 | Dex transcriptional response in keratinocytes is largely mediated by GR and not MR

To analyze the contribution of MR in GR-mediated transcriptional responses to GCs, we treated CO and MR^{EKO} keratinocytes with 100 nM Dex or vehicle for 3 h, and

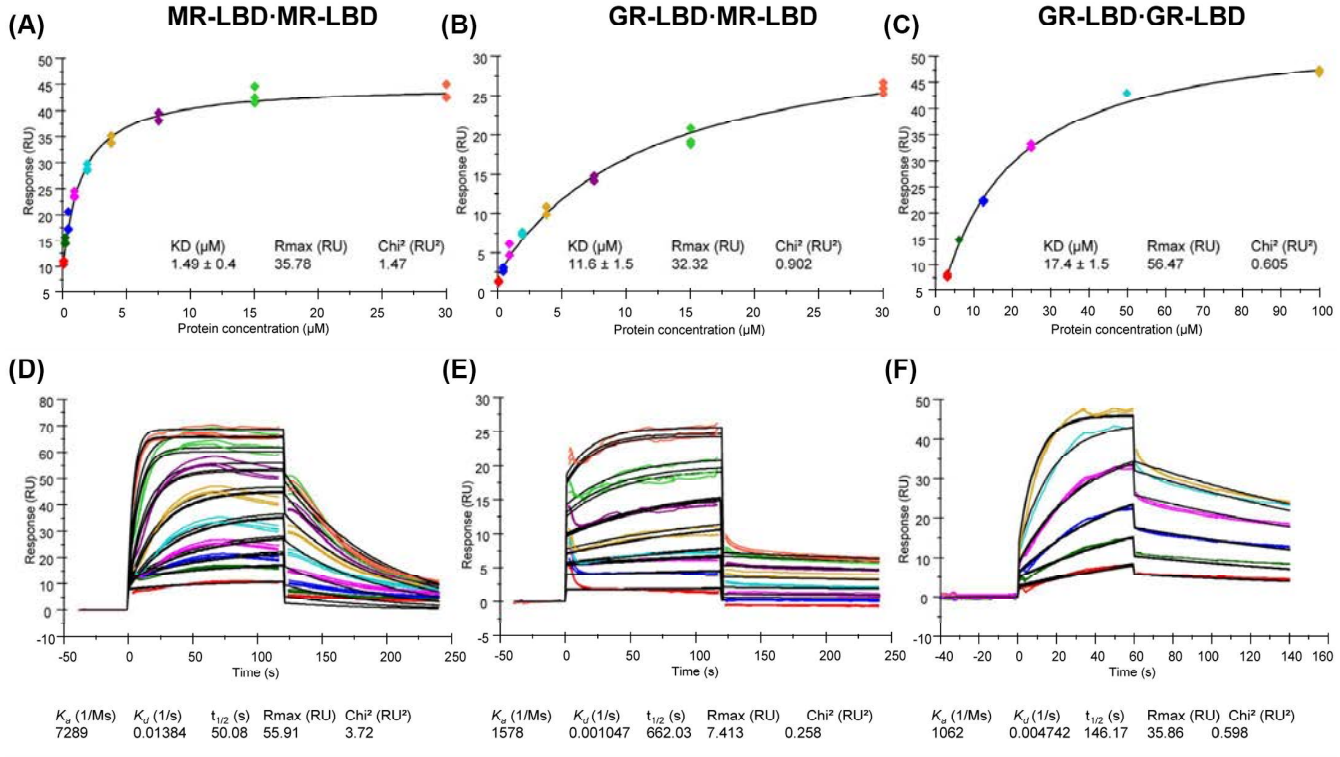

(G)

Interaction	Affinity constant (KD)	Dimer lifetime ($t_{1/2}$)
MR-LBD over MR-LBD	1.49 ± 0.4 μM	50 s
GR-LBD over GR-LBD	17.4 ± 1.5 μM	146 s
GR-LBD over MR-LBD	11.6 ± 1.5 μM	662 s

FIGURE 4 Affinity and kinetics of GR- and MR- protein–protein interactions. Surface plasmon resonance (SPR) analysis of either MR-LBD or GR-LBD self-association or heterodimerization were done by (A–C) affinity and (D–F) kinetics. Both immobilized protein and analyte protein run over the immobilized one were expressed and purified in the presence of 50 μM Dex. Concentrations specified under the X-axis correspond to the concentration gradient of the analyte protein past over the immobilized protein. Experiments were conducted in triplicates. The table (G) summarizes steady state affinity dissociation constants and complexes half-life.

15306860, 2023, 1, Downloaded from https://faseb.onlinelibrary.wiley.com/doi/10.1096/fj.202201199RR by Readcube (Labtiva Inc.), Wiley Online Library on [02/06/2023]. See the Terms and Conditions (https://onlinelibrary.wiley.com/terms-and-conditions) on Wiley Online Library for rules of use; OA articles are governed by the applicable Creative Commons License

performed *RNA-seq*. *Bioinformatics analyses identified* differentially expressed genes (DEGs) with statistical significance in both genotypes (FDR <0.05) (Table S3). A fold-change plot illustrates Dex versus vehicle gene expression in CO and MR^{EKO} cells (Figure 5A). The overall number of DEGs was almost identical in CO and MR^{EKO} cells (Figure 5B; 457 and 451 DEGs, respectively), with similar percentages of up- and downregulated genes (Figure 5B,C; 70% and 30% vs 64%, and 36%, respectively). Gene expression profiles between CO and MR^{EKO} were very similar, with high overlap between datasets and similar degrees of induction or repression among commonly regulated genes, suggesting a relatively small contribution of MR to the transcriptional response to Dex at this time point in keratinocytes. Upon evaluation of upregulated genes in both genotypes, we found that 16% of CO genes required MR for their regulation, while 8% of genes of the MR^{EKO} dataset were uniquely induced in the absence of this TF (Figure 5C). For downregulated genes, 22% of CO genes were dependent on MR for regulation, while a striking 33% of MR^{EKO} genes were uniquely repressed, suggesting that MR loss has greater impact on GR-mediated gene repression (Figure 5C).

The expression of selected candidate genes was validated in independent experiments by RT-qPCR. Differences between CO and MR^{EKO} reached statistical significance for genes such as *Tsc22d3/Gilz*, *Per1*, and *Sgk1* (Figure 5D). However, relative gene induction or repression by Dex was of similar magnitude in both genotypes for *Nfil3* and *Dusp10* (Figure 5D).

Functional enrichment analysis by DAVID identified regulation of transcription (23%), apoptosis (14%), T-cell activation (6%), and regulation of hormone secretion (5%) as the most overrepresented processes in Dex upregulated genes common to both genotypes (Figure S4). Most downregulated genes common to both genotypes were involved in signal transduction (60%), regulation of metabolism (43%), regulation of transcription (36%), cell migration (28%), response to stimulus (16%), and T-cell activation (12%), among others (Figure S6).

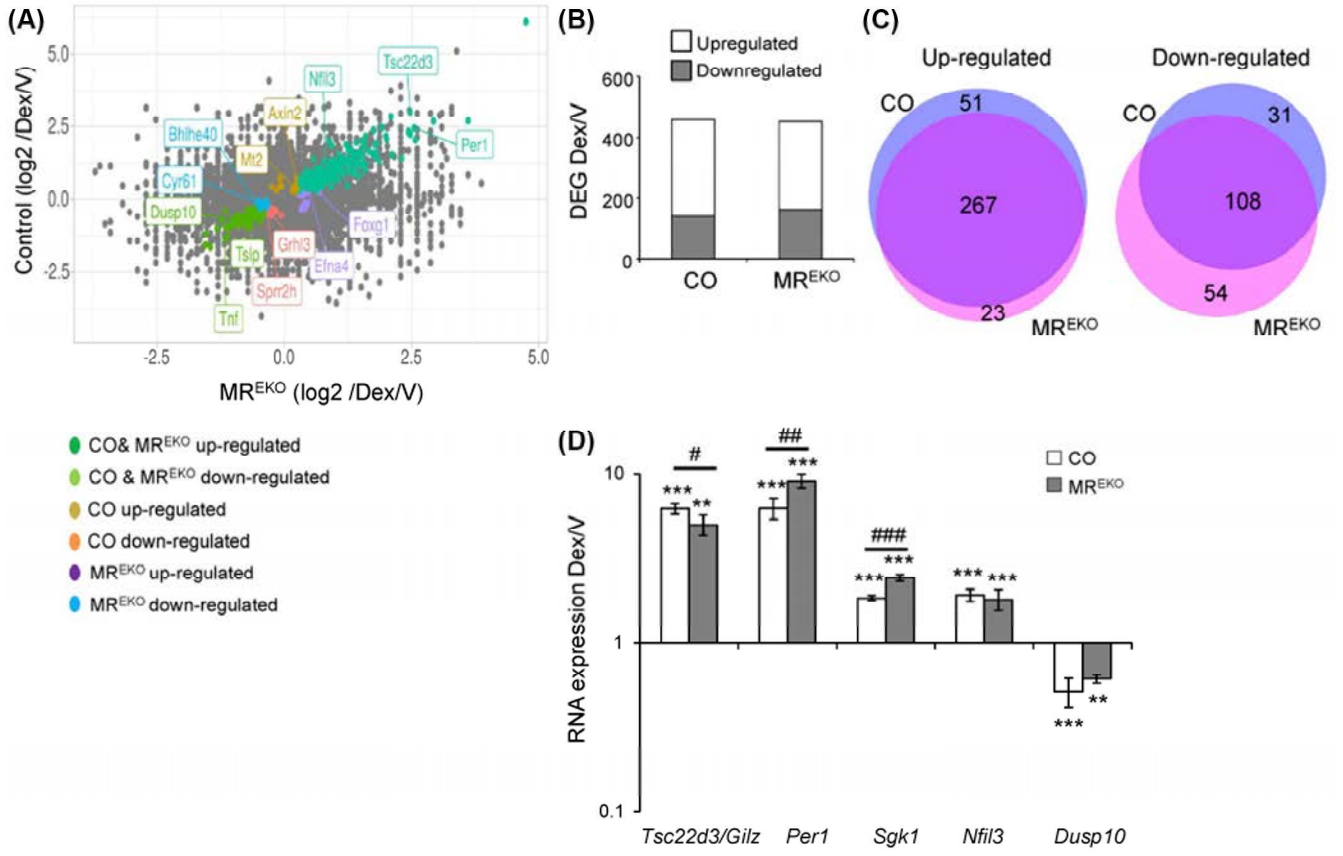

FIGURE 5 Transcriptomic profile in CO and MR^{EKO} keratinocytes upon Dex treatment. (A) Fold-change plot illustrates Dex versus vehicle gene expression *in* CO and MR^{EKO} cells. Differentially expressed genes (DEGs) with statistical significance in both genotypes (FDR <0.05), up- and downregulated, are highlighted in colors, including examples from indicated categories. (B) Bar graph showing number of DEGs, and (C) Venn diagram indicating overlap between up- and downregulated genes in Dex-treated CO and MR^{EKO} keratinocytes identified by RNA-Seq. (D) Validation of fold-change response (Dex vs vehicle) of the indicated genes in CO and MR^{EKO} keratinocytes by RT-qPCR. Mean values and SD are shown. Statistically significant differences relative to vehicle are denoted by asterisks and those between genotypes by hash symbols ($n = 3$–6; $^{\#}p < .05$; **, $^{\#\#}p < .01$; ***, $^{\#\#\#}p < .001$).

15306860, 2023, 1, Downloaded from https://faseb.onlinelibrary.wiley.com/doi/10.1096/fj.202201199RR by Readcube (Labtiva Inc.), Wiley Online Library on [02/06/2023]. See the Terms and Conditions (https://onlinelibrary.wiley.com/terms-and-conditions) on Wiley Online Library for rules of use; OA articles are governed by the applicable Creative Commons License

3.5 | MR modifies the kinetics of Dex-induced GR genomic binding

As GR nuclear/cytoplasmic ratio was significantly reduced in MR^{EKO} versus CO at 30–60 min following Dex treatment (Figure 3C), we performed time-course experiments to evaluate whether the loss of MR altered GR binding kinetics on GRE-containing GBS (Figure 6A). In Dex-treated CO cells, GR recruitment to *Nfil3* genomic sequence was detected at 10 min, and peaked at 30 min. However, in MR^{EKO}, GR binding was less pronounced and lagged behind CO only peaking 1 h after Dex (Figure 6A). When we assessed the time-course of *Nfil3* expression in MR^{EKO} versus CO, we found that transcript levels overall paralleled GR-binding kinetics; however, expression was similar in CO and MR^{EKO} 3 h after Dex treatment (Figure 6B).

GR binding to *Nr3c1* and *Dusp10* regulatory sequences followed similar early kinetics in CO and was dramatically decreased in MR-deficient cells (Figure 6A). The lack of GR binding to *Nr3c1* was particularly relevant as it is well known that GR mediates homologous downregulation of its own gene.[51,52] Importantly, *Nr3c1* repression by Dex occurred only in CO cells that co-express GR and MR (Figure 6B).

On the other hand, and despite marked differences of GR-binding kinetics between genotypes, *Tsc22d3/Gilz* followed similar expression kinetics, with significant differences between genotypes only at later time points (Figure 6B). This apparent discrepancy is likely due to the contribution of multiple GBS in this gene, of which four were common to both genotypes while one was unique for CO and one for MR^{EKO} (Table S2).

We also assessed GR binding to sequences identified uniquely in MR^{EKO} cells such as *Hlf* and *Lmnb2*. While in MR^{EKO} cells, Dex induced early GR binding to *Hlf*, which remained high up to 120 min, binding was not significant in CO cells through the time course (Figure S7). The differences in GR binding were less marked for *Lmnb2*, however, the extent of GR recruitment and delayed kinetics was decreased in CO cells (Figure S7). Altogether, these data indicate that MR modulates timing of GR genomic binding in keratinocytes in response to Dex. However, Dex did not elicit changes in *Hlf* or *Lmnb2* gene expression

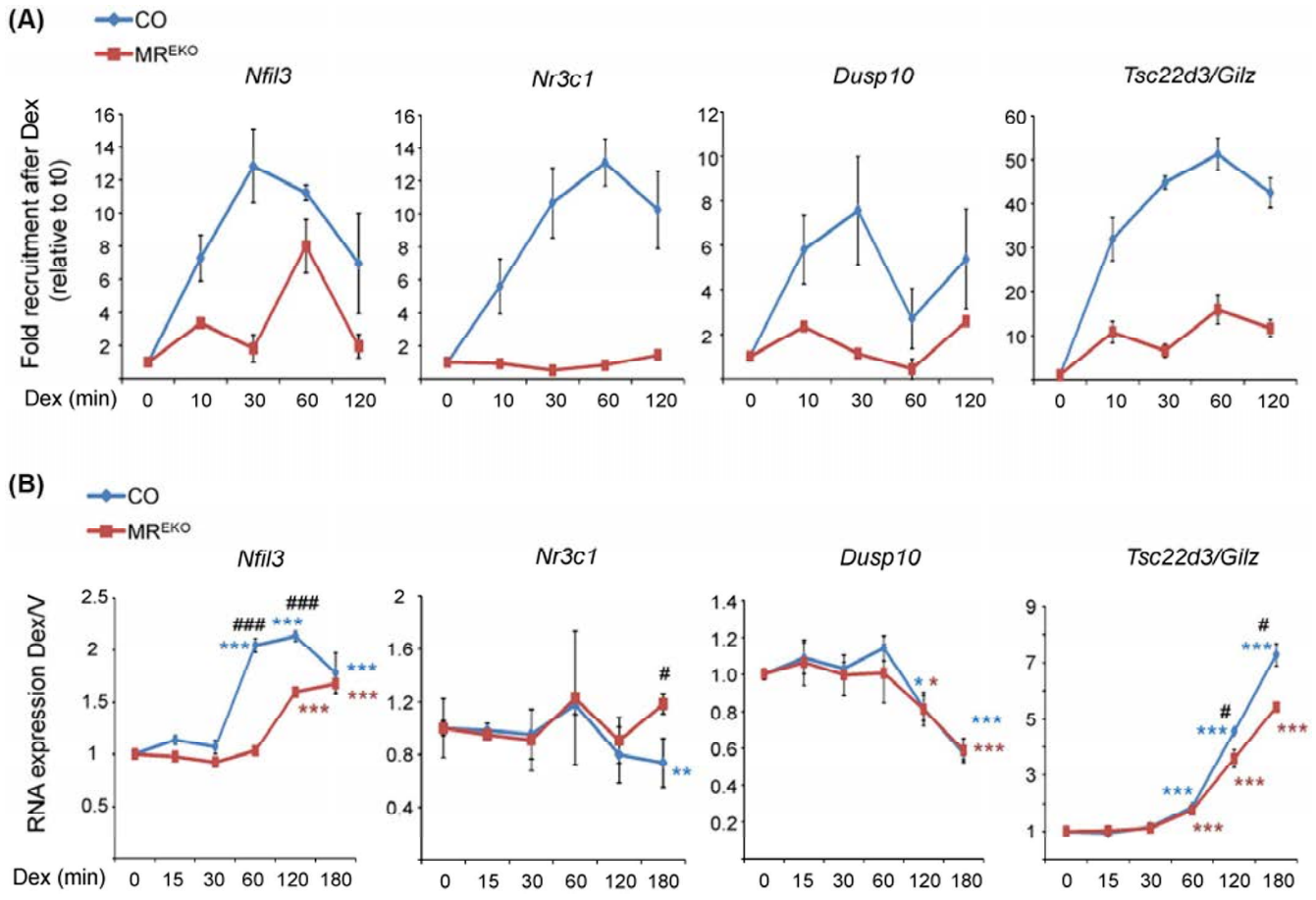

FIGURE 6 MR modifies the kinetics of Dex-induced GR genomic binding and transcriptional regulation. (A) GR ChIP carried out at indicated Dex treatment times to evaluate kinetics of binding to regulatory regions of indicated genes. (B) Dex time-course experiment to determine kinetics of gene expression in CO and MR^{EKO} cells. Mean values and SD are shown. Statistically significant differences relative to vehicle or between genotypes are represented by asterisks or hash symbols, respectively ($n = 3$; *, $^{\#}p < .05$; **, $^{\#\#}p < .01$; ***, $^{\#\#\#}p < .001$).

15306860, 2023, 1, Downloaded from https://faseb.onlinelibrary.wiley.com/doi/10.1096/fj.202201199RR by Readcube (Labtiva Inc.), Wiley Online Library on [02/06/2023]. See the Terms and Conditions (https://onlinelibrary.wiley.com/terms-and-conditions) on Wiley Online Library for rules of use; OA articles are governed by the applicable Creative Commons License

either in the RNA-seq data or the time points assessed (not shown) suggesting that GR binding to these regulatory sequences is unproductive.

Consistent with previous work,[50] comparison of ChIP-seq and RNA-seq datasets indicated that GR binding showed a higher correlation with gene induction; this was true in both genotypes (Figure S8; 11%–13% of induced genes were bound by GR). Altogether, our data indicate that differences in the magnitude of expression between genotypes upon Dex treatment are gene and time dependent.

4 | DISCUSSION

Our previous work demonstrated the central role of keratinocyte GR in mediating the GC transcriptional response in vitro and in vivo while keratinocyte MR was identified as an important modulator of GR-mediated transcription in this tissue in response to Dex.[24,30] These data prompted us to address the cell-type specific role of MR in GR genomic binding and transcriptional regulation in response to Dex in keratinocytes by integrated ChIP-seq and RNA-seq analyses.

In this study, we show that the absence of keratinocyte MR correlates with the global reduction of GR genomic binding, and elicits differential GR recruitment to specific TF-binding sites, in particular, a reduction in the number of GREs as well as number of palindromic motifs *per* GBS (Figure 2). Changes in MR^{EKO} versus CO were also in line with a decreased GR nuclear/cytoplasmic ratio (Figure 3D). Even in GRE-containing GBS present in both genotypes, we observed a lower tag count in MR^{EKO} (Figure 2D), suggesting an overall decreased affinity of GR for genomic targets. While these data strongly suggest that Dex induces GR and MR co-binding to DNA, direct proof of concurrent binding is lacking. Also, we cannot rule out that different association patterns of GR in MR^{EKO} versus CO cells after Dex are due to the lack of MR tethering.[16] However, the fact that CORT elicited robust MR binding to GBSs identified by GR ChIP-seq (Figure S3) indicates that distinct receptor–ligand complexes feature different affinities toward regulatory sequences.[23]

One major finding is the demonstration of physical complex formation between GR- and MR-LBDs by SPR analyses (Figure 4). The estimated K_D for GR homodimers is similar to previous data on GR and other steroid receptors such as AR and ER.[53] Importantly, to the best of our knowledge, this is the first report demonstrating the measurement of MR-LBD self-association affinity and kinetics constants. Indeed, the estimated K_D for MR homodimers was one order of magnitude lower than that obtained for GR homodimer, indicating higher affinity. However, homodimers of MR had the shortest lifetime, followed by those of GR and GR-MR heterodimers (Figure 4). Taken together, MR-containing dimers showed higher affinity while GR-containing dimers showed the longest lifetime. Therefore, as MR dimers likely represent a minor fraction due to low protein abundance, data indicate that MR mainly acts as modulator of GR-dependent transcription, placing the GR-MR heterodimer—with similar affinity to the GR homodimer but a 4.5-fold longer lifetime—as a key player in response to synthetic GCs.

Our data are also consistent with previous evidence demonstrating that GR-MR interactions can be mediated by alternative interfaces including the GR-LBD.[15,21] Also, while we demonstrated that GR is able to form oligomers,[15,53,54] preliminary data indicate that neither MR-MR nor MR-GR form higher order complexes (data not shown).

Collectively, our data not only emphasize the importance of the GR:MR balance in keratinocytes but also support the idea that GR-MR heterodimers represent an important mechanism to extend the regulatory potential of GCs in cells that co-express both receptors.[22] Indeed, combinatorial possibilities of GR-MR dimers likely contribute to cooperative or inhibitory transcriptional effects after Dex treatment. The fact that MR loss results in decreased (*Tsc22d3/Gilz*) or increased (*Per1* and *Sgk1*) gene expression (Figure 5C) is consistent with previous reports of MR as a cooperative or antagonistic partner for GR in the GC-dependent transcription.[16,19,30] It seems feasible that in pathological settings with altered GR:MR ratios, the formation of dimers may shift toward alternative complexes and result in changes in gene expression. This is in line with previous work demonstrating that MR inactivation in skin by genetic and pharmacological approaches reduced the GC-associated side effects in conditions of GC excess in mice and human.[36,55–57] Also, the fact that MR/*NR3C2* mRNA levels were decreased in human psoriatic lesions[58] highlights the importance of assessing the response of GR to synthetic GCs in face of the loss-of-function of endogenous MR.

The GR cistrome is cell-type specific and dynamic.[59] The mechanisms of GR genomic cooperation include its binding as distinct GR and/or GR-MR oligomers, and/or coordinated and synergistic GR-binding events with members of several TF family members including AP-1, C/EBP, STAT, NF-κB, TEAD, or p53.[60,61]

The top overrepresented motifs, common to CO and MR^{EKO} keratinocytes, were AP-1, GRE, TEAD, and p53 (Figure 2). It is well known that AP-1 has important roles in regulating gene expression during keratinocyte differentiation, consistent with differential expression of AP-1 family members in specific epidermal layers.[62,63] However, while AP-1 motifs showed the highest rate of

15306860, 2023, 1, Downloaded from https://faseb.onlinelibrary.wiley.com/doi/10.1096/fj.202201199RR by Readcube (Labtiva Inc.), Wiley Online Library on [02/06/2023]. See the Terms and Conditions (https://onlinelibrary.wiley.com/terms-and-conditions) on Wiley Online Library for rules of use; OA articles are governed by the applicable Creative Commons License

co-occurrence with GRE motifs in both CO and MR^{EKO} cells, bioinformatic analyses did not identify statistical differences between genotypes (Figure 2). It is feasible that the expression of distinct AP-1 family members has differential effects on the GR- and MR-mediated actions, as reported in HEK293 cells overexpressing these receptors.[64]

Enrichment analyses identified significant differences between TEAD (21% vs 42%) and p53 (7.5% vs 16%) motifs in CO and MR^{EKO} keratinocytes, respectively (Figure 2). The lack of detection of protein–protein interactions between GR and indicated TFs may be due to the experimental conditions used. In addition, there was higher co-occurrence of p53 and other TF motifs at GRE-containing GBS in MR^{EKO} versus CO cells (Figure 2F; 12% vs 6%, respectively), likely due to constitutive increased levels of p63 in MR^{EKO} keratinocytes (Figure 3A,B). We also identified additional TF motifs for STAT, KLF, and NF-1, although overrepresentation was not significant likely due to the restricted cut-off used (data not shown).

Despite the changes in GR genomic binding in MR^{EKO} relative to CO, the transcriptional profiles of both cells upon Dex treatment showed a high overlap (Figure 5 and Figure S5). Nonetheless, several known GC targets with important roles in keratinocytes were differentially expressed upon Dex treatment only in CO cells, including *Krt6a, Foxp1, Mt1, Mt2, Cxcl1, Spred2, Axin2*, *Grhl3*, and *Sprr2h*. This is likely due to the basal differences in the transcriptomic profile of MR^{EKO} versus CO keratinocytes, with overrepresentation of keratinocyte differentiation process, including p63 targets such as small proline-rich repeat (*Sprr*)*2* genes (data not shown). This is also consistent with more differentiated status of MR-deficient keratinocytes in vivo as shown by patches of increased keratinization in the epidermis of MR^{EKO} relative to CO mice.[36]

The choice of time points to perform ChIP-seq and RNA-seq (1 h vs 3 h) was based on previous analyses that showed optimal binding and gene expression changes at these time points.[38] However, genomic data showed poor association between these two parameters in both genotypes (Figure S5), consistent with previous reports in other cell types. This may be also due to the fact that binding of MR and GR to specific genomic sites is cyclic, as reported in renal cells.[23] Importantly, time-course experiments showed that gene-dependent differences in the magnitude of expression correlated with earlier and more pronounced GR binding to GRE sites unique to CO, which dramatically decreased in MR-deficient cells (Figure 6; *Nfil3, Nr3c1*, and *Dusp10*).

The lack of GR binding to *Nr3c1* in MR^{EKO} cells was particularly relevant as it constitutes, to the best of our knowledge, the first demonstration that homologous downregulation of *Nr3c1* requires the presence of MR. While in previous work, GC-mediated regulation of GRα mRNA was shown to be mediated through a direct interaction of the receptor with an intragenic nGRE in exon 6 of the gene,[51] here we identified a different genomic site located upstream of the gene (Table S2).

Overall, findings highlight the key role of MR to understand gene- and time-dependent specificity of GC actions, giving support to the combined use of MR antagonists plus GR ligands to improve the therapeutic index—or benefit:risk ratio—of GCs for the treatment of skin inflammatory disorders.[36,55–57]

AUTHOR CONTRIBUTIONS

Marc Lombès and Paloma Pérez designed the experiments; Elena Carceller-Zazo, Thi An Vu, Géraldine Vitellius, Say Viengchareun, and Yann Jaszczyszyn performed ChIPseq and RNAseq experiments; Elena Carceller-Zazo, Lisa M. Sevilla, and Omar Pons-Alonso performed cell culture work and ChIP-qPCR and RT-qPCR data validation; Elena Carceller-Zazo and Larbi Amazit performed immunofluorescence and high-throughput microscopy; Lisa M. Sevilla performed time-course experiments; Omar Pons-Alonso performed immunoprecipitation and immunoblotting experiments; Álvaro Chiner-Oms and Iñaki Comas performed data processing and bioinformatic analyses; Montserrat Abella, Andrea Alegre-Martí, and Eva Estébanez-Perpiñá did protein expression and purification studies, performed SPR assays, and analyzed data; Lisa M. Sevilla, Omar Pons-Alonso, and Paloma Pérez performed additional bioinformatic analyses; all authors analyzed data and contributed to the discussions; Elena Carceller-Zazo, Lisa M. Sevilla, Omar Pons-Alonso, Andrea Alegre-Martí, Eva Estébanez-Perpiñá, Marc Lombès, and Paloma Pérez contributed to manuscript writing and editing. We affirm that all authors have read and agree with the manuscript.

ACKNOWLEDGMENTS

We thank Mikhail Pachkov from the University of Basel Biozentrum for advice regarding the use of CREMA software. We kindly thank Eric Ortlund (Emory University) for sharing his GR and MR-LBD bacterial expression constructs.

FUNDING INFORMATION

This research is part of the grants PID2020-114652RB-I00 funded by MCIN/AEI/ 10.13039/501100011033 to PP, and PDC2021-121688-I00 to EE-P. The author's work was also supported by Inserm, Université Paris-Saclay. EC-Z was recipient of a postdoctoral fellowship from

15306860, 2023, 1, Downloaded from https://faseb.onlinelibrary.wiley.com/doi/10.1096/fj.202201199RR by Readcube (Labtiva Inc.), Wiley Online Library on [02/06/2023]. See the Terms and Conditions (https://onlinelibrary.wiley.com/terms-and-conditions) on Wiley Online Library for rules of use; OA articles are governed by the applicable Creative Commons License

the Alfonso Martín Escudero Foundation (Spain); OP-A was funded by EDGJID/2021/098 (Generalitat Valenciana) and by 'ESF Investing in your future.". We thank NuRCaMeIN (SAF2017-90604-REDT) for support for dissemination. PP is a member of the Scientific Network on ´Strategies for therapeutic targeting of the Aldosterone-Mineralocorticoid Receptor signaling pathway (ADMIRE network) funded by the German Research Foundation (DFG-ID 470188766). This work has benefited from the facilities and expertize of the high-throughput sequencing core facility of I2BC (Centre de Recherche de Gif – http://www.i2bc.paris-saclay.fr/). This work was supported by the DIM Thérapie Génique Paris Ile-de-France Région, IBiSA, and the Labex GR-Ex.

DISCLOSURES

The authors on the manuscript do not have any conflict of interest (either financial or personal).

DATA AVAILABILITY STATEMENT

Project sequencing data are publicly accessible at ENA-EBI under accession number PRJEB54880. Accession numbers for each sample can be found on Table S4.

ORCID

Paloma Pérez https://orcid.org/0000-0002-7166-2824

REFERENCES

1. Schäcke H, Döcke WD, Asadullah K. Mechanisms involved in the side effects of glucocorticoids. *Pharmacol Ther*. 2002;96:23-43.
2. Vandewalle J, Luypaert A, De Bosscher K, Libert C. Therapeutic mechanisms of glucocorticoids. *Trends Endocrinol Metab*. 2018;29:42-54. doi:10.1016/j.tem.2017.10.010
3. Desmet SJ, De BK. Glucocorticoid receptors: finding the middle ground. *J Clin Invest*. 2017;127:1136-1145. doi:10.1172/JCI88886
4. Menter A, Korman NJ, Elmets CA, et al. Guidelines of care for the management of psoriasis and psoriatic arthritis. Section 3. Guidelines of care for the management and treatment of psoriasis with topical therapies. *J Am Acad Dermatol*. 2009;60:643-659. doi:10.1016/j.jaad.2008.12.032
5. Timmermans S, Souffriau J, Libert C. A general introduction to glucocorticoid biology. *Front Immunol*. 2019;10:1545. doi:10.3389/FIMMU.2019.01545
6. Quax RA, Manenschijn L, Koper JW, et al. Glucocorticoid sensitivity in health and disease. *Nat Rev Endocrinol*. 2013;9:670-686. doi:10.1038/NRENDO.2013.183
7. Sacta MA, Chinenov Y, Rogatsky I. Glucocorticoid signaling: an update from a genomic perspective. *Annu Rev Physiol*. 2016;78:155-180. doi:10.1146/annurev-physiol-021115-105323
8. Gomez-Sanchez E, Gomez-Sanchez CE. the multifaceted mineralocorticoid receptor. *Compr Physiol*. 2014;4:965-994. doi:10.1002/CPHY.C130044
9. De Bosscher K, Desmet SJ, Clarisse D, Estébanez-Perpiña E, Brunsveld L. Nuclear receptor crosstalk - defining the mechanisms for therapeutic innovation. *Nat Rev Endocrinol*. 2020;16:363-377. doi:10.1038/S41574-020-0349-5
10. Escoter-Torres L, Greulich F, Quagliarini F, Wierer M, Uhlenhaut NH. Anti-inflammatory functions of the glucocorticoid receptor require DNA binding. *Nucleic Acids Res*. 2020;48:8393-8407. doi:10.1093/nar/gkaa565
11. Weikum ER, Knuesel MT, Ortlund EA, Yamamoto KR. Glucocorticoid receptor control of transcription: precision and plasticity via allostery. *Nat Rev Mol Cell Biol*. 2017;18:159-174. doi:10.1038/nrm.2016.152
12. Le Billan F, Khan JA, Lamribet K, et al. Cistrome of the aldosterone-activated mineralocorticoid receptor in human renal cells. *FASEB J*. 2015;29:3977-3989. doi:10.1096/FJ.15-274266
13. Surjit M, Ganti KP, Mukherji A, et al. Widespread negative response elements mediate direct repression by agonist- Liganded glucocorticoid receptor. *Cell*. 2011;145:224-241. doi:10.1016/J.CELL.2011.03.027
14. Jaisser F, Farman N. Emerging roles of the mineralocorticoid receptor in pathology: toward new paradigms in clinical pharmacology. *Pharmacol Rev*. 2016;68:49-75. doi:10.1124/pr.115.011106
15. Pooley JR, Rivers CA, Kilcooley MT, et al. Beyond the heterodimer model for mineralocorticoid and glucocorticoid receptor interactions in nuclei and at DNA. *PLoS One*. 2020;15:e0227520.
16. Rivers CA, Rogers MF, Stubbs FE, Conway-Campbell BL, Lightman SL, Pooley JR. Glucocorticoid receptor–tethered mineralocorticoid receptors increase glucocorticoid-induced transcriptional responses. *Endocrinology*. 2019;160:1044-1056. doi:10.1210/EN.2018-00819
17. Joëls M, De Kloet ER. Coordinative mineralocorticoid and glucocorticoid receptor-mediated control of responses to serotonin in rat hippocampus. *Neuroendocrinology*. 1992;55:344-350. doi:10.1159/000126135
18. Trapp T, Rupprecht R, Castren M, Reul JMHM, Holsboer F. Heterodimerization between mineralocorticoid and glucocorticoid receptor: a new principle of glucocorticoid action in the CNS. *Neuron*. 1994;13:1457-1462. doi:10.1016/0896-6273(94)90431-6
19. Liu W, Wang J, Sauter NK, Pearce D. Steroid receptor heterodimerization demonstrated in vitro and in vivo. *Proc Natl Acad Sci U S A*. 1995;92:12480-12484. doi:10.1073/PNAS.92.26.12480
20. Ou XM, Storring JM, Kushwaha N, Albert PR. Heterodimerization of mineralocorticoid and glucocorticoid receptors at a novel negative response element of the 5-HT1A receptor gene. *J Biol Chem*. 2001;276:14299-14307. doi:10.1074/JBC.M005363200
21. Savory JGA, Préfontaine GG, Lamprecht C, et al. Glucocorticoid receptor homodimers and glucocorticoid-mineralocorticoid receptor heterodimers form in the cytoplasm through alternative dimerization interfaces. *Mol Cell Biol*. 2001;21:781-793. doi:10.1128/MCB.21.3.781-793.2001
22. Koning ASCAM, Buurstede JC, Van Weert LTCM, Meijer OC. Glucocorticoid and mineralocorticoid receptors in the brain: a transcriptional perspective. *J Endocr Soc*. 2019;3:1917-1930. doi:10.1210/JS.2019-00158
23. Le Billan F, Amazit L, Bleakley K, et al. Corticosteroid receptors adopt distinct cyclical transcriptional signatures. *FASEB J*. 2018;32:5626-5639. doi:10.1096/FJ.201800391RR

15306860, 2023, 1, Downloaded from https://faseb.onlinelibrary.wiley.com/doi/10.1096/fj.202201199RR by Readcube (Labtiva Inc.), Wiley Online Library on [02/06/2023]. See the Terms and Conditions (https://onlinelibrary.wiley.com/terms-and-conditions) on Wiley Online Library for rules of use; OA articles are governed by the applicable Creative Commons License

24. Bigas J, Sevilla LM, Carceller E, Boix J, Pérez P. Epidermal glucocorticoid and mineralocorticoid receptors act cooperatively to regulate epidermal development and counteract skin inflammation article. *Cell Death Dis*. 2018;9:588-601. doi:10.1038/s41419-018-0673-z
25. Mifsud KR, Reul JMHM. Acute stress enhances heterodimerization and binding of corticosteroid receptors at glucocorticoid target genes in the hippocampus. *Proc Natl Acad Sci U S A*. 2016;113:11336-11341. doi:10.1073/PNAS.1605246113/-/DCSUPPLEMENTAL
26. Nishi M, Tanaka M, Matsuda KI, Sunaguchi M, Kawata M. Visualization of glucocorticoid receptor and mineralocorticoid receptor interactions in living cells with GFP-based fluorescence resonance energy transfer. *J Neurosci*. 2004;24:4918-4927. doi:10.1523/JNEUROSCI.5495-03.2004
27. Cato ACB, Weinmann J. Mineralocorticoid regulation of transcription of transfected mouse mammary tumor virus DNA in cultured kidney cells. *J Cell Biol*. 1988;106:2119-2125. doi:10.1083/JCB.106.6.2119
28. Gomez-Sanchez EP, Venkataraman MT, Thwaites D, Fort C. ICV infusion of corticosterone antagonizes ICV-aldosterone hypertension. *Am J Physiol Endocrinol Metab*. 1990;258:E649-E653. doi:10.1152/AJPENDO.1990.258.4.E649
29. Govindan MV, Leclerc S, Roy R, Rathanaswami P, Xie B. Differential regulation of mouse mammary tumor virus-bacterial chloramphenicol acetyltransferase chimeric gene by human mineralocorticoid hormone-receptor complexes. *J Steroid Biochem Mol Biol*. 1991;39:91-103. doi:10.1016/0960-0760(91)90017-Y
30. Sevilla LM, Bigas J, Chiner-Oms Á, Comas I, Sentandreu V, Pérez P. Glucocorticoid-dependent transcription in skin requires epidermal expression of the glucocorticoid receptor and is modulated by the mineralocorticoid receptor. *Sci Rep*. 2020;10:18954. doi:10.1038/s41598-020-75853-5
31. Pooley JR, Flynn BP, Grøntved L, et al. Genome-wide identification of basic helix-loop-helix and NF-1 motifs underlying GR binding sites in male rat hippocampus. *Endocrinology*. 2017;158:1486-1501. doi:10.1210/en.2016-1929
32. Watt FM. Mammalian skin cell biology: at the interface between laboratory and clinic. *Science*. 2014;346:937-940. doi:10.1126/SCIENCE.1253734
33. Elias PM, Wakefield JS. Therapeutic implications of a barrier-based pathogenesis of atopic dermatitis. *Clin Rev Allergy Immunol*. 2011;41:282-295. doi:10.1007/S12016-010-8231-1
34. Harris-Tryon TA, Grice EA. Microbiota and maintenance of skin barrier function. *Science*. 2022;376:940-945. doi:10.1126/science.abo0693
35. Sevilla LM, Pérez P. Roles of the glucocorticoid and mineralocorticoid receptors in skin pathophysiology. *Int J Mol Sci*. 2018;19:1906. doi:10.3390/ijms19071906
36. Boix J, Sevilla LM, Sáez Z, Carceller E, Pérez P. Epidermal mineralocorticoid receptor plays beneficial and adverse effects in skin and mediates glucocorticoid responses. *J Invest Dermatol*. 2016;136:2417-2426. doi:10.1016/j.jid.2016.07.018
37. Reichelt J, Haase I. Establishment of spontaneously immortalized keratinocyte lines from wild-type and mutant mice. *Methods Mol Biol*. 2010;585:59-69.
38. Sevilla LM, Latorre V, Carceller E, et al. Glucocorticoid receptor and Klf4 co-regulate anti-inflammatory genes in keratinocytes. *Mol Cell Endocrinol*. 2015;412:281-289. doi:10.1016/j.mce.2015.05.015
39. Heinz S, Benner C, Spann N, et al. Simple combinations of lineage-determining transcription factors prime cis-regulatory elements required for macrophage and B cell identities. *Mol Cell*. 2010;38:576-589. doi:10.1016/J.MOLCEL.2010.05.004
40. Severinova E, Alikunju S, Deng W, Dhawan P, Sayed N, Sayed D. Glucocorticoid receptor-binding and transcriptome signature in Cardiomyocytes. *J Am Heart Assoc*. 2019;8:e011484. doi:10.1161/JAHA.118.011484
41. Robinson JT, Thorvaldsdóttir H, Winckler W, et al. Integrative genomics viewer. *Nat Biotechnol*. 2011;29:24-26. doi:10.1038/nbt.1754
42. Grant CE, Bailey TL. XSTREME: comprehensive motif analysis of biological sequence datasets. *bioRxiv*. 2021;20210902458722. doi:10.1101/2021.09.02.458722
43. Huang DW, Sherman BT, Lempicki RA. Bioinformatics enrichment tools: paths toward the comprehensive functional analysis of large gene lists. *Nucleic Acids Res*. 2009;37:1-13. doi:10.1093/nar/gkn923
44. Huang DW, Sherman BT, Lempicki RA. Systematic and integrative analysis of large gene lists using DAVID bioinformatics resources. *Nat Protoc*. 2009;4:44-57. doi:10.1038/nprot.2008.211
45. Weikum ER, Okafor CD, D'Agostino EH, Colucci JK, Ortlund EA. Structural analysis of the glucocorticoid receptor ligand-binding domain in complex with triamcinolone Acetonide and a fragment of the atypical Coregulator, small heterodimer partner. *Mol Pharmacol*. 2017;92:12-21. doi:10.1124/MOL.117.108506
46. Frank F, Liu X, Ortlund EA. Glucocorticoid receptor condensates link DNA-dependent receptor dimerization and transcriptional transactivation. *Proc Natl Acad Sci U S A*. 2021;118:e2024685118. doi:10.1073/PNAS.2024685118/SUPPL_FILE/PNAS.2024685118.SAPP.PDF
47. Hulsen T, de Vlieg J, Alkema W. BioVenn - a web application for the comparison and visualization of biological lists using area-proportional Venn diagrams. *BMC Genomics*. 2008;9:488. doi:10.1186/1471-2164-9-488
48. Love MI, Huska MR, Jurk M, et al. Role of the chromatin landscape and sequence in determining cell type-specific genomic glucocorticoid receptor binding and gene regulation. *Nucleic Acids Res*. 2017;45:1805-1819. doi:10.1093/nar/gkw1163
49. So AYL, Chaivorapol C, Bolton EC, Li H, Yamamoto KR. Determinants of cell- and gene-specific transcriptional regulation by the glucocorticoid receptor. *PLoS Genet*. 2007;3:927-938. doi:10.1371/journal.pgen.0030094
50. Reddy TE, Pauli F, Sprouse RO, et al. Genomic determination of the glucocorticoid response reveals unexpected mechanisms of gene regulation. *Genome Res*. 2009;19:2163-2171. doi:10.1101/gr.097022.109
51. Ramamoorthy S, Cidlowski JA. Ligand-induced repression of the glucocorticoid receptor gene is mediated by an NCoR1 repression complex formed by long-range chromatin interactions with intragenic glucocorticoid response elements. *Mol Cell Biol*. 2013;33:1711-1722. doi:10.1128/MCB.01151-12
52. Spies LML, Verhoog NJD, Louw A. Acquired glucocorticoid resistance due to homologous glucocorticoid receptor downregulation: a modern look at an age-old problem. *Cell*. 2021;10:2529. doi:10.3390/CELLS10102529
53. Jiménez-Panizo A, Alegre-Martí A, Fettweis G, et al. The multivalency of the glucocorticoid receptor ligand-binding domain

15306860, 2023, 1, Downloaded from https://faseb.onlinelibrary.wiley.com/doi/10.1096/fj.202201199RR by Readcube (Labtiva Inc.), Wiley Online Library on [02/06/2023]. See the Terms and Conditions (https://onlinelibrary.wiley.com/terms-and-conditions) on Wiley Online Library for rules of use; OA articles are governed by the applicable Creative Commons License

explains its manifold physiological activities. *Nucleic Acids Res*. 2021;gkac1119. doi:10.1093/nar/gkac1119

54. Presman DM, Ganguly S, Schiltz RL, Johnson TA, Karpova TS, Hager GL. DNA binding triggers tetramerization of the glucocorticoid receptor in live cells. *Proc Natl Acad Sci U S A*. 2016;113:8236-8241. doi:10.1073/pnas.1606774113
55. Maubec E, Laouénan C, Deschamps L, et al. Topical mineralocorticoid receptor blockade limits glucocorticoid-induced epidermal atrophy in human skin. *J Invest Dermatol*. 2015;135:1781-1789. doi:10.1038/JID.2015.44
56. Boix J, Nguyen VT, Farman N, Aractingi S, Pérez P. Mineralocorticoid receptor blockade improves glucocorticoid-induced skin atrophy but partially ameliorates anti-inflammatory actions in an irritative model in human skin explants. *Exp Dermatol*. 2018;27:185-187. doi:10.1111/EXD.13473
57. Perez P. The mineralocorticoid receptor in skin disease. *Br J Pharmacol*. 2022;179:3178-3189. doi:10.1111/bph.15736
58. Suárez-Fariñas M, Li K, Fuentes-Duculan J, Hayden K, Brodmerkel C, Krueger JG. Expanding the psoriasis disease profile: interrogation of the skin and serum of patients with moderate-to-severe psoriasis. *J Invest Dermatol*. 2012;132:2552-2564. doi:10.1038/JID.2012.184
59. Escoter-Torres L, Caratti G, Mechtidou A, Tuckermann J, Uhlenhaut NH, Vettorazzi S. Fighting the fire: mechanisms of inflammatory gene regulation by the glucocorticoid receptor. *Front Immunol*. 2019;10:1859. doi:10.3389/FIMMU.2019.01859
60. Starick SR, Ibn-Salem J, Jurk M, et al. ChIP-exo signal associated with DNA-binding motifs provides insight into the genomic binding of the glucocorticoid receptor and cooperating transcription factors. *Genome Res*. 2015;25:825-835. doi:10.1101/gr.185157.114
61. Vockley CM, D'Ippolito AM, McDowell IC, et al. Direct GR binding sites potentiate clusters of TF binding across the human genome. *Cell*. 2016;166:1269-1281. doi:10.1016/J.CELL.2016.07.049
62. Welter JF, Eckert RL. Differential expression of the fos and Jun family members c-fos, fosB, Fra-1, Fra-2, c-jun, junB and junD during human epidermal keratinocyte differentiation. *Oncogene*. 1995;11:2681-2687.
63. Hanley K, Wood L, Ng DC, et al. Cholesterol sulfate stimulates involucrin transcription in keratinocytes by increasing Fra-1, Fra-2, and Jun D. *J Lipid Res*. 2001;42:390-398. doi:10.1016/S0022-2275(20)31663-1
64. Dougherty EJ, Elinoff JM, Ferreyra GA, et al. Mineralocorticoid receptor (MR) trans-activation of inflammatory AP-1 signaling: dependence on DNA sequence, MR conformation, and AP-1 family member expression. *J Biol Chem*. 2016;291:23628-23644. doi:10.1074/JBC.M116.732248

SUPPORTING INFORMATION

Additional supporting information can be found online in the Supporting Information section at the end of this article.

How to cite this article: Carceller-Zazo E, Sevilla LM, Pons-Alonso O, et al. The mineralocorticoid receptor modulates timing and location of genomic binding by glucocorticoid receptor in response to synthetic glucocorticoids in keratinocytes. *The FASEB Journal*. 2023;37:e22709. doi:10.1096/fj.202201199RR

15306860, 2023, 1, Downloaded from https://faseb.onlinelibrary.wiley.com/doi/10.1096/fj.202201199RR by Readcube (Labtiva Inc.), Wiley Online Library on [02/06/2023]. See the Terms and Conditions (https://onlinelibrary.wiley.com/terms-and-conditions) on Wiley Online Library for rules of use; OA articles are governed by the applicable Creative Commons License

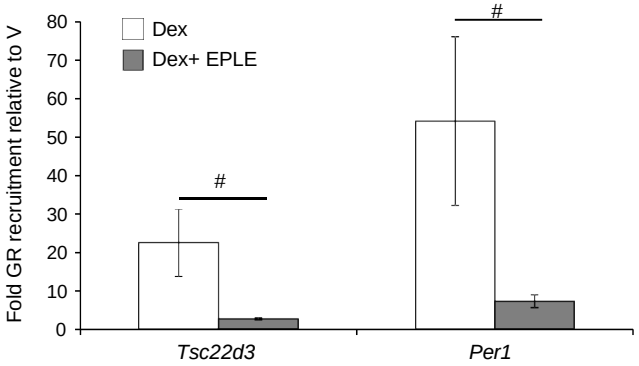

Figure S1. Treatment with MR antagonist Eplerenone impairs Dex-induced GR recruitment to genomic targets.
Control keratinocytes were treated for 1h with either Vehicle (V) or 100 nM Dex in the presence or absence of Eplenerone (Eple, 10 μM), followed by GR-ChIP. Binding to *Tsc22d3 and Per1* regulatory sequences was assessed by qPCR. Mean values and SD are shown. Hash signs indicate statistically significant differences in recruitment between treatments (n=3; #,p<0.05).

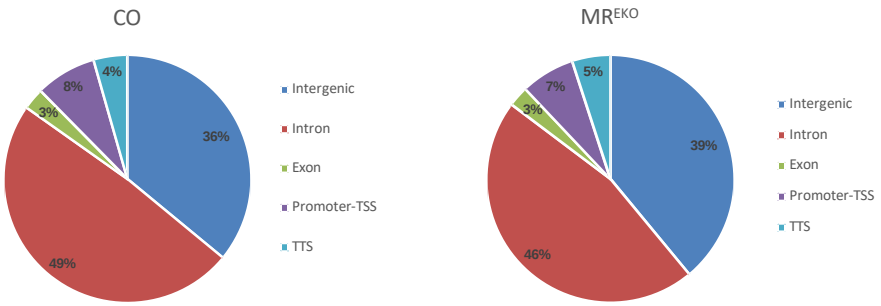

Figure S2. Genomic distribution of GR DNA binding sites.
Pie chart showing the percentage of genomic location distribution of GR in the presence (CO) and absence of MR (MR^{EKO}).

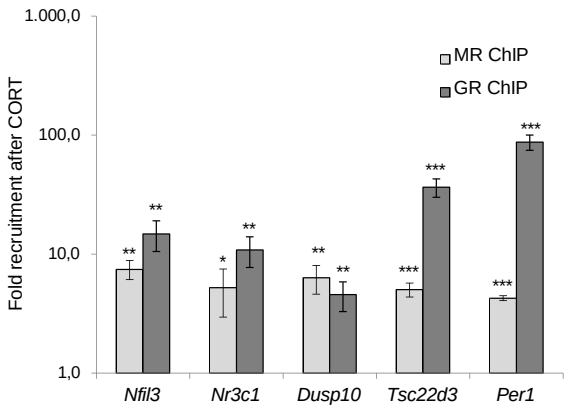

Figure S3. MR and GR genomic binding in response to corticosterone.
Control keratinocytes were treated 1h with either Vehicle (V), 100 nM Dex, or 100 nM corticosterone (CORT) followed by MR- or GR- ChIP; binding to indicated regulatory sequences was assessed by qPCR. Mean values and SD are shown. Asterisks indicate statistically significant differences in recruitment after CORT (n=3; *, p<0.05; **, p<0.01; ***, p<0.001).

CO only_GREs 408 genes

Term	Count	%	PValue
GO:0045944~positive regulation of transcription from RNA polymerase II promoter	33	8.8	0,009
GO:0000122~negative regulation of transcription from RNA polymerase II promoter	30	8	0,002
GO:0030154~cell differentiation	26	6.9	0,037

CO&MREKO_GREs 440 genes

Term	Count	%	PValue
GO:0006468~protein phosphorylation	38	8.8	8,34E-10
GO:0045944~positive regulation of transcription from RNA polymerase II promoter	38	8.8	0,0051671
GO:0000122~negative regulation of transcription from RNA polymerase II promoter	34	7.8	0,001495
GO:0007155~cell adhesion	29	6.7	1,88E-05
GO:0006915~apoptotic process	28	6.5	3,75E-05
GO:0035556~intracellular signal transduction	24	5.5	3,01E-05
GO:0001525~angiogenesis	16	3.7	4,19E-04
GO:0016477~cell migration	14	3.2	0,004201
GO:0051726~regulation of cell cycle	13	3	0,0044254
GO:0032922~circadian regulation of gene expression	9	2.1	8,18E-05

Figure S4. Functional clustering of GRE-containing genes in Dex-treated control and MR^{EKO} keratinocytes.
Gene ontology categorization of indicated gene subsets in control (CO) and MR^{EKO} keratinocytes was analyzed by DAVID (https://david.ncifcrf.gov/.)

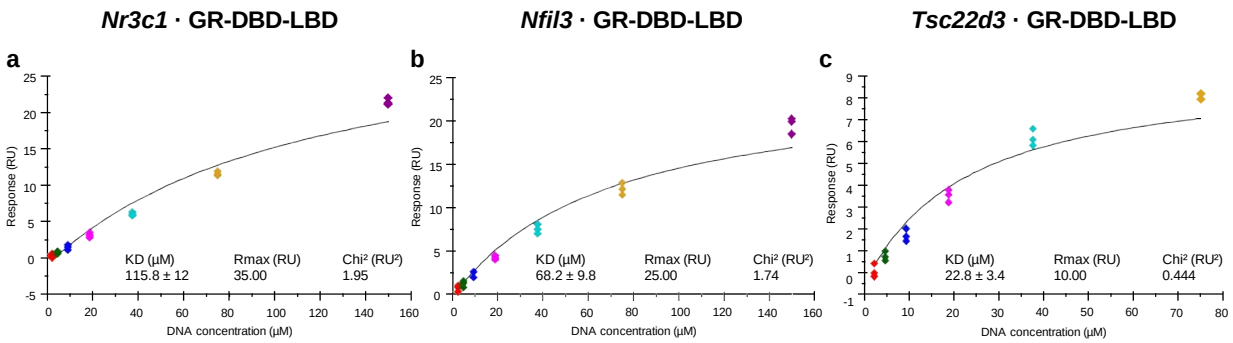

Figure S5. GR multidomain (GR-DBD-LBD) binding to DNA regulatory sequences identified by ChIP-seq.
Surface plasmon resonance (SPR) analysis of multidomain GR-DBD-LBD binding to increasing concentrations of regulatory sequences of *Nr3c1* (a), *Nfil3* (b) and *Tsc22d3* (c). Experiments were conducted in triplicates and analyzed by affinity.

OVERLAP CO&MREKO UP 266 genes

Gene Ontology Terms	**Count**	**%**	**PValue**
GO:0006355~regulation of transcription, DNA-templated	60	22.8	0,01554
GO:0042981~regulation of apoptotic process	36	13.7	4,78E-04
GO:0042110~T cell activation	15	5.7	0,00334
GO:0046883~regulation of hormone secretion	13	4.94	4,64E-04
GO:2000147~positive regulation of cell motility	13	4.94	0,01864

OVERLAP CO&MREKO DOWN 108 genes

Gene Ontology Terms	**Count**	**%**	**PValue**
GO:0007165~signal transduction	65	61.3	2,01E-11
GO:1901360~organic cyclic compound metabolic process	46	43.4	0,00279
GO:0006355~regulation of transcription, DNA-templated	38	35.8	1,55E-05
GO:0016477~cell migration	30	28.3	4,65E-12
GO:0009607~response to biotic stimulus	17	16	2,54E-04
GO:0071822~protein complex subunit organization	14	13.2	0,04456
GO:0042110~T cell activation	13	12.3	8,66E-06
GO:0018108~peptidyl-tyrosine phosphorylation	12	11.3	2,96E-07
GO:0007548~sex differentiation	10	9.43	5,11E-05

Figure S6. Functional clustering of DEGs in Dex-treated control and MR^{EKO} keratinocytes.
Gene ontology categorization of differentially expressed genes in control (CO) and MR^{EKO} keratinocytes was analyzed by DAVID (https://david.ncifcrf.gov/.). The table shows genes involved in specific biological processes. Fold-change of gene expression >1.5 and <0.7, FDR<0.05)

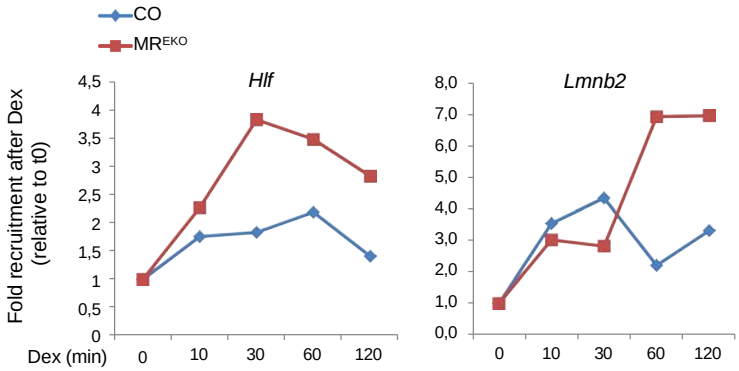

Figure S7. The absence of MR results in kinetics-dependent enhanced GR binding to specific regulatory regions after Dex treatment.
GR ChIP carried out at indicated Dex treatment times to evaluate kinetics of binding to indicated regulatory regions. Mean values and SD are shown. Statistically significant differences relative to vehicle or between genotypes are represented by asterisks or hash symbols, respectively (n = 3).

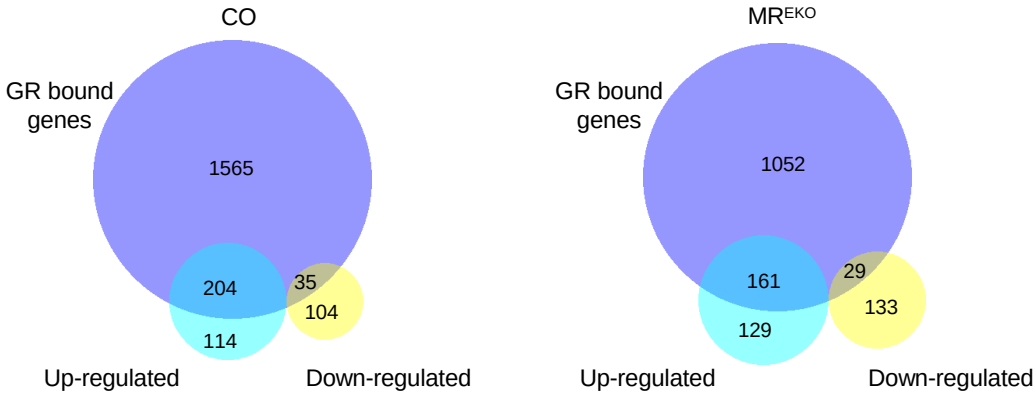

Figure S8. Correlation between GR genomic binding and gene expression changes in Dex-treated control and MR^{EKO} keratinocytes.
Venn diagram depicting the overlap between the genes associated with peaks identified by ChIP-Seq and DEGs identified by RNA-Seq in Dex-treated control (CO; left) and MR^{EKO} (right) keratinocytes.

3.5. Glucocorticoid resistance: Interference between the glucocorticoid receptor and the MAPK signalling pathways

Lisa M. Sevilla, Alba Jiménez-Panizo, **Andrea Alegre-Martí**, Eva Estébanez-Perpiñá, Carme Caelles and Paloma Pérez.

Published in: International Journal of Molecular Sciences, 2021
Impact factor: 6.208
Quartile: Q1
DOI: 10.3390/ijms221810049

For this review I designed and elaborated Figure 1 to show the gene organization of the different GR isoforms, and to give a structural presentation of GR LBD and DBD modules, as well as their individual dimeric crystal structures. I also prepared the bibliographic information file and contributed to the writing of the article.

International Journal of
Molecular Sciences

MDPI

Review

Glucocorticoid Resistance: Interference between the Glucocorticoid Receptor and the MAPK Signalling Pathways

Lisa M. Sevilla [1], Alba Jiménez-Panizo [2,3], Andrea Alegre-Martí [2,3], Eva Estébanez-Perpiñá [2,3], Carme Caelles [3,4] and Paloma Pérez [1,*]

1 Instituto de Biomedicina de Valencia (IBV)-CSIC, 46010 Valencia, Spain; lsevilla@ibv.csic.es
2 Department of Biochemistry and Molecular Biomedicine, Faculty of Biology, University of Barcelona (UB), 08028 Barcelona, Spain; alba.jimenez.panizo@gmail.com (A.J.-P.); andrea.alegre.marti@gmail.com (A.A.-M.); evaestebanez@ub.edu (E.E.-P.)
3 Institute of Biomedicine, University of Barcelona (IBUB), 08028 Barcelona, Spain; ccaelles@ub.edu
4 Department of Biochemistry and Physiology, School of Pharmacy and Food Sciences, University of Barcelona (UB), 08028 Barcelona, Spain
* Correspondence: pperez@ibv.csic.es; Tel.: +34-96-339-1766

Abstract: Endogenous glucocorticoids (GCs) are steroid hormones that signal in virtually all cell types to modulate tissue homeostasis throughout life. Also, synthetic GC derivatives (pharmacological GCs) constitute the first-line treatment in many chronic inflammatory conditions with unquestionable therapeutic benefits despite the associated adverse effects. GC actions are principally mediated through the GC receptor (GR), a ligand-dependent transcription factor. Despite the ubiquitous expression of GR, imbalances in GC signalling affect tissues differently, and with variable degrees of severity through mechanisms that are not completely deciphered. Congenital or acquired GC hypersensitivity or resistance syndromes can impact responsiveness to endogenous or pharmacological GCs, causing disease or inadequate therapeutic outcomes, respectively. Acquired GC resistance is defined as loss of efficacy or desensitization over time, and arises as a consequence of chronic inflammation, affecting around 30% of GC-treated patients. It represents an important limitation in the management of chronic inflammatory diseases and cancer, and can be due to impairment of multiple mechanisms along the GC signalling pathway. Among them, activation of the mitogen-activated protein kinases (MAPKs) and/or alterations in expression of their regulators, the dual-specific phosphatases (DUSPs), have been identified as common mechanisms of GC resistance. While many of the anti-inflammatory actions of GCs rely on GR-mediated inhibition of MAPKs and/or induction of DUSPs, the GC anti-inflammatory capacity is decreased or lost in conditions of excessive MAPK activation, contributing to disease susceptibility in tissue- and disease- specific manners. Here, we discuss potential strategies to modulate GC responsiveness, with the dual goal of overcoming GC resistance and minimizing the onset and severity of unwanted adverse effects while maintaining therapeutic potential.

Keywords: glucocorticoids; glucocorticoid receptor; resistance/sensitivity; mitogen-activated protein kinases (MAPKs); dual-specific phosphatases (DUSPs); chronic inflammation; leukaemia; therapeutics

check for updates

Citation: Sevilla, L.M.; Jiménez-Panizo, A.; Alegre-Martí, A.; Estébanez-Perpiñá, E.; Caelles, C.; Pérez, P. Glucocorticoid Resistance: Interference between the Glucocorticoid Receptor and the MAPK Signalling Pathways. *Int. J. Mol. Sci.* **2021**, *22*, 10049. https://doi.org/10.3390/ijms221810049

Academic Editor: Cristina Angeloni

Received: 26 July 2021
Accepted: 15 September 2021
Published: 17 September 2021

Publisher's Note: MDPI stays neutral with regard to jurisdictional claims in published maps and institutional affiliations.

Copyright: © 2021 by the authors. Licensee MDPI, Basel, Switzerland. This article is an open access article distributed under the terms and conditions of the Creative Commons Attribution (CC BY) license (https://creativecommons.org/licenses/by/4.0/).

1. Introduction

Glucocorticoids (GCs) are steroid hormones that regulate the physiology of all mammalian tissues throughout life due to their diverse roles in development, growth, metabolism, and inflammation [1–4]. In response to physiological cues and stressors, the hypothalamic-pituitary-adrenal (HPA) axis coordinates the systemic production and secretion of GCs from the adrenal glands in a circadian and stress-related manner to maintain tissue homeostasis. In turn, GCs mediate negative feed-back inhibiting secretion of the hypothalamic corticotropin-releasing hormone (CRH) and the adrenocorticotropic hormone (ACTH), limiting GC production.

The homeostatic control exerted by the HPA axis fits with an inverted U-shaped dose-response curve, where the equilibrium is achieved in the central range of the curve (optimal) while both GC excess or deficiency occur on either side of the curve (suboptimal effects) [2,5,6]. The disruption of this central HPA axis, due to pathophysiological triggers such as chronic stress, inflammation, or by prolonged exogenous GC treatments, results in abnormal endogenous GC levels. These GC imbalances contribute to disease and disease susceptibility in tissue-specific manners and with variable degrees of severity, by mechanisms that are not completely deciphered. Besides the adrenal GC production, certain tissues such as the thymus, intestine, brain, and skin, express functional equivalents of the HPA axis that allow for GC synthesis de novo [7,8]. This local GC production is increasingly recognized as a mechanism mediating rapid and critical control of immune activation [9].

Synthetic GCs are commonly prescribed to treat chronic inflammatory conditions including respiratory, autoimmune, and cutaneous diseases, as well as cancers of the hematopoietic lineage, mostly leukaemias [10]. The increasing number of GC-based prescriptions (around 3% of EU population uses GCs annually) [11] represents a high economic burden for health care systems, with demands rising as geriatric population and chronic diseases increase. However, despite their efficacy, long-term treatments and/or high doses with GCs trigger adverse effects, impacting metabolism (obesity, diabetes, and osteoporosis), and increasing susceptibility to stress and infections [10,12]. Another important limitation in the management of inflammatory diseases is resistance to GCs due to the lack of response or loss of efficacy over time [6,13–15]. The degrees of GC insensitivity are variable and highly dependent on the disease; for instance, while almost all patients with chronic obstructive pulmonary disease (COPD) and sepsis experience GC resistance, percentages are variable in patients with rheumatoid arthritis (30%), primary acute lymphoblastic leukaemia (ALL) (10–30%), or asthma (4–10%) [6].

Both endogenous and pharmacological GCs act through a dual system formed by the corticosteroid receptors GC receptor (GR/NR3C1) and mineralocorticoid receptor (MR/NR3C2), structurally and functionally close members of the nuclear receptor (NR) subclass NR3C that, upon hormone binding, act as ligand-activated transcription factors (TFs) [16–20]. While GR is ubiquitously expressed and almost exclusively activated by GCs, MR expression pattern is more restricted and can bind GCs and the mineralocorticoid aldosterone with similar high affinity. In tissues where GR and MR co-express, the selective activation of these TFs is achieved by pre-receptor mechanisms that modulate the local availability of active GCs. The enzymes 11β-hydroxysteroid dehydrogenase (HSD11B) type I and II, which catalyse the interconversion between active (cortisol) and inactive (cortisone) forms, represent a major regulatory mechanism for receptor selectivity [19,21,22].

2. Structure and Function of the Glucocorticoid Receptor (GR)

GR is encoded by *NR3C1*, a unique gene comprising nine exons (Figure 1A) that can give rise to multiple isoforms through alternative splicing (Figure 1B) and use of alternative translational initiation sites [10,17,18,23,24]. Similar to all NRs, GR is composed of modular domains required for ligand binding, receptor dimerization and binding of hormone receptor complexes to GC response elements (GREs) in target genes [10,16–18,25] (Figure 1B). The N-terminal domain features the activation function (AF)-1, which is ligand-independent, and also mediates interactions with the transcriptional machinery and co-regulators. Most sites for post-translational modifications (PTM) such as phosphorylation, acetylation, ubiquitination, and SUMOylation, map within this domain, contributing to modulation of receptor function [23]. The DNA-binding domain (DBD) is highly conserved among NR family members, and contains two zinc finger motifs that allow GR to recognize and bind to GREs (Figure 1C) as well as a nuclear localization signal (NLS)1. The DBD is connected to the C-terminal region by a flexible and poorly-conserved hinge region that is also target of PTMs. The C-terminal region includes the ligand-binding domain (LBD) that features the coregulatory binding pocket or AF-2 and an additional NLS2 (Figure 1D–F). The AF-2 groove, lined by helices 3, 5 and 12, is completed upon ligand-binding to the

encapsulated ligand-binding pocket (Figure 1G). The LBD uses the AF-2 pocket to establish interactions with the LXXLL motif (L, leucine; X, any amino acid), also called the NR box of co-activators.

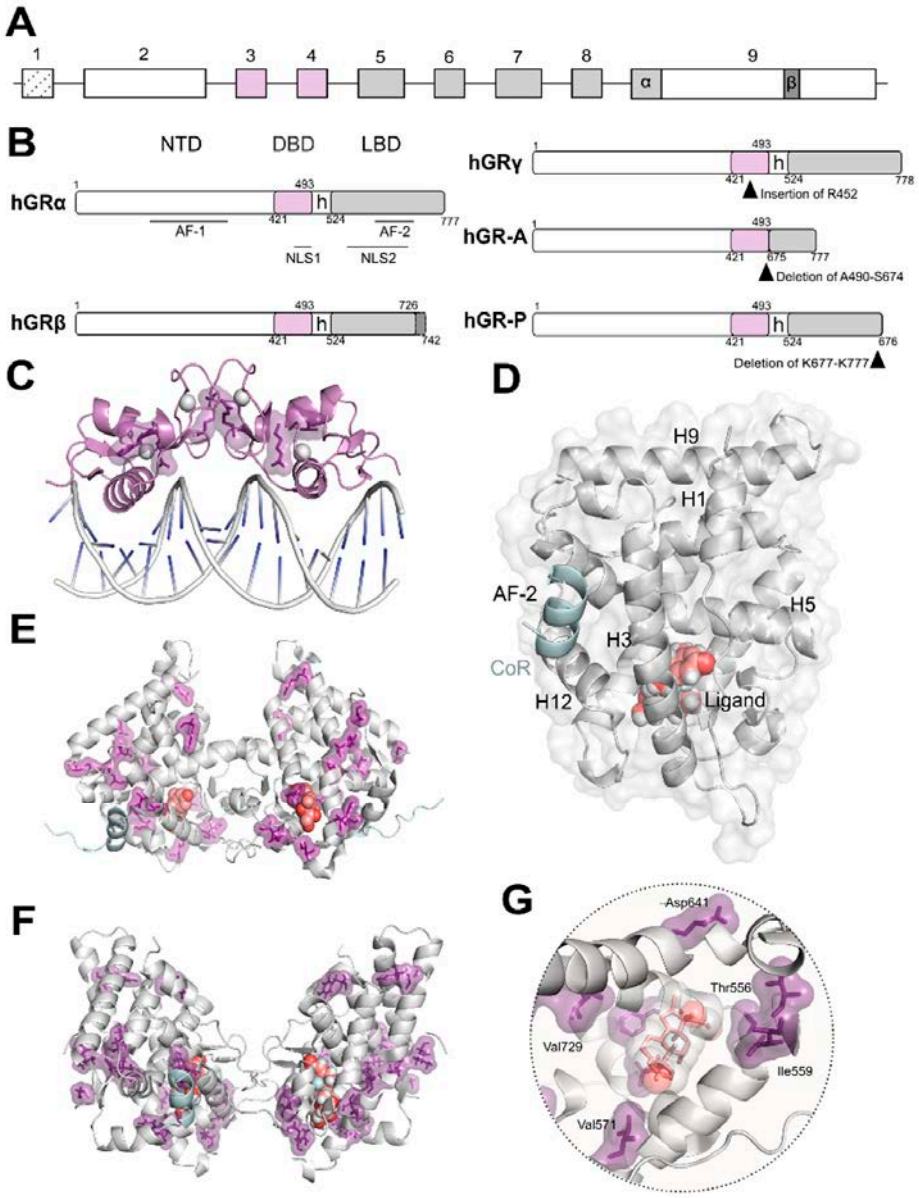

Figure 1. Glucocorticoid receptor (GR) isoforms: domain organization and crystal structures. (**A**) Schematic representation of *NR3C1/GR* gene organization. A unique gene gives rise to several isoforms through alternative splicing (**B**) and/or alternative transcription initiation. The exons encoding for the modular domains: N-terminal domain (NTD), DNA-binding domain (DBD), and ligand-binding domain (LBD), are indicated; exon 9 encodes the two alternative C-termini of the LBD in GRα and GRβ. (**B**) Schematic representation of GR isoforms domain organization generated by alternative splicing. hGRα modular domains include the intrinsically disordered NTD harboring the ligand-independent activation function (AF)-1; the DBD, the most conserved along the nuclear receptor superfamily; a poorly conserved hinge region (h); and the LBD displaying the surface-exposed co-regulator AF-2 groove. The five splice variants GRα, GRβ, GRγ, GR-A, and GR-P are shown; insertion/deletions are indicated by black arrowheads. (**C**) Crystal structure of the GR-DBD dimer bound to DNA shown in grey cartoon (PDB code 5CBX). This domain can dimerize on (+)GRE to activate transcription. Residues implicated in glucocorticoid (GC) resistance are shown (V423, R469, R477, F478) in purple as sticks and surface. The zinc ions are shown as grey spheres. (**D**) Cartoon

representation of the three-dimensional secondary structure of the GR-LBD monomer (PDB code 5UFS) and surface. The domain is depicted in standard orientation (i.e., with helices (H)1 and H3 displayed in the forefront and the AF-2 pocket, lined by H3, H5 and H12 on the left hand-side). The ligand is shown as salmon spheres and the co-regulator peptide (CoR) is shown in cyan. (**E**) Crystal structure of the first GR-LBD dimer reported (PDB code 1M2Z). The ligand is shown as salmon-coloured spheres and CoR is shown in cyan. Residues implicated in GC resistance are highlighted in purple (T556, I559, V571, V575, L595, D641, Y660, L672, G679, R714, H726, V729, F737, I747, I757, L773). (**F**) Crystal structure of a GR-LBD dimer reported (PDB code 5UFS) displaying a different self-recognition pose than in (**E**). The ligand is shown as salmon spheres and CoR is shown in cyan. Residues implicated in GC resistance (T556, I559, V571, V575, L595, D641, Y660, L672, G679, R714, H726, V729, F737, I747, I757, L773) are highlighted in purple. (**G**) Close-up of the ligand-binding pocket of GR occupied by the ligand dexamethasone shown in grey spheres and salmon sticks. Residues implicated in GC resistance contacting the ligand (T556, I559, V571, V729, F737, I747, I757) and lining the LBP are shown in purple.

GRα and GRβ are identical up to residue 727, then GRα diverges with an additional 50 residues and GRβ holds an additional 15 unrelated residues (Figure 1B). A single-residue insertion on the DBD results in GRγ. Furthermore, alternative splicing generates GR-A and GR-P in malignant cells, which lack N- and C-terminal halves of the LBD, respectively (Figure 1B). It has been reported that GR isoforms exhibit differential expression across tissues with distinct subcellular localization patterns that impact transcriptional activity [2,16]. In this review, and unless specified otherwise, we will refer to GRα, the classical and most studied receptor isoform capable of ligand binding, as GR.

The oligomerization of GR is still a matter of intense debate [26,27]. It has been observed that several of the GR domains contribute to self-association critical for functionality. Both the DBD (Figure 1C) and LBD (Figure 1D–F) domains dimerize and their crystal structures have been solved [28]. Despite common acceptance of DBD dimerization, LBD oligomerization is still debated with several models based on experimental structural data using X-ray crystallography and complimentary in silico methods [29]. Additionally, recent data in living cells obtained using the number and brightness technique have shown that the oligomeric state of GR bound to DNA may exhibit a more complex scenario where a monomer to dimer to tetramer transition is likely to occur [30]. To date, no detailed structural information is available either by X-ray crystallography or electron microscopy (EM) for full-length GR. However, recent EM data reported for the related androgen and oestrogen receptors may allow us to speculate that GR full length structure may resemble that of AR considering the higher degree of conservation of residues [31]. Furthermore, EM data have recently been published depicting how chaperones recognize the LBD of GR [32].

Upon ligand binding, GR dissociates from cytoplasmic heterocomplexes that include chaperones (HSP90, HSP70, and p23) and immunophilins (FKBP51 and FKBP52), undergoes PTMs, and translocates to the nucleus to regulate gene expression [4,10]. The GC-induced response is normally terminated by the autologous downregulation of GR following protein phosphorylation and subsequent ubiquitination through a PEST motif (rich in proline [P], glutamic acid [E], serine [S], and threonine [T]) in its C-terminus [4,10]. In a given cell type, the selective interactions of GR with TFs, co-regulators and/or chromatin modifying proteins determine receptor functionality [18,33–35]. This in part explains why different cell types vary in GR genomic binding and transcriptomic profile despite the ubiquitous expression of GR [36,37].

It is well established that GR anti-inflammatory properties rely on both DNA-binding–dependent and –independent receptor functions [36,38,39]. GR activates transcription of anti-inflammatory genes such as glucocorticoid induced leucine zipper (*GILZ/TSC22D3*) by binding to GREs in regulatory regions, and represses expression of pro-inflammatory genes such as *Il1-β* by binding negative (n)GREs, preventing the assembly of an active transcription complex. GR binding has also been reported at inverted repeat (IR) nGREs, unrelated to classical GREs [39,40]. Also, the expression of inflammatory genes can be

suppressed by the recruitment of histone deacetylases (HDAC) to acetylated GR complexes bound to GREs.

On the other hand, GR can regulate gene expression through protein–protein interactions (or tethering) to pro-inflammatory TFs (typically NF-κB or AP-1) bound to their respective DNA binding sites by a mechanism known as transrepression [4,38,39]. GR PTMs such as SUMOylation are required for GR-mediated inhibition of inflammatory genes via repression of IR nGRE genes as well as transrepression of NF-κB/AP-1-dependent transcription [10,18]. Besides their classic anti- inflammatory actions, GCs can also act as pro-inflammatory mediators, and even exert dual roles depending on the pathophysiological context [41]. Indeed, transcriptomic and cistromic studies have revealed that GR co-recruitment with key inflammatory TFs such as AP-1, NF-κB, or STATs, results in enhanced transcription at a subset of co-regulated targets [36]. Among the extensive crosstalk between GR and other signalling pathways, this review is focused on the mutual interference of GR with the mitogen-activated protein kinases (MAPKs).

3. Mutual Interference between GR and Mitogen-Activated Protein Kinases (MAPKs)

MAPKs are serine-threonine protein kinases that act as the meeting point for multiple upstream signalling pathways representing the final step of a phosphorylation cascade known as the MAPK module. In response to pleiotropic signals, including those from inflammatory cytokines, MAPKs dissociate from the MAPK module and can translocate to the nucleus to target TFs such as AP-1 and NF-κB or phosphorylate downstream protein kinases or other substrates to regulate gene expression [42,43] (Figure 2). Therefore, these kinases are critical in regulating inflammation although they also play key roles in regulating cell growth, apoptosis, and differentiation. In mammals, the MAPK family comprises extracellular signal-regulated kinases (ERK), c-Jun N-terminal kinases (JNK), and p38 MAPKs [43].

The ERK subfamily includes five members, among which ERK1 and ERK2 are the most extensively studied, being critical effectors of cell proliferation in response to growth factors. JNK family includes up to ten isoforms generated by alternative splicing from three genes (*Jnk*1-3). Importantly, JNK-mediated phosphorylation of the AP-1 component c-JUN is critical for AP-1-dependent transcription. The subgroup of p38 MAPK includes four isoforms (α, β, γ, δ), with different degrees of involvement in inflammatory disorders.

Within the MAPK module, MAPKs are activated by upstream specific kinases known as MAPK kinases, MKKs or MAP2Ks, through phosphorylation on tyrosine and threonine residues, which in turn are activated by MAPK kinase kinases, known as MKKKs or MAP3Ks, whose activation is triggered by several signals involving RAS GTPases. Specific combinations of scaffold proteins/MKKK/MKK/MAPK allow for specific cellular responses for diverse upstream events towards effector proteins. Each MKK isoform acts specifically onto downstream MAPKs. MKK1 and MKK2, MKK4 and MKK7, and MKK3, MKK4, and MKK6 activate ERK, JNK and p38 MAPK, respectively (Figure 2).

MAPK activities can be inhibited by dual-specificity phosphatases (DUSPs or MAPK phosphatases MKP). Among them, DUSP1/MKP1 has a key role as a crucial anti-inflammatory mediator and gatekeeper of the immune response by dephosphorylating and targeting preferentially, but not exclusively, JNK and p38 MAPK [44,45]. However, under certain settings, the JNK/c-JUN pathway can also transcriptionally up-regulate *DUSP1* to limit the expression of inflammatory genes, representing an important feedback regulatory loop [46–50] (Figure 2).

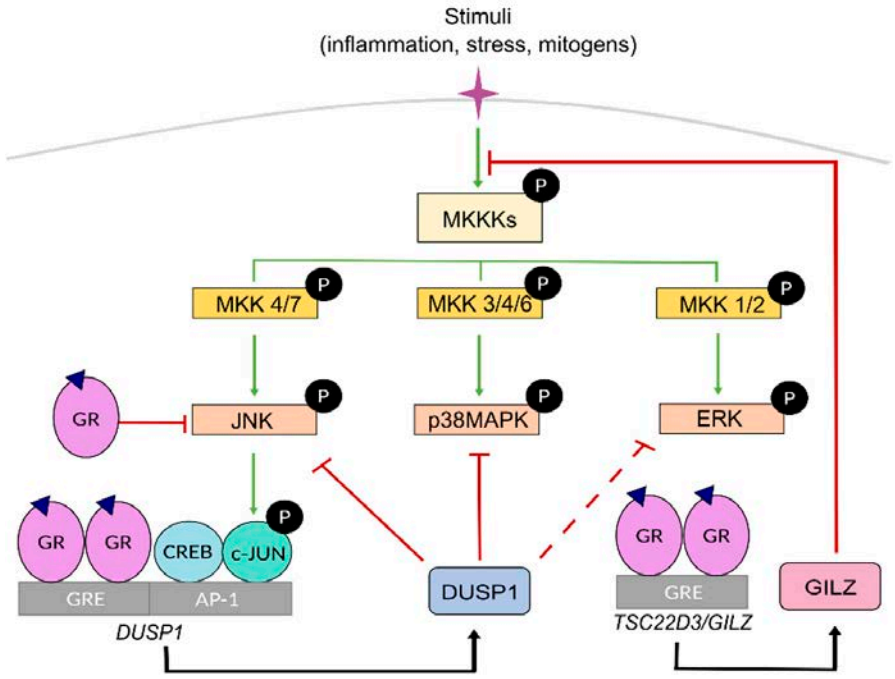

Figure 2. Mitogen-activated protein kinase (MAPK) signaling cascades and their inhibition by GR. MAPKs connect extracellular signaling with modulation of gene expression. In response to diverse stimuli, the kinases participating in the MAPK cascade phosphorylate and activate downstream kinases or other substrates including transcription factors. MAPK kinase kinases kinases (MKKKs) act on MAPK kinase kinases (MKKs) that specifically phosphorylate members of the MAPK JNK, p38, and ERK subfamilies which then signal downstream to regulate transcription of target genes dependent on AP-1 dimers (CREB/c-JUN) bound to AP-1 response elements. Ligand-bound GR negatively regulates MAPKs either by direct interference, as shown for JNK, or by regulating the expression of anti-inflammatory genes such as the MAPK phosphatase *DUSP1* or Glucocorticoid-induced leucine zipper (*GILZ/TSC22D3*). GILZ can also interact with proteins of the MAPK cascade to inhibit downstream activation of MKK1/2 and ERK. Green arrows and red blunt-ended lines indicate induction and inhibition, respectively. Dotted lines mark attenuated inhibition. Black arrows refer to the proteins encoded by GC-activated GR transcriptional targets *DUSP1* and *TSC22D3/GILZ*.

GR can inhibit MAPK function through direct and indirect mechanisms [51–56]. For instance, GC-activated GR antagonizes JNK by inhibiting its phosphorylation through interaction with MKK7 [57,58]. Also, GC-activated GR transcriptionally induces *DUSP1* [55], an effect that is further increased in the presence of pro-inflammatory cytokines, as a feedback mechanism that enhances MAPK inhibition [2,33,34,46] (Figure 2). In addition to triggering transcription, hormone-bound GR increases DUPS1 protein half-life [55]. However, other studies showed that the role of DUSP1 in GC-mediated MAPK inhibition is transient suggesting that additional effectors act at later time points [59]. For instance, GC-induced GILZ interacts with RAS/RAF1 blocking phosphorylation and inhibiting downstream activation of MKK and ERK [60] (Figure 2). Importantly, GR-MAPK interaction is mutual and, as it will be discussed below, GR is also targeted by MAPKs; indeed, excessive MAPK signalling can result in GC resistance.

4. Overview of the Mechanisms That Regulate Glucocorticoid (GC) Sensitivity

The sensitivity to GCs is influenced by multiple heterogeneous mechanisms whose impairment may result in GC hypersensitivity or resistance, which can be generalized or tissue-specific, congenital or acquired [2,5,6,61,62]. Generally speaking, the transient exposure to GCs, endogenous or pharmacological, is beneficial while the persistence of GCs is detrimental [63]. Paradoxically, the excess and deficiency of GCs often share common

features due to the existence of multiple feedforward and feedback loops aimed to limit the imbalances of GC signalling, which can ultimately lead to adaptation or induce disease [35]. The disparity of responses to a common trigger is directly related to the cell type- and context-specific actions of GCs [35,37,38]. This section summarizes the mechanisms that influence GC sensitivity, including impaired production and availability of GCs; GR polymorphisms and mutations; alterations in the levels, isoforms, or turnover of GR; GR PTMs; and GR crosstalk with other signalling pathways including MAPKs (Figure 3).

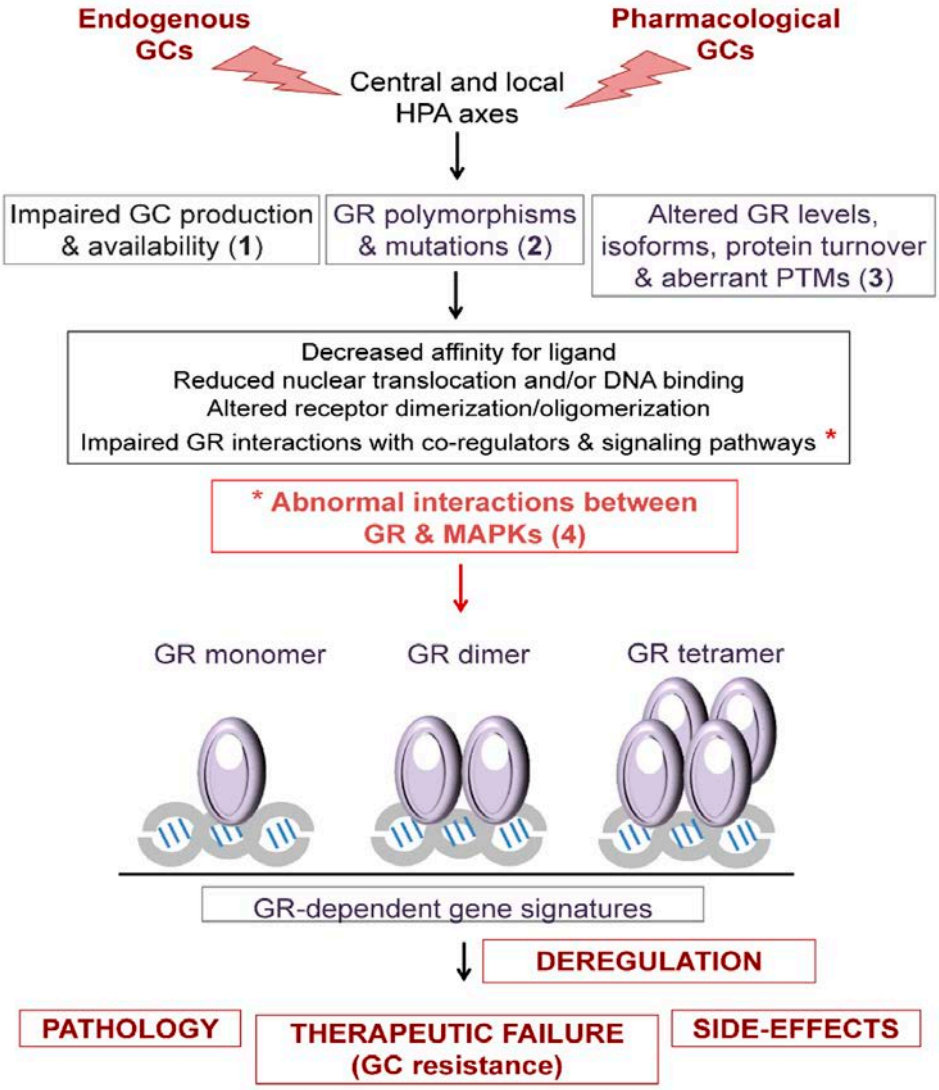

Figure 3. Mechanisms underlying GC sensitivity. Variations in the sensitivity to GCs can affect susceptibility to disease (endogenous) and to the capacity to respond to pharmacological doses of steroid analogs (exogenous). Impairments in either de novo production by the central and local hypothalamic-pituitary-adrenal (HPA) axes or in conversion from inactive to active GCs (availability) affect endogenous response and may lead to disease (1). GR polymorphisms and/or mutations (2), GR expression levels, protein stability, ratios of isoforms, and aberrant post-translational modifications (PTMs) (3) can reduce nuclear translocation and/or DNA binding, alter receptor dimerization/oligomerization, and affect GR interactions with co-regulators and signaling pathways. Among the abnormal interactions, those between GR and MAPKs can result in pathological changes to the GC response. Overall, defects in the mechanisms that influence GC sensitivity lead to deregulation of the GR-dependent transcriptional signatures.

4.1. GC Production and Availability

The synthesis and secretion of GCs is regulated by the central and local HPA axes [2,5,9], and dysregulation of these regulatory loops can result in GC excess or deficiency. Patients with Cushing syndrome present elevated endogenous systemic levels of cortisol due to pituitary ACTH-secreting or adrenal cortical ACTH-independent tumours [5,6]. The clinical features of Cushing's patients include immune dysfunction, depression, muscle wasting, skin atrophy, and adverse metabolic effects such as increased glycaemia, insulin resistance, hypertension, and adiposity, with associated increased morbidity and mortality rates [64]. Novel therapeutic strategies are envisaged after testing the use of MKK1/2 inhibitor MKK162, which show effectiveness in a mouse model of corticotroph tumor causal of Cushing's disease, reducing tumor growth and tumor-derived circulating levels of ACTH and, hence, corticosterone [65].

Endogenous GC production also increases during physiological aging and contributes to the development of diabetes, obesity, and hypertension [21,22]. Importantly, pharmacological inhibition of HSD11B1 was able to significantly reduce several of these age and GC-associated adverse metabolic effects in experimental models. Therefore, HSD11B1 targeting has become a promising therapeutic strategy to reverse or ameliorate the tissue-specific consequences of increased GCs [21].

Other patients present a rare GC hypersensitivity syndrome despite normal circulating cortisol levels, and can develop signs of metabolic syndrome either spontaneously or due to steroid treatments. This disease has been linked to different mechanisms that include elevated GR levels, augmented GR-dependent transcription, and one reported GR mutation [66].

4.2. GR Polymorphisms and Mutations

GR polymorphisms are commonly found in the general population and can result in GC hypersensitivity or resistance [2,5,6,61,62]. The most common GR polymorphisms ER22/23EK (rs6189 and rs6190), N363S (rs6195), and BcII (rs41423247) have been linked with the risk of developing obesity, metabolic syndrome, and cardiovascular problems.

The inactivating heterozygous mutations of the *NR3C1/GR* gene are the cause of congenital primary generalized GC resistance or Chrousos´ syndrome (OMIM #615962), a rare genetic condition characterized by hypercortisolism without signs of Cushing's syndrome. Due to the lack of the negative feedback loop on the HPA axis, patients also feature excess aldosterone and androgens, which result in hypertension, hypokalaemia and in women hirsutism and menstrual abnormalities. The overall impairment of GR-mediated signalling is highly variable in these patients, ranging from complete inability to respond to GCs to partially attenuated responses, and is also highly variable among tissues [2,5,62]. Most reported *NR3C1* mutations (approximately 30 cases) map at the GR-LBD, and only a few are located at the DBD [5,12]. In general, GR mutations result in decreased affinity for ligand, reduced nuclear translocation and/or DNA binding, and impaired interactions with coactivators such as GRIP [5,12,23,67].

It has been suggested that destabilization of the GR-LBD is the most common conformational change causing GC resistance; however, studies have mostly relied on computer simulations [68]. As the GR-LBD is implicated in oligomerization it is important to decipher the functional association between different GR oligomers and their pathophysiological function in Chrousos' syndrome. Residues implicated in GC resistance are indicated in Figure 1C, E–G. As functional characterization of the mutants has been thoroughly revised [5,12,23,67], it will not be discussed in detail in this chapter.

4.3. GR Levels, Isoforms, Protein Turnover, and Post-Translational Modifications

Reductions in the pool of available GR affect hormone sensitivity, and can ultimately result in GC resistance [61]. The decreased expression of GR can be due to increased circulating endogenous GCs or chronic exposure to GC treatments. Also, the increased expression and/or altered ratio of the GR isoforms reported in several inflammatory

diseases may be the origin of GC resistance [2,24]. The most characterized mechanism involves a dominant negative function of GRβ, unable to bind ligand, on GRα [24]. In fact, IL-1β imbalanced the GRα/GRβ ratio by increasing GRβ expression, resulting in a GC resistant phenotype that could be alleviated by JNK and p38 MAPK inhibitors [69]. The abnormal expression of other isoforms such as GRγ, GR-A, and GR-P has also been linked to GC resistance in patients with myeloma and leukaemia [2]. Imbalances in the relative levels of the GR chaperone complex proteins (high FKBP51 and low FKBP52) can also lead to GC resistance while the role of HSP90 and HSP70 in GC resistance is controversial.

GR is subjected to a variety of PTMs, including phosphorylation, acetylation, ubiquitination, SUMOylation, and oxidation, at evolutionally conserved sites (Figure 4). GR PTMs have a major impact on receptor function controlling GR half-life, subcellular location, and also modulate interactions with other signalling pathways that eventually affect GR-dependent gene expression [10,23,46].

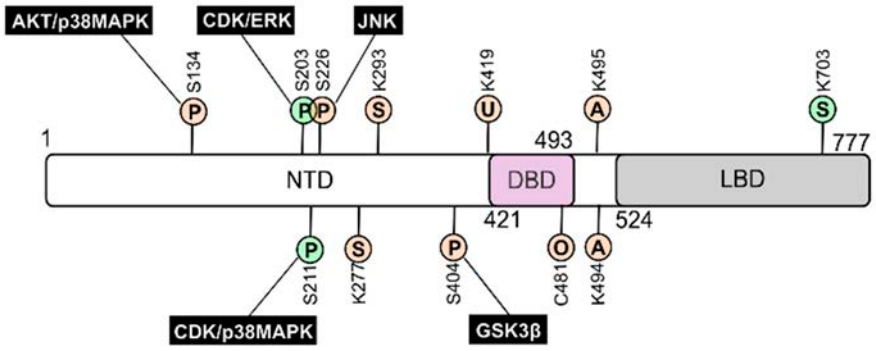

Figure 4. GR post-translational modifications: impact on receptor's function. GR is subjected to a variety of posttranslational modifications (PTMs), which have a major impact on receptor function. Scheme indicates PTM target residues for hGRα including phosphorylation (P), acetylation (A), ubiquitination (U), SUMOylation (S), and oxidation (O). The major kinases phosphorylating GR and the outcome of the corresponding PTMs are also indicated (green, activation; salmon, inhibition).

GR is substrate of multiple protein kinases including cycling-dependent kinases (CDKs), AKT, glycogen synthase kinase (GSK)-3β as well as all MAPKs (Figure 4). While it is accepted that GR phosphorylation is crucial for its functional impact, the in vivo relevance at some sites is still controversial. In addition to cell-type specificity clues, reported differences might be due to the requirement of multiple GR PTMs to drive functional specificity. For example, GR phosphorylation has a prominent role in receptor turnover mediated by K419 ubiquitination [70,71].

Upon hormone binding, p38 MAPK and CDKs induce GR phosphorylation at S211, an event regarded as a hallmark for GR transactivation; this effect is further enhanced by phosphorylation at S203 by ERK and CDK (Figure 4). In addition, similar to AKT, p38 MAPK can also inhibit GR function by phosphorylating S134, which results in impaired GR nuclear translocation and/or transcriptional activation of a subset of GR target genes [72,73]. On the other hand, GR phosphorylation at S226, mediated by JNK, induces nuclear to cytoplasmic shuttling of the receptor, consistently inhibiting GR-dependent transcription [74,75] (Figure 4). Finally, GSK-3β-mediated phosphorylation at S404 alters the GR transcriptional program [76].

The acetylation of GR on K494 and K495 decreases the receptor´s transcriptional activity, and also blunts its ability to inhibit NF-κB. The reduction of GR anti-inflammatory capacity may lead to GC resistance in COPD patients which can be alleviated by HDAC2 overexpression [77]. Moreover, it has been shown that these acetylation sites are targeted by the circadian rhythm TF CLOCK/BMAL1 [78] and might mediate GC resistance in response to hyperglycemic conditions [79].

GR is also target of SUMOylation at K277, K293, and K703, with opposite outcomes; while modification at N-terminal sites has a negative effect on GR transcription that of

K703 results in positive regulation [80,81]. Moreover, JNK phosphorylation on S226 promotes GR SUMOylation at N-terminal/inhibitory sites inhibiting GR transactivation [82]. Finally, there is evidence that, under oxidative conditions, C481 mediates suppression of GR functionality [83].

5. GC Resistance due to the Crosstalk between GR and MAPK Signalling

GR and MAPKs show strong interactions which normally result in mutual inhibition. In a given inflammatory context, the overall response to GCs is determined by multiple feedback and feedforward interactions between GR and cytokine-mediated signalling [13–15]. While many of the anti-inflammatory actions of GCs are achieved by the GR-mediated inhibition of MAPK activity, the GC anti-inflammatory capacity is decreased in conditions of excessive MAPK activation [13–15,33,46]. Given that chronic MAPK/AP-1-/NF-κB activation is a common denominator in multiple inflammatory diseases, the pharmacological inhibition of specific MAPK signalling pathway has become an add-on strategy intended to restore GC sensitivity [2,15,25]. As the interactions between GR and MAPK depend on the affected tissue(s) and are thus disease-dependent, the following sections have been organized according to the distinct pathologies associated to GC resistance.

5.1. Respiratory Diseases

Respiratory diseases such as asthma and COPD feature chronic inflammation of the airways. However, while asthma is characterized by allergic airway remodeling and hyper responsiveness with reversible airflow obstruction, COPD features chronic bronchitis, destruction of the peripheral airways and not fully reversible airflow limitation. Despite shared molecular mechanisms, these diseases differ greatly in their response to GC treatments. While most asthmatic patients have a relatively good response to GCs, almost all patients with COPD experience GC resistance [84]. It is accepted that the overexpression of pro-inflammatory cytokines such as tumor necrosis factor (TNF)-α, interleukin (IL)-17, IFN-γ, TGF-β, and IL-33, contributes to resistance in severe asthma and COPD, together with allergens, pathogens, and cigarette smoke. Among the mechanisms underlying impaired/lost GC sensitivity in these diseases, overactivation of the MAPK pathway and downstream AP-1-/NF-κB-dependent pro-inflammatory gene expression occupies a central position, as impairment of phosphorylation/dephosphorylation cascades ultimately results in defective GR binding, translocation, and function [13,52,85]. Consistently, several inhibitors targeting p38, JNK, and MKK1-2/ERK, such as SP600125, and trametinib, respectively, are in different stages of clinical development for treatment of respiratory diseases [86].

Asthma is a major health problem, with increasing incidence in western societies and the most common chronic disease in children [84]. The first-line therapy for patients with asthma with various degree of severity of all ages consists in inhaled corticosteroids, which achieve significant reductions in disease morbidity and mortality [13,84]. However, 4–10% of patients with severe asthma show poor responses to GCs, requiring higher doses to control the disease. About 1% of asthmatic patients are in need of treatment with oral GCs, which in addition to controlling asthma exacerbations, have undesired systemic effects [13,84].

In peripheral blood mononuclear cells (PBMCs) from severe asthmatic patients, GC-resistance correlates with higher levels of pro-inflammatory cytokines as well as increased expression and activity of the p38 α and β isoforms, relative to GC-responsive individuals [6,13,84]. The increased levels of cytokines in alveolar macrophages from asthmatic patients with reduced GC sensitivity result in the inhibition of GR function through its phosphorylation via p38α as well as the decreased induction of DUSP1 by GCs [13,87]. These findings are consistent with experimental models using macrophages from Dusp1 KO mice where the anti-inflammatory responses to GCs were reduced in vitro due to attenuated effects on gene expression and, as DUSP1 inactivates p38, as a consequence of increased p38 activation [88].

The anti-allergic actions of GCs are mediated through suppression of Th2-dependent pathways and involve the control of the TF GATA3 that regulates the transcription of Th2 cytokines such as IL4, IL-5, and IL-13. As both GATA3 and GR translocate to the nucleus via importin-α, GC treatments can inhibit nuclear translocation of GATA3 by competition and also by inducing DUSP1, which reverses the phosphorylation of GATA3 by p38 MAPK, necessary for its nuclear translocation [13,89]. These data highlight the importance of DUSP1 function to control p38 activity and thus modulate the sensitivity to GCs. Consistent with its causative role in steroid resistance, co-treatments with p38 inhibitors have proven useful in alveolar macrophages and PBMCs (SD-282 and SB 203580, respectively) isolated from severe asthmatics [84,90].

On the other hand, increased JNK activity due to the up-regulation of TNF-α and other pro-inflammatory cytokines has been reported in the airways of asthmatic patients, and associated to GC resistance in severe asthma. Augmented JNK1 activity results in increased phosphorylation at S226, resulting in decreased GR function [84]. These changes correlate with decreased expression of DUSP4/MKP2 in PBMCs from patients. The fact that enhancing DUSP4 activity restored corticosteroid sensitivity in vitro suggests that it might be a novel therapeutic target in severe asthma [84]. Corticosteroid resistance may also arise upon activation of PI3K and mammalian target of rapamycin (mTOR), leading to increased JNK1 activity [74,91]. Importantly, JNK inhibition (SP 600125) in mouse models for asthma had promising results in suppressing airway remodeling [84].

The activation of ERK by microbial antigens in severe non-allergic asthma also affects GR phosphorylation and can induce GC resistance in T cells in vitro [92]. ERK plays important roles in airway remodeling by regulating proliferation, extracellular matrix protein secretion, cytokine release, and eosinophil function in airway smooth muscle cells. ERK also promotes a Th2 phenotype and its inhibition blocks the production of Th2 cytokines in T lymphocytes. The use of MKK1/2 inhibitors to target the ERK pathway has proven effective for reduction of airway remodeling in several animal models of severe asthma. This is due to reductions in inflammation and in steroid resistance, as has been observed in airway type 2 innate lymphoid cells in severe asthma patients (trametinib) [85].

In COPD, airway inflammation results from the chronic inflammatory milieu in alveolar macrophages and the increased oxidative stress [84]. In PBMCs from COPD patients, basal and lipopolysaccharide-induced levels of IL-8 were higher relative to healthy smokers, along with higher increases in p38 activation. However, unlike in mild to moderate asthma, GCs are ineffective in reducing inflammation, which would rationally advise to limit this treatment to patients with severe disease in order to reduce exacerbations. Regardless, high doses of inhaled corticosteroids are routinely prescribed for patients diagnosed with COPD, increasing the risk of serious side metabolic effects such as diabetes and hypertension without proven benefits [84,90].

p38α also plays a central role in the pathobiology of COPD, and its activation seems critical for GC resistance. While p38 targeting in experimental mouse models of COPD was successful, the results of clinical trials assessing p38 inhibitors for COPD therapy have been so far disappointing [90,93]. Currently, the most promising strategy for the treatment of respiratory diseases such as asthma or COPD relies on the use of MAPK inhibitors as add-on therapies to inhaled corticosteroids or beta-blockers. A selective p38 inhibitor (GW856553) was reported to potentiate the repression of pro-inflammatory cytokines by GCs in PBMCs from COPD patients due to the decreased phosphorylation of GR-S211, mediated by p38 [87].

In addition, other therapies to restore GC sensitivity in COPD focus on upstream activators of the MAPK pathway. For instance, as PI3K/AKT overactivation in COPD can lead to reduced GR levels, PI3Kδ inhibition resulted in improved GC responses. Rapamycin, a immunosuppressant that inhibits the activity of mTOR, increased GC sensitivity in PBMCs from COPD patients through decreased phosphorylation of p70 S6 kinase, and concomitant reduction in c-JUN and cytokine (IL-8) levels. Phosphodiesterase 4 inhibitors potentiated the GC-induction of DUSP1 leading to reduction of p38 activity, and decreased

IL-8 production [90]. Also, resistance to GCs in COPD patients can be mediated by a defect in GR deacetylation due to decreased HDAC2 expression in alveolar macrophages, which specifically inhibits NF-κB transpression by hormone-bound GR [77].

GCs also exert their anti-inflammatory effects by inhibiting the activity of phospholipases A2 (PLA2), which regulate the production of arachidonic acid, a precursor of lipid inflammatory mediators, playing important roles in many inflammatory diseases [94]. The reduced response to GCs in respiratory disorders such as acute lung injury may be due to reduced GR binding to cortisol and/or GRα overexpression, resulting in excessive activation of the MAPK cascade and insufficient regulation of downstream PLA2 pathway, therefore accentuating the pathologic response [95].

GC resistance has also been reported in other respiratory diseases such as chronic sinusitis. In an in vitro model, treatment with IL-1β resulted in the increased expression of GRβ relative to GRα, leading to induction of p38 and JNK activities [69].

5.2. Leukemias

GCs are extensively used as therapeutic agents for the treatment of almost all lymphoid malignancies, including leukaemias, lymphomas, and multiple myeloma, due to their immunosuppressive and anti-inflammatory properties. Studies using various cell lines derived from human hematological malignancies showed that ERK and JNK inhibitors may restore sensitivity to GCs [96].

GCs have been classically used for treating acute lymphoblastic leukaemias (ALL), haematological malignancies that originate from progenitors of B (B-ALL) or T (T-ALL) cell lineages that due to oncogenic transformation fail to differentiate and gain unlimited proliferative capacity. Initially, these malignant cells invade the bone marrow interfering with haematopoiesis. As the disease progresses they also colonize extramedullary sites including lymph nodes, spleen, and liver. Typically, ALL treatment starts with one-week of GC monotherapy followed by combination with other chemotherapeutic agents such as spindle inhibitors, genotoxic drugs, or antimetabolites [97]. The therapeutic response of ALL patients to GCs is highly heterogeneous. In paediatric patients, 10–30% of primary cases are poor- or non-responders, reaching up to 70% in relapsed cases [98]. As GC resistance strongly correlates with poor prognosis, the outcome of GC treatments is the main basis to design therapeutic strategies [99].

In immune cells, GC anti-inflammatory and immunosuppressive properties are due to promotion of cell cycle arrest and apoptosis. The inhibition of cell growth is mediated by the induction of CDK inhibitors such as p21/CDKN1A and downregulation of proliferative effectors like c-Myc or CDK4. Also, GCs regulate the balance between pro- and anti-apoptotic effectors through the transcriptional regulation of genes of the B-cell lymphoma 2 (Bcl2) family [100]. Therefore, in addition to loss-of function mutations, polymorphisms, or epigenetic downregulation of the NR3C1 gene, GC resistance in leukaemias is frequently caused by alterations in other signaling pathways and downstream targets. Indeed, GC resistance in ALL is consistently associated with alterations in the regulation of apoptosis, involving abnormal expression Bcl2 family members, inactivation of the tumor suppressor TP53 or overexpression of its inhibitor, MDM2. It can also involve alterations in other signal transduction pathways including Notch, IL7R/JAK/STAT, PTEN/PI3K/AKT/mTOR and RAS/MAPKs. As the apoptotic-related mechanisms of GC resistance in immune cells have been recently reviewed [99], this section focuses on the GC resistance associated with impairment in the MAPK-related pathways.

Genome-wide transcriptomic analysis assessed the therapeutic response to GCs in ALL and identified several prednisolone-induced genes related to MAPK pathways in cell lines and clinical samples [101,102]. Consistently, while pharmacological inhibition of p38 MAPK protected leukemic cells from GC-induced apoptosis ERK or JNK inhibition had the opposite effect, correlating with GR phosphorylation on S211 [103]. However, genetic and pharmacological downregulation of MKK2 and MKK4 enhanced prednisolone-induced apoptosis in B-lineage leukemic cells through distinct mechanisms. While the effects of

MKK2 knockdown were mediated by increased TP53 expression and, hence, enhanced sensitivity to all chemotherapeutic agents, MKK4 downregulation specifically augmented sensitivity to GCs by increasing GR levels. Moreover, ERK activation was observed in patient samples at relapse compared to the time of diagnosis. Consequently, in xenograft models treatment with trametinib reduced leukemic cell burden from relapse but not from diagnosis samples [104].

In addition to upstream components of the MAPK pathways, downstream effectors have also been related to GC response in leukemia. Transcriptomic analysis in the leukemic Pre-B ALL cell line 697 subjected to GC treatment showed an unexpected repression of the GC target gene DUSP1 with concomitant induction of JNK activity [105]. Moreover, while DUSP1 overexpression did not influence GC-induced apoptosis, its silencing increased it [106]. These results are consistent with those obtained in GC-resistant T-ALL cell lines showing that a low dose of anisomycin, an activator of JNK and p38 MAPK, effectively sensitizes them to dexamethasone-induced cell cycle arrest and apoptosis [107]. However, other studies using a subset of GC-resistant lines derived from B-lineage cells, including Pre-B 697, showed that JNK inhibition re-sensitizes to GCs [108]. Therefore, further studies in primary and relapsed clinical samples are required to define the use of specific MAPK inhibitors to either enhance GC therapeutic response or alleviate GR resistance.

5.3. Skin Diseases

Despite the overall efficacy of topical GC treatments to combat prevalent inflammatory skin diseases such as psoriasis or atopic dermatitis [109], the response to GCs may be reduced or lost over time in some patients [6,110]. This phenomenon known as tachyphylaxis has been reported in human and mouse skin, and is defined by loss of the anti-proliferative actions of GCs on epidermal keratinocytes, vascular and lymphoid cells. Steroid tachyphylaxis is difficult to quantify as decreased effectiveness of GC treatments may be also due to the lack of adherence to prescription [111,112]. In mice, it was demonstrated that chronic exposure to GCs induced desensitization; instead of the initial rate of growth inhibition (around 10–15% of control level), keratinocyte proliferation returned to the basal levels and even increased after two weeks of treatment [113]. The activation of kallikrein (KLK)-related peptidase KLK6 may in part be responsible for the development of GC-desensitization [114]. KLK6 is induced by the phorbol ester PMA, a known inductor of MAPK, and is up-regulated in the skin of patients with several hyperproliferative/inflammatory diseases. Also, KLK6 is also induced upon chronic GC treatment likely as a mechanism aimed to regenerate the epidermis after GC-induced skin atrophy; in agreement with this, Klk6 KO mice showed decreased steroid tachyphylaxis [114].

Evidence from genetically modified mouse models demonstrate that the anti-proliferative, anti-inflammatory, and anti-tumor actions of topical GCs are mediated to a great extent through negative interference between epidermal GR and the MAPKs [109]. Upon topical application of PMA, mice with constitutive or adult-induced deletion of epidermal GR featured enhanced skin inflammation together with increases in p38 and ERK activities as well as in downstream expression of AP-1-target genes, relative to controls [40,115,116]. Also, when topical GCs were applied in combination with PMA, epidermal GR KO mice but not controls were partially resistant to the GC therapeutic actions [116]. The overactivation of MAPK/AP-1 activities was due to keratinocyte-autonomous actions upon GR loss, as shown in immortalized keratinocyte cell lines with GR deficiency, in which re-insertion of GR restored the altered MAPK activity to levels close to controls [117]. In addition, mice harboring a mutation that impairs GR SUMOylation (GR-K310 in mice/GR-K293 in humans) exhibited more severe responses to topical PMA and partial resistance to topically applied GCs highlighting the importance of this PTM for inhibition of NF-κB- and AP-1-transcriptional activities [118,119].

Increased MAPK activity has been observed in mouse and human psoriatic lesions and ERK, p38 and JNK are thought to play a pathogenic role in this disease [120–122]. Similar to PMA, repetitive treatment with imiquimod, a TLR7 agonist that induces psoriatic-lesions,

increased the severity of skin lesions in GR epidermal KO mice vs. controls, correlating with higher activation of p38 and ERK activities [117]. Indeed, lesional and non-lesional skin of psoriatic patients featured decreased GR expression as well as reductions in the local de novo GC synthesis [123,124]. These findings imply that defective cutaneous GC signaling can not only aggravate dermatological conditions but also be an etiopathogenic cause for inflammatory skin diseases. The cutaneous HPA axis appears as key regulator and therefore, the rescue of local GC production is a feasible strategy to improve psoriasis [8,109,123,125–127].

Studies on skin carcinogenesis have been classically addressed by the two-stage chemical protocol in mice, which consists of topical application of an unique dose of the mutagen DMBA followed by repetitive treatments with the tumor promoter PMA. During tumor progression, skin changes correlated with the sequential activation of AKT, NF-κB, and ERK; ERK activity rose only during the later stages of malignant conversion of papilomas to squamous tumors [128]. GCs were able to inhibit mouse skin tumor progression only if applied at the beginning of the promotion stage. We demonstrated that the gain-of epidermal GR function resulted in resistance to chemically-induced skin tumors while its loss caused increased sensitivity to develop these tumors [129,130]. The anti-tumor role of GR was mediated through interference with AKT and NF-κB, upstream activators of MAPKs [129–131].

5.4. Autoimmune Diseases

Many autoimmune diseases such as rheumatoid arthritis and inflammatory bowel diseases (IBD) show reduced effectiveness to routine treatments with GCs [132,133].

Rheumatoid arthritis is a chronic systemic autoimmune disease, with a prevalence around 0.5–1% of the population, affecting mostly the elderly, in particular women. The disease affects the synovial joints, which are progressively damaged and destroyed causing disability, and is comorbid with cardiovascular pathologies. It is well established that MAPK activation and/or DUSP1 deficiency are involved in the pathogenesis of rheumatoid arthritis and may contribute to disease progression. GC treatment alleviates joint swelling, stiffness and pain, at least in part by modulating the MAPK/DUSP pathways, directly or indirectly [134]. Unfortunately, long-term treatments with GCs may lead to bone loss (or GC-induced osteoporosis).

Among the proteins involved in GC resistance, the pro-inflammatory protein macrophage migration inhibitory factor (MIF), which increases the production of pro-inflammatory cytokines and positively regulates MAPK activation, and GILZ, play major roles. The mechanism by which MIF increases MAPK phosphorylation involves the inhibition of DUSP1, thus counteracting the anti-inflammatory effects of GCs [135]. The overexpression of GILZ in endothelial cells reduced adhesion and inflammation by increasing the expression DUSP1 along with the inhibition of the TNF-induced activation of all MAPKs [136]. Importantly, MIF-mediated inhibition of DUSP1 requires GILZ, exemplifying how feedforward and feedback loops are responsible for modulating the sensitivity to GCs [135]. These multilevel regulatory mechanisms also highlight the importance of the MAPK/DUSP pathway, as the reduction of DUSP1—either due to elevated levels of MIF or GILZ deficiency—amplifies MAPK-mediated signaling.

IBDs such as ulcerative colitis and Crohn´s disease are chronic diseases associated with dysregulation of the immune response in the intestinal mucosa. GCs are prescribed as the main anti-inflammatory treatment in patients with moderate to severe disease. While approximately half of patients respond to GC therapy, around 30% show partial responses, and 20% are GC-resistant. Also, upon long-term treatment, around 20% of IBD patients become dependent, requiring GCs to maintain remission [133]. Current efforts focus on second-generation steroids that maximize the amount of locally available steroid in the intestine and minimize systemic bioavailability.

The mechanisms underlying GC resistance in IBDs include high levels of TNFα, IL-6, and IL-8, and low IL-10 levels, in steroid-resistant relative to sensitive patients,

with activation of the MAPK/AP-1 and NF-κB pathways. MIF is also implicated in the pathogenesis of ulcerative colitis through activation of pro-inflammatory cytokines and subsequent anti-steroid effects [137,138]. As most cytokines are targets of major pro-inflammatory associated TFs, this scenario constitutes an auto-amplification loop for GC-resistance.

Besides their anti-inflammatory role, the therapeutic efficacy of GCs also relies on their capacity to restore the intestinal epithelial barrier function, which is impaired in IBDs. In Crohn's disease, the mechanisms of defective barrier are related with dysregulation of tight junction components such as claudins-2 and -4. Claudins were regulated via DUSP1 and consistently, inhibition of DUSP1 but not p38 or MKK1/2 prevented the GC control of tight junction permeability in intestinal epithelial cells, suggesting substrates in addition to MAPK [139].

In patients with Crohn´s disease, it was demonstrated that steroid-sensitive and -resistant patients show different cell type-specific patterns of activation of pro-inflammatory pathways. GC response correlated with activation of p38, JNK1, and NF-κB mainly in lamina propria macrophages while GC-resistance was associated to activation of these mediators mostly in epithelial cells [140]. In line with these studies, treatment of patients with p38 and JNK inhibitor CNI-1493 achieved significant improvement of Crohn's disease patients [141].

In ulcerative colitis patients, refraction to GC treatments correlated with higher levels of MIF in lamina propria macrophages, which resulted in p38 activation, and reduced inhibition of IL-8. Consistently, anti-MIF antibodies reduced p38 overactivation, ameliorating IL-8 production [142].

Given the major role of GCs in maintaining the equilibrium between pathogen clearance and tolerance mechanisms, abnormally high GCs can lead to excessive tolerance, contributing to chronic inflammation that may result in sepsis. Sepsis is a complex disease where generalized systemic inflammation and tissue damage lead to multiple organ failure and death. Sepsis is considered a global health priority with estimates around 30 million patients, and mortality rates around 30–50% annually [143]. In sepsis patients, the impaired inflammatory response transitions from excessive to immunosuppressive stages. There is no current treatment available other than antibiotics and fluids, and GC derivatives are routinely used as adjuvant therapy as almost all patients with sepsis undergo GC resistance.

During sepsis, MAPK activation features two phases, an early active phase of p38 up-regulation, followed by a second phase of ERK activation; both are suppressed by GR antagonists [144]. DUSP1 also exerts a main role on the efficacy of GC-mediated suppression of inflammation in sepsis, as shown by in vitro and in vivo evidences. Consistently, experiments in Dusp1$^{-/-}$ mice mimicking the consequences of septic shock (caecal ligation and puncture and peritonitis) demonstrated refraction to GC treatments [45]. As GILZ is expressed in many tissues, being downregulated during acute inflammation and up-regulated at immunosuppressive stages, it appears as a potential candidate for escaping GC resistance in sepsis. Experiments in mice have shown that GILZ has therapeutic effects in models of sepsis, and indeed mice overexpressing GILZ were protected against lethal septic peritonitis [145].

As TNFα is a major inducer of GC resistance in sepsis, the recent demonstration that the TNFα/GR antagonism is mediated by reshaping the nuclear GR´s interactome constitutes a major finding that should allow for development of more specific targeting approaches [146,147]. In sepsis, GC resistance seems to be associated with high GRβ levels that result in inhibition of GRα-mediated gene expression.

6. Conclusions and Perspectives

The impact and extent of GC resistance is highly variable among individuals, and is also heterogeneous depending on the tissue, which constitutes an intrinsic difficulty associated to GC prescriptions. An ideal scenario would allow the determination of GC sensitivity

prior to treatment, thus allowing for tailoring doses and regimes to patients ensuring an optimal personalized therapeutic treatment with an increased benefit vs. risk ratio.

The complexity of inflammatory networks and the multitude of signaling pathways involved in chronic inflammatory diseases justifies the efficacy of GC treatments as drugs that target all cell types by heterogeneous mechanisms. So far, targeting MAPKs represents a major therapeutic approach for chronic inflammatory diseases with GC resistance. Several p38 inhibitors for various uses have been patented, and multiple clinical trials have addressed the use of JNK and ERK inhibitors, mainly for hematologic malignancies. However, due to differences in the underlying mechanisms between inflammatory pathologies the development of an unique MAPK inhibitor that can be used as universal treatment is unfeasible. The failure or reduced efficacy of a given MAPK inhibitor is likely related to the intricate network formed by these kinases subjected to multiple feedback and feedforward loops that result in compensatory mechanisms. For instance, as p38 deficiency leads to increased activation of ERK and JNK, p38 targeting could lead to activation of other inflammatory cascades. Therefore, any therapy to restore GC sensitivity through MAPK inhibition would require careful adjustment of inhibitor dosage to keep compensatory mechanisms to a minimum. Once GC sensitivity is regained, GCs could be co-administered to sustain inhibition of inflammatory signaling.

Novel strategies should include targeting of alternative downstream regulators of the MAPKs, hopefully leading to minimize off-target inhibitory effects. Also, simultaneous targeting of more than one kinase along the cascade would potentially achieve synergistic effects.

Funding: This research was funded by grants to P.P. SAF2017-88046-R, PID2020-114652RB-I00, to E.E.-P. BFU-2017-86906-R, and to C.C. PID2020-119875RB-100 (from MICINN, Spanish Government); also, to E.E.-P. from G.E. Carretero Fund for Science.

Institutional Review Board Statement: Not applicable.

Informed Consent Statement: Not applicable.

Acknowledgments: We thank NURCAMEIN (SAF2015-71878-REDT and SAF2017-90604-REDT) for support for dissemination.

Conflicts of Interest: The authors declare no conflict of interest.

Abbreviations

ACTH	Adrenocorticotropic hormone
AF	Activation function
ALL	Acute lymphoblastic leukaemia
COPD	Chronic obstructive pulmonary disease
CRH	Corticotropin-releasing hormone
DBD	DNA-binding domain
DUSP	Dual-Specific Phosphatase
EM	Electron microscopy
ERK	Extracellular Signal-Regulated kinases
GCs	Glucocorticoids
GILZ	Glucocorticoid induced leucine zipper
GR	GC receptor
GRE	GC response element
GSK	Glycogen synthase kinase
HPA	Hypothalamic-pituitary-adrenal axis
HSD11B	11 beta hydroxysteroid dehydrogenase
IBD	Inflammatory bowel diseases
IL	Interleukin
JNK	c-Jun N-terminal kinase
LBD	Ligand-binding domain

MAPK	Mitogen-Activated Protein Kinase
mTOR	Mammalian target of rapamycin
NLS	Nuclear localization signal
NR	Nuclear receptor
PBMC	Peripheral blood mononuclear cells
PTM	Post-translational modification
TF	Transcription factor
TNF-α	Tumor necrosis factor α

References

1. Granner, D.K.; Wang, J.C.; Yamamoto, K.R. Regulatory Actions of Glucocorticoid Hormones: From Organisms to Mechanisms. *Adv. Exp. Med. Biol.* **2015**, *872*, 3–31.
2. Cain, D.W.; Cidlowski, J.A. Specificity and Sensitivity of Glucocorticoid Signaling in Health and Disease. *Best Pract. Res. Clin. Endocrinol. Metab.* **2015**, *29*, 545–556. [CrossRef] [PubMed]
3. Whirledge, S.; DeFranco, D.B. Glucocorticoid Signaling in Health and Disease: Insights from Tissue-Specific GR Knockout Mice. *Endocrinology* **2018**, *159*, 46–61. [CrossRef] [PubMed]
4. Timmermans, S.; Souffriau, J.; Libert, C. A General Introduction to Glucocorticoid Biology. *Front. Immunol.* **2019**, *10*, 1–17. [CrossRef]
5. Nicolaides, N.C.; Charmandari, E. Novel Insights into the Molecular Mechanisms Underlying Generalized Glucocorticoid Resistance and Hypersensitivity Syndromes. *Hormones* **2017**, *16*, 124–138. [PubMed]
6. Quax, R.A.; Manenschijn, L.; Koper, J.W.; Hazes, J.M.; Lamberts, S.W.J.; Van Rossum, E.F.C.; Feelders, R.A. Glucocorticoid Sensitivity in Health and Disease. *Nat. Rev. Endocrinol.* **2013**, *9*, 670–686. [CrossRef]
7. Talabér, G.; Jondal, M.; Okret, S. Extra-Adrenal Glucocorticoid Synthesis: Immune Regulation and Aspects on Local Organ Homeostasis. *Mol. Cell. Endocrinol.* **2013**, *380*, 89–98. [CrossRef]
8. Slominski, R.M.; Tuckey, R.C.; Manna, P.R.; Jetten, A.M.; Postlethwaite, A.; Raman, C.; Slominski, A.T. Extra-Adrenal Glucocorticoid Biosynthesis: Implications for Autoimmune and Inflammatory Disorders. *Genes Immun.* **2020**, *21*, 150–168. [CrossRef]
9. Merk, V.M.; Phan, T.S.; Brunner, T. Regulation of Tissue Immune Responses by Local Glucocorticoids at Epithelial Barriers and Their Impact on Interorgan Crosstalk. *Front. Immunol.* **2021**, *12*, 1–12. [CrossRef] [PubMed]
10. Vandewalle, J.; Luypaert, A.; De Bosscher, K.; Libert, C. Therapeutic Mechanisms of Glucocorticoids. *Trends Endocrinol. Metab.* **2018**, *29*, 42–54. [CrossRef]
11. Meijer, O.C.; Pereira, A.M. Three Percent Annually on Systemic Glucocorticoids: Facts, Worries and Perspectives. *Eur. J. Endocrinol.* **2019**, *181*, C23–C28. [CrossRef] [PubMed]
12. Vitellius, G.; Lombes, M. Genetics in Endocrinology: Glucocorticoid Resistance Syndrome. *Eur. J. Endocrinol.* **2020**, *182*, R15–R27. [CrossRef] [PubMed]
13. Barnes, P.J.; Adcock, I.M. Glucocorticoid Resistance in Inflammatory Diseases. *Lancet* **2009**, *373*, 1905–1917. [CrossRef]
14. Rodriguez, J.M.; Monsalves-Alvarez, M.; Henriquez, S.; Llanos, M.N.; Troncoso, R. Glucocorticoid Resistance in Chronic Diseases. *Steroids* **2016**, *115*, 182–192. [CrossRef]
15. Newton, R.; Shah, S.; Altonsy, M.O.; Gerber, A.N. Glucocorticoid and Cytokine Crosstalk: Feedback, Feedforward, and Co-Regulatory Interactions Determine Repression or Resistance. *J. Biol. Chem.* **2017**, *292*, 7163–7172. [CrossRef]
16. Kadmiel, M.; Cidlowski, J.A. Glucocorticoid Receptor Signaling in Health and Disease. *Trends Pharmacol. Sci.* **2013**, *34*, 518–530. [CrossRef] [PubMed]
17. Vandevyver, S.; Dejager, L.; Libert, C. Comprehensive Overview of the Structure and Regulation of the Glucocorticoid Receptor. *Endocr. Rev.* **2014**, *35*, 671–693. [CrossRef]
18. Weikum, E.R.; Knuesel, M.T.; Ortlund, E.A.; Yamamoto, K.R. Glucocorticoid Receptor Control of Transcription: Precision and Plasticity via Allostery. *Nat. Rev. Mol. Cell Biol.* **2017**, *18*, 159–174. [CrossRef]
19. Gomez-Sanchez, E.; Gomez-Sanchez, C.E. The Multifaceted Mineralocorticoid Receptor. *Compr. Physiol.* **2014**, *4*, 965–994.
20. Jaisser, F.; Farman, N. Emerging Roles of the Mineralocorticoid Receptor in Pathology: Toward New Paradigms in Clinical Pharmacology. *Pharmacol. Rev.* **2016**, *68*, 49–75. [CrossRef]
21. Gathercole, L.L.; Lavery, G.G.; Morgan, S.A.; Cooper, M.S.; Sinclair, A.J.; Tomlinson, J.W.; Stewart, P.M. 11β-Hydroxysteroid Dehydrogenase 1: Translational and Therapeutic Aspects. *Endocr. Rev.* **2013**, *34*, 525–555. [CrossRef]
22. Chapman, K.; Holmes, M.; Seckl, J. 11β-Hydroxysteroid Dehydrogenases Intracellular Gate-Keepers of Tissue Glucocorticoid Action. *Physiol. Rev.* **2013**, *93*, 1139–1206. [CrossRef] [PubMed]
23. Duma, D.; Cidlowski, J.A.; Cidlowski, J.A. Generating Diversity in Glucocorticoid Receptor Signaling: Mechanisms, Receptor Isoforms, and Post-Translational Modifications. *Horm. Mol. Biol. Clin. Investig.* **2010**, *3*, 319–328. [CrossRef]
24. Oakley, R.H.; Ramamoorthy, S.; Foley, J.F.; Busada, J.T.; Lu, N.Z.; Cidlowski, J.A. Glucocorticoid Receptor Isoform-Specific Regulation of Development, Circadian Rhythm, and Inflammation in Mice. *FASEB J.* **2018**, *32*, 5258–5271. [CrossRef]
25. De Bosscher, K.; Desmet, S.J.; Clarisse, D.; Estébanez-Perpiña, E.; Brunsveld, L. Nuclear Receptor Crosstalk—Defining the Mechanisms for Therapeutic Innovation. *Nat. Rev. Endocrinol.* **2020**, *16*, 363–377. [CrossRef] [PubMed]

26. Yang, M.; Chen, J.; Wei, W. Dimerization of Glucocorticoid Receptors and Its Role in Inflammation and Immune Responses. *Pharmacol. Res.* **2021**, *166*, 105334. [CrossRef]
27. Presman, D.M.; Hager, G.L. More than Meets the Dimer: What Is the Quaternary Structure of the Glucocorticoid Receptor? *Transcription* **2017**, *8*, 32–39. [CrossRef]
28. Frank, F.; Okafor, C.D.; Ortlund, E.A. The First Crystal Structure of a DNA-Free Nuclear Receptor DNA Binding Domain Sheds Light on DNA-Driven Allostery in the Glucocorticoid Receptor. *Sci. Rep.* **2018**, *8*, 13497. [CrossRef]
29. Bianchetti, L.; Wassmer, B.; Defosset, A.; Smertina, A.; Tiberti, M.L.; Stote, R.H.; Dejaegere, A. Alternative Dimerization Interfaces in the Glucocorticoid Receptor-α Ligand Binding Domain. *Biochim. Biophys. Acta Gen. Subj.* **2018**, *1862*, 1810–1825. [CrossRef] [PubMed]
30. Presman, D.M.; Ganguly, S.; Schiltz, R.L.; Johnson, T.A.; Karpova, T.S.; Hager, G.L. DNA Binding Triggers Tetramerization of the Glucocorticoid Receptor in Live Cells. *Proc. Natl. Acad. Sci. USA* **2016**, *113*, 8236–8241. [CrossRef]
31. Yu, X.; Yi, P.; Hamilton, R.A.; Shen, H.; Chen, M.; Foulds, C.E.; Mancini, M.A.; Ludtke, S.J.; Wang, Z.; O'Malley, B.W. Structural Insights of Transcriptionally Active, Full-Length Androgen Receptor Coactivator Complexes. *Mol. Cell* **2020**, *79*, 812–823.e4. [CrossRef] [PubMed]
32. Kirschke, E.; Goswami, D.; Southworth, D.; Griffin, P.R.; Agard, D.A. Glucocorticoid Receptor Function Regulated by Coordinated Action of the Hsp90 and Hsp70 Chaperone Cycles. *Cell* **2014**, *157*, 1685–1697. [CrossRef]
33. Ratman, D.; Vanden Berghe, W.; Dejager, L.; Libert, C.; Tavernier, J.; Beck, I.M.; De Bosscher, K. How Glucocorticoid Receptors Modulate the Activity of Other Transcription Factors: A Scope beyond Tethering. *Mol. Cell. Endocrinol.* **2013**, *380*, 41–54. [CrossRef] [PubMed]
34. Petta, I.; Dejager, L.; Ballegeer, M.; Lievens, S.; Tavernier, J.; De Bosscher, K.; Libert, C. The Interactome of the Glucocorticoid Receptor and Its Influence on the Actions of Glucocorticoids in Combatting Inflammatory and Infectious Diseases. *Microbiol. Mol. Biol. Rev.* **2016**, *80*, 495–522. [CrossRef]
35. Quatrini, L.; Ugolini, S. New Insights into the Cell- and Tissue-Specificity of Glucocorticoid Actions. *Cell. Mol. Immunol.* **2021**, *18*, 269–278. [CrossRef] [PubMed]
36. Sacta, M.A.; Chinenov, Y.; Rogatsky, I. Glucocorticoid Signaling: An Update from a Genomic Perspective. *Annu. Rev. Physiol.* **2016**, *78*, 155–180. [CrossRef]
37. Franco, L.M.; Gadkari, M.; Howe, K.N.; Sun, J.; Kardava, L.; Kumar, P.; Kumari, S.; Hu, Z.; Fraser, I.D.C.; Moir, S.; et al. Immune Regulation by Glucocorticoids Can Be Linked to Cell Type–Dependent Transcriptional Responses. *J. Exp. Med.* **2019**, *216*, 384–406. [CrossRef]
38. Desmet, S.J.; De Bosscher, K. Glucocorticoid Receptors: Finding the Middle Ground. *J. Clin. Investig.* **2017**, *127*, 1136–1145. [CrossRef]
39. Escoter-Torres, L.; Caratti, G.; Mechtidou, A.; Tuckermann, J.; Uhlenhaut, N.H.; Vettorazzi, S. Fighting the Fire: Mechanisms of Inflammatory Gene Regulation by the Glucocorticoid Receptor. *Front. Immunol.* **2019**, *10*, 1–17. [CrossRef]
40. Surjit, M.; Ganti, K.P.; Mukherji, A.; Ye, T.; Hua, G.; Metzger, D.; Li, M.; Chambon, P. Widespread Negative Response Elements Mediate Direct Repression by Agonist-Liganded Glucocorticoid Receptor. *Cell* **2011**, *145*, 224–241. [CrossRef]
41. Cain, D.W.; Cidlowski, J.A. Immune Regulation by Glucocorticoids. *Nat. Rev. Immunol.* **2017**, *17*, 233–247. [CrossRef] [PubMed]
42. Johnson, G.L.; Lapadat, R. Mitogen-Activated Protein Kinase Pathways Mediated by ERK, JNK, and P38 Protein Kinases. *Science* **2002**, *298*, 1911–1912. [CrossRef]
43. Kyriakis, J.M.; Avruch, J. Mammalian MAPK Signal Transduction Pathways Activated by Stress and Inflammation: A 10-Year Update. *Physiol. Rev.* **2012**, *92*, 689–737. [CrossRef]
44. Lang, R.; Raffi, F.A.M. Dual-Specificity Phosphatases in Immunity and Infection: An Update. *Int. J. Mol. Sci.* **2019**, *20*, 2710. [CrossRef]
45. Hoppstädter, J.; Ammit, A.J. Role of Dual-Specificity Phosphatase 1 in Glucocorticoid-Driven Antiinflammatory Responses. *Front. Immunol.* **2019**, *10*, 1–8. [CrossRef] [PubMed]
46. Beck, I.M.E.; Vanden Berghe, W.; Vermeulen, L.; Yamamoto, K.R.; Haegeman, G.; De Bosscher, K. Crosstalk in Inflammation: The Interplay of Glucocorticoid Receptor-Based Mechanisms and Kinases and Phosphatases. *Endocr. Rev.* **2009**, *30*, 830–882. [CrossRef] [PubMed]
47. Sánchez-Tilló, E.; Comalada, M.; Xaus, J.; Farrera, C.; Valledor, A.F.; Caelles, C.; Lloberas, J.; Celada, A. JNK1 Is Required for the Induction of Mkp1 Expression in Macrophages during Proliferation and Lipopolysaccharide-Dependent Activation. *J. Biol. Chem.* **2007**, *282*, 12566–12573. [CrossRef]
48. Casals-Casas, C.; Álvarez, E.; Serra, M.; de la Torre, C.; Farrera, C.; Sánchez-Tilló, E.; Caelles, C.; Lloberas, J.; Celada, A. CREB and AP-1 Activation Regulates MKP-1 Induction by LPS or M-CSF and Their Kinetics Correlate with Macrophage Activation versus Proliferation. *Eur. J. Immunol.* **2009**, *39*, 1902–1913. [CrossRef]
49. Chi, H.; Barry, S.P.; Roth, R.J.; Wu, J.J.; Jones, E.A.; Bennett, A.M.; Flavell, R.A. Dynamic Regulation of Pro- and Anti-Inflammatory Cytokines by MAPK Phosphatase 1 (MKP-1) in Innate Immune Responses. *Proc. Natl. Acad. Sci. USA* **2006**, *103*, 2274–2279. [CrossRef] [PubMed]
50. Salojin, K.V.; Owusu, I.B.; Millerchip, K.A.; Potter, M.; Platt, K.A.; Oravecz, T. Essential Role of MAPK Phosphatase-1 in the Negative Control of Innate Immune Responses. *J. Immunol.* **2006**, *176*, 1899–1907. [CrossRef] [PubMed]

51. Caelles, C.; Bruna, A.; Morales, M.; González-Sancho, J.M.; González, M.V.; Jiménez, B.; Muñoz, A. Glucocorticoid Receptor Antagonism of AP-1 Activity by Inhibition of MAPK Family. In *Recent Advances in Glucocorticoid Receptor Action. Ernst Schering Research Foundation Workshop*; Cato, A.C.B., Schäcke, H., Asadullah, K., Eds.; Springer: Berlin/Heidelberg, Germany, 2002; pp. 131–152.
52. Ayroldi, E.; Cannarile, L.; Migliorati, G.; Nocentini, G.; Delfino, D.V.; Riccardi, C. Mechanisms of the Anti-Inflammatory Effects of Glucocorticoids: Genomic and Nongenomic Interference with MAPK Signaling Pathways. *FASEB J.* **2012**, *26*, 4805–4820. [CrossRef] [PubMed]
53. Caelles, C.; González-Sancho, J.M.; Muñoz, A. Nuclear Hormone Receptor Antagonism with AP-1 by Inhibition of the JNK Pathway. *Genes Dev.* **1997**, *11*, 3351–3364. [CrossRef]
54. Swantek, J.L.; Cobb, M.H.; Geppert, T.D. Jun N-Terminal Kinase/Stress-Activated Protein Kinase (JNK/SAPK) Is Required for Lipopolysaccharide Stimulation of Tumor Necrosis Factor Alpha (TNF-Alpha) Translation: Glucocorticoids Inhibit TNF-Alpha Translation by Blocking JNK/SAPK. *Mol. Cell. Biol.* **1997**, *17*, 6274–6282. [CrossRef] [PubMed]
55. Kassel, O.; Sancono, A.; Krätzschmar, J.; Kreft, B.; Stassen, M.; Cato, A.C.B. Glucocorticoids Inhibit MAP Kinase via Increased Expression and Decreased Degradation of MKP-1. *EMBO J.* **2001**, *20*, 7108–7116. [CrossRef]
56. Lasa, M.; Abraham, S.M.; Boucheron, C.; Saklatvala, J.; Clark, A.R. Dexamethasone Causes Sustained Expression of Mitogen-Activated Protein Kinase (MAPK) Phosphatase 1 and Phosphatase-Mediated Inhibition of MAPK P38. *Mol. Cell. Biol.* **2002**, *22*, 7802–7811. [CrossRef]
57. González, M.V.; Jiménez, B.; Berciano, M.T.; González-Sancho, J.M.; Caelles, C.; Lafarga, M.; Muñoz, A. Glucocorticoids Antagonize AP-1 by Inhibiting the Activation/Phosphorylation of JNK without Affecting Its Subcellular Distribution. *J. Cell Biol.* **2000**, *150*, 1199–1207. [CrossRef]
58. Bruna, A.; Nicolàs, M.; Muñoz, A.; Kyriakis, J.M.; Caelles, C. Glucocorticoid Receptor-JNK Interaction Mediates Inhibition of the JNK Pathway by Glucocorticoids. *EMBO J.* **2003**, *22*, 6035–6044. [CrossRef] [PubMed]
59. Shah, S.; King, E.M.; Chandrasekhar, A.; Newton, R. Roles for the Mitogen-Activated Protein Kinase (MAPK) Phosphatase, DUSP1, in Feedback Control of Inflammatory Gene Expression and Repression by Dexamethasone. *J. Biol. Chem.* **2014**, *289*, 13667–13679. [CrossRef]
60. Ayroldi, E.; Zollo, O.; Macchiarulo, A.; Di Marco, B.; Marchetti, C.; Riccardi, C. Glucocorticoid-Induced Leucine Zipper Inhibits the Raf-Extracellular Signal-Regulated Kinase Pathway by Binding to Raf-1. *Mol. Cell. Biol.* **2002**, *22*, 7929. [CrossRef] [PubMed]
61. Wilkinson, L.; Verhoog, N.J.D.; Louw, A. Disease-and Treatment-Associated Acquired Glucocorticoid Resistance. *Endocr. Connect.* **2018**, *7*, R328–R349. [CrossRef] [PubMed]
62. Martins, C.S.; de Castro, M. Generalized and Tissue Specific Glucocorticoid Resistance. *Mol. Cell. Endocrinol.* **2021**, *530*, 1–23. [CrossRef] [PubMed]
63. Mariotti, A. The Effects of Chronic Stress on Health: New Insights into the Molecular Mechanisms of Brain–Body Communication. *Futur. Sci. OA* **2015**, *1*, 3. [CrossRef]
64. Ferraù, F.; Korbonits, M. Metabolic Syndrome in Cushing's Syndrome Patients. *Front. Horm. Res.* **2018**, *49*, 85–103.
65. Zhang, D.; Bergsneider, M.; Wang, M.B.; Heaney, A.P.; Zhang, D.; Bergsneider, M.; Wang, M.B.; Heaney, A.P. Targeting the ERK Pathway for the Treatment of Cushing's Disease. *Oncotarget* **2016**, *7*, 69149–69158. [CrossRef]
66. Charmandari, E.; Ichijo, T.; Jubiz, W.; Baid, S.; Zachman, K.; Chrousos, G.P.; Kino, T. A Novel Point Mutation in the Amino Terminal Domain of the Human Glucocorticoid Receptor (HGR) Gene Enhancing HGR-Mediated Gene Expression. *J. Clin. Endocrinol. Metab.* **2008**, *93*, 4963–4968. [CrossRef]
67. Santen, R.J.; Jewell, C.M.; Yue, W.; Heitjan, D.F.; Raff, H.; Katen, K.S.; Cidlowski, J.A. Glucocorticoid Receptor Mutations and Hypersensitivity to Endogenous and Exogenous Glucocorticoids. *J. Clin. Endocrinol. Metab.* **2018**, *103*, 3630–3639. [CrossRef] [PubMed]
68. Hurt, D.E.; Suzuki, S.; Mayama, T.; Charmandari, E.; Kino, T. Structural Analysis on the Pathologic Mutant Glucocorticoid Receptor Ligand-Binding Domains. *Mol. Endocrinol.* **2016**, *30*, 173–188. [CrossRef]
69. Wang, Z.; Li, P.; Zhang, Q.; Lv, H.; Liu, J.; Si, J. Interleukin-1β Regulates the Expression of Glucocorticoid Receptor Isoforms in Nasal Polyps in Vitro via P38 MAPK and JNK Signal Transduction Pathways. *J. Inflamm.* **2015**, *12*, 1–10. [CrossRef] [PubMed]
70. Wallace, A.D.; Cidlowski, J.A. Proteasome-Mediated Glucocorticoid Receptor Degradation Restricts Transcriptional Signaling by Glucocorticoids. *J. Biol. Chem.* **2001**, *276*, 42714–42721. [CrossRef]
71. Wallace, A.D.; Cao, Y.; Chandramouleeswaran, S.; Cidlowski, J.A. Lysine 419 Targets Human Glucocorticoid Receptor for Proteasomal Degradation. *Steroids* **2010**, *75*, 1016–1023. [CrossRef]
72. Galliher-Beckley, A.J.; Williams, J.G.; Cidlowski, J.A. Ligand-Independent Phosphorylation of the Glucocorticoid Receptor Integrates Cellular Stress Pathways with Nuclear Receptor Signaling. *Mol. Cell. Biol.* **2011**, *31*, 4663–4675. [CrossRef]
73. Piovan, E.; Yu, J.; Tosello, V.; Herranz, D.; Ambesi-Impiombato, A.; DaSilva, A.C.; Sanchez-Martin, M.; Perez-Garcia, A.; Rigo, I.; Castillo, M.; et al. Direct Reversal of Glucocorticoid Resistance by AKT Inhibition in Acute Lymphoblastic Leukemia. *Cancer Cell* **2013**, *24*, 766–776. [CrossRef] [PubMed]
74. Ismaili, N.; Garabedian, M.J. Modulation of Glucocorticoid Receptor Function via Phosphorylation. *Ann. N. Y. Acad. Sci.* **2004**, *1024*, 86–101. [CrossRef]
75. Itoh, M.; Adachi, M.; Yasui, H.; Takekawa, M.; Tanaka, H.; Imai, K. Nuclear Export of Glucocorticoid Receptor Is Enhanced by C-Jun N-Terminal Kinase-Mediated Phosphorylation. *Mol. Endocrinol.* **2002**, *16*, 2382–2392. [CrossRef] [PubMed]

76. Galliher-Beckley, A.J.; Williams, J.G.; Collins, J.B.; Cidlowski, J.A. Glycogen Synthase Kinase 3β-Mediated Serine Phosphorylation of the Human Glucocorticoid Receptor Redirects Gene Expression Profiles. *Mol. Cell. Biol.* **2008**, *28*, 7309–7322. [CrossRef]
77. Ito, K.; Yamamura, S.; E-Quaye, S.E.; Cosio, B.; Ito, M.; Barnes, P.J.; Adcock, I.M. Histone Deacetylase 2–Mediated Deacetylation of the Glucocorticoid Receptor Enables NF-KB Suppression. *J. Exp. Med.* **2006**, *203*, 7–13. [CrossRef]
78. Nader, N.; Chrousos, G.P.; Kino, T. Circadian Rhythm Transcription Factor CLOCK Regulates the Transcriptional Activity of the Glucocorticoid Receptor by Acetylating Its Hinge Region Lysine Cluster: Potential Physiological Implications. *FASEB J.* **2009**, *23*, 1572–1583. [CrossRef] [PubMed]
79. Kassi, E.; Papavassiliou, A.G. Glucose Can Promote a Glucocorticoid Resistance State. *J. Cell. Mol. Med.* **2012**, *16*, 1146–1149. [CrossRef]
80. Druker, J.; Liberman, A.C.; Antunica-Noguerol, M.; Gerez, J.; Paez-Pereda, M.; Rein, T.; Iñiguez-Lluhí, J.A.; Holsboer, F.; Arzt, E. RSUME Enhances Glucocorticoid Receptor SUMOylation and Transcriptional Activity. *Mol. Cell. Biol.* **2013**, *33*, 2116–2127. [CrossRef]
81. Paakinaho, V.; Kaikkonen, S.; Makkonen, H.; Benes, V.; Palvimo, J.J. SUMOylation Regulates the Chromatin Occupancy and Anti-Proliferative Gene Programs of Glucocorticoid Receptor. *Nucleic Acids Res.* **2014**, *42*, 1575–1592. [CrossRef]
82. Davies, L.; Karthikeyan, N.; Lynch, J.T.; Sial, E.A.; Gkourtsa, A.; Demonacos, C.; Krstic-Demonacos, M. Cross Talk of Signaling Pathways in the Regulation of the Glucocorticoid Receptor Function. *Mol. Endocrinol.* **2008**, *22*, 1331–1344. [CrossRef]
83. Okamoto, K.; Tanaka, H.; Ogawa, H.; Makino, Y.; Eguchi, H.; Hayashi, S.I.; Yoshikawa, N.; Poellinger, L.; Umesono, K.; Makino, I. Redox-Dependent Regulation of Nuclear Import of the Glucocorticoid Receptor. *J. Biol. Chem.* **1999**, *274*, 10363–10371. [CrossRef]
84. Kobayashi, Y.; Ito, K.; Kanda, A.; Tomoda, K.; Mercado, N.; Barnes, P.J. Impaired Dual-Specificity Protein Phosphatase DUSP4 Reduces Corticosteroid Sensitivity. *Mol. Pharmacol.* **2017**, *91*, 475–481. [CrossRef] [PubMed]
85. Khorasanizadeh, M.H.; Eskian, M.; Gelfand, E.W.; Rezaei, N. Mitogen-Activated Protein Kinases as Therapeutic Targets for Asthma. *Pharmacol. Ther.* **2017**, *174*, 112–126. [CrossRef]
86. Barnes, P.J. Kinases as Novel Therapeutic Targets in Asthma and Chronic Obstructive Pulmonary Disease. *Pharmacol. Rev.* **2016**, *68*, 788–815. [CrossRef]
87. Khorasani, N.; Baker, J.; Johnson, M.; Chung, K.F.; Bhavsar, P.K. Reversal of Corticosteroid Insensitivity by P38 MAPK Inhibition in Peripheral Blood Mononuclear Cells from COPD. *Int. J. COPD* **2015**, *10*, 283–291.
88. Abraham, S.M.; Lawrence, T.; Kleiman, A.; Warden, P.; Medghalchi, M.; Tuckermann, J.; Saklatvala, J.; Clark, A.R. Antiinflammatory Effects of Dexamethasone Are Partly Dependent on Induction of Dual Specificity Phosphatase 1. *J. Exp. Med.* **2006**, *203*, 1883–1889. [CrossRef] [PubMed]
89. Maneechotesuwan, K.; Yao, X.; Ito, K.; Jazrawi, E.; Usmani, O.S.; Adcock, I.M.; Barnes, P.J. Suppression of GATA-3 Nuclear Import and Phosphorylation: A Novel Mechanism of Corticosteroid Action in Allergic Disease. *PLoS Med.* **2009**, *6*, e1000076. [CrossRef]
90. Mei, D.; Tan, W.S.D.; Wong, W.S.F. Pharmacological Strategies to Regain Steroid Sensitivity in Severe Asthma and COPD. *Curr. Opin. Pharmacol.* **2019**, *46*, 73–81. [CrossRef] [PubMed]
91. Mitani, A.; Ito, K.; Vuppusetty, C.; Barnes, P.J.; Mercado, N. Restoration of Corticosteroid Sensitivity in Chronic Obstructive Pulmonary Disease by Inhibition of Mammalian Target of Rapamycin. *Am. J. Respir. Crit. Care Med.* **2016**, *193*, 143–153. [CrossRef]
92. Li, L.B.; Goleva, E.; Hall, C.F.; Ou, L.S.; Leung, D.Y.M. Superantigen-Induced Corticosteroid Resistance of Human T Cells Occurs through Activation of the Mitogen-Activated Protein Kinase Kinase/Extracellular Signal-Regulated Kinase (MEK-ERK) Pathway. *J. Allergy Clin. Immunol.* **2004**, *114*, 1059–1069. [CrossRef] [PubMed]
93. Pelaia, C.; Vatrella, A.; Sciacqua, A.; Terracciano, R.; Pelaia, G. Role of P38-Mitogen-Activated Protein Kinase in COPD: Pathobiological Implications and Therapeutic Perspectives. *Expert Rev. Respir. Med.* **2020**, *14*, 485–491. [CrossRef] [PubMed]
94. Pniewska, E.; Pawliczak, R. The Involvement of Phospholipases A2 in Asthma and Chronic Obstructive Pulmonary Disease. *Mediators Inflamm.* **2013**, *2013*, 793505–793516. [CrossRef]
95. Kitsiouli, E.; Nakos, G.; Lekka, M.E. Phospholipase A2 Subclasses in Acute Respiratory Distress Syndrome. *Biochim. Biophys. Acta* **2009**, *1792*, 941–953. [CrossRef]
96. Garza, A.S.; Miller, A.L.; Johnson, B.H.; Thompson, E.B. Converting Cell Lines Representing Hematological Malignancies from Glucocorticoid-Resistant to Glucocorticoid-Sensitive: Signaling Pathway Interactions. *Leuk. Res.* **2009**, *33*, 717–727. [CrossRef]
97. Lin, K.T.; Wang, L.H. New Dimension of Glucocorticoids in Cancer Treatment. *Steroids* **2016**, *111*, 84–88. [CrossRef]
98. Bhadri, V.A.; Trahair, T.N.; Lock, R.B. Glucocorticoid Resistance in Paediatric Acute Lymphoblastic Leukaemia. *J. Paediatr. Child Health.* **2012**, *48*, 634–640. [CrossRef]
99. Olivas-Aguirre, M.; Torres-López, L.; Pottosin, I.; Dobrovinskaya, O. Overcoming Glucocorticoid Resistance in Acute Lymphoblastic Leukemia: Repurposed Drugs Can Improve the Protocol. *Front. Oncol.* **2021**, *11*, 647. [CrossRef]
100. Renner, K.; Amberger, A.; Konwalinka, G.; Kofler, R.; Gnaiger, E. Changes of Mitochondrial Respiration, Mitochondrial Content and Cell Size after Induction of Apoptosis in Leukemia Cells. *Biochim. Biophys. Acta Mol. Cell Res.* **2003**, *1642*, 115–123. [CrossRef]
101. Tissing, W.J.E.; Den Boer, M.L.; Meijerink, J.P.P.; Menezes, R.X.; Swagemakers, S.; Van Der Spek, P.J.; Sallan, S.E.; Armstrong, S.A.; Pieters, R. Genomewide Identification of Prednisolone-Responsive Genes in Acute Lymphoblastic Leukemia Cells. *Blood* **2007**, *109*, 3929–3935. [CrossRef] [PubMed]
102. Webb, M.S.; Miller, A.L.; Howard, T.L.; Johnson, B.H.; Chumakov, S.; Fofanov, Y.; Nguyen-Vu, T.; Lin, C.Y.; Thompson, E.B. Sequential Gene Regulatory Events Leading to Glucocorticoid-Evoked Apoptosis of CEM Human Leukemic Cells:Interactions of MAPK, MYC and Glucocorticoid Pathways. *Mol. Cell. Endocrinol.* **2018**, *471*, 118–130. [CrossRef] [PubMed]

103. Miller, A.L.; Webb, M.S.; Copik, A.J.; Wang, Y.; Johnson, B.H.; Kumar, R.; Thompson, E.B. P38 Mitogen-Activated Protein Kinase (MAPK) Is a Key Mediator in Glucocorticoid-Induced Apoptosis of Lymphoid Cells: Correlation between P38 MAPK Activation and Site-Specific Phosphorylation of the Human Glucocorticoid Receptor at Serine 211. *Mol. Endocrinol.* **2005**, *19*, 1569–1583. [CrossRef]
104. Jones, C.L.; Gearheart, C.M.; Fosmire, S.; Delgado-Martin, C.; Evensen, N.A.; Bride, K.; Waanders, A.J.; Pais, F.; Wang, J.; Bhatla, T.; et al. MAPK Signaling Cascades Mediate Distinct Glucocorticoid Resistance Mechanisms in Pediatric Leukemia. *Blood* **2015**, *126*, 2202–2212. [CrossRef] [PubMed]
105. Planey, S.L.; Abrams, M.T.; Robertson, N.M.; Litwack, G. Role of Apical Caspases and Glucocorticoid-Regulated Genes in Glucocorticoid-Induced Apoptosis of Pre-B Leukemic Cells. *Cancer Res.* **2003**, *63*, 172–178.
106. Abrams, M.T.; Robertson, N.M.; Litwack, G.; Wickstrom, E. Evaluation of Glucocorticoid Sensitivity in 697 Pre-B Acute Lymphoblastic Leukemia Cells after Overexpression or Silencing of MAP Kinase Phosphatase-1. *J. Cancer Res. Clin. Oncol.* **2005**, *131*, 347–354. [CrossRef] [PubMed]
107. Liu, Y.; Ge, J.; Li, Q.; Guo, X.; Gu, L.; Ma, Z.G.; Li, X.H.; Zhu, Y.P. Low-Dose Anisomycin Sensitizes Glucocorticoid-Resistant T-Acute Lymphoblastic Leukemia CEM-C1 Cells to Dexamethasone-Induced Apoptosis through Activation of Glucocorticoid Receptor and P38-MAPK/JNK. *Leuk. Lymphoma* **2014**, *55*, 2179–2188. [CrossRef] [PubMed]
108. Nicholson, L.; Evans, C.A.; Matheson, E.; Minto, L.; Keilty, C.; Sanichar, M.; Case, M.; Schwab, C.; Williamson, D.; Rainer, J.; et al. Quantitative Proteomic Analysis Reveals Maturation as a Mechanism Underlying Glucocorticoid Resistance in B Lineage ALL and Re-Sensitization by JNK Inhibition. *Br. J. Haematol.* **2015**, *171*, 595–605. [CrossRef]
109. Sevilla, L.M.; Pérez, P. Roles of the Glucocorticoid and Mineralocorticoid Receptors in Skin Pathophysiology. *Int. J. Mol. Sci.* **2018**, *19*, 1906. [CrossRef]
110. Leung, D. Superantigens, Steroid Insensitivity and Innate Immunity in Atopic Eczema. *Acta Derm.-Venereol. Suppl.* **2005**, *215*, 11–15. [CrossRef]
111. Taheri, A.; Cantrell, J.; Feldman, S.R. Tachyphylaxis to Topical Glucocorticoids; What Is the Evidence? *Dermatol. Online J.* **2013**, *19*, 7.
112. Czarnowicki, T.; Linkner, R.V.; Suárez-Fariñas, M.; Ingber, A.; Lebwohl, M. An Investigator-Initiated, Double-Blind, Vehicle-Controlled Pilot Study: Assessment for Tachyphylaxis to Topically Occluded Halobetasol 0.05% Ointment in the Treatment of Psoriasis. *J. Am. Acad. Dermatol.* **2014**, *71*, 954–959.e1. [CrossRef] [PubMed]
113. Chebotaev, D.V.; Yemelyanov, A.Y.; Lavker, R.M.; Budunova, I.V. Epithelial Cells in the Hair Follicle Bulge Do Not Contribute to Epidermal Regeneration after Glucocorticoid-Induced Cutaneous Atrophy. *J. Investig. Dermatol.* **2007**, *127*, 2749–2758. [CrossRef]
114. Kishibe, M.; Baida, G.; Bhalla, P.; Lavker, R.M.; Schlosser, B.; Iinuma, S.; Yoshida, S.; Dudley, J.T.; Budunova, I. Important Role of Kallikrein 6 for the Development of Keratinocyte Proliferative Resistance to Topical Glucocorticoids. *Oncotarget* **2016**, *7*, 69479–69488. [CrossRef] [PubMed]
115. Sevilla, L.M.; Bayo, P.; Latorre, V.; Sanchis, A.; Pérez, P. Glucocorticoid Receptor Regulates Overlapping and Differential Gene Subsets in Developing and Adult Skin. *Mol. Endocrinol.* **2010**, *24*, 2166–2178. [CrossRef]
116. Sevilla, L.M.; Latorre, V.; Sanchis, A.; Pérez, P. Epidermal Inactivation of the Glucocorticoid Receptor Triggers Skin Barrier Defects and Cutaneous Inflammation. *J. Investig. Dermatol.* **2013**, *133*, 361–370. [CrossRef]
117. Bigas, J.; Sevilla, L.M.; Carceller, E.; Boix, J.; Pérez, P. Epidermal Glucocorticoid and Mineralocorticoid Receptors Act Cooperatively to Regulate Epidermal Development and Counteract Skin Inflammation Article. *Cell Death Dis.* **2018**, *9*, 1–14. [CrossRef] [PubMed]
118. Hua, G.; Ganti, K.P.; Chambon, P. Glucocorticoid-Induced Tethered Transrepression Requires SUMOylation of GR and Formation of a SUMO-SMRT/NCoR1-HDAC3 Repressing Complex. *Proc. Natl. Acad. Sci. USA* **2016**, *113*, E635–E643. [CrossRef]
119. Hua, G.; Paulen, L.; Chambon, P. GR SUMOylation and Formation of an SUMO-SMRT/ NCoR1-HDAC3 Repressing Complex Is Mandatory for GC-Induced IR NGRE-Mediated Transrepression. *Proc. Natl. Acad. Sci. USA* **2016**, *113*, E626–E634. [CrossRef]
120. Hobbs, R.M.; Silva-Vargas, V.; Groves, R.; Watt, F.M. Expression of Activated MEK1 in Differentiating Epidermal Cells Is Sufficient to Generate Hyperproliferative and Inflammatory Skin Lesions. *J. Investig. Dermatol.* **2004**, *123*, 503–515. [CrossRef]
121. Mavropoulos, A.; Rigopoulou, E.I.; Liaskos, C.; Bogdanos, D.P.; Sakkas, L.I. The Role of P38 Mapk in the Aetiopathogenesis of Psoriasis and Psoriatic Arthritis. *Clin. Dev. Immunol.* **2013**, *2013*, 569751. [CrossRef]
122. Hammouda, M.B.; Ford, A.E.; Liu, Y.; Zhang, J.Y. The JNK Signaling Pathway in Inflammatory Skin Disorders and Cancer. *Cells* **2020**, *9*, 857. [CrossRef]
123. Hannen, R.; Udeh-Momoh, C.; Upton, J.; Wright, M.; Michael, A.; Gulati, A.; Rajpopat, S.; Clayton, N.; Halsall, D.; Burrin, J.; et al. Dysfunctional Skin-Derived Glucocorticoid Synthesis Is a Pathogenic Mechanism of Psoriasis. *J. Investig. Dermatol.* **2017**, *137*, 1630–1637. [CrossRef]
124. Sarkar, M.K.; Kaplan, N.; Tsoi, L.C.; Xing, X.; Liang, Y.; Swindell, W.R.; Hoover, P.; Aravind, M.; Baida, G.; Clark, M.; et al. Endogenous Glucocorticoid Deficiency in Psoriasis Promotes Inflammation and Abnormal Differentiation. *J. Investig. Dermatol.* **2017**, *137*, 1474–1483. [CrossRef] [PubMed]
125. Jozic, I.; Stojadinovic, O.; Kirsner, R.S.; Tomic-Canic, M. Stressing the Steroids in Skin: Paradox or Fine-Tuning. *J. Investig. Dermatol.* **2014**, *134*, 2869–2872. [CrossRef] [PubMed]
126. Terao, M.; Katayama, I. Local Cortisol/Corticosterone Activation in Skin Physiology and Pathology. *J. Dermatol. Sci.* **2016**, *84*, 11–16. [CrossRef] [PubMed]

127. Nikolakis, G.; Stratakis, C.A.; Kanaki, T.; Slominski, A.; Zouboulis, C.C. Skin Steroidogenesis in Health and Disease. *Rev. Endocr. Metab. Disord.* **2016**, *17*, 247–258. [CrossRef]
128. Segrelles, C.; Ruiz, S.; Perez, P.; Murga, C.; Santos, M.; Budunova, I.V.; Martínez, J.; Larcher, F.; Slaga, T.J.; Gutkind, J.S.; et al. Functional Roles of Akt Signaling in Mouse Skin Tumorigenesis. *Oncogene* **2002**, *21*, 53–64. [CrossRef]
129. Budunova, I.V.; Carbajal, S.; Kang, H., II; Viaje, A.; Slaga, T.J. Altered Glucocorticoid Receptor Expression and Function during Mouse Skin Carcinogenesis. *Mol. Carcinog.* **1997**, *18*, 177–185. [CrossRef]
130. Latorre, V.; Sevilla, L.M.; Sanchis, A.; Pérez, P. Selective Ablation of Glucocorticoid Receptor in Mouse Keratinocytes Increases Susceptibility to Skin Tumorigenesis. *J. Investig. Dermatol.* **2013**, *133*, 2771–2779. [CrossRef]
131. Leis, H.; Page, A.; Ramírez, A.; Bravo, A.; Segrelles, C.; Paramio, J.; Barettino, D.; Jorcano, J.L.; Pérez, P. Glucocorticoid Receptor Counteracts Tumorigenic Activity of Akt in Skin through Interference with the Phosphatidylinositol 3-Kinase Signaling Pathway. *Mol. Endocrinol.* **2004**, *18*, 303–311. [CrossRef]
132. Straub, R.H. Rheumatoid Arthritis—A Neuroendocrine Immune Disorder: Glucocorticoid Resistance, Relative Glucocorticoid Defi Ciency, Low-Dose Glucocorticoid Therapy, and Insulin Resistance. *Arthritis Res. Ther.* **2014**, *16* (Suppl. 2), I1. [CrossRef]
133. Dubois-Camacho, K.; Ottum, P.A.; Franco-Muñoz, D.; De La Fuente, M.; Torres-Riquelme, A.; Díaz-Jiménez, D.; Olivares-Morales, M.; Astudillo, G.; Quera, R.; Hermoso, M.A. Glucocorticosteroid Therapy in Inflammatory Bowel Diseases: From Clinical Practice to Molecular Biology. *World J. Gastroenterol.* **2017**, *23*, 6628–6638.
134. Ralph, J.A.; Morand, E.F. MAPK Phosphatases as Novel Targets for Rheumatoid Arthritis. *Expert Opin. Ther. Targets* **2008**, *12*, 795–808. [CrossRef] [PubMed]
135. Fan, H.; Kao, W.; Yang, Y.H.; Gu, R.; Harris, J.; Fingerle-Rowson, G.; Bucala, R.; Ngo, D.; Beaulieu, E.; Morand, E.F. Macrophage Migration Inhibitory Factor Inhibits the Antiinflammatory Effects of Glucocorticoids via Glucocorticoid-Induced Leucine Zipper. *Arthritis Rheumatol.* **2014**, *66*, 2059–2070. [CrossRef] [PubMed]
136. Cheng, Q.; Fan, H.; Ngo, D.; Beaulieu, E.; Leung, P.; Lo, C.Y.; Burgess, R.; van der Zwan, Y.G.; White, S.J.; Khachigian, L.M.; et al. GILZ Overexpression Inhibits Endothelial Cell Adhesive Function through Regulation of NF-KB and MAPK Activity. *J. Immunol.* **2013**, *191*, 424–433. [CrossRef] [PubMed]
137. de Iudicibus, S.; Franca, R.; Martelossi, S.; Ventura, A.; Decorti, G. Molecular Mechanism of Glucocorticoid Resistance in Inflammatory Bowel Disease. *World J. Gastroenterol.* **2011**, *17*, 1095–1108. [CrossRef]
138. Lorén, V.; Cabré, E.; Ojanguren, I.; Domènech, E.; Pedrosa, E.; García-Jaraquemada, A.; Mañosa, M.; Manyé, J. Interleukin-10 Enhances the Intestinal Epithelial Barrier in the Presence of Corticosteroids through P38 MAPK Activity in Caco-2 Monolayers: A Possible Mechanism for Steroid Responsiveness in Ulcerative Colitis. *PLoS ONE* **2015**, *10*, e0130921.
139. Fischer, A.; Gluth, M.; Weege, F.; Pape, U.F.; Wiedenmann, B.; Baumgart, D.C.; Theuring, F. Glucocorticoids Regulate Barrier Function and Claudin Expression in Intestinal Epithelial Cells via MKP-1. *Am. J. Physiol. Gastrointest. Liver Physiol.* **2014**, *306*, G218–G228. [CrossRef]
140. Bantel, H.; Schmitz, M.L.; Raible, A.; Gregor, M.; Schulze-Osthoff, K. Critical Role of Nuclear Factor-κB and Stress-activated Protein Kinases in Steroid Unresponsiveness. *FASEB J.* **2002**, *16*, 1–19.
141. Hommes, D.; Van Den Blink, B.; Plasse, T.; Bartelsman, J.; Xu, C.; Macpherson, B.; Tytgat, G.; Peppelenbosch, M.; Van Deventer, S. Inhibition of Stress-Activated MAP Kinases Induces Clinical Improvement in Moderate to Severe Crohn's Disease. *Gastroenterology* **2002**, *122*, 7–14. [CrossRef]
142. Ishiguro, Y.; Ohkawara, T.; Sakuraba, H.; Yamagata, K.; Hiraga, H.; Yamaguchi, S.; Fukuda, S.; Munakata, A.; Nakane, A.; Nishihira, J. Macrophage Migration Inhibitory Factor Has a Proinflammatory Activity via the P38 Pathway in Glucocorticoid-Resistant Ulcerative Colitis. *Clin. Immunol.* **2006**, *120*, 335–341. [CrossRef] [PubMed]
143. He, Y.J.; Xu, J.Q.; Sun, M.M.; Fang, X.Z.; Peng, Z.K.; Pan, S.W.; Zhou, T.; Wang, Y.X.; Shang, Y. Glucocorticoid-Induced Leucine Zipper: A Promising Marker for Monitoring and Treating Sepsis. *Front. Immunol.* **2020**, *11*, 1–10. [CrossRef]
144. Maitra, S.R.; Chen, E.; Rosa, D.; Valane, P.D.; El-Maghrabi, M.R.; Brathwaite, C.E.M. Modulations of Signal Transduction Pathways during Sepsis and the Effects of Insulin and Mifepristone. *Acad. Emerg. Med.* **2003**, *10*, 1–8. [CrossRef] [PubMed]
145. Ballegeer, M.; Vandewalle, J.; Eggermont, M.; Van Isterdael, G.; Dejager, L.; De Bus, L.; Decruyenaere, J.; Vandenbroucke, R.E.; Libert, C. Overexpression of Gilz Protects Mice Against Lethal Septic Peritonitis. *Shock* **2019**, *52*, 208–214. [CrossRef] [PubMed]
146. Dendoncker, K.; Libert, C. Glucocorticoid Resistance as a Major Drive in Sepsis Pathology. *Cytokine Growth Factor Rev.* **2017**, *35*, 85–96. [CrossRef]
147. Dendoncker, K.; Timmermans, S.; Vandewalle, J.; Eggermont, M.; Lempiäinen, J.; Van Hamme, E.; Dewaele, S.; Vandevyver, S.; Ballegeer, M.; Souffriau, J.; et al. TNF-α Inhibits Glucocorticoid Receptor-Induced Gene Expression by Reshaping the GR Nuclear Cofactor Profile. *Proc. Natl. Acad. Sci. USA* **2019**, *116*, 12942–12951. [CrossRef]

Appendix

1. Manuscripts in preparation

(1) *Androgen receptor dimer interface inhibitors for the treatment of prostate cancer.* Jiménez-Panizo A*, **Alegre-Martí A***, Abella M, Fernández-Recio J, Hagler TA, Fuentes-Prior P, Estébanez-Perpiñá E.

(2) *Measuring N/C terminal interaction in the androgen receptor using optical tweezers.* Akulov V, Heling L, Sheikhhassani V, **Alegre-Martí A**, Estébanez-Perpiñá E, Mashaghi A.

(3) *Small compounds modulate glucocorticoid receptor function by binding to a novel allosteric pocket.* Jiménez-Panizo A, **Alegre-Martí A**, Abella M, Presman DM, Varticovski L, Arias I, Hager GL, Fuentes-Prior P, Estébanez-Perpiñá E.

(4) *Structural characterization of the heterodimerization of androgen and glucocorticoid receptors.* **Alegre-Martí A***, Jiménez-Panizo A*, Abella M, Poulard C, Le Romancer M, Fernández-Recio J, Fuentes-Prior P, Estébanez-Perpiñá E.

2. Conferences

2.1. Oral presentations

(1) Short talk at the *45º Congreso* organised by the Sociedad Española de Bioquímica y Biología Molecular (SEBBM), September 2023, Zaragoza, Spain. Title: The androgen receptor dimer interface harbours a posttranslational modification hub that drives pathology and anti-androgen resistance.

(2) Short talk at the *International Summer School in Epigenomics and Nuclear Receptors* organised by the Federation of European Biochemical Societies (FEBS), August 2023, Spetses, Greece. Title: A hotspot for posttranslational modifications on the androgen receptor dimer interface drives pathology and anti-androgen resistance.

(3) Short talk at the *Macromolecular Crystallography and Cryo-EM School* organised by Prof. Juan Hermoso and Prof. Armando Albert from CSIC, May 2023, Madrid, Spain. Title: Structure-function relationship study of androgen and glucocorticoid receptors.

(4) Short talk at *The 10th French Nuclear Receptors Meeting* at the Institut Universitaire du Cancer de Toulouse (IUCT Oncopole), May 2022, Toulouse, France. Title: Crystal structures of androgen receptor BF-3 mutants reveal allosteric coupling between the receptor's functional sites.

(5) Short talk at the *Uroncomol Network Meeting* organised by the Spanish Excellence Oncology network (URONCOMOL), October 2020, Virtual meeting. Title: Point-mutations in the androgen receptor linked to pathology reveal allosteric networks.

(6) Short talk at the *Nuclear Receptors and Cancer* Training Program "Nurcamein 3.0 Joint Meeting" by the Spanish Excellence Network of Nuclear Receptors (Nurcamein) and the Centro de Investigación Biomédica En Red, Oncología (CIBERONC), December 2019, Madrid, Spain. Title: Crystal structures of disease-linked androgen receptor mutants.

2.2. Poster presentation

(1) Poster presentation at the *International Summer School in Epigenomics and Nuclear Receptors* by FEBS, August 2023, Spetses, Greece. Title: A hotspot for posttranslational modifications on the androgen receptor dimer interface drives pathology and anti-androgen resistance. **Andrea Alegre-Martí**, Alba Jiménez-Panizo, Adrián Martínez-Tébar, Coralie Poulard, M. Núria Peralta-Moreno, Montserrat Abella, Rosa Antón, Marcos Chiñas, Ulrich Eckhard, Josep M. Piulats, Ana M. Rojas, Juan Fernández-Recio, Jaime Rubio-Martínez, Muriel Le Romancer, Álvaro Aytes, Pablo Fuentes-Prior, Eva Estébanez-Perpiñá.

(2) Poster presentation at the *Hormone-Dependent Cancers* by the Gordon Research Conference (CRG), August 2023, Maine, USA. Title: A hotspot for posttranslational modifications on the androgen receptor dimer interface drives pathology and anti-androgen resistance. **Andrea Alegre-Martí**, Alba Jiménez-Panizo, Adrián Martínez-Tébar, Coralie Poulard, M. Núria Peralta-Moreno, Montserrat Abella, Rosa Antón, Marcos Chiñas, Ulrich Eckhard, Josep M. Piulats, Ana M. Rojas, Juan Fernández-Recio, Jaime Rubio-Martínez, Muriel Le Romancer, Álvaro Aytes, Pablo Fuentes-Prior, Eva Estébanez-Perpiñá.

(3) Poster presentation at the *Imaging Cellular and Chromosome Dynamics Conference* by the FASEB Science Research Conference (SRC), August 2023, Accra, Ghana. Title: Live-cell imaging reveals key residues in glucocorticoid receptor ligand-binding domain structure that impact oligomerization and transcriptional activity. **Theophilus Tettey**, Alba Jiménez-Panizo,

Andrea Alegre-Martí, Gregory Fettweis, Montserrat Abella, Rosa Antón, Thomas A Johnson, Sohyoung Kim, R. Louis Schiltz, Israel Nuñez-Barrios, Joan Font-Díaz, Carme Caelles, Annabel F. Valledor, Paloma Pérez, Ana M. Rojas, Juan Fernández-Recio, Diego M. Presman, Gordon L. Hager, Pablo Fuentes-Prior, and Eva Estébanez-Perpiñá.

(4) Poster presentation at the *31st Intelligent Systems for Molecular Biology and the 22nd European Conference of Computational Biology* (ISMB/ECCB 2023) by the International School for Computational Biology (iSCB), July 2023, Lyon, France. Title: Identifying communications in the nuclear receptors' ligand binding domain. **Israel Barrios**, Ildefonso Cases, Alba Jiménez-Panizo, Andrea Alegre-Martí, Pablo Fuentes-Prior, Eva Estébanez-Perpiñá, Ana M. Rojas.

(5) Poster presentation at the *ENDO2023* by the Endocrine Society, June 2023, Chicago, USA. Title: Small compounds modulate glucocorticoid receptor function by binding to a novel allosteric pocket. **Jiménez-Panizo A**, **Alegre-Martí A**, Abella M, Presman DM, Varticovski L, Arias I, Hager GL, Fuentes-Prior P, Estébanez-Perpiñá E.

(6) Poster presentation at the workshop *A 20/20 vision of the future of nuclear receptors* by the European Molecular Biology Organization (EMBO), September 2022, La Valetta, Malta. Title: The multivalency of the glucocorticoid receptor ligand-binding domain explains its manifold physiological activities. Alba Jiménez-Panizo, **Andrea Alegre-Martí**, Theophilus Tettey, Gregory Fettweis, Montserrat Abella, Rosa Antón, Thomas A Johnson, Sohyoung Kim, R. Louis Schiltz, Israel Nuñez-Barrios, Joan Font-Díaz, Carme Caelles, Annabel F. Valledor, Paloma Pérez, Ana M. Rojas, Juan Fernández-Recio, Diego M. Presman, Gordon L. Hager, Pablo Fuentes-Prior, and Eva Estébanez-Perpiñá.

2.3. Congress attendance

(1) Attendance to the *Cancer Metabolism* conference by the Spanish Excellence Oncology network (URONCOMOL), October 2022, Bilbao, Spain.

3. Courses / Workshops

(1) *International Summer School in Epigenomics and Nuclear Receptors b*y FEBS, August 2023, Spetses, Greece.

(2) *Macromolecular Crystallography and Cryo-EM School*, Institute of Physical-Chemistry "Rocasolano", organized by Prof. Juan Hermoso and Prof. Armando Albert from CSIC, May 2023, Madrid, Spain.

(3) *Nuclear Receptors and Cancer*, Training Program "Nurcamein 3.0 Joint Meeting" organized by NURCAMEIN and CIBERONC, December 2019, Madrid, Spain.

(4) Course *CCP4 Virtual Study Weekend 2021*, organised by Dr. Atlanta Cook, Prof. Anastassis Perrakis and Prof. Dan Rigden from the CCP4 team. January 2021

(5) Course *Training in Laboratory Animal Science for Researchers*, Scientific and Technological Centres of the University of Barcelona (CCiTUB). March 2020, Barcelona, Spain.

(6) Course in *Kinetics and Affinity analysis in Biacore*, GE Healthcare Life Sciences. July 2019, Barcelona, Spain.

4. Short stays at collaborator laboratories

(1) Laboratory of *Programs of Molecular Mechanisms and Experimental Therapeutics in Oncology (ONCOBell) and Cancer Therapeutics Resistance (ProCURE)*, Dr. Álvaro Aytés, Catalan Institute of Oncology (ICO), Bellvitge Institute for Biomedical Research (IDIBELL). September 2020 – June 2022. Barcelona, Spain

(2) Laboratory of *GAT Therapeutics S.L.* at the Scientific Park of Barcelona (PCB). January – December 2021.

(3) Laboratory of *Molecular Immunology* (Prof. Annabel Valledor) Faculty of Biology, UB (January – December 2021).

5. Participation in funded research projects

(1) Prueba de Concepto (PDC2021-121688-100), Androgen receptor dimerization inhibitors (ARDIs).

(2) GAT Therapeutics (Service agreement, under CDA), Study of interaction between a protein and GAT ligands.

(3) CaixaImpulse (CI2018-0018), Dimerization inhibitors of Androgen Receptor.

(4) Programa Impulsa-Llavor (Llavor-003), Inhibitors of Androgen Receptor.

(5) Plan Nacional I+D+I (FBU2017-86906R), Structural Oncology of Androgen Receptor.

6. Other merits

(1) Supervision assistance of five undergraduate students during the realisation of their Final Degree Project or Final Master Project. Vinyet Esteve (2022-2023), Jana Bagan (2021-2022), Ana Alícia Martín (2021-2022), Bernat París (2019-2020), Mar Moré (2019-2020). Laboratory of Structural Biology of Nuclear Receptors of Prof. Eva Estébanez-Perpiñá. 2021 – present, Barcelona, Spain.

(2) Informal talk: *11th February. International Day of Women and Girls in Science*. Institut-Escola Costa i Llobera. 3rd and 4th courses of ESO. 11th of February 2021 and 11th of February 2023. Barcelona, Spain.